Ruthenium-based Light Harvesting Complexes

Dissertation
zur Erlangung des Grades
„Doktor der Naturwissenschaften“
im Promotionsfach Chemie

am Fachbereich Chemie, Pharmazie und Geowissenschaften
der Johannes Gutenberg-Universität in Mainz

Aaron Breivogel

geboren in Mainz

Mainz, 2014

Die vorliegende Arbeit wurde in der Zeit von August 2009 bis Mai 2014 am Institut für Anorganische Chemie und Analytische Chemie der Johannes Gutenberg-Universität Mainz unter Anleitung von Prof. Dr. [redacted] angefertigt.

Mainz, Mai 2014

Dekan: Prof. Dr. [redacted]
1. Berichterstatter: Prof. Dr. [redacted]
2. Berichterstatter: Prof. Dr. [redacted]

Tag der mündlichen Prüfung: 25.07.2014

Kurzzusammenfassung

Polypyridylkomplexe von Ruthenium(II) besitzen eine Vielzahl von Anwendungen, z. B. in Farbstoff-sensibilisierten Solarzellen und als Photokatalysatoren. $[Ru(bpy)_3]^{2+}$ ist einer der prominentesten Ruthenium(II)-Komplexe und besitzt langlebige angeregte ^{3}MLCT-Zustände mit einer Lebensdauer von 1 µs und einer Lumineszenz-Quantenausbeute von 10%. $[Ru(bpy)_3]^{2+}$ ist chiral und kann Stereoisomere bilden, wenn die Liganden unsymmetrisch substituiert sind oder im Falle von oligonuklearen *rac*/*meso*-Komplexen. Bis-tridentate Komplexe wie $[Ru(tpy)_2]^{2+}$ sind achiral und umgehen damit unerwünschte Stereoisomere. $[Ru(tpy)_2]^{2+}$ besitzt jedoch enttäuschende photophysikalische Eigenschaften mit einer ^{3}MLCT-Lebensdauer von nur etwa 0.2 ns und einer Quantenausbeute von $\leq$ 0.0007%. Die Anbringung von Substituenten an $[Ru(tpy)_2]^{2+}$ sowie die Aufweitung der Liganden-Bisswinkel auf 90° bewirken deutlich verbesserte Eigenschaften der emittierenden ^{3}MLCT-Zustände.

Dieser Strategie folgend wurden in der vorliegenden Arbeit neue bis-tridentate Ruthenium(II)-Komplexe entwickelt, synthetisiert und charakterisiert. Durch Anbringen von Ester-Substituenten und Verwenden von Liganden mit erweiterten Bisswinkeln konnten ^{3}MLCT-Lebensdauern von bis zu 841 ns und Quantenausbeuten von bis zu 1.1% erreicht werden. Die neuen bis-tridentaten Komplexe weisen eine deutlich erhöhte Photostabilität im Vergleich zu tris-bidentatem $[Ru(bpy)_3]^{2+}$ auf.

Die Komplexe wurden als Emitter in Licht-emittierenden elektrochemischen Zellen eingebaut und zeigen Elektrolumineszenz mit einer tiefroten Farbe, die bis ins NIR reicht. Ebenso wurden die Komplexe als Lichtsammler in Farbstoff-sensibilisierten Solarzellen getestet und erreichen Licht-zu-Energie-Effizienzen von bis zu 0.26%.

Dinukleare, stereochemisch einheitliche Ruthenium(II)-Komplexe wurden oxidiert um die Metall-Metall-Wechselwirkung zwischen Ru(II) und Ru(III) in der einfach oxidierten Spezies zu untersuchen. Die unterschiedlichen Redoxeigenschaften der beiden Rutheniumzentren in den verwendeten dinuklearen Verbindungen führt zu einer valenzlokalisierten Situation in der keine Metall-Metall-Wechselwirkung beobachtet wird. Ebenso wurde die Oxidation eines einkernigen Ruthenium(II)-Komplexes sowie dessen spontane Rückreduktion untersucht.

Energietransfersysteme wurden mittels Festphasensynthese hergestellt. Dabei ist ein Bis(terpyridin)ruthenium(II)-Komplex als Energie-Akzeptor über eine unterschiedliche Anzahl an Glycineinheiten mit einem Cumarin-Chromophor als Energie-Donor verknüpft. Bei einer kleinen Zahl an Glycineinheiten (0, 1) findet effektiver Energietransfer vom Cumarin- zum Ruthenium-Chromophor statt, wogegen bei zwei Glycineinheiten ein effektiver Energietransfer verhindert ist.

Licht-induzierte Ladungstrennung wurde erreicht, indem Bis(terpyridin)ruthenium(II)-Komplexe als Chromophore in einem Donor-Chromophor-Akzeptor-Nanokomposit eingesetzt wurden. Dabei wurde ein Triphenylamin-enthaltendes Blockcopolymer als Elektronendonor und ZnO-Nanostäbchen als Elektronenakzeptor verwendet. Bei Bestrahlung des Chromophors werden Elektronen in die ZnO-

Nanostäbchen injiziert und die Elektronenlöcher wandern in das Triphenylamin-enthaltende Blockcopolymer.

Abstract

Polypyridyl complexes of ruthenium(II) have a plethora of applications, e.g. in dye-sensitized solar cells and as photocatalysts. $[Ru(bpy)_3]^{2+}$ is one of the most prominent ruthenium(II) complexes featuring long-lived ^{3}MLCT excited states with a lifetime of 1 μs and a luminescence quantum yield of 10%. $[Ru(bpy)_3]^{2+}$ is chiral and can form stereoisomers when the ligands are substituted unsymmetrically or in the case of oligonuclear *rac*/*meso*-complexes. Bis(tridentate) complexes such as $[Ru(tpy)_2]^{2+}$ are achiral and thus, circumvent stereoisomers. However, $[Ru(tpy)_2]^{2+}$ features disappointing photophysical properties with a ^{3}MLCT lifetime of around 0.2 ns and a quantum yield $\leq 0.0007\%$. The attachment of substituents on $[Ru(tpy)_2]^{2+}$ as well as the enlargement of ligand bite angles to 90° provide considerably improved properties of the emitting ^{3}MLCT states.

Following this strategy, novel bis(tridentate) ruthenium(II) complexes were developed, synthesized and characterized in this work. The attachment of ester substituents and the use of ligands with enlarged bite angles lead to ^{3}MLCT lifetimes of up to 841 ns and quantum yields of up to 1.1%. The novel bis(tridentate) complexes feature a significantly higher photostability compared to tris(bidentate) $[Ru(bpy)_3]^{2+}$. The complexes were used as emitter in light-emitting electrochemical cells and show electroluminescence with a deep red color reaching into the NIR. Likewise, the complexes were tested as light harvesters in dye-sensitized solar cells and achieve light-to-energy efficiencies of up to 0.26%.

Dinuclear, stereochemically defined ruthenium(II) complexes were oxidized in order to study the metal-metal interaction between Ru(II) and Ru(III) in the one-electron oxidized species. The different redox properties of the two ruthenium centers in the dinuclear compounds lead to a valence-localized situation with no metal-metal interaction observed. Alike, the oxidation of a mononuclear ruthenium(II) complex and its spontaneous back reduction were studied.

Energy transfer systems were synthesized via a solid-phase synthesis. A bis(terpyridine) ruthenium(II) complex serves as energy acceptor and is connected via a different number of glycine units to a coumarin chromophore serving as energy donor. Efficient energy transfer from the coumarin to the ruthenium chromophore is feasible for a small number (0, 1) of glycine units while two glycine units prevent efficient energy transfer.

Light-induced charge separation was achieved when a bis(terpyridine) ruthenium(II) complex was used as chromophore in a donor-chromophore-acceptor nanocomposite. A triphenylamine-containing block-copolymer was used as electron donor and ZnO nanorods as electron acceptor. Upon irradiation of the chromophore electrons are injected into the ZnO nanorods and electron holes are transferred to the triphenylamine-containing block-copolymer.

Content

1 Abbreviations

δ	chemical shift
ε	molar extinction coefficient
λ	wavelength
η	efficiency
τ	lifetime
$\tilde{\nu}$	wave number
Φ	quantum yield
Ac	acetyl
AM	air mass
a.u.	arbitrary units
bpy	2,2‘-bipyridine
Bu	butyl
CIE	Commission International de l'Éclairage, International Commission on Illumination
COSY	correlated spectroscopy
d	day
DCC	*N*,*N*‘-dicyclohexylcarbodiimide
ddpd	*N*,*N*‘-dimethyl-*N*,*N*‘-dipyridin-2-ylpyridine-2,6-diamine
DIC	*N*,*N*‘-diisopropylcarbodiimide
DFT	density functional theory
DMF	*N*,*N*-dimethylformamide
DSSC	dye-sensitized solar cell
$E_{1/2}$	half wave potential
EPR	electron paramagnetic resonance
em	emission
equiv	equivalent
ESI	elektro spray ionisation
Et	ethyl
EQE	external quantum efficiency
exc	excitation
Fc	ferrocene
ff	fill factor
Fmoc	9-fluorenyl-methoxycarbonyl
Gly	glycine
GS	ground state
h	hour/ planck constant

HMBC	heteronuclear multiple bond correlation
HOBT	1-hydroxybenzotriazole
HOMO	highest occupied molecular orbital
HR	high resolution
IEFPCM	integral equation formalism polarizable continuum model
IL	intraligand
IPCE	incident photon-to-current conversion efficiency
ISC	intersystem crossing
IVCT	intervalence charge transfer
IQE	internal quantum efficiency
J	coupling constant
LEC	light-emitting electrochemical cell
LED	light-emitting device
LLCT	ligand-to-ligand charge transfer
LMCT	ligand-to-metal charge transfer
LUMO	lowest unoccupied molecular orbital
M	molar (mol l^{-1})
max	maximum
MC	metal-centered
Me	methyl
min	minute
MLCT	metal-to-ligand charge transfer
mpp	maximum power point
MS	mass spectrometry
m/*z*	mass per charge
NIR	near infrared
NMR	nuclear magnetic resonance
NOESY	nuclear Overhauser effect spectroscopy
OLED	organic light-emitting device
Ph	Phenyl
phen	1,10-phenanthroline
ppy	2-phenylpyridine
PyBOP	benzotriazole-1-yl-oxy-trispyrrolidino-phoshponium hexafluorophosphate
rac	racemic
RT	room temperature
SCE	saturated calomel electrode
SPPS	solid-phase peptide synthesis

^{t}BOC	*tert*-butyloxycarbonyl
^{t}Bu	*tert*-butyl
TFA	trifluoroacetic acid
THF	tetrahydrofurane
TPA	triphenylamine
tpy	2,2‘:6‘,2‘‘-terpyridine
UV	ultraviolet
Vis	visible
vs.	versus
WOC	water oxidation catalyst

2 Introduction

Polypyridine complexes of ruthenium(II) provide a unique class of complexes with unprecedented photophysical, chemical and electrochemical properties.[1] There is a plethora of applications dealing with polypyridine complexes of ruthenium(II) such as dye-sensitized solar cells,[2–4] light-emitting devices,[5–8] anticancer and photodynamic therapy,[9–11] sensing of ions,[12–14] sensing of small neutral molecules,[15–17] energy transfer,[18–20] mixed valency,[21–26] triplet-triplet annihilation upconversion,[27–30] and molecular data storage.[31–33] Applications also involve photocatalytic reactions such as splitting of H_2O,[34,35] generation of H_2,[36–40] reduction of CO_2,[38–40] and photocatalysis of organic redox reactions.[39,41–45] $[Ru(bpy)_3]^{2+}$ is one of the most prominent ruthenium(II) complexes (bpy = 2,2'-bipyridine). The absorption of a photon populates an excited ^{1}MLCT state (MLCT = metal-to-ligand charge transfer; Figure 1a). From this state quantitative intersystem crossing (ISC) into a ^{3}MLCT state occurs.[1] The long excited state lifetime ($\tau \approx 1$ µs) of the ^{3}MLCT state at room temperature in solution renders $[Ru(bpy)_3]^{2+}$ highly suitable as photoredox catalyst (Table 1).[39,46,47] The ^{3}MLCT state is emissive with a high luminescence quantum yield ($\Phi \approx 10\%$) which favors the application in light-emitting devices, as luminescent sensor or as imaging agent.[47]

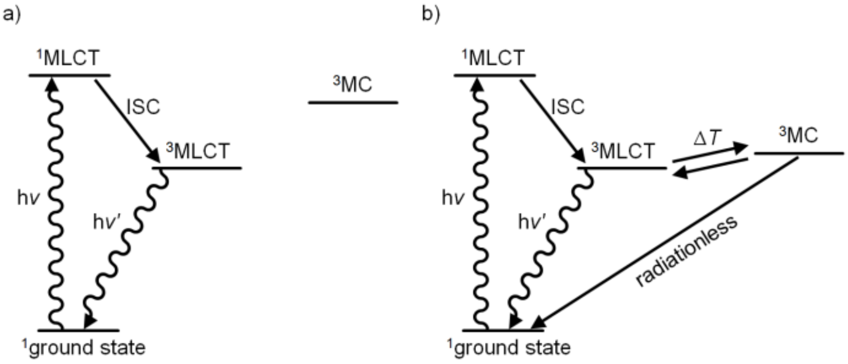

Figure 1. Qualitative Jablonski diagrams of a) $[Ru(bpy)_3]^{2+}$ and b) $[Ru(tpy)_2]^{2+}$ (MLCT = metal-to-ligand charge transfer, ISC = intersystem crossing, MC = metal-centered, bpy = 2,2'-bipyridine, tpy = 2,2';6',2''-terpyridine).

The properties of $[Ru(bpy)_3]^{2+}$ can be fine tuned via ligand design. However, the chirality of $[Ru(bpy)_3]^{2+}$ is a drawback when the bpy ligands are substituted unsymmetrically or in the case of oligonuclear *rac*/*meso*-complexes because stereoisomers are formed which have to be separated or avoided by complicated synthetic procedures.[48–50] Bis(tridentate) coordination as in $[Ru(tpy)_2]^{2+}$ ($[\mathbf{1}]^{2+}$, Figure 2) can avoid stereoisomers even in the case of heteroleptic complexes with 4',4'-substitution (tpy = 2,2';6',2''-terpyridine).[51] Furthermore, the stronger chelate effect of tridentate compared to bidentate ligands is favorable in terms of complex stability.[52,53] Despite the similar absorption characteristics and redox potentials of $[Ru(bpy)_3]^{2+}$ and $[\mathbf{1}]^{2+}$ the excited state properties differ significantly (Table 1). Unfortunately, $[\mathbf{1}]^{2+}$ has a dramatically reduced lifetime of the lowest excited ^{3}MLCT state ($\tau \approx 0.1 - 0.2$ ns) and quantum yield ($\Phi \leq 0.0007\%$; Table 1).[54–56] The reason for the poor excited state photophysical properties is an effective radiationless deactivation via ^{3}MC states which are thermally populated from ^{3}MLCT states (MC = metal-centered; Figure 1b). $[Ru(bpy)_3]^{2+}$ features three ligands which can create a coordination sphere that corresponds more to an ideal octahedron than in the case of $[Ru(tpy)_2]^{2+}$ with two constrained ligands. Therefore the overlap between the pyridine nitrogen lone pairs and the e_g* orbitals of Ru is higher in $[Ru(bpy)_3]^{2+}$. As a result the ligand field splitting is stronger in $[Ru(bpy)_3]^{2+}$ inducing less accessible ^{3}MC states with a higher ^{3}MLCT-^{3}MC energy difference compared to $[Ru(tpy)_2]^{2+}$ (Figure 1).[54–56] In order to improve ground and especially excited state photophysical properties of bis(terpyridine) ruthenium(II) complexes extensive efforts have been made in the last two decades. Long-lived and highly emissive excited states in bis(tridentate) complexes of ruthenium(II) can be obtained by the introduction of substituents in the 4'-position of the tpy ligand.[51] Electron-withdrawing substituents stabilize the ^{3}MLCT state compared to the ^{3}MC state while electron-donating substituents destabilize the ^{3}MC state compared to the ^{3}MLCT state. Both effects increase the ^{3}MLCT-^{3}MC state energy difference and can avoid radiationless deactivation via the ^{3}MC state.[57] In 4'-substituted $[(EtOOC\text{-}tpy)Ru(tpy)]^{2+}$ ($[\mathbf{2}]^{2+}$, Figure 2) prepared by Bolink the electron-withdrawing character of the ester group leads to a less accessible ^{3}MC state and a significantly higher lifetime (τ = 32 ns) and a higher quantum yield ($\Phi = 0.041\%$) compared to unsubstituted $[\mathbf{1}]^{2+}$ (Table 1).[8] Furthermore, $[\mathbf{2}]^{2+}$ has a red-shifted absorption maximum (λ_{max} = 485 nm; ε_{max} = 18140 M^{-1} cm^{-1}) and higher extinction coefficients compared to $[Ru(bpy)_3]^{2+}$ (λ_{max} = 452 nm; ε_{max} = 13000 M^{-1} cm^{-1}) and $[\mathbf{1}]^{2+}$ (λ_{max} = 474 nm; ε_{max} = 10400 M^{-1} cm^{-1}) which is beneficial for efficient light harvesting in dye-sensitized solar cells, especially in the low energy part of the electromagnetic spectrum (Table 1).[8]

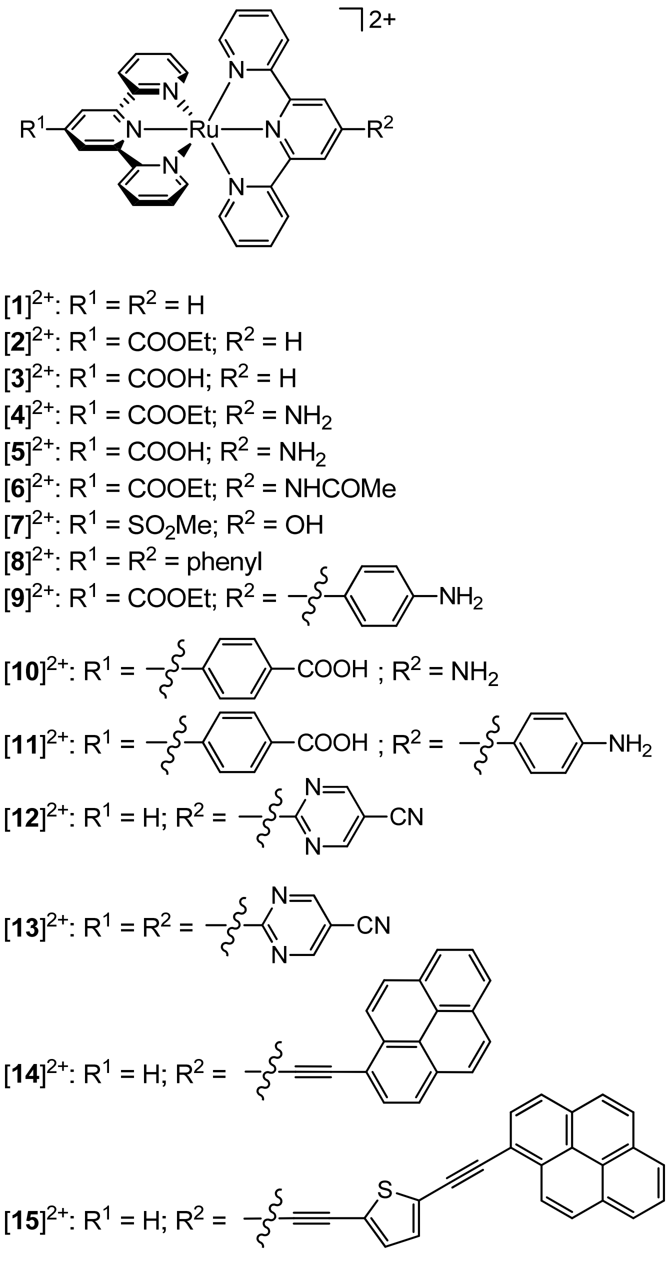

Figure 2. Bis(terpyridine) complexes of ruthenium(II).

Table 1. Photophysical and electrochemical properties of ruthenium(II) polypyridine complexes in CH_3CN at 295 K. See Figures 2 and 11 for complex numbering (bpy = 2,2'-bipyridine).

complex	absorption	emission			electrochemistry	
	λ_{max} [nm] (ε [M^{-1} cm^{-1}])	λ_{max} [nm]	Φ [%]	τ [ns]	$E_{½}$(Ru^{II}/Ru^{III})[a] [V]	$E_{½}^{red}$ [a] [V]
[Ru(bpy)$_3$]$^{2+}$ [47]	452 (13000)	615	9.4[58]	1100	+0.89	–1.73
[**1**]$^{2+}$ [51]	474 (10400)	629	≤ 0.0007[b]	0.1 – 0.2[55,c]	+0.92	–1.67
[**2**]$^{2+}$ [8]	485 (18100)	667	0.041[d]	32	+0.96[e]	–1.27[e]
[**3**]$^{2+}$ [59,60]	479 (19500)	637[f]	0.02[f,g]	-	+0.91	–1.69
[**4**]$^{2+}$ [61]	502 (19100)	734	0.27[d]	34	+0.68	–1.54
[**5**]$^{2+}$ [61,62]	501 (20700)	739	0.18[d,h]	26 (92%), 4 (8%)	+0.66	–1.60
[**6**]$^{2+}$ [63]	491 (21600)	690	0.24[d]	22	+0.85	-1.55
[**7**]$^{2+}$ [51]	490 (16800)	706	0.07[b]	50	+0.92	–1.53
[**8**]$^{2+}$ [51]	487 (26200)	715	0.006[b]	1.0	+0.90	–1.66
[**9**]$^{2+}$ [62]	502 (35600)	707	0.053[d]	23	-	-
[**10**]$^{2+}$ [62]	501 (24700)	659	0.053[d]	21 (3%), 3 (97%)	-	-
[**11**]$^{2+}$ [62]	498 (26600)	664	0.030[d]	23 (96%), 2 (4%)	-	-
[**12**]$^{2+}$ [64,65]	495 (31300)	713	0.13[b]	200	+0.95	–1.32
[**13**]$^{2+}$ [65]	506 (42000)	705	0.17[b]	231	+0.99	–1.29
[**14**]$^{2+}$ [66,67]	511 (44800)	698	0.76[d]	580	-	-
[**15**]$^{2+}$ [68]	500 (25000)	710	0.3[g,i]	2500	+0.94	–1.49
[**16**]$^{2+}$ [69]	463 (10000)	643[j]	11.4[g,j]	385[j]	+0.60	–1.95
[**17**]$^{2+}$ [69]	473 (10000)	694[j]	1.7[g,j]	7900[j]	+0.58	–1.88
[**18**]$^{2+}$ [70]	491 (14000)	700[j]	3.2[j,k]	3000[j]	+0.71	–1.73
[**19**]$^{2+}$ [71]	553 (10000)	693[j]	11.2[j,k]	5500[j]	+0.82	–1.52
[**20**]$^{2+}$ [72]	522 (6425)	608	30[g]	3300	+1.11	–1.36
[**21**]$^{2+}$ [57]	517 (7500)	729	0.45[d]	722[i]	+0.81	–1.47
[**22**]$^{2+}$ [57]	539 (6360)	744	1.1[d]	841[i]	+0.92	–1.25
[**23**]$^{2+}$ [57]	525 (8230)	762	0.042[d]	149[i]	+0.64	–1.50
[**24**]$^{2+}$ [57]	546 (7810)	788	0.052[d]	136[i]	+0.73	–1.32

[a] Versus FcH/FcH$^+$. [b] Recalculated from previously used value Φ = 0.028 for [Ru(bpy)$_3$]Cl_2 in H_2O to the updated [Ru(bpy)$_3$]Cl_2 standard Φ = 0.040 in H_2O.[58] [c] Various solvents. [d] Recalculated from previously used value Φ = 0.062[73] for [Ru(bpy)$_3$]Cl_2 in CH_3CN to the updated [Ru(bpy)$_3$]Cl_2 standard Φ = 0.094 in CH_3CN[58]. [e] No solvent denoted. [f] In DMF. [g] As given in the reference. [h] In acetone. [i] In PrCN. [j] In EtOH/MeOH (4:1, *v*/*v*). [k] Recalculated from previously used value Φ = 0.059 for [Ru(bpy)$_3$]Cl_2 in CH_3CN to the updated [Ru(bpy)$_3$]Cl_2 standard Φ = 0.094 in CH_3CN.[58]

3 Physicochemical Properties of Bis(tridentate) Ruthenium(II) Polypyridine Complexes

The physicochemical properties of bis(tridentate) ruthenium(II) polypyridine complexes will be discussed exemplarily in more detail on the donor-acceptor substituted bis(terpyridine)complex [**4**]$^{2+}$ (Figure 2) prepared by Hempel and Heinze.[61] Heteroleptic complexes such as [**4**]$^{2+}$ are readily synthesized in a stepwise approach. First one tpy ligand (tpy^1) coordinates to $RuCl_3$ forming the ruthenium(III) complex (tpy^1)$RuCl_3$ which can be isolated. Then the ruthenium center is reduced by *N*-ethylmorpholine from Ru^{III} to Ru^{II} in a microwave assisted reaction which enables coordination of the second tpy ligand (tpy^2) resulting in the desired heteroleptic complex [(tpy^1)Ru(tpy^2)]$^{2+}$ with *meridional* coordination.[61] The ester group of [**4**]$^{2+}$ can be hydrolyzed to the carboxylic acid derivative [**5**]$^{2+}$ by refluxing the complex in 20% sulfuric acid which offers the possibility of orthogonal functionalization either on the acid or on the amino group. The harsh reaction procedure also underlines the high thermal and chemical stability of bis(tridentate) complexes such as [**4**]$^{2+}$ and [**5**]$^{2+}$.[61]

Breivogel and Heinze showed that [**5**]$^{2+}$ is water soluble in the presence of NO_3^- ions enabling pH-dependent measurements. The Pourbaix diagram of [**5**]$^{2+}$ shows the redox potential $E_{½}$ of the Ru^{II}/Ru^{III} couple at different pH values (Figure 3) starting with 0.5 M HNO_3 in H_2O and stepwise titration with saturated aqueous NaOH. At pH = 0 – 1.6 the redox potential amounts to $E_{½} = 0.79$ V. Between pH 1.6 and 2.7 the redox potential drops to $E_{½} = 0.74$ V which is due to deprotonation of the carboxylic acid group (pK_a = 2.7).[61,74] For a proton-coupled electron transfer the expected slope of the redox potential is given by $-(m/n) \times 59$ mV per pH unit (m = number of transferred protons, n = number of transferred electrons).[75] The experimental slope amounts to approximately 46 ± 10 mV per pH unit suggesting that the electron transfer is indeed coupled to proton transfer in this pH region. The drop of the redox potential between pH 1.6 and 2.7 is rationalized by the fact that the deprotonated carboxylate group is a stronger electron donor than the protonated carboxyl group. Thus, the former can be oxidized at lower potential. From pH 2.7 – 9.5 the redox potential features a plateau with $E_{½} = 0.74$ V. At pH > 10 the redox potential again drops due to deprotonation of the amino group which is converted into an even stronger electron donor by deprotonation.[61,74] Oxidation is reversible at pH < 10 and irreversible at pH > 10. DFT-calculated spin densities of ruthenium(III) complexes [**5**]$^{3+}$, [**5** – H]$^{2+}$ and [**5** – 2 H]$^{+}$ are depicted in Figure 4. For [**5**]$^{3+}$ the spin density is located at the ruthenium center with a smaller contribution at the amino nitrogen atom. The Mulliken spin densities on Ru and on the amino nitrogen atom are calculated as 0.76 and 0.11, respectively. Similarly, for one-fold deprotonated [**5** – H]$^{2+}$ Mulliken spin densities amount to 0.78 and 0.10, respectively. Thus, when [**5**]$^{3+}$ is deprotonated at the carboxylic acid group the oxidation remains ruthenium-centered and reversible. The second deprotonation takes place at the amino group. The resulting species [**5** – 2 H]$^{+}$ features Mulliken spin densities on Ru and the amino nitrogen atom of 0.36 and 0.51, respectively

(Figure 4). Thus, oxidation takes place at the deprotonated amino group which induces the irreversibility of the oxidation. In summary, at pH < 10 $[\mathbf{5}]^{2+}$ is reversibly oxidized at the ruthenium center while at pH > 10 the amino group is irreversibly oxidized.[74]

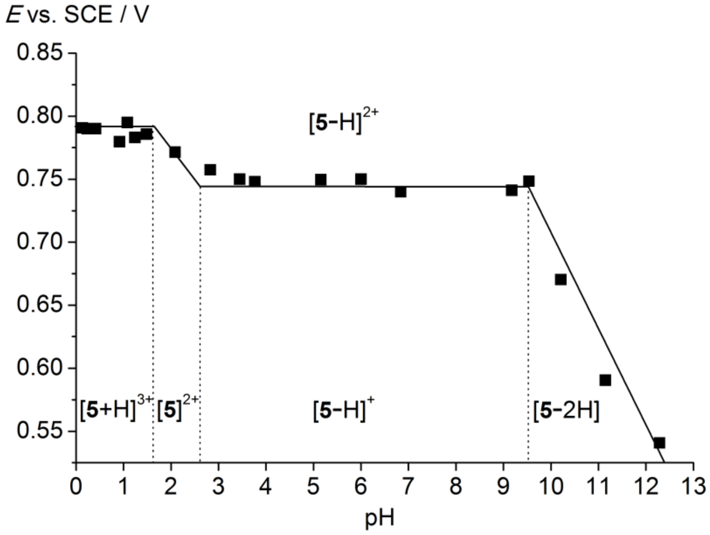

Figure 3. Pourbaix diagram of $[\mathbf{5}](PF_6)_2$ in 0.5 M HNO_3 in H_2O and stepwise titration with saturated aqueous NaOH.[74] E (vs. SCE) – 0.16 ≈ E (vs. FcH/FcH$^+$).[76] pK_a values are denoted by vertical dotted lines.

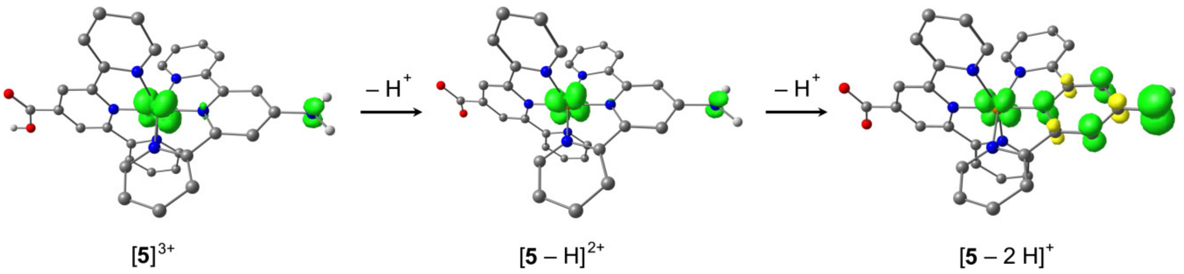

Figure 4. DFT-calculated spin density of ruthenium(III) complexes $[\mathbf{5}]^{3+}$, $[\mathbf{5} - \mathrm{H}]^{2+}$ and $[\mathbf{5} - 2\,\mathrm{H}]^{+}$ (B3LYP/LANL2DZ, IEFPCM, H_2O, contour value 0.01, CH hydrogen atoms omitted).[74]

The reversible one-electron oxidation of $[\mathbf{4}]^{2+}$ is found at $E_{½}$ = 0.68 V vs. FcH/FcH$^+$.[61] The EPR spectrum of $[\mathbf{4}]^{3+}$ in frozen solution shows a rhombic signal with $g_{1,2,3}$ = 2.347, 2.178, 1.843 (Δg = 0.504) confirming a characteristic Ru$^{\mathrm{III}}$ signature.[57,77] The reversible one-electron reduction of $[\mathbf{4}]^{2+}$ occurs at the COOEt-substituted tpy ligand.[57,61] The EPR spectrum of the N-acetylated analogue $[\mathbf{6}]^{+}$ (Figure 2) in frozen solution shows a less rhombic signal with $g_{1,2,3}$ = 2.005, 1.989, 1.955 (Δg = 0.050) which is in accord with a ligand-based reduction with some ruthenium admixture.[57] The DFT-calculated spin density of $[\mathbf{4}]^{+}$ confirms that oxidation takes place at the ruthenium center

(Mulliken spin density on Ru = 0.76) with some admixture from the amino nitrogen atom (Mulliken spin density on N = 0.11) while reduction is essentially localized at the tpy-COOEt ligand (Mulliken spin density on Ru = 0.10, Figure 5).

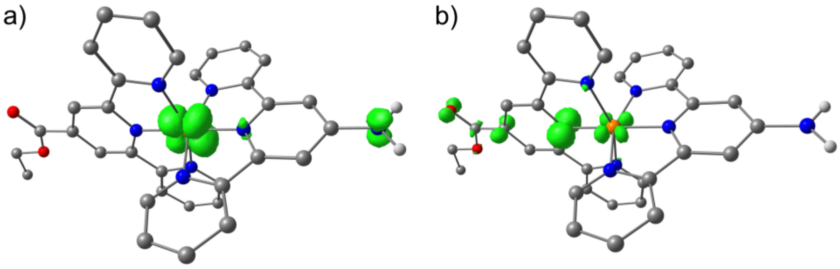

Figure 5. Spin densities of a) [**4**]$^{3+}$ and b) [**4**]$^{+}$ in CH_3CN calculated by DFT (B3LYP/LANL2DZ, IEFPCM, contour value 0.01 a.u., CH hydrogen atoms omitted).[20]

Breivogel and Heinze probed the stability of ruthenium(III) complex [**4**]$^{3+}$ in the presence of water and coordinating OH^- ions by spectroelectrochemical measurements. The ruthenium(II) complex [**4**]$^{2+}$ is reversibly oxidized to the ruthenium(III) complex [**4**]$^{3+}$ by gradually increasing the potential and then reduced back to [**4**]$^{2+}$ by gradually lowering the potential (Figure 6). Upon oxidation the MLCT band of [**4**]$^{2+}$ at λ = 502 nm disappears while a LMCT band of [**4**]$^{3+}$ at λ = 729 nm rises. Seven isosbestic points are observed and confirm the clean conversion from [**4**]$^{2+}$ to [**4**]$^{3+}$. Upon back reduction the initial spectrum is fully recovered and the same isosbestic points are observed clearly demonstrating the stability of the ruthenium(II/III) complexes [**4**]$^{2+}$ and [**4**]$^{3+}$ in the presence of water and coordinating OH^- ions.[78]

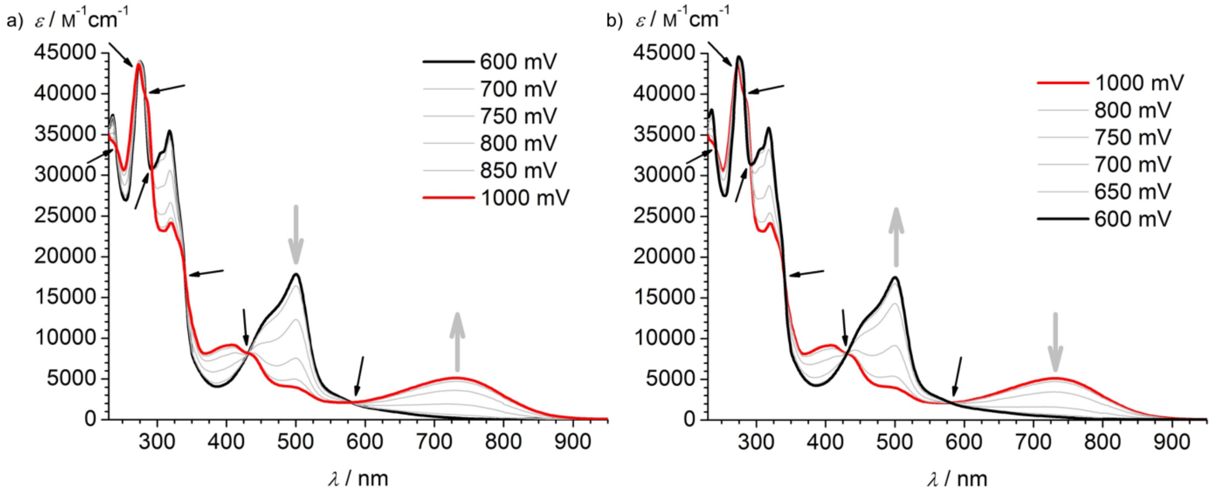

Figure 6. UV/Vis spectra during a) the electrochemical oxidation (E = 600 → 1000 mV) and b) back reduction (E = 1000 → 600 mV) of $[\mathbf{4}]^{2+}$ in an OTTLE cell in 10^{-3} M NaOH and 0.1 M $[n\text{-Bu}_4\text{N}](\text{PF}_6)$ in CH_3CN:H_2O (98:2, *v*%). Black arrows indicate isosbestic points.[78]

The absorption spectrum of $[\mathbf{4}]^{2+}$ features π → π* transitions below λ = 400 nm and a characteristic metal-to-ligand charge transfer band (MLCT) with a maximum at λ_{max} = 502 nm (ε_{max} = 19100 M ^{1} cm^{-1}; Figure 7).[61] TD-DFT calculations (B3LYP/LANL2DZ, IEFPCM, CH_3CN) confirm the ligand-centered character of the π → π* transitions at λ < 400 nm and the MLCT character of the transitions at λ > 400 nm.

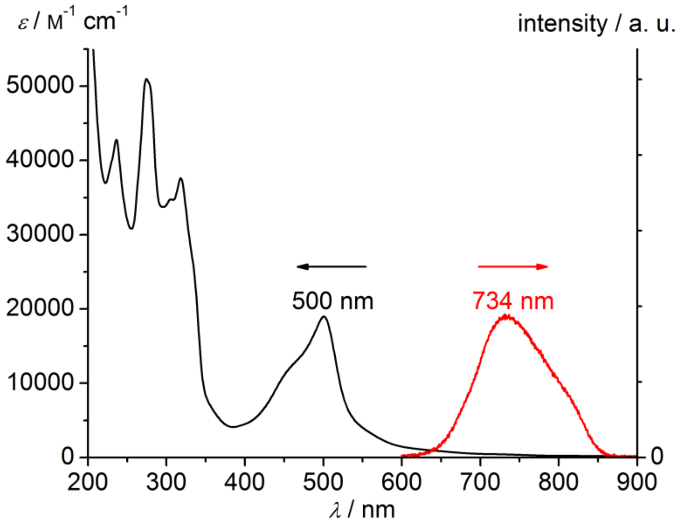

Figure 7. UV/Vis spectrum (black) and emission spectrum (red) of $[\mathbf{4}](PF_6)_2$ in CH_3CN at 295 K.

Relevant Kohn-Sham frontier molecular orbitals of $[\mathbf{4}]^{2+}$ are depicted in Figure 8. HOMO-2, HOMO-1, HOMO, LUMO and LUMO+1 represent the participating molecular orbitals in transitions with $\lambda > 400$ nm. HOMO to HOMO-2 correspond to the t_{2g} orbitals in O_h symmetry and are mainly ruthenium-centered with a small contribution from the amino nitrogen atom. The contribution of the amino group is experimentally verified by Resonance Raman experiments involving the MLCT excitation.[63] LUMO and LUMO+1 are located on the acceptor-functionalized tpy ligand. Thus, absorption is best described by a mixed ^{1}MLCT/^{1}LLCT character (LLCT = ligand-to-ligand charge transfer). LUMO+9 and LUMO+13 correspond to the higher energy e_g orbitals and do not participate in the MLCT absorption process (Figure 8).

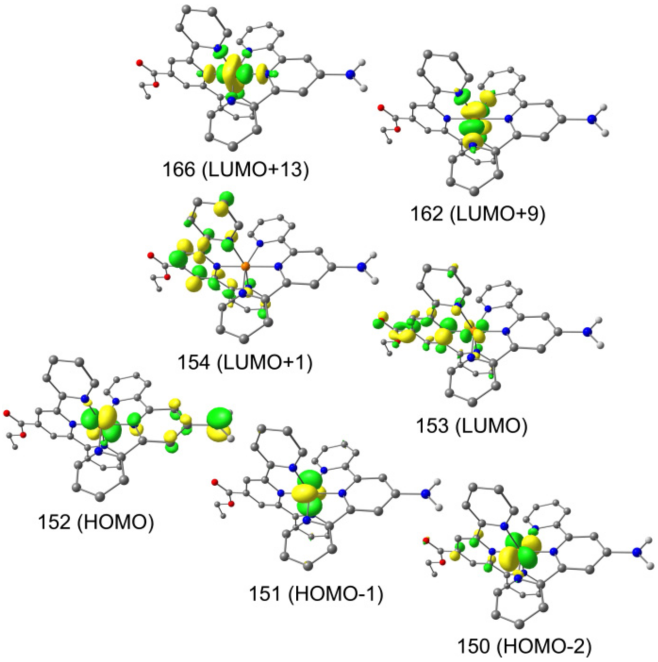

Figure 8. DFT-calculated Kohn-Sham frontier molecular orbitals (contour value 0.06 a.u.) of $[\mathbf{4}]^{2+}$ (B3LYP/LANL2DZ, IEFPCM, CH_3CN; CH hydrogen atoms omitted).

After population of the initial ^{1}MLCT/^{1}LLCT state ISC into the emissive ^{3}MLCT state occurs. Breivogel and Heinze have experimentally probed excited state dynamics of $[\mathbf{4}]^{2+}$ on the ps timescale by transient absorption measurements. When excited at $\lambda_{exc} = 400$ nm the transient absorption spectra of $[\mathbf{4}]^{2+}$ show an instant ground state bleach at $\lambda = 509$ nm together with a photoinduced absorption at $\lambda = 565 - 960$ nm (Figure 9). The region of the photoinduced absorption reveals a process with a time constant of 7.2 ps at 295 K before reaching the thermalized ^{3}MLCT state. This dynamics might be associated with localization of the excited electron on the tpy-COOEt ligand, intersystem crossing or vibrational relaxation within $^{1/3}$MLCT states.[57]

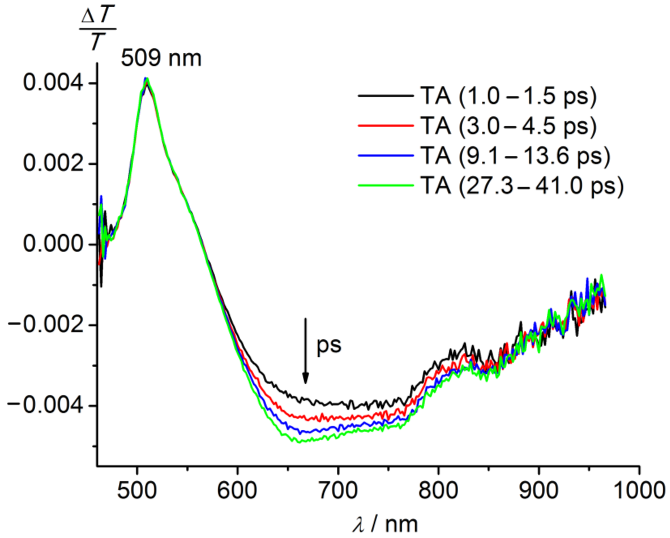

Figure 9. Transient absorption spectra of [**4**]$^{2+}$ (pulse λ_{exc} = 400 nm, 2600 nJ) in PrCN at 295 K.[57]

At 295 K complex [**4**]$^{2+}$ shows room temperature phosphorescence from the ^{3}MLCT state at λ_{max} = 734 nm with a ^{3}MLCT lifetime of τ = 34 ns and a quantum yield of Φ = 0.27% (Figure 7).[57] The emitting ^{3}MLCT state as well as the deactivating ^{3}MC state were modeled by DFT calculations by Breivogel and Heinze. The ^{3}MC state of [**4**]$^{2+}$ is higher in energy by 26.8 kJ mol^{-1} relative to the ^{3}MLCT state (Figure 10). In comparison, the corresponding triplet states of unsubstituted [**1**]$^{2+}$ are found to be essentially isoenergetic. While the geometry of the ^{3}MLCT state of [**4**]$^{2+}$ differs only slightly from the ^{1}GS geometry the ^{3}MC geometry is significantly distorted from that of the ^{1}GS (GS = ground state). For example, the bond lengths between Ru and the central N atom of EtOOC-tpy amount to 1.99, 2.04 and 2.17 Å for the ^{1}GS, the ^{3}MLCT and the ^{3}MC state, respectively. The N-C-C-N dihedral angle of the EtOOC-tpy ligand amount to 0°, 0° and 13° for the ^{1}GS, the ^{3}MLCT and the ^{3}MC state, respectively, showing that the EtOOC-tpy ligand loses its planarity in the ^{3}MC state. The spin density of the ^{3}MLCT state is localized on the ruthenium center as well as on the EtOOC-tpy ligand while for the ^{3}MC state the spin density is confined to the ruthenium center (Figure 10). The connecting transition state (^{3}TS) between the ^{3}MLCT and the ^{3}MC state is calculated with an energy 31.7 kJ mol^{-1} higher than the ^{3}MLCT state. Concerning the energy, spin density and geometry the transition state resembles more the ^{3}MC than the ^{3}MLCT state (Figure 10).[57]

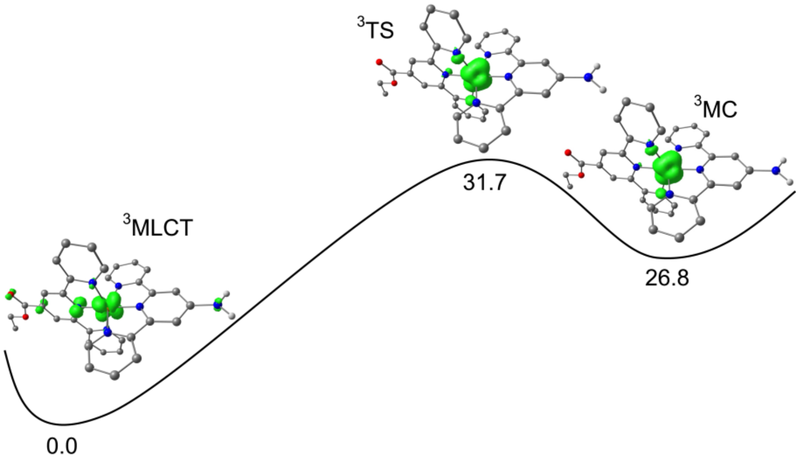

Figure 10. DFT-calculated geometries, relative energies, and spin densities of triplet states (^{3}MLCT and ^{3}MC) and the transition state (^{3}TS) of [**4**]$^{2+}$ (B3LYP/LANL2DZ, IEFPCM, CH_3CN; contour value 0.015 a.u.; energies in kJ mol^{-1}; CH hydrogen atoms omitted).[57]

4 Strategies Towards Long-Living and Highly Emissive Excited States

In the bis-4'-substituted heteroleptic complex $[(EtOOC\text{-}tpy)Ru(tpy\text{-}NH_2)]^{2+}$ ($[\mathbf{4}]^{2+}$, Figure 2) the electron-donating NH_2 group destabilizes the ^{3}MC state compared to the ^{3}MLCT state leading to a further improvement of the excited state properties (τ = 34 ns; Φ = 0.27%) compared to $[\mathbf{2}]^{2+}$ (τ = 32 ns; Φ = 0.041%; Table 1; Figure 1).[61] The push-pull substitution of $[\mathbf{4}]^{2+}$ induces a small HOMO-LUMO energy gap which red-shifts the absorption maximum (λ_{max} = 502 nm). In addition, the NH_2 group in $[\mathbf{4}]^{2+}$ enlarges the chromophoric system and raises the extinction coefficient (ε_{max} = 19080 M^{-1} cm^{-1}).[61] In push-pull substituted $[\mathbf{7}]^{2+}$ (Figure 2) the combination of an OH donor group and a SO_2Me acceptor group enables similar excited state properties (τ = 50 ns; Φ = 0.07%; Table 1).[51]

Enlargement of the chromophoric system stabilizes the ^{3}MLCT state relative to the ^{3}MC state. $[Ru(Ph\text{-}tpy)_2]^{2+}$ ($[\mathbf{8}]^{2+}$, Figure 2) features phenyl groups appended to the 4'-positions of the tpy ligands. The ^{3}MLCT lifetime (τ = 1 ns) and quantum yield (Φ = 0.006%) of $[\mathbf{8}]^{2+}$ are substantially enhanced compared to $[\mathbf{1}]^{2+}$ (Table 1).[51] The combination of donor-acceptor functionalization and an enlarged chromophoric system has been realized in complexes $[\mathbf{9}]^{2+}$ – $[\mathbf{11}]^{2+}$ featuring *para*-phenylene spacers between the 4'-substituents and the tpy ligands (Figure 2). However, this combination does not lead to a synergetic effect: $[\mathbf{9}]^{2+}$ features a lower ^{3}MLCT lifetime (τ = 23 ns) and a lower quantum yield (Φ = 0.053%) compared to the phenylene-free analogue $[\mathbf{4}]^{2+}$ (Table 1). $[\mathbf{10}]^{2+}$ and $[\mathbf{11}]^{2+}$ also have inferior excited state properties compared to the phenylene-free analogue $[\mathbf{5}]^{2+}$ (Figure 2).[61,62] The ring planes of the phenylene ring and the central pyridyl ring of a tpy ligand are twisted. Thus, the reduced π-conjugation dilutes the effect of donor-acceptor substitution.[62] Coplanarity in extended ligands could be achieved by replacing the *para*-phenylene rings with pyrimidine groups such as in complexes $[\mathbf{12}]^{2+}$ and $[\mathbf{13}]^{2+}$ (Figure 2). In these complexes the enhanced π-conjugation efficiently stabilizes the ^{3}MLCT state compared to the ^{3}MC state which was shown by high excited state lifetimes up to τ = 231 ns and quantum yields up to Φ = 0.17% (Table 1).[64,65]

High excited state lifetimes can also be achieved via the so-called multichromophore approach: Further chromophores such as pyrene and anthracene can have ^{3}IL states with energies similar to the ^{3}MLCT state (IL = intraligand). In this case a triplet-triplet equilibrium between these triplet states can significantly enhance the excited state lifetime.[79] Deactivation from the triplet state of the organic chromophore is slow due to the spin-forbidden nature such that the organic chromophore acts as an excited state reservoir for the emitting ^{3}MLCT state.[80] Complexes $[\mathbf{14}]^{2+}$ and $[\mathbf{15}]^{2+}$ (Figure 2) feature a pyrene unit as organic triplet reservoir and reach lifetimes of τ = 580 and 2500 ns, respectively.[66–68]

A pronounced push-pull situation is also present in complexes $[\mathbf{16}]^{2+}$ and $[\mathbf{17}]^{2+}$ (Figure 11) prepared by Schubert and Berlinguette where an electron accepting tpy ligand is used in combination with a strongly σ-donating carbene ligand [2',6'-bis(3-methyl-1,2,3-triazol-4-yl-5-idene)-pyridine] with CNC coordination. Unprecedented high excited state lifetimes and quantum yields up to τ = 7900 ns and

Φ = 11.4% have been obtained at room temperature (Table 1).[69] Carbene donor ligands and their ruthenium complexes will not be discussed here in more detail.[81–83]

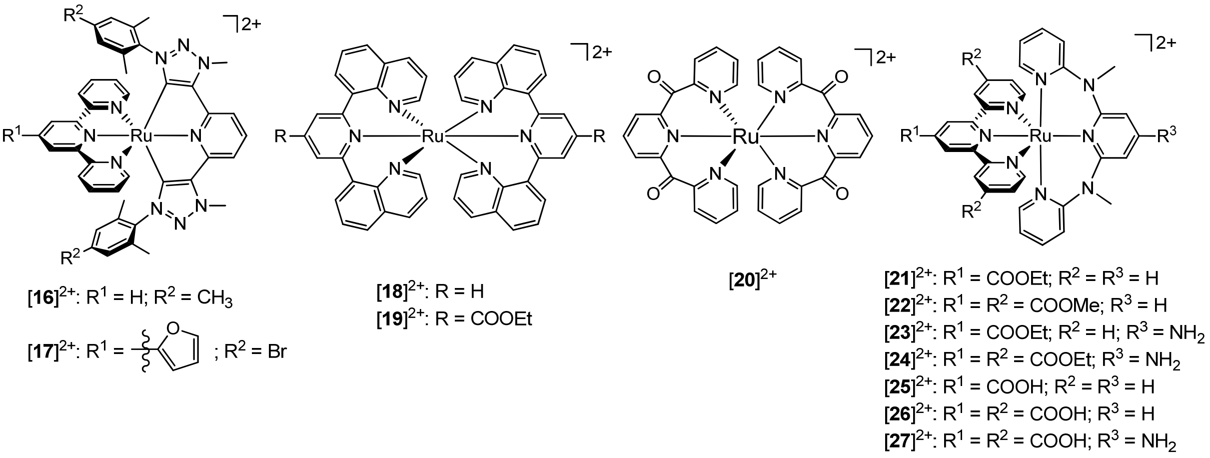

$[\mathbf{16}]^{2+}$: R^1 = H; R^2 = CH_3

$[\mathbf{17}]^{2+}$: R^1 = ; R^2 = Br

$[\mathbf{18}]^{2+}$: R = H

$[\mathbf{19}]^{2+}$: R = COOEt

$[\mathbf{20}]^{2+}$

$[\mathbf{21}]^{2+}$: R^1 = COOEt; R^2 = R^3 = H

$[\mathbf{22}]^{2+}$: R^1 = R^2 = COOMe; R^3 = H

$[\mathbf{23}]^{2+}$: R^1 = COOEt; R^2 = H; R^3 = NH_2

$[\mathbf{24}]^{2+}$: R^1 = R^2 = COOEt; R^3 = NH_2

$[\mathbf{25}]^{2+}$: R^1 = COOH; R^2 = R^3 = H

$[\mathbf{26}]^{2+}$: R^1 = R^2 = COOH; R^3 = H

$[\mathbf{27}]^{2+}$: R^1 = R^2 = COOH; R^3 = NH_2

Figure 11. Bis(tridentate) complexes of ruthenium(II).

A further strategy to improve the excited state properties in (bis)tridentate complexes is the optimization of N-Ru-N bite angles. All complexes $[\mathbf{1}]^{2+}$ – $[\mathbf{17}]^{2+}$ feature five-membered chelates and N-Ru-N bite angles of around 79°. The cyclometalated ligands in $[\mathbf{16}]^{2+}$ and $[\mathbf{17}]^{2+}$ have even smaller C-Ru-N bite angles of 77°.[8,61,69] An ideal octahedral coordination sphere with bite angles of 90° would afford a stronger ligand field due to maximization of the overlap between the pyridine nitrogen lone pairs and the e_g* orbitals of Ru. A stronger ligand field splitting increases the energy difference between ^{3}MLCT and ^{3}MC states which again hampers radiationless deactivation via the latter state (Figure 1).[56] Hammarström et al. introduced bite angles of 90° by using six-membered chelates in $[Ru(dpq)_2]^{2+}$ ($[\mathbf{18}]^{2+}$, Figure 11) leading to high room temperature lifetime (τ = 3000 ns) and quantum yield (Φ = 3.2%) of the excited state (dqp = 2,6-di(quinolin-8-yl)pyridine).[70,84] The homoleptic complex $[Ru(EtOOC\text{-}dpq)_2]^{2+}$ ($[\mathbf{19}]^{2+}$, Figure 11) features even higher values (τ = 5500 ns; Φ = 11%, Table 1).[71] Ruben et al. introduced $[Ru(dcpp)_2]^{2+}$ ($[\mathbf{20}]^{2+}$, Figure 11) featuring 90° bite angles and six-membered chelates by formal insertion of carbonyl spacers between the pyridine rings of the parent $[Ru(tpy)_2]^{2+}$ complex (dcpp = 2,6-di(2-carboxypyridyl)pyridine). $[\mathbf{20}]^{2+}$ has a long lived ^{3}MLCT state (τ = 3300 ns) and the highest room temperature quantum yield (Φ = 30%) reported to date among bis(tridentate) ruthenium(II) complexes (Table 1).[72]

Six-membered chelates such as in $[\mathbf{18}]^{2+}$ and $[\mathbf{19}]^{2+}$ are highly flexible and this can lead to undesired stereoisomers (*mer*, *cis-fac*, *trans-fac*).[85] The mixed-ligand complex $[(EtOOC\text{-}tpy)Ru(ddpd)]^{2+}$ ($[\mathbf{21}]^{2+}$, Figure 11) by Breivogel and Heinze overcomes the problem of stereoisomers by using the combination of a five-membered tpy and a six-membered ddpd chelate ligand (ddpd = *N*,*N*'-dimethyl-*N*,*N*'-dipyridin-2-ylpyridine-2,6-diamine).[57,86] $[\mathbf{21}]^{2+}$ can be prepared in a stepwise synthesis by first introducing the tpy ligand to obtain the ruthenium(III) complex (EtOOC-tpy)$RuCl_3$ which is converted to the final, pure meridional complex [**21**]$^{2+}$ by treating with the ddpd ligand. The tpy ligand only adopts a *meridional* coordination, thus forcing the ddpd ligand to adopt the *meridional* coordination as well. The bite angles of the ddpd ligand amount to 88°. Despite the presence of a tpy ligand with only 79° bite angles a quantum yield of Φ = 0.45% and a remarkable high ^{3}MLCT lifetime of τ = 722 ns were obtained for complex [**21**]$^{2+}$ at room temperature (Table 1). The synergy of the electron-accepting tpy ligand and the electron-donating ddpd ligand containing NCH_3 groups ([**21**]$^{2+}$) creates a push-pull situation and shifts the maximum absorption wavelength further to lower energy ($\lambda_{\max}$ = 517 nm) compared to [**2**]$^{2+}$ ($\lambda_{\max}$ = 485 nm) where the NCH_3 groups are lacking (Figure 2, Table 1). In complex [**22**]$^{2+}$ the two outer pyridine rings of the tpy ligand are functionalized by additional ester groups. The maximum absorption wavelength of [**22**]$^{2+}$ (Figure 11) is further red-shifted ($\lambda_{\max}$ = 539 nm) and even higher values for the ^{3}MLCT lifetime (τ = 841 ns) and the quantum yield (Φ = 1.1%) are obtained.[57]

However, the increase of ^{3}MLCT lifetimes and quantum yields by push-pull substitution tuning has a limit. A pronounced push-pull situation leads to small energy differences between the ^{3}MLCT state and the singlet ground state (^{1}GS). According to the energy gap law a small ^{3}MLCT-^{1}GS energy difference induces fast radiationless deactivation into the ground state.[73,87,88] Such a strong push-pull situation is given in complexes [**23**]$^{2+}$ and [**24**]$^{2+}$ (Figure 11), prepared by Breivogel and Heinze, which feature an additional NH_2 group on the electron-donating ddpd ligand compared to their NH_2-free counterparts [**21**]$^{2+}$ and [**22**]$^{2+}$, respectively. The push-pull character of [**23**]$^{2+}$ and [**24**]$^{2+}$ manifests itself by the red-shifted absorption maximum and by electrochemical data when compared to [**21**]$^{2+}$ and [**22**]$^{2+}$, respectively (Table 1). However, the NH_2 group dramatically reduces the ^{3}MLCT lifetimes of [**23**]$^{2+}$ and [**24**]$^{2+}$ by a factor of about 5 – 6 and quantum yields are reduced by an even higher factor compared to the NH_2-free analogues (Table 1). The faster excited state deactivation in [**23**]$^{2+}$ and [**24**]$^{2+}$ is induced by high energy oscillators (N–H). This is shown by ($NH_2 \rightarrow ND_2$) deuteration experiments with the deuterated complexes [**23^D**]$^{2+}$ and [**24^D**]$^{2+}$ featuring higher quantum yields than non-deuterated [**23**]$^{2+}$ and [**24**]$^{2+}$, respectively.[57] However, deuteration has only a small effect on the quantum yield. Hence, also the above mentioned ^{3}MLCT-^{1}GS energy gap is responsible for radiationless deactivation of the ^{3}MLCT state.

The tris(bidentate) benchmark complex $[Ru(bpy)_3]^{2+}$ has been reported to be photolabile in the presence of coordinating anions such as Cl^-, Br^-, I^-, SCN^- or NO_3^-. In its excited state $[Ru(bpy)_3]^{2+}$ is prone to photoinduced ligand substitution, photooxygenation and photoracemization.[89–93] In contrast, Breivogel and Heinze showed that bis(tridentate) ruthenium(II) complexes such as [**4**]$^{2+}$ and [**21**]$^{2+}$ feature significantly higher photostabilities compared to $[Ru(bpy)_3]^{2+}$ which is obviously favorable for photo applications of all kind.[71,78]

5 Amide Formation and Solid-Phase Peptide Synthesis

Amino acid [**5**]$^{2+}$ and its ester [**4**]$^{2+}$ (Figure 2) have been introduced as building blocks in peptide synthesis by coupling 1) in solution and 2) via solid-phase peptide synthesis. Photo-induced electron transfer in derivatives of [**4**]$^{2+}$ with amide-appended ferrocenyl substituents has been reported.[61] The dinuclear complex [**29**]$^{4+}$ is synthesized by Hempel and Heinze in solution by DCC/HOBT activation of [**28**]$^{2+}$ and treatment with [**4**]$^{2+}$ under basic conditions (Figure 12).[26]

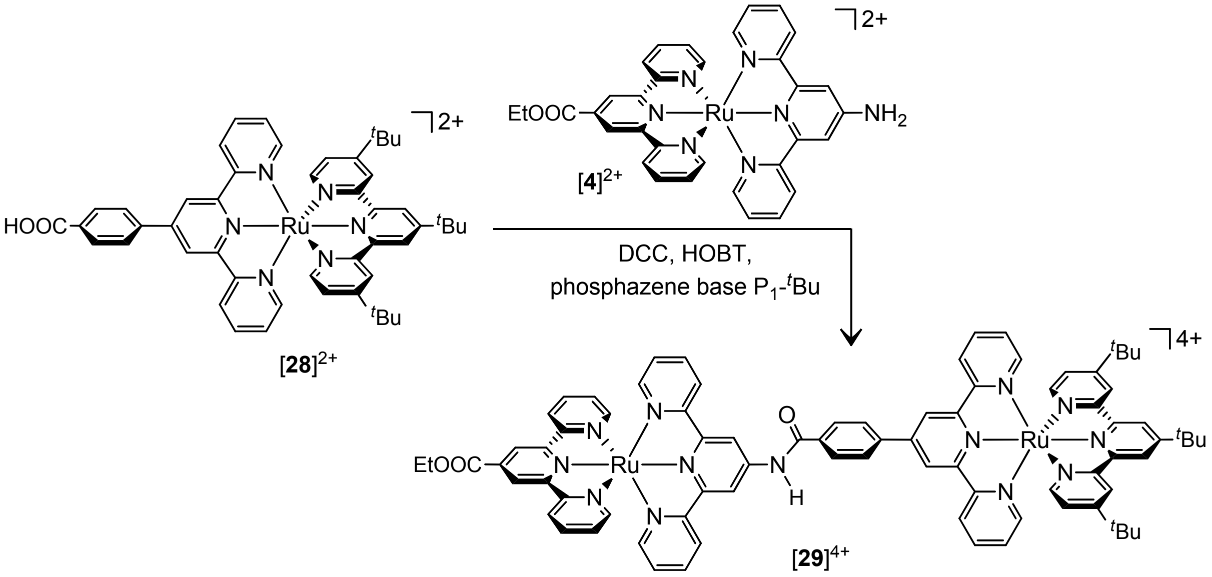

Figure 12. Synthesis of dinuclear [**29**]$^{4+}$ (DCC = *N*,*N*‘-dicyclohexylcarbodiimide, HOBT = 1-hydroxybenzotriazole, P$_1$-^{t}Bu = $(Me_2N)_3P=N^tBu$).[26]

Electrochemical measurements of [**29**]$^{4+}$ reveal different redox potentials for the two ruthenium(II) centers with $E_{½}$ = 0.68 and 0.91 V vs. FcH/FcH$^+$. Breivogel and Heinze studied the metal-metal interaction in the mixed valence complex [**29**]$^{5+}$ by UV/Vis/NIR spectroscopic measurements which indicate that one-electron oxidation of [**29**]$^{4+}$ to [**29**]$^{5+}$ is localized on the (tpy)Ru(tpy-^{t}Bu$_3$) part of [**29**]$^{5+}$. The locus of oxidation can be explained by the electron-donating positive inductive effect of the ^{t}Bu substituents. The lack of an IVCT band (IVCT = intervalence charge transfer) in the spectrum of [**29**]$^{5+}$ up to λ = 3000 nm reveals a negligible metal-metal interaction.[26] Thus, [**29**]$^{5+}$ can be assigned to the Robin-Day-Class I.[94] This is also confirmed by DFT-calculated spin densities with a Mulliken spin density on the Ru atom of the (tpy)Ru(tpy-^{t}Bu$_3$) part of 0.86 and of 0.00 for the second Ru atom (Figure 13a). In summary, the different environments of the two ruthenium(II) centers of [**29**]$^{4+}$ lead to a redox asymmetry which prevents metal-metal interaction. In addition, a metal-metal interaction is prevented by the *para*-phenylene bridge which enhances the distance between the metal centers and is responsible for a poor π-orbital overlap of the *para*-phenylene ring to the amide and to the pyridine plane.[26]

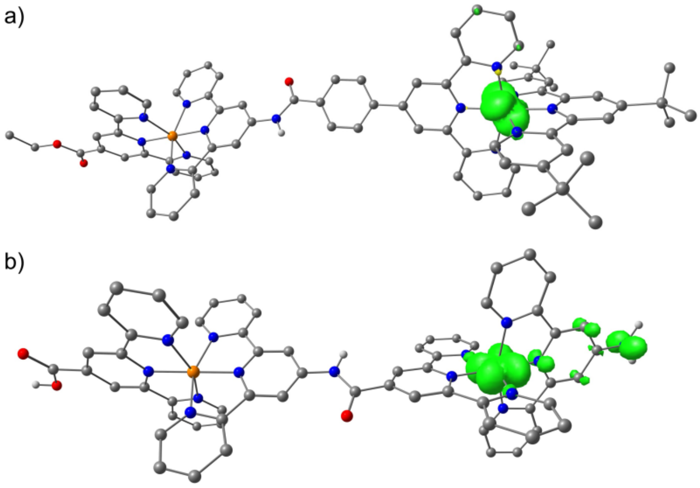

Figure 13. Spin densities of a) [**29**]$^{5+}$ and b) [**31**]$^{5+}$ in CH_3CN calculated by DFT (B3LYP/LANL2DZ, IEFPCM, contour value 0.004 a.u.). CH hydrogen atoms omitted.[26]

Hempel and Heinze realized a smaller redox asymmetry in the dinuclear dipeptide [**31**]$^{4+}$ (Figure 14). The redox potentials for the two ruthenium(II) centers are $E_{½}$ = 0.80 and 0.90 V vs. FcH/FcH^{+}. [**31**]$^{4+}$ is synthesized by PyBOP activation of [**30**]$^{2+}$ and treatment with [**4**]$^{2+}$ under basic conditions (PyBOP = benzotriazole-1-yl-oxy-trispyrrolidino-phoshponium hexafluorophosphate). After amide bond formation the ^{t}BOC and ethyl ester protecting groups are removed by aqueous acidic treatment to obtain [**31**]$^{4+}$ (Figure 14).[26] The amide bond induces a coplanar bridging ligand allowing for a better π-orbital overlap. In addition, the lack of the para-phenylene spacer provides a shorter metal-metal distance compared to [**29**]$^{4+}$. However, UV/Vis/NIR spectroscopic measurements of [**31**]$^{5+}$ by Breivogel and Heinze are analogue to the situation with [**29**]$^{5+}$. The spectra indicate that the NH_2-substituted bis(tpy) moiety is oxidized. This can be explained by the strong electron-donating character of the NH_2 group.[26,61] Still no IVCT is seen, so [**31**]$^{5+}$ can also be assigned to the Robin-Day-Class I.[94] The DFT-calculated spin density of [**31**]$^{5+}$ confirms the valence-localized situation showing spin density only on the *N*-terminal site. Mulliken spin densities of the Ru atom of the NH_2-substituted bis(tpy) moiety, the NH_2 nitrogen atom and the second Ru atom amount to 0.76, 0.11 and 0.00, respectively (Figure 13b).[26,57]

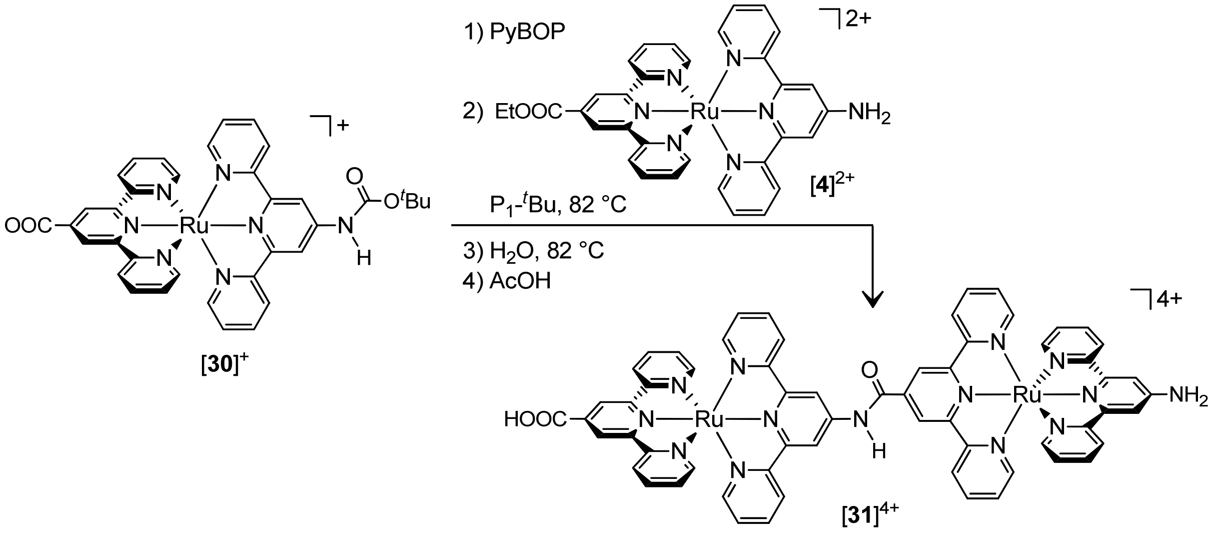

Figure 14. Synthesis of the dinuclear dipeptide [**31**]$^{4+}$ (PyBOP = benzotriazole-1-yl-oxy-trispyrrolidino-phoshponium hexafluorophosphate, P$_1$-^{t}Bu = (Me$_2$N)$_3$P=N^{t}Bu).[26]

The introduction of [**5**]$^{2+}$ by solid-phase peptide synthesis has been reported by Hempel and Heinze.[18] A general strategy is as follows: A TentaGel S resin[95,96] with a Wang linker[97] (**32**) is functionalized with Cl-Gly-Fmoc (Figure 15, Fmoc = fluorenylmethoxycarbonyl). The Fmoc group is cleaved by piperidine to obtain the free NH$_2$ group (**33**). The carboxylic acid group of [**5**]$^{2+}$ is activated by PyBOP and connected to the solid support via an amide bond to obtain [**34**]$^{2+}$ (PyBOP = benzotriazole-1-yl-oxy-tripyrrolidino-phosphonium hexafluorophosphate). Protection of the *N*-terminus of [**5**]$^{2+}$ is unnecessary due to the weak nucleophilicity of the aromatic NH$_2$ group of [**5**]$^{2+}$.[18,63] For the activation of the NH$_2$ group of [**34**]$^{2+}$ strong coupling reagents such as acid chlorides are necessary in order to form an amide bond such as in [**35**]$^{2+}$. The aliphatic NH$_2$ group of [**35**]$^{2+}$ readily forms amide bonds with carboxylic acids R-COOH by PyBOP activation. Several acids R-COOH have been used, e.g. R = CH$_3$, CF$_3$ and coumarin-3-carboxylic acid.[18] Finally, peptide [**36**]$^{2+}$ is cleaved from the solid phase by TFA to obtain the desired product [**37**]$^{2+}$ (TFA = trifuoroacetic acid).

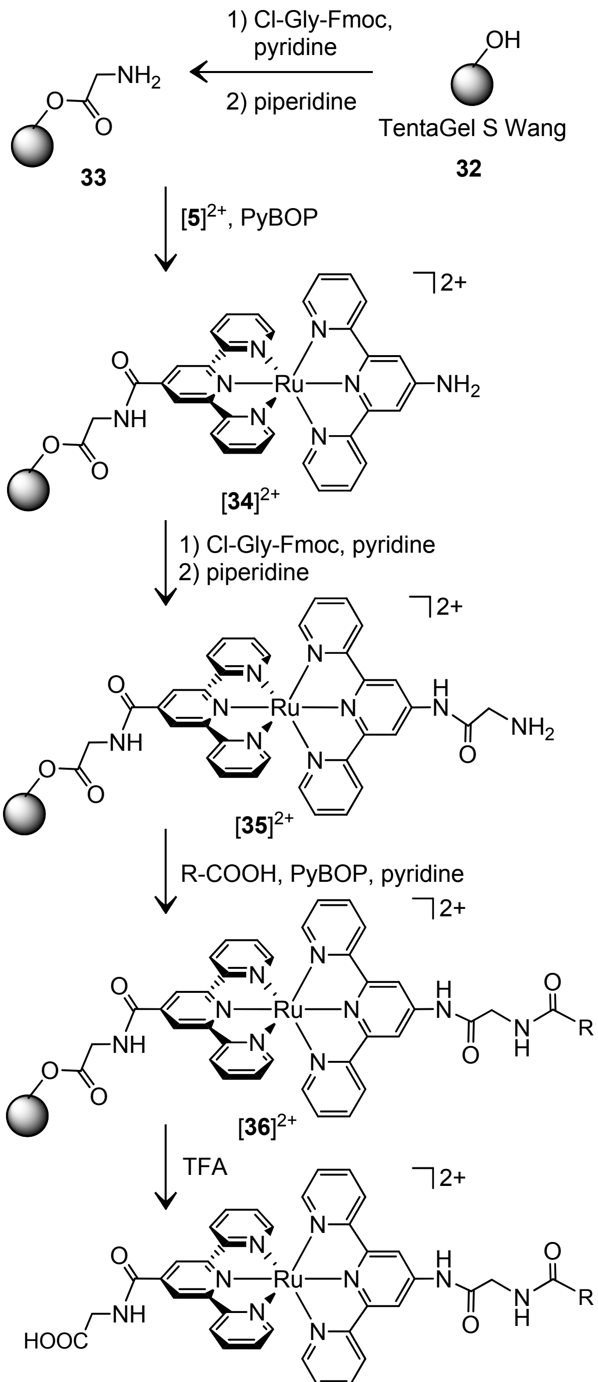

Figure 15. Solid-phase peptide synthesis including the ruthenium(II) amino acid [**5**]$^{2+}$.[18]

6 Applications

Polypyridine complexes of ruthenium(II), especially $[\mathrm{Ru(bpy)_3}]^{2+}$ type complexes, are suitable compounds for directional energy transfer and can act as donors and acceptors for photoinduced energy transfer.[98] Bis(tridentate) complexes of ruthenium(II) have been incorporated into energy transfer systems using ethynyl spacers between the $[\mathrm{Ru(tpy)_2}]^{2+}$ donor and thiophene units as acceptors.[99] Hempel and Heinze have connected the donor-acceptor substituted complex $[\mathbf{5}]^{2+}$ to organic chromophores by amide bridges via SPPS with a different number of glycine units in between (Figure 16). The use of one or none glycine unit with $n = 0$ ($[\mathbf{38}]^{2+}$) or 1 ($[\mathbf{39}]^{2+}$) allows for coplanarity of the coumarin dye and the adjacent tpy ligand which is favorable for efficient energy transfer via a Dexter mechanism.[18] In the case of short bridges excitation of the coumarin ($[\mathbf{39}]^{2+}$, $n = 1$, $\lambda_{\mathrm{exc}} = 422$ nm) induces energy transfer to the $[\mathrm{Ru(tpy)_2}]^{2+}$ core while the coumarin fluorescence is efficiently quenched.[18,20] Breivogel and Heinze measured excitation emission matrices of complexes $[\mathbf{39}]^{2+}$ – $[\mathbf{41}]^{2+}$. The excitation emission matrix of $[\mathbf{39}]^{2+}$ clearly shows that upon excitation at $\lambda_{\mathrm{exc}} = 400 - 500$ nm, emission occurs at $\lambda_{\mathrm{em}} = 670$ nm which corresponds to the wavelength of the coumarin-free reference $[\mathbf{41}]^{2+}$ (Figure 17). For a longer bridge ($[\mathbf{40}]^{2+}$, $n = 2$, Figure 16) efficient energy transfer is no more feasible. Excitation of the organic coumarin chromophore leads to fluorescence of the coumarin at $\lambda_{\mathrm{exc}} = 465$ nm while emission from the $[\mathrm{Ru(tpy)_2}]^{2+}$ core is not observed (Figure 17).[20]

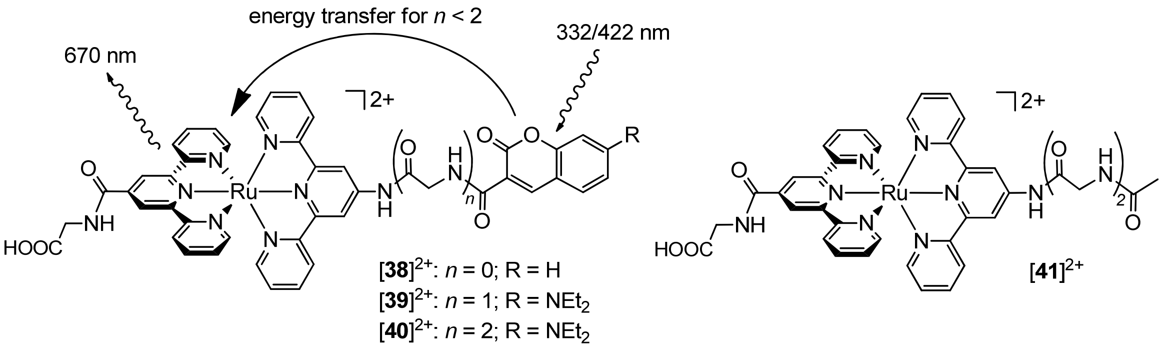

Figure 16. Bis(terpyridine) ruthenium(II) complexes for studying energy transfer.[18,20]

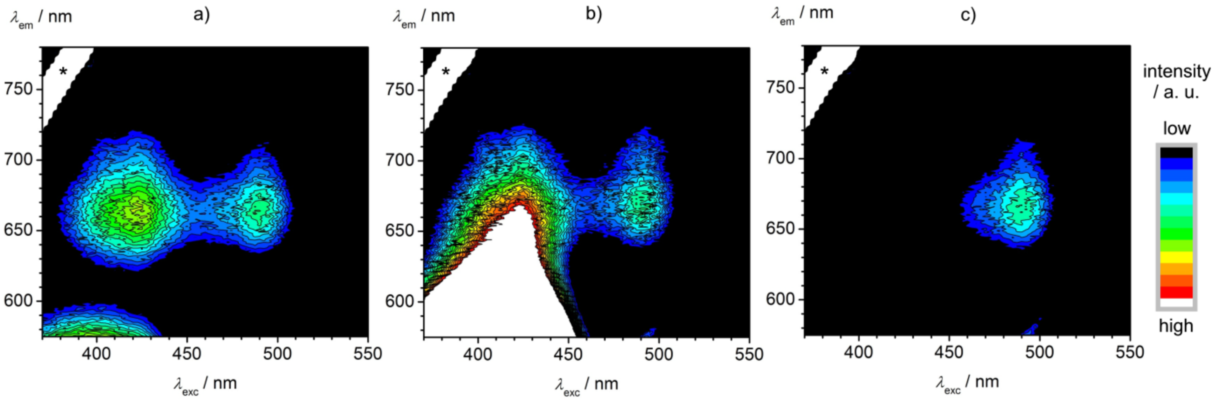

Figure 17. Excitation emission matrices of a) [**39**]$^{2+}$ (n = 1), b) [**40**]$^{2+}$ (n = 2) and c) reference complex [**41**]$^{2+}$. The color bar indicates the emission intensity. * = 2λ_{exc}.

Amino acid [**5**]$^{2+}$ has been used as chromophore in a donor-chromophore-acceptor electron transfer nanocomposite by zur Borg, Domanski, Breivogel, Bürger, Heinze and Zentel in order to probe light-induced charge separation.[100] As electron donor a polymer with triphenylamine units and as electron acceptor ZnO nanorods were used. [**5**]$^{2+}$ was converted to tripeptide [**42**]$^{2+}$ by a SPPS and the amino group of [**42**]$^{2+}$ forms an amide bond with the pentafluorophenol activated carboxylic acid of block-copolymer **43** to give [**44**]$^{(2m)+}$ (Figure 18). The free COOH group in [**44**]$^{(2m)+}$ acts as anchor to ZnO nanorods. Upon excitation of the [Ru(tpy)$_2$]$^{2+}$ chromophore by irradiation (λ_{exc} = 488 nm) into its absorption band (λ_{max} = 498 nm) excited electrons are injected into the ZnO nanorods and electron holes are generated in the triphenylamine-containing polymer. The phosphorescence of the [Ru(tpy)$_2$]$^{2+}$ core was completely quenched. Under irradiation a significant change of the surface potential of the polymer-coated nanorods is observed via Kelvin probe force microscopy and confirms the positive charge in the polymer.[100]

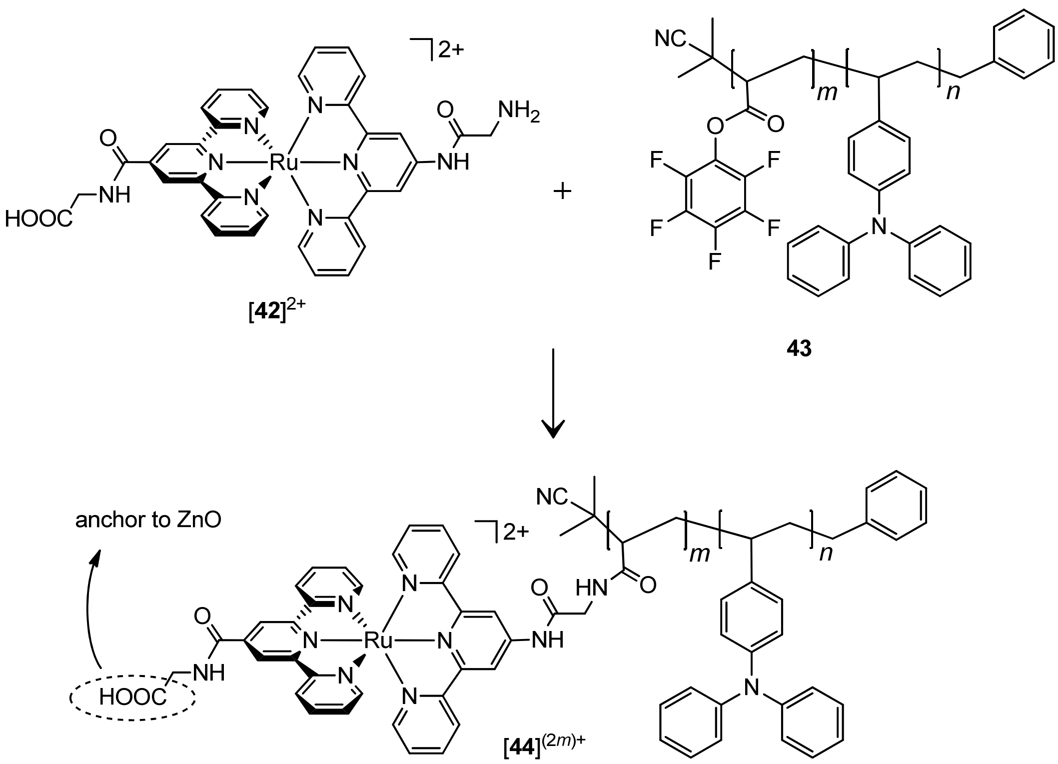

Figure 18. Synthesis of [**44**]$^{(2m)+}$ by coupling of [**42**]$^{2+}$ to **43** ($n \approx 50$, $m \approx 10$).[100]

Bis(tridentate) complexes [**5**]$^{2+}$, [**25**]$^{2+}$, [**26**]$^{2+}$, [**27**]$^{2+}$, [**45**]$^{2+}$ and [**46**]$^{2+}$ (Figure 2, 11 and 19) have been adsorbed to TiO_2 and tested as sensitizers in dye-sensitized solar cells with an I^-/I_3^- redox electrolyte by Breivogel and Heinze. The complexes feature absorption spectra comparable to the one of the standard ruthenium(II) sensitizer N719. However, the twofold positive charge of the complexes increases the I_3^- concentration near the TiO_2 electrode due to electrostatic interactions favoring electron recombination. Consequently, low cell power conversion efficiencies up to $\eta = 0.26\%$ were obtained with the twofold positively charged complexes. In contrast, N719 is twofold negatively charged and reaches a power conversion efficiency of $\eta = 5.03\%$ in cells under the same conditions.[78] The charge of bis(tridentate) complexes of ruthenium(II) can be reduced by introduction of negatively charged ligands such as pyrazolyl or cyclometalated ligands such as in complexes **52** and **53** reaching power conversion efficiencies up to $\eta = 10.7\%$ (Figure 23).[101–103] Another approach would be the use of other redox electrolytes such as positively charged metal complexes, e.g. $[Co(4,4'\text{-}({}^tBu)_2bpy)_3]^{2+/3+}$.[104]

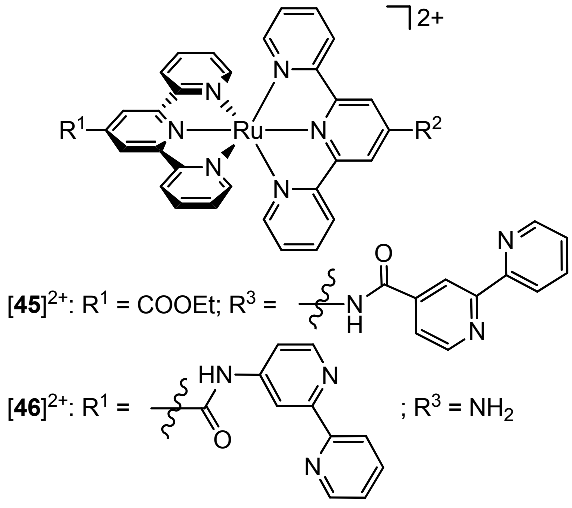

Figure 19. Complexes [**45**]$^{2+}$ and [**46**]$^{2+}$.[77,105]

Breivogel and Heinze employed bis(tridentate) complexes [**4**]$^{2+}$, [**21**]$^{2+}$ and [**22**]$^{2+}$ as emitters in light-emitting electrochemical cells (LECs). A simple device structure of ITO/PEDOT:PSS/ruthenium(II) complex/Ag is used and characterized by AFM (ITO = indium tin oxide, PEDOT = 3,4-ethylenedioxythiophene, PSS = poly(styrenesulfonate), AFM = atomic force microscopy). Deep red light emission up to a maximum emission wavelength of 755 nm is achieved. To the best of our knowledge this is the lowest emission energy for LECs containing bis(tridentate) ruthenium(II) complexes.[7,8,106] For such a low emission energy the energy gap law[73,87,88] predicts enhanced radiationless deactivation of the excited state explaining the small external quantum efficiencies. However, dilution of the ruthenium(II) complexes in PMMA enhances the external quantum efficiencies due to less radiationless excited state deactivation.[107]

7 Dye-Sensitized Solar Cells

7.1 Basic Principles

Dye-sensitized solar cells (DSSCs) were first reported in 1991 by O'Regan and Grätzel and provide a low cost alternative to widely used silicon-based solar cells.[2–4] The working principle and the schematic structure of a conventional DSSC are depicted in Figure 20. A DSSC consists of a mesoporous semiconductor layer of TiO_2 (anatase) on a transparent anode such as fluorine-doped tin oxide (FTO). Molecular sensitizers are adsorbed on top of the TiO_2 particles. The porous TiO_2 structure ensures a high surface area which allows for efficient light harvesting. The porous TiO_2 network is penetrated by a liquid redox electrolyte, typically the I^-/I_3^- system in CH_3CN, which is in contact to the cathode. When light passes through the transparent anode a sensitizer is excited ($S \rightarrow S^*$) and injects an electron into TiO_2 (k_1). The electrons percolate the TiO_2 network and are collected at the anode (k_2). The oxidized sensitizer (S^+) is regenerated by the redox electrolyte (k_3). The redox electrolyte diffuses to the cathode where it is reduced (k_4). The maximum attainable voltage V_{OC} is given by the potential difference between the Fermi level of TiO_2 and the redox potential of the electrolyte, hence it is independent of the sensitizer.[4]

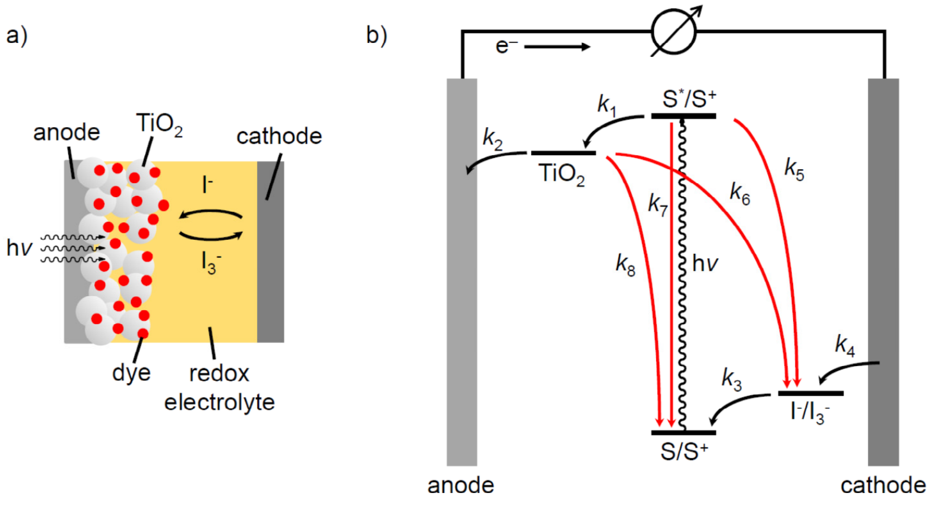

Figure 20. a) Schematic device structure and b) working principle of a DSSC. S denotes a sensitizer.

The efficiency η of a DSSC is defined by equation 1 with P_{out} being the maximum power per area that can be extracted and P_{in} being the power per area of the irradiated light.

(1) $$\eta = \frac{P_{\mathrm{out}}}{P_{\mathrm{in}}}$$

Usually, efficiencies are referred to standardized conditions with an irradiation power of P_{in} = 1000 W m^{-2} and a sample temperature of 25 °C. The standardized irradiation spectrum is the air mass (AM) 1.5 spectrum (Figure 21).[108] The factor "1.5" indicates that the solar light passes the thickness of 1.5 atmospheres which corresponds to a zenith angle of 48.2°.

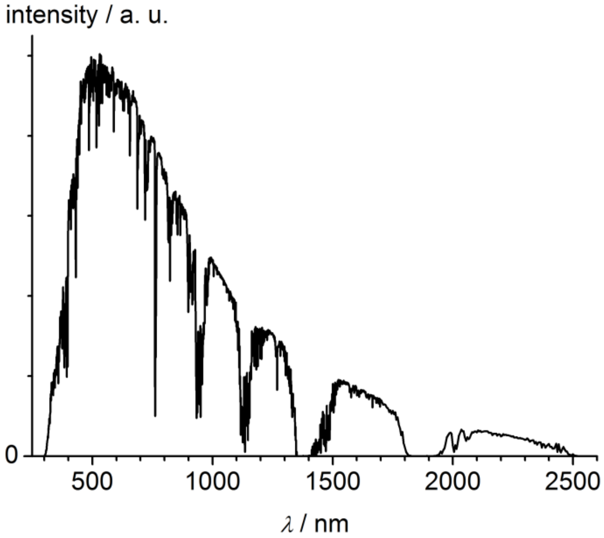

Figure 21. AM 1.5 spectrum of the sunlight reaching the surface of the earth under a zenith angle of 48.2°.[109]

Figure 22 shows the typical behavior of a current density-voltage (*I-U*) curve of a DSSC. I_{sc} is the maximum current density under short circuit conditions and U_{oc} is the maximum photovoltage at open circuit conditions. At a certain point, the maximum power point (mpp), the product of the current density and the photovoltage is maximal. This point defines the maximum output power P_{out} (equation 2).

(2) $$P_{\mathrm{out}} = U_{\mathrm{mpp}} \times I_{\mathrm{mpp}}$$

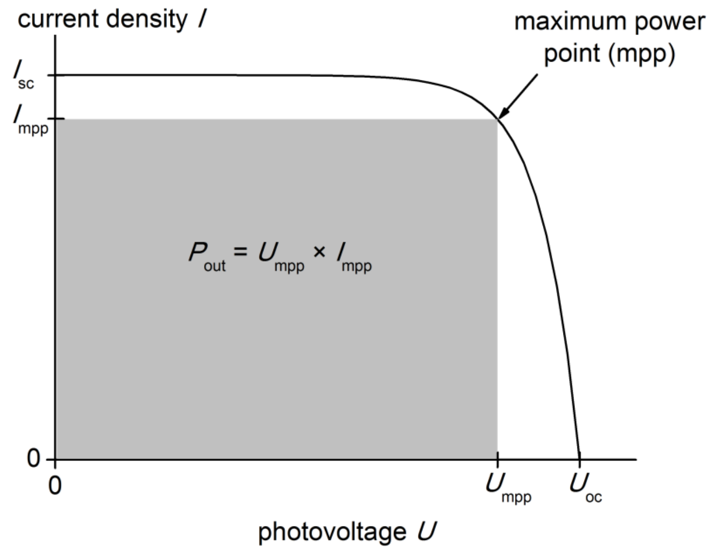

Figure 22. Current density-voltage (*I*-*U*) curve and indication of the short circuit current density (I_{sc}), the current density at the maximum power point (I_{mpp}), the open circuit voltage (U_{oc}) and the voltage at the maximum power point (U_{mpp}). The grey rectangle illustrates the maximum output power P_{out}.

The fill factor *ff* of a DSSC is given by equation 3 and describes the shape of the *I*-*U* curve. A rectangular shape of the *I*-*U* curve corresponds to a fill factor of *ff* = 1.

$$(3) \qquad ff = \frac{U_{mpp} \times I_{mpp}}{U_{oc} \times I_{sc}}$$

The incident photon-to-current conversion efficiency IPCE(λ) is defined by the number of collected electrons under short circuit conditions per number of incident photons at a given wavelength λ (equation 4).

$$(4) \qquad \mathrm{IPCE} = \frac{\#\,\text{electrons out}}{\#\,\text{photons in}} = \frac{\frac{I_{sc}(\lambda)}{\mathrm{e}}}{\frac{P_{in}(\lambda)}{\mathrm{h}\nu}} = \frac{\mathrm{hc}}{\lambda \mathrm{e}} \times \frac{I_{sc}(\lambda)}{P_{in}(\lambda)}$$

h denotes the Planck constant, *c* the velocity of light and *e* the elementary charge. Despite the defined DSSC parameters (equation 1 – 4) DSSC measurements of different laboratories are not directly comparable to each other because a manifold of other conditions is not standardized such as cell building procedures, solvents, additives, chemical and morphological nature of TiO_2, electrolyte compositions and electrode materials. For a better comparison standard dyes such as N719 should generally be employed as a reference under the used conditions and compared to the investigated dyes.[108]

7.2 Dye Design for DSSCs

Dyes for DSSCs should have a broad and intense absorption in order to efficiently harvest the sun light. Dyes should be photochemically, thermally and electrochemically stable to avoid degradation. For the immobilization on the nanoporous semiconductor anchor units such as carboxylic acids are advantageous. The LUMO of the dye needs to be higher in energy than the conduction band of TiO_2 while the HOMO of the dye needs to be lower in energy than the potential of the redox electrolyte. A high electronic directionality of the excited states is necessary for efficient electron injection into TiO_2. This means the HOMO of the dye is located remote from TiO_2 and the LUMO is in close contact to TiO_2.[3] Polypyridine complexes of ruthenium(II) have been shown to be excellent sensitizers for DSSCs. Two of the best performing and most prominent complexes are the so called black dye $(Bu_4N)_3[Ru(Htctpy)(NCS)_3]$ (**47**)[110] and N719 $(Bu_4N)_2[Ru(Hdcbpy)_2(NCS)_2]$ (**48**)[111,112] (Figure 23) reaching DSSC efficiencies of η = 10.4 and 11.2% under full air mass 1.5 (AM 1.5), respectively (tctpy = 4,4',4''-tricarboxy-2,2';6',2''-terpyridine, dcbpy = 4,4'-dicarboxy-2,2'-bipyridine).[4] Both, N719 and the black dye feature carboxylic acid/carboxylate anchor groups with a LUMO located on the anchoring ligand while the HOMO is located on the ruthenium center and the remote NCS$^-$ ligands.[78,113]

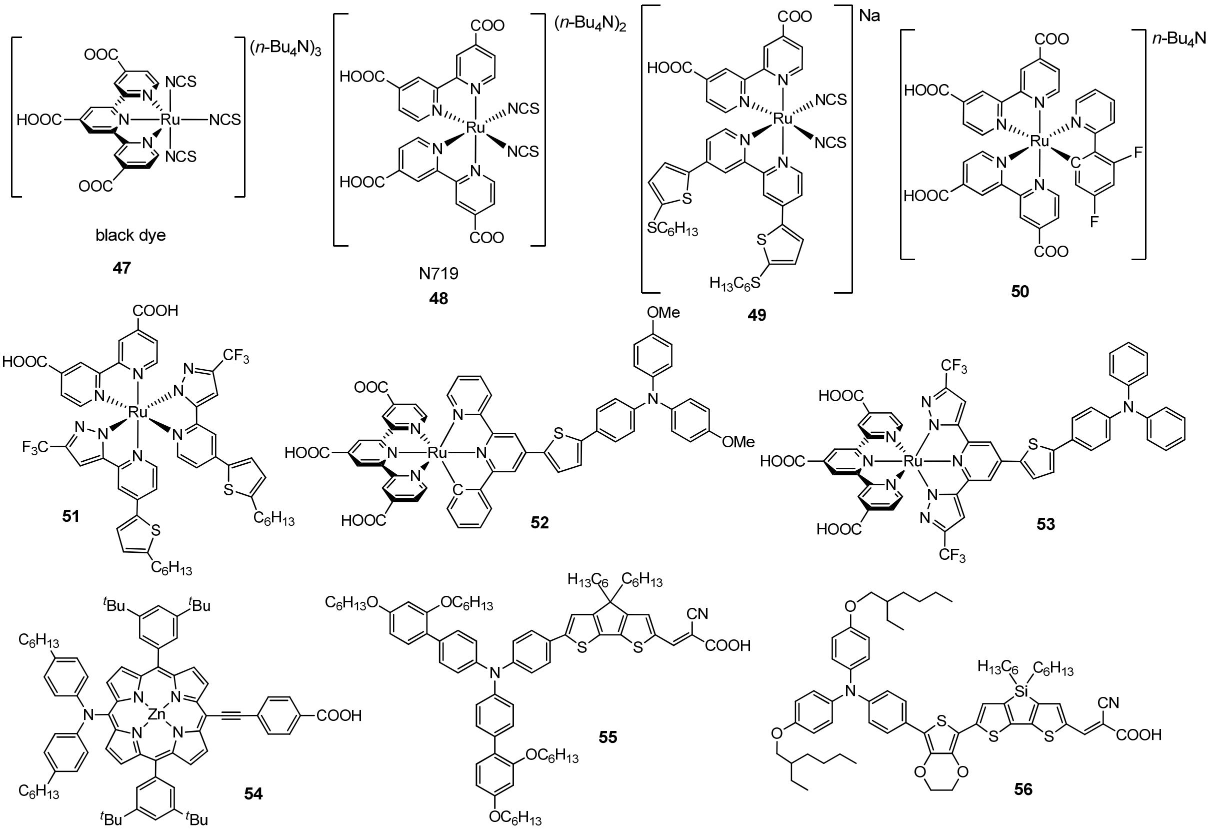

Figure 23. DSSC sensitizers **47** – **56**.

In order to improve DSSC characteristics a manifold of different design strategies for sensitizers has emerged in the last two decades. Complex **49** (Figure 23) is a derivative of N719 with thiophene units which extend the conjugated systems and significantly increase the extinction coefficients.[114] This is beneficial as more photons can be harvested by this dye compared to N719. In addition, the long alkyl chains prevent interfacial electron recombination leading to cell efficiencies of η = 11.4% under full AM 1.5.[4,114] Monodentate ligands such as NCS^- and pyridine are regarded as a drawback concerning the long term stability of sensitizers. Thermal- and photo-induced isomerization and ligand exchange has been reported for monodentate ligands leading to dye species with lower cell efficiencies.[115–122] Attempts to avoid monodentate ligands include the use of tris(bidentate) and bis(tridentate) complexes such as **50** (Figure 23).[4,123,124] **50** can also be seen as a derivative of N719 where both NCS^- ligands have been replaced by a bidentate cyclometalated 2-phenylpyridine ligand. DSSCs with **50** reach efficiencies of η = 10.1% under full AM 1.5.[4,124] Typically, the cyclometalated ligand contributes to the HOMO of ruthenium(II) complexes while the LUMO resides on the anchor ligand. A favorable electronic directionality is thus induced when the anchor ligand is situated opposite to the cyclometalated ligand.[125,126] Complex **51** (Figure 23) features a dcbpy ligand and two 2-pyridylpyrazole ligands. DSSCs with this complex reach efficiencies of η = 9.5% under full AM 1.5.[127] However, also complexes with bidentate ligands such as bpy or 4,4'-bi-1,2,3-triazolate are prone to photo-induced ligand loss and isomerization.[78,128,129] Furthermore, tris(bidentate) complexes of ruthenium(II) are chiral which complicates synthetic procedures as discussed above.[48–50] In contrast, bis(tridentate) complexes are achiral and feature higher stability constants compared to their bidentate analogues.[52,53] Bis(tridentate) complexes of ruthenium(II) have already been incorporated into DSSCs. Berlinguette et al. have employed complex **52** (Figure 23) featuring a tctpy anchor ligand and a cyclometalated pbpy ligand with an efficiency of η = 8.0% (pbpy = 6-phenyl-2,2'-bipyridine). The appended triarylamine moiety avoids electron recombination because after injection of an electron into TiO_2 the positive charge is shifted towards the triarylamine moiety and away from the TiO_2 surface.[101] Chi et al. reported the neutral bis(tridentate) ruthenium(II) complex **53** (Figure 23) with a dianionic donor ligand (2,6-bis(5-pyrazolyl)pyridine) and a tctpy acceptor ligand with DSSC efficiencies up to η = 10.7%.[102,103] Again, the thiophene unit in **52** and **53** extends the conjugated system and increases the extinction coefficients. Bis(tridentate) coordination of ruthenium(II) leads to more robust sensitizers concerning photostability and long term stability of DSSCs.[3,78,130,131]

To date, the highest DSSC efficiency of η = 12.3% could be obtained with a zinc porphyrin (**54**) in combination with **55** as organic cosensitizer (Figure 23).[132] Also metal-free all-organic sensitizers alone can reach high DSSC performances with η = 10.1% being the top efficiency obtained with dye **56** (Figure 23).[4]

Future work about DSSCs is headed towards solid-state DSSCs. In these cells the liquid electrolyte is substituted by a solid hole transporting material, typically spiro-OMeTAD (2,2'-7,7'-tetrakis(*N*,*N*-di-*p*-methoxyphenylamine)-9,9'-spirobifluorene). Solid-state DSSC are more robust than DSSCs containing a liquid electrolyte because of leaking problems with the liquid electrolyte. However, solid hole transport materials have several drawbacks such as low hole mobility, increased charge recombination between the semiconductor and the hole transporting material and low interfacial contact areas between dye molecules and the solid electrolyte resulting from incomplete penetration of the hole transport material into the pores of the semiconductor.[48] Nevertheless, new techniques in solid-state sensitized solar cells are very promising. The replacement of molecular sensitizers by perovskite $(CH_3NH_3)(PbX_3)$ (X = I, Cl) has lead to new record efficiencies of 14 – 15%.[133–136]

8 Light-Emitting Electrochemical Cells

Light-emitting electrochemical cells (LECs) were introduced in 1995 by Pei and provide a low-cost alternative to conventional organic light-emitting devices (OLEDs).[137,138] The main difference between OLEDs and LECs is the nature of the light-emitting layer which is neutral in OLEDs and ionic in LECs.[5,139–143] In principle, an LEC can simply consist of an ionic emitting layer between two electrodes (Figure 24a). Typically, the anode material is transparent (e.g. indium tin oxide) in order to enable light output while the cathode material can be nontransparent and reflective such as silver. When a voltage is applied ions in the emitting layer start to migrate. Cations migrate towards the cathode and anions towards the anode creating ionic layers at the electrodes (Figure 24b). These charge layers efficiently lower the injection barriers for electrons and holes at the interface which allows for low turn-on and driving voltages. Electrons and holes recombine in the emitting layer forming excited electron-hole pairs, called excitons which can degrade by emitting light. In contrast, high charge injection barriers are typically present in OLEDs due to the neutral emitting layer leading to high turn-on and driving voltages. Therefore OLEDs require additional ionic layers enabling electron and hole injection and controlling electron and hole transport, thus making OLED structures more complicated and cost-intensive (Figure 24a). Furthermore, OLEDs require air-sensitive low work function metals as cathode materials such as calcium or barium in order to allow electron injection which again raises fabrication costs due to expensive encapsulation. LECs offer the possibility to be essentially independent of electrode materials due to the ionic emitting layer.[5,139–143]

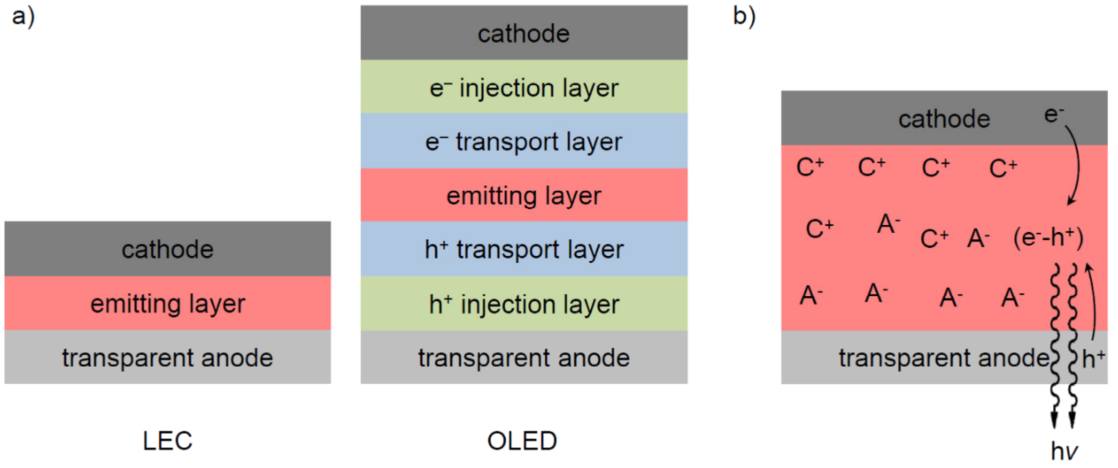

Figure 24. a) Structure of an LEC and a conventional OLED. b) Working principle of an LEC. C^+ denotes a cation and A^- an anion.

Important physical quantities in LECs are the internal quantum efficiency (IQE) which is the ratio of the number of generated photons per number of electrons passing through the cell (equation 5).

$$\text{(5)} \qquad \mathrm{IQE} = \frac{\#\,\text{generated photons}}{\#\,\text{electrons}}$$

Not all generated photons leave the cell due to photon reabsorption at the cathode, the emitting layer or the anode, reflection at the interface between the anode and the emitting layer or other loss mechanisms. The external quantum efficiency EQE defines the ratio of the number of photons coming out of the cell per number of electrons passing through the cell (equation 6).

$$\text{(6)} \qquad \mathrm{EQE} = \frac{\#\,\text{photons out}}{\#\,\text{electrons}}$$

A human eye has three color receptors. The normalized sensitivity curves X'(λ), Y'(λ) and Z'(λ) of these receptors are illustrated in Figure 25.[144]

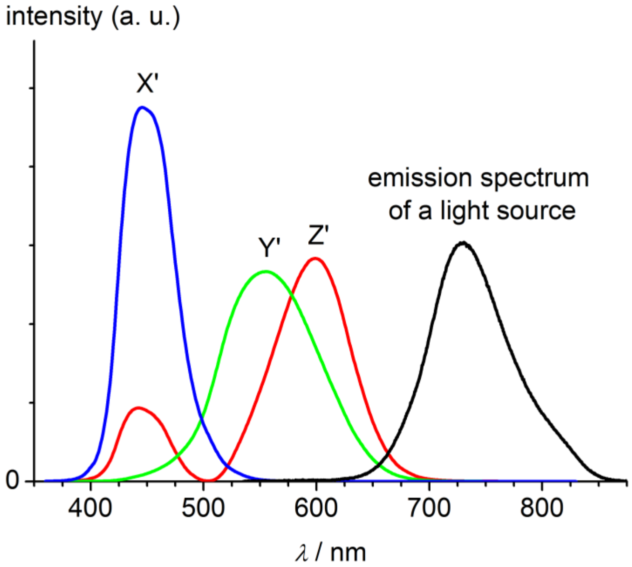

Figure 25. Integral-normalized sensitivity curves X'(λ), Y'(λ) and Z'(λ) of the three color receptors of the human eye.

The color impression of an emission spectrum to the standard human eye can be defined by the CIE coordinates x and y (CIE = commission international de l'éclairage). x and y are defined by equations 7.

$$(7) \qquad x = \frac{X}{X+Y+Z}; \qquad y = \frac{Y}{X+Y+Z}; \qquad z = \frac{Z}{X+Y+Z}; \qquad x+y+z=1$$

X, *Y*, and *Z* denote the overlap of the emission spectrum with the sensitivity curve X'(λ), Y'(λ) and Z'(λ), respectively. The sum of the three resulting coordinates *x*, *y* and *z* equals 1. For given values of *x* and *y* the value of *z* is predetermined. Therefore, the coordinates can be reduced to *x* and *y*. Figure 26 illustrates a chromaticity diagram which is the plot of *x* versus *y* and the corresponding colors. At $x = y = z = ⅓$ the color impression is white. Outside of the colored area there is still a color impression to the human eye. The color merely appears with lower intensity.

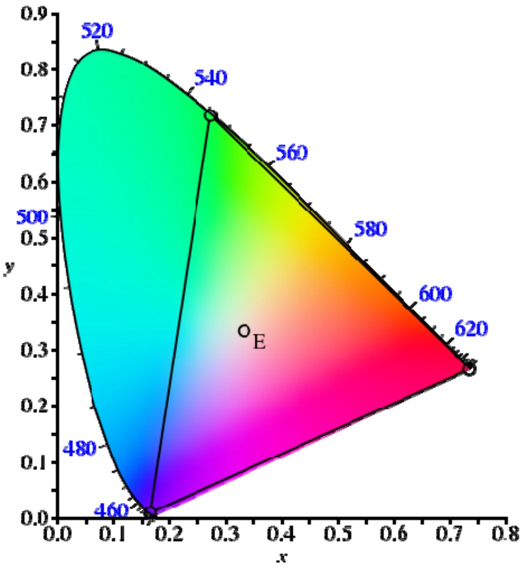

Figure 26. Chromaticity diagram.[145]

While CIE coordinates define the color impression of a spectrum to the human eye, the luminance *L* describes how bright a light source appears to the human eye. The sensitivity of the human eye is wavelength-dependent and is described by the human eye response curve V(λ) (Figure 27) with a maximum at $\lambda_{\max}$ = 555 nm. Two light sources might send out the same amount of photons but with different energy (spectrum 1 and 2 in Figure 27). The light source with spectrum 1 has a larger spectral overlap with the human eye response curve than the light source with spectrum 2. Therefore, the light source with spectrum 1 appears brighter to the human eye than the light source with spectrum 2.

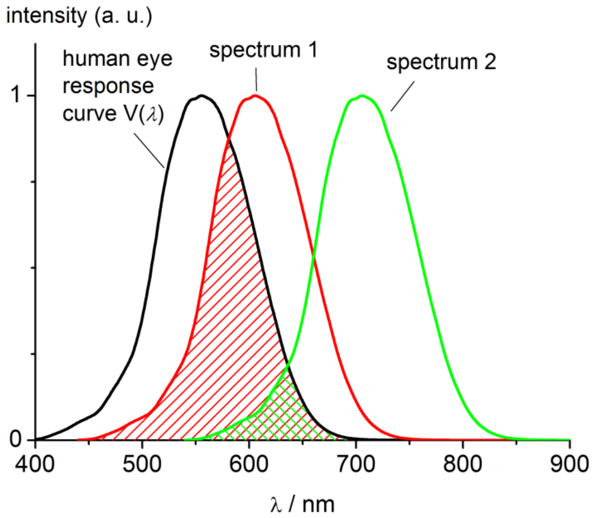

Figure 27. The human eye response curve V(λ) has a larger overlap with spectrum 1 (red) than with spectrum 2 (green). The overlap is illustrated by red and green hatchures, respectively.

The luminance L is defined by equation 8 where K_m = 683 lm W^{-1} at 555 nm, I is the current density, R is the distance between the LEC and the photodiode, A_{LEC} is the area of the limiting aperture, $A_{photodiode}$ is the area of the photodiode, $S_{emission}(\lambda)$ is the emission spectrum and $S_{responsivity}(\lambda)$ is the responsivity of the photodiode.[146,147]

$$(8) \qquad L = \frac{K_m \cdot I_{photodiode} \cdot R^2}{A_{LEC} \cdot A_{photodiode}} \times \frac{\int_{360nm}^{830nm} V(\lambda) \cdot \frac{S_{emission}(\lambda)}{S_{responsivity}(\lambda)} d\lambda}{\int_{360nm}^{830nm} S_{emission}(\lambda)\, d\lambda}$$

Simple spin statistics predict that 25% of the excitons are singlet excitons and 75% are triplet excitons. However, organic materials can only convert singlet excitons into photons while triplet excitons only produce heat.[148–151] The first LECs contained organic polymers as emitters, thus limiting the IQE to a theoretical maximum of 25%.[137,138] Instead, when transition metal complexes are used as emitters spin-orbit coupling enables the generation of photons from both singlet and triplet excitons which raises the theoretical limit for the IQE up to 100%. The first LEC with a transition metal complex was introduced by Lee in 1996 using a $[Ru(phen)_3]^{2+}$ derivative as emitter.[152] Among ruthenium complexes, the most efficient LECs (EQE = 6.4%) were obtained by using $[Ru(bpy)_3]^{2+}$ as emitter.[153] However, the chirality of substituted tris(bidentate) complexes of ruthenium(II) is problematic as discussed above. Furthermore, $[Ru(bpy)_3]^{2+}$ type complexes suffer from ligand loss in LECs which leads to degradation products in the presence of water such as $[Ru^{II}(bpy)_2(H_2O)_2]^{2+}$ and the oxido-bridged dimer $[\{Ru^{III}(bpy)_2(H_2O)\}_2O]^{4+}$.[143,154-156] In order to enhance the emitter stability bis(tridentate) complexes of ruthenium(II) have already been used in LECs.[7,8,107] However, EQE values for LECs with bis(tridentate) ruthenium(II) complexes remain low which is attributed to the lower solution quantum yields of these complexes compared to $[Ru(bpy)_3]^{2+}$ as discussed above.

Reasons for low EQEs in LECs are manifold: 1) Intrinsic properties of the emitter molecules such as too long luminescence lifetimes leading to saturation effects, low solution quantum yields due to deactivation via ^{3}MC states and vibrational coupling of the excited state to the ground state. 2) Energy transfer to impurities such as O_2. 3) The wrong choice of cell components and high applied biases can lead to charge imbalance, saturation effects due to triplet-triplet annihilation and losses due to inefficient light outcoupling (self-absorption of the emitted light, reflection at the transparent electrode).[157] Self-quenching of excited emitter molecules can be decreased by passivation with sterically demanding substituents[6,158] or dilution in polymeric matrices such as PMMA (PMMA = poly(methylmethacrylate).[107]

To date research for ionic emitters for LECs is focused on charged iridium(III) complexes such as $[Ir(ppy)_2(bpy)]^+$ ([**57**]$^+$, Figure 28).[140] Iridium(III) complexes have a stronger ligand field compared to ruthenium(II) complexes as the ligand field strength increases with the quantum number in the row 3d < 4d < 5d. Additionally, the higher charge of iridium(III) compared to ruthenium(II) also strengthens the ligand field of the former. The strong ligand field of iridium(III) complexes leads to less accessible dissociative ^{3}MC states and higher photostabilities compared to ruthenium(II) complexes. The lower accessibility of the ^{3}MC states also reduces radiationless deactivation into the ground state. Thus, solution quantum yields of iridium(III) complexes are generally higher than those of comparable ruthenium(II) complexes.[140] For example, the use of neutral *fac*-$Ir(ppy)_3$ (**58**, Figure 28) as emitter in OLEDs can be explained by its high room temperature solution quantum yield of $\Phi = 97\%$ (ppy = 2-phenylpyridine).[159] Furthermore, iridium(III) complexes of the $[Ir(ppy)_2(bpy)]^+$ type have spatially separated frontier orbitals with the HOMO residing on the cyclometalated ppy ligands and the LUMO on the bpy ligand. This offers the possibility to separately fine tune HOMO and LUMO energies by simple ligand modifications and has lead to iridium(III) complexes with emission maxima in the entire visible spectrum.[140] However, iridium is rare and expensive. The amount of iridium in the earth crust is around 1 ppb and the current price for 1 g iridium (99.9%) is around 70 €.

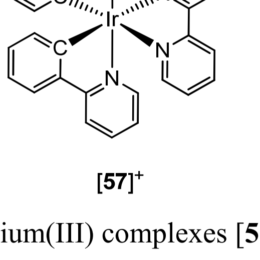

[57]$^+$

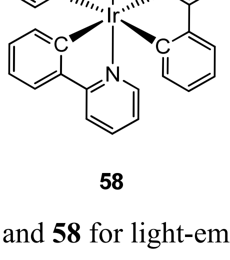

58

Figure 28. Iridium(III) complexes [**57**]$^+$ and **58** for light-emitting devices.

9 Publications and Manuscripts

9.1 Contribution of Aaron Breivogel to the Following Manuscripts and Publications

Prior to reproduction of the manuscripts and publications of my doctoral thesis I hereby clarify which contributions stem from other collaborators and which contributions stem from my own work. My contributions will be indicated by the initials "AB". Compounds mentioned herein refer to the compound numbering in the respective manuscript or publication.

Thermal and Photo Reactivity of a Donor-Acceptor-Substituted Bis(terpyridine) Ruthenium(III) Complex in Acidic Solutions: all ligand and complex syntheses, all spectroscopic and analytical measurements (NMR, MS, UV/Vis, EPR) and all DFT calculations were conducted by AB. EPR simulations were performed by [redacted] (group of Prof. Dr. [redacted]). The manuscript was written by AB.

Dinuclear Bis(terpyridine)ruthenium(II) Complexes by Amide Coupling of Ruthenium Amino Acids: Synthesis and Properties: the ruthenium complexes **1a** and **1b** were synthesized by AB and Dr. [redacted] (group of Prof. Dr. [redacted]). Ruthenium complexes **2a**, **2b**, **2c**, **3a** and **3b** were synthesized and spectroscopically and analytically characterized by Dr. [redacted] (group of Prof. Dr. [redacted]). All oxidation reactions (including UV/Vis spectroscopic measurements) and all DFT calculations were performed by AB. The manuscript was written by Prof. Dr. [redacted].

Light-induced Charge Separation in a Donor-Chromophore-Acceptor Nanocomposite Poly[TPA-Ru(tpy)$_2$]@ZnO: the ruthenium complex **A** was synthesized and spectroscopically and analytically characterized by AB. Polymer syntheses and characterizations were conducted by Dr. [redacted] (group of Prof. Dr. [redacted]). Emission spectroscopy and quantum yield determinations were done by AB and Dr. [redacted]. KPFM measurements were conducted by [redacted] (group of Dr. [redacted]). The manuscript was written by Dr. [redacted] (~ 60%), [redacted] (~ 20%) and AB (~ 20%).

A Heteroleptic Bis(tridentate)ruthenium(II) Polypyridine Complex with Improved Photophysical Properties and Integrated Functionalizability: all novel compounds were synthesized and spectroscopically and analytically characterized by AB. All DFT calculations were conducted by AB. The crystal structure was solved by Dr. [redacted] (group of Prof. Dr. [redacted]).

The emission lifetimes were measured by Dr. [redacted] (group of Dr. [redacted]). The manuscript was written by AB.

Excited State Tuning of Bis(tridentate) Ruthenium(II) Polypyridine Chromophores by Push-Pull Effects and Bite Angle Optimization: A Comprehensive Experimental and Theoretical Study: all novel compounds were synthesized and spectroscopically and analytically characterized by AB. The crystal structures were solved by Dr. [redacted] (group of Prof. Dr. [redacted]). The emission lifetimes were measured by Dr. [redacted] and [redacted] (group of Dr. [redacted]). EPR simulations were performed by [redacted] (group of Prof. Dr. [redacted]). All DFT calculations were conducted by AB. The manuscript was written by AB.

Push-Pull Design of Bis(tridentate) Ruthenium(II) Polypyridine Chromophores as Deep Red Light Emitters in Light-Emitting Electrochemical Cells: all ruthenium complexes were synthesized by AB. After instruction from [redacted], [redacted] (both from the group of Prof. Dr. [redacted]) and Prof. Dr. [redacted] the LECs were built and characterized by AB. AFM measurements were performed by [redacted] (group of Prof. Dr. [redacted]). All DFT calculations were conducted by AB. The manuscript was written by AB.

Anchor-Functionalized Push-Pull-Substituted Bis(tridentate) Ruthenium(II) Polypyridine Chromophores: Photostability and Evaluation as Photosensitizers: complexes $[\mathbf{1}]^{2+}$ – $[\mathbf{4}]^{2+}$ were synthesized and spectroscopically and analytically characterized by AB. Complexes $[\mathbf{5}]^{2+}$ and $[\mathbf{6}]^{2+}$ were synthesized and spectroscopically and analytically characterized by [redacted] (group of Prof. Dr. [redacted]). All photostability tests of the complexes were performed by AB. After instruction from [redacted] (group of Prof. Dr. [redacted]) and Prof. Dr. [redacted] the DSSCs were built and characterized by AB. The electron recombination lifetimes were measured by [redacted] (group of Prof. Dr. [redacted]). All DFT calculations were conducted by AB. The manuscript was written by AB.

9.2 Thermal and Photo Reactivity of a Donor-Acceptor-Substituted Bis(terpyridine) Ruthenium(III) Complex in Acidic Solutions

A. Breivogel, K. Heinze.

-to be submitted-

Thermal and Photo Reactivity of a Donor-Acceptor-Substituted Bis(terpyridine) Ruthenium(III) Complex in Acidic Solutions

Aaron Breivogel, and Katja Heinze*

Introduction

Polypyridine complexes of ruthenium(II) feature outstanding optical and electrochemical properties[1] and are applied in a manifold of research fields: as sensitizers in dye-sensitized solar cells (DSSCs),[2–5] phosphors in light-emitting electrochemical cells (LECs),[6–9] molecular catalysts for water oxidation,[10,11] hydrogen generation[12–15] and CO_2 reduction[12,14,16] and molecular mixed valence compounds.[17–22] Many complexes possess mono and bidentate ligands such as NCS^-, pyridine and bpy (bpy = 2,2'-bipyridine). The use of these mono and bidentate ligands renders the complexes prone to thermal and photo induced isomerization and ligand exchange reactions leading to undesired side products.[23–30]

Bis(tridentate) ruthenium(II) complexes are known for their high chemical and photochemical stability which is a consequence of the bis(tridentate) chelate effect.[3,5,31–35] $[Ru(tpy)_2]^{2+}$ is the prototype of bis(tridentate) ruthenium(II) complexes (tpy = 2,2';6',2"-terpyridine). However, poor photophysical properties prevent its use in optoelectronic applications. Excited ^{3}MLCT states are efficiently depopulated via low lying ^{3}MC states which leads to radiationless deactivation into the ground state ($\tau \approx 0.1 - 0.2$ ns, $\Phi \leq 0.0007\%$[36], MLCT = metal-to-ligand charge transfer, MC = metal-centered).[37–39] Electron withdrawing substituents on the 4'-position of the tpy ligand lower the energy of the ^{3}MLCT state compared to ^{3}MC state which is beneficial for the excited state properties. Exemplarily, 4'-ester-substituted $[(EtOOC\text{-}tpy)Ru(tpy)]^{2+}$ features a ^{3}MLCT lifetime of $\tau = 32$ ns and a quantum yield of $\Phi = 0.041\%$[36].[8] Addition of an electron donating substituent on the 4'-position of the unsubstituted tpy, e.g. $[(EtOOC\text{-}tpy)Ru(tpy\text{-}NH_2)]^{2+}$ ($[\mathbf{1}^{Et}]^{2+}$, Figure 1) further enhances the lifetime ($\tau = 34$ ns) and the quantum yield ($\Phi = 0.27\%$[36]).[40,41] Such a push-pull strategy is also applied in the combination of an electron accepting tpy ligand and a strong electron donating carbene ligand leading to unprecedented emission lifetimes of up to $\tau = 7.9$ µs and quantum yields of up to $\Phi = 17.3\%$[36].[42] ^{3}MC state energies can also be shifted to higher values by using ligands with ≈ 90° bite angles which allow for a better overlap between metal d orbitals and the pyridine lone pairs.[43–47] $[\mathbf{1}^{Et}]^{2+}$ has been shown to be highly photostable under conditions where tris(bidentate) $[Ru(bpy)_3]^{2+}$ undergoes photoaquation and photoanation.[5] The pronounced push-pull character of $[\mathbf{1}^{Et}]^{2+}$ reduces the HOMO-LUMO gap and shifts the absorption to lower energy compared to unsubstituted $[Ru(tpy)_2]^{2+}$ ($\lambda_{max} = 476$[39] → 502 nm[40]). $[\mathbf{1}^{Et}]^{2+}$ and similar complexes have been used as emitters in LECs and to the best of our knowledge show the lowest emission energy for bis(tridentate)ruthenium(II) emitters in LECs.[9] $[\mathbf{1}^{Et}]^{2+}$ has also been incorporated in energy and electron transfer systems and shows light-induced charge separation in a donor-chromophore-acceptor nanocomposite.[16,48–50] $[\mathbf{1}^{Et}]^{2+}$ can be hydrolyzed to obtain the carboxylic acid $[\mathbf{1}]^{2+}$ (Figure 1).[40] The carboxylic acid functionality can act as anchor to oxidic semiconductors (e.g. TiO_2) and $[\mathbf{1}]^{2+}$ has been tested as photosensitizer in DSSCs.[5] A dinuclear analogue of $[\mathbf{1}]^{2+}$ has been used to study mixed valency in redox asymmetric compounds. However, no electronic communication between Ru^{II} and Ru^{III} has been observed in the mixed valence species.[21,51]

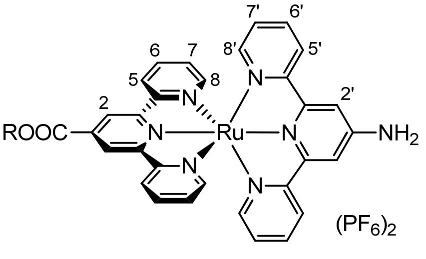

$[\mathbf{1}](PF_6)_2$, R = H
$[\mathbf{1}^{Et}](PF_6)_2$, R = Et

Figure 1. Bis(terpyridine)ruthenium(II) amino acid $[\mathbf{1}](PF_6)_2$ and its ester $[\mathbf{1}^{Et}](PF_6)_2$. Atom numbering for NMR assignments.

The oxidation of $[\mathbf{1}]^{2+}$ to $[\mathbf{1}]^{3+}$ is ruthenium-centered and has been reported previously.[21,43] The stability of oxidized state is particularly important for molecular ruthenium water oxidation catalysts (WOCs) which feature high metal oxidation states during the catalytic cycle.[52] Two main degradation pathways have been reported for molecular ruthenium WOCs: 1) Oxidative ligand degradation[53,54] and the formation of CO and CO_2 as decomposition products of $[Ru(bpy)_3]^{3+}$ and other ruthenium complexes.[52,55,56] 2) Ligand loss: monodentate ligands such as 4-picoline and isoquinoline are prone to ligand dissociation.[55,57] Even bidentate bpy is oxidized to 2,2'-bipyridine-*N*,*N*'-dioxide from $[Ru(tpy)(bpy)(OH_2)]^{2+}$ under catalytic conditions while no dissociation or degradation was observed for the tridentate tpy ligand.[54,56] This indicates that the chelate effect can significantly enhance stabilities of WOCs.[54,57]

Our work aims at maximizing the chelate effect in polypyridine complexes of ruthenium and describes the stability of the bis(tridentate) ruthenium(III) complex $[\mathbf{1}]^{3+}$. The $[\mathbf{1^{Et}}]^{2+/3+}$ couple is stable in the presence of potentially coordinating OH^- ions. However, a different reactivity is observed at low pH (in trifluoricacetic acid, H_2SO_4 and HNO_3) often in conjunction with the oxidant Ce^{IV}. After oxidation of $[\mathbf{1}]^{2+}$ to $[\mathbf{1}]^{3+}$ in acidic media an unexpected back reduction to $[\mathbf{1}]^{2+}$ is observed and described herein by means of UV/Vis, NMR and ESR spectroscopy, electrochemistry, mass spectrometry and DFT calculations.

Discussion

The ruthenium(II) complex $[\mathbf{1}](PF_6)_2$ (Figure 1) can be oxidized with $(NH_4)_2[Ce(NO_3)_6]$ in 0.5 M trifluoroacetic acid in CH_3CN.[21] Upon oxidation the MLCT band at $\lambda_{max} \approx 500$ nm disappears and a LMCT band at $\lambda_{max} \approx 750$ nm appears with a concomitant color change from orange to green.[21] Figure 2 compares experimental UV/Vis spectra of $[\mathbf{1}]^{2+}$ and $[\mathbf{1}]^{3+}$ in 0.125 M H_2SO_4 in H_2O with calculated stick spectra (TD-DFT, IEFPCM, H_2O). The experimental spectrum of $[\mathbf{1}]^{2+}$ features a characteristic MLCT band at $\lambda = 499$ nm ($\varepsilon = 17170$ M^{-1} cm^{-1}). Similarly, when oxidized with $Ce(SO_4)_2$ in 0.125 M H_2SO_4 in H_2O the MLCT band disappears and a LMCT band at $\lambda = 751$ nm ($\varepsilon = 6830$ M^{-1} cm^{-1}) appears.

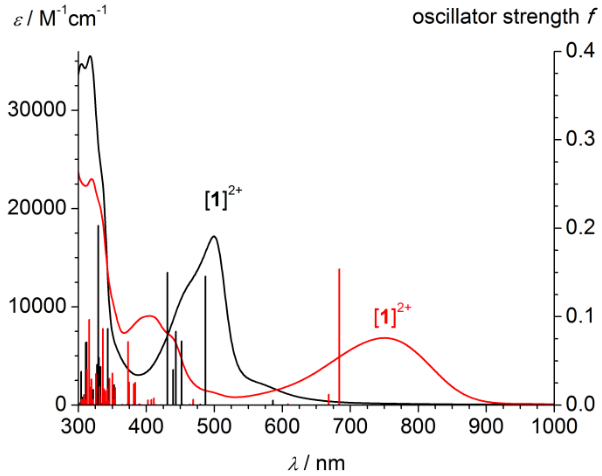

Figure 2. Experimental UV/Vis spectra of $[\mathbf{1}](PF_6)_2$ before (black) and directly after addition of $Ce(SO_4)_2$ (red) in 0.125 M H_2SO_4 in H_2O and calculated stick spectra (TD-DFT, B3LYP/LANL2DZ, IEFPCM, H_2O) of $[\mathbf{1}]^{2+}$ (black) and $[\mathbf{1}]^{3+}$ (red). For experimental details see *Oxidation 1* in the Experimental Section.

The experimental MLCT band of $[\mathbf{1}]^{2+}$ is nicely reproduced by the TD-DFT calculated stick spectrum with transitions at $\lambda = 487$ ($f = 0.1455$), 452 ($f = 0.0721$), 443 ($f = 0.0831$), 439 ($f = 0.0399$) and 431 nm ($f = 0.1498$). These transitions originate from ruthenium-centered orbitals HOMO to HOMO-2 corresponding to t_{2g} orbitals in O_h symmetry into ligand-centered orbitals LUMO to LUMO+3 residing on both tpy ligands (Figure S1 in the Supporting Information). The "e_g" orbitals LUMO+9 and LUMO+13 are found at higher energy. In contrast, the calculated stick spectrum of $[\mathbf{1}]^{3+}$ lacks transitions between $\lambda = 400$ and 650 nm with oscillator strengths $f \geq 0.01$. Instead, transitions are predicted at $\lambda = 684$ ($f = 0.1535$) and 668 nm ($f = 0.0118$). These transitions have predominantly LMCT character with the largest contribution stemming from the transition of molecular orbital 141β into 144β (Figure 3). Electron density is mainly shifted from the amino-substituted tpy ligand to the ruthenium(III) center. For more detailed results of the TD-DFT calculations of $[\mathbf{1}]^{2+}$ and $[\mathbf{1}]^{3+}$ see Figures S1 and S2 in the Supporting Information.

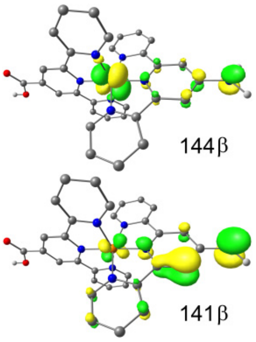

Figure 3. Relevant DFT-calculated Kohn-Sham frontier molecular orbitals of [**1**]$^{3+}$ (B3LYP/LANL2DZ, IEFPCM, H_2O, contour value 0.06 a. u., CH hydrogen atoms omitted).

The EPR spectrum of [**1**]$^{3+}$ (Figure 4) in 0.5 M trifluoroacetic acid in H_2O at 77 K is very similar to the one of its ester derivative [**1**^{Et}]$^{3+}$ which has already been reported.[16] It shows a rhombic signal ($g_{1,2,3}$ = 2.323, 2.175, 1.865; Δg = 0.458 by spectral simulation) and reveals that the oxidation is mainly located at the ruthenium center which is in full accordance with similar complexes of Ru^{III}.[16,43]

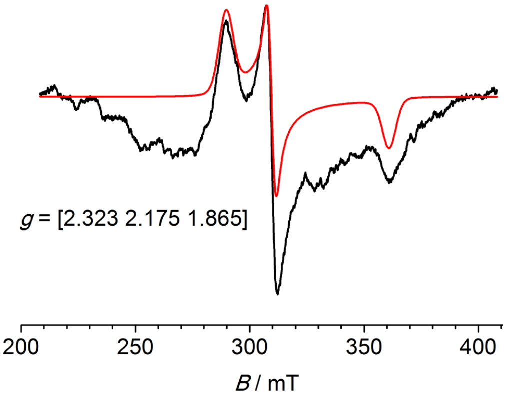

Figure 4. X-band EPR spectrum of [**1**]$^{3+}$ in 0.5 M trifluoroacetic acid in H_2O at 77 K. Black: experimental spectrum; red: simulation. For experimental details see *Oxidation 2* in the Experimental Section.

The DFT calculated spin density of the ruthenium(III) complex [**1**]$^{3+}$ is located at the ruthenium center with a smaller contribution at the amino nitrogen atom (Figure 5). The Mulliken spin densities on Ru and on the amino nitrogen atom are calculated as 0.76 and 0.11, respectively. Thus, DFT calculations substantiate the experimental finding of a largely ruthenium-centered oxidation.

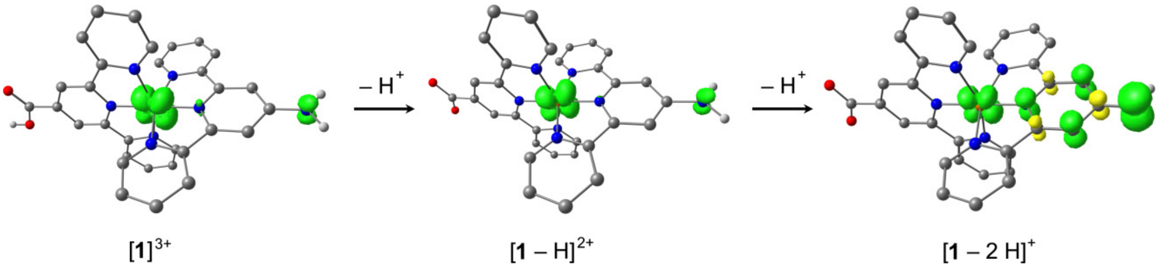

Figure 5. DFT-calculated spin density of ruthenium(III) complexes [**1**]$^{3+}$, [**1** – H]$^{2+}$ and [**1** – 2 H]$^+$ (B3LYP/LANL2DZ, IEFPCM, H_2O, contour value 0.01,CH hydrogen atoms omitted).

[**1**](PF_6)$_2$ is water soluble in the presence of NO_3^- ions enabling pH-dependent measurements. The Pourbaix diagram of [**1**](PF_6)$_2$ shows the redox potential $E_{½}$ of the Ru^{II}/Ru^{III} couple at different pH values (Figure 6) starting with 0.5 M HNO_3 in H_2O and stepwise titration with saturated aqueous NaOH. At pH = 0 – 1.6 the redox potential amounts to $E_{½}$ = 0.79 V. Between pH 1.6 and 2.7 the redox potential drops which is due to deprotonation of the carboxylic acid group (pK_a = 2.7).[40] For a proton-coupled electron transfer the expected

slope of the redox potential is given by –(*m*/*n*) × 59 mV per pH unit (*m* = number of transferred protons, *n* = number of transferred electrons).[52] The experimental slope amounts to approximately 46 ± 10 mV per pH unit suggesting that the electron transfer is indeed coupled to proton transfer in this pH region. The drop of the redox potential between pH 1.6 and 2.7 is rationalized by the fact that the deprotonated carboxylate group is a stronger electron donor than the protonated carboxyl group. Thus, the former can be oxidized at lower potential. From pH 2.7 – 9.5 the redox potential features a plateau with $E_{½}$ = 0.74 V. At pH > 10 the redox potential again drops due to deprotonation of the amino group which is converted into an even stronger electron donor by deprotonation.[40] Oxidation is reversible at pH < 10 and irreversible at pH > 10. Similar to $[\mathbf{1}]^{3+}$ for one-fold deprotonated $[\mathbf{1} - \mathrm{H}]^{2+}$ Mulliken spin densities on Ru and the amino nitrogen atom amount to 0.78 and 0.10, respectively (Figure 5). Thus, when $[\mathbf{1}]^{3+}$ is deprotonated at the carboxylic acid group the oxidation remains ruthenium-centered and reversible. However, the second deprotonation takes place at the amino group. The resulting species $[\mathbf{1} - 2\ \mathrm{H}]^{+}$ features Mulliken spin densities on Ru and the amino nitrogen atom of 0.36 and 0.51, respectively (Figure 5). Thus, oxidation takes place at the deprotonated amino group which induces the irreversibility of the oxidation. In summary, at pH < 10 $[\mathbf{1}]^{2+}$ is reversibly oxidized at the ruthenium center while at pH > 10 the amino group is irreversibly oxidized.

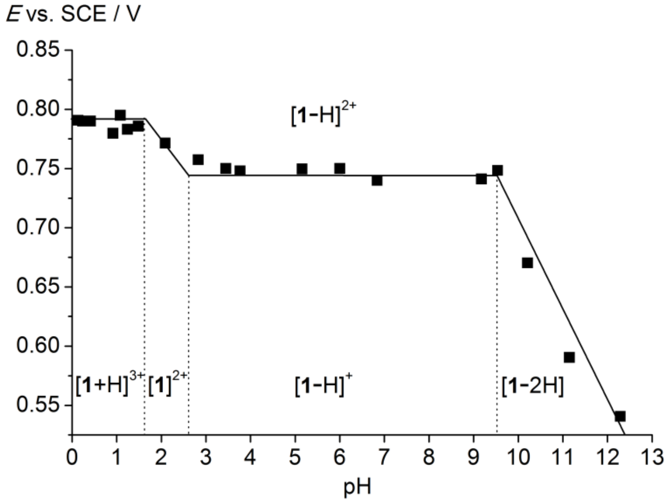

Figure 6. Pourbaix diagram of $[\mathbf{1}](PF_6)_2$ in 0.5 M HNO_3 in H_2O and stepwise titration with saturated aqueous NaOH. *E* (vs. SCE) – 0.16 ≈ *E* (vs. FcH/FcH^+).[58]

The ruthenium(III) complex $[\mathbf{1}]^{3+}$ is stable for at least several minutes or hours in 0.5 M trifluoroacetic acid. The slow decay/back reduction of $[\mathbf{1}]^{3+}$ can be followed by monitoring the decrease of the LMCT band. $[\mathbf{1}](PF_6)_2$ was oxidized in 0.125 M H_2SO_4 in H_2O with $Ce(SO_4)_2 \cdot 4\ H_2O$ as oxidant. Figure 7a shows solution UV/Vis spectra of $[\mathbf{1}](PF_6)_2$ before and after the addition of 1.1 equiv $Ce(SO_4)_2$ in 0.125 M H_2SO_4 in H_2O. For experimental details see *Oxidation 1* in the Experimental Section. The MLCT band of $[\mathbf{1}](PF_6)_2$ at λ = 499 nm (ε = 17170 $M^{-1}\ cm^{-1}$) immediately disappears upon addition of 1.1 equiv $Ce(SO_4)_2$. $[\mathbf{1}]^{3+}$ features a LMCT band at λ = 751 nm (ε = 6830 $M^{-1}\ cm^{-1}$). Upon standing the UV/Vis spectra of the solution change. After seven days the MLCT band is largely recovered (ε = 15850 $M^{-1}\ cm^{-1}$ at λ = 499 nm ≙ 92% recovery) and the LMCT band essentially disappeared. Isosbestic points at λ = 585, 432 and 342 nm clearly indicate the recovery of $[\mathbf{1}]^{2+}$ by conversion from $[\mathbf{1}]^{3+}$. Possible side products seem to be optically transparent in the observed spectral region. The addition of another 1.1 equiv $Ce(SO_4)_2$ again leads to the same color change with disappearance of the MLCT band and appearance of the LMCT band at λ = 751 nm (ε = 6250 $M^{-1}\ cm^{-1}$). The UV/Vis spectrum changes in the same manner as before. After four days the MLCT band is again largely recovered (ε = 13500 $M^{-1}\ cm^{-1}$ at λ = 499 nm ≙ 85% recovery with respect to the extinction coefficient before the second addition of $Ce(SO_4)_2$) and the LMCT band has nearly vanished (Figure 7b). The same isosbestic points are observed at λ = 583, 433 and 342 nm.

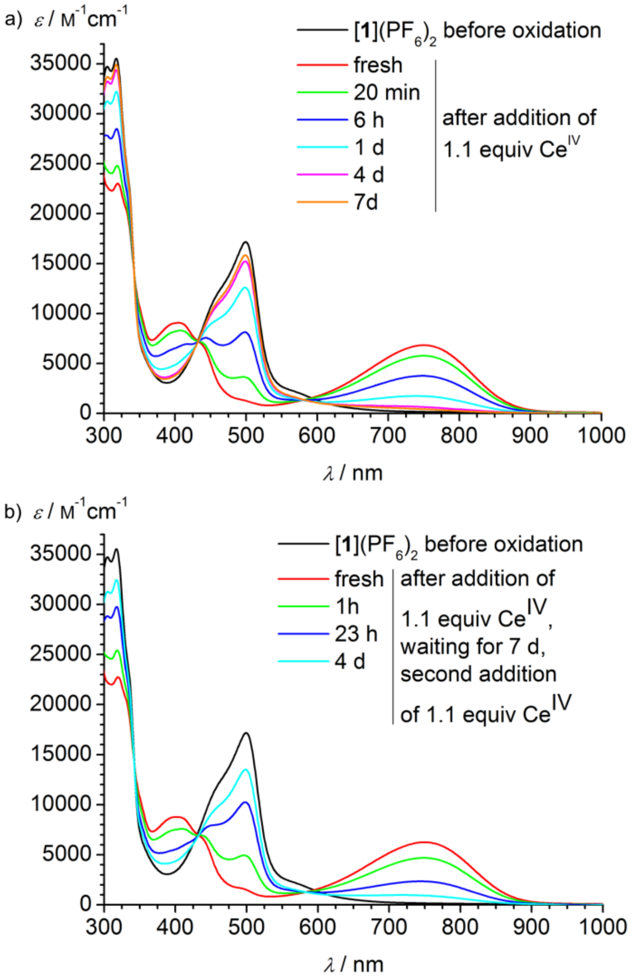

Figure 7. UV/Vis spectra of [**1**](PF_6)$_2$ before and after oxidation with a) 1.1 and b) 2.2 equiv Ce(SO_4)$_2$ in 0.125 M H_2SO_4 in H_2O. For experimental details see *Oxidation 1* in the Experimental Section.

[**1**](PF_6)$_2$ can also be oxidized in 0.125 M H_2SO_4 in H_2O:CH_3CN (1:1) with $(NH_4)_2[Ce(NO_3)_6]$ as oxidant showing the same spectral behavior as in *Oxidation 1* (see *Oxidation 3* in the Experimental Section).

An excess of Ce(SO_4)$_2$ (20 equiv) was added to a solution of [**1**](PF_6)$_2$ (*Oxidation 4*) in 0.125 M H_2SO_4 in H_2O. The orange solution of [**1**](PF_6)$_2$ immediately turned green upon addition of the Ce^{IV} salt. After 1 day the solution had a yellow color. UV/Vis spectra revealed that no absorption band above λ = 400 nm was present. No ruthenium complex could be detected in an ESI mass spectrum. Thus, complete degradation seems to have occurred under these conditions.

[**1**](PF_6)$_2$ was oxidized in 0.5 M trifluoroacetic acid in CH_3CN:H_2O (49:1) in an OTTLE cell (see *Oxidation 5* in the Experimental Section). Upon oxidation of [**1**]$^{2+}$ the intensity of the MLCT band is lowered (Figure 8a, $\varepsilon = 19300 \rightarrow 11900$ M^{-1} cm^{-1} at λ_{max} = 499 nm). Applying higher potentials does not lead to a further decrease of the MLCT band due to diffusion in the OTTLE cell solution. The LMCT band of [**1**]$^{3+}$ appears at λ_{max} = 733 nm (ε = 2620 M^{-1} cm^{-1}). During the oxidation isosbestic points are observed at λ = 554, 428, 340, 292, 282, 269, 241 and 231 nm. Upon back reduction new isosbestic points appear at λ = 606, 430, 342, 292, 283, 271, 242 and 219 nm (Figure 8a). After reaching the initial potential the MLCT band is not fully recovered (ε = 17600 M^{-1} cm^{-1} at λ_{max} = 499 nm, 91% recovery) even when the potential is further decreased. A new shoulder is observed at λ = 572 nm (ε = 2540 M^{-1} cm^{-1}). The appearance of this shoulder might be due to reduction of an intermediate species that is not reduced under the conditions with Ce(VI) as oxidant. These results are at odds with the high redox stability of the corresponding ester [**1**$^{\mathbf{Et}}$](PF_6)$_2$ in the presence of OH$^-$ reported by our group.[5] However, the redox stability of [**1**$^{\mathbf{Et}}$](PF_6)$_2$ was measured under basic conditions while here 0.5 M trifluoroacetic acid was used. Thus, the strong acidic conditions seem to be responsible for the redox instability of the [**1**]$^{3+}$ complex.

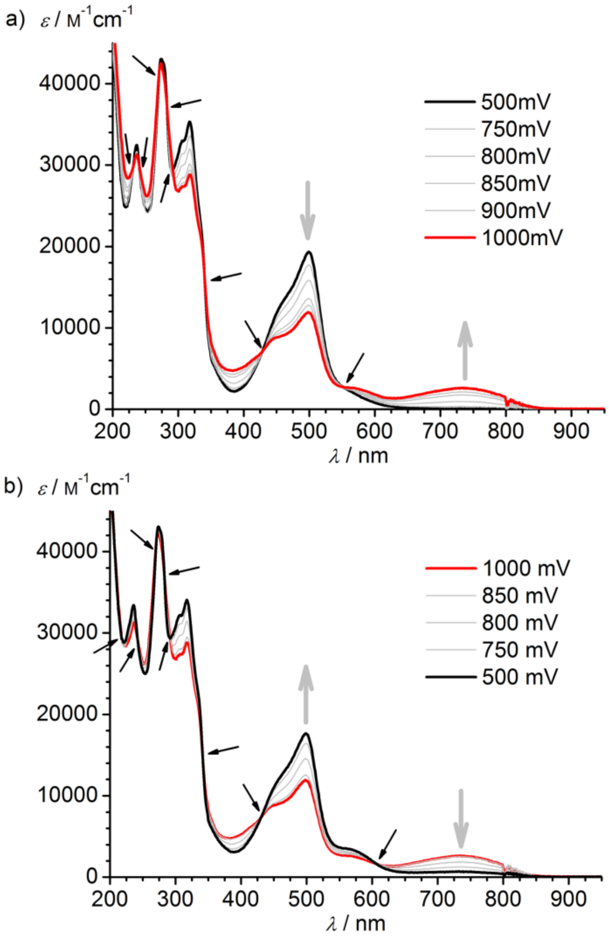

Figure 8. UV/Vis spectra during a) the electrochemical oxidation (500 → 1000 mV) and b) back reduction (1000 → 500 mV) of [**1**]$(PF_6)_2$ in an OTTLE cell in 0.5 M trifluoroacetic acid in CH_3CN:H_2O (49:1). Black arrows indicate isosbestic points.

In an NMR experiment [**1**]$(PF_6)_2$ was oxidized with 2.0 equiv $(NH_4)_2[Ce(NO_3)_6]$ in 0.5 M trifluoroacetic acid in CH_3CN. Immediately after the addition of $(NH_4)_2[Ce(NO_3)_6]$ and the concomitant color change from orange to green the solvent was removed under reduced pressure and D_2O was added. For experimental details see *Oxidation 6* in the Experimental Section. ^{1}H-NMR spectra were recorded at selected time intervals after the oxidation (Figure 9). In the fresh D_2O solution no sharp resonances could be obtained in the ^{1}H-NMR spectrum due to the paramagnetic nature of [**1**]$^{3+}$. Within 13 d resonances appear fitting excellently to pure [**1**]$^{2+}$ in D_2O. Resonances for the NH_2 group are not observed due to deuteration to ND_2. The self-exchange reaction [**1**]$^{2+}$ + [**1**]$^{3+}$ $\rightleftarrows$ [**1**]$^{3+}$ + [**1**]$^{2+}$ is expected to be fast and leads to averaged NMR resonances in the spectra after 17 h to 13 d (Figure 9). No hint for new signals could be detected at $\delta < 6.5$ ppm within the sensitivity of the ^{1}H NMR experiments.

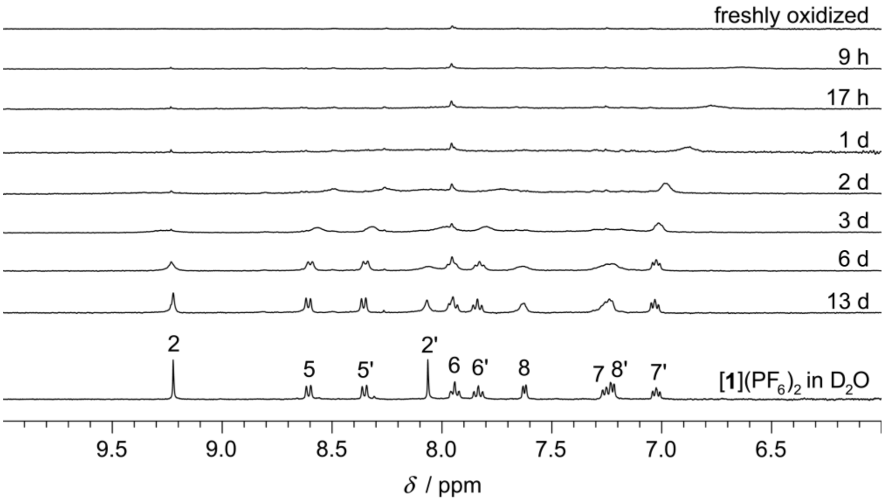

Figure 9. ^{1}H-NMR spectra of [**1**](PF_6)$_2$ in D_2O after oxidation with 2.0 equiv $(NH_4)_2[Ce(NO_3)_6]$ (freshly oxidized to 13 days after oxidation). The ^{1}H-NMR spectrum of pure [**1**](PF_6)$_2$ in D_2O is shown at the bottom for comparison. For experimental details see *Oxidation 6* in the Experimental Section.

After 13 days an ESI mass spectrum of the D_2O solution was recorded and showed signals with isotope distributions excellently fitting to the theoretical values for threefold deuterated [**1**]$^{2+}$ at m/z = 315.1 (100%) $[M - 2\ PF_6]^{2+}$, 628.1 (8%) $[M - 2\ PF_6 - D]^{+}$ and 775.1 (70%) $[M - PF_6]^{2+}$ where M is [(DOOC-tpy)Ru(tpy-ND_2)](PF_6)$_2$ (Figure 10). A signal at m/z = 606.1 (4%) with ruthenium isotope pattern was additionally found in the mass spectrum. This signal does not appear in the mass spectrum of neat [**1**](PF_6)$_2$ in D_2O. So far this signal could not be assigned to a structure. In summary, the nearly quantitative reformation of [**1**]$^{2+}$ by conversion from [**1**]$^{3+}$ could be shown by UV/Vis, NMR and mass spectra. The question arises which reducing agent is responsible for the reduction of [**1**]$^{3+}$. $[Ru(bpy)_3]^{3+}$ and other ruthenium polypyridine complexes are reported to oxidize water to O_2.[10,11,59] However, the exact mechanism for the reduction of $[Ru(bpy)_3]^{3+}$ to $[Ru(bpy)_3]^{2+}$ is still under debate. The attack of a H_2O or OH^- molecule to the ruthenium(III) center to form a seven-coordinate species has been proposed to be the initial reaction for water oxidation.[59] Ghosh et al. support the attack of water on a bpy ligand with further degradation of the ligand to CO_2. The thereby generated electrons enable 92 – 95% of $[Ru(bpy)_3]^{3+}$ to be reduced thermally or photochemically to $[Ru(bpy)_3]^{2+}$.[56] In the presence of colloidal RuO_2 or Co^{2+} ions $[Ru(bpy)_3]^{3+}$ efficiently catalyses the photo-oxidation of H_2O to O_2.[60] $[Ru(tpy)(bpy)(H_2O)]^{2+}$ and $[Ru(tpy)(py)_2(H_2O)]^{2+}$ are efficient WOCs and already contain a water molecule in the octahedral coordination sphere (py = pyridine).[61,62] Other ruthenium polypyridine catalysts expand their coordination sphere to a heptacoordinate pentagonal bipyramid in order to bind a water molecule to the metal.[63–65] $[Ru(tpy)_2]^{2+}$ is unable to adopt a heptacoordinate pentagonal bipyramid with a water molecule because no linear arrangement of the axial N-Ru-N bonds can be formed as is the case for bis(tridentate) complexes of ruthenium(II) with expanded ligands. This is regarded to be the reason why $[Ru(tpy)_2]^{2+}$ does not catalyze water oxidation and might also be applicable for [**1**]$^{2+}$.[62] H_2O as reducing agent would lead to the formation of H_2O_2, O_2^- or O_2. The formal equations for O_2 and H_2O_2 formation are:

(equation 1) $$4\,[\mathbf{1}]^{3+} + 2\,H_2O \rightarrow 4\,[\mathbf{1}]^{2+} + O_2 + 4\,H^+$$

(equation 2) $$2\,[\mathbf{1}]^{3+} + 2\,H_2O \rightarrow 2\,[\mathbf{1}]^{2+} + \underset{\substack{\downarrow \\ \text{attacks } [\mathbf{1}]^{2+} \text{ or } [\mathbf{1}]^{3+}}}{H_2O_2} + 2\,H^+$$

Oxidation of [**1**]$^{2+}$ to [**1**]$^{3+}$ and back reduction to [**1**]$^{2+}$ was conducted in closed reaction vessels and the gas phases above the reaction solutions were tested for O_2 via two methods: The gas phase was bubbled slowly through a solution of $IrCl(PEt_3)_3$ in d_8-THF. $Ir(O_2)(PEt_3)_3Cl$ should be formed in the presence of O_2 which was monitored by ^{31}P-NMR spectroscopy.[66] The second method is based on a ZrO_2-based oxygen sensor which measures the concentration of O_2 in the gas phase. Both methods reveal that no O_2 is produced during the reformation of [**1**]$^{2+}$ from [**1**]$^{3+}$ (*Oxidations 7* and *8*). H_2O_2 as possible intermediate in the oxidation of H_2O to O_2 is metastable in acidic solution with respect to disproportionation into H_2O to O_2. A solution of [**1**](PF_6)$_2$ (1.2×10^{-4} M) in 35% H_2O_2 in water is stable for at least 3 h (no changes in the UV/Vis spectra over time, stable MLCT band at 493 nm). However, in the presence of acid (0.1 M TFA) the ruthenium complex decomposes within 3 h which can be seen by the absence of any UV/Vis signal above 400 nm. The theoretical maximum amount of H_2O_2 would be half the amount of [**1**]$^{3+}$ according to equation 2. It is yet unclear whether H_2O_2 is produced during the reaction and which reaction products result from the reaction of H_2O_2 with [**1**]$^{2+}$ or [**1**]$^{3+}$. If H_2O_2 is produced quantitatively (0.50 equiv compared to 1.00 equiv of [**1**]$^{2+}$), then less than 0.12 equiv (of 1.00 equiv) of [**1**]$^{2+}$ are destroyed by 0.50 equiv of H_2O_2 (calculated from the observed 88% recovery of the MLCT band).

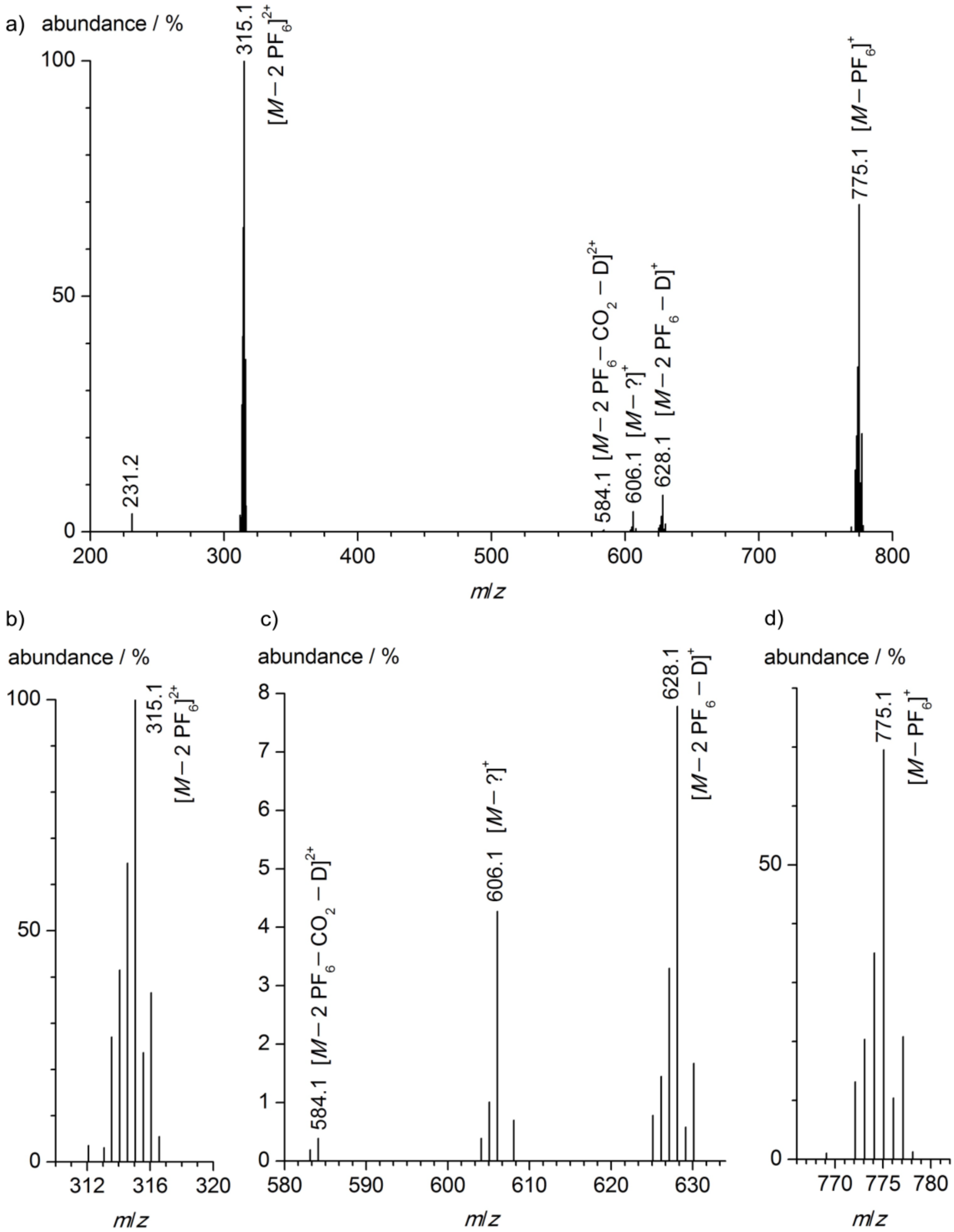

Figure 10. a) ESI$^+$ mass spectrum of [**1**]$(PF_6)_2$ in D_2O 13 days after oxidation with 2.0 equiv $(NH_4)_2[Ce(NO_3)_6]$ in 0.5 M trifluoroacetic acid in CH_3CN (See *Oxidation 6* for experimental details). b) c) and d) show the respective signals with ruthenium isotope patern. *M* = $[(DOOC\text{-}tpy)Ru(tpy\text{-}ND_2)](PF_6)_2$.

Further experiments are necessary to clarify whether H_2O_2 is indeed formed intermediately and subsequently consumed e.g. by oxygenation of a ligand to *N*-oxides or if other electron sources are responsible for the reduction of [**1**]$^{3+}$. For example a small part of the oxidized complex [**1**]$^{3+}$ could decompose and generate enough electrons to reduce the majority of [**1**]$^{3+}$ according to equation 3.

(equation 3) $n\,[\mathbf{1}]^{3+} + [\mathbf{1}]^{3+} \rightarrow n\,[\mathbf{1}]^{2+}$ + decomposition products

We tried to optimize a heptacoordinate species with one H_2O molecule coordinated to the ruthenium center of $[\mathbf{1}]^{3+}$ via DFT calculations. However, no energy minimum was found for a heptacoordinate species. Instead, only the hexacoordinate complexes "$[Ru(\kappa^3\text{-}H_2N\text{-tpy})(\kappa^3\text{-HOOC-tpy})]^{3+}$ + H_2O" and $[Ru(\kappa^2\text{-}H_2N\text{-tpy})(\kappa^3\text{-HOOC-tpy})(H_2O)]^{3+}$ lead to energy minima in the DFT calculations (Figure 11). In the latter the amino substituted ligand coordinates to ruthenium(III) in a bidentate κ^2-fashion via two pyridine nitrogen atoms while one outer pyridine nitrogen atom is involved in a hydrogen bond with a proton from the H_2O molecule. Indeed, the pyridine is protonated and the H_2O molecule deprotonated to OH^-, a well known phenomenon of H_2O ligands coordinated to metal centers with high oxidation states.[10,11] The bond length between the central pyridine nitrogen atom of the κ^2-H_2N-tpy ligand and the ruthenium atom is increased (2.20 Å) compared to the bis(tridentate) complex (1.97 Å). The N-C-C-N dihedral angles of the κ^2-H_2N-tpy ligand amount to 13° and 48°, respectively. In contrast the N-C-C-N dihedral angles of the κ^3-HOOC-tpy ligand amount to $\approx 0°$, similar to the bis(tridentate) complex "$[Ru(\kappa^3\text{-}H_2N\text{-tpy})(\kappa^3\text{-HOOC-tpy})]^{3+}$ + H_2O" where the dihedral angles of both tpy ligands are $\approx 0°$. Hence, $[Ru(\kappa^2\text{-}H_2N\text{-tpy})(\kappa^3\text{-HOOC-tpy})(H_2O)]^{3+}$ is highly distorted and activated towards potential chelate ligand loss. The bis(tridentate) complex has been calculated to be 35 kJ mol^{-1} more stable than $[Ru(\kappa^2\text{-}H_2N\text{-tpy})(\kappa^3\text{-HOOC-tpy})(H_2O)]^{3+}$. Thus, our DFT calculations support the above conclusion that bis(tpy) complexes of ruthenium(II) are not suitable for H_2O oxidation. $[\mathbf{1}]^{3+}$ is unable to adopt a heptacoordinate coordination with one H_2O molecule while the decoordination of an outer pyridine ring to form a free coordination site for H_2O is thermodynamically unfavorable. However, an energy barrier of 35 kJ mol^{-1} can be overcome at room temperature. Especially at low pH the protonation of pyridine is favored. $[Ru(\kappa^2\text{-}H_2N\text{-tpy})(\kappa^3\text{-HOOC-tpy})(H_2O)]^{3+}$ might be prone to loss of the H_2N-tpy ligand. Under acidic conditions H_2N-tpy ligand loss is irreversible due to protonation of the pyridine nitrogen atoms. Even if the reaction of "$[Ru(\kappa^3\text{-}H_2N\text{-tpy})(\kappa^3\text{-HOOC-tpy})]^{3+}$ + H_2O" to $[Ru(\kappa^2\text{-}H_2N\text{-tpy})(\kappa^3\text{-HOOC-tpy})(H_2O)]^{3+}$ is slow the irreversible H_2N-tpy ligand loss of the latter is a competing pathway to the back reduction to $[\mathbf{1}]^{2+}$.

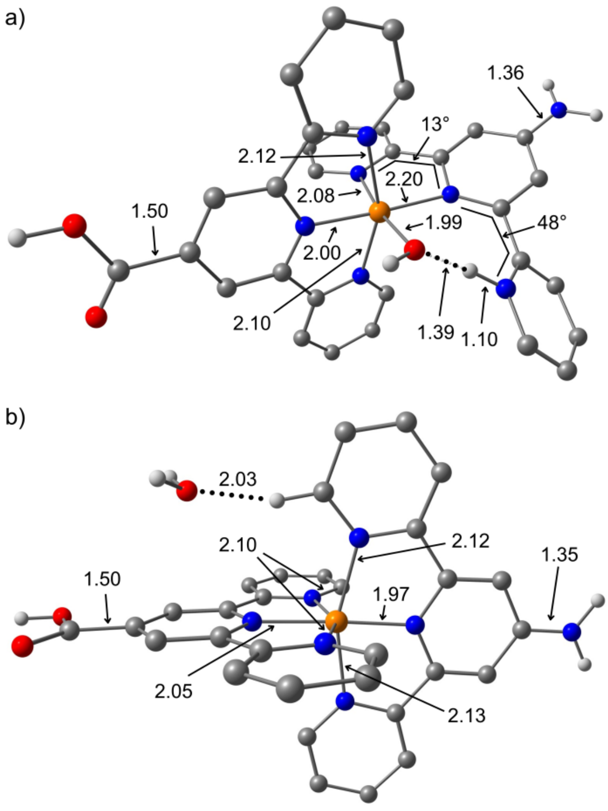

Figure 11. DFT (B3LYP/LANL2DZ, IEFPCM, H_2O, irrelevant CH hydrogen atoms omitted) optimized structures of a) $[Ru(\kappa^2\text{-}H_2N\text{-tpy})(\kappa^3\text{-HOOC-tpy})(H_2O)]^{3+}$ and b) "$[Ru(\kappa^3\text{-}H_2N\text{-tpy})(\kappa^3\text{-HOOC-tpy})]^{3+}$ + H_2O". Indicated bond lengths are given in Å.

In order to detect side products in the back reaction of $[\mathbf{1}]^{3+}$ to $[\mathbf{1}]^{2+}$ ESI mass spectra were conducted also in non-deuterated solvents before and after oxidation with $(NH_4)_2[Ce(NO_3)_6]$ in 0.5 M TFA in H_2O:CH_3CN (1:200;

Figure S3 and S4). The signal at *m*/*z* = 249.1 (50%) is observed before and after the oxidation and corresponds to the protonated ligand [tpy-NH_2 + H]$^+$. An unknown signal at *m*/*z* = 605.1 (40%) with ruthenium isotope pattern is observed besides the known signals with ruthenium isotope pattern at *m*/*z* = 313.6 (9%) [M – 2 PF_6]$^{2+}$, 582.2 (6%) [M – 2 PF_6 – CO_2 – H]$^+$, 626.1 (100%) [M – 2 PF_6 – H]$^+$ and 772.1 (19%) [M – PF_6]$^+$ where M is [(HOOC-tpy)Ru(tpy-NH_2)]$(PF_6)_2$. The signal at *m*/*z* = 605.1 does not appear in the ESI mass spectra before addition of $(NH_4)_2[Ce(NO_3)_6]$ (*Oxidation 9*, Figure S3 and S4). The signal at *m*/*z* = 606.1 which was observed in D_2O (*Oxidation 6*) indicates that one of the protons can be exchanged by deuteration. One could assume that the COOH-substituted tpy ligand is still intact while the NH_2-substituted tpy ligand underwent a structural change. The signal at *m*/*z* = 605.1 would fit to a complex where the tpy-NH_2 ligand has been substituted by two CF_3COO^- anions, namely [(HOOC-tpy)Ru$(CF_3COO)_2$]$^+$. However, the signal at *m*/*z* = 605.1 was also found when the oxidation and back reduction of [**1**]$^{2+}$ were performed in 0.5 M HNO_3 or 0.1 M H_2SO_4 instead of 0.5 M TFA (*Oxidation 10 and 11*, Figure S5 – S8). Thus, so far no complete structural assignment could be made to the signal with *m*/*z* = 605.1.

The reduction of [**1**]$^{3+}$ back to [**1**]$^{2+}$ was found to be faster in the presence of UV light (λ_{emiss} = 254 and 366 nm, Figure 12a, *Oxidation 12*). Upon oxidation the initial value of the extinction coefficient ε_{500} at λ = 500 nm dropped from ε_{500} = 16440 to 2330 M^{-1} cm^{-1} while the extinction coefficient ε_{760} at λ = 760 nm rose from ε_{760} = 20 to 6480 M^{-1} cm^{-1}. After exposing the solution to UV light (λ_{emiss} = 254 and 366 nm) for 10 min the MLCT band was largely recovered (ε_{500} = 15490 M^{-1} cm^{-1}, 94% recovery) and the LMCT band disappeared nearly completely (ε_{760} = 390 M^{-1} cm^{-1}). In a reference measurement in the darkness a much smaller part of the MLCT band was recovered after 10 min (ε_{500} = 5420 M^{-1} cm^{-1}, 33% recovery) and the LMCT band still featured a pronounced intensity (ε_{760} = 4950 M^{-1} cm^{-1}). Hence, the back reduction is significantly accelerated by UV light irradiation. This points to the existence of a dissociative rate-determining step in the back reduction of [**1**]$^{3+}$ back to [**1**]$^{2+}$. The loss of the κ^2-H_2N-tpy ligand of the above mentioned [Ru(κ^2-H_2N-tpy)(κ^3-HOOC-tpy)(H_2O)]$^{3+}$ might be the responsible dissociative rate-determining step which is accelerated by light.

In a second experiment five cycles of Ce^{IV} addition and UV light treatment were conducted. The extinction coefficients ε_{500} and ε_{760} are depicted in Figure 12b (*Oxidation 13*). The initial value of ε_{500} drops upon oxidation with 1.3 equiv Ce^{IV} from ε_{500} = 16840 to 1050 M^{-1} cm^{-1} with a concomitant rise of ε_{760} from ε_{760} = 110 to 6790 M^{-1} cm^{-1}. After irradiation with UV light for 10 min the extinction coefficients go back to ε_{500} = 14740 M^{-1} cm^{-1} (88% recovery) and ε_{760} = 450 M^{-1} cm^{-1}. For both, ε_{500} and ε_{760}, the initial values are not reached quantitatively under these conditions. The second addition of 1.3 equiv Ce^{IV} lets ε_{500} drop to 2710 M^{-1} cm^{-1} and ε_{760} rise to 5380 M^{-1} cm^{-1}. The treatment with UV light again leads to a rise of ε_{500} and a drop of ε_{760}. This procedure was conducted five times and in each step the respective starting values were not reached quantitatively (86 – 93% recovery) which is assigned to unknown side reactions such as ligand dissociation and decomposition as discussed above.

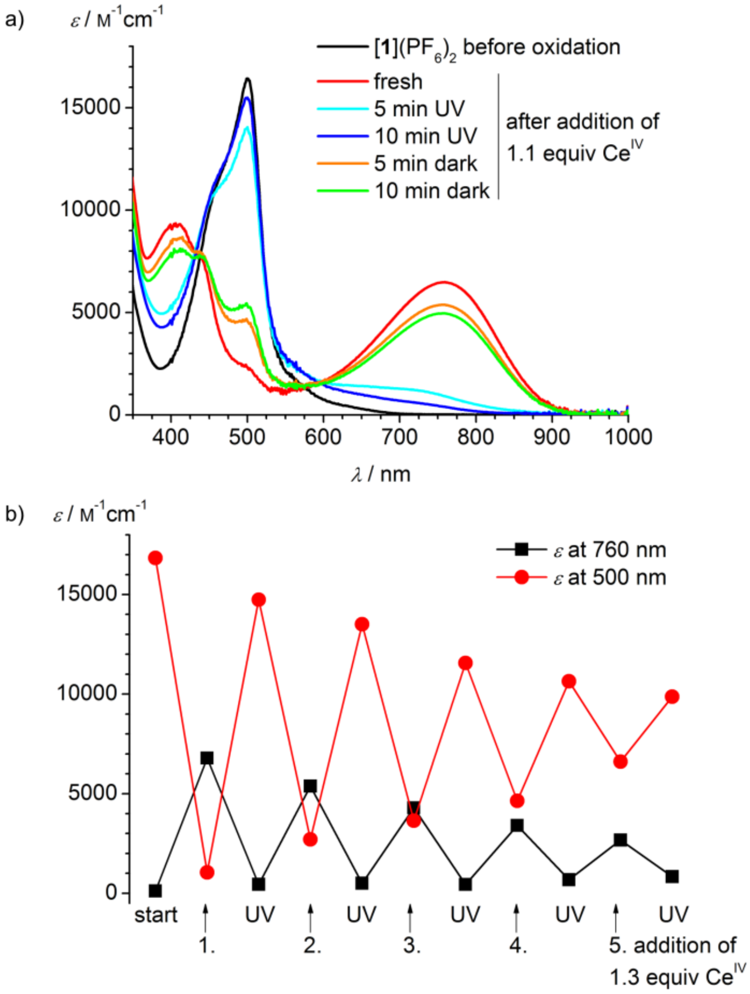

Figure 12. a) UV/Vis spectra of [**1**]$(PF_6)_2$ before and after oxidation with 1.1 equiv $(NH_4)_2[Ce(NO_3)_6]$ in 0.11 M H_2SO_4 in H_2O:CH_3CN (15:85) and treatment with UV light. For experimental details see *Oxidation 12* in the Experimental Section. b) Extinction coefficients at λ = 760 and 500 nm after alternating treatment with 1.3 equiv Ce^{IV} and UV light. For experimental details see *Oxidation 13* in the Experimental Section.

The reduction rate of $[\mathbf{1}]^{3+}$ to $[\mathbf{1}]^{2+}$ was also found to be higher in the presence of standard laboratory light conditions (mixture of fume hood light and scattered day light passing through the windows) than under darkness. After oxidation with 2.0 equiv $(NH_4)_2[Ce(NO_3)_6]$ in 0.5 M TFA in H_2O the temporal evolution of the extinction coefficients ε_{499} at λ = 499 nm and ε_{751} at λ = 751 nm is shown in Figure 13 (*Oxidation 14*). Under standard laboratory light conditions ε_{499} approaches ~17800 M^{-1} cm^{-1} after ~12 h. In the darkness ε_{499} approaches the same value after ~100 h. In both cases the initial value of ε_{499} = 19600 M^{-1} cm^{-1} is not fully recovered (91% recovery). ε_{751} shows a similar behavior with the difference that the LMCT band vanishes nearly completely. The temporal evolution of ε_{499} and ε_{751} nicely fits to first order (or pseudo first order) rate laws with rate constants amounting to $k(\varepsilon_{499,\text{light}})$ = 20.2 h^{-1}, $k(\varepsilon_{499,\text{dark}})$ = 5.2 h^{-1}, $k(\varepsilon_{751,\text{light}})$ = 18.4 h^{-1} and $k(\varepsilon_{751,\text{dark}})$ = 4.9 h^{-1}. Thus, under our conditions the reaction rate is four-fold increased under standard light conditions compared to darkness.

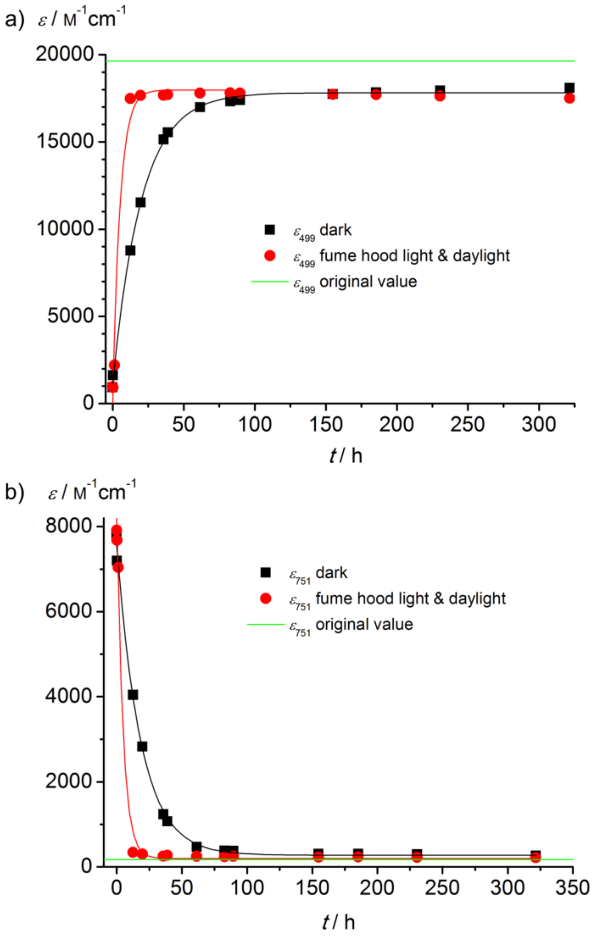

Figure 13. Temporal change of extinction coefficients at a) λ = 499 (MLCT) and b) λ = 751 nm (LMCT) after oxidation of [**1**]$(PF_6)_2$ with 2.0 equiv $(NH_4)_2[Ce(NO_3)_6]$ in 0.5 M TFA in H_2O. The solid black and red lines are monoexponential fits, respectively. For experimental details see *Oxidation 14* in the Experimental Section.

Furthermore, excited state redox potentials differ from their respective ground state redox potential by the energy of the 0–0' emission energy E_{00} and might be responsible for the faster back reduction in the presence of light.[67] For [**1**]$(PF_6)_2$ the 0–0' emission energy was obtained by the crossing point of the normalized absorption and emission spectra at a wavelength of λ = 626 nm which corresponds to a redox potential shift of ΔE = ± 1.98 V. $[Ru(bpy)_3]^{2+}$ features a comparable redox potential shift of ΔE = ± 2.13 V.[68] Similarly, [**1**]$^{3+}$ features excited state redox potentials that differ from its ground state redox potentials. Thus, [**1**]$^{3+*}$ is oxidized at lower potential than [**1**]$^{3+}$ which might be the reason for the decomposition of [**1**]$^{3+*}$. In analogy to the slow decomposition of [**1**]$^{3+}$ in the absence of light (equation 3), the decomposition of [**1**]$^{3+*}$ is faster and could generate electrons that reduce the majority of [**1**]$^{3+}$ according to:

(equation 4) $$n\,[\mathbf{1}]^{3+} + [\mathbf{1}]^{3+*} \rightarrow n\,[\mathbf{1}]^{2+} + \text{decomposition products}$$

Conclusion

The donor-acceptor-substituted bis(terpyridine)ruthenium(II) complex [**1**]$(PF_6)_2$ (Figure 1) can be chemically oxidized in acidic media by Ce^{IV}. The one electron oxidation of [**1**]$^{2+}$ to [**1**]$^{3+}$ is well understood and was characterized by UV/Vis and ESR spectroscopy, electrochemistry and DFT calculations. The generated [**1**]$^{3+}$ undergoes slow spontaneous back reduction to [**1**]$^{2+}$ without addition of a reducing agent. This was shown by UV/Vis and NMR spectroscopy and mass spectrometry. The rate of the back reaction depends on the used conditions like solvent and can be accelerated by light. However, the responsible reducing agent is yet unknown. Water as reducing agent would lead to the formation of O_2 or H_2O_2. H_2O_2 is unstable under the used conditions and would also form O_2 or lead to further side reactions. O_2 was not detected by trapping with $IrCl(PEt_3)_3$ and by gas phase measurements with a ZrO_2-based oxygen sensor. The ruthenium complex itself ([**1**]$^{3+}$) is assumed to behave as reducing agent as the full amount of [**1**]$^{2+}$ is not recovered (≈ 91 ± 3% recovery) in the back reaction of [**1**]$^{3+}$ to [**1**]$^{2+}$. [Ru(κ^2-H_2N-tpy)(κ^3-HOOC-tpy)(H_2O)]$^{3+}$ could be calculated by DFT and is 35 kJ mol^{-1} higher in energy than bis(tridentate) "[Ru(κ^3-H_2N-tpy)(κ^3-HOOC-tpy)]$^{3+}$ + H_2O". Under acidic conditions [Ru(κ^2-H_2N-tpy)(κ^3-HOOC-tpy)(H_2O)]$^{3+}$ might be prone to decomposition initiated by protonation of the κ^2-H_2N-tpy ligand and subsequent irreversible ligand loss which could explain the non-quantitative recovery of [**1**]$^{2+}$.

Experimental Section

General Procedures. CH_3CN was distilled from CaH_2 and THF from potassium under an argon atmosphere. All reagents were used as received from commercial suppliers (Acros and Sigma-Aldrich). $IrCl(PEt_3)_3$ was prepared according to a literature procedure (see the Supporting Information).[69] [**1**](PF_6)$_2$ was prepared as reported by Heinze et al.[40] NMR spectra were recorded on a Bruker Avance DRX 400 spectrometer at 400.31 MHz (^{1}H) and 162.05 MHz (^{31}P{^{1}H}). All resonances are reported in ppm versus the solvent signal as an internal standard [D_2O (^{1}H, δ = 4.80 ppm; d$_8$-THF (^{1}H, δ = 1.24, 3.57 ppm)] or versus external H_3PO_4 (85%; ^{31}P, δ = 0 ppm). Electrochemical experiments were carried out on a Bio Logic SP-50 voltammetric analyzer using platinum wires as counter and working electrodes and a saturated calomel electrode as reference electrode. The measurements were carried out at a scan rate of 50 – 100 mV s^{-1} for cyclic voltammetry experiments and at 50 – 200 mV s^{-1} for square-wave voltammetry experiments using 0.5 M HNO_3 as the supporting electrolyte and a 10^{-3} M solution of the analyte in degassed H_2O. Potentials are referenced to the saturated calomel electrode. UV/Vis/near-IR spectra were recorded on a Varian Cary 5000 spectrometer using 1.0 cm cells (Hellma, Suprasil). ESI MS spectra were recorded on a Micromass Q-TOF-Ultima spectrometer. X-band CW ESR spectra were measured on a Miniscope MS 300 (Magnettech GmbH, Germany). *g* values are referenced to external Mn^{2+} in ZnS (*g* = 2.118, 2.066, 2.027, 1.986, 1.946, 1.906). Measurements were conducted at 77 K and simulations were performed with the program package EasySpin. Irradiation experiments were performed with a UV lamp (Benda, NU-4 KL, 0.18 W, λ_{emiss} = 254 and 366 nm). Solutions of $(NH_4)_2[Ce(NO_3)_6]$ and $Ce(SO_4)_2$ always were freshly prepared and used directly after complete dissolution of the salts. Dissolution was achieved via ultrasonication. Oxygen measurements were conducted with a TOS 3.0 sensor (Ionic Systems).

DFT calculations were carried out with the *Gaussian09*/DFT[70] series of programs. The B3LYP formulation of DFT was used by employing the LANL2DZ basis set.[70] No symmetry constraints were imposed on the molecules. The presence of energy minima or first order saddle points was checked by analytical frequency calculations. For solvent modeling, the integral-equation-formalism polarizable continuum model (IEFPCM, H_2O) was employed. In general, data obtained including solvent modeling reproduced the experimental results better than those without solvent modeling. Therefore, solvent modeling is included in all calculations in this paper. For time-dependent DFT (TD-DFT) calculations at least 50 singlet transitions ($n \geq 50$) were used. All calculations were performed without explicit counterions.

Oxidation 1. A solvent mixture of 0.125 M H_2SO_4 in H_2O was used. A solution of [**1**](PF_6)$_2$ (3.58×10^{-5} M, 9 ml) was prepared and a solution of $Ce(SO_4)_2 \cdot 4\,H_2O$ (5.33×10^{-4} M, 0.74 ml, 1.1 equiv) was added. The orange solution of [**1**](PF_6)$_2$ immediately turned green after the addition of the $Ce(SO_4)_2 \cdot 4\,H_2O$ solution. Within 7 d the color of the solution turned back to orange. A fresh solution of $Ce(SO_4)_2 \cdot 4\,H_2O$ (5.51×10^{-4} M, 0.71 ml, 1.1 equiv) was added. Again, the solution immediately turned green and then slowly changed its color to orange. The measurement was made under normal laboratory light conditions (mixture of artificial light and sunlight passing through the window).

Oxidation 2. A solvent mixture of 0.5 M trifluoroacetic acid in H_2O was used. To a solution of [**1**](PF_6)$_2$ (3.21×10^{-4} M, 1.0 ml) a solution of $(NH_4)_2[Ce(NO_3)_6]$ (3.43×10^{-2} M, 34.6 µl, 3.7 equiv) was added. The dark red-brown solution immediately turned dark green upon addition of the cerium salt. The mixture was frozen directly after preparation (77 K). The oxidation was performed under normal laboratory light conditions (mixture of artificial light and sunlight passing through the window).

Oxidation 3. A solvent mixture of 0.125 M H_2SO_4 in H_2O:CH_3CN (1:1) was used. A solution of [**1**](PF_6)$_2$ (4.26×10^{-5} M, 10 ml) was prepared and a solution of $(NH_4)_2[Ce(NO_3)_6]$ (5.62×10^{-4} M, 0.84 ml, 1.1 equiv) was added. The orange solution of [**1**](PF_6)$_2$ immediately turned green after the addition of the $(NH_4)_2[Ce(NO_3)_6]$ solution. Within 18 h the color of the solution turned back to orange. 9.85 ml of the resulting solution were taken and a fresh solution of $(NH_4)_2[Ce(NO_3)_6]$ (4.39×10^{-4} M, 0.97 ml, 1.1 equiv) was added. Again, the solution immediately turned green and then slowly changed its color to orange. After 6 d a fresh solution of $(NH_4)_2[Ce(NO_3)_6]$ (4.64×10^{-4} M, 0.92 ml, 1.1 equiv) was added. Again, the solution immediately turned green and then slowly changed its color to orange. The measurement was made under normal laboratory light conditions (mixture of artificial light and sunlight passing through the window).

Figure 14a shows solution UV/Vis spectra of [**1**](PF_6)$_2$ before and after the addition of 1.1 equiv $(NH_4)_2[Ce(NO_3)_6]$ in 0.125 M H_2SO_4 in H_2O:CH_3CN (1:1). The MLCT band of [**1**](PF_6)$_2$ at λ = 501 nm (ε = 16920 M^{-1} cm^{-1}) immediately disappears upon addition of 1.1 equiv $(NH_4)_2[Ce(NO_3)_6]$. [**1**]$^{3+}$ features a LMCT band at λ = 753 nm (ε = 6670 M^{-1} cm^{-1}). The UV/Vis spectrum rapidly changes within minutes. After 18 h the MLCT band is largely recovered (ε = 15910 M^{-1} cm^{-1} at λ = 500 nm, 94% recovery) and the LMCT band essentially disappeared. Isosbestic points at λ = 586, 433 and 341 nm reveal the clean recovery of [**1**]$^{2+}$ by conversion from [**1**]$^{3+}$. The addition of another 1.1 equiv $(NH_4)_2[Ce(NO_3)_6]$ again leads to the same color change with the disappearance of the MLCT band and the appearance of the LMCT band at λ = 753 nm (ε = 6020 M ^{1} cm^{-1}). The UV/Vis spectrum then changes in the same manner as before. After 6 days the MLCT band is recovered (ε = 16140 M^{-1} cm^{-1} at λ = 500 nm, 101% recovery) and the LMCT band has vanished (Figure 14b). The same isosbestic points are observed at λ = 585, 433 and 341. The oxidation with 1.1 equiv $(NH_4)_2[Ce(NO_3)_6]$ can also be conducted a third time with an initial LMCT band at λ = 753 nm (ε = 4070 M^{-1} cm^{-1}) and a recovery of the MLCT band at λ = 500 nm (ε = 14700 M^{-1} cm^{-1} after 4 days, 91% recovery).

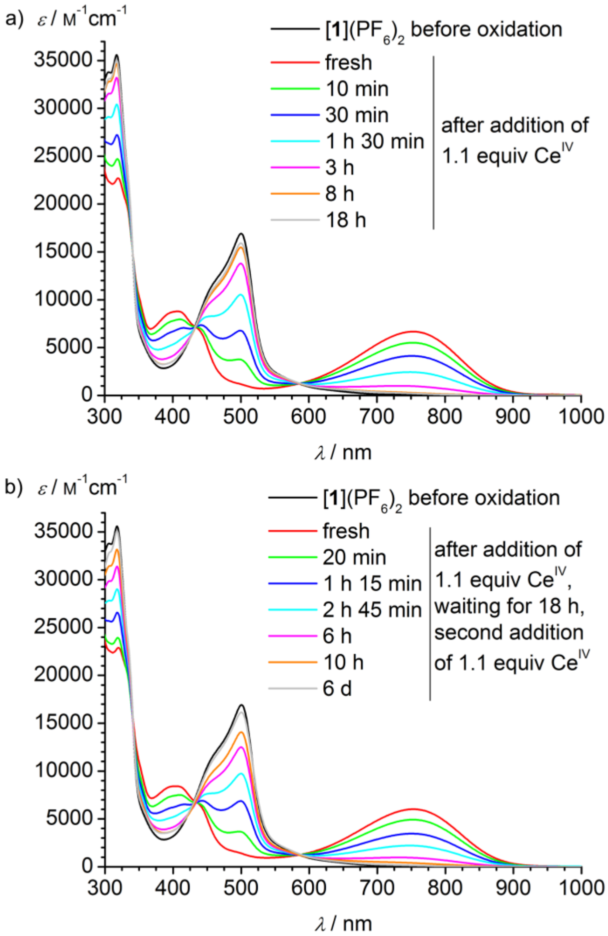

Figure 14. UV/Vis spectra of [**1**](PF_6)$_2$ before and after oxidation with a) 1.1 and b) 2.2 equiv $(NH_4)_2[Ce(NO_3)_6]$ in 0.125 M H_2SO_4 in H_2O:CH_3CN (1:1).

Oxidation 4. A solvent mixture of 0.125 M H_2SO_4 in H_2O was used. A solution of [**1**](PF_6)$_2$ (3.94×10^{-4} M, 1 ml) was prepared and a solution of $Ce(SO_4)_2 \cdot 4\ H_2O$ (8.11×10^{-2} M, 98.1 µl, 20 equiv) was added. The orange solution of [**1**](PF_6)$_2$ immediately turned green after the addition of the $Ce(SO_4)_2 \cdot 4\ H_2O$ solution. Within 1 day the color of the solution turned yellow. The measurement was made under normal laboratory light conditions (mixture of artificial light and sunlight passing through the window).

Oxidation 5. A solvent mixture of 0.5 M trifluoroacetic acid in CH_3CN:H_2O (49:1) was used. A solution of [**1**](PF_6)$_2$ (1.20×10^{-4} M, 0.3 ml) was prepared and oxidized in an OTTLE cell by gradually increasing the potential and then reduced back by gradually lowering the potential. UV/Vis spectra were recorded during this procedure. The measurement was made under normal laboratory light conditions (mixture of artificial light and sunlight passing through the window).

Oxidation 6. A solvent mixture of 0.5 M trifluoroacetic acid in CH_3CN was used. To a solution of [**1**]$(PF_6)_2$ (6.44×10^{-4} M, 2.5 ml) a solution of $(NH_4)_2[Ce(NO_3)_6]$ (3.51×10^{-3} M, 0.92 ml, 2.0 equiv) was added. The dark red-brown solution immediately turned dark green upon addition of the cerium salt. The solvent was removed under reduced pressure. The green solid was dissolved in D_2O (0.8 ml) and ^1H NMR spectra were recorded. The dark green color of the solution slowly turned dark red-brown. After 17 h the dark red-brown color of the starting solution is seen. After 13 days an ESI mass spectrum was recorded (Figure 10). The measurements were made under normal laboratory light conditions (mixture of artificial light and sunlight passing through the window).

Oxidation 7. The whole procedure was conducted in an Ar-filled glove box. [**1**]$(PF_6)_2$ (102 mg, 0.111 mmol, 1.00 equiv) was dissolved in degassed 0.5 M trifluoroacetic acid in H_2O:CH_3CN (200:1; 10 ml). A flask was filled with $(NH_4)_2[Ce(NO_3)_6]$ powder (57 mg, 0.104 mmol, 0.94 equiv) and closed with a septum (total volume: 86 ml). The dark red-brown solution of [**1**]$(PF_6)_2$ was added through the septum and the mixture was shaken thoroughly. The color turned to dark green upon dissolution of the cerium salt after shaking for a few seconds. After 5 h the solution had a dark brown color and after 17 h the solution again had the initial dark red-brown color. 24 ml of the gaseous phase were extracted by a gas-tight syringe and bubbled very slowly through a red d_8-THF solution of $IrCl(PEt_3)_3$ (55 mM, 2.0 ml, 0.11 mmol). No color change occurred during and after the bubbling of the gaseous phase, indicating that no oxygen was present in the gaseous phase. The measurement was made under normal laboratory light conditions (mixture of artificial light and sunlight passing through the window).

For the calculation the following assumptions were made:

1) [**1**]$^{3+}$ reacts quantitatively with water according to the equation 1. This assumption is reasonable because after oxidation the MLCT band regained 88% of its initial intensity.

2) The equilibrium between O_2 in the gas phase and in solution is totally on the side of the gas phase. This is reasonable due to literature known solubilities of O_2 in CH_3CN at 25 °C which amount to 8.1 mM O_2 at 1 atm (O_2 atmosphere) and 2.4 mM O_2 at 1 atm (air atmosphere).[71,72]

3) The mixing of Ar and O_2 is ideal. This assumption is surely wrong due to different densities of Ar and O_2 ($\rho_{273K}(\mathrm{Ar}) = 1.78$ kg m^{-3}, $\rho_{273K}(O_2) = 1.43$ kg m^{-3}). However, gas samples from the top of the reaction vessels were used for the attempted oxygen detection. The detected value for the O_2 concentration would then be an overestimation of the O_2 content.

4) The oxidative addition of O_2 by $IrCl(PEt_3)_3$ is quantitative. To ensure this the gas sample was bubbled very slowly through the solution of $IrCl(PEt_3)_3$. The reaction equation is: $IrCl(PEt_3)_3 + O_2 \rightarrow IrCl(O_2)(PEt_3)_3$.

$(NH_4)_2[Ce(NO_3)_6]$ is the limiting factor and its amount is $n(\mathrm{Ce}) = 0.104$ mmol. According to the equation "$2\ H_2O \rightarrow O_2 + 4\ H^+ + 4\ e^-$" four electrons are produced per molecule O_2. The reduction of [**1**]$^{3+}$ requires one electron. Hence, the total amount of O_2 is $n(O_2, \text{total}) = \frac{1}{4} \times n_{\mathrm{Ce}} = 0.026$ mmol which corresponds to a volume of $V(O_2, \text{total}) = n(O_2, \text{total}) \times 22.4\ \mathrm{l\ mol^{-1}} = 0.58$ ml. A sample of $V_1 = 24$ ml was taken out of the gas phase through the septum by a syringe. The total volume of the gas phase was $V(\text{gas phase}) = 76$ ml. This should correspond to maximum theoretical O_2 amount of $n(O_2 \text{ in } V_1) = n(O_2, \text{total}) \times V_1 \times [V(\text{gas phase})]^{-1} = 8.2 \times 10^{-3}$ mmol.
A d_8-THF solution of $IrCl(PEt_3)_3$ (55 mM) was prepared (see the Supporting Information). An NMR tube was filled with 2.0 ml of the $IrCl(PEt_3)_3$ solution and the sample was bubbled very slowly through the solution. ^{31}P-NMR spectra of the sample solution and of a blind sample (without cerium salt) were measured and the integrals I_x ($x = 1 - 4$, see Figure S9 of the Supporting Information) of the four relevant ^{31}P resonances were determined.

The amount of produced O_2 was calculated by the following procedure:

$$n(O_2) = \Delta n(\mathrm{IrCl(PEt_3)_3}) = n_{\mathrm{sample}}(\mathrm{IrCl(PEt_3)_3}) - n_{\mathrm{blind}}(\mathrm{IrCl(PEt_3)_3})$$

$$= n(\text{total amount of Ir}) \times \left[\frac{I_{1,\mathrm{sample}}+I_{2,\mathrm{sample}}}{I_{1,\mathrm{sample}}+I_{2,\mathrm{sample}}+I_{3,\mathrm{sample}}+I_{4,\mathrm{sample}}} - \frac{I_{1,\mathrm{blind}}+I_{2,\mathrm{blind}}}{I_{1,\mathrm{blind}}+I_{2,\mathrm{blind}}+I_{3,\mathrm{blind}}+I_{4,\mathrm{blind}}}\right]$$

$$= 1.1 \times 10^{-4}\ \mathrm{mmol} \times \left[\frac{0.968+2.000}{0.968+2.000+0.077+0.144} - \frac{0.975+2.000}{0.975+2.000+0.072+0.140}\right]$$

$$= 3.1 \times 10^{-7}\ \mathrm{mmol}$$

Thus, the experimental amount of produced O_2 was $n(O_2) = 3.1 \times 10^{-7}$ mmol. This corresponds to 0.0037% of the expected amount. Within the experimental error no oxygen was detected. In a positive sample 0.4 ml air (3.8×10^{-3} mmol O_2) were bubbled very slowly in an Ar atmosphere through a d_8-THF solution of $IrCl(PEt_3)_3$ (55 mM, 0.7 ml, 39 µmol). The full conversion of $IrCl(PEt_3)_3$ into its oxygen adduct $IrCl(O_2)(PEt_3)_3$ was observed via ^{31}P-NMR spectra.

Oxidation 8. The amount of produced O_2 was also measured with a ZrO_2-based sensor. The oxidation was performed exactly as described above (*Oxidation 7*) but in a reaction vessel with a total volume of 41 ml (instead of 86 ml) equipped with a septum, i.e. the volume of the gas phase was V_1 = 31 ml. After 17 h a sample with V_2 = 12 ml was taken out of the gas phase by a syringe and injected into a reaction vessel which had a volume of V_3 = 81 ml. The theoretical amount of generated O_2 is again $V(O_2, \text{total})$ = 5.8 ml.

The theoretical maximum concentration of produced O_2 is (with the same assumptions as for *Oxidation 7*):

$$c(O_2) = \frac{V(O_2,\text{total})}{V_1} \times \frac{V_2}{V_3} \times 10^6\ \mathrm{ppm} = \frac{5.8\ \mathrm{ml}}{31\ \mathrm{ml}} \times \frac{12\ \mathrm{ml}}{81\ \mathrm{ml}} \times 10^6\ \mathrm{ppm} = 2782\ \mathrm{ppm}$$

The experimentally determined concentration of produced O_2 was 0.6 ± 1.0 ppm. In a blind sample (without cerium salt) the concentration of produced O_2 was 1.5 ± 1.0 ppm. Again within experimental error no oxygen was detected.

Oxidation 9. A solvent mixture of 0.5 M TFA in $H_2O:CH_3CN$ (1:200) was used. A solution of [**1**]$(PF_6)_2$ (2.95×10^{-4} M, 1.0 ml) was prepared and a solution of $(NH_4)_2[Ce(NO_3)_6]$ (8.19×10^{-3} M, 72 µl, 2.0 equiv) was added. The orange solution of [**1**]$(PF_6)_2$ immediately turned green after addition of the $(NH_4)_2[Ce(NO_3)_6]$ solution. Within 2 days the color of the solution turned back to orange.

Oxidation 10. A solvent mixture of 0.5 M HNO_3 in H_2O was used. A solution of [**1**]$(PF_6)_2$ (8.00×10^{-4} M, 1.5 ml) was prepared and a solution of $(NH_4)_2[Ce(NO_3)_6]$ (1.51×10^{-2} M, 159 µl, 2.0 equiv) was added. The orange solution of [**1**]$(PF_6)_2$ immediately turned green after addition of the $(NH_4)_2[Ce(NO_3)_6]$ solution. Within 2 days the color of the solution turned back to orange.

Oxidation 11. A solvent mixture of 0.1 M H_2SO_4 in H_2O was used. A solution of [**1**]$(PF_6)_2$ (1.1×10^{-3} M, 1.0 ml) was prepared and a solution of $Ce(SO_4)_2 \cdot 4\ H_2O$ (16 mM, 1.34 ml, 2.0 equiv) was added. The orange solution of [**1**]$(PF_6)_2$ immediately turned green after addition of the $Ce(SO_4)_2 \cdot 4\ H_2O$ solution. Within 2 days the color of the solution turned back to orange.

Oxidation 12. A solvent mixture of 0.11 M H_2SO_4 in $H_2O:CH_3CN$ (15:85) was used. A solution of [**1**]$(PF_6)_2$ (9.69×10^{-5} M, 5 ml) was prepared and a solution of $(NH_4)_2[Ce(NO_3)_6]$ (1.70×10^{-3} M, 0.314 ml, 1.1 equiv) was added. The orange solution of [**1**]$(PF_6)_2$ immediately turned green after the addition of the $(NH_4)_2[Ce(NO_3)_6]$ solution. The freshly oxidized solution was filled into a 2 mm quartz cuvette and treated with UV light (Benda, NU-4 KL, 0.18 W, λ_{emiss} = 254 and 366 nm) and UV/Vis spectra were recorded. In a reference experiment the cuvette with the reaction mixture was kept in the dark.

Oxidation 13. A solvent mixture of 0.11 M H_2SO_4 in $H_2O:CH_3CN$ (15:85) was used. A solution of [**1**]$(PF_6)_2$ (9.69×10^{-5} M, 0.5 ml) was prepared and a solution of $(NH_4)_2[Ce(NO_3)_6]$ (2.56 M, 33 µl, 1.3 equiv) was added. The orange solution of [**1**]$(PF_6)_2$ immediately turned green after addition of the $(NH_4)_2[Ce(NO_3)_6]$ solution. The freshly oxidized solution was filled into a 2 mm quartz cuvette and treated with UV light (Benda, NU-4 KL, 0.18 W, λ_{exc} = 254 and 366 nm) for 10 min. Then a second portion of the same Ce^{IV} solution (2.56 M, 33 µl, 1.3 equiv) was added and again the solution was treated with UV light for 10 min. The procedure was repeated until five portions of Ce^{IV} and five periods of UV light treatments were conducted. UV/Vis spectra were recorded before, freshly after addition of Ce^{IV} and after treatment with UV light.

Oxidation 14. A solvent mixture of 0.5 M TFA in H_2O was used. A solution of [**1**]$(PF_6)_2$ (1.10×10^{-4} M, 3.0 ml) was prepared and a solution of $(NH_4)_2[Ce(NO_3)_6]$ (6.09×10^{-3} M, 109 µl, 2.0 equiv) was added. The orange solution of [**1**]$(PF_6)_2$ immediately turned green after addition of the $(NH_4)_2[Ce(NO_3)_6]$ solution. The freshly oxidized solution was filled into a 10 mm quartz cuvette and exposed to standard fume hood light conditions. In a reference experiment the cuvette with the reaction mixture was kept in the dark.

Acknowledgements

This work was supported by the International Research Training Group (IRTG 1404): Self Organized Materials for Optoelectronics supported by the Deutsche Forschungsgemeinschaft (DFG). We thank Anica Wünsche von Leupoldt for the EPR simulations.

Literature

[1] S. Campagna, F. Puntoriero, F. Nastasi, G. Bergamini, V. Balzani, *Top. Curr. Chem.* **2007**, *280*, 117–214.

[2] B. O'Regan, M. Grätzel, *Nature* **1991**, *353*, 737–740.

[3] J.-F. Yin, M. Velayudham, D. Bhattacharya, H.-C. Lin, K.-L. Lu, *Coord. Chem. Rev.* **2012**, *256*, 3008–3035.

[4] P. G. Bomben, K. C. D. Robson, B. D. Koivisto, C. P. Berlinguette, *Coord. Chem. Rev.* **2012**, *256*, 1438–1450.

[5] A. Breivogel, S. Wooh, J. Dietrich, T. Y. Kim, Y. S. Kang, K. Char, K. Heinze, *Eur. J. Inorg. Chem.* **2014**, 2720–2734.

[6] R. D. Costa, E. Ortí, H. J. Bolink, F. Monti, G. Accorsi, N. Armaroli, *Angew. Chem.* **2012**, *124*, 8300–8334; *Angew. Chem. Int. Ed.* **2012**, *51*, 8178–8211.

[7] H. J. Bolink, E. Coronado, R. D. Costa, P. Gaviña, E. Ortí, S. Tatay, *Inorg. Chem.* **2009**, *48*, 3907–3909.

[8] H. J. Bolink, L. Cappelli, E. Coronado, P. Gaviña, *Inorg. Chem.* **2005**, *44*, 5966–5968.

[9] A. Breivogel, M. Park, D. Lee, S. Klassen, A. Kühnle, C. Lee, K. Char, K. Heinze, *Eur. J. Inorg. Chem.* **2014**, 288–295.

[10] R. H. Crabtree *Energy Production and Storage: Inorganic Chemical Strategies for a Warming World*; Wiley-VCH: Weinheim, Germany, **2010**.

[11] X. Liu, F. Wang, *Coord. Chem. Rev.* **2012**, *256*, 1115–1136.

[12] M. Schulz, M. Karnahl, M. Schwalbe, J. G. Vos, *Coord. Chem. Rev.* **2012**, *256*, 1682–1705.

[13] W. T. Eckenhoff, R. Eisenberg, *Dalton Trans.* **2012**, *41*, 13004–13021.

[14] A. Inagaki, M. Akita, *Coord. Chem. Rev.* **2010**, *254*, 1220–1239.

[15] T. Stoll, M. Gennari, I. Serrano, J. Fortage, J. Chauvin, F. Odobel, M. Rebarz, O. Poizat, M. Sliwa, A. Deronizer, M.-N. Collomb, *Chem. Eur. J.* **2013**, *19*, 782–792.

[16] J. Dietrich, U. Thorenz, C. Förster, K. Heinze, *Inorg. Chem.* **2013**, *52*, 1248–1264.

[17] S. Roeser, M. Z. Ertem, C. Cady, R. Lomoth, J. Benet-Buchholz, L. Hammarström, B. Sarkar, W. Kaim, C. J. Cramer, A. Llobet, *Inorg. Chem.* **2012**, *51*, 320–327.

[18] L.-Z. Sui, W.-W. Yang, C.-J. Yao, H.-Y. Xie, Y.-W. Zhong, *Inorg. Chem.* **2012**, *51*, 1590–1598.

[19] O. S. Wenger, *Chem. Soc. Rev.* **2012**, *41*, 3772–3779.

[20] H.-J. Nie, X. Chen, C.-J. Yao, Y.-W. Zhong, G. R. Hutchison, J. Yao, *Chem. Eur. J.* **2012**, *18*, 14497–14509.

[21] A. Breivogel, K. Hempel, K. Heinze, *Inorg. Chim. Acta* **2011**, *374*, 152–162.

[22] C.-J. Yao, Y.-W. Zhong, J. Yao, *Inorg. Chem.* **2013**, *52*, 4040–4045.

[23] T. P. Brewster, W. Ding, N. D. Schley, N. Hazari, V. S. Batista, R. H. Crabtree, *Inorg. Chem.* **2011**, *50*, 11938–11946.

[24] S. Betanzos-Lara, L. Salassa, A. Habtemariam, O. Novakova, A. M. Pizarro, G. J. Clarkson, B. Liskova, V. Brabec, P. J. Sadler, *Organometallics* **2012**, *31*, 3466–3479.

[25] S. Kämper, A. Paretzki, J. Fiedler, S. Záliš, W. Kaim, *Inorg. Chem.* **2012**, *51*, 2097–2104.

[26] G. Xue, Y. Guo, T. Yu, J. Guan, X. Yu, J. Zhang, J. Liu, Z. Zou, *Int. J. Electrochem. Sci.* **2012**, *7*, 1496–1511.

[27] A. Bahreman, B. Limburg, M. A. Siegler, E. Bouwman, S. Bonnet, *Inorg. Chem.* **2013**, *52*, 9456–9469.

[28] P. T. Nguyen, B. X. T. Lam, A. R. Andersen, P. E. Hansen, T. Lund, *Eur. J. Inorg. Chem.* **2011**, 2533–2539.

[29] C. Dragonetti, A. Valore, A. Colombo, D. Roberto, V. Trifiletti, N. Manfredi, M. M. Salamone, R. Ruffo, A. Abbotto, *J. Organomet. Chem.* **2012**, *714*, 88–93.

[30] M. M. R. Choudhuri, R. J. Crutchley, *Inorg. Chem.* **2013**, *52*, 14404–14410.

[31] C.-W. Hsu, S.-T. Ho, K.-L. Wu, Y. Chi, S.-H. Liu, P.-T. Chou, *Energy Environ. Sci.* **2012**, *5*, 7549–7554.

[32] B. Schulze, D. Escudero, C. Friebe, R. Siebert, H. Görls, S. Sinn, M. Thomas, S. Mai, J. Popp, B. Dietzek, L. González, U. S. Schubert, *Chem. Eur. J.* **2012**, *18*, 4010–4025.

[33] R. Hogg, R. G. Wilkins, *J. Chem. Soc.* **1962**, 341–350.

[34] R. H. Holyer, C. D. Hubbard, S. F. A. Kettle, R. G. Wilkins, *Inorg. Chem.* **1966**, *5*, 622–625.

[35] M. Abrahamsson, M. Jäger, R. J. Kumar, T. Österman, P. Persson, H.-C. Becker, O. Johansson, L. Hammarström, *J. Am. Chem. Soc.* **2008**, *130*, 15533–15542.

[36] Recalculated from a previous value for $[Ru(bpy)_3]Cl_2$ to the updated $[Ru(bpy)_3]Cl_2$ standard according to A. Breivogel, C. Kreitner, K. Heinze, *Eur. J. Inorg. Chem.* **2014**, accepted.

[37] J.-P. Sauvage, J.-P. Collin, J.-C. Chambron, S. Guillerez, C. Coudret, V. Balzani, F. Barigelletti, L. D. Cola, L. Flamigni, *Chem. Rev.* **1994**, *94*, 993–1019.

[38] L. Hammarström, O. Johansson, *Coord. Chem. Rev.* **2010**, *254*, 2546–2559.

[39] Y. Liu, R. Hammitt, D. A. Lutterman, R. P. Thummel, C. Turro, *Inorg. Chem.* **2007**, *46*, 6011–6021.

[40] K. Heinze, K. Hempel, M. Beckmann, *Eur. J. Inorg. Chem.* **2006**, *10*, 2040–2050.

[41] K. Heinze, K. Hempel, A. Breivogel, *Z. Anorg. Allg. Chem.* **2009**, *635*, 2541–2549.

[42] D. G. Brown, N. Sanguantrakun, B. Schulze, U. S. Schubert, C. P. Berlinguette, *J. Am. Chem. Soc.* **2012**, *134*, 12354–12357.

[43] A. Breivogel, M. Meister, C. Förster, F. Laquei, K. Heinze, *Chem. Eur. J.* **2013**, *19*, 13745–13760.

[44] M. Abrahamsson, M. Jäger, T. Österman, L. Eriksson, P. Persson, H.-C. Becker, O. Johansson, L. Hammarström, *J. Am. Chem. Soc.* **2006**, *128*, 12616–12617.

[45] M. Abrahamsson, M. Jäger, R. J. Kumar, T. Österman, P. Persson, H.-C. Becker, O. Johansson, L. Hammarström, *J. Am. Chem. Soc.* **2008**, *130*, 15533–15542.

[46] F. Schramm, V. Meded, H. Fliegl, K. Fink, O. Fuhr, Z. Qu, W. Klopper, S. Finn, T. E. Keyes, M. Ruben, *Inorg. Chem.* **2009**, *48*, 5677–5684.

[47] G. A. Parada, L. A. Fredin, M.-P. Santoni, M. Jäger, R. Lomoth, L. Hammarström, O. Johansson, P. Persson, S. Ott, *Inorg. Chem.* **2013**, *52*, 5128–5137.

[48] J. Dietrich, A. Wünsche von Leupoldt, M. Grabolle, U. Resch-Genger, K. Heinze, *Eur. J. Inorg. Chem.* **2013**, 3009–3019.

[49] K. Heinze, K. Hempel, *Chem. Eur. J.* **2009**, *15*, 1346–1358.

[50] L. zur Borg, A. L. Domanski, A. Breivogel, M. Bürger, R. Berger, K. Heinze, R. Zentel, *J. Mater. Chem. C* **2013**, *1*, 1223–1230.

[51] C. Kreitner, K. Heinze, to be submitted.

[52] M. D. Kärkäs, T. Åkermark, H. Chen, J. Sun, B. Åkermark, *Angew. Chem.* **2013**, *125*, 4283–4287; *Angew. Chem. Int. Ed.* **2013**, *52*, 4189–4193.

[53] B.-L. Lee, M. D. Kärkäs, E. V. Johnston, A. K. Inge, L.-H. Tran, Y. Xu, Ö. Hansson, X. Zou, B. Åkermark, *Eur. J. Inorg. Chem.* **2010**, 5462–5470.

[54] D. J. Wasylenko, C. Ganesamoorthy, B. D. Koivisto, M. A. Henderson, C. P. Berlinguette, *Inorg. Chem.* **2010**, *49*, 2202–2209.

[55] M. D. Kärkäs, E. V. Johnston, E. A. Karlsson, B.-L. Lee, T. Åkermark, M. Shariatgorji, L. Ilag, Ö. Hansson, J.-E. Bäckvall, B. Åkermark, *Chem. Eur. J.* **2011**, *17*, 7953–7959.

[56] D. Kotkar, V. Joshi, P. K. Ghosh, *Inorg. Chem.* **1986**, *25*, 4334–4335.

[57] L. Duan, F. Bozoglian, S. Mandal, B. Stewart, T. Privalov, A. Llobet, L. Sun, *Nat. Chem.* **2012**, *4*, 418–423.

[58] N. G. Connelly, W. E. Geiger, *Chem. Rev.* **1996**, *96*, 877–910.

[59] P. A. Lay, W. H. F. Sasse, *Inorg. Chem.* **1985**, *24*, 4707–4710.

[60] A. Harriman, G. Porter, P. Walters, *J. Chem. Soc., Faraday Trans. 2* **1981**, *77*, 2373–2383.

[61] N. Kaveevivitchai, R. Zong, H.-W. Tseng, R. Chitta, R. P. Thummel, *Inorg. Chem.* **2012**, *51*, 2930–2939.

[62] N. Kaveevivitchai, L. Kohler, R. Zong, M. E. Ojaimi, N. Mehta, R. P. Thummel, *Inorg. Chem.* **2013**, *52*, 10615–10622.

[63] L. Duan, L. Wang, A. K. Inge, A. Fischer, X. Zou, L. Sun, *Inorg. Chem.* **2013**, *52*, 7844–7852.

[64] L. Wang, L. Duan, B. Stewart, M. Pu, J. Liu, T. Privalov, L. Sun, *J. Am. Chem. Soc.* **2012**, *134*, 18868–18880.

[65] H.-W. Tseng, R. Zong, J. T. Muckermann, R. Thummel, *Inorg. Chem.* **2008**, *47*, 11763–11773.

[66] S. W. Kohl, L. Weiner, L. Schwartsburd, L. Konstantinovski, L. J. W. Shimon, Y. Ben-David, M. A. Iron, D. Milstein, *Science* **2009**, *324*, 74–77.

[67] A. A. Vlcek, E. S. Dodsworth, W. J. Pietro, A. B. P. Lever, *Inorg. Chem.* **1995**, *34*, 1906–1913.

[68] C. R. Bock, J. A. Connor, A. R. Gutierrez, T. J. Meyer, D. G. Whitten, B. P. Sullivan, J. K. Nagle, *J. Am. Chem. Soc.* **1979**, *101*, 4815–4824.

[69] A. L. Casalnuovo, J. C. Calabrese, D. Milstein, *J. Am. Chem. Soc.* **1988**, *110*, 6738–6744.

[70] M. J. Frisch, G. W. Trucks, H. B. Schlegel, G. E. Scuseria, M. A. Robb, J. R. Cheeseman, G. Scalmani, V. Barone, B. Mennucci, G. A. Petersson, H. Nakatsuji, M. Caricato, X. Li, H. P. Hratchian, A. F. Izmaylov, J. Bloino, G. Zheng, J. L. Sonnenberg, M. Hada, M. Ehara, K. Toyota, R. Fukuda, J. Hasegawa, M. Ishida, T. Nakajima, Y. Honda, O. Kitao, H. Nakai, T. Vreven, J. A. Montgomery, Jr., J. E. Peralta, F. Ogliaro, M. Bearpark, J. J. Heyd, E. Brothers, K. N. Kudin, V. N. Staroverov, R. Kobayashi, J. Normand, K. Raghavachari, A. Rendell, J. C. Burant, S. S. Iyengar, J. Tomasi, M. Cossi, N. Rega, J. M. Millam, M. Klene, J. E. Knox, J. B. Cross, V. Bakken, C. Adamo, J. Jaramillo, R.

Gomperts, R. E. Stratmann, O. Yazyev, A. J. Austin, R. Cammi, C. Pomelli, J. W. Ochterski, R. L. Martin, K. Morokuma, V. G. Zakrzewski, G. A. Voth, P. Salvador, J. J. Dannenberg, S. Dapprich, A. D. Daniels, O. Farkas, J. B. Foresman, J. V. Ortiz, J. Cioslowski, D. J. Fox *Gaussian 09*, revision A.02, Gaussian, Inc.: Wallingford CT, 2009.

[71] J. M. Achord, C. L. Hussey, *Anal. Chem.* **1980**, *52*, 601–602.

[72] C. Franco, J. Olmsted III, *Talanta* **1990**, *37*, 905–909.

9.3 Dinuclear Bis(terpyridine)ruthenium(II) Complexes by Amide Coupling of Ruthenium Amino Acids: Synthesis and Properties

A. Breivogel, K. Hempel, K. Heinze, *Inorg. Chim. Acta* **2011**, *374*, 152–162.

DOI: 10.1016/j.ica.2011.03.046

Inorganica Chimica Acta 374 (2011) 152–162

Contents lists available at ScienceDirect

Inorganica Chimica Acta

journal homepage: www.elsevier.com/locate/ica

Dinuclear bis(terpyridine)ruthenium(II) complexes by amide coupling of ruthenium amino acids: Synthesis and properties

Aaron Breivogel [a], Klaus Hempel [b], Katja Heinze [a,*]

[a] Institute of Inorganic and Analytical Chemistry, Johannes Gutenberg-University of Mainz, Duesbergweg 10-14, 55128 Mainz, Germany
[b] Department of Inorganic Chemistry, Ruprecht Karls-University of Heidelberg, Im Neuenheimer Feld 270, 69120 Heidelberg, Germany

ARTICLE INFO

Article history:
Available online 27 March 2011

Dedicated to Prof. Dr. Wolfgang Kaim on the occasion of his 60th birthday

Keywords:
Amino acids
Charge transfer
Donor–acceptor systems
Mixed-valency
Ruthenium
Terpyridine

ABSTRACT

Two redox-asymmetric amide-bridged bis(terpyridine)ruthenium(II) complexes (**3a**, **3b**) have been prepared by amide coupling of a carboxylic acid functionalized complex with an amine substituted complex and they were fully characterized by spectroscopic analyses. They emit at 692 and 750 nm at room temperature in fluid solution with quantum yields larger than 10^{-3} and ^{3}MLCT lifetimes of 22 ns. Ru···Ru distances were estimated from DFT models as 17.7 and 13.4 Å for **3a** and **3b**, respectively. Cyclic voltammetry gives two oxidation potentials for the differently substituted ruthenium sites with splittings of 0.10 and 0.23 V for **3a** and **3b**, respectively. Oxidation of **3b** with Ce^{IV} ions gives the corresponding mixed-valent Ru^{II}–Ru^{III} system which is valence-localized according to NIR spectroscopic and theoretical analyses.

1. Introduction

The controlled assembly of multinuclear metal complexes in a precise fashion is a challenging task although several elegant solutions have been proposed, e.g. a chemistry-on-a-complex approach (complexes as ligands/complexes as metals) [1–4], solid-phase syntheses procedures [5] or supramolecular approaches [6,7]. For the first mentioned strategies rather stable metal complexes are needed while programmable labile systems can be employed in self-assembly processes.

Natural oligomeric systems often rely on directional connectors, e.g. sugar-phosphate esters in DNA/RNA or amide groups in peptides. Natural and artificial peptides with a precise amino acid sequence can be easily prepared employing adequate protection/deprotection and coupling techniques – even in an automated fashion on solid supports (solid-phase peptide synthesis) [8]. Amide connectors have been increasingly used to assemble multinuclear metal complexes in a controlled fashion [5,9–11]. As useful building blocks for metallo peptides metallo amino acids (e.g. **A** [9,12], **B** [13,14]; Scheme 1) have been developed.

Based on bis(terpyridine)ruthenium(II) fragments the ruthenium amino acid **1b** and its phenyl-elongated homologues **A** have been devised and realized (Scheme 1) [9,12]. Using ferrocene amino acid **B** [13,14] we have also reported amide bridged bis- and tris-ferrocenes **C** and their oxidized counterparts C^{x+} (Scheme 1) [10,11,15,16]. The neutral and the oxidized systems are potentially useful as molecular wires and as ion sensors [10,11,15–17]. Amide linked conjugates of the ruthenium amino acid **1b** and ferrocene derivatives have been shown to exhibit photoinduced electron transfer provided matching redox potentials are employed at the ferrocene electron donor site [9]. Energy transfer is observed in amide-linked conjugates of the ruthenium amino acid **1b** and matching organic chromophores (e.g. coumarins) [18].

We were then interested to study the interaction between two ruthenium centers in dinuclear systems based on ruthenium amino acid **1b**. Such long-range communication pathways in multimetallic assemblies are of fundamental importance and are furthermore of potential usage in molecular electronics. Oligonuclear ruthenium complexes have been proposed as components in photochemical molecular devices, for molecular recognition, information storage, energy conversion and catalysis applications [19,20].

Mixed-valence compounds containing metallic centers in different formal oxidation states ($M^{n+}/M^{(n+1)+}$) have been widely employed to study intramolecular electron transfer (ET) processes between donor and acceptor sites and several review articles have been published [21–36]. Robin and Day classified mixed-valence systems as a function of the strength of the electronic interaction (coupling) between donor and acceptor sites [37]. Species of Class I essentially exhibit negligible metal–metal interaction while Class II compounds include species with a nonzero barrier for valence exchange. Class III systems feature fully delocalized valencies.

---

* Corresponding author. Fax: +49 6131 3927277.
E-mail address: katja.heinze@uni-mainz.de (K. Heinze).

0020-1693/$ - see front matter © 2011 Elsevier B.V. All rights reserved.
doi:10.1016/j.ica.2011.03.046

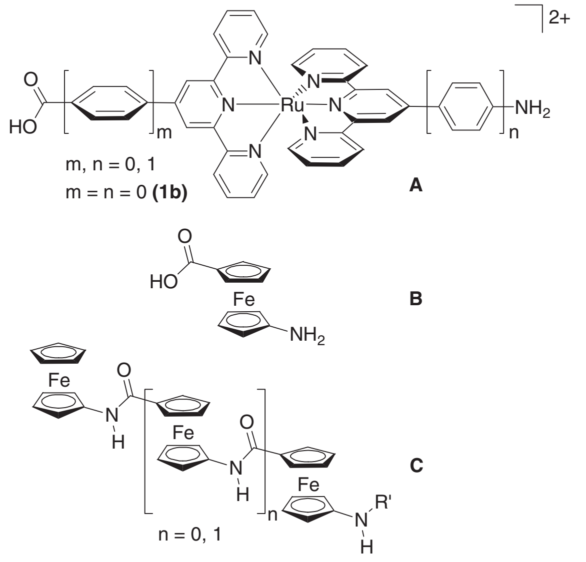

Scheme 1. Bis(terpyridine)ruthenium(II) amino acids **A** [9,12], ferrocene amino acid **B** [13,14] and oligoferroceneamides **C** [10,11,15,16].

A multitude of experimental and theoretical studies, especially on symmetrical systems with the textbook prototype being the Creutz–Taube ion $[(NH_3)_5Ru(pz)Ru(NH_3)_5]^{5+}$ (py = pyrazine) [38,39], have established that the molecular architecture – mainly the distance between redox sites and the bridging ligand planarity – controls the through-bond electronic coupling [21–36].

Directional electron transfer might be achieved using slightly asymmetric systems in terms of local redox potentials. This is an advanced extension of symmetrical homodinuclear systems possessing zero driving force for ET which have been thoroughly studied and are well understood [21–36]. Asymmetry can be introduced by differing metal centers (M, M′), differing terminal ligands (L, L′) or asymmetrical bridging ligands (L–L′). The amide bridge considered here naturally introduces an aspect of asymmetry and directionality in oligoamides and peptides (*N*-terminal end → *C*-terminal end).

The dinuclear complex $[(tpy)\ Ru\ (tpy\text{-}Ph\text{-}NHCO\text{-}Ph\text{-}tpy)\ Ru\ (tpy)]^{4+}$ **D** with an amide bridge and two *para*-phenylene units has been reported by Colbran (Scheme 2) [40]. As compared to mononuclear models an approximately doubled extinction coefficient (at λ_{max} = 487 nm, ε = 50 800 $M^{-1}\ cm^{-1}$) and an unshifted absorption MLCT maximum were observed. No splitting of the (two-electron) Ru^{II}/Ru^{III} couple at 1.25 V versus SCE in CH_3CN was reported. The data suggest that the ruthenium centers in **D** are isolated and electrochemically independent in the ground state. This is possibly due to the "dilution" with non-planar *para*-phenylene spacers [40]. However, no emission data has been reported to access the excited state properties. Similarly, the "expanded leucines" **E** [41] display additive extinction at 494 nm (unshifted λ_{max}) and one single Ru^{II}/Ru^{III} redox couple at +1.26 V versus SCE (Scheme 2). Again, these observations are very likely due to the separation of the redoxactive $[(tpy)Ru(tpy)]^{2+}$ units by non-planar *para*-phenylene and leucine spacers. Based on the observation of a single oxidation wave in electrochemical experiments metal–metal interaction in dinuclear complexes **F** with 'back-to-back' terpyridine and *para*-phenylene bridged bis-terpyridines seems to be absent (Scheme 2). However, in spite of the non-planar bridging ligand spectroelectrochemical investigations revealed a weak electronic interaction in the mixed-valent systems $\mathbf{F}^{+}$ [42–44]. Complexes of type **F** are non emissive at room temperature similar to the parent mononuclear complex $[(tpy)_2Ru]^{2+}$ [44]. Campagna and Hannan recently managed to planarize the briding π-system by replacing two CH groups by nitrogen atoms which allows for favourable CH···N interactions within the bridge (Scheme 2, **G**) [4]. The planarized bridge of **G** enhances the metal–metal interaction and two Ru^{II}/Ru^{III} oxidation processes were observed with $\Delta(E_{1/2})$ = 90 mV giving a comproportionation constant $K_C \sim 33$ for the mixed-valent cation $\mathbf{G}^{+}$. In addition a long-lived ^{3}MLCT emission has been observed for **G** [4]. A different successful strategy to planarize the bridging ligand in terpyridine-type ruthenium complexes has been introduced by Harriman using tethers of differing lengths within the bridge (Scheme 2, **H**). Although negligible Ru^{II}/Ru^{III} redox separations were found spectroelectrochemical studies revealed a weak electronic coupling (weakly coupled Class II) [45].

As an amide bridge allows for a rather coplanar arrangement of connected Ru(tpy) moieties we wish to address the question

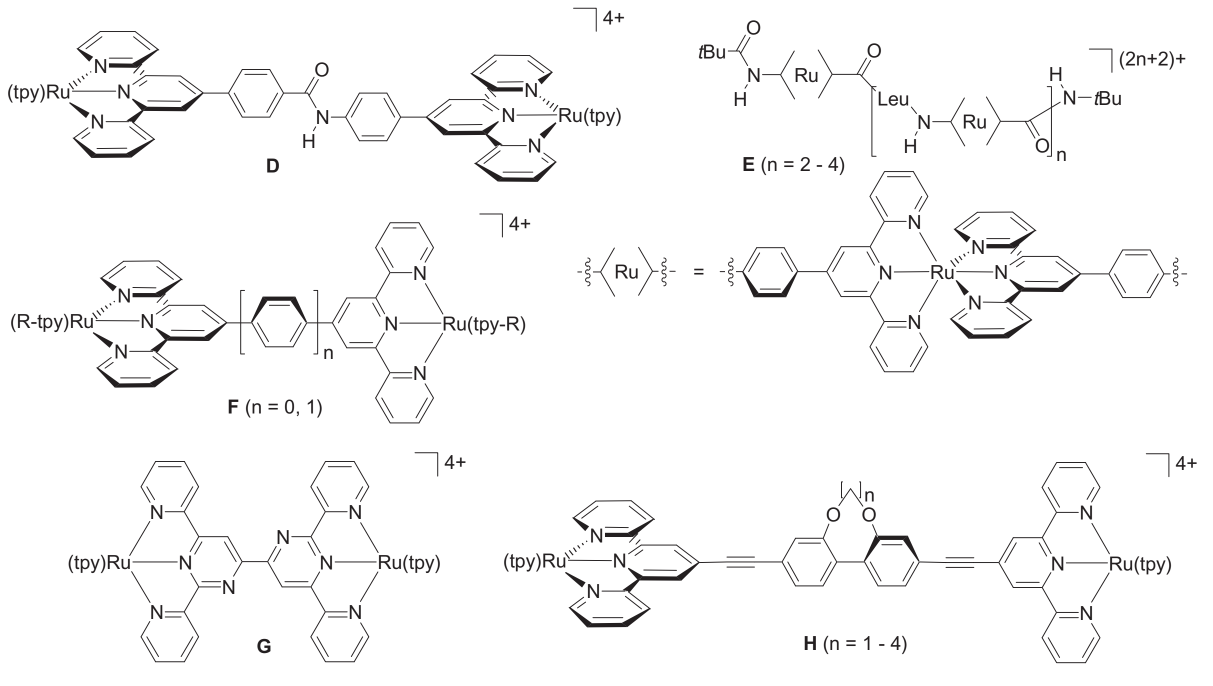

Scheme 2. Selection of linear oligonuclear bis(terpyridine)ruthenium(II) complexes **D**–**H** (tpy = 2,2′:6′,2″-terpyridine, R-tpy = 4′-p-tolyl-2,2′:6′,2″-terpyridine or tpy).

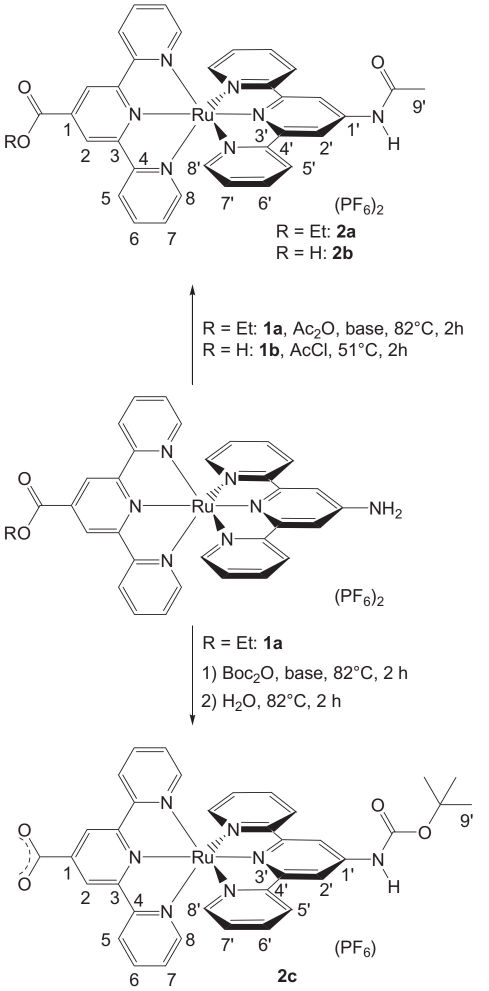

Scheme 3. *N*-Acylation of ruthenium amino acid ester **1a** and ruthenium amino acid **1b**–**2a** [46] and **2b** and Boc protection of **1a**–**2c** and atom numbering for NMR assignments.

whether metal–metal communication across an amide linkage is possible in dinuclear bis(terpyridine)ruthenium complexes. We report the synthesis of two amide bridged bis(terpyridine)ruthenium(II) complexes with one single *para*-phenylene spacer (**3a**) and without any *para*-phenylene spacers (**3b**) in addition to the connecting amide unit. The synthetic starting point is the bis(terpyridine)ruthenium(II) amino acid **1b** and its ethyl ester **1a** [9]. The *para*-phenylene spacer of **3a** is expected to disrupt any π-conjugation pathway, similar to the **D** case (Scheme 2), while in **3b** the bridge is expected to be rather planar. For comparison of optical and electrochemical data the mononuclear *N*-acetyl protected bis(terpyridine)ruthenium(II) amino acid **2b** and its ethyl ester **2a** [46] are reported together with the *N*-Boc protected bis(terpyridine)ruthenium(II) amino carboxylate **2c** as versatile synthetic intermediate for the construction of dinuclear amide linked bis(terpyridine)ruthenium(II) complexes.

2. Experimental

2.1. General procedures

Chemicals were obtained from commercial suppliers and used without further purification. Bis(terpyridine)ruthenium(II) complexes **1a**, **1b** [9] and **2a** [46] were synthesized as reported. [Ru(tpy-C_6H_4–COOH)(*t*Bu_3tpy)]$(PF_6)_2$ has been prepared by Prof. Dr. Sven Rau [47] IR spectra were recorded on a BioRad Excalibur FTS 3000 spectrometer using caesium iodide disks. UV/Vis spectra were recorded on a Perkin–Elmer Lambda 19 or on a Varian Cary 5000 spectrometer in 1.0 cm cells (Hellma, suprasil). FAB mass spectra were recorded with a Finnigan MAT 8400 mass spectrometer. ESI$^+$ mass spectra were recorded with a Finnigan TSQ 700 triple-quadrupole or a Q-Tof Ultima API mass spectrometer (Micromass/Waters) with analyte solutions in acetonitrile. NMR spectra were obtained on a Bruker Avance DPX 200 (200 MHz, ^1H) or a Bruker Avance II 400 (400 MHz, ^1H) at 30 °C. Chemical shifts (δ/ppm) are reported with respect to residual solvent peaks as internal standards: CD_3CN $\delta(^1H) = 1.94$ ppm, $\delta(^{13}C) = 1.24$ ppm. Cyclic voltammetry was performed on a Metrohm "Universal Mess- und Titriergefaess", Metrohm GC electrode RDE 628, platinum electrode, SCE electrode, Princeton Applied Research potentiostat Model 273; in 0.1 m *n*Bu_4NPF_6/CH_3CN. Potentials are given relative to that of SCE. Emission spectra were recorded on a Varian Cary Eclipse spectrometer. Quantum yields were determined by comparing the areas under the emission spectra on an energy scale [cm^{-1}] recorded for optically matched solutions of the samples and the reference $\{\phi([Ru(bpy)_3]^{2+}) = 0.062$ in $CH_3CN\}$ [48]; experimental uncertainty 15%. Luminescence lifetimes were determined on a PicoQuant FluoTime 100 time-correlated single-photon counting unit. Criteria for the best fit were the values of χ^2; experimental uncertainty 10%. Density functional calculations were carried out with the GAUSSIAN03/DFT [49] series of programs. The B3LYP formulation of density functional theory was used employing the LanL2DZ basis set [49]. All structures were characterized as minima by frequency analysis ($N_{imag} = 0$). No symmetry constraints were imposed on the molecules.

2.2. Synthesis of **2b**

Acid **1b** (150 mg, 0.16 mmol) was dissolved in acetyl chloride (20 mL) and the solution was heated under reflux for 2 h. After cooling to room temperature and removal of the solvent in vacuo the residue was dissolved in acetonitrile and the product was precipitated by the addition of diethyl ether. The product was collected by filtration, dissolved in hot water and precipitated by the addition of NH_4PF_6 (78 mg, 0.48 mmol) in water (1 ml). The product was collected by filtration and dried in vacuo to give a red powder. Yield 51% (80 mg, 0.08 mmol). Anal. Calc. $C_{33}H_{25}N_7O_3RuP_2F_{12}$ (958.60)·$4H_2O$: C, 38.46; H, 3.23; N, 9.51. Found: C, 38.63; H, 3.13; N, 9.68%. MS (FAB$^+$): m/z (%) = 814 (16) $[M+PF_6]^+$. ^1H NMR (CD_3CN, 200 MHz): $\delta = 9.46$ (s, 1H, NH), 9.19 (s, 2H, H^2), 8.96 (s, 2H, $H^{2'}$), 8.64 (d, $^3J_{HH} = 8.0$ Hz, 2H, H^5), 8.39 (d, $^3J_{HH} = 8.0$ Hz, 2H, $H^{5'}$), 7.86–7.98 (m, 4H, $H^{6,6'}$), 7.45 (d, $^3J_{HH} = 5.2$ Hz, 2H, H^8), 7.19–7.28 (m, 4H, $H^{7,7'}$), 7.11 (ddd, $^3J_{HH} = 6.6$ Hz, $^4J_{HH} = 1.20$ Hz, 2H, $H^{8'}$), 2.37 (s, 3H, $H^{9'}$). ^{13}C NMR (CD_3CN, 50 MHz): $\delta = 159.4$, 159.3, 158.1, 156.6 (4 s, $C^{3,3',4,4'}$), 154.4 (s, $C^{8'}$), 154.0 (s, C^8), 154.4 (s, $C^{1'}$), 139.9 (s, $C^{6'}$), 139.7 (s, C^6), 137.0 (s, C^1), 129.4 (s, C^7), 129.1 (s, $C^{7'}$), 126.4 (s, C^5), 126.1 (s, $C^{5'}$), 124.6 (s, C^2), 114.5 (s, $C^{2'}$), 25.5 (s, $C^{9'}$), COOH and NHCO were not observed. IR (CsI): $\nu = 3454$ (OH, NH), 3085 (CH_{aryl}), 2936 (CH_{alkyl}), 1711 (C=O), 1689 (amide I), 1525 (amide II), 1563 (C=N, C=C), 1246 (C–O), 841 (PF) cm^{-1}.

2.3. Synthesis of **2c**

Ester **1a** (200 mg, 0.21 mmol) and di-*tert*-butyldicarbonate (231 mg, 1.06 mmol) were dissolved in dry acetonitrile (15 mL) and phosphazene base P_1-*t*Bu[1] [51,52] (229 mg, 0.98 mmol) was added. The solution was heated under reflux for 2 h. After the

---

[1] Phosphazene base P_1-*t*Bu = tert-butylimino-tris(dimethylamino)-phosphorane.

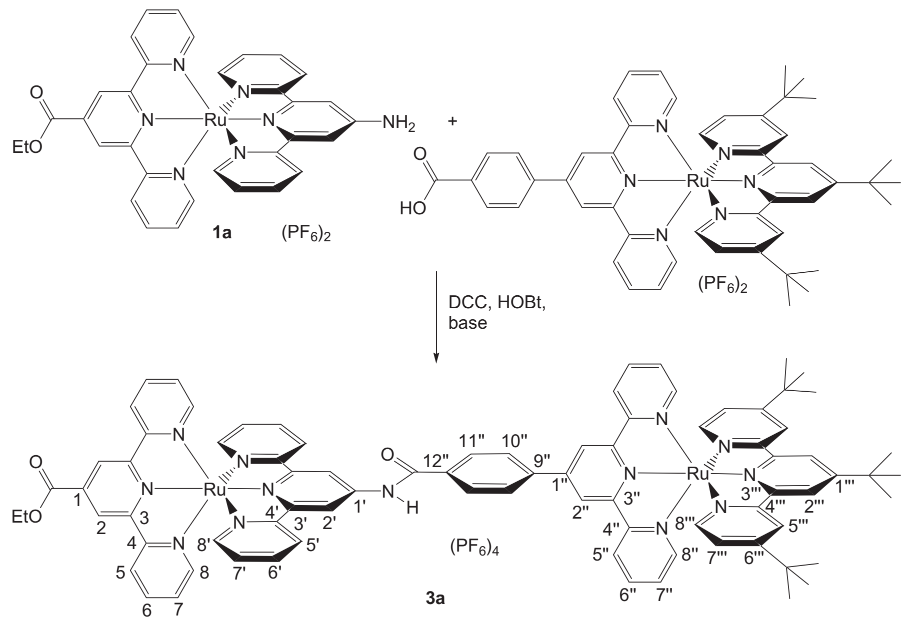

Scheme 4. Amide coupling of amino acid ester **1a** and [Ru(tpy-C_6H_4–COOH)($t$$Bu_3$tpy)]$(PF_6)_2$ to **3a** and atom numbering for NMR assignments.

addition of water (5 mL) the mixture was heated under reflux for 2 h. After cooling to room temperature and removal of the solvent in vacuo the residue was dissolved in acetonitrile and the product was precipitated by the addition of diethyl ether. The product was collected by filtration, dissolved in water and precipitated by the addition of NH_4PF_6 (78 mg, 0.48 mmol) in water (1 ml). The product was collected by filtration and dried in vacuo to give a red powder. Yield 93% (172 mg, 0.20 mmol). *Anal.* Calc. $C_{36}H_{30}N_7O_4RuPF_6$ (870.70)·$4H_2O$: C, 45.86; H, 4.06; N, 10.40. Found: C, 45.99; H, 4.16; N, 10.71%. MS (FAB$^+$): m/z (%) = 726 (8) $[M]^+$. ^{1}H NMR (CD_3CN, 200 MHz): δ = 10.30 (s, 1H, NH), 9.32 (s, 2H, H^2), 9.26 (s, 2H, $H^{2'}$), 8.61 (d, $^3J_{HH}$ = 8.0 Hz, 2H, H^5), 8.52 (d, $^3J_{HH}$ = 8.0 Hz, 2H, $H^{5'}$), 7.86–7.93 (m, 4H, $H^{6,6'}$), 7.44 (d, $^3J_{HH}$ = 5.5 Hz, 2H, H^8), 7.37 (d, $^3J_{HH}$ = 5.5 Hz, 2H, $H^{8'}$), 7.11–7.19 (m, 4H, $H^{7,7'}$), 1.68 (s, 9H, CH_3). ^{13}C NMR (CD_3CN, 50 MHz): δ = 167.0 (s, COO), 158.8 (s, C^3), 158.5 (s, $C^{3'}$), 156.5 (s, C^4), 155.6 (s, $C^{4'}$), 153.3 (s, CO^{Boc}), 153.2 (s, $C^{8'}$), 152.8 (s, C^8), 148.4 (s, C^1), 143.7 (s, $C^{1'}$), 138.7 (s, $C^{6'}$), 138.4 (s, C^6), 128.0 (s, C^7), 127.9 (s, $C^{7'}$), 125.1 (s, C^2), 124.6 (s, C^5), 123.8 (s, $C^{5'}$), 112.7 (s, $C^{2'}$), 82.7 (s, C_q^{Boc}), 28.0 (s, CH_3). IR (CsI): ν = 3431 (OH, NH), 3094 (CH_{aryl}), 2980 (CH_{alkyl}), 1722 (C=O), 1651 (amide I), 1564 (C=N, C=C), 1528 (amide II), 1249 (C–O), 843 (PF) cm^{-1}.

2.4. Synthesis of *3a*

[Ru(tpy-C_6H_4–COOH)($t$$Bu_3$tpy)]$(PF_6)_2$ (150 mg, 0.13 mmol), DCC (46 mg, 0.22 mmol) and HOBt (30 mg, 0.22 mmol) were dissolved in dry acetonitrile (15 mL) and stirred for 45 min at room temperature to activate the carboxylic acid. **1a** (140 mg, 0.15 mmol) and phosphazene base P_1-tBu (229 mg, 0.98 mmol) dissolved in acetonitrile (5 mL) were added and the solution was stirred for 8 h. The solution was filtered over Celite and the solvent was removed in vacuo. The residue was dissolved in hot ethanol (5 mL) and NH_4PF_6 (78 mg, 0.48 mmol) in water (1 ml) was added. After addition of excess water the precipitated product was collected by filtration. Recrystallization from ethanol/CH_2Cl_2 and drying in vacuo gave **3a** as a red powder. Yield 46% (125 mg, 0.06 mmol). *Anal.* Calc. $C_{82}H_{75}N_{13}O_3Ru_2P_4F_{24}$ (2072.56)·H_2O: C, 47.11; H, 3.71; N, 8.71. Found: C, 46.99; H, 3.71; N, 8.88%. MS (ESI$^+$): m/z (%) = 497.5 (100) $[M-H]^{3+}$, 373.4 (18) $[M]^{4+}$. ^{1}H NMR (CD_3CN, 200 MHz): δ = 10.07 (s, 1H, NH), 9.33 (s, 2H, $H^{2'}$), 9.21 (s, 2H, $H^{2''}$), 9.11 (s, 2H, H^2), 8.81 (s, 2H, $H^{2'''}$), 8.63–8.70 (m, 4H, $H^{5''}$, H^5), 8.41–8.52 (m, 8H, $H^{5'}$, $H^{5'''}$, $H^{10''}$, $H^{11''}$), 7.97–7.99 (m, 6H, H^6, $H^{6'}$, $H^{6''}$), 7.53 (d, $^3J_{HH}$ = 5.0 Hz, 2H, H^8), 7.25–7.31 (m, 10H, H^7, $H^{7''}$, $H^{8'}$, $H^{8''}$, $H^{8'''}$), 7.15–7.22 (m, 4H, $H^{7'}$, $H^{7'''}$), 4.64 (q, $^3J_{HH}$ = 6.8 Hz, 2H, CH_2), 1.77 (s, 9H, $CH_3{}'$), 1.59 (t, $^3J_{HH}$ = 6.8 Hz, 3H, CH_3), 1.33 (s, 18H, $CH_3{}''$). ^{13}C NMR (CD_3CN, 50 MHz): δ = 166.8 (s, CONH), 164.5 (s, COOEt), 163.5 (s, $C^{12''}$), 162.0 (s, $C^{9'}$), 158.6, 158.5, 158.3, 158.1, 156.6, 156.3, 155.5, 155.3 (8 s, $C^{3,3',3'',3''',4,4',4'',4'''}$), 153.3, 152.8, 152.7, 152.2 (4 s, $C^{8,8',8'',8'''}$), 147.6 (s, $C^{1'}$), 146.4 (s, $C^{1''}$), 141.6 (s, C^1), 138.9, 138.6, 138.3 (3 s, $C^{6,6',6''}$), 136.7 (s, $C^{1'''}$), 135.3 (s, $C^{6'''}$), 129.7, 128.7, 128.3, 128.0 (4 s, $C^{7,7',7'',7'''}$), 125.3, 125.0, 124.9, 124.7 (4 s, $C^{5,5',5'',5'''}$), 123.2 (s, C^2), 122.4 (s, $C^{2''}$), 122.2, 121.7 (2 s, $C^{10'',11''}$), 114.3 (2C) (s, $C^{2',2'''}$), 63.3 (s, CH_2), 36.8 (s, $C_q{}'$), 35.7 (s, $C_q{}''$), 30.6 (s, $CH_3{}'$), 29.9 (s, $CH_3{}''$), 14.9 (s, CH_3). IR (CsI): ν = 3453 (OH, NH), 3076 (CH_{aryl}), 2968 (CH_{alkyl}), 1689 (C=O, amide I), 1612 (C=N, C=C), 1526 (amide II), 1255 (C–O), 841 (PF) cm^{-1}.

2.5. Synthesis of *3b*

Boc protected **2c** (100 mg, 0.11 mmol) and PyBOP (72 mg, 0.14 mmol) were dissolved in acetonitrile (15 mL) and stirred at room temperature for 45 min to activate the carboxylic acid. **1a** (109 mg, 0.12 mmol) and phosphazene base P_1-tBu (229 mg, 0.98 mmol) dissolved in acetonitrile (5 mL) were added and the solution was heated under reflux for 2 h. Water (5 mL) was added and the mixture was heated under reflux for further 2 h. After cooling to room temperature the solvents were removed in vacuo and the residue was dissolved in acetonitrile (2 mL). Acetic acid (0.5 mL) was added and the product was precipitated by the addition of excess water. The product was collected by filtration and recrystallized from acetone/water to give a red powder. Yield 82% (170 mg, 0.09 mmol). *Anal.* Calc. $C_{62}H_{44}N_{14}O_3Ru_2P_4F_{24}$ (1815.10)·C_3H_6O: C, 41.68; H, 2.69; N, 10.47. Found: C, 41.53; H, 2.85; N, 10.22%. MS (ESI$^+$): m/z (%) = 309.0 (100) $[M]^{4+}$, 411.6 (94) $[M-H]^{3+}$. ^{1}H NMR (CD_3CN, 200 MHz): δ = 11.30 (s, 1H, NH), 9.51 (s, 2H, $H^{2'}$), 9.45 (s, 2H, $H^{2''}$), 9.24 (s, 2H, H^2), 8.77 (d, $^3J_{HH}$ = 7.8 Hz, 2H, $H^{5''}$), 8.69 (d, $^3J_{HH}$ = 7.8 Hz, 2H, H^5), 8.61 (d, $^3J_{HH}$ = 7.8 Hz, 2H, $H^{5'}$), 8.33 (d, $^3J_{HH}$ = 7.8 Hz, 2H, $H^{5'''}$), 7.86–8.07 (m, 10H, $H^{2'''}$, H^6, $H^{6'}$, $H^{6''}$, $H^{6'''}$), 7.65 (d, $^3J_{HH}$ = 7.2 Hz, 2H, H^8),

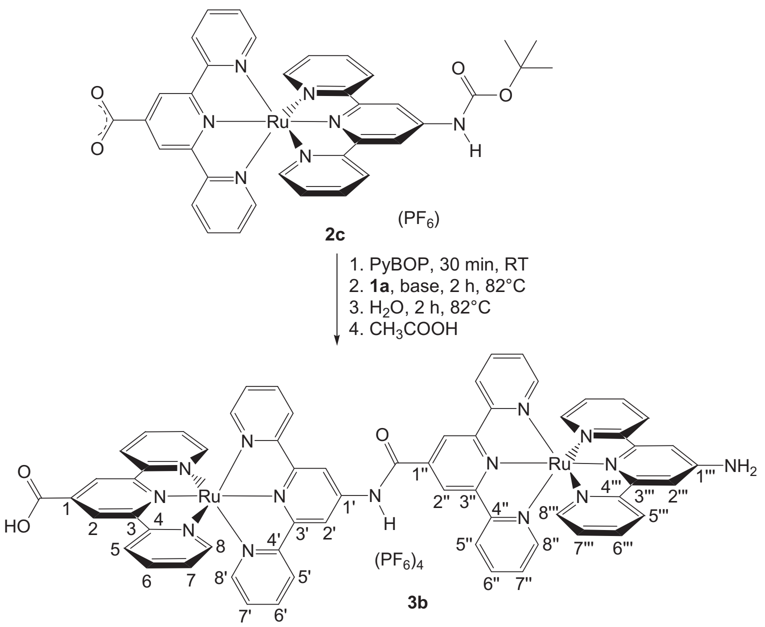

Scheme 5. Amide coupling of amino acid ester **1a** and and Boc protected **2c** to give fully deprotected **3b** and atom numbering for NMR assignments.

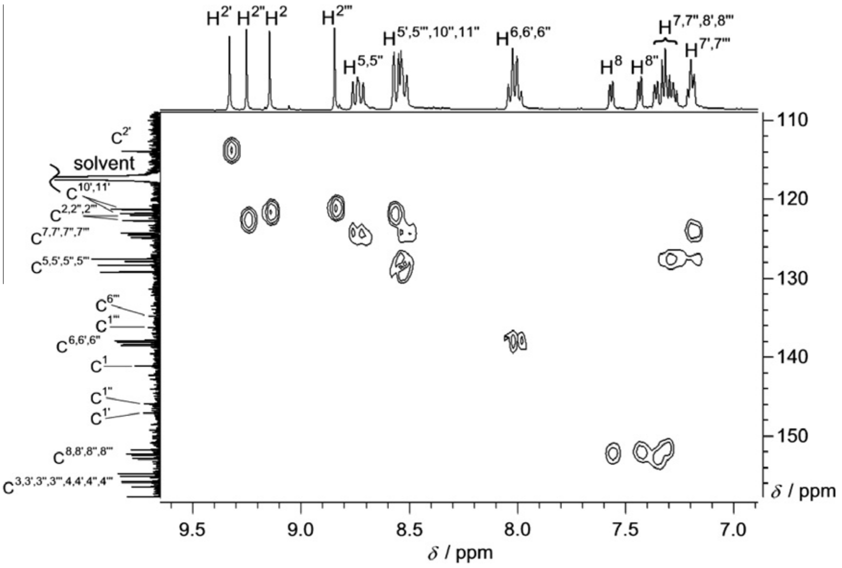

Fig. 1. Partial CH-COSY spectrum of **3a** in CD_3CN.

7.57 (ddd, $^3J_{HH}$ = 5.2 Hz, $^4J_{HH}$ = 1.20 Hz, 2H, $H^{8''}$), 7.29–7.37 (m, 8H, H^7, $H^{7''}$, $H^{8'}$, $H^{8'''}$), 7.08–7.22 (m, 2H, $H^{7'}$, $H^{7'''}$), 5.83 (bs, 2H, NH_2). ^{13}C NMR (CD_3CN, 50 MHz): δ = 165.0 (s, COOH), 159.4, 159.0, 158.8, 158.7, 158.1, 157.4, 156.3, 155.0 (8 s, $C^{3,3',3'',3''',4,4',4'',4'''}$), 157.1 (s, $C^{1''}$), 153.8 (s, $C^{8'}$), 153.7 (s, $C^{8'''}$), 153.4 (s, $C^{8''}$), 153.2 (s, C^8), 147.9 (s, $C^{1'}$), 139.4, 139.2, 139.2, 138.8 (4 s, $C^{6,6',6'',6'''}$), 138.9 (s, C^1), 137.3 (s, $C^{1'''}$), 128.9, 128.8, 128.6, 128.0 (4 s, $C^{7,7',7'',7'''}$), 125.9, 125.6, 125.5, 124.9 (4 s, $C^{5,5',5'',5'''}$), 124.0 (s, C^2), 122.6 (s, $C^{2''}$), 115.3 (s, $C^{2'}$), 109.7 (s, $C^{2'''}$), CONH not observed. IR (CsI): ν = 3458 (OH, NH), 3077 (CH_{aryl}), 1687 (C=O, amide I), 1562 (C=N, C=C), 1526 (amide II), 1245 (C–O), 838 (PF) cm^{-1}.

2.6. Oxidation of **1b**

A solution of **1b** (3.9×10^{-5} M) was titrated stepwise with a solution of $(NH_4)_2Ce(NO_3)_6$ (4.1×10^{-3} M). A solution of trifluoroacetic acid in acetonitrile (0.5 M) was used as solvent. During titration the colour of the solution turned from orange to yellow and finally to green. UV/Vis spectra revealed a decreasing band (MLCT) at 500 nm, an increasing band at 729 nm (LMCT) and isosbestic points at 432 und 578 nm.

2.7. Oxidation of **3a**

A solution of **3a** (1.5×10^{-5} M) was titrated stepwise with a solution of $(NH_4)_2Ce(NO_3)_6$ (1.8×10^{-3} M). A solution of trifluoroacetic acid in acetonitrile (0.5 M) was used as solvent. During titration the colour of the solution turned from orange to yellowish brown. UV/Vis spectra revealed a decreasing band (MLCT) at 492 nm, an increasing band at 705 nm (shoulder, LMCT) and isosbestic points at 418 und 574 nm.

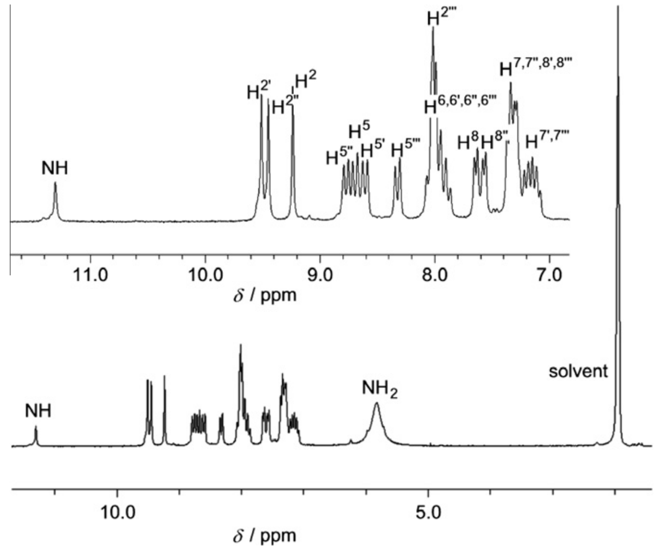

Fig. 2. ^{1}H NMR spectrum of **3b** in CD_3CN (bottom); aromatic region (top).

2.8. Oxidation of 3b

A solution of **3b** (2.0×10^{-5} M) was titrated stepwise with a solution of $(NH_4)_2Ce(NO_3)_6$ (2.4×10^{-3} M). A solution of trifluoroacetic acid in acetonitrile (0.5 M) was used as solvent. During titration the colour of the solution turned from orange to yellowish brown. UV/Vis spectra revealed a decreasing band (MLCT) at 504 nm, an increasing band at 733 nm (LMCT) and isosbestic points at 436 und 583 nm.

3. Results and discussion

3.1. Syntheses of mono- and dinuclear amides

One challenge when using ruthenium amino acid **1b** or its ester **1a** in amide coupling reactions is the extremely poor nucleophilicity of the pyridylamine coordinated to the cationic ruthenium(II) center. We have tackled this problem by using a strong base to deprotonate the NH_2 group [9] or by employing highly reactive acid chlorides as acylating agents [18]. The mononuclear *N*-acetyl derivatives **2b** and **2a** [46] were prepared by acylation of the amino acid **1b** and its ester **1a**, respectively. The latter is acylated using acetic anhydride and activation of the unreactive amino group of **1a** by the phosphazene base P_1-*t*Bu (*tert*-butylimino-tris(dimethylamino)-phosphorane) [51,52] in 96% isolated yield [46] while amino acid **1b** is acyclated by acetyl chloride in 51% isolated yield (Scheme 3). The Boc protected derivative **2c** is prepared by activation of **1a** with P_1-*t*Bu and reaction with Boc_2O (di-*tert*-butyl dicarbonate). As traces of water inevitably result in hydrolysis of the ester function under these alkaline conditions water was added on purpose after the Boc protection step and the carboxylate derivative **2c** was isolated in 93% yield and high purity (Scheme 3). **2c** is an excellent starting material for the construction of dinuclear ruthenium complexes from **1b** as the Boc group is compatible with the activation of NH_2 groups by strong bases.

When using amino acid ester **1a** as the amine part and a COOH-functionalized bis(terpyridine)ruthenium(II) complex without any further NH_2 group as the acid part no protection groups are necessary. Thus, coupling of **1a** with [Ru(tpy-C_6H_4–COOH)(*t*Bu_3tpy)]$(PF_6)_2$ [47] (*t*Bu_3tpy = 4,4′,4″-tri-*tert*-butyl-2,2′:6′,2″-terpyridine) is accomplished by activation of **1a** with P_1-*t*Bu and activation of

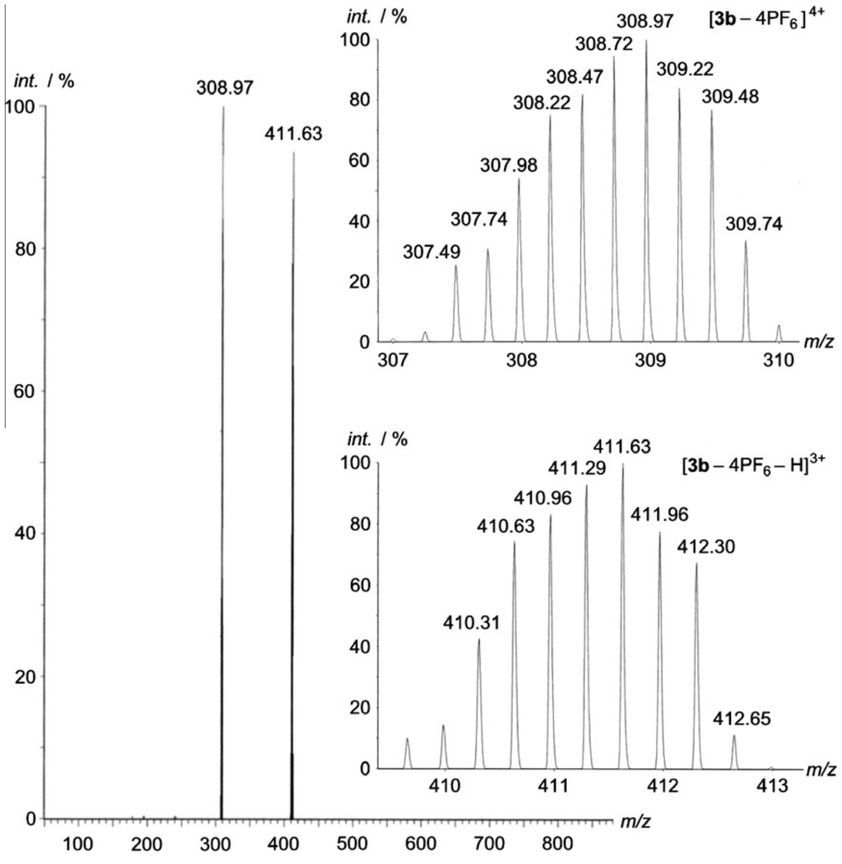

Fig. 3. ESI$^+$ mass spectrum of **3b** and isotopic pattern of relevant peaks.

Table 1
Optical properties of mononuclear **2a**, **2b**, **2c** and dinuclear **3a** and **3b** in CH_3CN at room temperature.

	Abs: λ_{max} (nm) (ε/M^{-1} cm^{-1})	Emission: λ_{max} (nm)	$\Phi/\times 10^4$	τ/ns (%)[a]
2a	491 (21 600) [46]	690 [46]	16 [46]	21.7 (100) [46]
2b	493 (22 210)	699	13	21.3 (95) 4.1 (5)
2c	489 (19 990)	699	1.0	20.9 (92) 1.1 (8)
3a	496 (46 550)	692	14	21.6 (100)
3b	522 (50 620)	750	16	22.4 (99) 1.8 (1)

[a] λ_{exc} = 500 nm.

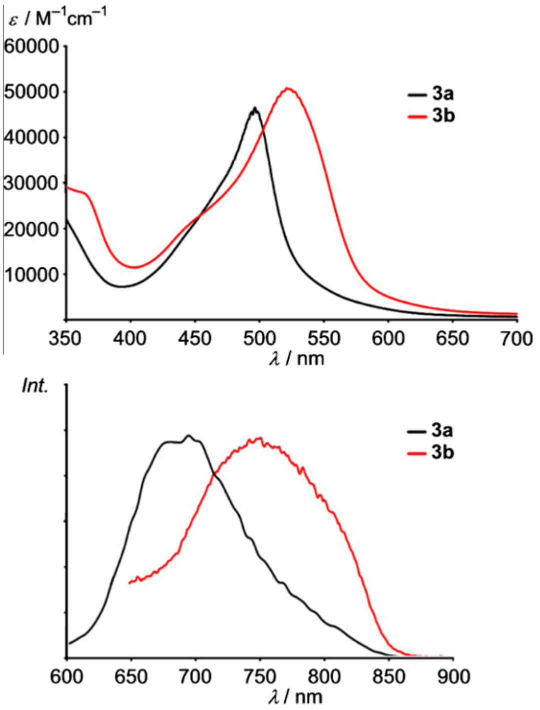

Fig. 4. Absorption spectra (top) and emission spectra (bottom) of **3a** and **3b** in CH_3CN at room temperature.

Table 2
Electrochemical data of **2a**, **2c**, **3a** and **3b** in nBu_4NPF_6/CH_3CN at room temperature.

	E_{ox}[a] (V)	$E_{p,red}$[a,b] (V)
2a	1.25	−1.15; −1.73
2c	1.27	−1.39; −1.66
3a	1.18; 1.28	−1.11; −1.24; −1.57; −1.87
3b	1.06; 1.29	−1.10; −1.32; −1.53

[a] vs. SCE; $E_{½}(FcH/FcH^+)$ = 0.38 V.
[b] Pseudoreversible or irreversible reductions; peak potential given.

the acid by DCC/HOBt (DCC = *N*,*N*′-dicyclohexylcarbodiimide, HOBt = 1-hydroxybenzotriazole) to give dinuclear **3a** in 46% isolated yield (Scheme 4).

More challenging is the amide coupling of **1a** and **2c**. Activation of the carboxylate group of **2c** as benzotriazole ester requires slightly acidic conditions when using the standard DCC/HOBt protocol but these conditions would result in Boc deprotection. However, installing an acid-stable but base-labile Fmoc group (Fmoc = fluorenylmethoxycarbonyl) instead of Boc is prohibited as the coupling conditions with **1a** require a strong base. This dilemma is circumvented by using PyBOP (benzotriazole-1-yl-oxy-tris-pyrrolidino-phosphonium hexafluorophosphate) as the carboxylate activating agent for **2c** as PyBOP is compatible with the carboxylate group (Scheme 5). Thus the amino group of **1a** is activated by P_1-*t*Bu and the carboxylate group of **2c** is activated by PyBOP to give a fully protected dinuclear complex. Addition of water hydrolyzes the ester of the dinuclear complex and acidification with acetic acid removes the Boc group giving fully deprotected **3b** in 82% overall yield (Scheme 5).

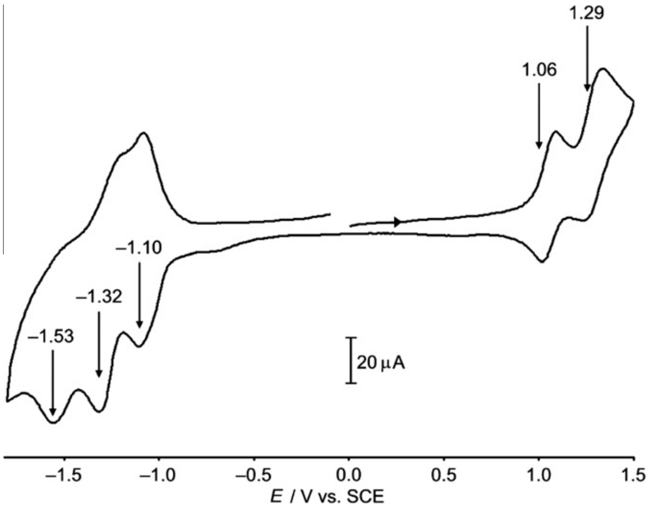

Fig. 5. Cyclic voltammogram of **3b** in CH_3CN/nBu_4NPF_6.

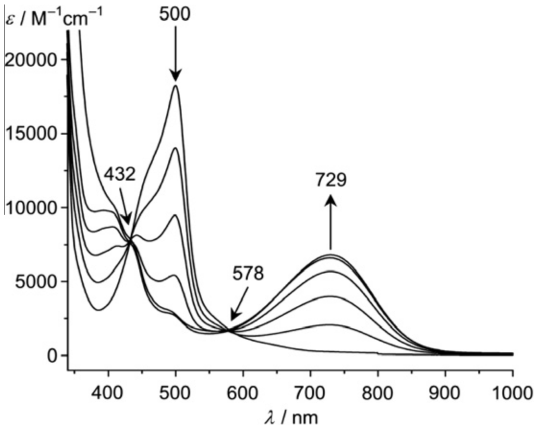

Fig. 6. UV/Vis/NIR spectra of **1b** during oxidation with Ce^{IV} in 0.5 M TFA/CH_3CN.

3.2. Characterization of mono- and dinuclear amides

The successful amide coupling reactions yielding the mononuclear complexes **2a**–**2c** are easily evidenced in the proton NMR spectra of the acetyl derivatives **2a** and **2b** as the resonances of the protons H2′ are significantly shifted to lower field by about one ppm as compared to those of the starting materials **1a**/**1b** [9] (see Scheme 3 for atom numbering). The amide protons of **2a**/**2b** resonate around δ = 9.4 ppm and the protons of the methyl group H9′ at δ = 2.37 ppm. The Boc protected derivative **2c** is characterized by the carbamate NH resonance at δ = 10.30 ppm, the signal of the *tert*-butyl protons H9′ at δ = 1.68 ppm and the downfield shifted H2′ proton resonances at δ = 9.26 ppm. All other proton resonances are found at typical chemical shifts. In these mononuclear complexes the ^{13}C resonances are easily assigned by CH-correlation spectroscopy (see Section 2). The FAB^+ mass spectra

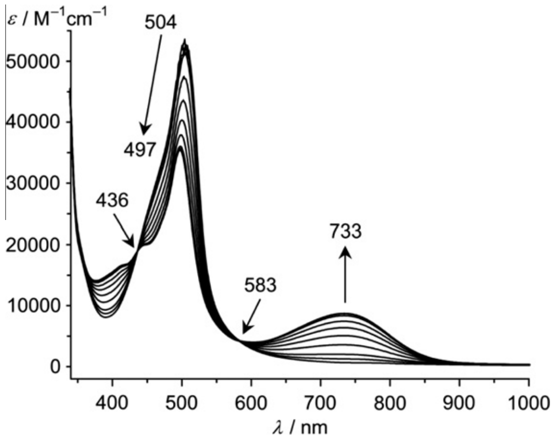

Fig. 7. UV/Vis/NIR spectra of **3b** during oxidation with Ce^{IV} in 0.5 M TFA/CH_3CN.

of **2b** and **2c** show peaks for the compounds devoid of one hexafluorophosphate counter ion (see Section 2). As the complexes **2a**–**2c** tend to adsorb water (see Section 2) the IR spectra are little informative concerning characteristic NH stretching frequencies. However, characteristic group frequencies are observed for CH_{aryl}, CH_{alkyl}, C=O, amide I, amide II, C–O and P–F stretching vibrations of **2b** and **2c** (see Section 2).

As expected the ^1H NMR spectra of the dinuclear species **3a** and **3b** are somewhat more complicated and many multiplet signals are overlapping. However, 2D correlation spectroscopy allowed assigning all signal groups (Figs. 1 and 2). The amide resonances are found at δ = 10.07 ppm (**3a**) and δ = 11.30 ppm (**3b**) and the characteristic H2′ resonances are observed at δ = 9.33 ppm (**3a**) and δ = 9.51 ppm (**3b**). In the high field region **3a** shows the expected triplet/quartet pattern for the ethyl ester at δ = 1.59 ppm and δ = 4.64 ppm as well as the singlet resonances for the different *tert*-butyl groups of the terpyridine ligand at δ = 1.77 ppm and δ = 1.33 ppm. The amine protons of fully deprotected **3b** resonate at δ = 5.83 ppm.

The ESI + mass spectra of the dinuclear complexes **3a** and **3b** display signals corresponding to quadruply charged $[M]^{4+}$ ions and triply charged $[M-H]^{3+}$ ions with correct isotopic patterns and signal spacings of $\Delta(m/z) = 0.25$ (tetracation) and $\Delta(m/z) = 0.33$ (trication) confirming the product identity and purity (Fig. 3).

IR spectroscopy confirms the presence of aliphatic CH groups in **3a** (ethyl, *tert*-butyl) and the absence of aliphatic CH groups in fully deprotected **3b**. Characteristic signatures of expected functional groups (CO, amide, PF; see Section 2) further corroborate the constitution of **3a** and **3b**.

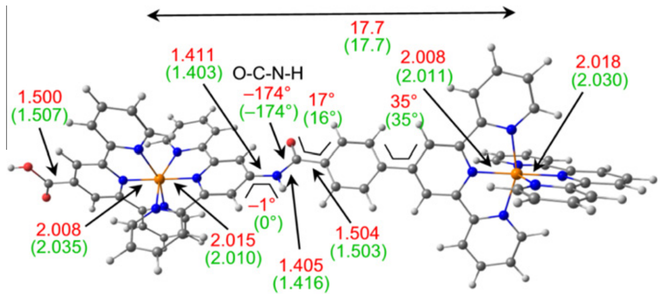

Fig. 8. Relevant DFT calculated metrical parameters of a model of **3a** (red) and **[3a]⁺** (green, in parentheses) (distances in Å). (For interpretation of the references to colour in this figure legend, the reader is referred to the web version of this article.)

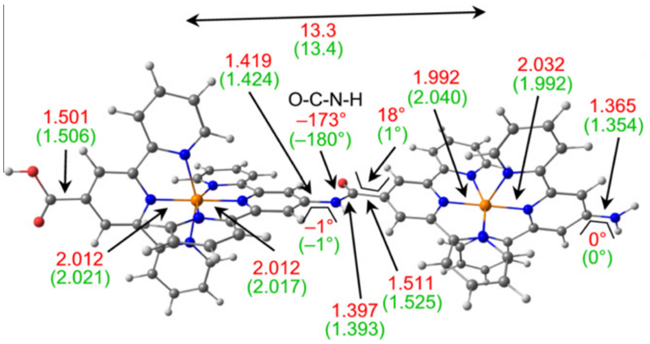

Fig. 9. Relevant DFT calculated metrical parameters of a model of **3b** (red) and **[3b]⁺** (green, in parentheses) (distances in Å). (For interpretation of the references to colour in this figure legend, the reader is referred to the web version of this article.)

3.3. Optical and redox properties of mono- and dinuclear amides

The mononuclear bis(terpyridine)ruthenium(II) complexes **2a**–**2c** display the expected ^1MLCT absorption band at around λ_{max} = 490 nm ($\varepsilon \approx 20\,000\ M^{-1}\ cm^{-1}$) slightly hypsochromically shifted relative to the maximum of the amino acid **1b** and its ester **1a** [9,46]. For the dinuclear complexes **3a** and **3b** the extinction coefficients are more than twice as large (Table 1, Fig. 4). For **3b** a significant bathochromic shift of the ^1MLCT absorption band to λ_{max} = 522 nm is noted, together with a strong hyperchromic effect (Table 1). Thus, the optical properties of **3b** appear not as a simple superposition of individual spectra (e.g. of amide **2b** and ester **1a**). A straightforward explanation would be a cooperative effect of the electron donating character of the NH_2 group paired with the strong electron accepting character of the amide linked cationic bis(terpyridine)ruthenium(II) moiety (push–pull chromophore). In **3a** the electron donating effect of *tert*-butyl substituents is weaker than that of an NH_2 group and the electron accepting effect of the attached $[Ru(tpy)_2]^{2+}$ unit is attenuated by the additional *para*-phenylene spacer resulting in unremarkable absorption properties.

In contrast to the parent $[(tpy)_2Ru]^{2+}$ complex all compounds **2** and **3** show room temperature emission around $\lambda_{max} \approx 700$ nm in CH_3CN due to the favorable donor–acceptor substitution pattern [46,53]. The emission of **3b** is bathochromically shifted to 750 nm parallel to its low-energy absorption maximum (Table 1, Fig. 4). All compounds feature similar quantum yields (except for the carboxylate derivative **2c**, see Table 1) and ^3MLCT excited state lifetimes $\tau \approx 20$ ns. For carboxylic acids and carboxylate compounds **2b**, **2c** and **3b** a biexponential decay is observed which might be a result of an additional deactivation pathway to a non-emissive state, e.g. by excited state proton transfer [54,55]. Biexponential rate laws have been observed consistently in several luminescent COOH substituted derivatives of bis(terpyridine) ruthenium(II) complexes [12,18].

The cyclic voltammograms of mononuclear **2a** and **2c** (the poor solubility of the acid **2b** prevented recording of reliable CVs) show very similar reversible Ru^{II}/Ru^{III} couples at ca. 1.26 V versus SCE, similar to comparable systems [53]. Two couples (pseudoreversible or irreversible) are assigned to terpyridine reductions (Table 2). The dinuclear complexes **3a** and **3b** can be oxidized twice (Fig. 5) – first at a lower potential round 1.1 V versus SCE and secondly at around 1.28 V versus SCE. The difference in oxidation potentials (0.10 V for **3a** and 0.23 V for **3b**) can be largely ascribed to the different substitution pattern and is not necessarily a sign of electronic communication or electrostatic interaction of the metal sites. However, electronic communication of the redox sites in **3b** cannot be excluded at this stage of the investigation and spectroscopic and theoretical investigations were performed.

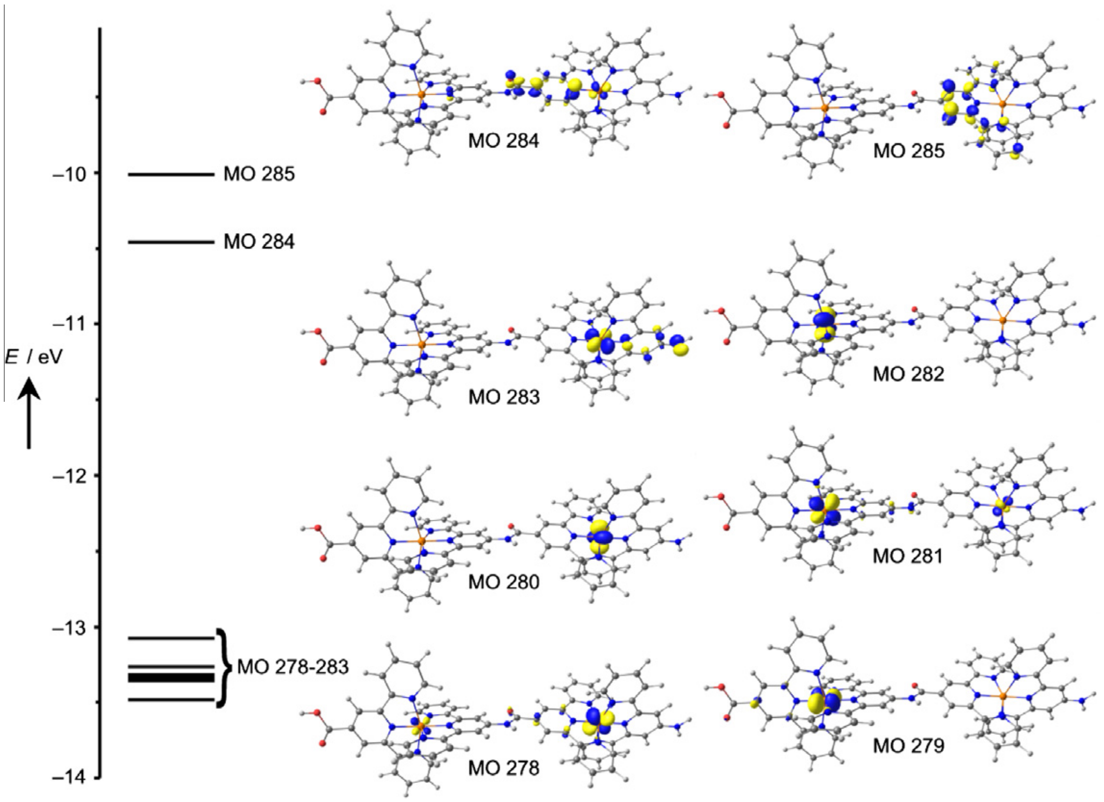

Fig. 10. MO scheme of **3b** (contour level 0.07 a.u.).

3.4. Oxidation to mixed-valent cations

In order to elucidate a possible electronic communication between ruthenium centers **3b** was titrated with diammonium cerium(IV) hexanitrate $(NH_4)_2Ce(NO_3)_6$ in 0.5 M TFA/CH_3CN solution. The potential of Ce^{IV} could be sufficient for the oxidation of Ru^{II} depending on the solvent employed ($E_{½}(HClO_4) = 1.3$ V, $E_{½}(H_2O) = 0.88$ V versus FcH/FcH$^+$) [56]. For comparison the acetylated derivative **2b** and the amino acid **1b** were also treated with Ce^{IV} under the same conditions. The extremely weak basic amine function of **1b** is not protonated under these conditions [9]. In order to observe possible IVCT bands UV/Vis/NIR spectra were recorded during oxidation.

The *N*-acetylated derivative **2b** is resistant towards oxidation with Ce^{IV} under these conditions as its MLCT absorption band ($\lambda_{max} = 492$ nm) remains unchanged upon addition of up to 7.2 equivalents Ce^{IV} and no new bands arise.

The amino acid **1b**, however, is oxidized by Ce^{IV} ions to the corresponding green Ru^{III} complex **[1b]**$^+$. The MLCT band of **1b** ($\lambda_{max} = 500$ nm, $\varepsilon = 18\,230\ M^{-1}\ cm^{-1}$) decays while a new LMCT band (**[1b]**$^+$) at 729 nm ($\varepsilon = 6810\ M^{-1}\ cm^{-1}$) rises (Fig. 6). Isosbestic points are observed at 432 and 578 nm. The oxidation has to be done quite fast as the TFA solution of **[1b]**$^+$ changes with time (within hours). The nature of this slow reaction of **[1b]**$^+$ and the products are currently investigated in greater detail.

The data show that the *amino* functionalized Ruthenium complex **1b** can be oxidized by Ce^{IV} while the *amido* functionalized Ruthenium complex **2b** is resistant towards Ce^{IV} oxidation. Thus, it is expected that Ce^{IV} oxidizes the dinuclear NH_2 substituted complex **3b** only once – namely at the *N*-terminal end. Treating **3b** with Ce^{IV} in 0.5 M TFA solution decreases the MLCT absorption band at 504 nm from $\varepsilon = 52\,690$ to $35\,350\ M^{-1}\ cm^{-1}$ (now at 497 nm) and a new LMCT band at 733 nm ($\varepsilon = 8720\ M^{-1}\ cm^{-1}$) rises (Fig. 7). Two isosbestic points are observed at 436 and 583 nm. Addition of excess Ce^{IV} does not further change the spectrum. Thus, the data supports the interpretation that the tetracation of **3b** is oxidized to the mixed-valent pentacation **[3b]**$^+$ by Ce^{IV}. No bands assignable to intervalence charge transfer bands (IVCT) are observed up to 3000 nm for **[3b]**$^+$. The UV/Vis/NIR data allow us to describe the mixed-valent cation **[3b]**$^+$ as largely localized system (Class I) as no IVCT could be observed. The valence trapping is likely due to the quite substantial redox asymmetry at the *N*- and *C*-terminal site (estimated as 0.15–0.20 V from mononuclear model compounds).

Similarly, **3a** has been oxidized to **[3a]**$^+$ by Ce^{IV}. During oxidation isosbestic points are observed at 418 and 574 nm. The LMCT band of **[3a]**$^+$ is found at 705 nm together with a remaining MLCT band at 492 nm, very similar to the observations made during the **3b** → **[3b]**$^+$ oxidation. Up to 3000 nm no bands attributable to IVCT have been observed also suggesting trapped valences in **[3a]**$^+$.

3.5. Theoretical calculations

The ground state geometric structures of models of the dinuclear complex tetracations **3a** and **3b** were optimized at the B3LYP/LanL2DZ level and the calculated molecular structures are depicted in Fig. 8 and 9. In order to save computational costs the alkyl periphery of **3a** (*tert*-butyl and ethyl groups) has been replaced by hydrogen atoms in the model complex. The Ru···Ru distance increases from 13.4 Å in **3b** to 17.7 Å in **3a** due to the additional *para*-phenylene spacer. The calculations show that the amide linker in **3b** is almost perfectly planar and also co-planar to both adjacent pyridine rings so that π-conjugation is principally possible. In **3a**, however, the *para*-phenylene spacer is twisted relative to the amide plane by 17° and also relative to the pyridine plane by 35° suggesting only poor π-orbital overlap (Fig. 8).

The molecular orbital schemes of **3a** and **3b** are depicted in Fig. S1 (Supporting Information) and Fig. 10. The occupied "t_{2g}" orbitals of both ruthenium sites are well separated from the π^*

terpyridine orbitals in both dinuclear systems. The highest occupied molecular orbital is centered on the *C*-terminal site for **3a** (see Supporting Information; MO 297-299) and on the *N*-terminal site for **3b** (MO 283, Fig. 10) suggesting differing sites of oxidation for **3a** and **3b**. The participation of the nitrogen p-orbital in the HOMO of amino-substituted ruthenium complex **1b** has been previously suggested on the basis of Resonance Raman spectroscopic results.[46] This feature is also seen here for **3b** (MO 283, Fig. 10). Fully analogous observations have been made for amino substituted free-base porphyrins and zink(II) porphyrinato complexes [57]. In order to clarify the site of oxidation (*N*-terminus, *C*-terminus) open-shell calculations on the oxidized complexes [3**a**]$^+$ and **[3b]**$^+$ have been performed.

No dramatic metrical changes are observed in the redox pairs **3a**/**[3a]**$^+$ and **3b**/**[3b]**$^+$ (Figs. 8 and 9) which is within expectation for $Ru^{II/III}$ complexes with polypyridine ligands.[50] For the **3a**/**[3a]**$^+$ model some differences in Ru–N(py) distances are calculated at the *C*-terminal site (from 2.008 to 2.035 Å) while for **3b**/**[3b]**$^+$ two Ru–N(py) distances at the *N*-terminal site are influenced (from 1.992 to 2.040 Å and from 2.032 to 1.992 Å). In addition, the C–N(amine) bond length varies from 1.365 to 1.354 Å, similar to the changes calculated for the pair **1b**/**[1b]**$^+$ (Fig. S2, Supporting Information).

These DFT data suggest that the site of oxidation is mainly localized on the "*C*-terminal" ruthenium complex in the model of **3a** and on the "*N*-terminal" ruthenium site in **3b**. In amine substituted Ru^{III} complexes **[3b]**$^+$ and **[1b]**$^+$ a significant part of the additional positive charge is delocalized onto the NH_2 substituent strengthening the intrinsic iminium-like structure. This $[Ru^{II}–\{Ru^{III}–NH_2\}]^{5+}$/$[Ru^{II}–\{Ru^{II}{=}N^{(+)}H_2\}]^{5+}$ description supports the class I assignment based on spectroscopic data (see Section 3.4).

4. Conclusions

Asymmetrically substituted dinuclear terpyridine ruthenium complexes **3a** and **3b** have been synthesized by amide coupling with Ru···Ru distances of 17.7 and 13.4 Å, respectively. The differences in the local redox potentials in the dinuclear complexes should increase the barrier for (thermal and optical) electron transfer in singly oxidized mixed-valent complexes. In the mixed-valent complex **[3b]**$^+$ with relatively small Ru···Ru distance and a rather planar bridging ligand no communication is observed by spectroscopic analysis. This finding is likely due to the redox asymmetry (ca. 0.15–0.20 V) featured in these systems with directional amide units. Future studies will focus on systems based on ruthenium amino acids with less differing redox potentials, e.g. by adjusting the substituents to –C(O)–NHR at the *C*-terminus and to NH–C(O)R at the *N*-terminus. This should result in similar redox potentials of the individual ruthenium centers due to the similar substitution pattern $[(RHN\text{-}(O)C\text{-}tpy)Ru(tpy\text{-}NHC(O)\text{-}tpy)Ru(tpy\text{-}NHC(O)R)]^{4+}$ but simultaneously preserve the directionality of oligoamides and peptides (*N*-terminus/*C*-terminus).

Acknowledgments

This work was financially supported by the Deutsche Forschungsgemeinschaft (Grant No. HE 2778/5-1). We thank Prof. Dr. Sven Rau for the generous donation of a sample of $[Ru(tpy\text{-}C_6H_4\text{–}COOH)(tBu_3tpy)](PF_6)_2$.

Appendix A. Supplementary material

Supplementary data associated with this article can be found, in the online version, at doi:10.1016/j.ica.2011.03.046.

References

[1] S. Campagna, G. Denti, S. Serroni, M. Ciano, A. Juris, V. Balzani, Inorg. Chem. 31 (1992) 2982.
[2] K.O. Johansson, J.A. Lotoski, C.C. Tong, G.S. Hanan, Chem. Commun. (2000) 819.
[3] Y.-Q. Fang, M.I.J. Polson, G.S. Hanan, Inorg. Chem. 42 (2003) 5.
[4] M.I.J. Polson, F. Loiseau, S. Campagna, G.S. Hanan, Chem. Commun. (2006) 1301.
[5] K. Heinze, M. Beckmann, K. Hempel, Chem. Eur. J. 14 (2008) 9468.
[6] U.S. Schubert, H. Hofmeier, G.R. Newkome, Modern Terpyridine Chemistry, Wiley-VCH, 2006.
[7] H. Hofmeier, U.S. Schubert, Chem. Soc. Rev. 33 (2004) 373.
[8] W.C. Chan, P.D. White (Eds.), Fmoc Solid Phase Peptide Synthesis, Oxford University Press, Oxford, 2000.
[9] K. Heinze, K. Hempel, M. Beckmann, Eur. J. Inorg. Chem. (2006) 2040.
[10] K. Heinze, U. Wild, M. Beckmann, Eur. J. Inorg. Chem. (2007) 617.
[11] K. Heinze, M. Schlenker, Eur. J. Inorg. Chem. (2005) 66.
[12] K. Heinze, K. Hempel, A. Breivogel, Z. Anorg. Allg. Chem. 635 (2009) 2541.
[13] L. Barišić, V. Rapić, V. Kovač, Croat. Chem. Acta 75 (2002) 199.
[14] K. Heinze, M. Schlenker, Eur. J. Inorg. Chem. (2004) 2974.
[15] D. Siebler, M. Linseis, T. Gasi, L.M. Carrella, R.F. Winter, C. Förster, K. Heinze, Chem. Eur. J. 17 (2011) 4540.
[16] K. Heinze, D. Siebler, Z. Anorg. Allg. Chem. 633 (2007) 2223.
[17] D. Siebler, C. Förster, K. Heinze, Eur. J. Inorg. Chem. (2010) 523.
[18] K. Heinze, K. Hempel, Chem. Eur. J. 15 (2009) 1346.
[19] V. Balzani, A. Juris, M. Venturi, S. Campagna, S. Serroni, Chem. Rev. 96 (1996) 759.
[20] J.-P. Sauvage, J.-P. Collin, J.-C. Chambron, S. Guillerez, C. Coudret, V. Balzani, F. Barigelletti, L. De Cola, L. Flamigni, Chem. Rev. 94 (1994) 993.
[21] C. Creutz, Prog. Inorg. Chem. 30 (1983) 1.
[22] D.E. Richardson, H. Taube, Coord. Chem. Rev. 60 (1984) 107.
[23] R.J. Crutchley, Adv. Inorg. Chem. 41 (1994) 273.
[24] M.D. Ward, Chem. Soc. Rev. 24 (1995) 121.
[25] D. Astruc, Acc. Chem. Res. 30 (1997) 383.
[26] J.A. McCleverty, M.D. Ward, Acc. Chem. Res. 31 (1998) 842.
[27] W. Kaim, A. Klein, M. Göckle, Acc. Chem. Res. 33 (2000) 755.
[28] K.D. Demadis, C.M. Hartshorn, T.J. Meyer, Chem. Rev. 101 (2001) 2655.
[29] J.-P. Launay, Chem. Soc. Rev. 30 (2001) 386.
[30] B.S. Brunschwig, C. Creutz, N. Sutin, Chem. Soc. Rev. 31 (2002) 168.
[31] J.T. Hupp, in: J.A. McCleverty, T.J. Meyer (Eds.), Comprehensive Coordination Chemistry II, Elsevier Science, Amsterdam, 2003, p. 709.
[32] R.J. Crutchley, in: J.A. McCleverty, T.J. Meyer (Eds.), Comprehensive Coordination Chemistry II, Elsevier Science, Amsterdam, 2003, p. 235.
[33] D.M. D'Alessandro, F.R. Keene, Chem. Soc. Rev. 35 (2006) 424.
[34] D.M. D'Alessandro, F.R. Keene, Chem. Rev. 106 (2006) 2270.
[35] (a) W. Kaim, G.K. Lahiri, Angew. Chem. 119 (2007) 1808;
(b) W. Kaim, G.K. Lahiri, Angew. Chem., Int. Ed. 46 (2007) 1778.
[36] W. Kaim, B. Sarkar, Coord. Chem. Rev. 251 (2007) 584.
[37] M.B. Robin, P. Day, Adv. Inorg. Chem. Radiochem. 10 (1968) 247.
[38] C. Creutz, H. Taube, J. Am. Chem. Soc. 91 (1969) 3988.
[39] C. Creutz, H. Taube, J. Am. Chem. Soc. 95 (1973) 1086.
[40] G.D. Storrier, S.B. Colbran, Inorg. Chim. Acta 284 (1999) 76.
[41] T. Okamura, T. Iwamura, S. Seno, H. Yamamoto, N. Ueyama, J. Am. Chem. Soc. 126 (2004) 15972.
[42] E.C. Constable, M.D. Ward, J. Chem. Soc., Dalton Trans. (1990) 1405.
[43] J.-P. Collin, P. Lainé, J.-P. Launay, J.-P. Sauvage, A. Sour, J. Chem. Soc., Chem. Commun. (1993) 434.
[44] S. Vaduvescu, P.G. Potvin, Inorg. Chem. 41 (2002) 4081.
[45] A.C. Benniston, A. Harriman, P. Li, C.A. Sams, M.D. Ward, J. Am. Chem. Soc. 126 (2004) 13630.
[46] K. Heinze, K. Hempel, S. Tschierlei, M. Schmitt, J. Popp, S. Rau, Eur. J. Inorg. Chem. (2009) 3119.
[47] A sample of this ruthenium(II) complex has been kindly donated by Prof. Dr. Sven Rau, University of Erlangen-Nürnberg, Germany.
[48] J.V. Caspar, T.J. Meyer, J. Am. Chem. Soc. 105 (1983) 5583.
[49] M.J. Frisch, G.W. Trucks, H.B. Schlegel, G.E. Scuseria, M.A. Robb, J.R. Cheeseman, J.A. Montgomery Jr., T. Vreven, K.N. Kudin, J.C. Burant, J.M. Millam, S.S. Iyengar, J. Tomasi, V. Barone, B. Mennucci, M. Cossi, G. Scalmani, N. Rega, G.A. Petersson, H. Nakatsuji, M. Hada, M. Ehara, K. Toyota, R. Fukuda, J. Hasegawa, M. Ishida, T. Nakajima, Y. Honda, O. Kitao, H. Nakai, M. Klene, X. Li, J.E. Knox, H.P. Hratchian, J.B. Cross, C. Adamo, J. Jaramillo, R. Gomperts, R.E. Stratmann, O. Yazyev, A.J. Austin, R. Cammi, C. Pomelli, J.W. Ochterski, P.Y. Ayala, K. Morokuma, G.A. Voth, P. Salvador, J.J. Dannenberg, V.G. Zakrzewski, S. Dapprich, A.D. Daniels, M.C. Strain, O. Farkas, D.K. Malick, A.D. Rabuck, K. Raghavachari, J.B. Foresman, J.V. Ortiz, Q. Cui, A.G. Baboul, S. Clifford, J. Cioslowski, B.B. Stefanov, G. Liu, A. Liashenko, P. Piskorz, I. Komaromi, R.L. Martin, D.J. Fox, T. Keith, M.A. Al-Laham, C.Y. Peng, A. Nanayakkara, M. Challacombe, P.M.W. Gill, B. Johnson, W. Chen, M.W. Wong, C. Gonzalez, J.A. Pople, GAUSSIAN 03, Revision B.03, Gaussian, Inc., Pittsburgh PA, 2003.
[50] M. Biner, H.-B. Bürgi, A. Ludi, C. Röhr, J. Am. Chem. Soc. 114 (1992) 5197.
[51] (a) R. Schwesinger, C. Hasenfratz, H. Schlemper, L. Walz, E.-M. Peters, K. Peters, H.G. von Schnering, Angew. Chem. 105 (1993) 1420;
(b) R. Schwesinger, C. Hasenfratz, H. Schlemper, L. Walz, E.-M. Peters, K. Peters, H.G. von Schnering, Angew. Chem., Int. Ed. 32 (1993) 1361.

[52] R. Schwesinger, Nachr. Chem. Tech. Lab. 38 (1990) 1214.
[53] M. Maestri, N. Armaroli, V. Balzani, E.C. Constable, A.M.W. Cargill Thompson, Inorg. Chem. 34 (1995) 2759.
[54] G. Ulrich, F. Nastasi, P. Retailleau, F. Puntoriero, R. Ziessel, S. Campagna, Chem. Eur. J. 14 (2008) 4381.
[55] C. Turro, S.H. Bossmann, Y. Jenkins, J.K. Barton, N.J. Turro, J. Am. Chem. Soc. 117 (1995) 9026.
[56] N.G. Connelly, W.E. Geiger, Chem. Rev. 96 (1996) 877.
[57] K. Heinze, A. Reinhart, Dalton Trans. (2008) 469.

9.4 Light-induced Charge Separation in a Donor-Chromophore-Acceptor Nanocomposite Poly[TPA-Ru(tpy)$_2$]@ZnO

L. zur Borg, A. L. Domanski, A. Breivogel, M. Bürger, R. Berger, K. Heinze, R. Zentel, *J. Mater. Chem. C* **2013**, *1*, 1223–1230.

DOI: 10.1039/c2tc00535b

Journal of
Materials Chemistry C

RSCPublishing

PAPER

View Article Online
View Journal | View Issue

Cite this: *J. Mater. Chem. C*, 2013, **1**, 1223

Light-induced charge separation in a donor–chromophore–acceptor nanocomposite poly[TPA-Ru(tpy)$_2$]@ZnO†

Lisa zur Borg,[a] Anna L. Domanski,‡[b] Aaron Breivogel,‡[c] Mareike Bürger,[a] Rüdiger Berger,[b] Katja Heinze*[c] and Rudolf Zentel*[a]

Received 31st October 2012
Accepted 29th November 2012

DOI: 10.1039/c2tc00535b

www.rsc.org/MaterialsC

The synthesis and characterisation of a new donor–chromophore–acceptor system based on poly(vinyltriphenylamine) as the electron donor and a glycine-functionalised bis(2,2′;6′,2″-terpyridine) ruthenium(II) complex acting both as a chromophore and as an anchor group attached to ZnO nanorods as the electron acceptor are described. The TPA-containing block copolymer was synthesised by Reversible Addition Fragmentation Chain Transfer (RAFT) polymerisation and the ruthenium complex glycine conjugates prepared by Solid Phase Peptide Synthesis (SPPS) were attached *via* post-polymerisation esterification. GPC, NMR, IR and UV-Visible spectroscopy were used to characterise the multifunctional chromophore–donor polymer. Zinc oxide nanorods were functionalised with the block copolymer by multisite adsorption *via* the glycine COOH groups. The functionalised nanoparticles were well dispersible in organic solvents. Photoluminescence studies showed a complete quenching of the phosphorescence of the ruthenium chromophore (^{3}MLCT state). Kelvin probe force microscopy (KPFM) was used to confirm that under continuous excitation of the Ru^{II} complex (^{1}MLCT) the polymer corona develops a positive charge and thus efficient charge separation between ZnO and the polymer is achieved.

Introduction

Since O'Regan and Grätzel reported the first dye-sensitised solar cells (DSSCs) in 1991,[1] much effort has been devoted to enhancing their efficiency. The benefit to our environment is obvious, but the DSSCs suffer from the possibility of leaking of the I_3^-/I^- hole conductor dissolved in a liquid solvent. To avoid leaking, solid state dye-sensitised solar cells (ssDSSCs) were introduced in 1996.[2] Oligoethylene glycol methacrylate doped with lithium ions was used as a p-type conductor. In the following years, different polymers were used to improve the efficiency.[3,4] Conducting polymers like poly(vinyltriphenylamine) (PTPA), poly(*para*-phenylene vinylene) (PPV) or poly(3-hexylthiophene) (P3HT) have been used as hole transporting layers.[5] Transient absorption spectroscopy studies showed that the dye regeneration in ssDSSCs was at least one order of magnitude faster than in conventional DSSCs. However, the efficiencies of ssDSSCs remained low. The major drawback in this system is the low penetration rate of the polymer within the mesoporous film of TiO$_2$ nanoparticles. Several approaches were reported to increase the penetration. P3HT with carboxylate end groups has been synthesised and was used as a sensitiser in ssDSSCs.[6] A higher adsorption of the polymer onto the TiO$_2$ was observed compared to methyl terminated P3HT. Oligotriarylamine groups were directly bound to ruthenium(II) polypyridine dyes, enhancing the contact between the donor and the chromophore.[7–11] Furthermore, it has been shown that these systems show higher extinction coefficients compared to standard polypyridine complexes.[12] To further improve the ssDSSCs, a tris(2,2′-bipyridine) ruthenium(II) dye was incorporated directly inside a hole transporting PTPA and indeed these devices showed enhanced performances.[13] However, they carry only a single ruthenium(II) complex within each polymer chain. To increase the amount of the chromophore in each polymeric chain, block copolymers with the first block based on a semiconducting PTPA and a second block with perylene units as chromophores and separated dopamine units as anchor groups were synthesised.[14] These polymers were attached to ZnO nanorods and characterised by Kelvin probe force microscopy (KPFM) on the level of the individual nanoparticle. A negative

---

[a] *Institute of Organic Chemistry, Johannes Gutenberg-University, Duesberweg 10-14, 55099 Mainz, Germany. E-mail: Zentel@uni-mainz.de; Fax: +49-6131-3924778; Tel: +49-6131-3920361*

[b] *Max Planck Institute for Polymer Research, Ackermannweg 10, 55128 Mainz, Germany. E-mail: berger@mpip-mainz.mpg.de; Fax: +49-6131-379100; Tel: +49-6131-379114*

[c] *Institute of Analytical and Inorganic Chemistry, Johannes Gutenberg-University, Duesberweg 10-14, 55128 Mainz, Germany. E-mail: katja.heinze@uni-mainz.de; Fax: +49-6131-3927277; Tel: +49-6131-3925886*

† Electronic supplementary information (ESI) available: FTIR of **A**, **P2**, **P3a** and **P3b**, ^{19}F NMR spectra of **P2** and **P3a**, AFM of **P3a@ZnO** and KPFM of **P3b@ZnO**, atom numbering of **A** used for NMR assignment, UV-vis spectrum of **P3b**. See DOI: 10.1039/c2tc00535b

‡ These authors contributed equally to this work.

charging of the inorganic nanoparticles and a positive charging of the polymer corona were observed upon laser irradiation.[14] However, a more proximate contact of the dye with the ZnO is desirable for a more efficient electron injection.

Herein, we present the synthesis of a nanoscale donor–chromophore–acceptor (D–C–A) system with a PTPA based block copolymer carrying several directional bis(terpyridine) ruthenium(II) side groups in the second block. A carboxyl group is attached to each Ru^{II} dye which binds to the oxidic surface of ZnO nanorods. This allows for a large amount of dyes in proximity to the surface of the ZnO with the direct binding of the dye to the acceptor being beneficial for an efficient electron injection and charge separation. The TPA polymer acts as a hole transporting matrix and the directional ruthenium complexes act both as light harvesting units and as anchor groups. Upon irradiation into the dye MLCT absorption band, charges are created and separated, as proven by photoluminescence (PL) spectra and KPFM measurements.

Experimental

Materials

Unless otherwise mentioned, all chemical reagents were used as purchased without any further purification. Pentafluorophenol was obtained from Fluorochem (UK). Anhydrous THF and dioxane were freshly distilled from sodium. DMF was freshly distilled from calcium hydride and not exposed to light until it was used. 2,2′-Azobis(isobutyronitrile) (AIBN) was recrystallised from diethyl ether and stored at −18 °C. Diphenyl-(4-vinylphenyl)-amine[15a] and ZnO nanorods[15b] were synthesised as reported in the literature.

Instrumentation

^1H NMR spectra were recorded on a Bruker 300 MHz FT NMR spectrometer. Chemical shifts (δ) are given in parts per million relative to TMS. Samples were prepared in deuterated solvents and their signals referenced to residual nondeuterated solvent signals. ^{19}F NMR spectra were recorded on a Bruker 400 MHz FT NMR spectrometer. The molecular weight of the polymers was determined by gel permeation chromatography (GPC) in THF as the solvent and with the following equipment: pump PU 1580, auto sampler AS1555, UV detector UV 1575 (detection at 254 nm), RI detector RI 1530 from JASCO. Columns were used from MZ-Analysentechnik: MZ-Gel SDplus 10 2 Å and MZ-Gel SDplus 10 6 Å. Calibration was done using polystyrene standards purchased from Polymer Standard Services. IR spectra were recorded on a Perkin-Elmer 100 FTIR spectrometer using an ATR unit. UV-Vis spectra were recorded using a Jasco V-630 spectrophotometer (1 cm × 1 cm quartz cell). Emission spectra were recorded on a Varian Cary Eclipse spectrometer. Quantum yields were calculated by comparing the areas under the emission spectra on an energy scale/cm^{-1} recorded for optically matched solutions of the sample and the reference $[Ru(bpy)_3]Cl_2 = 0.094$ in CH_3CN.[16] ESI MS spectra were recorded on a Micromass Q-TOF-Ultima spectrometer. TEM pictures were taken on a Philips EM-420: 120 kV with a CCD-Camera.

KPFM measurements were performed at a MFP-3D standalone setup (Asylum Research, Santa Barbara). In order to prevent any degradation of the sample during the KPFM measurements the setup was placed in a glove box that was continuously purged with dry nitrogen ($H_2O < 0.1\%$, $O_2 < 0.01\%$). For simultaneous sample illumination during the KPFM measurement the setup was equipped with a diode laser (Point Source, iFLEX2000) with a wavelength of 488 nm, an intensity of 13.3 mW on the sample, and a spot diameter of 640 μm.[17a] We used Pt/Ir coated cantilevers with a nominal vertical resonance frequency of 70 kHz (Nanosensors, PPP-EFM). The measurements were performed in the dual pass mode at a lift height of 5 nm and with an AC voltage of 1.5 V. In KPFM, the contact potential difference (CPD) is measured which is defined as the difference in the work function between the tip and sample. By using the amplitude modulation mode for KPFM both the tip apex and the cantilever contribute to the measured CPD.[17b] Thus, local changes in the CPD are not exclusively related to the sample area underneath the tip apex but also to the one underneath the cantilever. In case the work function of the tip remains constant, it is possible to attribute changes in the measured CPD owing to sample illumination to changes in the surface potential of the sample.[20] However, studies on P3HT:PCBM blends have shown that the CPD changes significantly for consecutive scanning on the same position. These shifts of the measured CPDs can be attributed to changes in the cantilever tip, such as coating thickness and adsorbates. Thus, it is important to have one surface within the scan area that does not participate in the photo-induced reaction and can therefore serve as an internal reference.[21,22] For sample preparation, glass substrates were coated with 100 nm of ITO (99.9%, MaTeck GmbH) and cleaned in Ar plasma (PDC-002, Harrick plasma) for 2 min prior to their usage. The ITO surface acted as a reference surface for the KPFM study. A highly diluted dispersion of **P3a@ZnO** in THF was spin cast on the substrates.

Synthesis of chromophore A

The ruthenium dye $[(H_2N{-}CH_2{-}CONH{-}tpy)Ru(tpy{-}CONH{-}CH_2{-}COOH)](PF_6)_2$ (**A**) was synthesised from $[(H_2N{-}tpy)Ru(tpy{-}COOH)](PF_6)_2$ according to a solid phase peptide synthesis procedure.[18,19] After cleavage from the TentaGel S Wang solid phase chromophore **A** was precipitated as its PF_6 salt by adding aqueous NH_4PF_6 to give **A** as a dark red powder. ν_{max}/cm^{-1} 3090w (=C–H), 2920w (C–H), 1717m (C=O(acid)), 1663m (amide I), 1603m (C=C stretching), 1528s (amide II), 1477s (C=C stretching), 1427s, 1354s, 1289s, 1260, 1095m, 1028s, 826vs (PF_6), 789s, 752s, 555s (see Fig. S1†). ^1H NMR: δ_H (600 MHz; CD_3CN; Me_4Si) 9.09 (s, 2H, H^2), 9.05 (s, 2H, $H^{2'}$), 8.59 (s, 1H, NH^b), 8.59 (m, 2H, H^5), 8.41 (m, 2H, $H^{5'}$), 8.16 (m, 1H, NH^a), 7.95 (m, 2H, H^6), 7.93 (m, 2H, $H^{6'}$), 7.44 (m, 2H, H^8), 7.31 (m, 2H, $H^{8'}$), 7.21 (m, 2H, H^7), 7.12 (m, 2H, $H^{7'}$), 4.32–4.30 (m, 2H, $CH_2{}^a$), 4.32–4.30 (m, 2H $CH_2{}^b$), NH_2 not observed probably due to protonation (for atom numbering see ESI†). $\lambda_{abs,max}$(DMF)/nm (ε/dm^3 mol^{-1} cm^{-1}) 279 (87 900, $\pi \rightarrow \pi^*$), 311 (72 600, $\pi \rightarrow \pi^*$), 498 (29 400, MLCT), $c = 0.09$ mg mL^{-1}. $\lambda_{em,max}$(DMF)/nm

667 (λ_{ex}/nm 498). Quantum yield $\Phi = 1.4 \times 10^{-3}$). MS (ESI$^+$): $m/z = 370.6$ (22%) $[M - (PF_6)_2]^{2+}$, 886.1 (100%) $[M - PF_6]^+$.

Synthesis of P1

Diphenyl-(4-vinyl-phenyl)-amine (1.71 g, 6.3 mmol), dithiobenzoic acid benzyl ester (6.6 mg, 0.03 mmol), and 2,2′-azobis(2-methylpropionitrile) (AIBN) (0.6 mg, 4.5 μmol) were placed in a Schlenk tube and equipped with a stir bar. Dioxane (9 mL) was added and the solution was degassed by three freeze–pump–thaw cycles. The flask was then immersed in a preheated oil bath at 75 °C and the polymerisation was carried out for 42 h. The polymer was precipitated in methanol, collected by centrifugation, redissolved in THF and reprecipitated in methanol. This procedure was repeated three times. The light yellow powder **P1** (540 mg, 32%) was dried at 45 °C under reduced pressure for 12 h. λ_{max}(THF)/nm 300 (ε/dm^3 mol^{-1} cm^{-1} 205 800, $c = 0.13$ mg mL^{-1}). GPC: $M_n = 12{,}800$, $M_w = 15{,}600$, PDI: 1.2.

Synthesis of P2

P1 (180 mg, 0.01 mmol), pentafluorophenyl acrylate (90 mg, 0.4 mmol) and AIBN (0.2 mg, 1.5 μmol) were placed in a Schlenk tube and equipped with a stir bar. Dioxane (2 mL) was added and the solution was degassed by three freeze–pump–thaw cycles. The flask was then immersed in a preheated oil bath at 80 °C and the polymerisation was carried out for 48 h. The polymer was precipitated in methanol, collected by centrifugation, redissolved in THF and reprecipitated in methanol. This procedure was repeated three times. The light yellow powder (171 mg) was dried at 45 °C under reduced pressure for 12 h. To remove the end group, the polymer (171 mg) was dissolved in dioxane (2 mL) and AIBN (47 mg, 0.28 mmol) was added. The solution was immersed in a preheated oil bath at 80 °C and stirred for 4 h. The polymer was precipitated in methanol, collected by centrifugation, redissolved in THF and reprecipitated in methanol. This procedure was repeated three times. The light yellow powder **P2** (151 mg) was dried at 45 °C under reduced pressure for 12 h. ν_{max}/cm^{-1} 3082w (=C–H), 2914w (C–H), 1784m (COOR), 1587vs, 1515vs (Ar–F), 1507vs, 1489vs, 1312s, 1272s, 1175s, 1029s, 835s, 750vs, 692vs, 623vs. ^{1}H NMR: δ_H (300 MHz; CDCl$_3$; Me$_4$Si) 1.55 (br, s), 1.97 (br, s), 6.54 (br), 6.87 (br). ^{19}F NMR δ_F (400 MHz; CDCl$_3$; Me$_4$Si) −153.21 (2F, br, s, F$_{ortho}$), −157.36 (1F, br, d, F$_{para}$), −164.28 (2F, br, s, F$_{meta}$). GPC: $M_n = 14{,}900$, $M_w = 19{,}000$, PDI: 1.3.

Synthesis of P3a

P2 (37 mg, 2.8 μmol) was dissolved in dry THF (0.5 mL) in a nitrogen atmosphere. **A** (88 mg, 90 μmol) was dissolved in dry DMF (0.5 mL) in a nitrogen atmosphere and triethylamine (0.01 mg, 10 μmol) was added. The solutions were combined and stirred at 45 °C for 90 h. A white precipitate was observed after some time. The polymer was precipitated in methanol, redissolved in THF and reprecipitated in methanol seven more times until the supernatant was colourless. The dark red polymer **P3a** (18 mg) was dried under reduced pressure at 45 °C for 12 h. λ_{max}(THF)/nm 300, 498 (MLCT). ν_{max}/cm^{-1} 3082w (=C–H), 2914w (C–H), 1664m (amide I), 1587vs (amide II), 1402s, 1507vs, 1489vs, 1312s, 1272s, 1175s, 835s, 780 s, 750vs, 692vs, 623vs. GPC: $M_n = 18{,}000$, $M_w = 22{,}000$, PDI: 1.2. ^{19}F NMR δ_F (400 MHz; CDCl$_3$; Me$_4$Si) no signal.

Synthesis of P3b

P2 (300 mg, 0.02 mmol), 4-(aminomethyl)benzoic acid (139 mg, 0.9 mmol) and triethylamine (0.1 mL, 0.9 mmol) were placed in a Schlenk tube and dispersed in anhydrous DMF (2 mL). The suspension was stirred for 21 h at 80 °C in a nitrogen atmosphere and the resulting polymer was purified by dialysis against methanol (molecular weight cut off of 3.500 g mol^{-1}). **P3b** (275 mg) was obtained as a light brown powder after drying in vacuum at 45 °C for 12 h. λ_{max}(THF)/nm (ε/dm^3 mol^{-1} cm^{-1}) 301 (102 400), $c = 0.16$ mg mL^{-1}. ν_{max}/cm^{-1} 3082w (=C–H), 2914w (C–H), 1700m (amide I), 1655m (amide I), 1587vs (amide II), 1507vs, 1489vs, 1312s, 1272s, 1175s, 1029s, 835s, 750vs, 692vs, 623vs. ^{19}F NMR δ_F (400 MHz; CDCl$_3$; Me$_4$Si) no signal.

Functionalisation of ZnO with P3a and P3b

For both polymers **P3a** and **P3b** the same procedure was applied. **P3a** (15 mg) or **P3b** (15 mg) and ZnO nanorods (15 mg) were dispersed in THF (1 mL) in a Schlenk tube and degassed by three freeze–pump–thaw cycles. The tube was then immersed in a preheated oil bath at 65 °C and stirred for 18 h. The dispersion was then centrifuged at 4000 rpm for 5 min to remove the non-functionalised nanorods which precipitated. A few drops of ethanol were then added to the supernatant and the dispersion was centrifuged at 13 000 rpm for 5 min. The supernatant was removed and the precipitate redispersed in THF (0.5 mL). The washing cycle was repeated four more times. The functionalised nanoparticles **P3a@ZnO** and **P3b@ZnO** were dispersed in 1 mL anhydrous THF and kept under nitrogen and in the dark until they were used. **P3a@ZnO**: λ_{max}(THF)/nm 300, 498 (MLCT). $\lambda_{em,max}$(DMF)/nm practically no emission observed (λ_{ex}/nm 498).

Results and discussion

Polypyridine complexes of ruthenium(ɪɪ) have been extensively used as photoactive compounds in light to energy conversion devices. Compared to organic dyes they exhibit higher photo and thermal stabilities.[23] In many cases, ruthenium(ɪɪ) polypyridine complexes contain bidentate (*e.g.* 2,2′-bipyridine) and monodentate ligands (*e.g.* pyridine, NCS$^-$). Especially monodentate ligands are believed to cause long term stability problems because of photo-induced and thermal ligand dissociation and degradation.[24–26] We employed tridentate 2,2′;6′,2″-terpyridine (tpy) ligands in the ruthenium complex **A** which imparts high photo and thermal stability because of the chelating effect.[19,27,28] In addition, the 4′-substituents on the $[Ru(tpy)_2]^{2+}$ core lead to a push–pull system with the two amide substituents pointing in the same direction. This vectorial arrangement is beneficial for charge separation and charge injection into inorganic semiconductors like ZnO or TiO$_2$.

The ruthenium dye conjugate [(H$_2$N–CH$_2$–CONH–tpy)Ru(tpy–CONH–CH$_2$–COOH)](PF$_6$)$_2$ (**A**) was obtained *via* a solid phase peptide synthesis (SPPS) (Scheme 1) with a TentaGel S Wang resin used as the solid phase and an Fmoc protecting group strategy.[18] SPPS allows high yield and high purity over several reaction steps because the reagents can be used in excess and purification is done by a simple washing procedure. A glycine unit was attached to the resin before the ruthenium(II) complex [(H$_2$N–tpy)Ru(tpy–COOH)](PF$_6$)$_2$ was anchored to the solid support by an amide bond. As aromatic amino groups are known to be less reactive towards activated esters[29] the amino group of the complex was decorated with a further glycine at the *N*-terminus which provides a reactive aliphatic amine functionality. In the last step the complex was cleaved from the solid phase by trifluoroacetic acid and precipitated by addition of an aqueous NH$_4$PF$_6$ solution.

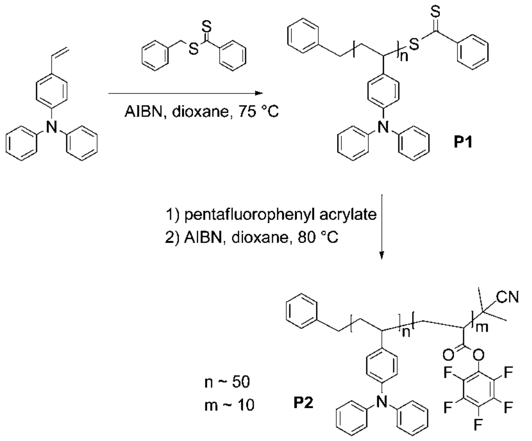

Scheme 2 Synthesis of **P1** and **P2** by RAFT polymerisation.

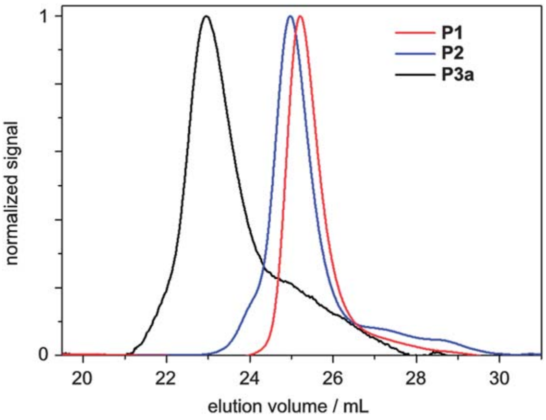

Fig. 1 GPC traces of **P1** (red), **P2** (blue) and **P3a** (black).

The polymer poly(vinyltriphenylamine) PTPA (**P1**) was prepared by Reversible Addition Fragmentation Chain Transfer (RAFT) polymerisation from vinyltriphenylamine (Scheme 2). PTPA is well known as a p-type semiconducting polymer and has already been used in solar cells.[30] The controlled radical polymerisation allows a good control of the molecular weight, a narrow polydispersity index (PDI) and the possibility to synthesise block copolymers. **P1** had a molecular weight of 13,000 g mol^{-1} (by GPC, polystyrene standard) and a PDI of 1.2. The second block was subsequently grafted onto **P1**, using pentafluorophenyl acrylate as the monomer and giving the block copolymer **P2**. Characterisation of **P2** by GPC (Fig. 1) showed a small shift to higher molecular weight and by referring it to the polystyrene standard, the degree of polymerisation of the first block was calculated to be around 50 ($n \approx 50$) and of the second block around 10 ($m \approx 10$). The ^{19}F NMR spectrum shows the expected resonances of the five fluorine nuclei attached to the aromatic ring (Fig. S2†). The activated pentafluorophenyl ester of **P2** can subsequently be treated with primary amines to introduce functionalities in quantitative yields.[31,32] The activated ester block was chosen to be relatively short ($m \approx 10$), since short anchor blocks were shown to bind the most effectively to ZnO surfaces.[33]

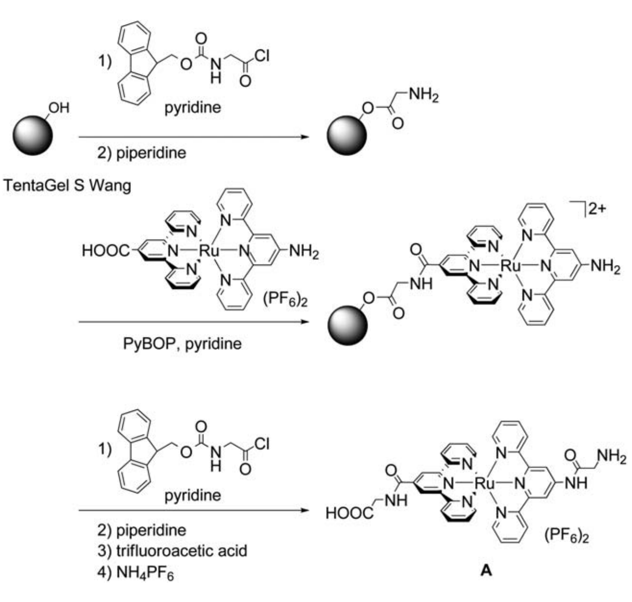

Scheme 1 Synthesis of directional chromophore **A** by SPPS.

In order to attach the ruthenium dye **A** to polymer **P2** a polymer analog reaction was carried out. The amine functionality of dye **A** readily reacts with the activated ester moieties of **P2** (Scheme 3). An excess of the dye and the polymer were dissolved in *N*,*N*′-dimethylformamide and heated to 45 °C for 90 h. Excessive washing by precipitation/dissolving yielded the pure dark red block copolymer **P3a**. Characterisation by Fourier transform infrared (FT-IR) spectroscopy showed the absence of the ester band at 1784 cm^{-1} and the new band of amide bonds at 1664 cm^{-1} (Fig. S2†). Additionally, a ^{19}F NMR spectrum proves that all pentafluorophenyl groups were removed from the polymer (Fig. S3†). Furthermore, the PF$_6$ counterions were exchanged by other anions as judged by the absence of a resonance at 73.2 ppm. A significantly higher molecular weight of **P3a** was observed by GPC (Fig. 1) compared to the block copolymer **P2**, so that the covalent attachment of the dye to the polymer is proven. As a control, **P2** was treated with 4-(aminomethyl)benzoic acid giving **P3b**. The synthesis and characterisation of **P3b** are analogous to the reaction of **P2** with **A**. The

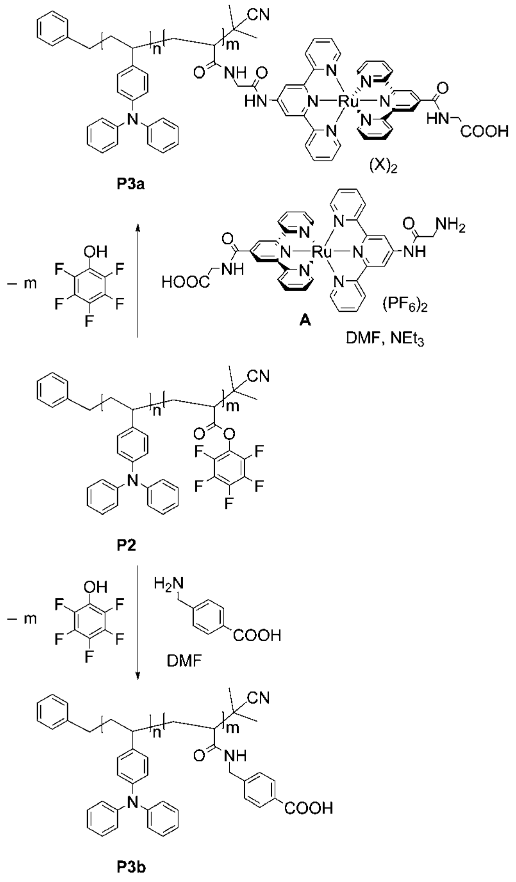

Scheme 3 Functionalisation of **P2** with **A** to give **P3a** (top) and with 4-(aminomethyl)benzoic acid to give **P3b** (bottom).

carboxyl groups of **P3b** can also adsorb to ZnO surfaces but no charge generation is expected under irradiation with visible light.

UV-Visible and photoluminescence (PL) measurements were carried out (Fig. 2). In the absorption spectrum of **P3a** the bands at 250–350 nm arise from $\pi \rightarrow \pi^*$ transitions mainly of the triphenylamine groups and a small contribution from the ruthenium dye. The absorption of the dye in the visible region was observed at 498 nm and is attributed to the characteristic metal-to-ligand charge transfer (MLCT) of the complex.[18] For **P3b** no absorption is observed in that spectral region (Fig. S8†). Photoluminescence measurements in THF (λ_{exc} = 498 nm) show that the dye functionalised polymer **P3a** emits at 667 nm, which is the same value as for the pristine dye **A** (667 nm in DMF). Thus the emission of the dye is not reductively quenched by the TPA polymer.

ZnO nanorods were synthesised according to the literature with a size distribution of several hundreds of nanometers to two micrometers.[15b] For functionalisation with polymers **P3a** and **P3b**, the nanorods were dispersed in a small amount of THF and the respective polymer was added subsequently. The dispersion was stirred at 65 °C overnight under an inert atmosphere. Centrifugation (4000 rpm) for 2 min removed all insufficiently functionalised nanoparticles. Ethanol was then added to the clear dispersion to precipitate the nanocomposite.

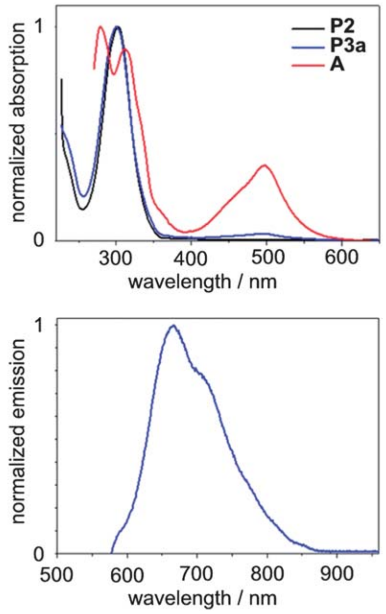

Fig. 2 UV-Vis spectra of **P2** in THF (black), **P3a** in THF (blue) and **A** in DMF (red) (top) and PL spectrum of **P3a** in THF at 498 nm excitation (bottom).

Subsequent centrifugation, redispersion and repetition of the washing cycle for several times gave the pure hybrid materials **P3a@ZnO** and **P3b@ZnO**, respectively. **P3a@ZnO** was a stable red dispersion, which showed some scattering of the light due to the large nanoparticles (length >800 nm). TEM images drop cast from the THF dispersion showed that **P3a@ZnO** nanoparticles were well dispersed and did not aggregate. In contrast, the as-synthesised sample of pristine ZnO showed strong aggregation (Fig. S4†).

The Jablonski diagram of the nanocomposite (Fig. 3) shows the estimated energy levels of the system **P3a@ZnO** together with the possible charge separation/recombination pathways in the D–C–A array.[42] Irradiation of ZnO–⟨Ru⟩$^{2+}$–TPA at 498 nm leads to the singlet MLCT excited state ZnO–^{1}⟨Ru⟩$^{2+}$*–TPA

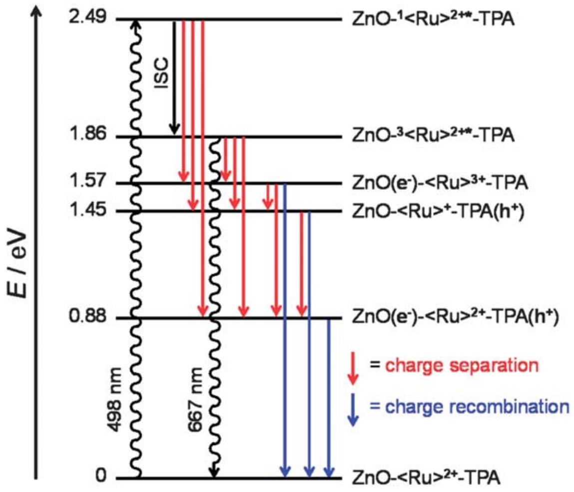

Fig. 3 Jablonski diagram of **P3a@ZnO**.

(2.49 eV), which subsequently undergoes intersystem crossing (ISC) to the triplet excited state ^{3}MLCT ZnO–$^3\langle\mathrm{Ru}\rangle^{2+}*$–TPA (1.86 eV) typically with unit efficiency. Both MLCT states are thermodynamically competent to inject an electron into ZnO or to accept an electron from TPA. Photoluminescence measurements show that the phosphorescence of **P3a@ZnO** is indeed efficiently quenched as compared to **P3a** lacking the ZnO acceptor. From the singlet and triplet MLCT excited states ZnO–$^1\langle\mathrm{Ru}\rangle^{2+}*$–TPA/ZnO–$^3\langle\mathrm{Ru}\rangle^{2+}*$–TPA the fully charge separated state ZnO(e$^-$)–$\langle\mathrm{Ru}\rangle^{2+}$–TPA(h$^+$)[14,34] can principally be populated *via* the partially charge separated states ZnO–$\langle\mathrm{Ru}\rangle^{+}$–TPA(h$^+$) (1.45 eV) or ZnO(e$^-$)–$\langle\mathrm{Ru}\rangle^{3+}$–TPA (1.57 eV).[18] In the fully charge separated state ZnO(e$^-$)–$\langle\mathrm{Ru}\rangle^{2+}$–TPA(h$^+$) (0.88 eV), the ZnO carries the negative and the TPA the positive charge.

By performing PL measurements the quantum yield of **P3a** was determined to be $\Phi = 2.0 \times 10^{-3}$ which is very similar to the value of **A** without TPA attachment ($\Phi = 1.4 \times 10^{-3}$).[18] This shows that no luminescence quenching occurs when the dye is bound to the polymer backbone, *i.e.* photo-induced electron transfer from TPA to the excited ruthenium units $^1\langle\mathrm{Ru}\rangle^{2+}*$ and $^3\langle\mathrm{Ru}\rangle^{2+}*$ is inefficient in this polymer. However, after anchoring of **P3a** to ZnO, the quantum yield of the hybrid **P3a@ZnO** drops below $\Phi = 6.5 \times 10^{-5}$. This low quantum yield clearly corroborates the efficiency of the oxidative quenching in the system, *i.e.* the first electron transfer step after excitation is electron injection into ZnO, likely followed by dye regeneration by TPA.

In order to study the photo-induced interfacial charge transfer in more detail on a single particle level KPFM measurements were carried out in analogy to the measurements we performed on the D–C–A system consisting of a PTPA–perylene block copolymer covalently bound to a ZnO system.[14] KPFM is a very powerful tool to detect local variations of the surface potential in the nanometer regime.[35] Illuminating samples with light allows studying the photo-response of optoelectronic materials.[36–41] Sample illumination of **P3a@ZnO** is realised from underneath the sample through transparent indium tin oxide (ITO) (Fig. 4a) The surface potential was first measured without illumination (Fig. 4b) on a single particle with a length of around 1 μm and a diameter of approximately 120 nm (Fig. S5†). The particle displays an approximately 45 mV higher surface potential than the surrounding ITO substrate. By subsequently comparing that to the surface potential recorded under illumination with $\lambda = 488$ nm (Fig. 4c), the photo-induced change in the surface potential of the **P3a@ZnO** particles is determined. Upon illumination, the surface potential on the **P3a@ZnO** particle increases. This effect was completely reversible after switching off the laser and could be observed for all particles at different positions. Upon laser illumination at a wavelength of 488 nm an electron of the chromophore is excited. Charge separation occurs at the interface of the ZnO particle by transfer of the electron to the conduction band of the ZnO. The oxidised ruthenium dye regenerates by collecting an electron from the HOMO level of the TPA polymer.

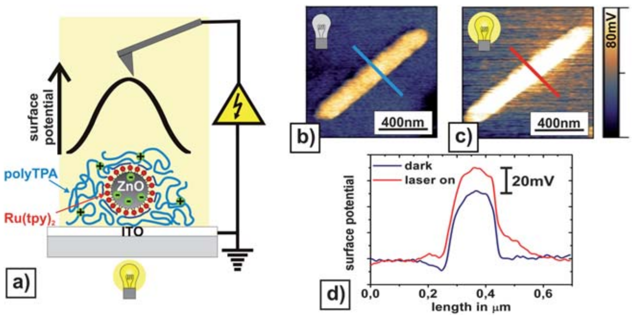

Fig. 4 Study of interfacial charge transfer by KPFM on **P3a@ZnO** spun cast from THF in the dark and under laser illumination ($\lambda = 488$ nm). (a) Schematic of the KPFM measurement on the D–C–A system (TPA in blue, Ru(tpy)$_2$ in red and ZnO in grey) under laser illumination through the ITO coated glass substrate. The surface potential on the functionalised ZnO particle upon illumination is qualitatively depicted in the upper graph. (b) and (c) Surface potential maps measured in the dark and under illumination on the same position. The measured potential values were adjusted relative to the constant potential value of the ITO at a large distance from the **P3a@ZnO**. (d) Line profiles of the surface potentials taken across the particle show an increase in surface potential of around 20 mV upon illumination.

In order to quantitatively discuss this photo-response, the surface potential profile was analyzed in detail across the particle as indicated by the blue and red line for laser off and on in the corresponding surface potential images (Fig. 4d). The increase in surface potential of around 20 mV on the **P3a@ZnO** particle and up to a distance of around 100 nm around the particle was attributed to the build-up of positive charges in the TPA block as a consequence of the charge separation at the interface. Negative charges of the ZnO particle could not be detected by KPFM. This observation indicates a high grafting density of the **P3a** to the ZnO and therefore results in a densely packed and thick polymer layer. Thus, the effect of the build-up of electrons inside the ZnO on the surface potential change is shielded by the positive charges of the TPA.[43]

The estimated energy level difference of 0.88 eV between the ground state ZnO–$\langle\mathrm{Ru}\rangle^{2+}$–TPA and the charge separated state ZnO(e$^-$)–$\langle\mathrm{Ru}\rangle^{2+}$–TPA(h$^+$) (Fig. 3) is significantly larger than the value obtained by KPFM. We attribute this difference to the screening of the positively charged TPA by the counter ions of the $\langle\mathrm{Ru}\rangle^{2+}$ which diffuse from the D–A interface into the polymer matrix. Finally, an additional control experiment performed on **P3b@ZnO** showed no photo-response under irradiation with $\lambda = 488$ nm (Fig. S6†). Without the chromophore as the anchoring group at the interface between ZnO and TPA no excitons can be generated under similar conditions. Thus, for an efficient charge transfer the complete donor–chromophore–acceptor system is required.

Conclusions

Herein we demonstrated the synthesis and characterisation of a new nanoscale D–C–A system with polytriphenylamine as the electron donor (D) and a directional $[\mathrm{Ru^{II}(tpy)_2}]^{2+}$ complex as the chromophore (C) which is directly bound to ZnO nanorods as the electron acceptor (A).

The ruthenium complex $[\mathrm{Ru^{II}(tpy)_2}]^{2+}$ with tridentate ligands has a higher thermal and photostability compared to organic dyes or 2,2′-bipyridine ruthenium(II) complexes. Additionally, the push–pull substituted terpyridine ligands induce spatially separated frontier orbitals which support the charge separation at the interphase. Since the polymer carries several chromophores within each chain, the local concentration of the light harvesting units at the ZnO surface is very high. The chromophore–acceptor contact is very intimate through the direct attachment *via* the carboxyl groups of the Ru^{II} complex. The donor–chromophore contact on the other side is enhanced by the covalent binding of the triphenylamine polymer to the chromophores. Charge separation occurs under light excitation of the chromophore and was proven by phosphorescence quenching and KPFM measurements. Based on these results, we believe that the system is especially suitable to build high performance ssDSSCs.

Acknowledgements

This work was financially supported by the International Research Training Group (IRTG): Self Organized Materials for Optoelectronics supported by the Deutsche Forschungsgemeinschaft (DFG). We thank Dr Stefan Frank for the synthesis of the ZnO nanorods and Gabi Herrmann for the preparation of the ITO coated glass substrates. In addition, we thank Esha Sengupta and Stefan Weber for discussions and the BMBF (contract # 03SF0334) for partial financial support in building up the photo-KPFM.

Notes and references

1 B. O'Regan and M. Grätzel, *Nature*, 1991, **353**, 737–740.

2 M. Matsumoto, H. Miyazaki, K. Matsuhiro, Y. Kumashiro and Y. Takaoka, *Solid State Ionics*, 1996, **89**, 263–267.

3 U. Bach, D. Lupo, P. Comte, J. E. Moser, F. Weissortel, J. Salbeck, H. Spreitzer and M. Grätzel, *Nature*, 1998, **395**, 583–585.

4 J. Boucle and J. Ackermann, *Polym. Int.*, 2012, **61**, 355–373.

5 W. Zhang, Y. Cheng, X. Yin and B. Liu, *Macromol. Chem. Phys.*, 2011, **212**, 15–23.

6 R. H. Lohwasser, J. Bandara and M. Thelakkat, *J. Mater. Chem.*, 2009, **19**, 4126–4130.

7 K. C. D. Robson, B. D. Koivisto, T. J. Gordon, T. Baumgartner and C. P. Berlinguette, *Inorg. Chem.*, 2010, **49**, 5335–5337.

8 K. C. D. Robson, B. Sporinova, B. D. Koivisto, E. Schott, D. G. Brown and C. P. Berlinguette, *Inorg. Chem.*, 2011, **50**, 6019–6028.

9 C. S. Karthikeyan, K. Peter, H. Wietasch and M. Thelakkat, *Sol. Energy Mater. Sol. Cells*, 2007, **91**, 432–439.

10 J.-H. Yum, S.-J. Moon, C. S. Karthikeyan, H. Wietasch, M. Thelakkat, S. M. Zakeeruddin, M. K. Nazeeruddin and M. Grätzel, *Nano Energy*, 2012, **1**, 6–12.

11 Z. Jin, H. Masuda, N. Yamanaka, M. Minami, T. Nakamura and Y. Nishikitani, *Chem. Lett.*, 2009, **38**, 44–45.

12 H. J. Snaith, C. S. Karthikeyan, A. Petrozza, J. Teuscher, J. E. Moser, M. K. Nazeeruddin, M. Thelakkat and M. Grätzel, *J. Phys. Chem. C*, 2008, **112**, 7562–7566.

13 K. Peter and M. Thelakkat, *Macromolecules*, 2003, **36**, 1779–1785.

14 M. Zorn, S. A. L. Weber, M. N. Tahir, W. Tremel, H. J. Butt, R. Berger and R. Zentel, *Nano Lett.*, 2010, **10**, 2812–2816.

15 (*a*) M. Behl, E. Hattemer, M. Brehmer and R. Zentel, *Macromol. Chem. Phys.*, 2002, **203**, 503–510; (*b*) B. Cheng, W. Shi, J. M. Russell-Tanner, L. Zhang and E. T. Samulski, *Inorg. Chem.*, 2006, **45**, 1208–1214.

16 K. Suzuki, A. Kobayashi, S. Kaneko, K. Takehira, T. Yoshihara, H. Ishida, Y. Shiina, S. Oishi and S. Tobita, *Phys. Chem. Chem. Phys.*, 2009, **11**, 9850–9860.

17 (*a*) S. L. Weber, H.-J. Butt and R. Berger, Electrical Characterization of Solar Cell Materials Using Scanning Probe Microscopy, in *Scanning Probe Microscopy in Nanoscience and Nanotechnology 3*, ed. B. Bhushan, Springer Berlin Heidelberg, 2013, pp. 551–573; (*b*) S. V. Kalinin and D. A. Bonnell, *Phys. Rev. B: Condens. Matter Mater. Phys.*, 2001, **63**, 125411.

18 K. Heinze and K. Hempel, *Chem.–Eur. J.*, 2009, **15**, 1346–1358.

19 K. Heinze, K. Hempel and M. Beckmann, *Eur. J. Inorg. Chem.*, 2006, **2006**, 2040–2050.

20 V. Palermo, M. Palma and P. Samorì, *Adv. Mater.*, 2006, **18**, 145–164.

21 E. Sengupta, A. L. Domanski, S. A. L. Weber, M. B. Untch, H.-J. Butt, T. Sauermann, H. J. Egelhaaf and R. Berger, *J. Phys. Chem. C*, 2011, **115**, 19994–20001.

22 A. L. Domanski, E. Sengupta, K. Bley, M. B. Untch, S. A. L. Weber, K. Landfester, C. K. Weiss, H.-J. Butt and R. Berger, *Langmuir*, 2012, **28**, 13892–13899.

23 A. Reynal and E. Palomares, *Eur. J. Inorg. Chem.*, 2011, **2011**, 4509–4526.

24 P. T. Nguyen, B. X. T. Lam, A. R. Andersen, P. E. Hansen and T. Lund, *Eur. J. Inorg. Chem.*, 2011, **2011**, 2533–2539.

25 T. P. Brewster, W. Ding, N. D. Schley, N. Hazari, V. S. Batista and R. H. Crabtree, *Inorg. Chem.*, 2011, **50**, 11938–11946.

26 S. Kämper, A. Paretzki, J. Fiedler, S. Záliš and W. Kaim, *Inorg. Chem.*, 2012, **51**, 2097–2104.

27 A. Breivogel, C. Förster and K. Heinze, *Inorg. Chem.*, 2010, **49**, 7052–7056.

28 A. Breivogel, K. Hempel and K. Heinze, *Inorg. Chim. Acta*, 2011, **374**, 152–162.

29 K. Nilles and P. Theato, *J. Polym. Sci., Part A: Polym. Chem.*, 2010, **48**, 3683–3692.

30 M. Sommer, S. M. Lindner and M. Thelakkat, *Adv. Funct. Mater.*, 2007, **17**, 1493–1500.

31 M. Eberhardt, R. Mruk, R. Zentel and P. Théato, *Eur. Polym. J.*, 2005, **41**, 1569–1575.

32 M. Eberhardt and P. Theato, *Macromol. Rapid Commun.*, 2005, **26**, 1488–1493.

33 M. Zorn, S. Meuer, M. N. Tahir, Y. Khalavka, C. Sonnichsen, W. Tremel and R. Zentel, *J. Mater. Chem.*, 2008, **18**, 3050–3058.

34 E. Hattemer, *Synthesen und Charakterisierungen Arylaminhaltiger Polymere: Multifunktionelle hoch-T_g-Copolymere für photorefraktive Anwendungen*, Johannes Gutenberg-Universität, Mainz, 2000.

35 M. Nonnenmacher, M. P. O'Boyle and H. K. Wickramasinghe, *Appl. Phys. Lett.*, 1991, **58**, 2921–2923.

36 J. M. R. Weaver and H. K. Wickramasinghe, *J. Vac. Sci. Technol., B: Microelectron. Nanometer Struct.–Process., Meas., Phenom.*, 1991, **9**, 1562–1565.

37 H. Hoppe, T. Glatzel, M. Niggemann, A. Hinsch, M. C. Lux-Steiner and N. S. Sariciftci, *Nano Lett.*, 2005, **5**, 269–274.

38 J. Cao, J.-Z. Sun, J. Hong, X.-G. Yang, H.-Z. Chen and M. Wang, *Appl. Phys. Lett.*, 2003, **83**, 1896–1898.

39 V. Palermo, G. Ridolfi, A. M. Talarico, L. Favaretto, G. Barbarella, N. Camaioni and P. Samorì, *Adv. Funct. Mater.*, 2007, **17**, 472–478.

40 S. Sadewasser and M. C. Lux-Steiner, *J. Vac. Sci. Technol., B: Microelectron. Nanometer Struct.–Process., Meas., Phenom.*, 2010, **28**, C4D29–C24D33.

41 E. J. Spadafora, R. Demadrille, B. Ratier and B. Grevin, *Nano Lett.*, 2010, **10**, 3337–3342.

42 The energy levels of the Jablonski diagram were estimated from the absorption and emission maxima (ZnO–$^1\langle\mathrm{Ru}\rangle^{2+*}$–TPA: 498 nm; 2.49 eV; ZnO–$^3\langle\mathrm{Ru}\rangle^{2+*}$–TPA: 667 nm; 1.86 eV) as well as from potential differences of literature known energy levels and redox potentials. The conduction band of ZnO is at −4.4 eV *vs.* vacuum.[14] The oxidation potential of the TPA units in **P3@ZnO** is estimated to be +0.84 V *vs.* NHE which is the oxidation potential of monomeric tolyldiphenylamine.[34] The oxidation and reduction potentials of the ⟨Ru⟩ unit in **P3@ZnO** were estimated to be +1.285 and −0.850 V *vs.* SCE, respectively, from the values of the molecular ruthenium dye [(H_3C–CONH–tpy)Ru(tpy–CONH–CH_2–COOH)](PF6)$_2$.[18] With E(vacuum)/eV = −4.44 − E(NHE) = −4.68 − E(SCE) we estimate ZnO–$\langle\mathrm{Ru}\rangle^{+}$–TPA$^+$ at +1.45 eV, ZnO(e$^-$)–$\langle\mathrm{Ru}\rangle^{3+}$–TPA at +1.565 eV and ZnO(e$^-$)–$\langle\mathrm{Ru}\rangle^{2+}$–TPA$^+$ at 0.88 eV.

43 S. V. Kalinin and D. A. Bonnell, *Nano Lett.*, 2004, **4**, 555–560.

9.5 A Heteroleptic Bis(tridentate)ruthenium(II) Polypyridine Complex with Improved Photophysical Properties and Integrated Functionalizability

A. Breivogel, C. Förster, K. Heinze, *Inorg. Chem.* **2010**, *49*, 7052–7056.

DOI: 10.1021/ic1007236

7052 *Inorg. Chem.* **2010**, *49*, 7052–7056
DOI: 10.1021/ic1007236

Inorganic Chemistry
Article

A Heteroleptic Bis(tridentate)ruthenium(II) Polypyridine Complex with Improved Photophysical Properties and Integrated Functionalizability

Aaron Breivogel, Christoph Förster, and Katja Heinze*

Institute of Inorganic Chemistry and Analytical Chemistry, Johannes Gutenberg-University of Mainz, Duesbergweg 10−14, 55128 Mainz, Germany

Received April 15, 2010

The synthesis and photophysical properties of a ruthenium(II) complex bearing an electron-accepting 2,2′;6′,2″-terpyridine ligand and an electron-donating *N,N*′-dimethyl-*N,N*′-dipyridin-2-ylpyridine-2,6-diamine (ddpd) ligand are presented. The heteroleptic complex is easily prepared isomerically pure and features intense low-energy metal-to-ligand charge-transfer (MLCT) absorption bands and intense room temperature ^{3}MLCT emission with a long ^{3}MLCT lifetime. The favorable photophysical properties are due to the strong ligand field imposed by the ddpd ligand.

Introduction

Meridional-coordinating tridentate ligands are preferred over bidentate ligands because of increased (photo)stability, absence of chirality (Δ and Λ), and simple functionalization in central mutually trans positions. For example, switching from tris(bidentate) [Ir(ppy)$_2$(bpy)]$^+$ to bis(tridentate) [Ir(phbpy)$_2$]$^+$ has been beneficial in terms of the stability and excited-state lifetime (ppy = 2-phenylpyridine; bpy = 2,2′-bipyridine; phbpy = 6-phenyl-2,2′-bipyridine).[1] However, in ruthenium oligopyridine chemistry, [Ru(tpy)$_2$]$^{2+}$ (**1**) shows disappointing photophysical properties [essentially nonluminescent at room temperature and a low triplet-state metal-to-ligand charge-transfer (^{3}MLCT) lifetime] compared to [Ru(bpy)$_3$]$^{2+}$ (**2**). Thermal population of a low-lying ^{3}MC state of **1** provides an efficient deactivating pathway.[2−4]

Two strategies have emerged to improve the excited-state properties of bis(tridentate) ruthenium complexes: (i) increasing the M−L orbital overlap by adjusting the bite angles from N−Ru−N $<80°$ in five-membered chelate rings to $\sim 90°$ in six-membered chelate rings, which raises the energy of the ^{3}MC state relative to that of the ^{3}MLCT state,[5−10] and (ii) attaching an electron-withdrawing substituent to lower the oligopyridine π^* orbitals and thus the energy of the MLCT states relative to the deactivating ^{3}MC state (which should overcompensate for the effect of increased nonradiative decay at low emission energies).[11−14] Concomitant attachment of an electron-donating substituent at the second chelate ligand further improves the emission properties.[14,15] These effects are clearly seen in the series [Ru(tpy)$_2$]$^{2+}$ (**1**; $\lambda_{\text{abs/emiss}}$ = 474/629 nm[11]) → [Ru(EtOOC-tpy)(tpy)]$^{2+}$ (**3**; 485/667 nm[13]) → [Ru(EtOOC-tpy)(H$_2$N-tpy)]$^{2+}$ (**4**; 500/744 nm[14,15]) (Chart 1). At room temperature, the luminescence quantum yield increases from $< 5 \times 10^{-6}$ to 2.7×10^{-4} to 1.8×10^{-3} and the excited-state lifetime from 0.25 to 32 to 34 ns.[11,13−15] Hammarström et al. have switched five-membered chelate rings to six-membered chelate rings by employing (bipyridylpyridyl)methane derivatives (bpy-CR$_2$-py) instead of terpyridine.[5] The homoleptic

---

*To whom correspondence should be addressed. E-mail: katja.heinze@uni-mainz.de. Fax: +49-6131-39-27277.

(1) Tinker, L. L.; Bernhard, S. *Inorg. Chem.* **2009**, *48*, 10507.

(2) Sauvage, J.-P.; Collin, J.-P.; Chambron, J.-C.; Guillerez, S.; Coudret, C.; Balzani, V.; Barigelletti, F.; De Cola, L.; Flamigni, L. *Chem. Rev.* **1994**, *94*, 993.

(3) Winkler, J. R.; Netzel, T. L.; Creutz, C.; Sutin, N. *J. Am. Chem. Soc.* **1987**, *109*, 2381.

(4) Siemeling, U.; Vor der Brüggen, J.; Vorfeld, U.; Neumann, B.; Stammler, A.; Stammler, H.-G.; Brockhinke, A.; Plessow, R.; Zanello, P.; Laschi, F.; Fabrizi de Biani, F.; Fontani, M.; Steenken, S.; Stapper, M.; Gurzadyan, G. *Chem.—Eur. J.* **2003**, *9*, 2819.

(5) Abrahamsson, M.; Wolpher, H.; Johansson, O.; Larsson, J.; Kritikos, M.; Eriksson, L.; Norrby, P.-O.; Bergquist, J.; Sun, L.; Åkermark, B.; Hammarström, L. *Inorg. Chem.* **2005**, *44*, 3215.

(6) Abrahamsson, M.; Jäger, M.; Österman, T.; Eriksson, L.; Persson, P.; Becker, H.-C.; Johansson, O.; Hammarström, L. *J. Am. Chem. Soc.* **2006**, *128*, 12616.

(7) Abrahamsson, M.; Jäger, M.; Kumar, R. J.; Österman, T.; Persson, P.; Becker, H.-C.; Johansson, O.; Hammarström, L. *J. Am. Chem. Soc.* **2008**, *130*, 15533.

(8) Jäger, M.; Kumar, R. J.; Görls, H.; Bergquist, J.; Johansson, O. *Inorg. Chem.* **2009**, *48*, 3228.

(9) Kumar, R. J.; Karlsson, S.; Streich, D.; Rolandini Jensen, A.; Jäger, M.; Becker, H.-C.; Bergquist, J.; Johansson, O.; Hammarström, L. *Chem.—Eur. J.* **2010**, *16*, 2830.

(10) Jäger, M.; Smeigh, A.; Lombeck, F.; Görls, H.; Collin, J.-P.; Sauvage, J.-P.; Hammarström, L.; Johansson, O. *Inorg. Chem.* **2010**, *49*, 374.

(11) Maestri, M.; Armaroli, N.; Balzani, V.; Constable, E. C.; Cargill Thompson, A. M. W. *Inorg. Chem.* **1995**, *34*, 2759.

(12) Schubert, U. S.; Hofmeier, H.; Newkome, G. R. *Modern Terpyridine Chemistry*; Wiley-VCH: Weinheim, Germany, 2006.

(13) Bolink, H. J.; Cappelli, L.; Coronado, E.; Gaviña, P. *Inorg. Chem.* **2005**, *44*, 5966.

(14) Heinze, K.; Hempel, K.; Beckmann, M. *Eur. J. Inorg. Chem.* **2006**, 2040.

(15) Heinze, K.; Hempel, K.; Tschierlei, S.; Schmitt, M.; Popp, J.; Rau, S. *Eur. J. Inorg. Chem.* **2009**, 3119.

Chart 1. Bis(tridentate) Ruthenium(II) Oligopyridine Complexes

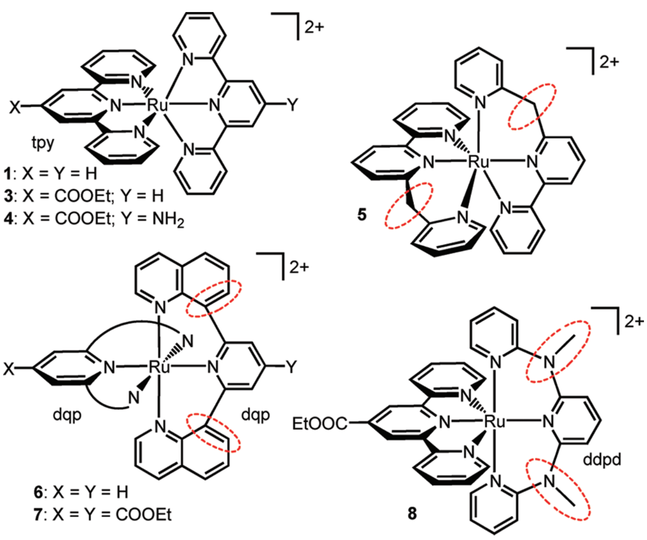

bis[(bipyridylpyridyl)methane]ruthenium complex **5** features $\tau = 15$ ns and $\Phi = 10^{-3}$ ($\lambda_{abs/emiss} = 477/655$ nm; Chart 1).[5] However, the values are still well below those of the tris-bpy complex **2** ($\tau = 1\ \mu$s, $\Phi = 8.9 \times 10^{-2}$[6,7]), and **5** is still chiral. These properties have been surpassed by the homoleptic complex $[Ru(dqp)_2]^{2+}$ (**6**, Chart 1). Almost 90° N−Ru−N bite angles are observed and excellent photophysical properties are achieved ($\Phi = 2 \times 10^{-2}$; $\tau = 3\ \mu$s; $\lambda_{abs/emiss} = 490/700$ nm). Further enhancement is achieved by COOEt substitution (**7**, Chart 1; $\Phi = 7 \times 10^{-2}$; $\tau = 5.5\ \mu$s; $\lambda_{abs/emiss} = 553/693$ nm).[6,7]

However, these homoleptic dqp complexes show *fac*/*mer* stereoisomerism because of the flexible six-membered chelate rings (the *fac* isomers even come in cis-*fac* and trans-*fac* isomers), and, in addition, N_5Cl-coordinated complexes $[RuCl(dqp)_2]^+$ are formed.[8] Heteroleptic-type **6** complexes with X ≠ Y (e.g., donor/acceptor substitution) are quite difficult to obtain,[8] but very recently Hammarström et al. succeeded in incorporating dqp complexes in donor/chromophor/acceptor triads.[9]

Results and Discussion

Here we describe the synthesis and properties of the heteroleptic ruthenium oligopyridine complex **8** (Chart 1), which has several beneficial features: a 2-fold rotation axis, setup for simple functionalization in the direction of this C_2 axis,[16] absence of *fac*/*mer* stereoisomerism, an electron-donating *N*,*N*′-dimethyl-*N*,*N*′-dipyridin-2-ylpyridine-2,6-diamine (ddpd) ligand forming six-membered chelate rings together with an electron-withdrawing 4′-(ethylcarboxy)terpyridine ligand (push−pull substitution). The methyl substituents of ddpd are necessary because tripyridyldiamines lacking alkyl groups at the amine are easily deprotonated, yielding chain complexes that are interesting by themselves for other reasons but undesirable for our purposes.[17]

First, we performed quantum chemical calculations on the homoleptic complex $[Ru(ddpd)_2]^{2+}$ (**9**). The calculations suggest that *fac*/*mer* stereoisomers are analogous to those of **6**, with *mer*-**9** being more stable than *trans*-*fac*-**9** (31 kJ mol^{-1}) and *cis*-*fac*-**9** (34 kJ mol^{-1}). Attempts to synthesize and purify **9** are indeed complicated because of the formation of *fac*/*mer* isomers and N_5Cl coordination. Coordinated chloride is easily removed by silver cations, but heating (dimethyl sulfoxide, reflux, microwave, 10 h) does not furnish pure *mer*-**9**. The photophysical properties of the *fac*/*mer* mixture were also disappointing ($\lambda_{abs/emiss} = 393/468$ nm, very weak emission). Thus, we switched to the mixed donor/acceptor-substituted ruthenium(II) complex **8** with an electron-donating ddpd ligand and an electron-withdrawing EtOOC-tpy ligand. **8** is easily prepared from $RuCl_3$(EtOOC-tpy)[18−20] and ddpd in a microwave-assisted synthesis at 80 °C (after chloride abstraction with silver nitrate and precipitation with NH_4PF_6) as a purple powder in 62% yield.

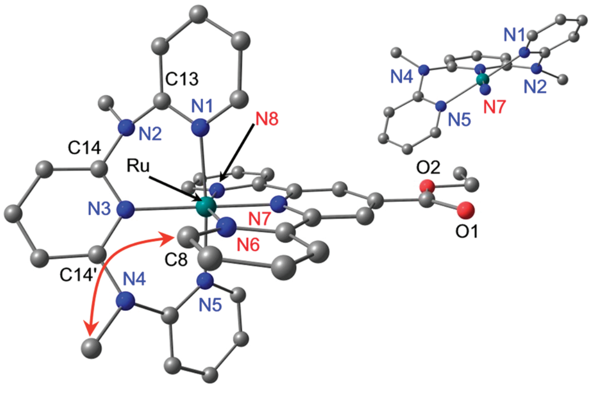

Figure 1. DFT (B3LYP, LANL2DZ)-optimized geometry of **8** (inset: Newman projection viewed approximately along the C_2 axis; tpy-COOEt ligand omitted). Hydrogen atoms are omitted for clarity. The arrow indicates an interligand NOE contact between protons.

High-resolution electrospray ionization [(HR)ESI] mass spectrometry (MS), IR spectrometry, multinuclear and correlation NMR spectroscopy, and elemental analysis are consistent with the formulated structure of **8**. Because the tpy ligand only coordinates in a meridional fashion, *fac*/*mer* stereoisomers are absent. A single resonance is observed for the $N-CH_3$ hydrogen, carbon, and nitrogen nuclei, respectively (Supporting Information). Singlet ground-state density functional theory (DFT) calculations on **8** reveal that the N−Ru−N angles involving the ddpd ligand are around 88° while the corresponding angles involving the tpy ligand are around 79° (Figure 1). The six-membered chelate rings of the ddpd ligand form boat conformations, resulting in an overall small twist of the ddpd ligand, with one terminal pyridine ring pointing up and the other one pointing down relative to the plane of the central pyridine ring (Figure 1, inset). Similarly, the $N-CH_3$ groups point up and below the central pyridine plane ($H_3\underline{C}-\underline{N}2-\underline{C}14-\underline{N}3/H_3\underline{C}-\underline{N}4-\underline{C}14'-\underline{N}3 = 150.4°/150.2°$), which allows for an nuclear Overhauser enhancement (NOE) contact to the tpy proton H8 vis-à-vis (indicated by an orange-colored arrow, Figure 1). Gratifyingly, the DFT-calculated metrical parameters match those obtained from a single-crystal X-ray diffraction analysis of **8** [triclinic, $P\bar{1}$; N1−Ru−N3/N5−Ru−N3 = 87.5°/87.7°; N6−Ru−N7/N7−Ru−N8 = 79.6°/79.7°; $H_3\underline{C}-\underline{N}2-\underline{C}14-\underline{N}3/H_3\underline{C}-\underline{N}4-\underline{C}14'-\underline{N}3 = 156.2°/153.2°$; the atom numbering refers to that used in Figure 1 for the sake of comparison].

---

[16] Heinze, K.; Hempel, K. *Chem.—Eur. J.* **2009**, *15*, 1346.

[17] Yin, C.; Huang, G.-C.; Kuo, C.-K.; Fu, M.-D.; Lu, H.-C.; Ke, J.-H.; Shih, K.-N.; Huang, Y.-L.; Lee, G.-H.; Yeh, C.-Y.; Chen, C.-h.; Peng, S.-M. *J. Am. Chem. Soc.* **2008**, *130*, 10090.

[18] Fallahpour, R.-A. *Synthesis* **2000**, *8*, 1138.

[19] Fallahpour, R.-A. *Eur. J. Inorg. Chem.* **1998**, 1205.

[20] Fallahpour, R.-A.; Neuburger, M.; Zehnder, M. *New J. Chem.* **1999**, *23*, 53.

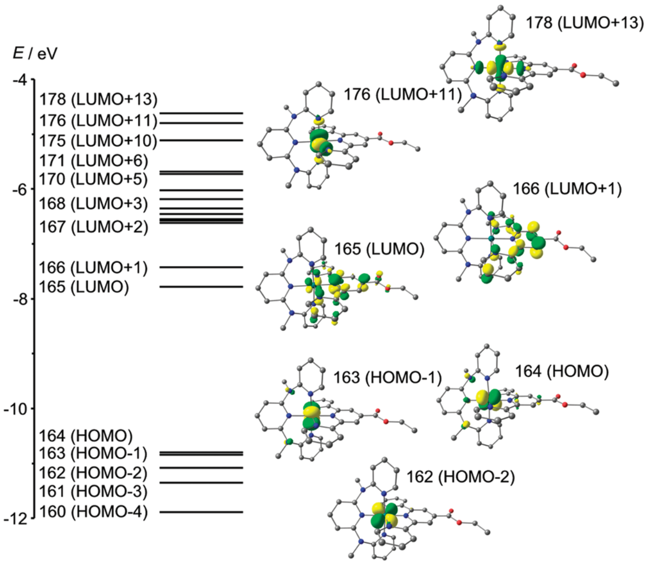

Figure 2. Molecular orbital diagram of **8** and some relevant molecular orbitals (contour value 0.06 au).

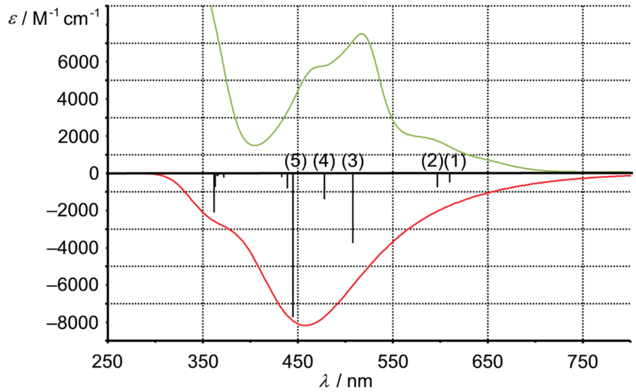

Figure 3. Experimental electronic absorption spectrum of **8** in CH_3CN (top) and calculated stick spectrum (TD-DFT, IEFPCM, CH_3CN) of **8** (the intensity of the sticks is proportional to the calculated oscillator strength, and the calculated spectrum is composed of δ functions at the excitation energies) (bottom).

Kohn–Sham frontier orbitals of the singlet ground state of **8** are shown in Figure 2. The lowest unoccupied molecular orbitals (LUMOs) of **8** are mainly localized on the EtOOC-tpy ligand, while the highest occupied molecular orbitals (HOMOs) are essentially ruthenium-based orbitals (t_{2g} in octahedral symmetry) with some ddpd contribution (especially the nitrogen atoms of the $N-CH_3$ groups). The experimental electronic spectrum of **8** is dominated by intense $\pi \rightarrow \pi^*$ transitions at $\lambda < 350$ nm (Supporting Information). The broad absorption band around $\lambda = 500$ nm corresponds to several MLCT transitions (Figure 3).[21] On the basis of time-dependent DFT (TD-DFT) calculations (gas-phase and polarizable continuum solvation model, CH_3CN)[21] on **8** involving the first 12 spin-allowed singlet excitations, the most intense peaks in the visible spectral region are assigned to MLCT "t_{2g}(Ru)" → π^*(tpy-COOEt) transitions, e.g., transitions (3), (4), and (5) involve mainly HOMO, HOMO−1, and HOMO−2 (d_{Ru}) to LUMO and LUMO+1 [π^*(tpy-COOEt)] transitions at 508, 478, and 445 nm (Figures 2 and 3).

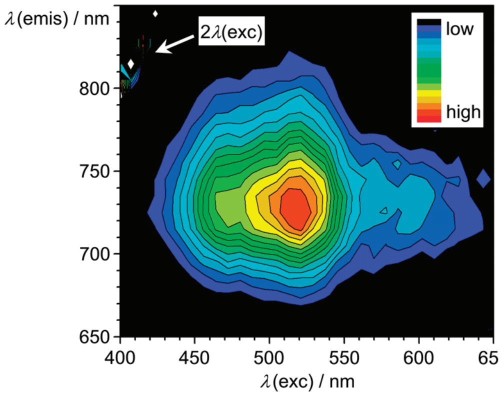

Figure 4. Excitation emission matrix of **8**.

The TD-DFT results compare well with the experimental data of **8** ($\lambda_{abs} = 517$ nm; $\varepsilon = 7500\ M^{-1}\ cm^{-1}$; Figure 3). The difference between experimental and calculated absorption maxima of $\Delta E = 0.35$ eV (gas phase) [$\Delta E = 0.30$ eV (CH_3CN)] is similar to the one obtained for **1** using the same method [$\Delta E = 0.38$ eV (acetone)].[21] The experimental maximum of **8** is bathochromically shifted by 1275 cm^{-1} relative to that of **3** because of the π-electron-donating effect of ddpd, raising the energy of the Ru d orbitals.

The room temperature emission is also shifted from 667 nm (**3**) to 729 nm (**8**),[13] with the maximum intensity observed upon excitation of the ^{1}MLCT transitions (Figure 4). The excitation spectrum closely follows the absorption spectrum in the visible spectral region. In spite of the lower ^{3}MLCT energy, **8** features a more than 10-fold higher quantum yield compared to **3** [$\Phi = 3.0 \times 10^{-3}$ (**8**)]. Also, the ^{3}MLCT lifetime has dramatically increased to $\tau = 722(5)$ ns (**8**). This is appreciable considering the fact that a lower ^{3}MLCT energy should lead to faster nonradiative decay.[22,23]

In frozen butyronitrile at 77 K, emission is observed at higher energy and with a higher lifetime [$\lambda_{emiss} = 707$ nm; $\tau = 3309(15)$ ns]. The first observation is due to the lower stabilization of the excited state in the frozen matrix, and the second finding is due to less accessible thermal deactivation pathways. The DFT-calculated energy difference between the ^{3}MLCT state and the ground state (gas phase) amounts to 1.64 eV (756 nm for the 0 → 0 transition), in quite good agreement with the experiment.[21]

The photophysical properties of **8** are thus dramatically improved when compared to those of **1** and are approaching those of **2** ($\Phi = 6.2 \times 10^{-2}$; $\tau = 962$ ns[24,25]).

The $Ru^{II/III}$ oxidation of **8** is found at $E_{1/2} = 0.81$ V (vs Fc/Fc^+). Thus, **8** is harder to oxidize than **4** ($E_{1/2} = 0.68$ V[14]) but easier to oxidize than **1** ($E_{1/2} = 0.92$ V[11]) or **3** ($E_{1/2} = 0.96$ V[13]). This reflects the stronger donor ability of ddpd as compared to tpy, raising the energy of the Ru d levels. **8** is reduced at $E_{1/2} = -1.40$ V in a quasi-two-electron process, precluding assignments to individual ligands.

To place the ddpd ligand in the context of other donor ligands, a computational analysis was conducted. The net donor strength ($\sigma + \pi$) is estimated from DFT-calculated A_1 carbonyl stretching modes of tricarbonyl(nickel) fragments

---

[21] Jakubikova, E.; Chen, W.; Dattelbaum, D. M.; Rein, F. N.; Rocha, R. C.; Martin, R. L.; Batista, E. R. *Inorg. Chem.* **2009**, *48*, 10720.

[22] Meyer, T. J. *Pure Appl. Chem.* **1986**, *58*, 1193.

[23] Caspar, J. V.; Meyer, T. J. *J. Phys. Chem.* **1983**, *87*, 952.

[24] Caspar, J. V.; Meyer, T. J. *J. Am. Chem. Soc.* **1983**, *105*, 5583.

[25] Ding, Z.; Wellington, R. G.; Brevet, P. F.; Girault, H. H. *J. Phys. Chem.* **1996**, *100*, 10658.

coordinated to the ligands.[26,27] On this basis, the ddpd ligand was ranked between trimethylamine and N-heterocyclic carbene ligands (Supporting Information).

Conclusion

We have prepared a novel heteroleptic ruthenium(II) complex with a terpyridine acceptor ligand and a meridional-coordinating tridentate ddpd donator ligand. The latter forms six-membered chelate rings with the metal center. This ligand combination results in long-wavelength absorption and emission as well as an extended ^{3}MLCT lifetime of 722 ns.

The effects of ddpd are 3-fold: improved σ-orbital overlap with Ru "e_g" orbitals due to $\approx$90° bite angles (LUMO+11 and LUMO+13; Figure 2) raising their energies and thus the energy of the deactivating ^{3}MC state, increased σ-donation boosting this effect, and increased π donation raising the energy of the Ru "t_{2g}" orbitals and resulting in quite low absorption and emission energies. These aspects of ddpd will also be exploited in other ddpd metal complexes currently prepared in our group. The use of **8** and functionalized derivatives in organic light-emitting devices, dye-sensitized solar cells (DSSCs), or biolabeling applications is actively pursued in our group.

Experimental Section

General Procedures. CH_3CN and dioxane were distilled from CaH_2 and sodium, respectively. All reagents were used as received from commercial suppliers (Acros and Sigma-Aldrich). Microwave heating was performed in a Discover Benchmate Plus (CEM Synthesis) single-mode microwave cavity, producing continuous irradiation at 2.455 GHz with 100 W (maximum power). Reaction mixtures were stirred with a magnetic stir bar during irradiation. The temperature and irradiation power were monitored during the course of the reaction. NMR spectra were recorded on a Bruker Avance DRX 400 spectrometer at 400.31 MHz (^{1}H), 100.66 MHz (^{13}C{^{1}H}), and 40.56 MHz (^{15}N). All resonances are reported in ppm versus the solvent signal as an internal standard [CD_3CN (^{1}H, $\delta = 1.94$; ^{13}C, $\delta = 1.24$ ppm)] or versus external CH_3NO_2 (90% in $CDCl_3$; ^{15}N, $\delta = 0$ ppm). IR spectra were recorded with a BioRad Excalibur FTS 3100 spectrometer as KBr disks. Electrochemical experiments were carried out on a BioLogic SP-50 voltammetric analyzer using platinum wires as counter and working electrodes and 0.01 M $Ag/AgNO_3$ as the reference electrode. The measurements were carried out at a scan rate of 150 mV s^{-1} for cyclic voltammetry experiments and at 50−200 mV s^{-1} for square-wave voltammetry experiments using 0.1 M (nBu$_4$N)(PF$_6$) as the supporting electrolyte in CH_3CN. Potentials are referenced to the ferrocene/ferrocenium couple ($E_{1/2} = 85 \pm 5$ mV under the experimental conditions). UV/vis/near-IR spectra were recorded on a Varian Cary 5000 spectrometer using 1.0 cm cells (Hellma, Suprasil). Emission spectra were recorded on a Varian Cary Eclipse spectrometer. Quantum yields were determined by comparing the areas under the emission spectra on an energy scale/cm^{-1} recorded for optically matched solutions of the sample and the reference {([Ru(bpy)$_3$]$^{2+}$) = 0.062 in CH_3CN}.[24] For time-resolved photoluminescence measurements, a solution ($c = 4.5 \times 10^{-6}$ M in butyronitrile) was filled into a homemade cuvette (tin-plated copper with quartz windows; indium-sealed; 4 mm optical path length) inside a nitrogen-filled glovebox and the cuvette was sealed and transferred to a home-built cryostat. It was kept under a dynamic vacuum (typically 10^{-6} mbar) for low-temperature experiments. The sample was excited by the 517 nm output of an optical parametric oscillator (OPO; GWU Lasertechnik) itself pumped by the frequency-tripled (10 Hz) output of a pulsed Nd:YAG nanosecond laser (INDI Quanta Ray Spectra Physics). The luminescence of the sample was dispersed by a Shamrock SR-303i spectrograph with a 150 L/mm grating and detected by a gated intensified CCD detector (Andor IStar DH740 ICCD camera). The solution was illuminated with the laser beam from the detector side, and measurements were conducted at room temperature (295 K) and liquid-nitrogen temperature (77 K). Single exponentials were used to fit the experimental data. Field desorption (FD) MS spectra were recorded on a FD Finnigan MAT90 spectrometer. ESI MS spectra were recorded on a Micromass Q-TOF-Ultima spectrometer. Elemental analyses were performed by the microanalytical laboratory of the chemical institutes of the University of Mainz.

Crystal Structure Determination. Intensity data were collected with a Bruker AXS Smart1000 CCD diffractometer with an APEX II detector and an Oxford cooling system and corrected for absorption and other effects using Mo Kα radiation ($\lambda = 0.71073$ Å) at 173(2) K. The diffraction frames were integrated using the *SAINT* package, and most were corrected for absorption with *MULABS*.[28,29] The structures were solved by direct methods and refined by the full-matrix method based on F^2 using the *SHELXTL* software package.[30,31] All non-hydrogen atoms were refined anisotropically, while the positions of all hydrogen atoms were generated with appropriate geometric constraints and allowed to ride on their respective parent carbon atoms with fixed isotropic thermal parameters. The asymmetric unit of a crystal of **8** contains one molecule of an acetonitrile solvent and two [PF$_6$]$^-$ counterions, one of which is disordered over two positions (site occupancy 0.73:0.27). Crystallographic data (excluding structure factors) for the structure reported in this paper have been deposited with the Cambridge Crystallographic Data Centre as supplementary publication no. CCDC-773229. Copies of the data can be obtained free of charge upon application to CCDC, 12 Union Road, Cambridge CB2 1EZ, U.K. [fax (0.44) 1223-336-033; e-mail deposit@ccdc.cam.ac.uk].

DFT calculations were carried out with the *Gaussian03*/DFT[32] series of programs. The B3LYP formulation of DFT was used by employing the LANL2DZ basis set.[32] No symmetry constraints were imposed on the molecules. For solvent modeling, the integral-equation-formalism polarizable continuum model (IEFPCM) was employed.

---

[26] Tolman, C. A. *Chem. Rev.* **1977**, *77*, 313.

[27] Shi, Q.; Thatcher, R. J.; Slattery, J.; Sauari, P. S.; Whitwood, A. C.; McGowan, P. C.; Douthwaite, R. E. *Chem.—Eur. J.* **2009**, *15*, 11346.

[28] *SMART Data Collection and SAINT-Plus Data Processing Software for the SMART System*, various versions; Bruker Analytical X-ray Instruments, Inc.: Madison, WI, 2000.

[29] Blessing, B. *Acta Crystallogr.* **1995**, *A51*, 33.

[30] Sheldrick, G. M. *SHELXTL*, version 5.1; Bruker AXS: Madison, WI, 1998.

[31] Sheldrick, G. M. *SHELXL-97*; University of Göttingen: Göttingen, Germany, 1997.

[32] Frisch, M. J.; Trucks, G. W.; Schlegel, H. B.; Scuseria, G. E.; Robb, M. A.; Cheeseman, J. R.; Montgomery, J. A.; Vreven, T., Jr.; Kudin, K. N.; Burant, J. C.; Millam, J. M.; Iyengar, S. S.; Tomasi, J.; Barone, V.; Mennucci, B.; Cossi, M.; Scalmani, G.; Rega, N.; Petersson, G. A.; Nakatsuji, H.; Hada, M.; Ehara, M.; Toyota, K.; Fukuda, R.; Hasegawa, J.; Ishida, M.; Nakajima, T.; Honda, Y.; Kitao, O.; Nakai, H.; Klene, M.; Li, X.; Knox, J. E.; Hratchian, H. P.; Cross, J. B.; Adamo, C.; Jaramillo, J.; Gomperts, R.; Stratmann, R. E.; Yazyev, O.; Austin, A. J.; Cammi, R.; Pomelli, C.; Ochterski, J. W.; Ayala, P. Y.; Morokuma, K.; Voth, G. A.; Salvador, P.; Dannenberg, J. J.; Zakrzewski, V. G.; Dapprich, S.; Daniels, A. D.; Strain, M. C.; Farkas, O.; Malick, D. K.; Rabuck, A. D.; Raghavachari, K.; Foresman, J. B.; Ortiz, J. V.; Cui, Q.; Baboul, A. G.; Clifford, S.; Cioslowski, J.; Stefanov, B. B.; Liu, G.; Liashenko, A.; Piskorz, P.; Komaromi, I.; Martin, R. L.; Fox, D. J.; Keith, T.; Al-Laham, M. A.; Peng, C. Y.; Nanayakkara, A.; Challacombe, M.; Gill, P. M. W.; Johnson, B.; Chen, W.; Wong, M. W.; Gonzalez, C.; Pople, J. A. *Gaussian 03*, revision B.03; Gaussian, Inc.: Pittsburgh, PA, 2003.

Chart 2. Atom Numbering of ddpd for NMR Assignment

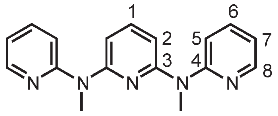

Chart 3. Atom Numbering of **8** for NMR Assignment

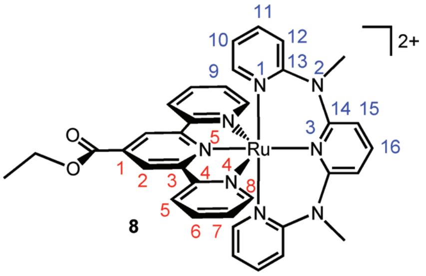

Synthesis of ddpd (Chart 2). Potassium bis(trimethylsilyl)amide (5.670 g, 28.42 mmol, 2.6 equiv) was dissolved in dioxane (100 mL) under argon. After the addition of *N*-methylpyridin-2-ylamine (3.00 mL, 29.2 mmol, 2.7 equiv), the solution turned yellow. A solution of 2,6-dibromopyridine (2.555 g, 10.79 mmol, 1.0 equiv) in dioxane (30 mL) was added, and the mixture was heated to reflux for 64 h, resulting in a brown solution. After cooling to room temperature, water (250 mL) was added, and the aqueous phase was extracted three times with tetrahydrofuran/Et_2O (1:1, 100 mL). The combined organic phases were washed three times with a 1 M aqueous Na_2CO_3 solution and finally dried over $MgSO_4$. After removal of the solvent under reduced pressure, the product was purified by column chromatography (silica gel, 3:1 petroleum ether 40−60/ethyl acetate), yielding a yellow viscous liquid. Yield: 2.82 g (9.68 mmol, 90%). ^1H NMR (CD_3CN, 300 K): δ 8.29 (m, 2 H, H^8), 7.57 (m, 2 H, H^6), 7.50 (t, $^3J_{HH}$ = 8.0 Hz, 1 H, H^1), 7.26 (m, 2 H, H^5), 6.89 (m, 2 H, H^7), 6.71 (d, $^3J_{HH}$ = 8.0 Hz, 2 H, H^2), 3.50 (s, 6 H, CH_3). $^{13}C\{^1H\}$ NMR (CD_3CN, 300 K): δ 158.7 (s, C^4), 157.2 (s, C^3), 148.8 (s, C^8), 139.8 (s, C^1), 137.8 (s, C^6), 117.9 (s, C^7), 116.3 (s, C^5), 106.6 (s, C^2), 36.3 (s, CH_3). MS (FD): *m/z* 291.2 (100%) $[M]^+$. HR-MS (ESI^+): Calcd for $C_{17}H_{17}N_5Na$: *m/z* 314.1382. Obsd: *m/z* 314.1375. Elem anal. Calcd for $C_{17}H_{17}N_5$ (291.35): C, 70.08; H, 5.88; N, 24.04. Found: C, 70.12; H, 5.52; N, 24.34.

Synthesis of 8 (Chart 3). A solution of ddpd (216.4 mg, 0.743 mmol, 1.5 equiv) in ethanol (15 mL) was added to $RuCl_3$(EtOOC-tpy)[33−35] (251.0 mg, 0.490 mmol, 1.0 equiv). After the addition of *N*-ethylmorpholine (0.20 mL, 0.18 mg, 3.2 equiv), the mixture was sonicated for 1 min and heated to reflux in a laboratory microwave oven for 15 min (80 °C). The mixture was filtered over Celite (1.5 cm; diameter 3.5 cm) and rinsed with ethanol. The solvent was removed under reduced pressure, and the dark-red-brown residue was dissolved in ethanol (3 mL). The addition of an aqueous solution of NH_4PF_6 (239.0 mg, 1.466 mmol, 3.0 equiv, 3 mL of H_2O) resulted in the precipitation of a purple solid. After the precipitate was washed with water, the precipitate was dissolved in CH_3CN (10 mL) and a solution of $AgNO_3$ (52 mg, 0.31 mmol, 0.4 equiv) in CH_3CN (10 mL) was added. The mixture was refluxed for 4 h. The resulting AgCl was removed by filtration, and the filtrate was concentrated to 3 mL under reduced pressure. The addition of an aqueous solution of NH_4PF_6 (156.0 mg, 0.957 mmol, 2.0 equiv, 3 mL of H_2O) resulted in the precipitation of a purple solid, which was collected by filtration and dried under reduced pressure. Yield: 298.6 mg (0.3023 mmol, 62%). Crystals suitable for single-crystal X-ray diffraction were obtained by the slow diffusion of diethyl ether into a solution of **8** in CH_3CN. ^1H NMR (CD_3CN, 300 K): δ 8.97 (s, 2 H, H^2), 8.56 (m, 2 H, H^5), 8.27 (t, $^3J_{HH}$ = 8.2 Hz, 1 H, H^{16}), 8.11 (m, 2 H, H^8), 8.02 (m, 2 H, H^6), 7.61 (m, 2 H, H^{11}), 7.56 (d, $^3J_{HH}$ = 8.2 Hz, 2 H, H^{15}), 7.47 (m, 2 H, H^7), 7.17 (m, 2 H, H^{12}), 6.57 (m, 2 H, H^{10}), 6.42 (m, 2 H, H^9), 4.58 (q, $^3J_{HH}$ = 7.1 Hz, 2 H, $C\underline{H_2}CH_3$), 3.46 (s, 6 H, $N{-}C\underline{H_3}$), 1.52 (t, $^3J_{HH}$ = 7.1 Hz, 3 H, $CH_2C\underline{H_3}$). $^{13}C\{^1H\}$ NMR (CD_3CN, 300 K): δ 164.9 (s, C=O), 159.8, 159.7 (2s, C^3, C^{13}), 158.7 (s, C^4), 157.2 (s, C^{14}), 155.1 (s, C^8), 149.4 (s, C^9), 141.8 (s, C^{16}), 140.2 (s, C^{11}), 139.2 (s, C^6), 136.3 (s, C^1), 128.0 (s, C^7), 125.7 (s, C^5), 123.8 (s, C^2), 121.5 (s, C^{10}), 116.3 (s, C^{12}), 113.6 (s, C^{15}), 63.7 (s, $\underline{C}H_2CH_3$), 41.8 (s, $N\underline{C}H_3$), 14.6 (s, $CH_2\underline{C}H_3$). $^1H-^{15}N$ HMBC (CD_3CN, 300 K): δ −288.1 (N^2), −168.6 (N^1), −162.2 (N^3), −142.2 (N^4), −85.8 (N^5). MS (ESI^+): *m/z* 349.1 (7%) $[M - 2PF_6]^{2+}$, 843.1 (100) $[M - PF_6]^+$. HR-MS (ESI^+): Calcd for $C_{35}H_{32}F_6N_8O_2P^{96}Ru$: *m/z* 837.1366. Obsd: *m/z* 837.1360. IR (KBr): $\tilde{\nu}$ 3432 (br, crystal water), 3092 (m, CH_{ar}), 2922 (m, CH_{al}), 1729 (s, CO_{ester}), 1603 (s), 1583 (m), 1492 (m), 1454 (s), 1441 (s), 1372 (m), 1343 (s), 1280 (m), 1254 (s), 1126 (m), 1100 (m), 1023 (m), 841 (vs, PF), 768 (m), 752 (m), 560 (s) cm^{-1}. UV/vis (CH_3CN): λ_{abs} (ε) 517 (7500), 319 (28 800), 276 (34 700), 236 (29 900), 205 nm (31500 M^{-1} cm^{-1}). Emission (CH_3CN, 295 K, λ_{exc} = 517 nm): λ_{emiss} = 729 nm [τ = 722(5) ns]. Emission ($CH_3CH_2CH_2CN$, 77 K, λ_{exc} = 517 nm): λ_{emiss} = 707 nm [τ = 3309(15) ns]. Quantum yield (CH_3CN, λ_{exc} = 469 nm, 295 K): Φ = 0.003. CV (CH_3CN): $E_{1/2}$ = +0.81 (1e), −1.40 V (2e) vs Fc/Fc^+. Elem anal. Calcd for $C_{35}H_{32}F_{12}N_8O_2P_2Ru$ (987.68)·$5H_2O$: C, 39.00; H, 3.93; N, 10.40. Found: C, 39.03; H, 3.60; N, 10.40.

Acknowledgment. This work was supported by the Deutsche Forschungsgemeinschaft (Grant HE 2778/5-2). We thank Dr. F. Laquai and M. Meister (Max Planck Institute for Polymer Research, Mainz) for measuring the excited-state lifetime of **8**.

Supporting Information Available: X-ray crystallographic data for complex **8** in CIF format, X-ray structure of complex **8** (Figure S1), crystal and structure refinement data for complex **8** (Table S1), bond lengths and angles of complex **8** (Table S2), IR spectrum, UV/vis absorption and emission spectra, ^1H NMR spectrum, $^{13}C\{^1H\}$ NMR spectrum, HH COSY, NOESY, CH COSY, $^{13}C-^1H$ HMBC, and $^{15}N-^1H$ HMBC of **8** (Figures S2−S10), Cartesian coordinates of *cis-fac*-**9**, *trans-fac*-**9**, *mer*-**9**, the singlet ground state of **8**, the ^3MLCT state of **8**, graphical representation of the frontier orbitals of **8**, results of the TD-DFT (singlet) calculation of **8** (gas phase and CH_3CN), Cartesian coordinates of $Ni(CO)_3L$ complexes [L = κN(central pyridine)-ddpd, κN(terminal pyridine)-ddpd, NMe_3, NHC (1,3-dimethyl-2,3-dihydro-1*H*-imidazol-2-ylidene), PMe_3, PH_3, PF_3, pyridine, NH_3, CH_3CN, CH_3NC, correlation of A_1 stretching frequencies with C−O distances in $Ni(CO)_3L$ complexes. This material is available free of charge via the Internet at http://pubs.acs.org.

---

(33) Fallahpour, R.-A. *Synthesis* **2000**, *8*, 1138.
(34) Fallahpour, R.-A. *Eur. J. Inorg. Chem.* **1998**, 1205.
(35) Fallahpour, R.-A.; Neuburger, M.; Zehnder, M. *New J. Chem.* **1999**, *23*, 53.

9.6 Excited State Tuning of Bis(tridentate) Ruthenium(II) Polypyridine Chromophores by Push-Pull Effects and Bite Angle Optimization: A Comprehensive Experimental and Theoretical Study

A. Breivogel, M. Meister, C. Förster, F. Laquai, K. Heinze, *Chem. Eur. J.* **2013**, *19*, 13745–13760.

DOI: 10.1002/chem.201302231

CHEMISTRY
A EUROPEAN JOURNAL

DOI: 10.1002/chem.201302231

Excited State Tuning of Bis(tridentate) Ruthenium(II) Polypyridine Chromophores by Push–Pull Effects and Bite Angle Optimization: A Comprehensive Experimental and Theoretical Study

Aaron Breivogel,[a] Michael Meister,[b] Christoph Förster,[a] Frédéric Laquai,[b] and Katja Heinze*[a]

Abstract: The synergy of push–pull substitution and enlarged ligand bite angles has been used in functionalized heteroleptic bis(tridentate) polypyridine complexes of ruthenium(II) to shift the ^{1}MLCT absorption and the ^{3}MLCT emission to lower energy, enhance the emission quantum yield, and to prolong the ^{3}MLCT excited-state lifetime. In these complexes, that is, [Ru(ddpd)(EtOOC-tpy)][PF$_6$]$_2$, [Ru(ddpd-NH$_2$)(EtOOC-tpy)][PF$_6$]$_2$, [Ru(ddpd){(MeOOC)$_3$-tpy}][PF$_6$]$_2$, and [Ru(ddpd-NH$_2$){(EtOOC)$_3$-tpy}][PF$_6$]$_2$ the combination of the electron-accepting 2,2′;6′,2″-terpyridine (tpy) ligand equipped with one or three COOR substituents with the electron-donating *N*,*N*′-dimethyl-*N*,*N*′-dipyridin-2-ylpyridine-2,6-diamine (ddpd) ligand decorated with none or one NH$_2$ group enforces spatially separated and orthogonal frontier orbitals with a small HOMO–LUMO gap resulting in low-energy ^{1}MLCT and ^{3}MLCT states. The extended bite angle of the ddpd ligand increases the ligand field splitting and pushes the deactivating ^{3}MC state to higher energy. The properties of the new isomerically pure mixed ligand complexes have been studied by using electrochemistry, UV/Vis absorption spectroscopy, static and time-resolved luminescence spectroscopy, and transient absorption spectroscopy. The experimental data were rationalized by using density functional calculations on differently charged species (charge $n=0$–4) and on triplet excited states (^{3}MLCT and ^{3}MC) as well as by time-dependent density functional calculations (excited singlet states).

Keywords: density functional calculations · excited states · ligands · luminescence · ruthenium

Introduction

Polypyridine complexes of ruthenium(II) have attracted great interest due to their outstanding and tunable photophysical and electrochemical properties combined with high thermal and chemical robustness.[1] They are used as light harvesters in dye-sensitized solar cells,[2–4] luminescent emitters in light-emitting electrochemical cells,[5–7] possible anticancer and imaging agents in phototherapy,[8–10] sensors for ions[11–16] and small molecules,[17,18] photocatalysts for water splitting,[19,20] hydrogen production,[21–24] CO$_2$ reduction,[21,23,25] and many other chemical reactions,[23,26–29] components in mixed valence systems,[30–35] light upconversion systems[36–39] and molecular memory devices.[40–42]

The most prominent ruthenium(II) polypyridine complexes are [Ru(bpy)$_3$]$^{2+}$ (bpy = 2,2′-bipyridine) and its analogues thanks to their high ^{3}MLCT state lifetimes ($\tau \approx 1$ μs) and luminescence quantum yields ($\Phi \approx 10\%$) at room temperature in solution.[1,43] However, the intrinsic chirality of Δ,Λ-[Ru(bpy)$_3$]$^{2+}$ leads to the formation of stereoisomers for unsymmetrically substituted bpy ligands, which heavily complicates synthetic procedures.[44,45] In contrast, [Ru(tpy)$_2$]$^{2+}$ ([**5**]$^{2+}$, tpy = 2,2′;6′,2″-terpyridine) type complexes are achiral and can be synthesized free of stereoisomers even in the case of unsymmetrical substitution of the tpy 4′-positions.[46] Additionally, the tridentate coordination should provide a higher photo and chemical stability compared with the bidentate mode with respect to ligand substitution. Despite the structural similarity of the parent complexes [Ru(bpy)$_3$]$^{2+}$ and [Ru(tpy)$_2$]$^{2+}$, the triplet metal-to-ligand charge transfer (^{3}MLCT) lifetime of the latter is dramatically reduced due to an efficient radiationless deactivation through triplet metal-centered (^{3}MC) states ($\tau \approx 0.1$–0.2 ns, $\Phi \leq 0.0005\%$; Scheme 1).[47–49]

Two strategies have emerged to impede radiationless deactivation in bis(tridentate) ruthenium(II) complexes and to improve ^{3}MLCT lifetimes and luminescence quantum yields:

---

[a] A. Breivogel, Dr. C. Förster, Prof. Dr. K. Heinze
Institute of Inorganic Chemistry and Analytical Chemistry
Johannes Gutenberg-University of Mainz
Duesbergweg 10-14, 55128 Mainz (Germany)
Fax: (+49) 6131-39-27-277
E-mail: katja.heinze@uni-mainz.de

[b] M. Meister, Dr. F. Laquai
Max Planck Institute for Polymer Research
Ackermannweg 10, 55128 Mainz (Germany)

Supporting information for this article is available on the WWW under http://dx.doi.org/10.1002/chem.201302231.

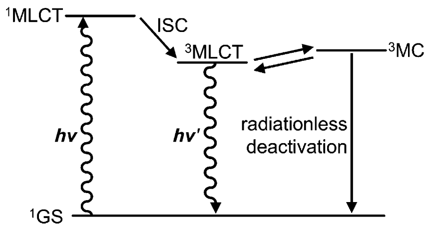

Scheme 1. Qualitative Jablonski diagram of Ru^{II} oligopyridine complexes (GS = ground state, MLCT = metal-to-ligand charge transfer, ISC = intersystem crossing, MC = metal-centered).

1) Push–pull substituents at the 4-position of the central pyridine rings: Electron-withdrawing substituents lower the ^{3}MLCT state energy, whereas electron-donating substituents raise the ^{3}MC state energy, which increases the energy difference between the two states.[46] For example, the bis-4′-substituted complex $[(\text{EtOOC-tpy})\text{Ru}(\text{tpy-NH}_2)]^{2+}$ ($[\mathbf{7}]^{2+}$, Scheme 2) possesses a significantly higher lifetime ($\tau = 34$ ns) and a higher quantum yield ($\Phi = 0.18\,\%$) compared with unsubstituted $[\text{Ru(tpy)}_2]^{2+}$. This amino acid derivative $[\mathbf{7}]^{2+}$ has been successfully incorporated in peptidic energy and electron-transfer systems and shows light-induced charge separation in a donor–chromophore–acceptor nanocomposite.[25,50–54] Exceptionally high room temperature emission lifetimes and quantum yields were obtained by Schubert and Berlinguette et al. by using heteroleptic bis(tridentate) ruthenium(II) complexes incorporating electron-accepting tpy and strongly σ-electron-donating tridentate bis(carbene)pyridine ligands (τ up to 7.9 μs, Φ up to 11 %).[55]

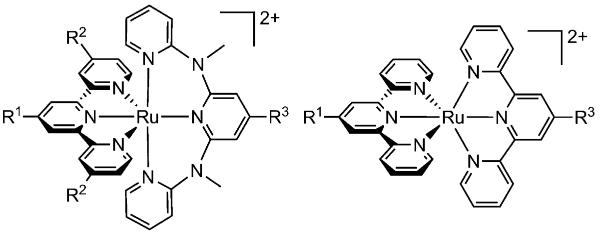

1: R^1 = COOEt; R^2 = H; R^3 = H
2: R^1 = COOEt; R^2 = H; R^3 = NH$_2$
3: R^1 = R^2 = COOMe; R^3 = H
4: R^1 = R^2 = COOEt; R^3 = NH$_2$

5: R^1 = R^3 = H
6: R^1 = COOEt; R^3 = H
7: R^1 = COOEt; R^3 = NH$_2$

Scheme 2. Bis(tridentate) ruthenium(II) oligopyridine complexes.

2) Enlargement of N-Ru-N bite angles: Typically, N-Ru-N bite angles in tpy complexes of ruthenium are around 79°. Larger bite angles (ideally 90°) would create a stronger ligand field splitting due to the better overlap between the Ru d orbitals and the pyridine nitrogen lone pairs. In a stronger ligand field the ^{3}MC–^{3}MLCT energy difference increases and the deactivating ^{3}MC states are less accessible.[48] Bite angles of close to 90° could be achieved by Hammarström et al. in $[\text{Ru(dqp)}_2]^{2+}$ (dqp = 2,6-di(quinolin-8-yl)pyridine) with a high lifetime and quantum yield at room temperature ($\tau = 3.0$ μs, $\Phi = 2\,\%$).[56] The 4′-substituted analogue $[\text{Ru(dqp-COOEt)}_2]^{2+}$ even surpasses the values of the latter ($\tau = 5.5$ μs, $\Phi = 7\,\%$) and $[\text{Ru(dqp)}_2]^{2+}$ complexes have already been used in donor–acceptor arrays with long-lived photoinduced charge-separated states.[57,58] A homoleptic analogue of $[\text{Ru(tpy)}_2]^{2+}$ containing carbonyl bridges between the pyridine rings synthesized by Ruben et al. shows bite angles of 90° and, to the best of our knowledge, features the highest reported room temperature quantum yield for a bis(tridentate) ruthenium(II) complex ($\tau = 3.3$ μs, $\Phi = 30\,\%$).[59] Ligands with large bite angles like dqp are flexible and therefore can lead to the formation of stereoisomers (*mer*, *cis-fac*, *trans-fac*).[60] For this reason we developed the heteroleptic bis(tridentate) ruthenium(II) complex $[\mathbf{1}][\text{PF}_6]_2$ (Scheme 2), which is the first example for the combination of a tpy ligand and a ddpd ligand (ddpd = *N*,*N*′-dimethyl-*N*,*N*′-dipyridin-2-ylpyridine-2,6-diamine, **11**). The tpy ligand only allows for a *meridional* coordination of both ligands and avoids the formation of undesired stereoisomers. The ddpd ligand is a tpy analogue and shows large bite angles due to the additional NCH_3 bridges between the pyridine rings. The ^{3}MLCT room temperature lifetime of $[\mathbf{1}][\text{PF}_6]_2$ and its room temperature quantum yield are significantly higher than for comparable bis(tpy) complexes ($\tau = 722$ ns, $\Phi = 0.45\,\%$).[7,61]

Herein, we apply the push–pull strategy to the complex $[\mathbf{1}][\text{PF}_6]_2$ by stepwise boosting its push–pull substitution pattern with additional electron-accepting (-COOR) and electron-donating (-NH_2) substituents ($[\mathbf{1}][\text{PF}_6]_2$–$[\mathbf{4}][\text{PF}_6]_2$, Scheme 2). The amino and the (hydrolyzed) ester groups can be easily functionalized and principally connected to semiconductors, polymers, biomolecules, or potential catalysts in a directional way.[25,50–53] A 2,2′;6′,2′′-terpyridine (R^{1}R^2-tpy) ligand as electron acceptor and a R^3-ddpd ligand as electron donor are used in combination with additional substituents on both tridentate ligands enhancing their acceptor or donor strength, respectively. This choice of acceptor and donor abilities should lead to a small HOMO–LUMO gap, which should shift the MLCT absorption and emission energies towards the red spectral region. Additionally, the different donor–acceptor characteristics of the *meridional* coordinating ligands should enforce spatially separated (orthogonal) frontier orbitals and should equip the systems with a high electronic directionality. The second strategy aims at shifting the energy of the thermally accessible ^{3}MC state, which is a funnel for radiationless deactivation,[48] to higher values by employing the ddpd ligand with its large bite angle. Thus, to enhance the emission quantum yield and ^{3}MLCT state lifetime, the ^{3}MC–^{3}MLCT energy difference is increased by increasing the energy of the ^{3}MC state and by decreasing the energy of the ^{3}MLCT state. As the latter strategy also decreases the energy between the emitting ^{3}MLCT state and the ground state ^{1}GS, the effects of the energy gap law[62–64] also need to be considered (Scheme 1). The properties of $[\mathbf{1}]^{2+}$–$[\mathbf{4}]^{2+}$ and bis(tpy) reference complexes $[\mathbf{5}]^{2+}$–$[\mathbf{7}]^{2+}$ will be disclosed by electrochemistry, UV/Vis, static and time-resolved emission, transient absorption spectroscopy, and by DFT calculations (Scheme 2).

Results and Discussion

Ligand and complex synthesis and analytical characterization: The terpyridine ligands EtOOC-tpy and $(\text{MeOOC})_3$-tpy, the unsubstituted ddpd ligand **11**, the trichlorido ruthenium(III) complexes **12** and **13**, and the heteroleptic complex $[\mathbf{1}][\text{PF}_6]_2$ have been reported previously.[61,65–67] The synthesis of the new amino-functionalized ddpd ligand precursor **10** is depicted in Scheme 3. The N-protected ligand **10** was prepared by a Pd-catalyzed Buchwald–Hartwig amination of 2,6-dichloro-4-phthalimidopyridine **8** or its bromo derivative **9**. The reasons for this protecting-group strategy are outlined in the Supporting Information. All compounds **8**–**11**[61] were characterized by using mass spectrometry, infrared (Figure S1–S4, the Supporting Information), ^{1}H, ^{13}C, and ^{15}N NMR 1D- and 2D spectroscopy (Figure S5–S16, the Supporting Information) and elemental analysis. Single crystals of **8** and **9** have been obtained and X-ray diffraction analyses show a dihedral angle of 43° between the pyridine and the phthalimido substituent in both cases (Figures S17 and S18, Tables S1–S3, the Supporting Information).

The syntheses of heteroleptic ruthenium(II) complexes $[\mathbf{1}][\text{PF}_6]_2$–$[\mathbf{4}][\text{PF}_6]_2$ are depicted in Scheme 4. Starting from the trichlorido(terpyridine)ruthenium(III) precursors **12** and **13**[65–67] all mixed ligand complexes were obtained in isomerically pure form (*mer*) in a microwave-assisted reaction with the respective ddpd ligand **10** or **11** in ethanol and *N*-ethylmorpholine as reducing agent. For a successful synthesis of $[\mathbf{1}]^{2+}$[61] and $[\mathbf{3}]^{2+}$ comprising the unsubstituted ddpd ligand **11** the chloride ions have to be removed with AgNO_3 as AgCl. In the last step, the complexes $[\mathbf{1}][\text{PF}_6]_2$ and $[\mathbf{3}][\text{PF}_6]_2$ are precipitated by addition of an aqueous NH_4PF_6 solution. For $[\mathbf{2}]^{2+}$ and $[\mathbf{4}]^{2+}$ bearing the N-protected amino ligand **10** the phthalimido group is partially deprotected during the microwave-assisted reaction to give a mixture of phthalimide, monoethylester monoamide, and free amino group functionality of the coordinated ddpd ligand. Full deprotection is achieved in situ by treating the mixture with hydrazine hydrate. The use of AgNO_3 to remove the chloride anions proved unnecessary. During the hydrazine deprotection to give $[\mathbf{4}]^{2+}$, the methyl ester groups are partially hydrolyzed. Therefore, the free acid groups are re-alkylated by treating the mixture with ethanol and sulfuric acid to obtain $[\mathbf{4}]^{2+}$ as pure tris(ethylester). All complexes $[\mathbf{1}][\text{PF}_6]_2$–$[\mathbf{4}][\text{PF}_6]_2$ were characterized by using ESI and HR-ESI mass

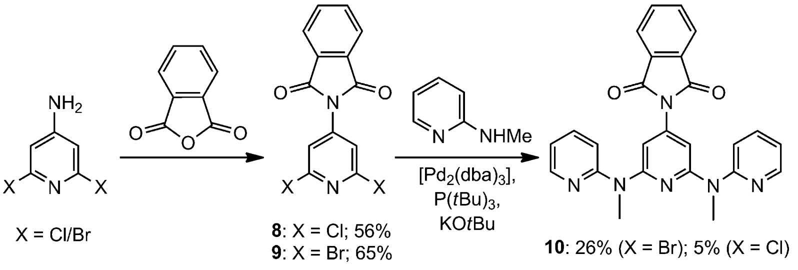

Scheme 3. Synthesis of functionalized ddpd ligand **10**.

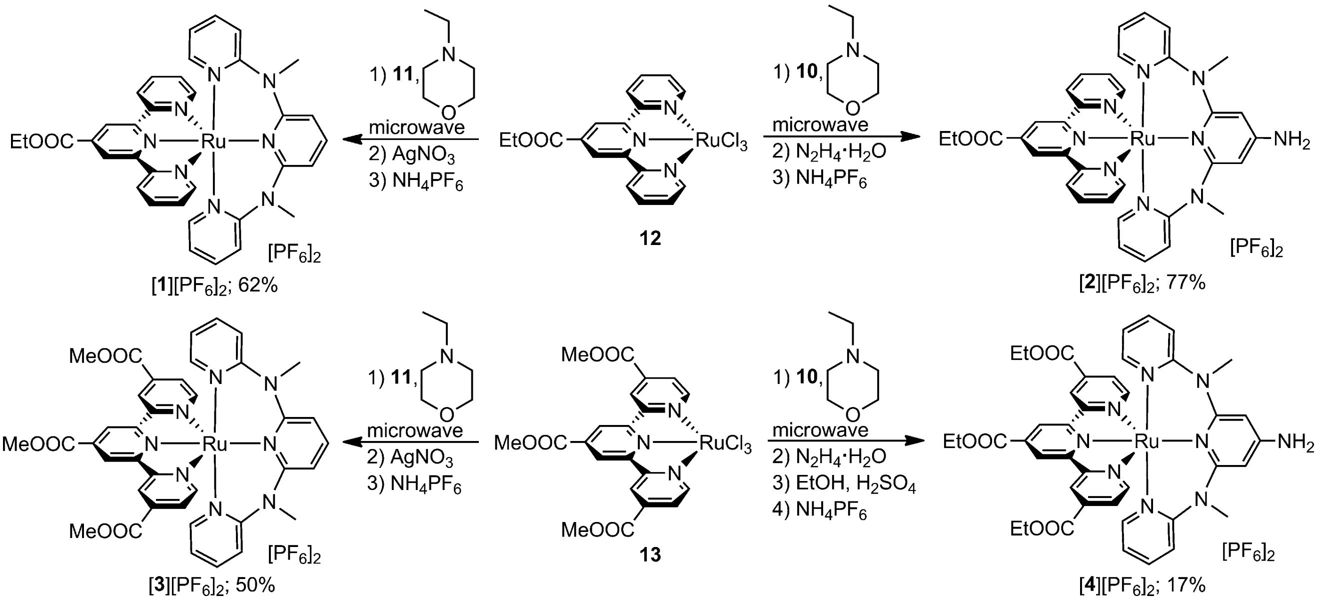

Scheme 4. Synthesis of the heteroleptic ruthenium(II) complexes $[\mathbf{1}][\text{PF}_6]_2$–$[\mathbf{4}][\text{PF}_6]_2$.

spectrometry, infrared, ^{1}H, ^{13}C and ^{15}N NMR 1D and 2D spectroscopy, and elemental analysis. For all complexes, the ion peaks for $[M-PF_6]^+$ and for $[M-2PF_6]^{2+}$ were observed in the ESI mass spectrum with m/z values and isotope distributions fitting excellently to the theoretical values. Moreover, the HR-ESI spectra verify the molecular formulae of all the complex cations (see the Experimental Section). ^{1}H NMR spectral data of [**1**][PF$_6$]$_2$–[**4**][PF$_6$]$_2$ are summarized in the Supporting Information (Table S4) and the corresponding spectra of [**2**][PF$_6$]$_2$–[**4**][PF$_6$]$_2$ are shown in Figures S19–S21. All NMR data confirm the presence of a single stereoisomer in each case, namely, the *meridional* one. Exemplarily, the ^{1}H NMR spectrum of [**2**][PF$_6$]$_2$ and its atom numbering are depicted in Figure 1. All resonances of the pyridine protons appear in the expected range from $\delta = 6$ to 9 ppm. The most downfield-shifted resonance is assigned to H^{2} and appears as a singlet at $\delta = 8.95$ ppm. The amino protons resonate at $\delta = 5.72$ and the protons of the bridging NCH$_3$ unit at $\delta = 3.36$ ppm. Compared with [**1**]$^{2+}$ ($\delta =$ 7.56 ppm)[61] the resonance of H^{15} in [**2**]$^{2+}$ is shifted to higher field ($\delta = 6.80$ ppm) due to the presence of the NH$_2$ group as expected.[68] For the NCH$_3$ moieties a single resonance is observed for each of the ^{1}H, ^{13}C and ^{15}N nuclei in the respective NMR spectra. The two NCH$_3$ units in the ddpd ligand point up and below the plane of the central pyridine plane, respectively, enforcing an interligand nuclear Overhauser effect (NOE) between NCH$_3$ of the ddpd ligand and H^{8} of the tpy ligand vis-à-vis. ^{13}C{^{1}H} NMR spectra of [**1**][PF$_6$]$_2$–[**4**][PF$_6$]$_2$ show resonances of all carbon atoms (Table S5 and Figures S22–S24, the Supporting Information). The ^{13}C resonances were successfully assigned by using 2D NMR correlation spectroscopy. ^{15}N-^{1}H HMBC spectral data of [**1**][PF$_6$]$_2$–[**4**][PF$_6$]$_2$ and of ligands **10**, **11**, and EtOOC-tpy are summarized in Table S6 and Figures S15, S16, and S25–S27 (the Supporting Information). All ^{15}N resonances, including pyridyl, amino, and phthalimido nitrogen atoms have been identified and assigned by correlation to the respective adjacent hydrogen nuclei. The coordinating pyridine nitrogen atoms of the ligands are much more affected by Ru^{2+} coordination (coordination shift) than the remote and non-coordinating NCH$_3$ ^{15}N nuclei substantiating that the NCH$_3$ groups remain indeed non-coordinated.

Solid-state IR spectra of complexes [**1**][PF$_6$]$_2$–[**4**][PF$_6$]$_2$ show very strong bands at 841–843 cm^{-1}, which are assigned to the PF stretching vibration of the counterions. Functional groups of the cations are identified by strong bands at 1726–1734 cm^{-1} belonging to C=O stretching vibrations of the ester moieties and by bands at 3400–3468 cm^{-1} and 3240 cm^{-1} assigned to asymmetric and symmetric NH stretching vibrations (Figure S28–S30, the Supporting Information).

Single crystals of [**2**][PF$_6$]$_2$ and [**3**][PF$_6$]$_2$ were obtained by diffusion of diethyl ether into an acetonitrile solution of the complexes. The single-crystal X-ray diffraction analysis of [**1**][PF$_6$]$_2$ has been described previously.[61] Selected bond lengths and angles obtained by X-ray diffraction and from DFT optimized geometries are summarized in Table 1. All complex cations [**1**]$^{2+}$–[**3**]$^{2+}$ exhibit *meridional* coordination of the tridentate ligands as expected (Figure 2 and the Supporting Information, Figures S31–S32 and Tables S7–S9). Cations [**1**]$^{2+}$–[**3**]$^{2+}$ feature very similar Ru–N bond lengths and N-Ru-N bond angles. The shortest Ru–N distance in [**1**]$^{2+}$–[**3**]$^{2+}$ is the one between ruthenium and the central tpy-nitrogen atom N2 (1.94–1.95 Å) due to the small bite angle of tpy. All other Ru–N bond lengths in [**1**]$^{2+}$–[**3**]$^{2+}$ are around 2.07–2.09 Å. The DFT-calculated values are about 0.03–0.04 Å longer (1.98 Å for Ru–N2 and 2.11–2.12 Å for all other Ru–N bonds) but reproduce the short central Ru–N(tpy) distance. The N-Ru-N bite angles are well reproduced by DFT calculations with tpy bite angles of 79–80° and ddpd bite angles of 87–88°. The latter nearly approach the value of an ideal octahedron (90°) allowing for an opti-

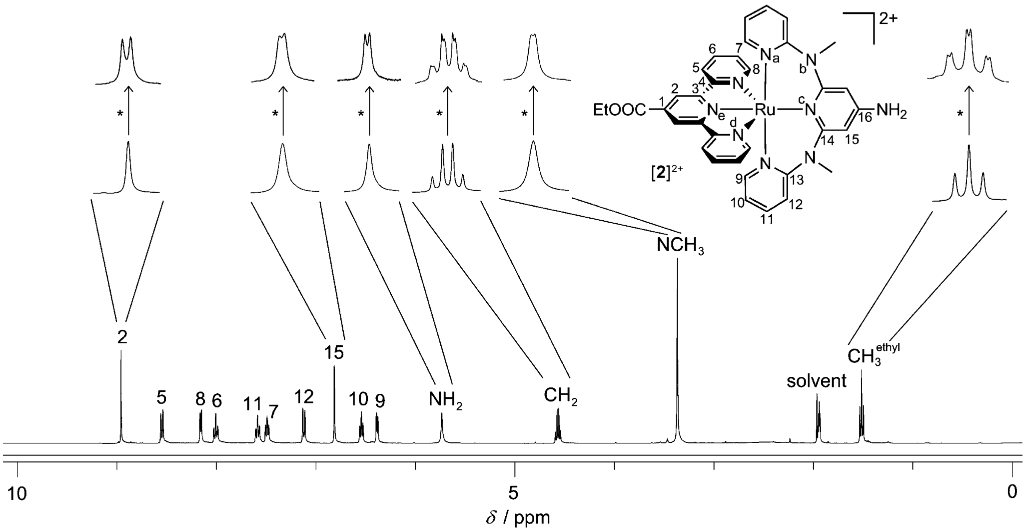

Figure 1. ^{1}H NMR spectrum of [**2**][PF$_6$]$_2$ and atom numbering in CD$_3$CN. The asterisk (*) indicates the splitting of the proton resonances of [**2**]$^{2+}$ after addition of chiral (Δ-TRISPHAT)$^{-}$ counterions.

Table 1. Experimental (X-ray diffraction) and DFT calculated (singlet ground state, B3LYP/LANL2DZ, IEFPCM in CH_3CN), selected bond lengths [Å] and angles [°] of $[\mathbf{1}]^{2+}$–$[\mathbf{4}]^{2+}$.

	$[\mathbf{1}]^{2+}$ exp	$[\mathbf{1}]^{2+}$ DFT	$[\mathbf{2}]^{2+}$ exp	$[\mathbf{2}]^{2+}$ DFT	$[\mathbf{3}]^{2+}$ exp	$[\mathbf{3}]^{2+}$ DFT	$[\mathbf{4}]^{2+}$ DFT
Ru–N1	2.079(2)	2.117	2.0804(17)	2.114	2.0777(15)	2.109	2.107
Ru–N2	1.944(2)	1.983	1.9465(16)	1.980	1.9481(14)	1.984	1.982
Ru–N3	2.078(2)	2.117	2.0869(16)	2.116	2.0921(15)	2.108	2.107
Ru–N4	2.076(2)	2.119	2.0750(16)	2.118	2.0800(15)	2.119	2.119
Ru–N5	2.078(2)	2.114	2.0806(16)	2.113	2.0858(15)	2.114	2.111
Ru–N6	2.072(2)	2.119	2.0766(16)	2.118	2.0784(15)	2.119	2.118
N1-Ru-N2	79.68(8)	79.23	79.80(7)	79.28	79.84(6)	79.28	79.33
N1-Ru-N3	159.22(8)	158.46	159.53(7)	158.56	159.10(6)	158.59	158.72
N2-Ru-N5	178.29(9)	179.85	178.19(7)	179.91	177.18(6)	179.95	179.92
N4-Ru-N5	87.51(8)	87.55	87.33(6)	87.28	87.34(6)	87.54	87.31
N4-Ru-N6	174.70(8)	175.12	174.83(6)	174.56	174.74(6)	175.04	174.58

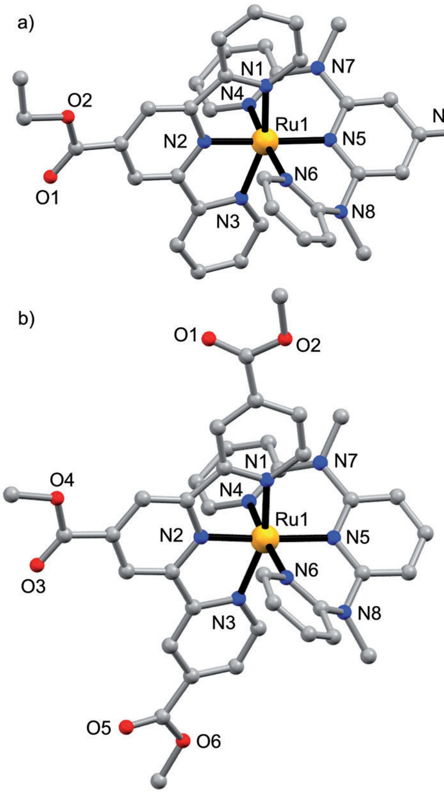

Figure 2. Molecular structures of cations of a) $[\mathbf{2}]^{2+}$ and b) $[\mathbf{3}]^{2+}$ in the solid state (CH hydrogen atoms omitted).

mal σ-overlap of metal d orbitals ("e_g") with the lone pairs of the ddpd nitrogen donor atoms. The coordinated ddpd ligand is slightly twisted with the NCH_3 groups pointing up and below the plane of the central pyridine ring as already deduced from the nuclear Overhauser effect (NOE) data.

To explore this helical twist of the coordinated ddpd ligand, a solution of $[\mathbf{2}][PF_6]_2$ was treated with the chiral anion [Δ-tris(tetrachloro-1,2-benzenediolato)phosphate(V)] ((Δ-TRISPHAT)$^-$).[45,69] This splits the ^1H NMR resonances of $[\mathbf{2}]^{2+}$ (H^2, H^{15}, NH_2, CH_2, NCH_3, CH_3; Figure 1; Figure S33, the Supporting Information) into two signal sets (≈1.0:1.3 by integration of ^1H NMR spectrum) revealing the helical chirality of $[\mathbf{2}]^{2+}$. The formation of diasteromeric ion pairs is a result of the electrostatic attraction between the cations and anions leading to a high proximity between $[\mathbf{2}]^{2+}$ and the (Δ-TRISPHAT)$^-$ or $[PF_6]^-$ counterions. Indeed, the solid-state structures of $[\mathbf{2}][PF_6]_2$ and $[\mathbf{3}][PF_6]_2$ reveal that the $[PF_6]^-$ counterions are situated in chiral "pockets" formed by the tridentate ligands (Figure 3). The two $[PF_6]^-$ counterions with the shortest Ru···P distance (≈6 Å) lie vis-à-vis on both sides of the ruthenium atom. Each hexafluorophosphate is embraced by two neighboring pyridine rings of one chelate ligand and by one additional pyridine ring of the other tridentate ligand, respectively, with distances between the phosphorus atom and the center of the pyridine rings of 4.4–5.7 Å. Similar contact ion pairs are expected for the (Δ-TRISPHAT)$^-$ anion and $[\mathbf{2}]^{2+}$ with the anion inserted into the chiral "pockets" of the cation.

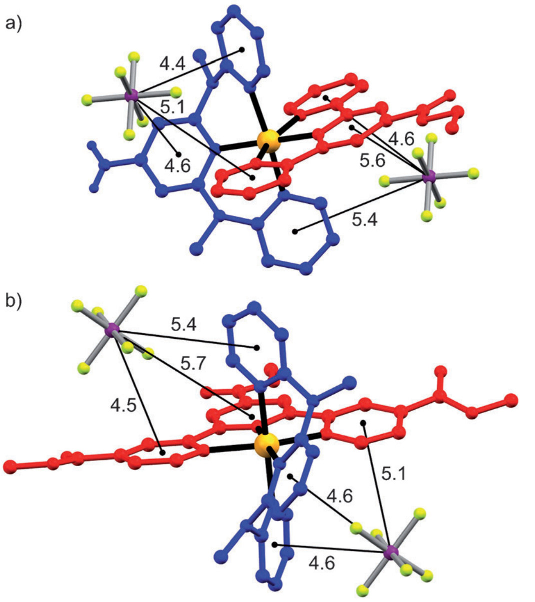

Figure 3. Arrangement of cations and the two nearest $[PF_6]^-$ counterions of a) $[\mathbf{2}]^{2+}$ and b) $[\mathbf{3}]^{2+}$ in the solid state (red: tpy, blue: ddpd, CH hydrogen atoms omitted). Distances between the phosphorus atoms and the center of the surrounding pyridine rings are indicated in Å.

Electrochemistry of [1][PF$_6$]$_2$–[4][PF$_6$]$_2$ and reference complexes: Electrochemical data of $[\mathbf{1}][PF_6]_2$–$[\mathbf{4}][PF_6]_2$ are obtained by cyclic and square wave voltametry in acetonitrile solution and $[n\text{-}Bu_4N][PF_6]$ as the supporting electrolyte. All potential values are referenced to the Fc/Fc^+ couple. Electrochemical data of all complexes $[\mathbf{1}][PF_6]_2$–$[\mathbf{7}][PF_6]_2$ are summarized in Table 2 (Figures S34–S36, the Supporting Information). Exemplarily, Figure 4 depicts cyclic and square wave voltammograms of $[\mathbf{4}][PF_6]_2$. The reversible one-elec-

Table 2. Electrochemical data[a] of complexes [**1**][PF$_6$]$_2$–[**7**][PF$_6$]$_2$.

	$E_{1/2}$ ddpd/ddpd$^+$	$E_{1/2}$ Ru^{II}/Ru^{III}	$E_{1/2}$ tpy/tpy$^-$
[**1**][PF$_6$]$_2$[a]	+1.80[b]	+0.81	−1.47, −2.09[b]
[**2**][PF$_6$]$_2$[a]	+1.73[b]	+0.64	−1.50, −2.11,[b] −2.21[b]
[**3**][PF$_6$]$_2$[a]	+1.80[b]	+0.92	−1.25,[b] −1.70[b]
[**4**][PF$_6$]$_2$[a]	+1.70[b]	+0.73	−1.32, −1.75
[**5**][PF$_6$]$_2$[46][a]	–	+0.92	−1.67
[**6**][PF$_6$]$_2$[7][c]	–	+0.96	−1.27, −1.45
[**7**][PF$_6$]$_2$[53,70][a]	–	+0.68	−1.54, −1.99

[a] In CH$_3$CN in V versus Fc/Fc$^+$. [b] Irreversible, E_p given. [c] No solvent denoted.

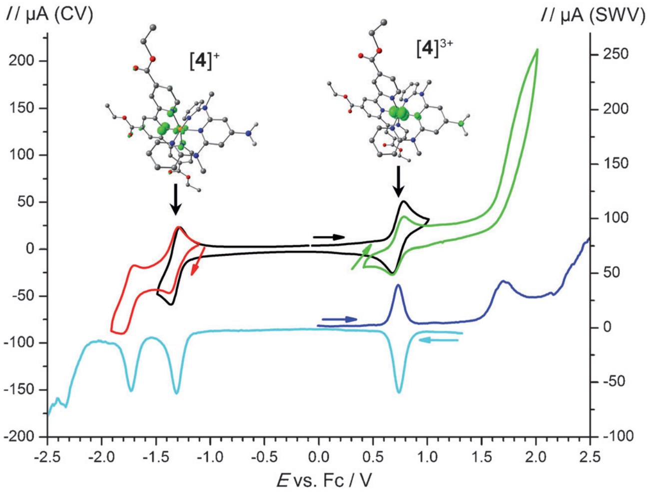

Figure 4. Cyclic voltammogram (top) and square wave voltammogram (bottom) of [**4**][PF$_6$]$_2$ in CH$_3$CN; 0.1 M [nBu$_4$][PF$_6$]. The inset structures show the DFT calculated spin densities (contour value 0.01 au) of the reduced and oxidized species [**4**]$^+$ and [**4**]$^{3+}$, respectively.

tron oxidation of [**4**]$^{2+}$ to [**4**]$^{3+}$ at 0.73 V is assigned to the Ru$^{II/III}$ redox couple in analogy to similar complexes.[7,53,54,61] To further confirm this assignment, DFT calculations (B3LYP/LANL2DZ, IEFPCM, CH$_3$CN) were performed on singly oxidized species [**1**]$^{3+}$–[**4**]$^{3+}$ and on bis(tpy) ruthenium reference compounds [**5**]$^{3+}$–[**7**]$^{3+}$ (without (PF$_6$)$^-$ counterions, multiplicity $M=2$). Indeed, the spin density is largely located on the ruthenium atom with Mulliken spin densities calculated as 0.85, 0.78, 0.83, 0.77, 0.88, 0.88, and 0.76 for [**1**]$^{3+}$–[**7**]$^{3+}$, respectively (Figure S37, the Supporting Information). For [**2**]$^{3+}$, [**4**]$^{3+}$, and [**7**]$^{3+}$ bearing NH$_2$ groups, a small amount of spin density is delocalized onto the nitrogen atom of the NH$_2$ group (Mulliken spin density on N: 0.06, 0.07, and 0.11), which underlines the electron-donating character of the amino group in these complexes (Figure 4).[25,53,54] This electron donation is experimentally clearly observed in the oxidation potentials of complexes with and without an NH$_2$ group [**2**]$^{2+}$/[**1**]$^{2+}$, [**4**]$^{2+}$/[**3**]$^{2+}$ and [**7**]$^{2+}$/[**6**]$^{2+}$ (Table 2).[7,53,54,61] On the other hand, comparing the Ru$^{II/III}$ potential of complexes with one or three ester substituents [**1**]$^{2+}$/[**3**]$^{2+}$ and [**2**]$^{2+}$/[**4**]$^{2+}$ reveals that their electron-withdrawing nature hampers the largely metal-centered oxidation by roughly 0.1 V.

The second experimentally observed oxidation of [**1**]$^{2+}$–[**4**]$^{2+}$ at 1.70–1.80 V is irreversible. DFT calculations of doubly oxidized complexes [**1**]$^{4+}$–[**4**]$^{4+}$ ($M=3$) and reference compounds [**5**]$^{4+}$–[**7**]$^{4+}$ are depicted in Figure S38 (the Supporting Information). The spin density in bis(tpy) complexes [**5**]$^{4+}$ and [**6**]$^{4+}$ is located almost entirely on the metal center and for [**7**]$^{4+}$ also partly on the NH$_2$ group. However, in ddpd complexes [**1**]$^{4+}$–[**4**]$^{4+}$ a significant amount of spin density is delocalized onto the nitrogen atoms of the NCH$_3$ groups. Therefore, we assign the second oxidation in complexes [**1**]$^{2+}$–[**4**]$^{2+}$ to the irreversible oxidation of the NCH$_3$ groups of the ddpd ligands. Again, the second oxidation potential of NH$_2$-containing ddpd complexes [**2**]$^{2+}$ and [**4**]$^{2+}$ is lower than that of their NH$_2$-free counterparts [**1**]$^{2+}$ and [**3**]$^{2+}$, respectively (Table 2).

Two reduction waves are observed for [**1**]$^{2+}$–[**4**]$^{2+}$ and assigned to ligand-based reductions.[53,61] The first reduction is clearly centered on the tpy ligand as it is strongly affected by the number of ester substituents on the tpy ligand ([**1**]$^{2+}$/[**3**]$^{2+}$; [**2**]$^{2+}$/[**4**]$^{2+}$) and only marginally affected by the presence of NH$_2$ groups on the ddpd ligand ([**1**]$^{2+}$/[**2**]$^{2+}$; [**3**]$^{2+}$/[**4**]$^{2+}$). The second reduction follows the trend of the first reduction, with triesters [**3**]$^+$ and [**4**]$^+$ being much more easily reduced than [**1**]$^+$ and [**2**]$^+$ (Table 2). This leads to the conclusion that both the first and the second reduction are related to the tpy ligands.

DFT calculated spin densities of the singly reduced species [**1**]$^+$–[**7**]$^+$ ($M=2$) and doubly ($M=3$) reduced species [**1**]^0–[**7**]^0 are depicted in Figures S39 and S40 of the Supporting Information, respectively. As spin densities are mainly localized on the tpy ligand(s) in all cases the experimental assignment to tpy reductions is confirmed. In some cases the singlet species [**1**]^0–[**7**]^0 ($M=1$) are calculated slightly lower in energy than their triplet counterparts ($M=3$). Thus, for a pictorial comparison, the highest occupied molecular orbitals (HOMOs) of these singlet species were also calculated (the Supporting Information, Figure S40). The HOMOs of [**1**]^0–[**4**]^0 ($M=1$) are fully localized on the (ROOC)$_n$-tpy ligand leading to the same conclusion as the spin density in the triplet species.

Exemplarily, complex [**2**]$^{2+}$ was chemically oxidized by ammonium cerium(IV) nitrate to [**2**]$^{3+}$ and reduced by decamethylcobaltocene to [**2**]$^+$. EPR spectra of the resulting radicals were measured at 77 K. The radical [**2**]$^{3+}$ gives a rhombic signal ($g_{1,2,3}=2.4440$, 2.2694, 2.0300; $\Delta g=0.4140$ by spectral simulation; Figure S41, the Supporting Information). This signal is in full accordance with similar complexes of Ru^{III}[52] and the DFT calculations of [**2**]$^{3+}$ (Figure S37, the Supporting Information). For the one-electron-reduced radical [**2**]$^+$ a less rhombic signal is obtained ($g_{1,2,3}=2.0089$, 1.9865, 1.9720; $\Delta g=0.0387$ by spectral simulation; Figure S42, the Supporting Information). The reduced g anisotropy points to a ligand-based reduction with some ruthenium admixture,[25,52] which is fully corroborated by DFT calculations for [**2**]$^+$ (Mulliken spin density of 0.10 on Ru; Figure S39, the Supporting Information).

In summary, oxidation occurs at the ruthenium center (plus some ddpd-NH_2 admixture for $[\mathbf{2}]^{2+}$ and $[\mathbf{4}]^{2+}$), whereas reduction is confined to the tpy ligand. Consequently, oxidation is favored by NH_2 substitution at ddpd, whereas reduction is facilitated by COOR substitution at tpy leading to the smallest difference between oxidation and reduction potentials in $[\mathbf{4}]^{2+}$ in the series $[\mathbf{1}]^{2+}$–$[\mathbf{4}]^{2+}$ (Table 2). This electronic situation should also be reflected in the optical properties.

Optical properties of $[\mathbf{1}][PF_6]_2$–$[\mathbf{4}][PF_6]_2$ and reference complexes: Experimental UV/Vis data together with time-dependent (TD) DFT (IEFPCM, CH_3CN) calculated stick spectra showing the oscillator strength f of the calculated transitions are graphically depicted in Figure 5 and numerically listed in Table 3.

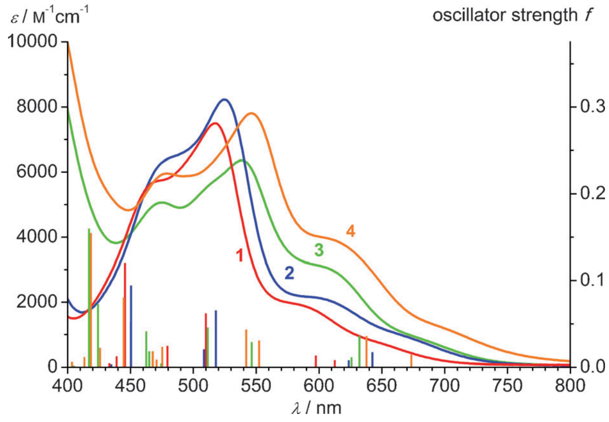

Figure 5. Experimental UV/Vis spectra and calculated stick spectra (TD-DFT, IEFPCM, CH_3CN) of $[\mathbf{1}]^{2+}$–$[\mathbf{4}]^{2+}$ in CH_3CN.

Table 3. UV/Vis data of complexes $[\mathbf{1}][PF_6]_2$–$[\mathbf{7}][PF_6]_2$ in CH_3CN and TD-DFT data (B3LYP/LANL2DZ, IEFPCM in CH_3CN) data.

	Experimental MLCT λ_{max} [nm] (ε [M^{-1} cm^{-1}])	π→π* λ_{max} [nm] (ε [$M^{-1}cm^{-1}$])	DFT[a] λ [nm] (f)
$[\mathbf{1}][PF_6]_2$	630 (1000, sh), 582 (1900, sh), 517 (7500), 473 (5700, sh)	319 (28800), 276 (34700), 236 (29900), 205 (31500)	596.70 (0.0116), 507.85 (0.0576), 478.37 (0.0215), 444.82 (0.1188)
$[\mathbf{2}][PF_6]_2$	648 (1200, sh), 595 (2200, sh), 525 (8230), 475 (6300, sh)	323 (26700), 273 (42000), 238 (43600)	642.20 (0.0167), 623.45 (0.0072), 517.71 (0.0649), 508.21 (0.0198), 450.24 (0.0937), 450.08 (0.0516)
$[\mathbf{3}][PF_6]_2$	687 (800, sh), 603 (3100, sh), 539 (6360), 508 (5400, sh), 475 (5060)	340 (31000), 292 (34200), 210 (52400)	631.34 (0.0356), 625.10 (0.0106), 545.59 (0.0283), 510.71 (0.0451), 464.10 (0.0174), 461.70 (0.0405), 423.32 (0.0725), 416.11 (0.1591)
$[\mathbf{4}][PF_6]_2$	696 (1200, sh), 622 (3700, sh), 546 (7810), 479 (5960)	341 (32000), 292 (37200), 223 (45600)	674.37 (0.0139), 638.74 (0.0352), 553.25 (0.0300), 543.00 (0.0428), 476.16 (0.0226), 468.56 (0.0175), 445.44 (0.0797), 426.62 (0.0214), 419.40 (0.1538)
$[\mathbf{5}][PF_6]_2$[49]	476 (14400)	308 (57400), 269 (38800)	555.80 (0.0063), 489.74 (0.0144), 471.01 (0.1314), 441.43 (0.0262), 426.47 (0.1782), 425.02 (0.0372), 415.02 (0.0447)
$[\mathbf{6}][PF_6]_2$[7]	485 (18140)	309 (51690), 272 (42450), 225 (39620)	502.22 (0.0151), 502.22 (0.0151), 456.98 (0.0526), 429.73 (0.1659), 428.54 (0.0190), 428.54 (0.0192), 425.14 (0.0297), 425.14 (0.0297)
$[\mathbf{7}][PF_6]_2$[53]	502 (19080)	318 (37610), 306 (34760), 274 (50990), 236 (42800)	572.52 (0.0064), 483.95 (0.1485), 453.79 (0.0593), 446.09 (0.0838), 439.61 (0.0411), 432.21 (0.1618)

[a] Highest calculated oscillator strengths f at $\lambda > 400$ nm (TD-DFT, IEFPCM, CH_3CN). For a complete list see the Supporting Information.

The absorption spectra of $[\mathbf{1}][PF_6]_2$–$[\mathbf{4}][PF_6]_2$ in acetonitrile show ligand-centered π→π* transitions below $\lambda = 350$ nm. In the visible spectral region characteristic metal-to-ligand charge transfer (MLCT) bands with maxima at $\lambda_{max} = 517$–546 nm and further maxima (or shoulders) at around $\lambda \approx 470$, 600, and 665 nm are found. Similar to the electrochemical data, the MLCT maxima are affected by the ligand type and the ligand-substitution pattern.

Replacing a tpy ligand by ddpd ($[\mathbf{6}]^{2+} \rightarrow [\mathbf{1}]^{2+}$; $[\mathbf{7}]^{2+} \rightarrow [\mathbf{2}]^{2+}$) causes a bathochromic shift of the MLCT band (485[7]→517 nm;[61] 502[53]→525 nm) due to the electron-donating NCH_3 groups, which raise the energy of the (mainly ruthenium-centered) HOMO, leaving the lowest occupied molecular orbital (LUMO) of the tpy acceptor essentially unaffected. This results in a smaller HOMO–LUMO gap (Table 3). Attaching electron-donating NH_2 groups to the ddpd ligand further decreases the HOMO–LUMO gap ($[\mathbf{1}][PF_6]_2 \rightarrow [\mathbf{2}][PF_6]_2$; $[\mathbf{3}][PF_6]_2 \rightarrow [\mathbf{4}][PF_6]_2$, Table 3, Figure 6). Installing more electron-withdrawing ester substituents at the acceptor tpy ligand also results in bathochromically shifted MLCT absorptions ($[\mathbf{1}]^{2+} \rightarrow [\mathbf{3}]^{2+}$; $[\mathbf{2}]^{2+} \rightarrow [\mathbf{4}]^{2+}$, Table 3, Figure 5). The strongest push–pull combination is realized in $[\mathbf{4}]^{2+}$, which displays its MLCT band at the lowest energy in the reported series, consistent with the redox data. We note that $[\mathbf{1}]^{2+}$–$[\mathbf{4}]^{2+}$ have more structured MLCT absorption bands than their bis(tpy) counterparts $[\mathbf{6}]^{2+}$ and $[\mathbf{7}]^{2+}$. Extinction coefficients at the band maxima of $[\mathbf{1}]^{2+}$–$[\mathbf{4}]^{2+}$ are significantly lower than for $[\mathbf{6}]^{2+}$ and $[\mathbf{7}]^{2+}$,[7,53,54] which might be due to the fact that the low-energy MLCT excitations only involve tpy ligands but no ddpd ligands. The extinction coefficients of the amino derivatives $[\mathbf{2}]^{2+}$, $[\mathbf{4}]^{2+}$,

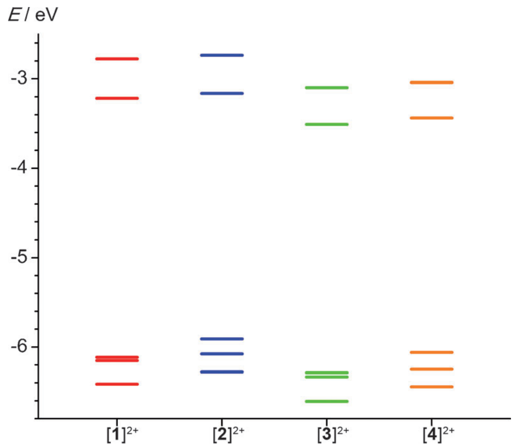

Figure 6. Energies of relevant frontier molecular orbitals (HOMO-2, HOMO-1, HOMO, LUMO, and LUMO+1) of [**1**]$^{2+}$–[**4**]$^{2+}$.

and [**7**]$^{2+}$ are consistently larger than that of their respective NH_2-free parent complexes [**1**]$^{2+}$, [**3**]$^{2+}$, and [**6**]$^{2+}$. This is based on the enlarged chromophore system, which extends onto the NH_2 group in [**2**]$^{2+}$, [**4**]$^{2+}$, and [**7**]$^{2+}$.

The Kohn–Sham frontier molecular orbitals have been calculated by using DFT (B3LYP/LANL2DZ, IEFPCM, CH_3CN) for [**1**]$^{2+}$–[**4**]$^{2+}$ and their energies are presented in Figure 6. Figure 7 exemplarily depicts the frontier molecular orbitals of [**2**]$^{2+}$. HOMO to HOMO-2 are essentially ruthenium-centered corresponding to the t_{2g} orbitals in O_h symmetry, whereas LUMO and LUMO+1 are localized on the tpy ligand.[55] The "e_g" orbitals LUMO+11 and LUMO+13 are found at a higher energy. Introduction of an NH_2 group at the ddpd ligand ([**1**]$^{2+}$→[**2**]$^{2+}$) raises the HOMO energy by $\Delta E_{\text{HOMO}}=0.21$ eV, whereas the LUMO energy is hardly affected ($\Delta E_{\text{LUMO}}=0.05$ eV). Similar values are calculated for the pair [**3**]$^{2+}$→[**4**]$^{2+}$ ($\Delta E_{\text{HOMO}}=0.23$; $\Delta E_{\text{LUMO}}=0.07$ eV). Installing more ester substituents at the tpy ligand lowers the LUMO energy more than the HOMO energy ([**1**]$^{2+}$→[**3**]$^{2+}$: $\Delta E_{\text{LUMO}}=0.29$; $\Delta E_{\text{HOMO}}=0.17$ eV and [**2**]$^{2+}$→[**4**]$^{2+}$: $\Delta E_{\text{LUMO}}=0.27$; $\Delta E_{\text{HOMO}}=0.15$ eV) resulting in a net smaller HOMO–LUMO gap consistent with a bathochromically shifted MLCT absorption (Figures 5 and 6). The HOMO of the NH_2-substituted ddpd complexes [**2**]$^{2+}$ and [**4**]$^{2+}$ extends onto the NH_2 group similar to that of [**7**]$^{2+}$ and thus enhances the transition dipole moment leading to higher extinction coefficients (Table 3).[54]

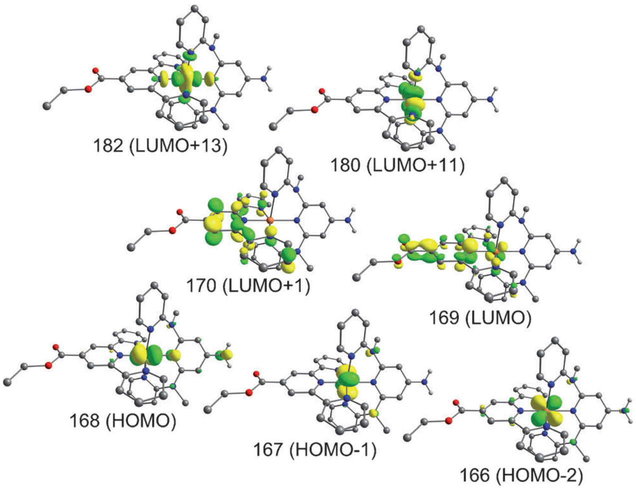

Figure 7. Relevant Kohn–Sham frontier molecular orbitals (contour value 0.06 au) of [**2**]$^{2+}$ (CH hydrogen atoms omitted).

The absorption spectra of [**1**]$^{2+}$–[**4**]$^{2+}$ were also estimated by TD-DFT calculations including a polarizable solvent continuum model.[55,71,72] The characteristic experimental bandshape with four discernible features (Table 3, Figure 5) is reproduced as MLCT transitions originating from the metal-centered orbitals (HOMO to HOMO-2) to the tpy-based π* orbitals (LUMO and LUMO+1). For [**2**]$^{2+}$ the MLCT band is composed of four sets of transitions centered at 450.1 ($f=0.0516$)/450.2 ($f=0.0937$), 508.2 ($f=0.0198$)/517.5 ($f=0.0649$), 623.5 ($f=0.0072$), and 642.2 nm ($f=0.0167$). The bathochromic shift and the shape of the MLCT band of [**4**]$^{2+}$ is also fully reproduced by the TD-DFT calculation by 468.6 ($f=0.0175$)/476.2 ($f=0.0226$), 543.0 ($f=0.0428$)/553.3 ($f=0.0300$), 638.7 ($f=0.0352$), and 674.4 ($f=0.0139$). Furthermore, the individual sum of oscillator strengths Σf at $\lambda>400$ nm increases by attaching an amino group ($\Sigma f=0.2408$ ([**1**]$^{2+}$)→0.2564 ([**2**]$^{2+}$) and $\Sigma f=0.4153$ ([**3**]$^{2+}$)→0.4410 ([**4**]$^{2+}$)). The total experimental integrated intensity $\int I$ of the MLCT absorption bands was calculated on an energy scale (cm^{-1}). In the range $\lambda=400$–1000 nm (25000–10000 cm^{-1}), the integrated intensity $\int I$ increases in the same direction ($\int I=3.57\times10^{7}\,\text{M}^{-1}\,cm^{-2}$ ([**1**]$^{2+}$)→$4.01\times10^{7}\,\text{M}^{-1}\,cm^{-2}$ ([**2**]$^{2+}$) and $\int I=4.58\times10^{7}\,\text{M}^{-1}\,cm^{-2}$ ([**3**]$^{2+}$)→$5.86\times10^{7}\,\text{M}^{-1}\,cm^{-2}$ ([**4**]$^{2+}$)). The high absorptivity in the visible spectral region up to 700 nm of the amino-substituted complexes [**2**]$^{2+}$ and [**4**]$^{2+}$ would be especially beneficial for harvesting the low-energy red light in dye-sensitized solar cells. For reference compounds [**5**]$^{2+}$–[**7**]$^{2+}$, the sums of the oscillator strengths Σf at $\lambda>400$ nm ($\Sigma f=0.3463$ ([**5**]$^{2+}$) $<\Sigma f=0.4395$ ([**6**]$^{2+}$) $<\Sigma f=0.5026$ [**7**]$^{2+}$) is also nicely in accordance with the trend of their respective experimental extinction coefficients of their lowest-energy MLCT band (Table 3).

Emission data of [**1**][PF_6]$_2$–[**7**][PF_6]$_2$ are summarized in Table 4. In a solution of CH_3CN at room temperature, complexes [**1**]$^{2+}$–[**4**]$^{2+}$ emit red to near-infrared light with emission maxima at $\lambda_{\text{max}}>720$ nm bathochromically shifted in the series [**1**]$^{2+}$<[**3**]$^{2+}$<[**2**]$^{2+}$<[**4**]$^{2+}$ ($\lambda_{\text{max}}=729$, 744, 762, and 788 nm; Figure 8). Both the amino groups at the push-substituted side and the ester groups at the pull-substituted side act in a cooperative manner and lower the energy of the emitting ^{3}MLCT state. The mixed ligand complex [**2**]$^{2+}$ emits at significantly lower energy than the bis(tpy) complex [**7**]$^{2+}$ ([**2**]$^{2+}$: $\lambda_{\text{max}}=762$ nm; [**7**]$^{2+}$: $\lambda_{\text{max}}=734$ nm), which is essentially due to the electron-donating NCH_3 groups present in the ddpd ligand.

Emission energies were estimated by using DFT calculations (B3LYP/LANL2DZ, IEFPCM, CH_3CN) as energy difference of the energy of the optimized ^{3}MLCT state and the

Table 4. Experimental and DFT calculated emission data of complexes [**1**][PF$_6$]$_2$–[**7**][PF$_6$]$_2$.

	Experimental						DFT[d]
	$\lambda_{max,295K}$[a] [nm] ($E_{max,295K}$ [eV])	Φ_{295K}[a] [%] (λ_{ex} [nm])	τ_{295K} [ns]	$\lambda_{max,77K}$[b] [nm] ($E_{max,77K}$ [eV])	τ_{77K}[b] [ns]	τ_{TA}[b,c] [ps]	$\lambda_{max,298K}$[a] [nm] ($E_{max,298K}$ [eV]
[**1**][PF$_6$]$_2$	729 (1.70)	0.45 (469.0)	722[b]	707 (1.75)	3309	9.3	932 (1.33)
[**2**][PF$_6$]$_2$	762 (1.63)	0.042 (474.5)	149[b]	749 (1.66)	1123	8.4	1047 (1.18)
[**3**][PF$_6$]$_2$	744 (1.67)	1.1 (467.5)	841[b]	728 (1.70)	3251	16.7	979 (1.27)
[**4**][PF$_6$]$_2$	788 (1.57)	0.052 (467.5)	136[b]	779 (1.59)	1002	7.5	1181 (1.05)
[**5**][PF$_6$]$_2$[49]	629 (1.97)	$\leq$0.0005 (n.a.)	$\approx$0.1–0.2[e]	n.a.	10600	n.a.	716 (1.73)
[**6**][PF$_6$]$_2$[7][f]	667 (1.86)	0.027 (n.a.)	32	n.a.	n.a.	8.7	816 (1.52)
[**7**][PF$_6$]$_2$[54]	734 (1.69)	0.18 (n.a.)	34[a]	702 (1.77)	n.a.	7.2	916 (1.35)

[a] In CH$_3$CN. [b] In PrCN. [c] Time constants from picosecond TA spectroscopy at 295 K. [d] Calculated from the energy difference of the optimized ^{3}MLCT state and the singlet state with ^{3}MLCT geometry. [e] Various solvents. [f] No solvent denoted.

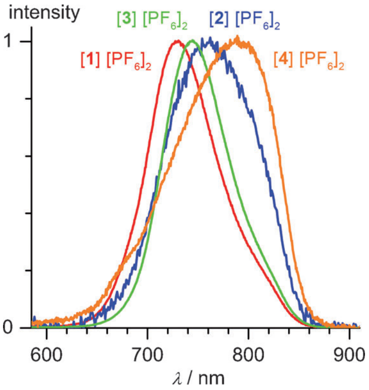

Figure 8. Normalized emission spectra of [**1**][PF$_6$]$_2$–[**4**][PF$_6$]$_2$ in CH$_3$CN at room temperature.

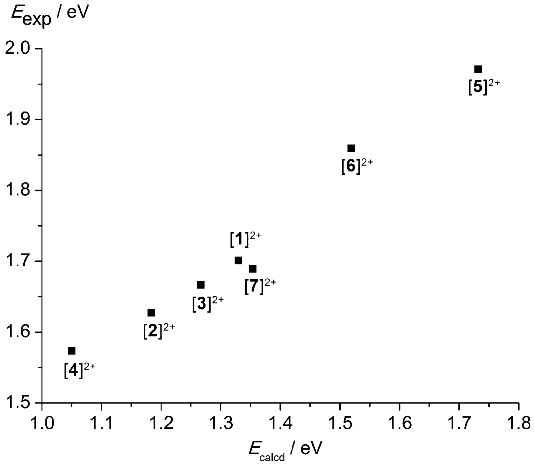

Figure 9. DFT calculated and experimental emission energies (E_{max} at 295 K) of [**1**]$^{2+}$–[**4**]$^{2+}$ and reference compounds [**5**]$^{2+}$–[**7**]$^{2+}$ in CH$_3$CN. Experimental emission data of [**5**]$^{2+}$ and [**6**]$^{2+}$ were taken from the literature.[7,49]

energy of the singlet ground state at the ^{3}MLCT state geometry. Figure 9 shows a clear correlation of the DFT-calculated values of [**1**]$^{2+}$–[**7**]$^{2+}$ with the experimentally determined ones. Thus, the DFT derived conclusions corroborate the experimental findings and underpin the successful push–pull concept to manipulate absorption and emission energies.

All mixed ligand complexes [**1**]$^{2+}$–[**4**]$^{2+}$ display high room temperature emission quantum yields and long ^{3}MLCT-state lifetimes in fluid solution in comparison to the essentially non-emissive bis(tpy) complex [**5**]$^{2+}$ (Table 4). Recently, cyclometalated ligands as strong donors in ruthenium(II) complexes have been reported with quantum yields of 0.001–0.025 % and lifetimes of 1–30 ns.[73,74] The significantly higher values for [**1**]$^{2+}$–[**4**]$^{2+}$ are based on a synergetic effect of the push–pull substitution (lower ^{3}MLCT state) and the stronger ligand field imposed by the ddpd ligand with the large bite angle (higher ^{3}MC state). However, for the low-energy emitting complexes [**2**]$^{2+}$ and [**4**]$^{2+}$ a further effect is noted. The lower emission energy of the amino-substituted complexes renders them susceptible to radiationless deactivation to the ground state (energy-gap law[62–64]) especially due to the presence of high-energy oscillators such as the N–H stretch ($\approx$3450 cm^{-1}). This detrimental effect of the NH$_2$ group significantly reduces the quantum yield and room temperature ^{3}MLCT lifetime ([**1**]$^{2+}$→[**2**]$^{2+}$ τ_{295K}= 722→149 ns and [**3**]$^{2+}$→[**4**]$^{2+}$ τ_{295K}=841→136 ns; Figure 10a). The effect of the N–H oscillators is removed by deuteration of the NH$_2$ groups in [**2**]$^{2+}$ and [**4**]$^{2+}$. Successful deuteration is proven by the absence of amine resonances in the ^{1}H NMR spectra, by the absence of N–H bands in the solid state IR spectra and by the appearance of corresponding N–D bands ([**2^D**]$^{2+}$: 2631/2477 cm^{-1} (asymmetric/symmetric); [**4^D**]$^{2+}$: 2629/2475 cm^{-1} (asymmetric/symmetric)) in the solid-state IR spectra. Hence, high-energy N–H oscillators ($\approx$3450 cm^{-1}) are replaced by lower-energy N–D oscillators ($\approx$2630 cm^{-1}). Intersystem crossing from the ^{3}MLCT state to the ^{1}GS ground state is feasible through the second vibrational NH overtone of the ^{1}GS ([**2**]$^{2+}$/[**4**]$^{2+}$) and through the third ND overtone ([**2^D**]$^{2+}$/[**4^D**]$^{2+}$; Figure 11). As multiphonon deactivation is more probable for fewer phonons, the deuterated derivatives are less prone to quenching by high-energy vibrations (Figure 11). Indeed, deuteration of the amino group significantly increases the quantum yields ([**2**]$^{2+}$→[**2^D**]$^{2+}$: Φ= 0.042→0.100 %; [**4**]$^{2+}$→[**4^D**]$^{2+}$: Φ=0.052→0.073 %). Possibly, the replacement of C–H in the ligands by C–D would further improve the quantum yield and lifetime but this is beyond the scope of this study.[75–78]

^{3}MLCT lifetimes for [**1**]$^{2+}$–[**4**]$^{2+}$ (τ_{77K}=3309, 1123, 3251, 1002 ns) at 77 K in frozen butyronitrile are higher than room temperature lifetimes by a factor of 4–8 (Table 4, Figure 10) showing that deactivation through thermally accessible ^{3}MC states is still a deactivation pathway at room temperature in fluid solution. The presence of an amino group reduces τ_{77K} by a factor of approximately three ([**1**]$^{2+}$

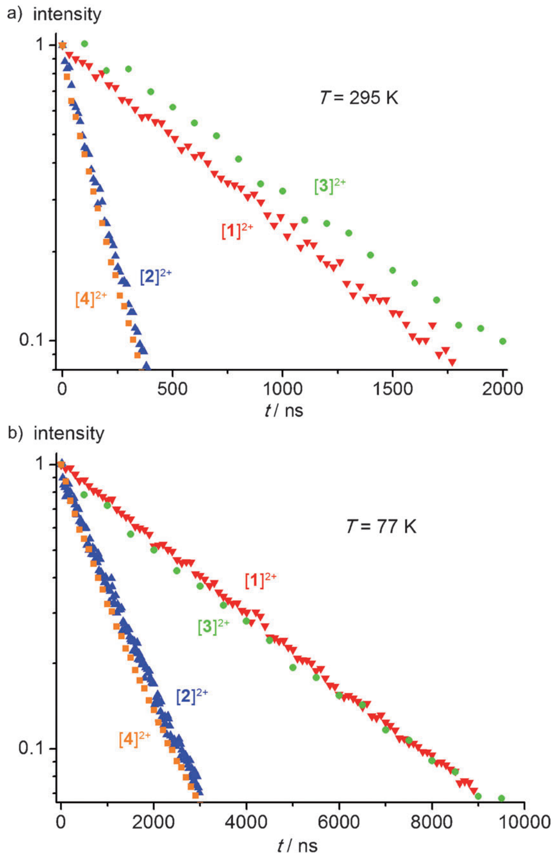

Figure 10. Monoexponential emission decay of $[\mathbf{1}]^{2+}$–$[\mathbf{4}]^{2+}$ in PrCN a) at 295 K and b) at 77 K.

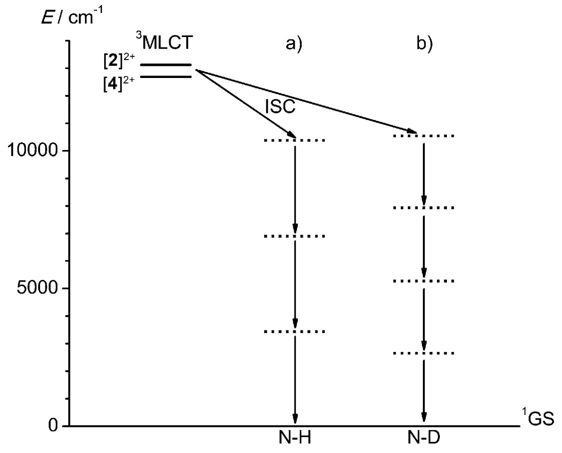

Figure 11. Proposed radiationless deactivation from the vibrationally relaxed ^{3}MLCT states of $[\mathbf{2}]^{2+}$ and $[\mathbf{4}]^{2+}$ (estimated by $\lambda_{\text{max,emiss}}$ at 295 K) into their respective ground states (^{1}GS) in the presence of a) N–H and b) N–D harmonic oscillators.

$\rightarrow[\mathbf{2}]^{2+}$; $[\mathbf{3}]^{2+}\rightarrow[\mathbf{4}]^{2+}$). Emission maxima at 77 K are shifted to higher energy ($\Delta E = 0.02$–0.05 eV) compared with room temperature values because the excited state is less stabilized in the frozen matrix than in solution, which also prolongs the lifetime at low temperature (energy-gap law).

In summary, emission quantum yields and ^{3}MLCT lifetimes are improved by 1) using the push–pull concept decreasing the energy of the ^{3}MLCT state and 2) increasing the ligand bite angle to strengthen the ligand field and thus raising the energy of the deactivating ^{3}MC state. The first approach, however, seems to reach its limits at around 750 nm emission energy due to the energy-gap law in this type of complexes, especially when high-energy oscillators are present.

DFT modeling of excited triplet states: Relevant electronic triplet states ^{3}MLCT and ^{3}MC have been successfully modeled by DFT methods for all complexes $[\mathbf{1}]^{2+}$–$[\mathbf{7}]^{2+}$ (Figure 12), except for the ^{3}MC state of $[\mathbf{4}]^{2+}$, which we were unable to localize. It appears that the ^{3}MC state of $[\mathbf{4}]^{2+}$ corresponds only a very shallow minimum, which connects to the ^{3}MLCT state without a significant barrier. In addition, we were able to locate the transition states (^{3}TS) for the excited state equilibrium between ^{3}MLCT and ^{3}MC

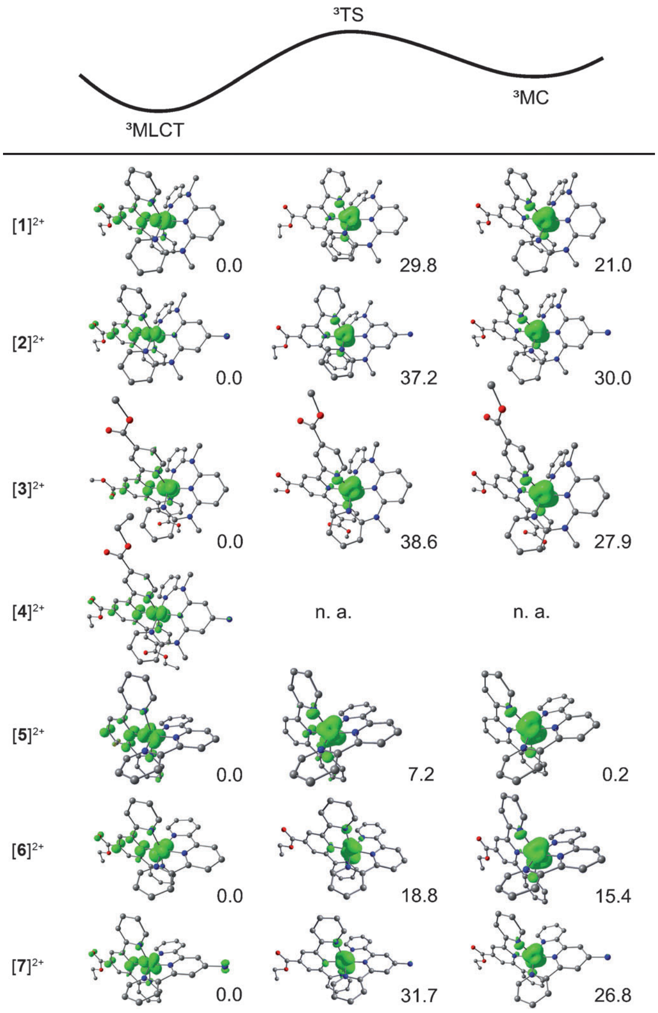

Figure 12. Geometries, relative energies, and spin densities of triplet states (^{3}MLCT and ^{3}MC) as well as the connecting transition state (^{3}TS) of $[\mathbf{1}]^{2+}$–$[\mathbf{7}]^{2+}$. Contour value 0.01; energies in kJ mol^{-1}; hydrogen atoms are omitted.

states for all complexes [**1**]$^{2+}$–[**7**]$^{2+}$ except [**4**]$^{2+}$. Optimized geometries and spin densities of the triplet states are depicted in Figure 12 together with their energy relative to the ^{3}MLCT state. Selected bond lengths and angles are summarized in Table S10 (the Supporting Information). For complexes [**1**]$^{2+}$–[**7**]$^{2+}$ (except [**5**]$^{2+}$), the Ru–N2 bond is slightly elongated (0.02–0.05 Å) from the ^{1}GS to the ^{3}MLCT state, whereas the Ru–N5 bond *trans* to N2 is slightly shortened (0.01–0.06 Å). Consequently, bite angles of the ester substituted tpy ligand (N1-Ru-N2, N2-Ru-N3) in the ^{3}MLCT state (77–78°) are slightly smaller than in the ^{1}GS state (79°). The majority of the spin density in the ^{3}MLCT state is located on the ester substituted tpy ligand and on the ruthenium atom as can be seen from Mulliken spin density values (Table S11, the Supporting Information) and spin densities (Figure 12). The elongation of the Ru–N2 bond as well as the spin density distribution clearly demonstrate that the excited ^{3}MLCT state is located on both the ruthenium atom as well as on the tpy ligand as expected from electrochemical and optical investigations.

Geometries of ^{3}MC states are obtained as local energy minima. The Ru–N bond lengths of the ester substituted tpy ligand of [**1**]$^{2+}$–[**4**]$^{2+}$, [**6**]$^{2+}$ and [**7**]$^{2+}$ are significantly longer in the ^{3}MC state than in the ^{3}MLCT state, whereas for the second ligand (ddpd or tpy) the Ru–N bond lengths change only marginally. N-Ru-N angles with the ester-substituted tpy ligand are smaller due to the larger distance between the ruthenium atom and the ester-substituted ligand. Furthermore, dihedral angles (N1-C-C-N2 and N2-C-C-N3) of the ester substituted tpy ligand are significantly larger in the ^{3}MC state than in the ^{1}GS and ^{3}MLCT states. Spin density plots (Figure 12) and Mulliken spin densities (Table S11, Supporting Information) show that the ^{3}MC state is predominantly located on the ruthenium atom with only small contributions from both ligands, which corresponds to the expected spin density of a "$(t_{2g})^5(e_g)^1$" electronic configuration (see "e_g" orbitals LUMO+11 and LUMO+13 in Figure 7). All ^{3}MC states are calculated to be higher in energy than corresponding ^{3}MLCT states. For bis(tpy) complexes [**6**]$^{2+}$ and [**7**]$^{2+}$ the energy difference amounts to 15.4 and 26.8 kJ mol^{-1}, respectively. Substituting one tpy ligand in [**6**]$^{2+}$ and [**7**]$^{2+}$ by a ddpd ligand ([**1**]$^{2+}$ and [**2**]$^{2+}$) raises the energy difference between the ^{3}MC and the ^{3}MLCT state by 3–6 kJ mol^{-1} ([**6**]$^{2+}$→[**1**]$^{2+}$: 15.4→21.0 kJ mol^{-1}; [**7**]$^{2+}$→[**2**]$^{2+}$: 26.8→30.0 kJ mol^{-1}). This finding is in accordance with experimental ^{3}MLCT lifetimes, which are higher for the ddpd complexes [**1**]$^{2+}$ and [**2**]$^{2+}$ compared with [**6**]$^{2+}$ and [**7**]$^{2+}$ (Table 4). Additionally, the ^{3}MC–^{3}MLCT energy difference of a given complex type dramatically increases by push–pull substitution ([**7**]$^{2+}$ (26.8 kJ mol^{-1}) > [**6**]$^{2+}$ (15.4 kJ mol^{-1}) > [**5**]$^{2+}$ (0.2 kJ mol^{-1}); [**2**]$^{2+}$ (30.0 kJ mol^{-1}) ≈ [**3**]$^{2+}$ (27.9 kJ mol^{-1}) > [**1**]$^{2+}$ (21.0 kJ mol^{-1})). The calculated transition states ^{3}TS are more similar to the ^{3}MC than to the ^{3}MLCT states with respect to energies, bond lengths, N-Ru-N angles and N-C-C-N dihedral angles as well as from spin density distributions, suggesting a late transition state on the reaction coordinate. The homoleptic complex [Ru(tpy)$_2$]$^{2+}$ ([**5**]$^{2+}$) is unique when compared with heteroleptic analogues due to its higher symmetry. In the ^{1}GS, both ligands have similar Ru–N bond lengths, whereas in the ^{3}MLCT state, one central pyridine nitrogen atom moves towards and the other central pyridine nitrogen atom moves away from the ruthenium atom, indicating that the excited state is distorted and the spin density is localized on one of the two tpy ligands. Spin densities are higher on the tpy ligand with the shorter central Ru–N bond. With respect to the ^{3}TS and the ^{3}MC state, complex [**5**]$^{2+}$ is similar to the aforementioned heteroleptic complexes.[79]

Early-time dynamics by transient absorption spectroscopy: Before reaching the ^{3}MLCT state and its thermal equilibration with the ^{3}MC state, the Franck–Condon excited ^{1}MLCT state has to undergo localization of the excited electron onto a single oligopyridyl ligand, intersystem crossing (ISC), solvent reorganization, and vibrational relaxation.[1] Early-time dynamics occurring shortly after excitation to the Franck–Condon state and before reaching the emitting ^{3}MLCT state and the deactivating ^{3}MC state were probed by picosecond transient absorption (TA) spectroscopy for [**1**]$^{2+}$–[**4**]$^{2+}$, and [**6**]$^{2+}$ and [**7**]$^{2+}$ at 298 K in CH_3CN (pulse λ_{exc} = 400–425 nm). The TA spectra of [**2**]$^{2+}$ and [**7**]$^{2+}$ are exemplarily depicted in Figure 13 (Figures S43–S46 in the Supporting Information for [**1**]$^{2+}$, [**3**]$^{2+}$, [**4**]$^{2+}$, and [**6**]$^{2+}$). All complexes exhibit ground-state bleaching from 480 to 550 nm and absorption features of the MLCT state from 550 to 1000 nm similar to the reported data of [Ru(tpy)$_2$]$^{2+}$ in CH_3CN.[49,80]

To assign absorption and bleaching in the TA spectra, UV/Vis spectra of chemically oxidized and reduced [**2**]$^{2+}$ were recorded (Figure S47, the Supporting Information). In [**2**]$^{3+}$ the MLCT band at 450–550 nm is replaced by LMCT bands at 600–950 nm with maxima at 647 (4300 M^{-1}cm^{-1}) and at 770 nm (3100 M^{-1}cm^{-1}).[34] In the reduced form [**2**]$^{+}$ absorption bands appear at 372 (27500 M^{-1}cm^{-1}) and 466 nm (18600 M^{-1}cm^{-1}). Similar absorptions are also present in the spectra of reduced [Ru(tpy)$_2$]$^{2+}$ complexes.[25,52] A third absorption band of [**2**]$^{+}$ is found at 695 nm (4100 M^{-1}cm^{-1}). The absorption features of [**2**]$^{+}$ are tentatively assigned to the coordinated tpy radical ligand. The difference spectrum "[**2**]$^{2+}$–½ ([**2**]$^{3+}$ + [**2**]$^{+}$)" emulates the TA spectrum concerning ground state bleach at 530 nm and excited state absorption at 560–900 nm (Figure 13). Thus, the excited ^{3}MLCT state of [**2**]$^{2+}$ is well formulated by [Ru^{III}(ddpd-NH$_2$)(EtOOC-tpy$^{(-)}$)]$^{2+}$, with the spin density localized on the tpy ligand and a Ru^{III} center.

Time-resolved transient absorption features evolve within the first picoseconds after the laser pulse. The time constants of [**1**]$^{2+}$–[**4**]$^{2+}$, and [**6**]$^{2+}$ and [**7**]$^{2+}$ are summarized in Table 4. TA spectra of [Ru(bpy)$_3$]$^{2+}$ had revealed that no significant changes occur in the spectrum within ≈0.3 ps after a laser pulse with λ_{exc} = 475 nm.[81] On the other hand, time constants of 5 ps had been observed by TA measurements for [Ru(dmb)$_3$]$^{2+}$ (dmb = 4,4′-dimethyl-2,2′-bipyridine) when irradiated at 400 nm and had been assigned to

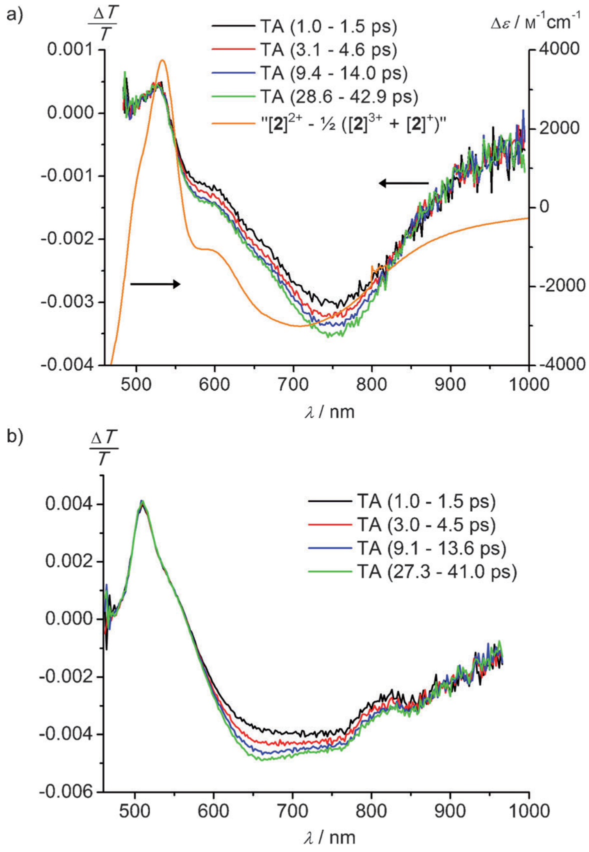

Figure 13. Transient absorption spectra of a) $[\mathbf{2}]^{2+}$ (pulse $\lambda_{exc}=425$ nm, 2050 nJ) with difference spectrum "$[\mathbf{2}]^{2+}-{}^{1}/_{2}([\mathbf{2}]^{3+}+[\mathbf{2}]^{+})$" and b) $[\mathbf{7}]^{2+}$ (pulse $\lambda_{exc}=400$ nm, 2600 nJ) in PrCN at 295 K.

vibrational cooling within the ^{3}MLCT state.[82] A time constant of 2 ps had been found for $[Ru(tpy)_2]^{2+}$ and had been assigned to the equilibrium between ^{3}MLCT and ^{3}MC states. This interpretation is clearly not applicable for $[\mathbf{1}]^{2+}$–$[\mathbf{4}]^{2+}$, and $[\mathbf{6}]^{2+}$ and $[\mathbf{7}]^{2+}$ because the ^{3}MLCT/^{3}MC equilibration occurs in the nanosecond regime. For heteroleptic [Ru(tpy)(ttpy)]$^{2+}$ (ttpy=4′-(4-methylphenyl)-2,2′;6′,2″-terpyridine) a 3 ps dynamics had been discussed to be an interligand electron-transfer process.[80] Whatever the exact nature of the observed dynamics in $[\mathbf{1}]^{2+}$–$[\mathbf{4}]^{2+}$ and $[\mathbf{6}]^{2+}$ and $[\mathbf{7}]^{2+}$ (localization of the electron on the tpy ligand, ISC, or vibrational relaxation within MLCT states), all these processes together from the ^{1}MLCT Franck–Condon state to the thermalized ^{3}MLCT state are completed within several picoseconds in all cases. The thermalized ^{3}MLCT state equilibrates with the ^{3}MC state, relaxes to the ground state by radiationless deactivation through high-energy oscillators, or emits a photon.

Conclusion

Heteroleptic bis(tridentate) ruthenium(II) complexes $[\mathbf{1}]^{2+}$–$[\mathbf{4}]^{2+}$ with long ^{3}MLCT lifetimes (up to 841 ns) and high quantum yields (up to 1.1%) have been synthesized by using the combination of an electron-accepting tpy and an electron-donating ddpd ligand. The favorable push–pull substitution of the complexes leads to a small HOMO–LUMO gap, a spatial separation of the frontier orbitals, and to low-energy absorption and emission. The large 88° bite angle of ddpd ligands induces a strong ligand field and increases the energy difference between ^{3}MLCT and ^{3}MC states, thus reducing radiationless decay pathways through the latter state. Excited states of $[\mathbf{1}]^{2+}$–$[\mathbf{4}]^{2+}$ have been probed experimentally by using ultrafast transient absorption spectroscopy and theoretically by DFT calculations. The $^1\text{MLCT}\rightarrow{}^3\text{MLCT}$ relaxation occurs within picoseconds, whereas the $^3\text{MLCT}\rightarrow{}^3\text{MC}$ equilibration is shifted to the nanosecond timescale (Scheme 1). The fairly long lifetime of >100 ns of the ^{3}MLCT state of complexes $[\mathbf{1}]^{2+}$–$[\mathbf{4}]^{2+}$ should allow for efficient electron-transfer processes in solution or at semiconductor interfaces. Furthermore, the quantum yields together with the functional groups present will allow labeling applications in the field of luminescent sensors and in other luminescent devices. Future applications of $[\mathbf{1}]^{2+}$–$[\mathbf{4}]^{2+}$ are dye-sensitized solar cells, light-emitting electrochemical cells, labeling, and photocatalysis. This research is currently being pursued in our group and results will be reported in due course.

Experimental Section

General procedures: Dioxane, diethyl ether, and petroleum ether (b.p. 40–60°C) were distilled from sodium, CH_3CN and CH_2Cl_2 from CaH_2, and THF from potassium under an argon atmosphere. All reagents were used as received from commercial suppliers (Acros and Sigma–Aldrich). Microwave heating was performed in a Discover Benchmate Plus (CEM Synthesis) single-mode microwave cavity, producing continuous irradiation at 2.455 GHz with 100 W (maximum power). Reaction mixtures were stirred with a magnetic stir bar during irradiation. The temperature and irradiation power were monitored during the course of the reaction. NMR spectra were recorded on a Bruker Avance DRX 400 spectrometer at 400.31 MHz (^{1}H), 100.66 MHz (^{13}C{^{1}H}), and 40.56 MHz (^{15}N). All resonances are reported in ppm versus the solvent signal as an internal standard (CD_3CN (^{1}H, $\delta=1.94$; ^{13}C, $\delta=1.24$ ppm); CD_2Cl_2 (^{1}H, $\delta=5.32$); [D$_6$]DMSO (^{1}H, $\delta=2.50$); ^{13}C, $\delta=39.43$ ppm)) or versus external CH_3NO_2 (90% in $CDCl_3$ $\delta=380.23$ ppm vs. NH_3(l)) and referenced to NH_3 (^{15}N, $\delta=0$ ppm). IR spectra were recorded with a BioRad Excalibur FTS 3100 spectrometer as KBr or CsI disks. Electrochemical experiments were carried out on a Bio Logic SP-50 voltammetric analyzer using platinum wires as counter- and working electrodes and 0.01 M Ag/AgNO$_3$ as reference electrode. The measurements were carried out at a scan rate of 100–333 mV s^{-1} for cyclic voltammetry experiments and at 25–333 mV s^{-1} for square-wave voltammetry experiments using 0.1 M [nBu$_4$N][PF$_6$] as the supporting electrolyte and a 10^{-3} M solution of the sample in dry and degassed CH_3CN. Potentials are referenced to the ferrocene/ferrocenium couple ($E_{1/2}=90\pm5$ mV under experimental conditions). UV/Vis/near-IR spectra were recorded on a Varian Cary 5000 spectrometer using 1.0 cm cells (Hellma, Suprasil). Emission spectra were recorded on a Varian Cary Eclipse spectrometer. Quantum yields were determined by comparing the areas under the emission spectra on an energy scale cm^{-1} recorded for optically matched solutions of the sample and the reference $\Phi([Ru(bpy)_3]Cl_2)=0.094$ in deaerated CH_3CN.[83] Time-resolved photoluminescence measurements were recorded with a gated intensified charge-coupled device camera (Andor IStar iCCD Detector DH740 ICCD) connected to a spectrograph (Andor Shamrock SR-303i) employing gratings with 150 or 300 lines per millimeter. Photoexcitation at wavelengths corresponding to the maximum absorption of the complexes in solution was provided by 10 ns pulses of an optical parametric oscillator (GWU VisIR2 OPO System) pumped by the third harmonic of a Nd:YAG Laser (Spectra-Physics Quanta Ray-INDI) at a repetition rate of 10 Hz. Solutions ($c=5\times10^{-6}$ M) in degased butyronitrile were prepared under a nitrogen atmosphere. The measurements were performed at 295 and 77 K in a self-made indium sealed brass cuvette with quartz windows and an optical path of 1 mm. Single exponentials were used to fit the experimental data. Transient absorption measurements were performed with a home-built pump-probe setup.[84] To measure a time range up to 3 ns with a resolution of ≈100 fs, the output of a commercial titanium:sapphire amplifier (Coherent LIBRA HE, 3.5 mJ, 1 kHz, 100 fs) was split with one portion used to generate a 400–425 nm excitation pulse using an optical parametric amplifier (Coherent OPerA Solo), and another used to generate a 1300 nm seed pulse (output of an optical parametric amplifier (Coherent OPerA Solo)) for white-light generation in the visible to NIR (500–1000 nm) in a c-cut 3 mm thick sapphire window. The variable delay of up to 3 ns between pump and probe was introduced by using a broadband retroreflector mounted on a mechanical delay stage. The excitation pulse was chopped at 500 Hz, while the white light pulses were dispersed onto a linear silicon (Hamamatsu NMOS linear image sensor S3901) photodiode. The array was read out at 1 kHz. Adjacent diode readings corresponding to the transmission of the sample after an excitation pulse and without an excitation pulse were used to calculate $\Delta T/T$. Samples were excited with fluences between 50 and 500 μJ cm^{-2}. No fluence dependent kinetics were observed. The complexes were dissolved in degased butyronitrile ($c=0.2$–0.6 mM) under a nitrogen atmosphere and measured in a quartz cuvette with 1 mm optical path length. Field desorption (FD) mass spectra were recorded on a FD Finnigan MAT90 spectrometer. ESI mass spectra were recorded on a Micromass Q-TOF-Ultima spectrometer. X-band CW ESR spectra were measured on a Miniscope MS 300 (Magnettech GmbH, Germany). g values are referenced to external Mn^{2+} in ZnS ($g=2.118$, 2.066, 2.027, 1.986, 1.946, 1.906). Measurements were conducted at 77 K and simulations were performed with the program package EasySpin.[85] Elemental analyses were performed by the microanalytical laboratory of the chemical institutes of the University of Mainz.

Crystal structure determinations: Intensity data were collected with a Bruker AXS Smart 1000 CCD diffractometer with an APEX II detector and an Oxford cooling system and corrected for absorption and other effects using Mo$_{K\alpha}$ radiation ($\lambda=0.71073$ Å) at 173(2) K. The diffraction frames were integrated using the SAINT package, and most were corrected for absorption with MULABS.[86,87] The structures were solved by direct methods and refined by the full-matrix method based on F^2 using the SHELXTL software package.[88,89] All non-hydrogen atoms were refined anisotropically, whereas the positions of all hydrogen atoms were generated with appropriate geometric constraints and allowed to ride on their respective parent carbon atoms with fixed isotropic thermal parameters. The asymmetric unit of a crystal of [**3**][PF$_6$]$_2$ contains one molecule of an acetonitrile solvent and one molecule of diethylether. Both [PF$_6$]$^-$ counterions and one ester group are disordered over two positions (site occupancy 0.55:0.45 (P1); 0.68:0.32 (P2); 0.76:0.24 (ester)). In the refinement one [PF$_6$]$^-$ counterion (P1) of [**3**][PF$_6$]$_2$ restraints were applied (same, simu, delu). Crystallographic data (excluding structure factors) for the structure reported in this paper have been deposited as CCDC-930312 ([**2**][PF$_6$]$_2$), CCDC-930313 ([**3**][PF$_6$]$_2$), CCDC-930310 (**8**) and CCDC-930311 (**9**). These data can be obtained free of charge from The Cambridge Crystallographic Data Centre via www.ccdc.cam.ac.uk/data_request/cif..

DFT calculations: Calculations were performed by using the Gaussian 09/DFT[90] series of programs. The B3LYP formulation of DFT was used employing the LANL2DZ basis set.[90] No symmetry constraints were imposed on the molecules. The presence of energy minima or first order saddle points was checked by analytical frequency calculations. The integral-equation-formalism polarizable continuum model (IEFPCM, CH$_3$CN) was employed for solvent modeling. As data obtained including solvent modeling reproduced the experimental results better than those without solvent modeling the IEFPCM formalism is used in all calculations in this paper. In TD-DFT calculations at least 100 singlet transitions ($n\geq100$) were calculated. For thermodynamic energy values, the sum of electronic and thermal free-energies ($T=298.15$ K) from the output file was used. All calculations were performed without explicit counterions and solvent molecules.

Syntheses: The synthesis of [Ru(ddpd)(EtOOC-tpy)][PF$_6$]$_2$ ([**1**][PF$_6$]$_2$), [RuCl$_3$(EtOOC-tpy)] (**12**) and ddpd (**11**) have been reported previously.[61] [(RuCl$_3${(MeOOC)$_3$-tpy}] (**13**) was synthesized according to literature procedures.[55,66,67] Syntheses of **8**, 4-amino-2,6-dibromopyridine, **9** and **10** can be found in the Supporting Information.

*[Ru(ddpd-NH$_2$)(EtOOC-tpy)][PF$_6$]$_2$ ([**2**][PF$_6$]$_2$)*: [RuCl$_3$(EtOOC-tpy)] (**12**, 103.7 mg, 0.2022 mmol, 1.0 equiv) and **10** (95.4 mg, 0.219 mmol, 1.1 equiv) were suspended in ethanol (15 mL). The dark red-brown suspension was ultrasonicated for 1 min and *N*-ethylmorpholine (0.15 mL, 1.2 mmol, 5.9 equiv) was added. The mixture was heated to reflux in a laboratory microwave oven for 30 min (80 °C). The mixture was filtered over Celite (1.5 cm; Ø 3.5 cm) and rinsed with ethanol. The solvent was removed under reduced pressure, and the dark-purple solid was dissolved in ethanol (5 mL). Addition of diethylether (50 mL) resulted in the precipitation of a dark-purple solid, which was filtered and dissolved in ethanol (25 mL). Hydrazine hydrate (50 μL, 1.0 mmol, 5.1 equiv) was added and the mixture was heated to reflux (16 h). After cooling to room temperature a second portion of hydrazine hydrate (70 μL, 1.4 mmol, 7.1 equiv) was added. The mixture was heated to reflux (17 h), cooled to room temperature and the solvent was removed under reduced pressure. The dark purple solid was dissolved in ethanol (2 mL) and precipitated by adding diethylether (26 mL). The solid was filtered and dissolved in water (11 mL). The dark-purple product was precipitated by the addition of an aqueous solution of NH$_4$PF$_6$ (166.2 mg, 1.020 mmol, 5.0 equiv, 13 mL). The precipitate was filtered, washed with water (10 mL) and diethyl ether (30 mL) and dried under reduced pressure. A dark-purple powder was obtained. Yield: 155.2 mg (0.1548 mmol, 77 %). ^{1}H NMR (CD$_3$CN, 300 K): $\delta=8.95$ (s, 2H, H^2), 8.54 (m, 2H, H^5), 8.15 (m, 2H, H^8), 8.00 (m, 2H, H^6), 7.58 (m, 2H, H^{11}), 7.48 (m, 2H, H^7), 7.12 (m, 2H, H^{12}), 6.80 (s, 2H, H^{15}), 6.54 (m, 2H, H^{10}), 6.38 (m, 2H, H^9), 5.72 (br, s, 2H, NH$_2$), 4.57 (q, $^3J_{HH}=7.1$ Hz, 2H, CH_2CH$_3$), 3.36 (s, 6H, NCH$_3$), 1.51 ppm (t, $^3J_{HH}=7.1$ Hz, 3H, CH$_2$CH_3); ^{13}C{^{1}H} NMR (CD$_3$CN, 300 K): $\delta=165.0$ (s, C=O), 160.2 (s, C^{13}), 160.0 (s, C^{16}), 159.1 (s, C^3), 158.8 (s, C^4), 156.8 (s, C^{14}), 155.0 (s, C^8), 149.3 (s, C^9), 140.0 (s, C^{11}), 138.8 (s, C^6), 135.1 (s, C^1), 127.8 (s, C^7), 125.4 (s, C^5), 123.6 (s, C^2), 121.1 (s, C^{10}), 116.2 (s, C^{12}), 98.7 (s, C^{15}), 63.5 (s, CH_2CH$_3$), 41.4 (s, NCH$_3$), 14.5 ppm (s, CH$_2$CH_3); ^{1}H-^{15}N HMBC (CD$_3$CN, 300 K): $\delta=297.2$ (N^e), 238.6 (N^d), 212.7 (N^a), 183.1 (N^c), 90.1 (N^b), 72.1 ppm (NH$_2$) ppm; MS (ESI$^+$): *m*/*z* 356.6 (100 %) [$M-2$PF$_6$]$^{2+}$, 858.2 (25 %) [$M-$PF$_6$]$^+$; HR-MS (ESI$^+$): *m*/*z* calcd for C$_{35}$H$_{33}$F$_6$N$_9$O$_2$P^{96}Ru$^+$: 852.1475; found: 852.1500; IR (CsI): $\tilde{\nu}=3468$ (m, NH), 3400 (m, NH), 3240 (w, NH), 3125 (w, NH, CH), 2920 (m, CH), 2853 (w, CH), 1726 (s, C=O), 1641 (s, NH$_2$, NH, C=C), 1620 (s, NH, C=N), 1605 (s, NH, C=N), 1574 (m, NH, C=N), 1462 (s, CH$_3$, CH$_2$), 1433 (s, CH$_3$, CH$_2$), 1367 (s, CH$_3$), 1344 (s, C-N), 1327 (s, C-N), 1281 (s, C-N, C-O-C), 1254 (s, C-N, C-O-C), 1170 (m, C-N, C-O-C), 1132 (m, C-N, C-O-C), 1097 (m, C-O-C), 1049 (m, C-O-C), 1026 (m, C-O-C), 966 (w), 843 (vs, PF), 781 (m), 767 (m), 650 (w), 613 (w), 559 (s), 527 cm^{-1} (w); UV/Vis (CH$_3$CN): λ_{abs} (ε)$=525$ (8230), 323 (26 700), 273 (42 000), 238 nm (43 600 M^{-1} cm^{-1}); emission (CH$_3$CN, 295 K, $\lambda_{exc}=525$ nm): $\lambda_{emiss}=762$ nm [$\tau=149(2)$ ns]; emission (CH$_3$CH$_2$CH$_2$CN, 77 K, $\lambda_{exc}=525$ nm): $\lambda_{emiss}=749$ nm [$\tau=1123(9)$ ns]; Φ (CH$_3$CN, $\lambda_{exc}=474.5$ nm, 295 K): 0.00042 %; CV (CH$_3$CN): $E_{1/2}=+1.73$ (1e, irrev.), +0.64 (1e, rev.), −1.50 (1e, rev.), −2.11 (1e, irrev.), −2.21 (1e, irrev.) vs. Fc/Fc$^+$; elemental analysis calcd (%) for C$_{35}$H$_{33}$F$_{12}$N$_9$O$_2$P$_2$Ru·$^1/_2$Et$_2$O: C 42.74, H 3.68, N 12.12; found: C 42.97, H 3.48, N 11.96.

*[Ru(ddpd){(MeOOC)$_3$-tpy}][PF$_6$]$_2$ ([**3**][PF$_6$]$_2$)*: A solution of **11** (524.7 mg, 1.801 mmol, 2.1 equiv) in methanol (40 mL) was added to [RuCl$_3${(MeOOC)$_3$-tpy}] (**13**, 523.1 mg, 0.851 mmol, 1.0 equiv). *N*-ethylmorpholine (1.50 mL, 11.9 mmol, 13.9 equiv) was added, the black mixture was ultrasonicated (1 min) and heated to reflux in a laboratory microwave oven for 30 min (70 °C). A dark purple-brown solution was obtained which was filtered over Celite (1.5 cm; Ø 3.0 cm) and rinsed with methanol. The solvent was removed under reduced pressure, and the viscous dark purple-brown residue was dissolved in methanol (10 mL). Addition of an aqueous solution of NH$_4$PF$_6$ (5.768 g, 35.39 mmol, 41.6 equiv,

100 mL) led to the precipitation of a dark purple-brown solid which was filtered and washed with a dilute aqueous solution of NH_4PF_6 (50.5 mg in 100 mL; pale-brown filtrate). The filtrate was washed with dioxane (≈200 mL) until the filtrate was colorless (the color of the filtrate turned from dark-green to colorless). The black residue on the filter paper was redissolved in acetone. The solvent of the dark purple solution was removed under reduced pressure and the residue was dissolved in CH_3CN, filtered again and the filter was washed with CH_3CN (a dark-green residue remained on the filter paper). The solvent was removed under reduced pressure and the residue was dissolved in acetone (10 mL). Dioxane (90 mL) was added and the mixture was concentrated to half of its volume under reduced pressure. The suspension was filtered (greenish filtrate). The solid residue was dried in vacuo. $AgNO_3$ (0.5025 g, 2.958 mmol, 3.5 equiv) and absolute CH_3CN (43 mL) were added and the solution was heated to reflux (30 min) under an argon atmosphere. After cooling to room temperature AgCl was filtered and washed with CH_3CN. The solvent of the combined filtrates was removed under reduced pressure and the residue was dissolved in CH_3CN (14 mL). An aqueous solution of NH_4PF_6 (1.037 g, 6.362 mmol, 7.5 equiv, 10 mL) was added and the dark-purple product precipitated. CH_3CN was removed under reduced pressure and the suspension was filtered, washed with diethyl ether, and dried in vacuo. A dark-purple powder was obtained. Yield: 464 mg (0.426 mmol, 50 %). ^{1}H NMR (CD_3CN, 300 K): $\delta=9.17$ (s, 2H, H^2), 8.99 (m, 2H, H^5), 8.30 (t, $^3J_{HH}=8.2$ Hz, 1H, H^{16}), 8.28 (m, 2H, H^8), 7.91 (m, 2H, H^7), 7.62 (m, 2H, H^{11}), 7.60 (d, $^3J_{HH}=8.2$ Hz, 2H, H^{15}), 7.19 (m, 2H, H^{12}), 6.56 (m, 2H, H^{10}), 6.36 (m, 2H, H^9), 4.13 (s, 3H, H^{19}), 3.99 (s, 6H, H^{18}), 3.48 ppm (s, 6H, NCH_3); $^{13}C\{^1H\}$ NMR (CD_3CN, 300 K): $\delta=$ 165.2 (s, $C{=}O^{center}$), 164.8 (s, $C{=}O^{outer}$), 159.7 (s, C^4), 159.5 (s, C^{13}), 159.3 (s, C^3), 157.1 (s, C^{14}), 155.8 (s, C^8), 149.2 (s, C^9), 142.1 (s, C^{16}), 140.4 (s, C^{11}), 140.0 (s, C^6), 136.4 (s, C^1), 126.8 (s, C^7), 124.8 (s, C^2), 124.7 (s, C^5), 121.6 (s, C^{10}), 116.6 (s, C^{12}), 113.7 (s, C^{15}), 54.1 (s, $OCH_3{}^{center}$), 53.9 (s, $OCH_3{}^{outer}$), 41.7 ppm (s, NCH_3); ^{1}H-^{15}N HMBC (CD_3CN, 300 K): $\delta=$ 294.4 (N^e), 249.1 (N^d), 216.2 (N^c), 209.2 (N^a), 92.0 (N^b) ppm. MS (ESI$^+$): $m/z=400.2$ (84 %) $[M-2\ PF_6]^{2+}$, 945.3 (100 %) $[M-PF_6]^+$; HR-MS (ESI$^+$): m/z calcd for $C_{38}H_{34}F_6N_8O_6P^{96}Ru^+$: 939.1319; found: 939.1343; IR (CsI): $\tilde{\nu}=3120$ (w, CH), 2959 (w, CH), 2922 (w, CH), 2853 (w, CH), 1734 (s, C=O), 1607 (m, C=N), 1582 (w, C=N), 1491 (m, C=N), 1450 (m, CH_3), 1408 (m, CH_3), 1358 (s, CH_3, C-N), 1337 (s, C-O-C), 1308 (m, C-N, C-O-C), 1238 (s, C-N, C-O-C), 1165 (w, C-N, C-O-C), 1123 (m, C-N, C-O-C), 1099 (m, C-N), 841 (vs, PF), 768 (m), 727 (w), 613 (w), 559 (s), 538 (w), 467 (w), 444 (w), 349 (w) cm^{-1}; UV/Vis (CH_3CN): λ_{abs} (ε)$=539$ (6360), 475 (5060), 340 (31 000), 292 (34 200), 210 nm (52 400 $M^{-1}cm^{-1}$); emission (CH_3CN, 295 K, $\lambda_{exc}=539$ nm): $\lambda_{emiss}=744$ nm [$\tau=841(26)$ ns]. Emission ($CH_3CH_2CH_2CN$, 77 K, $\lambda_{exc}=539$ nm): $\lambda_{emiss}=728$ nm [$\tau=3251(55)$ ns]; Φ (CH_3CN, $\lambda_{exc}=467.5$ nm, 295 K): 0.011 %; CV (CH_3CN): $E_{1/2}=+1.80$ (1e, irrev.), +0.92 (1e, rev.), –1.25 (1e, irrev.), –1.70 (1e, irrev.) vs. Fc/Fc$^+$; elemental analysis calcd (%) for $C_{38}H_{34}F_{12}N_8O_6P_2Ru\cdot H_2O\cdot {}^1/_2Et_2O$: C 41.97, H 3.61, N 9.79; found: C 41.22, H 3.33, N 8.79.

*[Ru(ddpd-NH$_2$){(EtOOC)$_3$-tpy}][PF$_6$]$_2$ [**4**][PF$_6$]$_2$*: [$RuCl_3$\{(MeOOC)$_3$-tpy\}] (**13**, 141.9 mg, 0.2308 mmol, 1.0 equiv) and ddpd-phthalimide (**10**, 98.6 mg, 0.2259 mmol, 1.0 equiv) were placed in a flask and ethanol (15 mL) was added. The dark red-brown suspension was ultrasonicated (1 min) and *N*-ethylmorpholine (0.15 mL, 1.2 mmol, 5.2 equiv) was added. The mixture was heated to reflux in a laboratory microwave oven for 30 min (80 °C). A dark-purple solution was obtained that was filtered over Celite (1.5 cm; diameter 3.5 cm) and rinsed with ethanol. The solvent was removed under reduced pressure, the solid residue was dissolved in CH_3CN (5 mL) and precipitated by the addition of diethyl ether (100 mL). After filtration and washing with diethyl ether half of the obtained solid was used for further treatment. The solid was dissolved in ethanol (25 mL) and hydrazine hydrate (1.00 mL, 20.6 mmol, 178 equiv) was added. The mixture was heated to reflux (18 h). After cooling to room temperature the solvent was removed under reduced pressure. The dark-purple solid was dissolved in water (13 mL) and a dark-purple solid was precipitated by the addition of an aqueous NH_4PF_6 (1.088 g, 6.675 mmol, 58 equiv, 10 mL) solution. A pH of 7 was adjusted with concentrated H_2SO_4, the suspension was filtered and the solid was washed with water. The solid was dissolved in CH_3CN (2.5 mL) and precipitated by the addition of dioxane (25 mL). After filtration and washing with distilled dioxane and distilled diethyl ether, the solid was dried in a vacuo and dissolved in absolute ethanol (25 mL). Concentrated H_2SO_4 (0.25 mL) was added and the mixture was heated to reflux (21 h). After cooling to room temperature, an aqueous solution of NH_4PF_6 (1.552 g, 9.521 mmol, 84 equiv, 10 mL) was added. Ethanol was removed under reduced pressure and the precipitate was filtered, washed with water and dried in a vacuo. A dark-purple powder was obtained. Yield: 19.9 mg (0.0187 mmol, 17 %). ^{1}H NMR (CD_3CN, 300 K): $\delta=9.15$ (s, 2H, H^2), 8.96 (m, 2H, H^5), 8.31 (m, 2H, H^8), 7.91 (m, 2H, H^7), 7.59 (m, 2H, H^{11}), 7.13 (m, 2H, H^{12}), 6.82 (s, 2H, H^{15}), 6.52 (m, 2H, H^{10}), 6.30 (m, 2H, H^9), 5.77 (br, s, 2H, NH_2), 4.60 (q, $^3J_{HH}=7.1$ Hz, 2H, $\mathit{CH_2}CH_3{}^{center}$), 4.45 (q, $^3J_{HH}=$ 7.1 Hz, 4H, $\mathit{CH_2}CH_{3^\circ}{}^{uter}$), 3.36 (s, 6H, NCH_3), 1.54 (t, $^3J_{HH}=7.1$ Hz, 3H, $CH_2\mathit{CH_3}{}^{center}$), 1.41 ppm (q, $^3J_{HH}=7.1$ Hz, 6H, $CH_2\mathit{CH_3}{}^{outer}$); $^{13}C\{^1H\}$ NMR (CD_3CN, 300 K): $\delta=164.8$ (s, $C{=}O^{center}$), 164.4 (s, $C{=}O^{outer}$), 160.0 (s, C^{13}), 159.8 (s, C^4), 159.6 (s, C^3), 159.3 (s, C^{16}), 156.7 (s, C^{14}), 155.7 (s, C^8), 149.2 (s, C^9), 140.3 (s, C^{11}), 140.0 (s, C^6), 135.8 (s, C^1), 126.7 (s, C^7), 124.6 (s, C^2), 124.4 (s, C^5), 121.2 (s, C^{10}), 116.5 (s, C^{12}), 98.8 (s, C^{15}), 63.6 (s, $\mathit{CH_2}CH_3{}^{center}$), 63.5 (s, $\mathit{CH_2}CH_3{}^{outer}$), 41.3 (s, NCH_3), 14.6 (s, $CH_2\mathit{CH_3}{}^{center}$), 14.4 ppm (s, $CH_2\mathit{CH_3}{}^{outer}$); ^{1}H-^{15}N HMBC ($CD_3CN$, 300 K): $\delta=296.6$ (N^e), 249.7 (N_d), 209.9 (N_a), 181.7 (N_c), 89.5 (N_b), 72.7 ppm (NH_2); MS (ESI$^+$): $m/z=428.6$ (100 %) $[M-2PF_6]^{2+}$, 1002.2 (55 %) $[M-PF_6]^+$; HR-MS (ESI$^+$): m/z calcd for $C_{41}H_{41}F_6N_9O_6P^{96}Ru^+$: 996.1898; found: 996.1891; IR (CsI): $\tilde{\nu}=3109$ (w, CH), 2957 (w, CH), 2926 (m, CH), 2855 (w, CH), 1726 (s, C=O), 1636 (m, NH, C=C, C=N), 1607 (m, NH, C=N), 1574 (w, NH, C=N), 1556 (w, NH, C=N), 1464 (m, CH), 1441 (w, CH), 1408 (m), 1364 (s, CH, C-N), 1325 (s, C-O-C), 1304 (m, C-N, C-O-C), 1238 (s, C-N, C-O-C), 1169 (w, C-N, C-O-C), 1117 (m, C-N, C-O-C), 1051 (w, C-N, C-O-C), 1016 (w, C-O-C), 843 (vs, PF), 768 (w), 615 (w), 559 (m) cm^{-1}; UV/Vis (CH_3CN): λ_{abs} (ε)$=546$ (7810), 479 (5960), 341 (32 000), 292 (37 200), 223 nm (45 600 $M^{-1}cm^{-1}$); emission (CH_3CN, 295 K, $\lambda_{exc}=546$ nm): $\lambda_{emiss}=788$ nm [$\tau=136(3)$ ns]; emission ($CH_3CH_2CH_2CN$, 77 K, $\lambda_{exc}=546$ nm): $\lambda_{emiss}=779$ nm [$\tau=1002(17)$ ns]; Φ (CH_3CN, $\lambda_{exc}=467.5$ nm, 295 K): 0.00052 %; CV (CH_3CN): $E_{1/2}=+1.70$ (1e, irrev.), +0.73 (1e, rev.), –1.32 (1e, rev.), –1.75 (1e, rev.) vs. Fc/Fc$^+$; elemental analysis calcd (%) for $C_{41}H_{41}F_{12}N_9O_6P_2Ru\cdot 5EtOH$: C 44.48, H 5.20, N 9.15; found: C 44.76, H 5.06, N 8.78.

Anion exchange with Δ-TRISPHAT: ^{1}H NMR spectra of [**2**][PF_6]$_2$ (2.7 mg, 2.7 μmol, 1 equiv) in CD_3CN (0.55 mL) were measured before and after addition of tetra(*n*-butyl)ammonium(Δ-tris(tetrachloro-1,2-benzenediolato) phosphate(V)) (4.8 mg, 4.7 μmol, 1.8 equiv). A small but clear splitting of around $\Delta\delta=0.01$ ppm is obtained for the proton resonances of H^2, H^{15}, NH_2, CH_2, NCH_3, and $CH_3{}^{ethyl}$ in the presence of (Δ-TRISPHAT)$^-$ (see Figure 1). The ^{31}P NMR spectrum revealed no splitting of the phosphorus resonance of (Δ-TRISPHAT)$^-$ at $\delta=-81.6$ ppm.

Deuteration: A few milligrams of [**2**][PF_6]$_2$ or [**4**][PF_6]$_2$ were dissolved in dry CD_3CN (0.5 mL). D_2O (99.96 % D; 2–3 drops) was then added. A proton NMR spectrum revealed the instantaneous absence of the NH_2 resonance due to proton–deuterium exchange. The solvent was removed under reduced pressure and the resulting deuterated complex was kept under a dry argon atmosphere. Solid-state IR spectra of [**2^D**][PF_6]$_2$ or [**4^D**][PF_6]$_2$ revealed the presence of N–D vibrational bands and the absence of N–H vibrational bands (the Supporting information, Figures S48 and S49).

*[**2^D**][PF$_6$]$_2$*: IR (CsI): $\tilde{\nu}=3120$ (w, CH), 2984 (w, CH), 2924 (w, CH), 2851 (w, CH), 2631 (w, ND_{asym}), 2477 (w, ND_{sym}), 1728 (s, C=O), 1628 (s, C=C, C=N), 1605 (s, C=N), 1574 (m, C=N), 1477 (s, CH), 1462 (s, CH), 1435 (m, CH_3, CH_2), 1368 (m, CH_3), 1344 (s, C-N), 1335 (s, C-N), 1283 (s, C-N, C-O-C), 1258 (s, C-N, C-O-C), 1175 (m, C-N, C-O-C), 1134 (m, C-N, C-O-C), 1105 (w, C-O-C), 1047 (m, C-O-C), 1026 (w, C-O-C), 1013 (w, C-O-C), 980 (w), 843 (vs, PF), 781 (m), 766 (s), 557 (s), 527 cm^{-1} (w); Φ (CH_3CN, $\lambda_{exc}=472.2$ nm, 295 K): 0.0010 %.

*[**4^D**][PF$_6$]$_2$*: IR (CsI): $\tilde{\nu}=3105$ (w, CH), 2955 (m, CH), 2926 (m, CH), 2855 (m, CH), 2629 (w, ND_{asym}), 2475 (w, ND_{sym}), 1732 (s, C=O), 1628 (s, C=C, C=N), 1607 (m, C=N), 1576 (w, C=N), 1553 (w, C=N), 1464 (s, CH), 1416 (w, CH), 1371 (m, CH, C-N), 1310 (s, C-N, C-O-C), 1246 (s, C-N, C-O-C), 1184 (m, C-N, C-O-C), 1134 (s, C-N, C-O-C), 1049 (w, C-N,

C-O-C), 1024 (w, C-O-C), 986 (m), 843 (vs, PF), 768 (m), 557 cm^{-1} (s); Φ (CH_3CN, $\lambda_{exc}=477.4$ nm, 295 K): 0.00073 %.

Oxidation and reduction of [2][PF_6]$_2$: For UV/Vis oxidation measurements a solution of [**2**][PF_6]$_2$ (7.7×10^{-5} M) was titrated with a solution of $(NH_4)_2[Ce(NO_3)_6]$ (3.0×10^{-2} M) in 0.5 M trifluoroacetic acid in water. UV/Vis reduction measurements were performed by titration of a solution of [**2**][PF_6]$_2$ (1.3×10^{-4} M, 0.5 mL) with a solution of $[Co(Cp^*)_2]$ (2.0×10^{-3} M) in CH_3CN. For EPR oxidation measurements a solution of $(NH_4)_2[Ce(NO_3)_6]$ (5.0×10^{-2} M, 3.1 equiv) was added to a solution of [**2**][PF_6]$_2$ (1.3×10^{-3} M, 0.5 mL) in CH_3CN. EPR reduction was performed by addition of a solution of $[Co(Cp^*)_2]$ (1.0×10^{-2} M, 3.0 equiv) to a solution of [**2**][PF_6]$_2$ (1.7×10^{-3} M) in CH_3CN. For all EPR measurements the solution was immediately frozen to 77 K in an EPR tube. [**2**]$^+$: EPR: $g_{1,2,3}=2.0089$, 1.9865, 1.9720; $\Delta g=0.0387$ by spectral simulation; Figure S42, the Supporting Information). [**2**]$^{3+}$: EPR: $g_{1,2,3}=2.4440$, 2.2694, 2.0300; $\Delta g=0.4140$ by spectral simulation; Figure S41, the Supporting Information).

Acknowledgements

This work was supported by the International Research Training Group (IRTG 1404): Self Organized Materials for Optoelectronics supported by the Deutsche Forschungsgemeinschaft (DFG). M.M. thanks the Max Planck Graduate Center for support and F.L. (all Max Planck Institute for Polymer Research of Mainz, Germany) thanks the Max Planck Society for funding a Max Planck Research group. We thank Anica Wünsche von Leupoldt for the EPR simulations, Regine Jung-Pothmann for the X-ray data collection (all Johannes Gutenberg-University of Mainz, Germany), Julian Ochsmann (MPI-P Mainz) for transient absorption measurements and Prof. Dr. Doris Kunz (Eberhard Karls-University of Tübingen, Germany) for helpful discussions.

---

[1] S. Campagna, F. Puntoriero, F. Nastasi, G. Bergamini, V. Balzani, *Top. Curr. Chem.* **2007**, *280*, 117–214.
[2] B. O'Regan, M. Grätzel, *Nature* **1991**, *353*, 737–740.
[3] J.-F. Yin, M. Velayudham, D. Bhattacharya, H.-C. Lin, K.-L. Lu, *Coord. Chem. Rev.* **2012**, *256*, 3008–3035.
[4] P. G. Bomben, K. C. D. Robson, B. D. Koivisto, C. P. Berlinguette, *Coord. Chem. Rev.* **2012**, *256*, 1438–1450.
[5] R. D. Costa, E. Ortí, H. J. Bolink, F. Monti, G. Accorsi, N. Armaroli, *Angew. Chem.* **2012**, *124*, 8300–8334; *Angew. Chem. Int. Ed.* **2012**, *51*, 8178–8211.
[6] H. J. Bolink, E. Coronado, R. D. Costa, P. Gaviña, E. Ortí, S. Tatay, *Inorg. Chem.* **2009**, *48*, 3907–3909.
[7] H. J. Bolink, L. Cappelli, E. Coronado, P. Gaviña, *Inorg. Chem.* **2005**, *44*, 5966–5968.
[8] L. Marcélis, J. Ghesquière, K. Garnir, A. K.-D. Mesmaeker, C. Moucheron, *Coord. Chem. Rev.* **2012**, *256*, 1569–1582.
[9] M. R. Gill, J. A. Thomas, *Chem. Soc. Rev.* **2012**, *41*, 3179–3192.
[10] H. Komatsu, K. Yoshihara, H. Yamada, Y. Kimura, A. Son, S.-i. Nishimoto, K. Tanabe, *Chem. Eur. J.* **2013**, *19*, 1971–1977.
[11] C. Bhaumik, D. Saha, S. Das, S. Baitalik, *Inorg. Chem.* **2011**, *50*, 12586–12600.
[12] L. M. Hancock, E. Marchi, P. Ceroni, P. D. Beer, *Chem. Eur. J.* **2012**, *18*, 11277–11283.
[13] T. Kundu, A. D. Chowdhury, D. De, S. M. Mobin, V. G. Puranik, A. Datta, G. K. Lahiri, *Dalton Trans.* **2012**, *41*, 4484–4496.
[14] S. Khatua, D. Samanta, J. W. Bats, M. Schmittel, *Inorg. Chem.* **2012**, *51*, 7075–7086.
[15] H.-J. Mo, Y. Shen, B.-H. Ye, *Inorg. Chem.* **2012**, *51*, 7174–7184.
[16] Z.-B. Zheng, Z.-M. Duan, Y.-Y. Ma, K.-Z. Wang, *Inorg. Chem.* **2013**, *52*, 2306–2316.
[17] R. Zhang, Z. Ye, G. Wang, W. Zhang, J. Yuan, *Chem. Eur. J.* **2010**, *16*, 6884–6891.
[18] H. Chen, X. Li, Y. Wu, W. Gao, R. Bai, *Dalton Trans.* **2012**, *41*, 13292–13297.
[19] R. H. Crabtree, *Energy Production and Storage: Inorganic Chemical Strategies for a Warming World*, Wiley-VCH, Weinheim, **2010**.
[20] X. Liu, F. Wang, *Coord. Chem. Rev.* **2012**, *256*, 1115–1136.
[21] M. Schulz, M. Karnahl, M. Schwalbe, J. G. Vos, *Coord. Chem. Rev.* **2012**, *256*, 1682–1705.
[22] W. T. Eckenhoff, R. Eisenberg, *Dalton Trans.* **2012**, *41*, 13004–13021.
[23] A. Inagaki, M. Akita, *Coord. Chem. Rev.* **2010**, *254*, 1220–1239.
[24] T. Stoll, M. Gennari, I. Serrano, J. Fortage, J. Chauvin, F. Odobel, M. Rebarz, O. Poizat, M. Sliwa, A. Deronizer, M.-N. Collomb, *Chem. Eur. J.* **2013**, *19*, 782–792.
[25] J. Dietrich, U. Thorenz, C. Förster, K. Heinze, *Inorg. Chem.* **2013**, *52*, 1248–1264.
[26] S. Ohzu, T. Ishizuka, Y. Hirai, S. Fukuzumi, T. Kojima, *Chem. Eur. J.* **2013**, *19*, 1563–1567.
[27] H. Nitadori, T. Takahashi, A. Inagaki, M. Akita, *Inorg. Chem.* **2012**, *51*, 51–62.
[28] P. Guillo, O. Hamelin, P. Batat, G. Jonusauskas, N. D. McClenaghan, S. Ménage, *Inorg. Chem.* **2012**, *51*, 2222–2230.
[29] F. Li, M. Yu, Y. Jiang, F. Huang, Y. Li, B. Zhang, L. Sun, *Chem. Commun.* **2011**, *47*, 8949–8951.
[30] S. Roeser, M. Z. Ertem, C. Cady, R. Lomoth, J. Benet-Buchholz, L. Hammarström, B. Sarkar, W. Kaim, C. J. Cramer, A. Llobet, *Inorg. Chem.* **2012**, *51*, 320–327.
[31] L.-Z. Sui, W.-W. Yang, C.-J. Yao, H.-Y. Xie, Y.-W. Zhong, *Inorg. Chem.* **2012**, *51*, 1590–1598.
[32] O. S. Wenger, *Chem. Soc. Rev.* **2012**, *41*, 3772–3779.
[33] H.-J. Nie, X. Chen, C.-J. Yao, Y.-W. Zhong, G. R. Hutchison, J. Yao, *Chem. Eur. J.* **2012**, *18*, 14497–14509.
[34] A. Breivogel, K. Hempel, K. Heinze, *Inorg. Chim. Acta* **2011**, *374*, 152–162.
[35] C. J. Yao, Y.-W. Zhong, J. Yao, *Inorg. Chem.* **2013**, *52*, 4040–4045.
[36] P. Ceroni, *Chem. Eur. J.* **2011**, *17*, 9560–9564.
[37] T. N. Singh-Rachford, F. N. Castellano, *Coord. Chem. Rev.* **2010**, *254*, 2560–2573.
[38] W. Wu, S. Ji, W. Wu, J. Shao, H. Guo, T. D. James, J. Zhao, *Chem. Eur. J.* **2012**, *18*, 4953–4964.
[39] P. Hanczyc, B. Norden, M. Samoc, *Dalton Trans.* **2012**, *41*, 3123–3125.
[40] P. Ceroni, G. Bergamini, V. Balzani, *Angew. Chem.* **2009**, *121*, 8668–8670; *Angew. Chem. Int. Ed.* **2009**, *48*, 8516–8518.
[41] J. Lee, H. Chang, S. Kim, G. S. Bang, H. Lee, *Angew. Chem.* **2009**, *121*, 8653–8656; *Angew. Chem. Int. Ed.* **2009**, *48*, 8501–8504.
[42] K. Terada, K. Kanaizuka, V. M. Iyer, M. Sannodo, S. Saito, K. Kobayashi, M.-a. Haga, *Angew. Chem.* **2011**, *123*, 6411–6415; *Angew. Chem. Int. Ed.* **2011**, *50*, 6287–6291.
[43] A. Juris, V. Balzani, F. Barigelletti, S. Campagna, P. Belser, A. von Zelewsky, *Coord. Chem. Rev.* **1988**, *84*, 85–277.
[44] C. Fu, M. Wenzel, E. Treutlein, K. Harms, E. Meggers, *Inorg. Chem.* **2012**, *51*, 10004–10011.
[45] E. Meggers, *Chem. Eur. J.* **2010**, *16*, 752–758.
[46] M. Maestri, N. Armaroli, V. Balzani, E. C. Constable, A. M. W. Cargill Thompson, *Inorg. Chem.* **1995**, *34*, 2759–2767.
[47] J.-P. Sauvage, J.-P. Collin, J.-C. Chambron, S. Guillerez, C. Coudret, V. Balzani, F. Barigelletti, L. D. Cola, L. Flamigni, *Chem. Rev.* **1994**, *94*, 993–1019.
[48] L. Hammarström, O. Johansson, *Coord. Chem. Rev.* **2010**, *254*, 2546–2559.
[49] Y. Liu, R. Hammitt, D. A. Lutterman, R. P. Thummel, C. Turro, *Inorg. Chem.* **2007**, *46*, 6011–6021.
[50] K. Heinze, K. Hempel, *Chem. Eur. J.* **2009**, *15*, 1346–1358.
[51] L. zur Borg, A. L. Domanski, A. Breivogel, M. Bürger, R. Berger, K. Heinze, R. Zentel, *J. Mater. Chem. C* **2013**, *1*, 1223–1230.
[52] J. Dietrich, A. Wünsche von Leupoldt, M. Grabolle, U. Resch-Genger, K. Heinze, *Eur. J. Inorg. Chem.* **2013**, 3009–3019.
[53] K. Heinze, K. Hempel, M. Beckmann, *Eur. J. Inorg. Chem.* **2006**, 2040–2050.
[54] K. Heinze, K. Hempel, S. Tschierlei, M. Schmitt, J. Popp, S. Rau, *Eur. J. Inorg. Chem.* **2009**, 3119–3126.

[55] D. G. Brown, N. Sanguantrakun, B. Schulze, U. S. Schubert, C. P. Berlinguette, *J. Am. Chem. Soc.* **2012**, *134*, 12354–12357.
[56] M. Abrahamsson, M. Jäger, T. Österman, L. Eriksson, P. Persson, H.-C. Becker, O. Johansson, L. Hammarström, *J. Am. Chem. Soc.* **2006**, *128*, 12616–12617.
[57] M. Abrahamsson, M. Jäger, R. J. Kumar, T. Österman, P. Persson, H.-C. Becker, O. Johansson, L. Hammarström, *J. Am. Chem. Soc.* **2008**, *130*, 15533–15542.
[58] R. J. Kumar, S. Karlsson, D. Streich, A. R. Jensen, M. Jäger, H.-C. Becker, J. Bergquist, O. Johansson, L. Hammarström, *Chem. Eur. J.* **2010**, *16*, 2830–2842.
[59] F. Schramm, V. Meded, H. Fliegl, K. Fink, O. Fuhr, Z. Qu, W. Klopper, S. Finn, T. E. Keyes, M. Ruben, *Inorg. Chem.* **2009**, *48*, 5677–5684.
[60] M. Jäger, R. J. Kumar, H. Görls, J. Bergquist, O. Johansson, *Inorg. Chem.* **2009**, *48*, 3228–3238.
[61] A. Breivogel, C. Förster, K. Heinze, *Inorg. Chem.* **2010**, *49*, 7052–7056.
[62] T. J. Meyer, *Pure Appl. Chem.* **1986**, *58*, 1193–1206.
[63] J. V. Caspar, T. J. Meyer, *J. Am. Chem. Soc.* **1983**, *105*, 5583–5590.
[64] J. V. Caspar, T. J. Meyer, *J. Phys. Chem.* **1983**, *87*, 952–957.
[65] M. K. Nazeeruddin, P. Péchy, T. Renouard, S. M. Zakeeruddin, R. Humphry-Baker, P. Comte, P. Liska, L. Cevey, E. Costa, V. Shklover, S. Spiccia, G. B. Deacon, C. A. Bignozzi, M. Grätzel, *J. Am. Chem. Soc.* **2001**, *123*, 1613–1624.
[66] L. Giribabu, T. Bessho, M. Srinivasu, C. Vijaykumar, Y. Soujanya, V. G. Reddy, P. Y. Reddy, J.-H. Yum, M. Grätzel, M. K. Nazeeruddin, *Dalton Trans.* **2011**, *40*, 4497–4504.
[67] J. Dehaudt, J. Husson, L. Guyard, *Green Chem.* **2011**, *13*, 3337–3340.
[68] M. Hesse, H. Meier, B. Zeeh, *Spektroskopische Methoden in der organischen Chemie*, Thieme, Stuttgart, **1991**.
[69] S. Sharma, F. Lombeck, L. Eriksson, O. Johansson, *Chem. Eur. J.* **2010**, *16*, 7078–7081.
[70] E(vs. Fc/Fc$^+$)/V = E(vs. SCE)/V−0.4 V.
[71] E. Jakubikova, W. Chen, D. M. Dattelbaum, F. N. Rein, R. C. Rocha, R. L. Martin, E. R. Batista, *Inorg. Chem.* **2009**, *48*, 10720–10725.
[72] T. Österman, P. Persson, *Chem. Phys.* **2012**, *407*, 76–82.
[73] B. Schulze, D. Escudero, C. Friebe, R. Siebert, H. Görls, S. Sinn, M. Thomas, S. Mai, J. Popp, B. Dietzek, L. González, U. S. Schubert, *Chem. Eur. J.* **2012**, *18*, 4010–4025.
[74] W.-W. Yang, Y.-W. Zhong, S. Yoshikawa, J.-Y. Shao, S. Masaoka, K. Sakai, J. Yao, M.-a. Haga, *Inorg. Chem.* **2012**, *51*, 890–899.
[75] J. Van Houten, R. J. Watts, *J. Am. Chem. Soc.* **1975**, *97*, 3843–3844.
[76] J. Van Houten, R. J. Watts, *J. Am. Chem. Soc.* **1976**, *98*, 4853–4858.
[77] S. F. McClanahan, J. R. Kincaid, *J. Am. Chem. Soc.* **1986**, *108*, 3840–3841.
[78] T. E. Keyes, C. M. O'Connor, U. O'Dwyer, C. G. Coates, P. Callaghan, J. J. McGarvey, J. G. Vos, *J. Phys. Chem. A* **1999**, *103*, 8915–8920.
[79] T. Österman, M. Abrahamsson, H.-C. Becker, L. Hammarström, P. Persson, *J. Phys. Chem. A* **2012**, *116*, 1041–1050.
[80] J. T. Hewitt, P. J. Vallet, N. H. Damrauer, *J. Phys. Chem. A* **2012**, *116*, 11536–11547.
[81] N. H. Damrauer, G. Cerullo, A. Yeh, T. R. Boussie, C. V. Shank, J. K. McCusker, *Science* **1997**, *275*, 54–57.
[82] N. H. Damrauer, J. K. McCusker, *J. Phys. Chem. A* **1999**, *103*, 8440–8446.
[83] K. Suzuki, A. Kobayashi, S. Kaneko, K. Takehira, T. Yoshihara, H. Ishida, Y. Shiina, S. Oishi, S. Tobita, *Phys. Chem. Chem. Phys.* **2009**, *11*, 9850–9860.
[84] F. Etzold, I. A. Howard, N. Forler, D. M. Cho, M. Meister, H. Mangold, J. Shu, M. R. Hansen, K. Müllen, F. Laquai, *J. Am. Chem. Soc.* **2012**, *134*, 10569–10583.
[85] S. Stoll, A. Schweiger, *J. Magn. Reson.* **2006**, *178*, 42–55.
[86] *SMART Data Collection and SAINT-Plus Data Processing Software for the SMART System, various versions*, Bruker Analytical X-ray Instruments, Madison, **2000**.
[87] R. H. Blessing, *Acta Crystallogr. A* **1995**, *51*, 33–38.
[88] G. M. Sheldrick, *SHELXTL, Version 5.1*, Bruker AXS, Madison, **1998**.
[89] G. M. Sheldrick, *SHELXL-97*, University of Göttingen, Göttingen, **1997**.
[90] Gaussian 09, Revision A.02, M. J. Frisch, G. W. Trucks, H. B. Schlegel, G. E. Scuseria, M. A. Robb, J. R. Cheeseman, G. Scalmani, V. Barone, B. Mennucci, G. A. Petersson, H. Nakatsuji, M. Caricato, X. Li, H. P. Hratchian, A. F. Izmaylov, J. Bloino, G. Zheng, J. L. Sonnenberg, M. Hada, M. Ehara, K. Toyota, R. Fukuda, J. Hasegawa, M. Ishida, T. Nakajima, Y. Honda, O. Kitao, H. Nakai, T. Vreven, J. A. Montgomery, Jr., J. E. Peralta, F. Ogliaro, M. Bearpark, J. J. Heyd, E. Brothers, K. N. Kudin, V. N. Staroverov, R. Kobayashi, J. Normand, K. Raghavachari, A. Rendell, J. C. Burant, S. S. Iyengar, J. Tomasi, M. Cossi, N. Rega, J. M. Millam, M. Klene, J. E. Knox, J. B. Cross, V. Bakken, C. Adamo, J. Jaramillo, R. Gomperts, R. E. Stratmann, O. Yazyev, A. J. Austin, R. Cammi, C. Pomelli, J. W. Ochterski, R. L. Martin, K. Morokuma, V. G. Zakrzewski, G. A. Voth, P. Salvador, J. J. Dannenberg, S. Dapprich, A. D. Daniels, Ö. Farkas, J. B. Foresman, J. V. Ortiz, J. Cioslowski, D. J. Fox, Gaussian, Inc., Wallingford CT, **2009**.

Received: June 12, 2013
Published online: September 2, 2013

9.7 Push-Pull Design of Bis(tridentate) Ruthenium(II) Polypyridine Chromophores as Deep Red Light Emitters in Light-Emitting Electrochemical Cells

A. Breivogel, M. Park, D. Lee, S. Klassen, A. Kühnle, C. Lee, K. Char, K. Heinze, *Eur. J. Inorg. Chem.* **2014**, 288–295.

DOI: 10.1002/ejic.201301226

EurJIC European Journal of Inorganic Chemistry

ChemPubSoc Europe

FULL PAPER

DOI:10.1002/ejic.201301226

Push-Pull Design of Bis(tridentate) Ruthenium(II) Polypyridine Chromophores as Deep Red Light Emitters in Light-Emitting Electrochemical Cells

**Aaron Breivogel,[a] Myeongjin Park,[b] Donggu Lee,[b]
Stefanie Klassen,[c] Angelika Kühnle,[c] Changhee Lee,[b]
Kookheon Char,[d] and Katja Heinze*[a]**

Dedicated to Professor Rudolf Zentel on the occasion of his 60th birthday

Keywords: Ruthenium / Molecular electronics / Tridentate ligands / Luminescence / N ligands

Light-emitting electrochemical cells (LECs) with a simple device structure were prepared by using heteroleptic bis(tridentate) ruthenium(II) complexes [**1**]$(PF_6)_2$–[**3**]$(PF_6)_2$ as emitters. The push-pull substitution shifts the emission energy to low energy, into the NIR region. The devices emit deep red light up to a maximum emission wavelength of 755 nm [CIE (International Commission on Illumination) coordinates: x = 0.731, y = 0.269 for [**3**]$(PF_6)_2$], which, to the best of our knowledge, is the lowest emission energy for LECs containing bis(tridentate) ruthenium(II) complexes. A device structure of ITO/PEDOT:PSS/ruthenium(II) complex/Ag was used, and the thickness of the emitting layer was measured by AFM [ITO: indium tin oxide, PEDOT: poly(3,4-ethylenedioxythiophene), PSS: poly(styrenesulfonate), AFM: atomic force microscopy]. To enhance the external quantum efficiency (EQE), cells were fabricated with and without poly(methyl methacrylate) (PMMA) as additive in the emitting layer.

Introduction

Light-emitting electrochemical cells (LECs) provide a low-cost alternative to conventional organic light emitting devices (OLEDs) due to their simple device structures and solution processability. LECs feature an ionic emitting layer that enables low turn-on and driving voltages, as well as independence of the work function of electrode materials.[1–6] LECs introduced in 1995 by Pei contained organic polymers as emitters.[7,8] While for all-organic emitters spin statistics predicts a maximum internal quantum efficiency of 25%, transition metal complexes have a theoretical limit of 100%, because in the latter both singlet and triplet excitons can lead to light emission.[9–12] The first LEC with an ionic transition metal complex was reported in 1996 by Lee employing a $[Ru(phen)_3]^{2+}$ derivative as emitter (phen: 1,10-phenanthroline).[13] The use of ruthenium(II) complexes as emitters is reasonable because of their outstanding photophysical and electrochemical properties combined with their high thermal and chemical stabilities.[14] So far $[Ru(bpy)_3]^{2+}$ (bpy: 2,2′-bipyridine) and its analogues are the most studied ruthenium(II) polypyridine complexes because they have high ^{3}MLCT (MLCT: metal-to-ligand charge transfer) excited state lifetimes ($\tau \approx 1$ µs) and luminescence quantum yields ($\Phi \approx 10\%$) at room temperature in solution.[14–16] $[Ru(bpy)_3]^{2+}$ and its derivatives have already been used in LECs showing high external quantum efficiencies (EQEs) of up to 6.4%.[17–20]

However, $[Ru(bpy)_3]^{2+}$ is chiral (Δ, Λ), and unsymmetrical substitution of bpy ligands leads to the formation of stereoisomers, which complicates synthetic procedures.[21,22] The formation of stereoisomers can be avoided by using tridentate, meridional coordinating ligands. For instance achiral $[Ru(tpy)_2]^{2+}$ (tpy: 2,2′;6′,2′′-terpyridine) gives rise to only a single isomer even in the case of unsymmetrical substitution of the tpy 4′-positions.[23] Additionally, the tridentate coordination provides a higher photostability and

---

[a] Institute of Inorganic Chemistry and Analytical Chemistry, Johannes Gutenberg University of Mainz,
Duesbergweg 10-14, 55128 Mainz, Germany
E-mail: katja.heinze@uni-mainz.de
http://www.ak-heinze.chemie.uni-mainz.de/
[b] Department of Electrical and Computer Engineering, Inter-University Semiconductor Research Center, Seoul National University,
1 Gwanak-ro, Gwanak-gu, Seoul 151-744, Korea
[c] Institute of Physical Chemistry, Johannes Gutenberg University of Mainz,
Duesbergweg 10-14, 55099 Mainz, Germany
[d] The National Creative Research Initiative Center for Intelligent Hybrids, The WCU Program on Chemical Convergence for Energy and Environment, School of Chemical and Biological Engineering, Seoul National University,
1 Gwanak-ro, Gwanak-gu, Seoul, 151-744, Korea

Supporting information for this article is available on the WWW under http://dx.doi.org/10.1002/ejic.201301226.

chemical stability relative to the bidentate mode.[24,25] This should prevent thermal and photoinduced ligand exchange, favoring longevity of luminescent and solar cell devices.[26–29] Degradation products due to ligand loss have been identified in LECs with $[Ru(bpy)_3]^{2+}$ complexes, namely bis(aqua)complex $[Ru(bpy)_2(H_2O)_2]^{2+}$ and oxido-bridged dimer $[\{Ru(bpy)_2(H_2O)\}_2O]^{4+}$, which have been formed by photoaquation in the presence of water.[6,30–32] A better stabilization towards (photo) ligand substitution might be achieved by using tridentate ligands.

Unfortunately, excited state features of $[Ru(tpy)_2]^{2+}$ in solution are very unfavorable ($\tau \approx 0.1$–0.2 ns, $\Phi \leq 0.0005\,\%$) because of rapid radiationless deactivation of the radiative ^{3}MLCT states via thermally accessible ^{3}MC states (MC: metal-centered; Figure 1).[33,34] Increased excited state lifetimes τ and quantum yields Φ have been obtained by structurally modifying $[Ru(tpy)_2]^{2+}$ in order to increase the energy difference between the ^{3}MLCT and ^{3}MC states and hence to avoid radiationless deactivation via the latter states. Push-pull substitution like that in $[(EtOOC\text{-}tpy)Ru(tpy\text{-}NH_2)]^{2+}$ ([**1**]$(PF_6)_2$, Figure 2) is favorable, as the electron-withdrawing ester group lowers the energy of the ^{3}MLCT state while the electron-donating amino group increases the energy of the ^{3}MC state, thus reducing radiationless deactivation via the latter state and enhancing the excited state lifetime and luminescence quantum yield significantly ($\tau = 34$ ns, $\Phi = 0.18\,\%$).[23,35–37] Another strategy employs a strong ligand field to increase the energy difference between the ^{3}MLCT and ^{3}MC states. This can be achieved by N–Ru–N bite angles of 90° as in an ideal octahedron allowing for an optimal overlap of ruthenium and nitrogen orbitals. The N–Ru–N bite angle of tpy is 79° because its five-membered chelate rings result in a suboptimal orbital overlap.[38] Hammarström et al. designed a complex $\{[Ru(dqp)_2]^{2+}$; dpq: 2,6-di(quinolin-8-yl)pyridine$\}$ with six-membered chelate rings and 90° bite angles featuring high room-temperature lifetime and quantum yield in solution ($\tau = 3.0$ µs, $\Phi = 2\,\%$).[39,40] The substituted complex $[Ru(dpq\text{-}COOEt)_2]^{2+}$ with ester substituents on the 4′-positions reaches even higher values ($\tau = 5.5$ µs, $\Phi = 7\,\%$).[41] Ruben et al. incorporated carbonyl bridges between the pyridine rings of $[Ru(tpy)_2]^{2+}$ and thus obtained six-membered chelate rings and 90° bite angles leading to high ^{3}MLCT lifetimes and, to the best of our knowledge, to the highest reported quantum yield of bis(tridentate) ruthenium(II) complexes ($\tau = 3.3$ µs, $\Phi = 30\,\%$).[42] Bis(tridentate) ruthenium(II) complexes have been incorporated in LECs, but until now only complexes with small bite angles (ca. 79°) and hence low solution luminescence quantum yields have been utilized, leading to low EQEs ($\leq 0.1\,\%$) of the devices.[43–45]

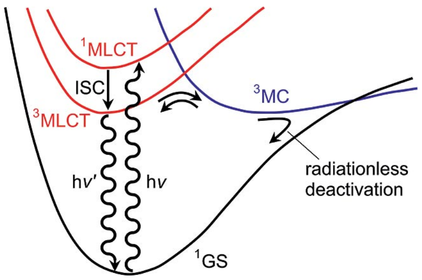

Figure 1. Jablonski diagram of ruthenium(II) polypyridine complexes (GS: ground state, MLCT: metal-to-ligand charge transfer, ISC: intersystem crossing, MC: metal centered).

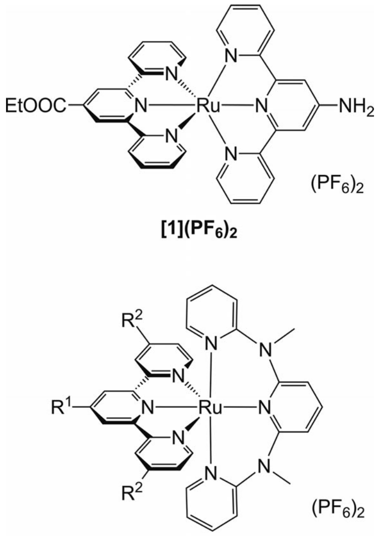

[1](PF$_6$)$_2$

[2](PF$_6$)$_2$: R^1 = COOEt; R^2 = H
[3](PF$_6$)$_2$: R^1 = R^2 = COOMe

Figure 2. Bis(tridentate) ruthenium(II) oligopyridine complexes [**1**]$(PF_6)_2$–[**3**]$(PF_6)_2$.

In this paper, we incorporate bis(tridentate) ruthenium(II) complexes [**1**]$(PF_6)_2$–[**3**]$(PF_6)_2$ as low-energy emitters in LECs (Figure 2). [**1**]$(PF_6)_2$–[**3**]$(PF_6)_2$ are photostable and chemically stable as a result of their tridentate coordination mode; they feature a sophisticated push-pull substitution with high directionality due to electron-withdrawing ester and electron-donating amino groups.[35–37,46–48] The push-pull substitution lowers the HOMO–LUMO gap (and hence increases the energy difference between the ^{3}MLCT and ^{3}MC states) and leads to emission in the red spectral region (λ_{em} = 729–744 nm, Table 1).[35,36,46,47] Red light and NIR emission are particularly favorable for noninvasive bioimaging, telecommunication, night-vision-readable displays, downconversion and triplet–triplet annihilation upconversion.[1,2,49–57] However, according to the energy gap law, low-energy emission is correlated to low luminescence quantum yields and short luminescence lifetimes due to effective radiationless deactivation into the ground state.[58–60] In spite of their low emission energy, complexes [**1**]$(PF_6)_2$–[**3**]$(PF_6)_2$ possess comparably high luminescence lifetimes and quantum yields at room temperature in solution (τ = 34, 722, and 841 ns; Φ = 0.18, 0.45, and 1.1 %, Table 1). While complex [**1**]$(PF_6)_2$ consists of two tpy ligands with 79° N–Ru–N bite angles, complexes [**2**]$(PF_6)_2$ and [**3**]$(PF_6)_2$ consist of a tpy ligand and a ddpd ligand (ddpd: *N*,*N*′-dimethyl-*N*,*N*′-dipyridin-2-ylpyridine-2,6-diamine).[35,46,47] The larger bite angle (88°) of the latter ligand favors the high luminescence lifetimes and quantum yields of [**2**]$(\mathrm{PF}_6)_2$ and [**3**]$(\mathrm{PF}_6)_2$ (Φ = 0.45 and 1.1 %, Table 1) and their choice as red light to NIR emitters in LECs.

Table 1. Electrochemical and photophysical properties of complexes [**1**]$(\mathrm{PF}_6)_2$–[**3**]$(\mathrm{PF}_6)_2$.[35–37,46]

	[**1**]$(\mathrm{PF}_6)_2$	[**2**]$(\mathrm{PF}_6)_2$	[**3**]$(\mathrm{PF}_6)_2$
$E_{1/2}^{\mathrm{ox}}$ /V[a]	+0.68	+0.81	+0.92
$E_{1/2}^{\mathrm{red}}$ /V[a]	–1.54, –1.99	–1.47, –2.09[b]	–1.25[b], –1.70[b]
λ_{abs} /nm (ε/M^{-1} cm^{-1})[c]	502 (19080)	517 (7500)	539 (6360), 475 (5060)
$\lambda_{\mathrm{em,295\,K}}$ /nm[c]	734	729	744
$\Phi_{295\,\mathrm{K}}$ /%[c]	0.18	0.45	1.1
$\tau_{295\,\mathrm{K}}$ /ns	34[c]	722[d]	841[d]

[a] In 0.1 M $[n\mathrm{Bu_4N}][\mathrm{PF_6}]$ in $\mathrm{CH_3CN}$ vs. Fc/Fc$^+$. [b] Irreversible, E_p given. [c] In $\mathrm{CH_3CN}$. [d] In PrCN.

Results and Discussion

The electrochemical and photophysical properties of complexes [**1**]$(\mathrm{PF}_6)_2$–[**3**]$(\mathrm{PF}_6)_2$ have been described previously and are summarized in Table 1.[35–37,46] The oxidation potential, $E_{1/2}^{\mathrm{ox}}$, follows the order [**1**]$(\mathrm{PF}_6)_2 <$ [**2**]$(\mathrm{PF}_6)_2 <$ [**3**]$(\mathrm{PF}_6)_2$ (Table 1). [**1**]$(\mathrm{PF}_6)_2$ is oxidized at the lowest potential because of the electron-donating effect of the $\mathrm{NH_2}$ substituent. [**3**]$(\mathrm{PF}_6)_2$ is oxidized at the highest potential because of the electron-withdrawing effect of the three ester groups.[46] The first reduction potential, $E_{1/2}^{\mathrm{red}}$, follows the same order [**1**]$(\mathrm{PF}_6)_2 <$ [**2**]$(\mathrm{PF}_6)_2 <$ [**3**]$(\mathrm{PF}_6)_2$ (Table 1) for the same reasons as those for the trend in $E_{1/2}^{\mathrm{ox}}$. The oxidation of [**1**]$(\mathrm{PF}_6)_2$–[**3**]$(\mathrm{PF}_6)_2$ is reversible on the time scale of electrochemical experiments, while reduction is only reversible for [**1**]$(\mathrm{PF}_6)_2$ and [**2**]$(\mathrm{PF}_6)_2$ on this time scale. The reduction of [**3**]$(\mathrm{PF}_6)_2$ seems to be only quasireversible.[35,36,46] Thus, for all complexes sufficient reversibility in oxidation and reduction processes is given for the application in LECs.

HOMO and LUMO energies of emitting compounds [**1**]$(\mathrm{PF}_6)_2$–[**3**]$(\mathrm{PF}_6)_2$ were estimated from electrochemical redox potentials (Table 1) and are depicted in Figure 3.[61] The parent $[\mathrm{Ru(tpy)_2}]^{2+}$ complex has a HOMO–LUMO energy gap of ΔE = 2.59 eV with E_{HOMO} = –6.00 eV and E_{LUMO} = –3.41 eV.[23] The effect of donor–acceptor substitution in [**1**]$(\mathrm{PF}_6)_2$ can be clearly seen as the electron-withdrawing ester group lowers the LUMO energy (E_{LUMO} = –3.54 eV) while the electron-donating amino group raises the HOMO energy (E_{HOMO} = –5.76 eV) resulting in a smaller ΔE = 2.22 eV compared to that of $[\mathrm{Ru(tpy)_2}]^{2+}$. [**2**]$(\mathrm{PF}_6)_2$ and [**3**]$(\mathrm{PF}_6)_2$ have lower HOMO and LUMO energies than [**1**]$(\mathrm{PF}_6)_2$ because of the strong electron-donating effect of the primary amino group present in [**1**]$(\mathrm{PF}_6)_2$.[35–37,46] [**3**]$(\mathrm{PF}_6)_2$ has even lower HOMO and LUMO energies than [**2**]$(\mathrm{PF}_6)_2$, which results from the electron-withdrawing character of the additional ester groups on the tpy ligand. The push-pull effect is most pronounced in [**3**]$(\mathrm{PF}_6)_2$, leading to the smallest HOMO–LUMO energy gap in this series (E_{HOMO} = –6.00 eV, E_{LUMO} = –3.83 eV, ΔE = 2.17 eV). HOMO and LUMO energies were also obtained by DFT calculations and are summarized in Figure 3.

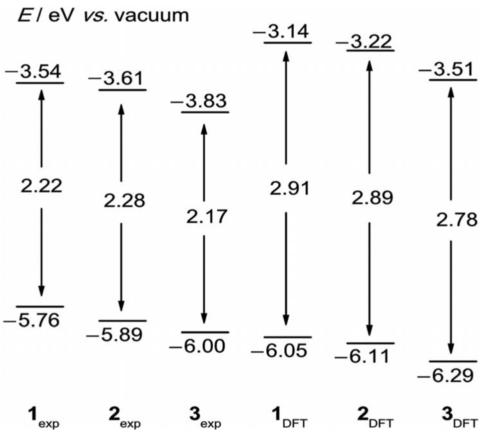

Figure 3. HOMO and LUMO levels of complexes [**1**]$(\mathrm{PF}_6)_2$–[**3**]$(\mathrm{PF}_6)_2$ from experimentally determined redox potentials in $\mathrm{CH_3CN}$[35,46] and from DFT calculations (B3LYP/LANL2DZ, IEFPCM, $\mathrm{CH_3CN}$).

HOMO energies calculated by DFT (B3LYP/LANL2DZ, IEFPCM, $\mathrm{CH_3CN}$) are lower (0.2–0.3 eV) and LUMO energies are higher (0.3–0.4 eV) than values obtained from electrochemical data. Nevertheless, the trend of the HOMO and LUMO energies (E_{HOMO} and E_{LUMO}) is correctly reproduced: [**1**]$^{2+} >$ [**2**]$^{2+} >$ [**3**]$^{2+}$.

The injection of electrons and holes from opposite electrodes leads to the formation of radical species. Electron capture and loss both occur on the doubly charged ruthenium complex cation. Reduction is located at the ester-substituted tpy ligands, while oxidation is essentially confined to the ruthenium center.[35,46–48] Spin densities calculated by DFT are exemplarily depicted for complex [**3**]$^{2+}$ in its reduced and oxidized forms ([**3**]$^{+}$ and [**3**]$^{3+}$; Figures 4a and 4b). The plot illustrates the location of reduction and oxidation processes in [**3**]$^{2+}$. Electron transfer from [**3**]$^{+}$ to [**3**]$^{3+}$ leads to one ^{1,3}MLCT excited state species ^{1,3}[**3**]$^{2+}$ and [**3**]$^{2+}$ in the ground state.[62] The excited ^{1}MLCT state undergoes efficient ISC to the ^{3}MLCT state (Figure 1).[16] Finally, the ^{3}MLCT state emits light upon returning to the singlet ground state [**3**]$^{2+}$ (Figure 1). The spin density of ^{3}[**3**]$^{2+}$ is located on both the ruthenium center and the ester-substituted tpy ligand (Figure 4c), which is in accord with a ruthenium(III) center and a one-electron-reduced tpy ligand.

LECs incorporating [**1**]$(\mathrm{PF}_6)_2$–[**3**]$(\mathrm{PF}_6)_2$ were built with a configuration of ITO/PEDOT:PSS/ruthenium(II) complex/Ag [Figure 5; ITO: indium tin oxide; PEDOT: poly(3,4-ethylenedioxythiophene); PSS: poly(styrenesulfonate)]. PEDOT:PSS was found to increase reproducibility[45] and shows a HOMO energy level of E_{HOMO} = –5.1 eV.[63] Ag was used as cathode material because it greatly improves lifetimes of LECs compared to other electrode materials like Al.[20] Cells were fabricated with and without 20 % (w/w) PMMA in the emitting layer [PMMA: poly(methyl methacrylate)]. PMMA acts as insulator, improves the film

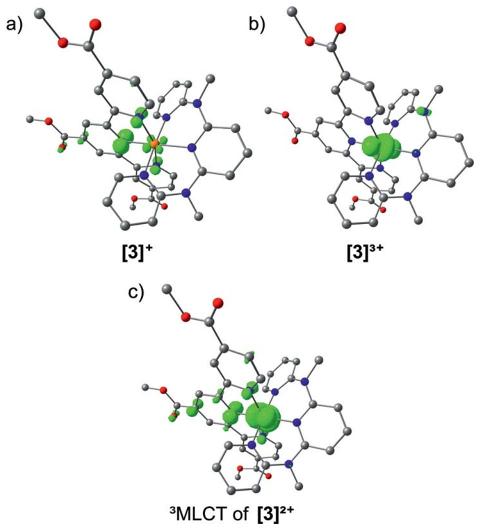

Figure 4. Spin densities of (a) one-electron-reduced complex [**3**]$^+$, (b) one-electron-oxidized complex [**3**]$^{3+}$ and (c) the lowest excited triplet species ^{3}MLCT of [**3**]$^{2+}$ in CH_3CN calculated by DFT (B3LYP/LANL2DZ, IEFPCM, contour value 0.01 a. u.). Hydrogen atoms are omitted.

quality, and increases the distance between ruthenium(II) complexes to avoid self-quenching processes to enhance the EQE and to prolong device lifetimes.[18,20,44,45,64] The PEDOT:PSS and ruthenium(II) complex layers were spin-coated onto an ITO substrate. The Ag cathode was deposited in vacuo by thermal evaporation. The thicknesses of the PEDOT:PSS and the ruthenium complex:PMMA layers were determined by AFM measurements after scratching the layer with a razor (AFM: atomic force microscopy). The thicknesses are 45 ± 5 nm (PEDOT:PSS), 229 ± 19 nm (total thickness of PEDOT:PSS and ruthenium complex without PMMA), and 237 ± 23 nm (total thickness of PEDOT:PSS and ruthenium complex with PMMA). Figure 6 shows a representative AFM image of the scratched LEC with [**1**]$(PF_6)_2$ and PMMA. AFM images for all scratched LECs are depicted in the Supporting Information (Figure S1).

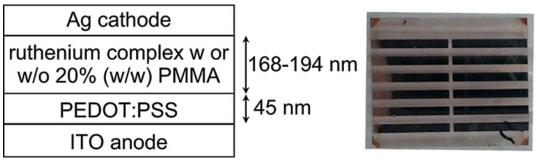

Figure 5. General device structure of the LECs and photograph of the LEC with [**1**]$(PF_6)_2$ without PMMA.

A voltage of 3 V was applied to each cell for at least 10 min. The LEC incorporating complex [**2**]$(PF_6)_2$ (without PMMA) shows red light emission. The other cells did not emit under these conditions. For these cells, a higher voltage on a new pixel was applied in steps of 0.5–1 V until emission was observed. LEC characteristics are summarized in Table 2. The reported voltage is the minimum voltage for which emission is observed, and all other data refer to this voltage. Cells with [**1**]$(PF_6)_2$ without PMMA do not emit up to a voltage of 6 V. When PMMA is present, the LEC with [**1**]$(PF_6)_2$ emits with a turn on voltage of 4 V. The driving voltages are generally a few volts higher for cells with PMMA, which is consistent with the insulating character of PMMA.[20] Emission wavelengths of the devices are fully comparable to the emissions in solution and differ only by $\Delta E = \pm 0.02$ eV (Tables 1 and 2, Figures S2 and S3). [**3**]$(PF_6)_2$ features a slightly redshifted electroluminescence in LECs in the absence of PMMA (Figure S4, Tables 1 and 2). Figure 7a exemplarily depicts the emission spectra of [**2**]$(PF_6)_2$ in CH_3CN and in LECs with and without PMMA.

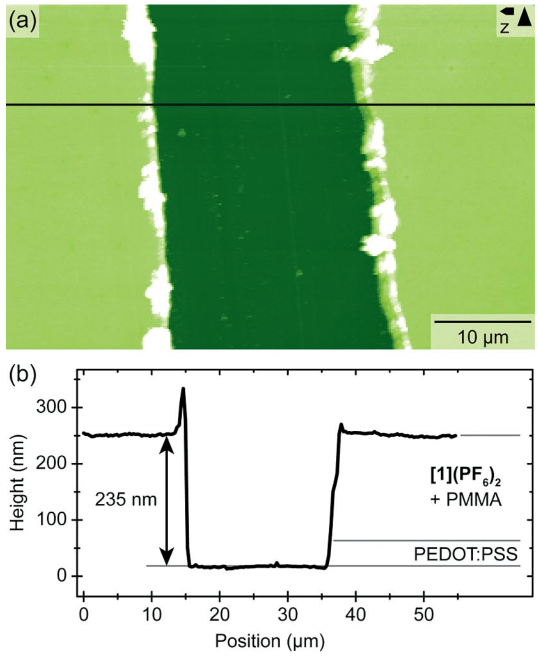

Figure 6. AFM image taken in intermittent contact mode of a scratched PEDOT:PSS/[**1**]$(PF_6)_2$ with PMMA layer. (a) Topographical height scan with indicated cross section. (b) Height profile along the indicated cross section.

The longest emission wavelength maximum ($\lambda_{em,max}$ = 755 nm) was obtained for the LEC with [**3**]$(PF_6)_2$ without PMMA at an applied voltage of 4 V. To the best of our knowledge, this is the longest emission wavelength of a LEC with a mononuclear bis(tridentate) ruthenium(II) complex. The CIE (International Commission on Illumination) coordinates[65] of the emitted light are given in Table 2 and in all cases correspond to deep red light at the edge of the CIE chromaticity diagram. Light intensity, current density, and EQE curves are plotted against time (Supporting Information, Figures S4–S7). Exemplarily, Figure 7b shows the EQE-intensity-current density vs. time plots for the LEC with [**2**]$(PF_6)_2$ without PMMA at an applied voltage of 3 V. All values increase at initial stages until they reach a maximum after a few minutes. Then they slowly decrease as typically observed for this kind of LECs.[44,45] Maximum light emission occurs after $t_{em,max}$ = 2–14 min. Devices with PMMA should have a higher $t_{em,max}$ than devices without PMMA, because PMMA hinders ion migration and forma-

Table 2. LEC device characteristics for complexes [**1**]$(PF_6)_2$–[**3**]$(PF_6)_2$.

	[**1**]$(PF_6)_2$ without PMMA	with PMMA[a]	[**2**]$(PF_6)_2$ without PMMA	with PMMA[a]	[**3**]$(PF_6)_2$ without PMMA	with PMMA[a]
Height of emitting layer /nm	182 ± 16	190 ± 12	168 ± 33	191 ± 31	193 ± 27	194 ± 12
U /V	–	4	3	6	4	5
$\lambda_{em,max,LEC}$ /nm	–	733$^{(6V)}$	731	722	755	745
$\lambda_{em,max,acetonitrile}$ /nm	734	734	729	729	744	744
$t_{em,max}$ /min	–	ca. 11–14	13	2	9	4
L_{max} /cd m^{-2}	–	0.32	1.81	3.36	0.75	0.64
$t_{current,max}$ /min	–	13	31	3	8	8
$I_{d,max}$ /mA cm^{-2}	–	313	103	518	213	231
EQE$_{max}$ /%	–	0.001	0.016	0.028	0.007	0.013
$t_{EQE,max}$ /min	–	14–15	10	1	9	1
CIE coordinates (x, y)	–	0.709, 0.291	0.725, 0.275	0.717, 0.283	0.731, 0.269	0.729; 0.271

[a] 20% (w/w).

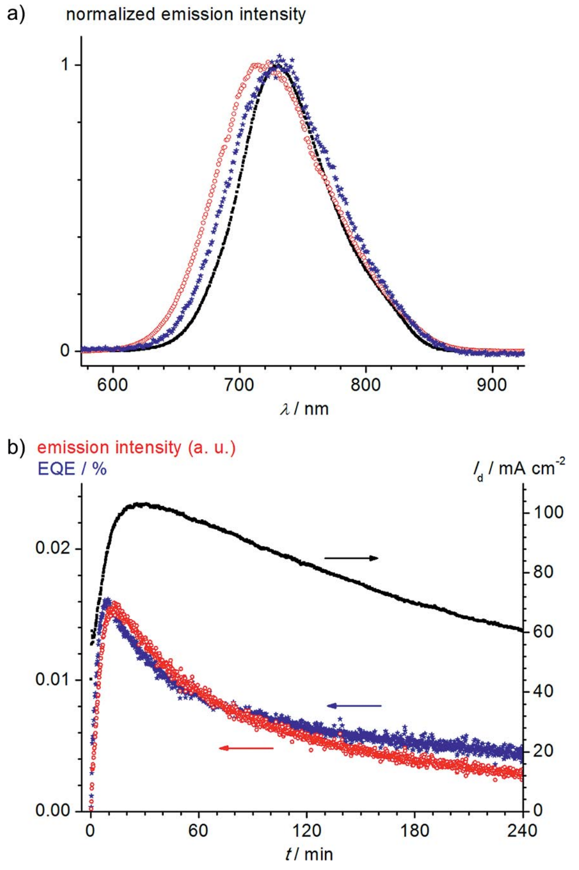

Figure 7. (a) Normalized emission spectra of [**2**]$(PF_6)_2$ (black squares: CH_3CN solution; red hollow circles: LEC with PMMA, 6 V; blue stars: LEC without PMMA, 3 V). (b) Current density (black squares), emission intensity (red hollow circles), and EQE (blue stars) as a function of time in the LEC with [**2**]$(PF_6)_2$ without PMMA at an applied voltage of 3 V.

tion of electric double layers. However, a smaller $t_{em,max}$ value is measured for devices with PMMA than for those without PMMA (see LECs with [**2**]$(PF_6)_2$ and [**3**]$(PF_6)_2$, Table 2). The higher voltages applied for devices with PMMA to compensate the insulating behavior of PMMA might be responsible for this observation.[6] Luminances L were calculated with Equation (1), which assumes that the device was a Lambertian source and a calibrated Si photodiode was placed at an angle normal to the device surface.[66,67]

$$L=\frac{K_m\cdot I_{photodiode}\cdot R^2}{A_{LEC}\cdot A_{photodiode}}\,\frac{\int_{360nm}^{830nm}V(\lambda)\frac{S_{emission}(\lambda)}{S_{responsivity}(\lambda)}d\lambda}{\int_{360nm}^{830nm}S_{emission}(\lambda)d\lambda} \qquad (1)$$

where K_m = 683 lm W^{-1} at 555 nm, I: current, R: distance between LEC and photodiode, A_{LEC}: area of the limiting aperture, $A_{photodiode}$: area of the photodiode, V(λ): photopic response curve, $S_{emission}(\lambda)$: emission spectrum, $S_{responsivity}(\lambda)$: responsivity of the Si photodiode, λ: wavelength).

The highest luminance is L = 3.4 cd m^{-2} for the LEC with [**2**]$(PF_6)_2$ with PMMA at an applied voltage of 6 V. The smaller luminance of LECs with [**1**]$(PF_6)_2$ (L = 0.3 cd m^{-2}) is likely due to the lower luminescence quantum yield of [**1**]$(PF_6)_2$ in solution (Table 2). The lower luminance of [**3**]$(PF_6)_2$ ($L \approx 0.7$ cd m^{-2}) might be due to the small overlap of its NIR emission ($\lambda_{em} \approx 750$ nm) with the human eye response curve (Figure S8). The current density reaches its maximum after $t_{current,max}$ = 3–31 min. For LECs with complex [**3**]$(PF_6)_2$ there is no clear dependency of $t_{current,max}$ on the voltage or the presence of PMMA. In contrast, $t_{current,max}$ values in LECs with [**2**]$(PF_6)_2$ are smaller at high voltages (6 V, 3 min) and larger at lower voltages (3 V, 31 min), which confirms that ion migration is faster at higher voltages.[6] Current densities are in the range I_d = 103–518 mA cm^{-2}, which is consistent with previously reported LECs with a bis(terpyridine)ruthenium(II) complex (ca. 200–300 mA cm^{-2}).[44] As expected, current densities are high for high applied voltages (Table 2). EQE values are 0.001–0.028%. The highest EQE value (0.028%) is obtained for the LEC with [**2**]$(PF_6)_2$ with PMMA. LECs containing [**1**]$(PF_6)_2$ only lead to a small EQE (0.001%), which is probably caused by the smaller solution quantum yield of [**1**]$(PF_6)_2$ relative to those of [**2**]$(PF_6)_2$ and [**3**]$(PF_6)_2$ (Table 1). The maximum EQE of the LEC with [**3**]$(PF_6)_2$ (0.013%) is less than the EQE for the LEC with [**2**]$(PF_6)_2$ (0.028%), which is in contrast to the relative emission quantum yields (Table 1 and Table 2). Possibly this observation can be explained by the redshifted emission of **[3]**$(PF_6)_2$ (λ = 745–755 nm) within the LEC compared to its emission in solution (λ = 744 nm, Figure S5, Table 1 and Table 2). The low-energy emissive state might be prone to enhanced radiationless deactivation according to the energy gap law.[58–60] Interestingly, **[2]**$(PF_6)_2$ shows no redshifted emission in the LECs (Figure 7a, Table 1 and Table 2).

For OLEDs, saturation and quenching effects like triplet–triplet annihilation resulting from high luminescence lifetimes and high current densities can lead to decreasing EQEs.[68] Typically, luminescent emitters are doped into host matrices like PMMA or CBP in order to enhance the EQE [CBP: 4,4′-bis(9-carbazolyl)-2,2′-biphenyl]. For instance, *fac*-Ir$(ppy)_3$ (ppy: 2-phenylpyridine) features lifetimes of 1.4 µs (less than 0.1 w/w% in PMMA) to 630 ns (8 w/w% in CBP), which is regarded sufficiently short to avoid saturation and quenching effects up to a current density of I_d = 1000 mA cm^{-2}.[69,70] Saturation thresholds for the current density also depend on the concentration of the dopant. For PtOEP (PtOEP: 2,3,7,8,12,13,17,18-octaethylporphyrine platinum) with a phosphorescence lifetime of $\tau \approx$ 30 µs, the critical current density rises from I_d = 40 (1 w/w% in CBP) to 800 mA cm^{-2} (16 w/w% in CBP).[71] For neat films of *fac*-Ir$(ppy)_3$ the EQE drops to 0.8% with a concomitant drop in phosphorescence lifetime to $\tau \approx$ 100 ns relative to doped devices.[72] This drop is caused by self-quenching due to Ir$(ppy)_3$–Ir$(ppy)_3$ exciton interactions.[68,73] In neat films of *fac*-Ir$(ppy)_3$ critical current densities for quenching mechanisms like triplet–triplet annihilation are reported to be in the range I_d = 500–1400 mA cm^{-2}.[74,75] However, depending on the device structure, a decrease of EQE in neat films of *fac*-Ir$(ppy)_3$ can already be observed at current densities of $I_d \approx$ 300 mA cm^{-2}.[76] In LECs such quenching effects have also been studied in a few cases apart from the above-mentioned deactivation due to ligand loss and the formation of aqua complexes. The cationic iridium(III) complex [Ir$(ppy)_2$-(pzpy)]PF_6 [pzpy: 2-(1*H*-pyrazol-1-yl)pyridine] was tested in a LEC. The doping of this complex into a PMMA film (5 w/w%) increases its luminescence quantum yield (Φ = 23 → 61%) and lifetime (τ = 1.6 → 3.3 µs). However, luminescence quantum yield and lifetime drop dramatically when going from the doped (5 w/w % in PMMA) to the neat film (Φ = 3%, τ = 0.2 µs), which is attributed to the efficient excited state quenching in the neat film.[77] Quenching effects in LECs also depend on the thickness of the (neat) emitting layer. The EQE of a LEC with $[Ru(bpy)_3](PF_6)_2$ decreases monotonically from 1% for a 192 nm thick complex layer to less than 0.01% for a 46 nm thick layer. The quenching is believed to occur by triplet–triplet annihilation and higher charge carrier densities near the electrode surfaces.[78–80] Self-quenching can be avoided by using sterically demanding substituents.[81,82] As a result of the high local concentration (neat or 80 w/w%), high current densities (up to 518 mA cm^{-2}), and high solution luminescence lifetimes (up to 841 ns), saturation and quenching effects might also be present in our LECs. Indeed, dilution with PMMA has a positive effect on the EQE. In LECs with **[2]**$(PF_6)_2$ and **[3]**$(PF_6)_2$, the EQE is increased by a factor of two by using PMMA.[20,83] The maximum values of the EQE are obtained after 1–15 min. In LECs with PMMA of **[2]**$(PF_6)_2$ and **[3]**$(PF_6)_2$, the maximum EQE is reached after only one minute, which is attributed to the fast ion migration and rapid device degradation due to the high applied voltages of 5–6 V.[6]

Conclusions

Heteroleptic bis(tridentate) ruthenium(II) complexes **[1]**$(PF_6)_2$–**[3]**$(PF_6)_2$ (Figure 1) were used as emitters in LECs with a ITO/PEDOT:PSS/ruthenium(II) complex/Ag device structure. Red to NIR light emission was observed in the solid-state devices (λ_{em} = 722–755 nm; CIE: x = 0.709–0.731, y = 0.291–0.269). To the best of our knowledge, these are the lowest emission energies for LECs containing bis(tridentate) ruthenium(II) complexes. The low-energy emission is favored by the pronounced push-pull character of the complexes, which results in a small HOMO–LUMO gap. PMMA as additive (20% w/w) in the ruthenium complex layer requires higher driving voltages but yields higher external quantum efficiencies. Future perspectives include the steric protection of the ruthenium core by bulkier ligands to prevent a change in the coordination sphere by ligand substitution and self-quenching as well as the usage of other counterions to investigate their effect on the LEC performance.

Experimental Section

General Procedures: Complexes **[1]**$(PF_6)_2$–**[3]**$(PF_6)_2$ were prepared as described previously.[35,36,46,47] Before spin-coating, the complexes were further purified by reversed phase HPLC with a JASCO semipreparative HPLC system with a Reprosil C_{18} column (5 µm) by using CH_3CN/water (96:4, v/v) as an eluent (10 mL min^{-1}) and UV/Vis detection at 502–539 nm. Patterned ITO glass substrates, which were cleaned in an ultrasonic bath, sequentially with acetone, isopropyl alcohol, and deionized water, were treated with UV/O_3 for 10 min before spin-coating. PEDOT:PSS (1:6 weight%, Al 4083; suspension in water; 1.3–1.7% solid content) was filtered (HP, 0.45 µm) and spin-coated (4000 rpm, 30 s, 4 s acceleration) onto the ITO substrate. After drying (1 h, 120 °C under reduced pressure), the substrate was transferred into an argon atmosphere. Ruthenium complexes (10 mg mL^{-1}) and PMMA (0 or 2 mg mL^{-1}, M_W 120000) were dissolved in acetonitrile in an argon atmosphere and spin-coated onto the PEDOT:PSS layer (1000 rpm, 20 s, no acceleration). Silver electrodes were vapor-deposited on the substrates under a pressure of 3×10^{-6} Torr. The current–voltage characteristics were measured by using a source measurement unit (Keithley 236). The luminance and efficiencies were calculated from photocurrent measurement data obtained with a calibrated Si photodiode (Hamamatsu S5227–1010BQ). Electroluminescence spectra of the devices were obtained by an ICCD camera through an ARC 275 monochromator. AFM measurements were conducted in intermittent contact mode with two different instruments: A Veeco Dimension AFM was used for the measurement of the total height of the PEDOT:PSS and the emitting layers and a XE-100 AFM was used to measure the thickness of the PEDOT:PSS layer. The spin-coated PEDOT:PSS and PEDOT:PSS-ruthenium complex layers were scratched with a razor, and the thickness of the layers was determined by the measured height differences.

DFT Studies: The DFT calculations were carried out with the *Gaussian 09*/DFT[84] series of programs. The LANL2DZ basis set[84] was used in the B3LYP formulation of DFT. No symmetry constraints were imposed on the molecules. The presence of energy minima was checked by analytical frequency calculations. The integral-equation-formalism polarizable continuum model (IEFPCM, CH_3CN) was employed for solvent modeling in all calculations. All calculations were performed without explicit counterions and solvent molecules.

Supporting Information (see footnote on the first page of this article): AFM images of scratched PEDOT:PSS/ruthenium complex:PMMA layers; emission spectra of [**1**]$(PF_6)_2$ and [**3**]$(PF_6)_2$ in solution and in LECs; current density vs. EQE intensity curves of the LECs; human eye response curve and emission spectra of [**1**]$(PF_6)_2$–[**3**]$(PF_6)_2$ in LECs.

Acknowledgments

This work was supported by the Deutsche Forschungsgemeinschaft (DFG) [International Research Training Group: Self-Organized Materials for Optoelectronics (IRTG 1404)].

---

[1] H. Xiang, J. Cheng, X. Ma, X. Zhou, J. J. Chruma, *Chem. Soc. Rev.* **2013**, *42*, 6128–6185.
[2] R. D. Costa, E. Ortí, H. J. Bolink, F. Monti, G. Accorsi, N. Armaroli, *Angew. Chem.* **2012**, *124*, 8300–8334; *Angew. Chem. Int. Ed.* **2012**, *51*, 8178–8211.
[3] R. D. Costa, E. Ortí, H. J. Bolink, *Pure Appl. Chem.* **2011**, *83*, 2115–2128.
[4] J. Slinker, D. Bernards, P. L. Houston, H. D. Abruña, S. Bernhard, G. G. Malliaras, *Chem. Commun.* **2003**, *19*, 2392–2399.
[5] E. Holder, B. M. W. Langeveld, U. S. Schubert, *Adv. Mater.* **2005**, *17*, 1109–1121.
[6] J. D. Slinker, J. Rivnay, J. S. Moskowitz, J. B. Parker, S. Bernhard, H. D. Abruña, G. G. Malliaras, *J. Mater. Chem.* **2007**, *17*, 2976–2988.
[7] Q. Pei, G. Yu, C. Zhang, Y. Yang, A. J. Heeger, *Science* **1995**, *269*, 1086–1088.
[8] Q. Pei, Y. Yang, G. Yu, C. Zhang, A. J. Heeger, *J. Am. Chem. Soc.* **1996**, *118*, 3922–3929.
[9] A. P. Monkman, *ISRN Mater. Sci.* **2013**, DOI: 10.1155/2013/670130.
[10] J. Wang, A. Chepelianskii, F. Gao, N. C. Greenham, *Nat. Commun.* **2012**, *3*, DOI: 10.1038/ncomms2194.
[11] A. Köhler, H. Bässler, *Mater. Sci. Eng.* **2009**, *R66*, 71–109.
[12] H. Yersin, *Highly Efficient OLEDs with Phosphorescent Materials*, Wiley-VCH, Weinheim, Germany, **2008**.
[13] J.-K. Lee, D. S. Yoo, E. S. Handy, M. F. Rubner, *Appl. Phys. Lett.* **1996**, *69*, 1686–1688.
[14] S. Campagna, F. Puntoriero, F. Nastasi, G. Bergamini, V. Balzani, *Top. Curr. Chem.* **2007**, *280*, 117–214.
[15] J. R. Lakowicz, *Principles of Fluorescence Spectroscopy*, Springer, New York, **2006**.
[16] A. Juris, V. Balzani, F. Barigelletti, S. Campagna, P. Belser, A. von Zelewsky, *Coord. Chem. Rev.* **1988**, *84*, 85–277.
[17] C.-Y. Liu, A. J. Bard, *Appl. Phys. Lett.* **2005**, *87*, 061110.
[18] H. Rudmann, S. Shimada, M. F. Rubner, *J. Am. Chem. Soc.* **2002**, *124*, 4918–4921.
[19] S. Xun, J. Zhang, X. Li, D. Ma, Z. Y. Wang, *Synth. Met.* **2008**, *158*, 484–488.
[20] H. Rudmann, M. F. Rubner, *J. Appl. Phys.* **2001**, *90*, 4338–4345.
[21] C. Fu, M. Wenzel, E. Treutlein, K. Harms, E. Meggers, *Inorg. Chem.* **2012**, *51*, 10004–10011.
[22] E. Meggers, *Chem. Eur. J.* **2010**, *16*, 752–758.
[23] M. Maestri, N. Armaroli, V. Balzani, E. C. Constable, A. M. W. Cargill Thompson, *Inorg. Chem.* **1995**, *34*, 2759–2767.
[24] R. Hogg, R. G. Wilkins, *J. Chem. Soc.* **1962**, 341–350.
[25] R. H. Holyer, C. D. Hubbard, S. F. A. Kettle, R. G. Wilkins, *Inorg. Chem.* **1966**, *5*, 622–625.
[26] A. Reynald, E. Palomares, *Eur. J. Inorg. Chem.* **2011**, *29*, 4509–4526.
[27] C.-W. Hsu, S.-T. Ho, K.-L. Wu, Y. Chi, S.-H. Liu, P.-T. Chou, *Energy Environ. Sci.* **2012**, *5*, 7549–7554.
[28] J.-F. Yin, M. Velayudham, D. Bhattacharya, H.-C. Lin, K.-L. Lu, *Coord. Chem. Rev.* **2012**, *256*, 3008–3035.
[29] B. Schulze, D. Escudero, C. Friebe, R. Siebert, H. Görls, S. Sinn, M. Thomas, S. Mai, J. Popp, B. Dietzek, L. González, U. S. Schubert, *Chem. Eur. J.* **2012**, *18*, 4010–4025.
[30] J. D. Slinker, J.-S. Kim, S. Flores-Torres, J. H. Delcamp, H. D. Abruña, R. H. Friend, G. G. Malliaras, *J. Mater. Chem.* **2007**, *17*, 76–81.
[31] L. J. Soltzberg, J. D. Slinker, S. Flores-Torres, D. A. Bernards, G. G. Malliaras, H. D. Abruña, J.-S. Kim, R. H. Friend, M. D. Kaplan, V. Goldberg, *J. Am. Chem. Soc.* **2006**, *128*, 7761–7764.
[32] G. Kalyuzhny, M. Buda, J. McNeill, P. Barbara, A. J. Bard, *J. Am. Chem. Soc.* **2003**, *125*, 6272–6283.
[33] J.-P. Sauvage, J.-P. Collin, J.-C. Chambron, S. Guillerez, C. Coudret, *Chem. Rev.* **1994**, *94*, 993–1019.
[34] Y. Liu, R. Hammitt, D. A. Lutterman, R. P. Thummel, C. Turro, *Inorg. Chem.* **2007**, *46*, 6011–6021.
[35] K. Heinze, K. Hempel, M. Beckmann, *Eur. J. Inorg. Chem.* **2006**, *10*, 2040–2050.
[36] K. Heinze, K. Hempel, S. Tschierlei, M. Schmitt, J. Popp, S. Rau, *Eur. J. Inorg. Chem.* **2009**, *21*, 3119–3126.
[37] K. Heinze, K. Hempel, A. Breivogel, *Z. Anorg. Allg. Chem.* **2009**, *635*, 2541–2549.
[38] K. Lashgari, M. Kritikos, R. Norrestam, T. Norrby, *Acta Crystallogr., Sect. C* **1999**, *55*, 64–67.
[39] M. Abrahamsson, M. Jäger, T. Österman, L. Eriksson, P. Persson, H.-C. Becker, O. Johansson, L. Hammarström, *J. Am. Chem. Soc.* **2006**, *128*, 12616–12617.
[40] G. A. Parada, L. A. Fredin, M.-P. Santoni, M. Jäger, R. Lomoth, L. Hammarström, O. Johansson, P. Persson, S. Ott, *Inorg. Chem.* **2013**, *52*, 5128–5137.
[41] M. Abrahamsson, M. Jäger, R. J. Kumar, T. Österman, P. Persson, H.-C. Becker, O. Johansson, L. Hammarström, *J. Am. Chem. Soc.* **2008**, *130*, 15533–15542.
[42] F. Schramm, V. Meded, H. Fliegl, K. Fink, O. Fuhr, Z. Qu, W. Klopper, S. Finn, T. E. Keyes, M. Ruben, *Inorg. Chem.* **2009**, *48*, 5677–5684.
[43] W. Y. Ng, X. Gong, W. K. Chan, *Chem. Mater.* **1999**, *11*, 1165–1170.
[44] H. J. Bolink, L. Cappelli, E. Coronado, P. Gaviña, *Inorg. Chem.* **2005**, *44*, 5966–5968.
[45] H. J. Bolink, E. Coronado, R. D. Costa, P. Gaviña, E. Ortí, S. Tatay, *Inorg. Chem.* **2009**, *48*, 3907–3909.
[46] A. Breivogel, M. Meister, C. Förster, F. Laquai, K. Heinze, *Chem. Eur. J.* **2013**, *19*, 13745–13760.
[47] A. Breivogel, C. Förster, K. Heinze, *Inorg. Chem.* **2010**, *49*, 7052–7056.
[48] A. Breivogel, K. Hempel, K. Heinze, *Inorg. Chim. Acta* **2011**, *374*, 152–162.
[49] H. Komatsu, K. Yoshihara, H. Yamada, Y. Kimura, A. Son, S.-i. Nishimoto, K. Tanabe, *Chem. Eur. J.* **2013**, *19*, 1971–1977.
[50] M. R. Gill, J. A. Thomas, *Chem. Soc. Rev.* **2012**, *41*, 3179–3192.
[51] P. Ceroni, *Chem. Eur. J.* **2011**, *17*, 9560–9564.
[52] T. N. Singh-Rachford, F. N. Castellano, *Coord. Chem. Rev.* **2010**, *254*, 2560–2573.

[53] W. Wu, S. Ji, W. Wu, J. Shao, H. Guo, T. D. James, J. Zhao, *Chem. Eur. J.* **2012**, *18*, 4953–4964.

[54] P. Hanczyc, B. Norden, M. Samoc, *Dalton Trans.* **2012**, *41*, 3123–3125.

[55] M. D. Ward, *Coord. Chem. Rev.* **2007**, *251*, 1663–1677.

[56] S. V. Eliseeva, J.-C. G. Bünzli, *Chem. Soc. Rev.* **2010**, *39*, 189–227.

[57] J. C. G. Bünzli, S. V. Eliseeva, *J. Rare Earths* **2010**, *28*, 824–842.

[58] T. J. Meyer, *Pure Appl. Chem.* **1986**, *58*, 1193–1206.

[59] J. V. Caspar, T. J. Meyer, *J. Am. Chem. Soc.* **1983**, *105*, 5583–5590.

[60] J. V. Caspar, T. J. Meyer, *J. Phys. Chem.* **1983**, *87*, 952–957.

[61] E(vacuum) /eV = –4.68 – E(SCE) /V = –5.08 – E(Fc/Fc$^+$) /V.

[62] F. Bolletta, S. Bonafede, *Pure Appl. Chem.* **1986**, *58*, 1229–1232.

[63] F. Xu, J.-Y. Kwon, J.-H. Kim, H. U. Kim, J. M. Lim, H. Cho, C. Lee, J. Lee, J.-I. Lee, D.-H. Hwang, *Synth. Met.* **2012**, *162*, 1421–1428.

[64] H. J. Bolink, L. Cappelli, E. Coronado, M. Grätzel, Md. K. Nazeeruddin, *J. Am. Chem. Soc.* **2006**, *128*, 46–47.

[65] International Commission on Illumination (CIE), 1931.

[66] P. Toivanen, J. Hovila, P. Kärhä, E. Ikonen, *Metrologia* **2000**, *37*, 527–530.

[67] P. Toivanen, P. Kärhä, F. Manoochehri, E. Ikonen, *Metrologia* **2000**, *37*, 131–140.

[68] H. Yersin, A. F. Rausch, R. Czerwieniec, T. Hofbeck, T. Fischer, *Coord. Chem. Rev.* **2011**, *255*, 2622–2652.

[69] N. C. Giebink, S. R. Forrest, *Phys. Rev. B* **2008**, *77*, 235215.

[70] T. Hofbeck, H. Yersin, *Inorg. Chem.* **2010**, *49*, 9290–9299.

[71] M. A. Baldo, C. Adachi, S. R. Forrest, *Phys. Rev. B* **2000**, *62*, 10967–10977.

[72] M. A. Baldo, M. E. Thompson, S. R. Forrest, *Pure Appl. Chem.* **1999**, *71*, 2095–2106.

[73] C. Adachi, M. A. Baldo, S. R. Forrest, M. E. Thompson, *Appl. Phys. Lett.* **2000**, *77*, 904–906.

[74] J. Kalinowski, J. Mżyk, F. Meinardi, R. Tubino, M. Cocchi, D. Virgili, *J. Appl. Phys.* **2005**, *98*, 063532.

[75] J. Kalinowski, W. Stampor, J. Szmytkowski, D. Virgili, M. Cocchi, V. Fattori, C. Sabatini, *Phys. Rev. B* **2006**, *74*, 085316.

[76] M. A. Baldo, S. Lamansky, P. E. Burrows, M. E. Thompson, S. R. Forrest, *Appl. Phys. Lett.* **1999**, *75*, 4–6.

[77] L. He, L. Duan, J. Qiao, R. Wang, P. Wei, L. Wang, Y. Qiu, *Adv. Funct. Mater.* **2008**, *18*, 2123–2131.

[78] K. W. Lee, J. D. Slinker, A. A. Gorodetsky, S. Flores-Torres, H. D. Abruña, P. L. Houston, G. G. Malliaras, *Phys. Chem. Chem. Phys.* **2003**, *5*, 2706–2709.

[79] S. Bernhard, X. Gao, G. G. Malliaras, H. D. Abruña, *Adv. Mater.* **2002**, *14*, 433–436.

[80] N. R. Armstrong, R. M. Wightman, E. M. Gross, *Annu. Rev. Phys. Chem.* **2001**, *52*, 391–422.

[81] P. Dreyse, B. Loeb, M. Soto-Arriaza, D. Tordera, E. Ortí, J. J. Serrano-Pérez, H. J. Bolink, *Dalton Trans.* **2013**, *42*, 15502–15513.

[82] S. Bernhard, J. A. Barron, P. L. Houston, H. D. Abruña, J. L. Ruglovksy, X. Gao, G. G. Malliaras, *J. Am. Chem. Soc.* **2002**, *124*, 13624–13628.

[83] D. W. Thompson, C. N. Fleming, B. D. Myron, T. J. Meyer, *J. Phys. Chem. B* **2007**, *111*, 6930–6941.

[84] M. J. Frisch, G. W. Trucks, H. B. Schlegel, G. E. Scuseria, M. A. Robb, J. R. Cheeseman, G. Scalmani, V. Barone, B. Mennucci, G. A. Petersson, H. Nakatsuji, M. Caricato, X. Li, H. P. Hratchian, A. F. Izmaylov, J. Bloino, G. Zheng, J. L. Sonnenberg, M. Hada, M. Ehara, K. Toyota, R. Fukuda, J. Hasegawa, M. Ishida, T. Nakajima, Y. Honda, O. Kitao, H. Nakai, T. Vreven, J. A. Montgomery Jr., J. E. Peralta, F. Ogliaro, M. Bearpark, J. J. Heyd, E. Brothers, K. N. Kudin, V. N. Staroverov, R. Kobayashi, J. Normand, K. Raghavachari, A. Rendell, J. C. Burant, S. S. Iyengar, J. Tomasi, M. Cossi, N. Rega, J. M. Millam, M. Klene, J. E. Knox, J. B. Cross, V. Bakken, C. Adamo, J. Jaramillo, R. Gomperts, R. E. Stratmann, O. Yazyev, A. J. Austin, R. Cammi, C. Pomelli, J. W. Ochterski, R. L. Martin, K. Morokuma, V. G. Zakrzewski, G. A. Voth, P. Salvador, J. J. Dannenberg, S. Dapprich, A. D. Daniels, O. Farkas, J. B. Foresman, J. V. Ortiz, J. Cioslowski, D. J. Fox *Gaussian 09*, revision A.02, Gaussian, Inc., Wallingford CT, **2009**.

Received: September 19, 2013

9.8 Anchor-Functionalized Push-Pull-Substituted Bis(tridentate) Ruthenium(II) Polypyridine Chromophores: Photostability and Evaluation as Photosensitizers

A. Breivogel, S. Wooh, J. Dietrich, T. Y. Kim, Y. S. Kang, K. Char, K. Heinze, *Eur. J. Inorg. Chem.* **2014**, 2720–2734.

DOI: 10.1002/ejic.201402091

DOI:10.1002/ejic.201402091

Anchor-Functionalized Push-Pull-Substituted Bis(tridentate) Ruthenium(II) Polypyridine Chromophores: Photostability and Evaluation as Photosensitizers

Aaron Breivogel,[a] Sanghyuk Wooh,[b] Jan Dietrich,[a]
Tea Yon Kim,[c] Yong Soo Kang,[c] Kookheon Char,[b] and
Katja Heinze*[a]

Keywords: Ruthenium / Tridentate ligands / Sensitizers / Photochemistry / N ligands

Stable push-pull substituted heteroleptic bis(tridentate) ruthenium(II) polypyridine complexes with COOH or 2,2′-bipyridine anchor groups have been prepared and characterized by ^{1}H, ^{13}C and ^{15}N NMR 1D and 2D spectroscopy, infrared spectroscopy, elemental analysis, high-resolution ESI mass spectrometry, electrochemistry, UV/Vis absorption spectroscopy, luminescence spectroscopy, and density functional calculations. The complexes feature a pronounced electronic directionality and high absorption wavelengths up to $\lambda_{\max}$ = 544 nm extending to 720 nm as a result of favorable push-pull substitutions. A remarkable photostability in the presence of water and coordinating ions (I^-) was discovered for the tridentate complexes when compared with the standard ruthenium sensitizer N719 and tris(bidentate) [Ru(bpy)$_3$]-(PF$_6$)$_2$, which are highly photolabile under the same conditions (photodissociation/photosubstitution). The complexes were studied as photosensitizers in dye-sensitized solar cells. The incident photon-to-current conversion efficiency follows the absorption spectra into the NIR region. However, the high positive charge of the complexes (2+) favors the recombination of the injected electrons with I_3^- of the redox electrolyte, which is evidenced by high dark currents and short electron recombination lifetimes, leading to low cell performances compared with cells with the negatively charged N719 dye.

Introduction

Dye-sensitized solar cells (DSSCs) were introduced in 1991 by O'Regan and Grätzel[1] and provide a promising class of light-to-energy conversion systems.[2–8] In a typical DSSC, molecular dyes are adsorbed onto a nanoporous inorganic semiconductor electrode (e.g., TiO$_2$, ZnO). After being excited by light, the dyes inject electrons into the conduction band of the semiconductor. A redox electrolyte (typically I^-/I_3^-) regenerates the dye and diffuses to the counter electrolyte where positive charges are collected. DSSCs are an attractive alternative to conventional silicon-based solar cells due to low-cost of fabrication and the possibility to finely tune the sensitizers, cell morphologies, and redox mediators.[2–8] Currently, the highest power conversion efficiency amounts to η = 12.3 % under full air mass 1.5 (AM 1.5) solar light using a designed zinc porphyrin as sensitizer in concert with an organic dye as cosensitizer.[9] Polypyridine complexes of ruthenium(II) have emerged as a prominent class of sensitizers for DSSCs due to their useful photophysical properties,[10] high cell efficiencies, and long-term stabilities.[2–8] Well-known standard ruthenium(II) sensitizers for DSSCs are N719 (Bu$_4$N)$_2$[Ru(Hdcbpy)$_2$-(NCS)$_2$][11,12] and the so-called black dye (Bu$_4$N)$_3$-[Ru(Htctpy)(NCS)$_3$],[13] reaching solar cell efficiencies of η = 10–11 % under full AM 1.5 (dcbpy = 4,4′-dicarboxy-2,2′-bipyridine, tctpy = 4,4′,4′′-tricarboxy-2,2′;6′,2′′-terpyridine). However, the presence of monodentate ligands in these complexes is a key detrimental factor reducing the long-term stability in DSSCs. Monodentate ligands, such as NCS$^-$ and pyridine, support thermal- and photo-induced isomerization and ligand-exchange reactions, leading to dye species with lower cell efficiencies.[14–21] The replacement of monodentate ligands in DSSCs is realized in complexes with tris(bidentate) and bis(tridentate) coordination and offers a better opportunity for tuning the sensitizer properties.[5,22] The two NCS$^-$ ligands of N719 can be replaced by one bidentate cyclometalated 2-phenylpyridine ligand, reaching DSSC efficiencies of η = 10.1 %.[5,20,23] In another

---

[a] Institute of Inorganic Chemistry and Analytical Chemistry,
Johannes Gutenberg University of Mainz,
Duesbergweg 10–14, 55128 Mainz, Germany
E-mail: katja.heinze@uni-mainz.de
http://www.ak-heinze.chemie.uni-mainz.de/
[b] The National Creative Research Initiative Center for Intelligent Hybrids, The WCU Program on Chemical Convergence for Energy and Environment, School of Chemical and Biological Engineering, Seoul National University,
1 Gwanak-ro, Gwanak-gu, Seoul 151-744, Korea
[c] The WCU Department of Energy Engineering and Center for Next Generation Dye-Sensitized Solar Cells, Hanyang University,
222 Wangsimni-ro, Seongdong-gu, Seoul 133-791, Korea

Supporting information for this article is available on the WWW under http://dx.doi.org/10.1002/ejic.201402091.

strategy, a NCS⁻-free complex with bidentate 2-pyridylpyrazole ligands achieves an efficiency of η = 9.5% in a DSSC.[4,24] However, even ruthenium complexes with bidentate ligands such as 4,4′-bi-1,2,3-triazolate suffer from photoinduced ligand loss or photoisomerization.[25,26] Ligand loss is also known for $[Ru(bpy)_3]^{2+}$ in light-emitting electrochemical cells, leading to degradation products such as $[Ru(bpy)_2(H_2O)_2]^{2+}$ and the oxido-bridged ruthenium(III) dimer $[(Ru(bpy)_2(H_2O))_2(\mu\text{-}O)]^{4+}$.[27–30] Moreover, tris(bidentate) complexes are chiral, thus diastereomers can be formed in the case of unsymmetrically substituted ligands, leading to complex synthetic procedures.[3,31,32] The presence of stereoisomers can be circumvented with bis(tridentate) complexes such as $[Ru(tpy)_2]^{2+}$, which are achiral, even when the ligands are functionalized unsymmetrically in the 4′-positions (tpy = 2,2′;6′,2′′-terpyridine).[33] Tridentate chelate complexes are expected to feature higher photo- and chemical-stability compared with bidentate chelates.[34,35] The drawback of $[Ru(tpy)_2]^{2+}$ is its fast excited state deactivation via ^{3}MC states with a time constant of τ = 0.1–0.2 ns,[36–38] thus competing with electron injection into semiconductor electrodes (MC = metal-centered).[39,40] The detrimental effect of radiationless deactivation via ^{3}MC states can be avoided by substitution at the 4′-positions of tpy. In 4′-substituted $[(EtOOC\text{-}tpy)Ru(tpy)]^{2+}$, the electron-withdrawing ester group stabilizes the ^{3}MLCT state with respect to the ^{3}MC state, thus radiationless deactivation via the latter state is hampered (MLCT = metal-to-ligand charge transfer).[41,42] This is reflected by the enhanced excited state lifetime of τ = 32 ns, which is sufficiently long for quantitative charge injection into TiO_2.[39,40] The ester group also reduces the HOMO–LUMO gap because it effectively reduces the LUMO energy. This is beneficial due to the redshift of the absorption maximum (λ = 485 nm) compared with $[Ru(tpy)_2]^{2+}$ (λ = 476 nm), thus enabling the harvest of lower energy photons.[38,42] The carboxylic acid analogue $[(HOOC\text{-}tpy)Ru(tpy)]^{2+}$ has been incorporated into DSSCs. Efficiencies were not reported, but the incident photon-to-current conversion efficiency (IPCE) shows a maximum of 35% at λ = 500 nm.[43] The phosphonic acid derivative $[(H_2O_3P\text{-}tpy)Ru(tpy)]^{2+}$ reaches only a low DSSC efficiency of η = 0.17%, which has been attributed to the low injection yield.[44] Push-pull substituted $[(HOOC\text{-}tpy)Ru(tpy\text{-}NH_2)]^{2+}$ ([**4**]$(PF_6)_2$, Figure 1) features both an electron-withdrawing and an electron-donating moiety. The excited state lifetime is further enhanced (τ = 34 ns) and the absorption is redshifted (λ = 502 nm) because the electron-donating NH_2 group destabilizes both the HOMO and the ^{3}MC state.[41,45–47] Asymmetric substitution with a carboxylic acid and an amino group offers the possibility for orthogonal functionalization. Bis(tridentate) ruthenium(II) complexes have been used in donor-acceptor arrays with photoinduced charge-separated states.[48] Complex [**4**]$(PF_6)_2$ has been covalently linked to ferrocene, Pt^{II} and Re^{I} complexes, which show photoinduced electron transfer.[45,49,50] Light-induced charge separation has been achieved by using [**4**]$(PF_6)_2$ as a chromophore in a donor-chromophore-acceptor nanocomposite with triphenylamine as donor and ZnO nanorods as acceptor.[51] The push-pull character of [**4**]$(PF_6)_2$ can be further intensified by the inclusion of additional electron-withdrawing groups on the acceptor ligand as well as electron-donating groups on the donor ligand. This has been shown by our group employing a tpy acceptor ligand containing one or three ester groups and a ddpd donor ligand featuring two or three amine functionalities (ddpd = *N*,*N*′-dimethyl-*N*,*N*′-dipyridin-2-ylpyridine-2,6-diamine). The absorption is redshifted up to λ = 546 nm, while maintaining excited state lifetimes of $\tau > 100$ ns in spite of increased radiationless deactivation due to the energy gap law.[41,52–54] In these dyes, a directional electron transfer is enforced by spatially separated and orthogonal frontier orbitals.[41,55]

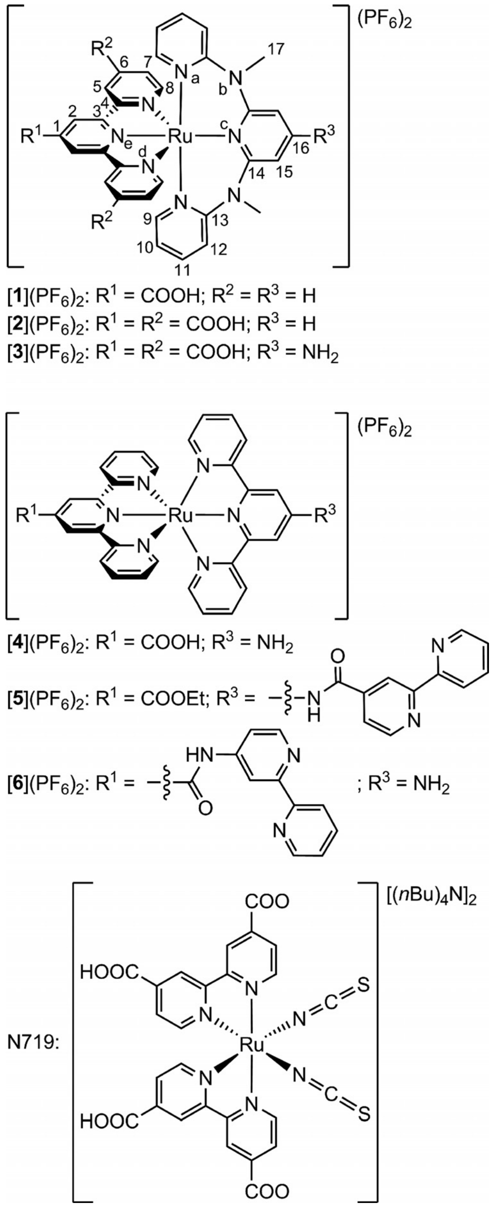

[**1**]$(PF_6)_2$: R^1 = COOH; R^2 = R^3 = H

[**2**]$(PF_6)_2$: R^1 = R^2 = COOH; R^3 = H

[**3**]$(PF_6)_2$: R^1 = R^2 = COOH; R^3 = NH_2

[**4**]$(PF_6)_2$: R^1 = COOH; R^3 = NH_2

[**5**]$(PF_6)_2$: R^1 = COOEt; R^3 =

[**6**]$(PF_6)_2$: R^1 = ; R^3 = NH_2

Figure 1. Bis(tridentate) ruthenium(II) oligopyridine complexes [**1**]$(PF_6)_2$ – [**6**]$(PF_6)_2$ and reference dye N719. Atom numbering for NMR assignments.

Cyclometalation is another striking tool that can be used to create a push-pull situation in ruthenium(II) complexes and to shift the absorption further into the red spectral region. Spatially separated frontier orbitals are obtained when the cyclometalated functionality is situated face to face with the anchoring ligand with the HOMO located on the cyclometalated ligand and the metal center while the LUMO is located on the anchoring ligand.[56] The donor–acceptor motive was also realized by Berlinguette et al. in a bis(tridentate) ruthenium(II) complex with tctpy as acceptor ligand and a cyclometalating pbpy ligand with a triarylamine substituent (pbpy = 6-phenyl-2,2′-bipyridine). After the injection of an electron into TiO$_2$, the positive charge is shifted away from the TiO$_2$ surface towards the appended triarylamine moiety, thus avoiding charge recombination and reaching a DSSC efficiency of $\eta = 8.0\%$.[57] Recently, bis(tridentate) ruthenium(II) complexes with a dianionic donor ligand [2,6-bis(5-pyrazolyl)pyridine] and tctpy acceptor ligand have been presented in DSSCs with efficiencies up to $\eta = 10.7\%$.[58,59] The use of ruthenium(II) complexes with two tridentate ligands has a favorable effect on the long-term stability of DSSCs.[4,60,61]

In this work, we present the synthesis of three novel, push-pull substituted bis(tridentate) ruthenium(II) complexes [**1**](PF$_6$)$_2$ – [**3**](PF$_6$)$_2$ together with three previously reported, push-pull-substituted bis(tridentate) complexes [**4**](PF$_6$)$_2$ – [**6**](PF$_6$)$_2$ and their performance in DSSCs in comparison with the standard ruthenium(II) sensitizer N719 (Figure 1).[45,49,50,62] Binding to TiO$_2$ occurs through carboxylic acid/carboxylate groups {[**1**](PF$_6$)$_2$ – [**4**](PF$_6$)$_2$, N719} and for the first time complexes with bidentate 2,2′-bpy as anchor {[**5**](PF$_6$)$_2$, [**6**](PF$_6$)$_2$} were used in DSSCs. Dicarboxylic acid[63] and bidentate acetylacetonato[64,65] or catecholato[39,66,67] anchors have been employed previously. Bidentate bpy anchors might be favored compared with monodentate pyridine anchors because dye desorption from the semiconductor is a critical issue for the long-term stability of DSSCs.[68] The photostability under irradiation (λ_{exc} = 400 and 500 nm) of ethyl esters [**1^{Et}**](PF$_6$)$_2$ and [**4^{Et}**](PF$_6$)$_2$ was studied and compared to that of [Ru(bpy)$_3$](PF$_6$)$_2$ and N719. In addition, the stability of the ruthenium(III) complexes [**1^{Et}**]$^{3+}$, [**4^{Et}**]$^{3+}$, [Ru(bpy)$_3$]$^{3+}$, and oxidized N719 was investigated by spectroelectrochemical measurements.

Results and Discussion

Synthesis and Analytical Characterization

The ester analogues of complexes [**1**](PF$_6$)$_2$ – [**3**](PF$_6$)$_2$ as well as complexes [**4**](PF$_6$)$_2$ – [**6**](PF$_6$)$_2$ have been reported previously.[41,45,49,50,55] Complexes [**1**](PF$_6$)$_2$ and [**2**](PF$_6$)$_2$ have been synthesized by hydrolysis of their respective ester derivatives with sulfuric acid.[41,55] [**3**](PF$_6$)$_2$ has been obtained in a microwave-assisted reaction of [(MeOOC)$_3$-tpy]RuCl$_3$[13,69–71] and ddpd-4′-phthalimide[41] in methanol with *N*-ethylmorpholine as reducing agent. Subsequently, the ester groups and the phthalimide protecting group were hydrolyzed in a single step by acidic treatment. Finally, [**1**](PF$_6$)$_2$ – [**3**](PF$_6$)$_2$ were precipitated by addition of [NH$_4$](PF$_6$) and obtained as (PF$_6$)$^-$ salts. Complexes [**1**](PF$_6$)$_2$ – [**3**](PF$_6$)$_2$ were characterized by ESI and HR-ESI mass spectrometry, infrared, ^{1}H, ^{13}C and ^{15}N NMR 1D and 2D spectroscopy, and by elemental analysis. The ion peaks for $[M - PF_6]^+$ and $[M - 2PF_6]^{2+}$ were found in the ESI mass spectra of [**1**](PF$_6$)$_2$ – [**3**](PF$_6$)$_2$ with *m*/*z* values and isotope distributions being in excellent accord with theoretical values. Additionally, HRMS (ESI) clearly confirmed the molecular formulae of all complex cations (see Experimental Section). ^{1}H, ^{13}C and ^{15}N NMR spectroscopic data of [**1**](PF$_6$)$_2$ – [**3**](PF$_6$)$_2$ corroborate that the structural integrity remained intact during the harsh synthetic conditions (reflux, acidic medium) by showing only a single stereoisomer (*meridional*), similar to their ester derivatives (Tables S1–S3 in the Supporting Information; see Figure 1 for atom assignment).[41,55] NMR spectra of [**1**](PF$_6$)$_2$ – [**3**](PF$_6$)$_2$ do not differ significantly from the spectra of their respective ester derivatives,[41,55] with the exception that the resonances for the alkyl ester groups were not present. The resonances of all pyridine protons of [**1**](PF$_6$)$_2$ – [**3**](PF$_6$)$_2$ appear in the expected range between δ = 6.2 and 9.2 ppm. The highest chemical shift originates from to H-2 (δ = 8.99–9.15 ppm), due to the electron-withdrawing COOH moiety at the central pyridine of the tpy ligand. The addition of two carboxylic acid groups {[**1**](PF$_6$)$_2$→[**2**](PF$_6$)$_2$} strengthens the electron-accepting character of the tpy ligand, which is reflected in the downfield shift of H-5 and H-7 by about 0.4 ppm. The protons of the NCH$_3$ group of the ddpd ligand appear as a singlet at δ = 3.4–3.5 ppm. The amino protons of [**3**](PF$_6$)$_2$ resonate at δ = 5.75 ppm. The electron-donating character of the NH$_2$ group is clearly seen in the high-field shift of the H-15 resonance for [**3**](PF$_6$)$_2$ (δ = 6.81 ppm) compared with [**2**](PF$_6$)$_2$ (δ = 7.58 ppm).[72] For [**1**](PF$_6$)$_2$ – [**3**](PF$_6$)$_2$ an interligand nuclear Overhauser effect is observed between proton H-8 of the tpy ligand and the NCH$_3$ protons of the ddpd ligand, supporting the twisted *meridional* coordination of the ddpd ligand, with the two NCH$_3$ groups lying above and below the plane of the tpy ligand.[41,55] ^{13}C{^{1}H} NMR spectra of [**1**](PF$_6$)$_2$ – [**3**](PF$_6$)$_2$ show resonances for all carbon atoms, including quaternary carbon atoms. All carbon atoms were assigned unambiguously on the basis of 2D NMR correlation spectroscopic methods (HMQC, HMBC) and appear with expected chemical shifts (Table S2 in the Supporting Information). Again, the electron-donating effect of the NH$_2$ group of [**3**](PF$_6$)$_2$ is revealed when comparing the chemical shifts of C-15 {δ = 113.7 ([**2**](PF$_6$)$_2$)→98.8 ppm ([**3**](PF$_6$)$_2$)}. ^{15}N NMR chemical shifts of [**1**](PF$_6$)$_2$ – [**3**](PF$_6$)$_2$ were recorded with ^{15}N-^{1}H HMBC spectroscopy and also underline the electron-withdrawing effect of two additional COOH groups {$\delta(N^d)$ = 238.3 ([**1**](PF$_6$)$_2$)→249.5 ppm ([**2**](PF$_6$)$_2$)} and the electron-donating character of the NH$_2$ group {$\delta(N^c)$ = 216.3 ([**2**](PF$_6$)$_2$)→181.6 ppm ([**3**](PF$_6$)$_2$)}. IR spectra of [**1**](PF$_6$)$_2$ – [**3**](PF$_6$)$_2$ in CsI disks were recorded, and these feature characteristic bands of the functional groups and counterions. Broad bands at $\tilde{\nu}$ = 3440–3443 cm^{-1} arise from OH stretching vibrations. Absorption bands at $\tilde{\nu}$ = 1713–1728 cm^{-1} are assigned to C=O stretching vibrations, and very strong bands at $\tilde{\nu}$ = 839–843 cm^{-1} are caused by PF stretching vibrations of the $(PF_6)^-$ counterions.

Electrochemical Properties of [1](PF$_6$)$_2$ – [3](PF$_6$)$_2$

Cyclic and square wave voltammetry in CH_3CN and [*n*Bu$_4$N](PF$_6$) as supporting electrolyte have been performed for complexes **[1]**(PF$_6$)$_2$ – **[3]**(PF$_6$)$_2$ (Figures S1–S3 in the Supporting Information). The FcH/FcH$^+$ redox couple was used as internal reference. Electrochemical data of **[1]**(PF$_6$)$_2$ – **[6]**(PF$_6$)$_2$ and N719 are summarized in Table 1. The one-electron oxidation of **[1]**(PF$_6$)$_2$ – **[3]**(PF$_6$)$_2$ is reversible and occurs at $E_{1/2}$ = 0.81, 0.87, and 0.71 V, respectively, which essentially matches the oxidation potentials of the corresponding ester counterparts.[41] The oxidation is assigned to the Ru^{II}/Ru^{III} redox couple.[41,55] Spin density plots of the DFT optimized one-electron oxidized complexes corroborate the ruthenium-centered oxidation (Figure 2). **[1]**(PF$_6$)$_2$ ($E_{1/2}$ = 0.81 V) is more easily oxidized than **[2]**(PF$_6$)$_2$ ($E_{1/2}$ = 0.87 V) due to the two additional electron-withdrawing COOH groups of the latter. **[3]**(PF$_6$)$_2$ ($E_{1/2}$ = 0.71 V) is more easily oxidized than **[2]**(PF$_6$)$_2$ ($E_{1/2}$ = 0.87 V) due to the electron-donating NH_2 group of **[3]**(PF$_6$)$_2$. In **[3]**$^{3+}$, a small amount of spin density is also located on the NH_2 group, similar to complexes **[4]**$^{3+}$ and **[6]**$^{3+}$, with Mulliken spin densities on the amino nitrogen atom of 0.07, 0.11, and 0.12, respectively (Figure 2).[45,55] Reduction of **[1]**(PF$_6$)$_2$ – **[3]**(PF$_6$)$_2$ is irreversible and initially occurs at E_p = –1.50, –1.37, and –1.53 V, respectively, and is confined to the acid-substituted tpy ligand, which is illustrated by spin density plots of the one-electron reduced species **[1]**$^+$, **[2]**$^+$, and **[3]**$^+$ (Figure S4 in the Supporting Information).[41] Because the ester derivatives of **[1]**(PF$_6$)$_2$ – **[3]**(PF$_6$)$_2$ show reversible reductions, the irreversibility is associated with the COOH group.[41,55] The reduced radical ligand (tpy-COOH)$^{\cdot-}$ has a higher proton affinity compared with tpy-COOH. This might lead to the protonation reaction (tpy-COOH)$^{\cdot-}$ + H$^+$ → [tpy-C(OH)$_2$]$^{\cdot}$ and explains the irreversibility of the reduction in complexes **[1]**(PF$_6$)$_2$ – **[3]**(PF$_6$)$_2$. Reductive H_2 evolution, as in the reaction R-COOH + e$^-$ → R-COO$^-$ + 1/2 H_2, has also been reported to be responsible for the irreversible reduction of carboxylic acids attached to bpy.[73] Complex **[2]**(PF$_6$)$_2$ is more easily reduced than **[1]**(PF$_6$)$_2$ due to the additional electron-withdrawing COOH groups of the former. **[3]**(PF$_6$)$_2$ is reduced at lower potential than **[2]**(PF$_6$)$_2$ due to presence of the electron-donating NH_2 group.[41]

Table 1. Electrochemical data of complexes **[1]**(PF$_6$)$_2$ – **[6]**(PF$_6$)$_2$ and reference compound N719 in CH_3CN ($E_{1/2}$ given in V vs. FcH/FcH$^+$).

	$E_{1/2}$ (Ru^{II}/Ru^{III})	$E_{1/2}$ (tpy/tpy$^{\cdot-}$)
[1](PF$_6$)$_2$	+0.810	–1.500[a]
[2](PF$_6$)$_2$	+0.870	–1.370[a]
[3](PF$_6$)$_2$	+0.710	–1.530[a]
[4](PF$_6$)$_2$[45]	+0.680	–1.540[a]
[5](PF$_6$)$_2$[49]	+0.915	–1.565
[6](PF$_6$)$_2$[50]	+0.680	–1.505
N719[12][b]	+0.500	–1.790

[a] Irreversible, E_p given. [b] In DMF.

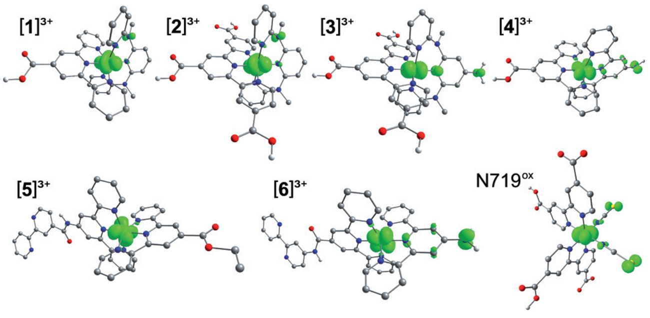

Figure 2. Spin densities of ruthenium(III) complexes **[1]**$^{3+}$ – **[6]**$^{3+}$ and one-electron oxidized N719 (contour value 0.005 a. u.; CH hydrogen atoms omitted).

Optical Properties of [1](PF$_6$)$_2$ – [3](PF$_6$)$_2$

Figure 3 depicts experimental UV/Vis spectra of **[1]**(PF$_6$)$_2$ – **[3]**(PF$_6$)$_2$ in CH_3CN. The data are summarized together with complexes **[4]**(PF$_6$)$_2$ – **[6]**(PF$_6$)$_2$ and N719 in Table 2. Intense bands at $\lambda < 400$ nm are assigned to $\pi \rightarrow \pi^*$ transitions of the ligands. The bands in the visible spectral range are predominantly of MLCT parentage. **[1]**(PF$_6$)$_2$ features its MLCT band maximum at λ = 517 nm (ε = 8110 M^{-1} cm^{-1}) with a high-energy shoulder at λ = 472 nm and two low-energy shoulders at λ = 583 and 635 nm. The spectrum of **[2]**(PF$_6$)$_2$ shows two maxima at λ = 537 (ε = 6600 M^{-1} cm^{-1}) and 473 nm (ε = 5820 M^{-1} cm^{-1}) and two shoulders at λ = 608 and 661 nm. A distinct redshift compared with **[1]**(PF$_6$)$_2$ can be noticed. This is due to the smaller HOMO–LUMO energy gap in the case of **[2]**(PF$_6$)$_2$ caused by the additional COOH groups lowering the LUMO energy by a greater extent than the HOMO energy

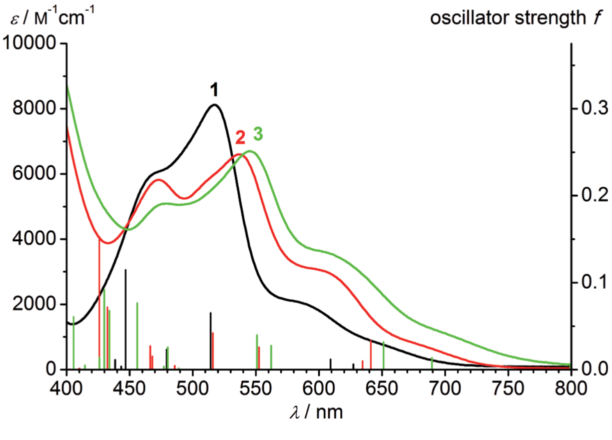

Figure 3. Experimental UV/Vis spectra in CH_3CN and calculated stick spectra (TD-DFT, B3LYP/LANL2DZ, IEFPCM in CH_3CN) of **[1]**$^{2+}$ – **[3]**$^{2+}$.

($[\mathbf{1}]^{2+} \rightarrow [\mathbf{2}]^{2+}$: $\Delta E_{LUMO} = 0.30$; $\Delta E_{HOMO} = 0.19$ eV by DFT; Figure 4). For $[\mathbf{3}](PF_6)_2$, the HOMO–LUMO gap is further reduced because the addition of the electron-donating NH_2 group raises the HOMO energy more than the LUMO energy ($[\mathbf{2}]^{2+} \rightarrow [\mathbf{3}]^{2+}$: $\Delta E_{LUMO} = 0.05$; $\Delta E_{HOMO} = 0.22$ eV by DFT; Figure 4). This can be seen in the electronic spectra because the absorption bands of $[\mathbf{3}](PF_6)_2$ are further red-shifted compared with those of $[\mathbf{2}](PF_6)_2$ (Table 2, Figure 3). Calculated stick spectra were obtained by time-dependent DFT calculations including solvent modeling (TD-DFT, B3LYP/LANL2DZ, IEFPCM in CH_3CN) and these appropriately reproduce the experimental spectra (Figure 3). For example, the bands and shoulders of the experimental spectrum of $[\mathbf{3}]^{2+}$ at λ = 680, 610, 544 and 480 nm appear as calculated transitions at λ = 689.5 (f = 0.0137), 651.3 (f = 0.0319), 562.1 (f = 0.0319)/550.9 (f = 0.0400) and 480.2 (f = 0.0260)/456.0 nm (f = 0.0768). Absorptions at $\lambda > 400$ nm arise predominantly from transitions from metal-centered "t_{2g}" orbitals (HOMO, HOMO–1 and HOMO–2) to tpy-based π* orbitals (LUMO and LUMO+1). Relevant Kohn–Sham frontier molecular orbitals are depicted for $[\mathbf{3}]^{2+}$ in Figure 5. The unoccupied "e_g"

Table 2. UV/Vis data of complexes $[\mathbf{1}](PF_6)_2$ – $[\mathbf{6}](PF_6)_2$ and reference compound N719 in CH_3CN and TD-DFT data (B3LYP/LANL2DZ, IEFPCM in CH_3CN).

	Experimental		DFT[a]
	π→π* λ_{max} [nm] (ε [$M^{-1}cm^{-1}$])	MLCT λ_{max} [nm] (ε [$M^{-1}cm^{-1}$])	λ [nm] (f)
$[\mathbf{1}](PF_6)_2$	319 (31200), 279 (37600), 221 (37500)	635 (970, sh), 583 (2080, sh), 517 (8110), 472 (6060, sh)	627.28 (0.0064), 609.06 (0.0119), 514.10 (0.0653), 479.27 (0.0233), 446.70 (0.1147), 438.60 (0.0114)
$[\mathbf{2}](PF_6)_2$	340 (34400), 291 (37100), 211 (55300)	661 (1010, sh), 608 (2960, sh), 537 (6600), 473 (5820)	641.06 (0.0337), 634.53 (0.0100), 552.49 (0.0261), 515.85 (0.0423), 467.83 (0.0155), 466.40 (0.0273), 432.33 (0.0718), 425.85 (0.1511)
$[\mathbf{3}](PF_6)_2$	340 (30400), 292 (34400), 217 (59900)	680 (1400, sh), 610 (3540, sh), 544 (6690), 480 (5090)	689.49 (0.0137), 651.28 (0.0319), 562.06 (0.0276), 550.87 (0.0400), 480.21 (0.0260), 455.99 (0.0768), 433.95 (0.0681), 426.03 (0.0142), 405.47 (0.0608)
$[\mathbf{4}](PF_6)_2$[45]	318 (41100), 306 (38000), 274 (55700), 236 (46700)	570 (1900, sh), 501 (20700), 467 (14400, sh)	585.50 (0.0053), 486.60 (0.1460), 451.84 (0.0719), 443.55 (0.0837), 439.16 (0.0402), 431.24 (0.1507)
$[\mathbf{5}](PF_6)_2$[49]	305 (56800), 276 (77800)	493 (24400)	555.74 (0.0059), 490.41 (0.0137), 475.62 (0.2638), 452.00 (0.0416), 432.90 (0.0382), 430.92 (0.2257), 427.40 (0.0372)
$[\mathbf{6}](PF_6)_2$[50]	313 (43900, sh), 278 (63900)	502 (23000)	562.43 (0.0079), 485.06 (0.1427), 457.57 (0.0134), 456.09 (0.0963), 448.27 (0.0421), 446.75 (0.0828), 435.76 (0.1837)
N719[11]	312 (49100)[b]	535 (14700)[b], 395 (14300)[b]	682.20 (0.0586), 653.33 (0.0131), 591.98 (0.1223), 541.43 (0.0857), 473.58 (0.0312), 455.74 (0.0595), 449.54 (0.0443), 440.46 (0.0180), 435.66 (0.0298), 433.88 (0.0260), 414.86 (0.0149), 408.02 (0.0087)

[a] Highest calculated oscillator strengths f at $\lambda > 400$ nm (TD-DFT, B3LYP/LANL2DZ, IEFPCM in CH_3CN). For a complete list see the Supporting Information. [b] In ethanol.

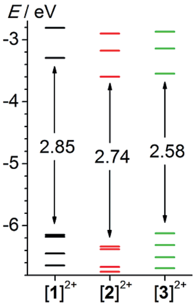

Figure 4. DFT (B3LYP/LANL2DZ, IEFPCM in CH_3CN) calculated frontier orbital energies of $[\mathbf{1}]^{2+}$ – $[\mathbf{3}]^{2+}$.

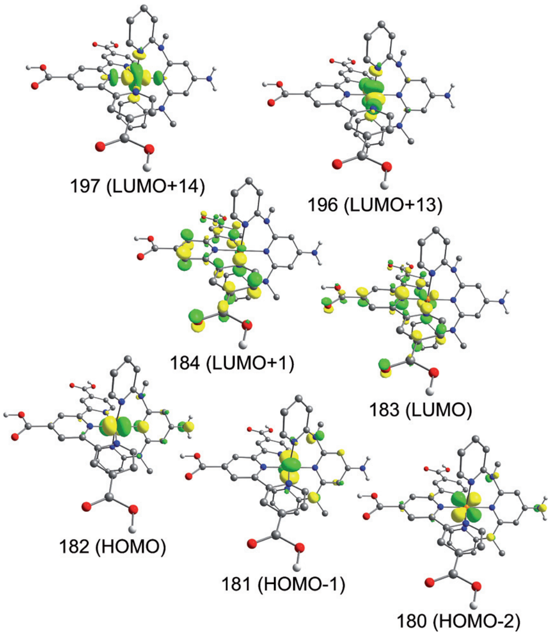

Figure 5. Relevant Kohn–Sham frontier molecular orbitals (contour value 0.06 a. u.) of $[\mathbf{3}]^{2+}$ (CH hydrogen atoms omitted).

orbitals of the d-manifold (LUMO+13 and LUMO+14) appear at higher energy.

In a more detailed analysis, we compare the frontier orbitals (HOMO–3 to LUMO+3) that are relevant for transitions at $\lambda > 400$ nm, as calculated by TD-DFT calculations for complexes $[\mathbf{1}]^{2+}$ – $[\mathbf{6}]^{2+}$ and N719 (Figures S5–S6 in the Supporting Information). HOMO, HOMO–1, and HOMO–2 of complexes $[\mathbf{1}]^{2+}$ – $[\mathbf{6}]^{2+}$ are located at the metal center, formally corresponding to "t_{2g}" orbitals. For complexes $[\mathbf{3}]^{2+}$, $[\mathbf{4}]^{2+}$, and $[\mathbf{6}]^{2+}$, the p(N) orbitals of the NH_2 substituent also contribute to the HOMO.[41,62] This is regarded as being beneficial for directional electron injection into solid semiconductors, e.g., TiO_2.[2–4] HOMO-3 of complexes $[\mathbf{1}]^{2+}$ – $[\mathbf{4}]^{2+}$ is situated at the remote amine donor ligand, which also favors directional electron injection into TiO_2. Similarly, HOMO to HOMO–2 of N719 are metal-centered, but large contributions from the NCS^- ligands are present. HOMO-3 of N719 is even essentially NCS^--based. LUMO to LUMO+3 of $[\mathbf{1}]^{2+}$ – $[\mathbf{3}]^{2+}$ and N719 are mainly located at the anchoring ligand and should therefore facilitate electron injection.[2–4] In contrast, LUMO to LUMO+3 of $[\mathbf{4}]^{2+}$ – $[\mathbf{6}]^{2+}$ are distributed over both tpy ligands. In the case of $[\mathbf{5}]^{2+}$, the LUMO is not even located on the anchor ligand as is the case for all other complexes (Figure S6). Thus, for complexes $[\mathbf{4}]^{2+}$ – $[\mathbf{6}]^{2+}$, the local separation of frontier orbitals is less pronounced and might retard efficient charge injection into TiO_2.

The individual sum of oscillator strengths Σf at $\lambda > 400$ nm increases by attaching two COOH groups $\{\Sigma f = 0.2368\ ([\mathbf{1}]^{2+}) \rightarrow 0.3849\ ([\mathbf{2}]^{2+})\}$ as well as by attaching an amino group $\{\Sigma f = 0.3849\ ([\mathbf{2}]^{2+}) \rightarrow 0.4619\ ([\mathbf{3}]^{2+})\}$, which is a behavior similar to the ester derivatives and is due to the enlargement of the chromophoric system.[41] The total experimental integrated intensity $\int I$ was calculated in the visible spectral range (λ = 400–800 nm) on an energy scale (cm^{-1}) and increases in the same order $\{\int I = 3.77 \times 10^7\ \mathrm{M}^{-1}\,cm^{-2}\ ([\mathbf{1}](PF_6)_2) \rightarrow 4.69 \times 10^7\ \mathrm{M}^{-1}\,cm^{-2}\ ([\mathbf{2}](PF_6)_2) \rightarrow 5.16 \times 10^7\ \mathrm{M}^{-1}\,cm^{-2}\ ([\mathbf{3}](PF_6)_2)\}$. This increased absorptivity favors photon collection over the entire spectral range.

DFT-calculated spin densities of the emissive ^{3}MLCT states of complexes $[\mathbf{1}]^{2+}$ – $[\mathbf{6}]^{2+}$ and N719[12,74] are illustrated in Figure 6. For all complexes, the spin density is distributed over both the ruthenium atom and the carbonyl-substituted polypyridine ligand. For all complexes except $[\mathbf{5}]^{2+}$, spin density is transferred towards the anchor groups in the ^{3}MLCT state compared with the ground state. This is beneficial for efficient charge injection into semiconductors.[2–4] For $[\mathbf{5}]^{2+}$ however, the carbonyl-substituted terpyridine ligand is opposite to the bpy anchor group, which should be rather detrimental for charge injection (see below).[4]

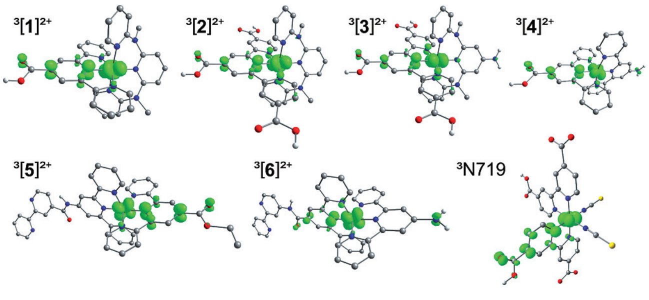

Figure 6. Spin densities of the ^{3}MLCT state of $[\mathbf{1}]^{2+}$ – $[\mathbf{6}]^{2+}$ and N719 (contour value 0.01 a. u.; CH hydrogen atoms omitted).

Figure 7 compares the experimental UV/Vis spectra of $[\mathbf{1}](PF_6)_2$ – $[\mathbf{6}](PF_6)_2$ and N719 in CH_3CN/*t*BuOH (1:1) solution. $[\mathbf{2}](PF_6)_2$ features a very similar absorption maximum to that of N719, with additional low energy shoulders at λ = 661 and 608 nm. The absorption maxima of $[\mathbf{3}](PF_6)_2$ are even bathochromically shifted with respect to those of N719 (Table 2).

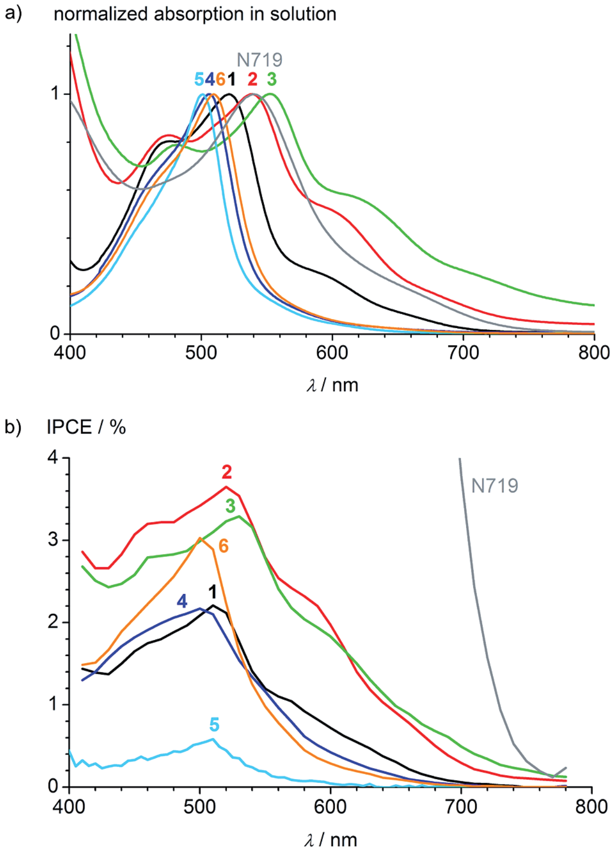

Figure 7. (a) Normalized experimental UV/Vis spectra of $[\mathbf{1}](PF_6)_2$ – $[\mathbf{6}](PF_6)_2$ and N719 in CH_3CN/*t*BuOH (1:1); (b) IPCE of cells with $[\mathbf{1}](PF_6)_2$ – $[\mathbf{6}](PF_6)_2$ and N719.

Emission of $[\mathbf{1}](PF_6)_2$ – $[\mathbf{3}](PF_6)_2$ in CH_3CN at 295 K occurs at λ = 732, 743, and 771 nm, respectively. The redshift of the emission wavelength in the series $[\mathbf{1}](PF_6)_2$, $[\mathbf{2}](PF_6)_2$, $[\mathbf{3}](PF_6)_2$ is due to the consecutive lowering of the HOMO–LUMO gap, as already discussed for absorption (see above, Figure 4). Emission quantum yields of $[\mathbf{1}](PF_6)_2$ – $[\mathbf{3}](PF_6)_2$ were measured in deaerated CH_3CN at 295 K. The quantum yield of $[\mathbf{3}](PF_6)_2$ (Φ = 0.067 %) is similar to its ester derivative (Φ = 0.052 %).[41] In contrast, the quantum yields of $[\mathbf{1}](PF_6)_2$ (Φ = 0.068 %) and $[\mathbf{2}](PF_6)_2$ (Φ = 0.590 %) are smaller by a factor of 2–7 compared with their ester derivatives,[41,75] which is due to the presence of carboxylic acid functionalities. Carboxylic acids are known to form hydrogen-bonding networks, and proton transfer along hydrogen bonds can be responsible for excited-state deactivation.[76–80] Furthermore, excited-state deactivation can occur through high energy oscillators (O–H, N–H), typically leading to smaller quantum yields.[41,45] For [**3**]$(PF_6)_2$, we assume that efficient excited-state deactivation already occurs through N–H oscillators and clearly does not increase significantly by additional deactivation through the three extra O–H oscillators. This would explain the similar quantum yields of [**3**]$(PF_6)_2$ and its ester derivative.[41]

For example, the excited state pK_a^* $[pK_a^* = pK_a + 0.625 \times T^{-1} \times (\tilde{\nu} - \tilde{\nu}')]$ was calculated for complex [**1**]$(PF_6)_2$ from the ground state pK_a and the 0–0 transitions of $[\mathbf{1}]^{2+}$ ($\tilde{\nu}'$/cm^{-1}) and the deprotonated ($\tilde{\nu}$/cm^{-1}) form $[\mathbf{1}\text{–H}]^+$.[81] 0–0 transitions were estimated from the intersection points of the normalized absorption and emission spectrum, which were found at λ = 659 and 621 nm for $[\mathbf{1}]^{2+}$ and $[\mathbf{1}\text{–H}]^+$, respectively. The ground state pK_a amounts to 2.3 and the excited state pK_a^* to 4.3 (T = 295 K). A similar difference between pK_a (3.0) and pK_a^* (4.85) was found in $[Ru(bpy)_2(bpy\text{-}4\text{-}COOH)]^{2+}$.[82] The lower acidity of the excited state compared to the ground state corroborates the metal-to-ligand charge transfer character of the excited state mentioned above.[81]

Photostability Tests

Photostability tests were conducted to investigate possible ligand loss during DSSC operation. The ethyl ester derivatives [**1**$^{\mathbf{Et}}$]$(PF_6)_2$ and [**4**$^{\mathbf{Et}}$]$(PF_6)_2$ of carboxylic acids [**1**]$(PF_6)_2$ and [**4**]$(PF_6)_2$ as well as N719 and $[Ru(bpy)_3](PF_6)_2$ were continuously irradiated under an Ar atmosphere in 0.1 M $[nBu_4N]I$ in CH_3CN/H_2O (98:2, v/v) at λ_{exc} = 400 and 500 nm. The solutions of [**1**$^{\mathbf{Et}}$]$(PF_6)_2$, [**4**$^{\mathbf{Et}}$]$(PF_6)_2$, N719, and $[Ru(bpy)_3](PF_6)_2$ were isoabsorptive at the respective irradiation wavelength. The presence of water and potentially coordinating iodide simulates DSSCs conditions, with I^- being present in the liquid electrolyte and H_2O penetrating into the cell. The emission intensity of the complexes was measured over a period of at least 4 h and compared to the evolution of the emission intensity of N719 and $[Ru(bpy)_3](PF_6)_2$ (Figure 8). In the absence of coordinating anions, $[Ru(bpy)_3](PF_6)_2$ is photoinert.[83,84] However, in the presence of coordinating anions such as Cl^-, Br^-, I^-, SCN^-, or NO_3^-, $[Ru(bpy)_3]^{2+}$ readily undergoes photoinduced ligand substitution, photooxygenation (in the presence of O_2), and photoracemization.[83–87] When irradiated at λ_{exc} = 400 nm, the normalized emission intensities of N719 and $[Ru(bpy)_3](PF_6)_2$ drop within 4 h to 68 and 5% of the initial emission intensity, respectively (Figure 8, a). In contrast, for [**1**$^{\mathbf{Et}}$]$(PF_6)_2$ and [**4**$^{\mathbf{Et}}$]$(PF_6)_2$, more than 95% of the initial emission intensity is maintained after the same irradiation time under identical conditions. Irradiation at λ_{exc} = 500 nm shows similar results, with a drop in the initial emission intensity to 79 and 47% for N719 and $[Ru(bpy)_3](PF_6)_2$, respectively, after 5 h (Figure 8, b). Under the same conditions, [**1**$^{\mathbf{Et}}$]$(PF_6)_2$ and [**4**$^{\mathbf{Et}}$]$(PF_6)_2$ retain more than 97% of the initial emission intensity. The results clearly show that under the applied conditions bis(tridentate) complexes [**1**$^{\mathbf{Et}}$]$(PF_6)_2$ and [**4**$^{\mathbf{Et}}$]$(PF_6)_2$ are much more photostable than N719 and $[Ru(bpy)_3](PF_6)_2$, which is a result of the tridentate coordination compared with mono- and bidentate modes.[14–21,88]

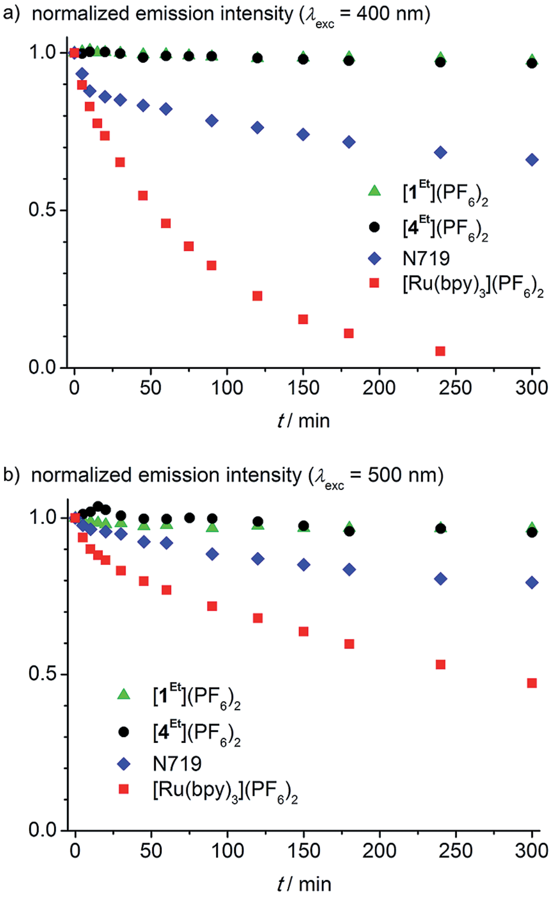

Figure 8. Normalized emission intensities of [**1**$^{\mathbf{Et}}$]$(PF_6)_2$, [**4**$^{\mathbf{Et}}$]$(PF_6)_2$, N719, and $[Ru(bpy)_3](PF_6)_2$ in 0.1 M $[nBu_4N]I$ in CH_3CN/H_2O (98:2, v%) under continuous irradiation at (a) λ_{exc} = 400 and (b) λ_{exc} = 500 nm.

Photodecomposition products of $[Ru(bpy)_3]^{2+}$ were indeed detected when a solution of $[Ru(bpy)_3](PF_6)_2$ (11 mM) was irradiated at λ_{exc} = 400 nm in the presence of $[nBu_4N]I$ (2.2 equiv.) and trace amounts of H_2O. ^1H NMR spectra reveal resonances corresponding to the noncoordinated 2,2′-bipyridine ligand (Figure S7 in the Supporting Information). The ESI$^+$ mass spectrum after irradiation shows signals with characteristic ruthenium isotope patterns at m/z = 559.0 $[Ru(bpy)_2(H_2O)I]^+$, 541.0 $[Ru(bpy)_2I]^+$, 467.1 $[Ru(bpy)_2(H_2O)_2(OH)]^+$, and 449.1 $[Ru(bpy)_2(H_2O)(OH)]^+$ in addition to intense signals for intact $[Ru(bpy)_3]^{2+}$ (Figure S8 in the Supporting Information). Hence, one bpy ligand of $[Ru(bpy)_3]^{2+}$ is efficiently photo-substituted by H_2O and/or I^-. The high photostability of ruthenium(II) complexes with bis(tridentate) coordination should thus be favorable in applications such as DSSCs and light-emitting devices.[3,4,27–30,60,61]

Photodecomposition products of N719 could be detected when a solution of N719 (4.4 mм) was irradiated at λ_{exc} = 400 nm in the presence of $[n\mathrm{Bu_4N}]\mathrm{I}$ (4.5 equiv.) and H_2O. ^{1}H NMR spectra after irradiation show new signals with similar resonances ($\Delta\delta < 0.1$ ppm) to those obtained from N719 (Figure S9 in the Supporting Information). No signals from degradation compounds could be observed in FD, ESI$^+$, or ESI$^-$ mass spectra. However, the small changes of the chemical shifts indicate that both dcbpy ligands remain coordinated and that NCS$^-$ ligands are replaced by I$^-$ or by H_2O.[11] This is reasonable because NCS$^-$ coordinates in a monodentate fashion and is substituted faster than the bidentate dcbpy ligand. Indeed, for N719 and related compounds, the photochemical and thermal substitution of both NCS$^-$ by I$^-$ and other monodentate ligands has previously been reported.[17,19,20,89,90]

Redox Stability

The redox stability of sensitizers is an important issue in DSSCs because electron injection leads to ruthenium(III) complexes, which can be prone to ligand exchange reactions. The ethyl esters of $[\mathbf{1^{Et}}]^{2+}$ and $[\mathbf{4^{Et}}]^{2+}$ were oxidized and the stability of the oxidized species ($[\mathbf{1^{Et}}]^{3+}$ and $[\mathbf{4^{Et}}]^{3+}$) in the presence of coordinating OH$^-$ ions was investigated by spectroelectrochemical measurements. Oxidized N719 and $[\mathrm{Ru(bpy)_3}]^{3+}$ were used for comparison. The ruthenium(II) complexes were oxidized to ruthenium(III) by gradually increasing the potential and then reduced back to the starting ruthenium(II) complexes by gradually lowering the potential. The reactions were monitored by following changes to the UV/Vis spectra. Figure 9 exemplarily shows that, upon oxidation of $[\mathbf{4^{Et}}]^{2+}$ to $[\mathbf{4^{Et}}]^{3+}$, the MLCT band disappears while a LMCT band at λ = 729 nm (ε = 5120 $\mathrm{M^{-1}\,cm^{-1}}$) appears.[46] Isosbestic points at λ = 581, 431, 340, 292, 283, 272, and 241 nm reveal a clean conversion from $[\mathbf{4^{Et}}]^{2+}$ into $[\mathbf{4^{Et}}]^{3+}$.[46] Upon lowering the potential, the spectra clearly show a clean reduction back to $[\mathbf{4^{Et}}]^{2+}$ with the same isosbestic points as for the oxidation and a perfect overlap with the spectra of the initial ruthenium(II) complex could be achieved.

Experiments with $[\mathbf{1^{Et}}](\mathrm{PF_6})_2$ and $[\mathrm{Ru(bpy)_3}](\mathrm{PF_6})_2$ show essentially the same spectral behavior upon oxidation and back reduction (Figures S10–S11 in the Supporting Information). LMCT bands for the oxidized complexes $[\mathbf{1^{Et}}]^{3+}$, N719^{ox}, and $[\mathrm{Ru(bpy)_3}]^{3+}$ appear at λ = 702 (shoulder; ε = 770 $\mathrm{M^{-1}\,cm^{-1}}$), λ = 662 (shoulder; ε = 860 $\mathrm{M^{-1}\,cm^{-1}}$), and 662 nm (ε = 370 $\mathrm{M^{-1}\,cm^{-1}}$), respectively. The smaller LMCT band intensity of $[\mathbf{1^{Et}}]^{3+}$, N719^{ox}, and $[\mathrm{Ru(bpy)_3}]^{3+}$ compared with NH$_2$-substituted $[\mathbf{4^{Et}}]^{3+}$ is due to the strong electron-donating character of the primary amino group of $[\mathbf{4^{Et}}]^{3+}$. Isosbestic points for $[\mathbf{1^{Et}}](\mathrm{PF_6})_2$ appear at λ = 664, 423, 373, 352, 296, 285, and 258 nm and for $[\mathrm{Ru(bpy)_3}](\mathrm{PF_6})_2$ at λ = 573, 329, 298, and 267 nm.

During the oxidation of N719, isosbestic points were observed at λ = 316, 333, and 550 nm (Figure S12a). However, during the back reduction, no isosbestic points were observed. The spectrum of N719 before oxidation (E = 200 mV, Figure S12 a) features maxima at λ_{max} = 249 (ε = 31810 $\mathrm{M^{-1}\,cm^{-1}}$), 308 (ε = 44640 $\mathrm{M^{-1}\,cm^{-1}}$), 374 (ε = 14090 $\mathrm{M^{-1}\,cm^{-1}}$), and 512 nm (ε = 12270 $\mathrm{M^{-1}\,cm^{-1}}$) whereas the spectrum after gradually increasing and then lowering the potential (E = 200 mV, Figure S12b) features maxima at λ_{max} = 249 (ε = 33190 $\mathrm{M^{-1}\,cm^{-1}}$), 307 (ε = 47040 $\mathrm{M^{-1}\,cm^{-1}}$), 372 (ε = 14700 $\mathrm{M^{-1}\,cm^{-1}}$), and 508 nm (ε = 12270 $\mathrm{M^{-1}\,cm^{-1}}$) indicating that the majority of N719 could be recovered and a small part of oxidized N719 underwent side reactions. Indeed the oxidation of the ester-protected analogue of N719 is irreversible, and desulfuration of the NCS$^-$ ligands has been reported.[90] In essence, $[\mathbf{1^{Et}}]^{3+}$, $[\mathbf{4^{Et}}]^{3+}$, and $[\mathrm{Ru(bpy)_3}]^{3+}$ are stable in the presence of coordinating OH$^-$. No hint of instability of the ruthenium(III) complexes could be found on the electrochemical time-scale under the applied conditions. In contrast, oxidized N719 is less stable and undergoes irreversible side reactions. Thus, compared with N719, our bis(tridentate) ruthenium(II) complexes feature a superior redox stability, which is important for applications such as DSSCs.[2]

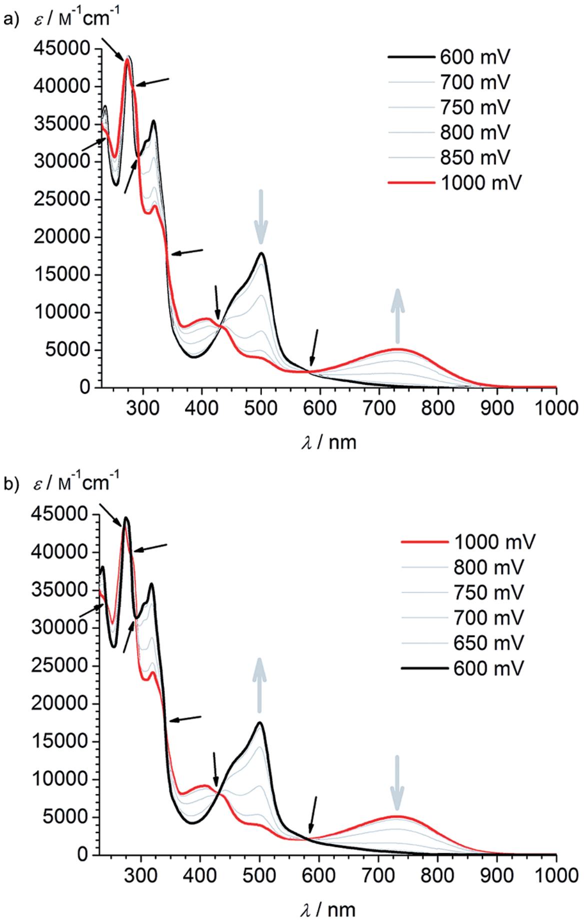

Figure 9. UV/Vis spectra of (a) the electrochemical oxidation (E = 600→1000 mV) and (b) back reduction (E = 1000→600 mV) of $[\mathbf{4^{Et}}](\mathrm{PF_6})_2$ in an OTTLE cell in 10^{-3} м NaOH and 0.1 м $[n\mathrm{Bu_4N}](\mathrm{PF_6})$ in $\mathrm{CH_3CN/H_2O}$ (98:2, v/v). Black arrows indicate isosbestic points.

Device Testing

DSSCs were prepared with a FTO/TiO_2/dye/electrolyte/Pt/FTO structure. As redox electrolyte the I^-/I_3^- redox couple in CH_3CN was used. Ground state (^{1}GS) and excited state (^{3}MLCT and ^{1}MLCT) energy levels of sensitizers [**1**]$(PF_6)_2$ – [**6**]$(PF_6)_2$ at E = –5.89, –4.20, –3.49 ([**1**]$(PF_6)_2$), –5.95, –4.28, –3.64 ([**2**]$(PF_6)_2$), –5.79, –4.18, –3.51 ([**3**]$(PF_6)_2$), –5.74, –4.06, –3.26 ([**4**]$(PF_6)_2$), –6.00, –4.15, –3.48 ([**5**]$(PF_6)_2$), –5.58, –4.09, –3.26 eV ([**6**]$(PF_6)_2$) and N719 at –5.58, –4.09, –3.26 eV are depicted together with the conduction band edge of TiO_2 (E = –3.94 eV) and the redox potential of the I^-/I_2^- redox couple (E = –5.24 eV), which is assumed to be responsible for dye regeneration in the I^-/I_3^- system (Figure 10).[5,91] ^{1}GS energies were derived from experimental Ru^{II}/Ru^{III} redox potentials, ^{1}MLCT state energies were estimated from lowest energy absorption maxima in solution (Table 2) and ^{3}MLCT state energies from the room temperature emission maxima in solution.[11,45,49,50] ^{1}MLCT state energies are higher in energy than the TiO_2 conduction band edge by ΔE = 0.30–0.68 eV. Thus, injection of electrons into the TiO_2 conduction band is thermodynamically feasible from hot and thermally equilibrated ^{1}MLCT states for all tested dyes.[39] Typically, electron injection occurs on the femto to picosecond timescale with high efficiency.[39,40] In contrast, injection from thermally equilibrated ^{3}MLCT states would be thermodynamically uphill for all dyes by ΔE = 0.13–0.34 eV. Injection rates from vibrationally hot ^{3}MLCT states depend on the vibrational state and the relaxation rate to the vibrational ground state. Vibrational cooling in complexes of type [**1**]$(PF_6)_2$ – [**4**]$(PF_6)_2$ occurs on the timescale of several picoseconds.[41] The ^{1}GS energies of all dyes is lower than the I^-/I_2^- redox potential by ΔE = 0.34–0.76 eV and therefore allows for the regeneration of oxidized dyes.

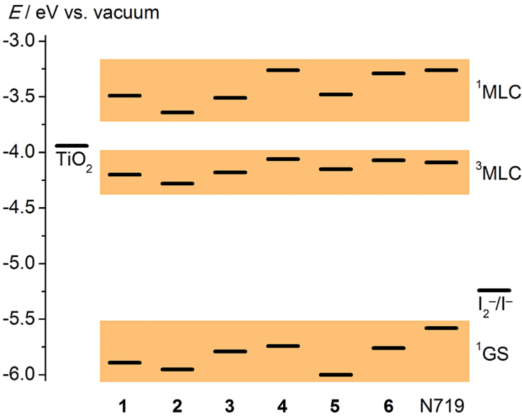

Figure 10. Energy levels of the ground state (^{1}GS) and excited states (^{1}MLCT and ^{3}MLCT) of [**1**]$(PF_6)_2$ – [**6**]$(PF_6)_2$ and N719, the conduction band edge of TiO_2, and the I_2^-/I^- redox potential.

Dye loadings of [**1**]$(PF_6)_2$ – [**6**]$(PF_6)_2$ and N719 on TiO_2 were measured by the difference of absorption maxima of the dipping solution (CH_3CN/*t*BuOH, 1:1) before and after dipping of the TiO_2 electrodes. Whereas high dye loading was obtained for [**1**]$(PF_6)_2$ – [**4**]$(PF_6)_2$ and N719 (6–11 × 10^{-8} mol cm^{-2}), the dye loading for [**5**]$(PF_6)_2$ (1 × 10^{-8} mol cm^{-2}) and [**6**]$(PF_6)_2$ (3 × 10^{-8} mol cm^{-2}) remained low (Table 3). This can be explained by the nature of the anchor group, which are 2,2′-bpy anchors for [**5**]$(PF_6)_2$ and [**6**]$(PF_6)_2$ and carboxylic acids and carboxylate anchors for [**1**]$(PF_6)_2$ – [**4**]$(PF_6)_2$ and N719. So far, only *para*-substituted pyridine anchors have been used for binding to TiO_2 and, to the best of our knowledge, this is the first example of a 2,2′-bpy anchor.[92,93] The low dye loadings with our 2,2′-bpy anchor might have two reasons: One reason could be that both pyridines in 2,2′-bpy hinder each other sterically in binding to TiO_2 due to the 2,2′-constitution, resulting in low dye loadings for [**5**]$(PF_6)_2$ and [**6**]$(PF_6)_2$. A carboxylic acid/carboxylate anchor might be able to bind to TiO_2 surface atoms that are not sufficiently accessible for a 2,2′-bpy anchor. The dye loading of [**6**]$(PF_6)_2$ is higher than of [**5**]$(PF_6)_2$, which is due to the more electron-rich bpy moiety in [**6**]$(PF_6)_2$ in which bpy is bound to the nitrogen atom of the amide functionality. In contrast, bpy is bound to the carbonyl carbon atom of the amide functionality in complex [**5**]$(PF_6)_2$. The more electron-rich bpy of [**6**]$(PF_6)_2$ might form stronger interactions to the electrophilic surface Ti ions of TiO_2. A second reason might be the larger area per molecule required for binding of [**5**]$(PF_6)_2$ and [**6**]$(PF_6)_2$ to the TiO_2 surface compared with [**1**]$(PF_6)_2$ – [**4**]$(PF_6)_2$ and N719, which is due to the canted orientation with respect to the surface. In addition, the 2,2′-bpy anchor has more steric bulk than a carboxylic acid/carboxylate anchor.

Table 3. Characteristics of the DSSCs with [**1**]$(PF_6)_2$ – [**6**]$(PF_6)_2$ and reference compound N719.

	Dye loading [mol cm^{-2}]	U_{oc} [V]	I_{sc} [mA cm^{-2}]	Fill factor [%]	η [%]	IPCE [%] (λ_{max} [nm])
[**1**]$(PF_6)_2$	5.6 × 10^{-8}	0.41	0.50	63	0.13	2.2 (510)
[**2**]$(PF_6)_2$	9.7 × 10^{-8}	0.49	0.75	70	0.26	3.6 (520)
[**3**]$(PF_6)_2$	8.7 × 10^{-8}	0.45	0.74	67	0.22	3.3 (530)
[**4**]$(PF_6)_2$	11.0 × 10^{-8}	0.49	0.48	62	0.15	2.2 (500)
[**5**]$(PF_6)_2$	1.0 × 10^{-8}	0.44	0.24	61	0.06	0.5 (510)
[**6**]$(PF_6)_2$	2.6 × 10^{-8}	0.46	0.59	61	0.18	3.0 (500)
N719	6.4 × 10^{-8}	0.76	9.30	71	5.03	51.6 (520)

IPCE were measured (Figure 7, b, Table 3) and these nicely follow the absorption spectrum of the respective dipping solution (Figure S13). The maximum IPCE of 3.7% was obtained for the cell with [**2**]$(PF_6)_2$ at $\lambda \approx$ 520 nm. For the cell with [**3**]$(PF_6)_2$, the maximum IPCE (3.3%) is redshifted to $\lambda \approx$ 530 nm, whereas for the cell with [**1**]$(PF_6)_2$ it is blueshifted to $\lambda \approx$ 510 nm. This is consistent with the tendency for λ_{max} in the solution absorption mentioned above: [**3**]$(PF_6)_2$ > [**2**]$(PF_6)_2$ > [**1**]$(PF_6)_2$. The cell with [**2**]$(PF_6)_2$ features higher IPCE and efficiency than the cell with [**1**]$(PF_6)_2$ and [**3**]$(PF_6)_2$. This can be ascribed to the higher dye loading (Table 3) in the case of [**2**]$(PF_6)_2$ and the less intimate contact to TiO_2 in the case of [**1**]$(PF_6)_2$ due to the presence of only one carboxylic acid anchor group.[94] The IPCE maxima of cells with [**4**]$(PF_6)_2$ (2.2%), [**5**]$(PF_6)_2$ (0.6%), and [**6**]$(PF_6)_2$ (3.0%) are at $\lambda \approx$ 500–510 nm, which is consistent with the respective absorption maxima in solution (Table 2). The reference cell with N719 features a maximum IPCE of 51.6% at $\lambda \approx 520$ nm. The maximum IPCE of the cell with [**5**](PF_6)$_2$ remains low (0.5% at 510 nm) due to the low dye loading (Table 3) and the poor electronic directionality of complex [**5**](PF_6)$_2$, as already discussed (Figure S6).

Current-voltage curves of DSSCs with [**1**](PF_6)$_2$ – [**6**](PF_6)$_2$ are depicted in Figure 11 and data are listed in Table 3. Open circuit voltages of cells with [**1**](PF_6)$_2$ – [**6**](PF_6)$_2$ reach values of U_{oc} = 0.41–0.49 V compared with U_{oc} = 0.76 V for the cell with N719. Short circuit currents are low for cells with [**1**](PF_6)$_2$ – [**6**](PF_6)$_2$ (I_{sc} = 0.2–0.8 mA cm^{-2}) whereas the cell with N719 features a much higher value (I_{sc} = 9.3 mA cm^{-2}). Fill factors amount to 61–71% for all cells, with the highest fill factor belonging to the one with N719. At the maximum power point, the cell with N719 has an efficiency of η = 5.03%. Nazeeruddin, Angelis et al. have reported a maximum efficiency of 11.2% for the N719 dye, which is attributed to the optimized cell building procedure, including the addition of tetra-*n*-butylammonium chenodeoxycholic acid salt to the dipping solution.[12] Efficiencies of cells with [**1**](PF_6)$_2$ – [**6**](PF_6)$_2$ are much lower (η = 0.06–0.26%) than for the cell with N719 under the same conditions (η = 5.03%), which is primarily due to the poor short circuit current in these cells. The low efficiency of the cell with [**5**](PF_6)$_2$ can further be attributed to the low dye loading (Table 3) as well as to the poor electronic directionality (Figure S6).

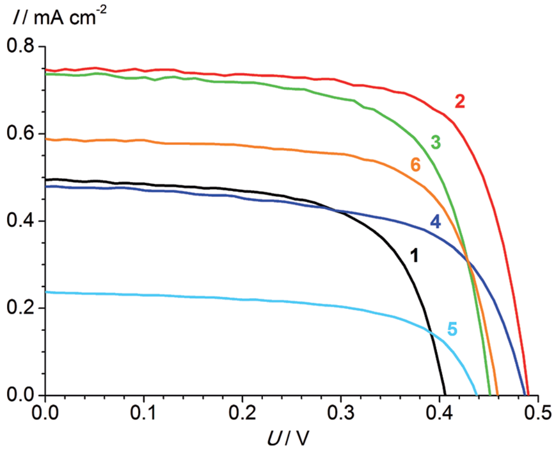

Figure 11. Current-voltage characteristics of DSSCs containing complexes [**1**](PF_6)$_2$ – [**6**](PF_6)$_2$.

A reverse bias was applied to all cells to measure the dark currents. Recombination was shown to be negligible at the TiO_2-dye interface when the I_3^-/I^- redox couple was used because regeneration of the oxidized dye is significantly faster than back electron transfer from TiO_2 to the oxidized dye.[95,96] Instead, efficient recombination is supposed to occur at the TiO_2-electrolyte interface.[95] The recombination efficiency depends on the excitation intensity, the electrolyte composition, and the presence of dyes and additives.[96,97] Figure 12 shows that for the cell with N719 a significantly higher voltage is necessary to produce the same amount of dark current compared with cells containing complexes [**1**](PF_6)$_2$ – [**6**](PF_6)$_2$. This can be explained by the twofold positive charge of the complex cations of [**1**](PF_6)$_2$ – [**6**](PF_6)$_2$ as compared to the twofold negative charge of N719 (Figure 1). Electrostatic interactions between the cationic complexes and I_3^- favor a higher concentration of I_3^- near the TiO_2 surface than in the bulk solution, which leads to an enhanced recombination rate.[95,98] In contrast, the negative charge of N719 effectively repels I_3^- ions from the TiO_2 surface. Consequently, it is not surprising that all top-performing dyes are neutral or even negatively charged.[6–9] Among the cells with [**1**](PF_6)$_2$ – [**6**](PF_6)$_2$, the cell with [**4**](PF_6)$_2$ shows the smallest dark current (Figure 12). This is possibly due to the high dye loading of [**4**](PF_6)$_2$, which acts as a blocking layer and reduces recombination at the TiO_2-electrolyte interface (Table 3).[96] Indeed, the dye loading order of [**1**](PF_6)$_2$ – [**4**](PF_6)$_2$ is the inverse of the amount of dark current (Table 3, Figure 12). Regarding the low dye loading of [**5**](PF_6)$_2$ and [**6**](PF_6)$_2$, one would expect a high dark current for cells with these dyes. However, the amount of dark current of cells with [**5**](PF_6)$_2$ and [**6**](PF_6)$_2$ is moderate and can be compared to the cell with [**2**](PF_6)$_2$.

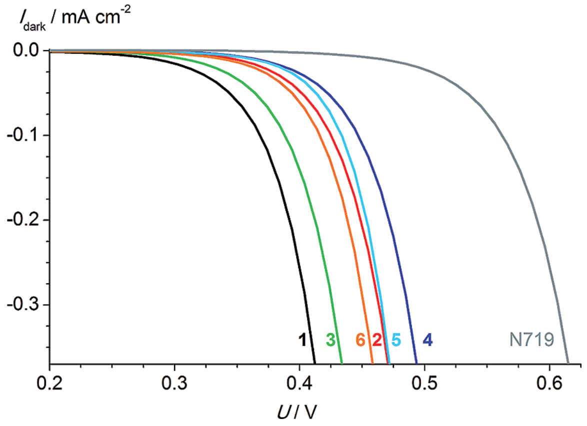

Figure 12. Dark current characteristics of DSSCs with complexes [**1**](PF_6)$_2$ – [**6**](PF_6)$_2$ and N719.

Two reasons might be responsible for this effect: (1) Dyes can also protonate (or deprotonate) the TiO_2 surface, shifting the conduction band edge of TiO_2 to lower (or higher) energy, which influences recombination rates.[95,96,99] Protonation of TiO_2 by protons from N719 was found to increase the dark current, which might be due to the enhanced concentration of I_3^- near the surface.[95,96] [**1**](PF_6)$_2$ – [**4**](PF_6)$_2$ are even more acidic than N719 [N719: pK_{a1} = 3.5, pK_{a2} = 4.2; [**4**](PF_6)$_2$: pK_a = 2.7; [**1**](PF_6)$_2$: pK_a = 2.3][45,100] and therefore protonate the TiO_2 surface, which lowers the energy of the conduction band. [**5**](PF_6)$_2$ and [**6**](PF_6)$_2$ cannot protonate the TiO_2 surface, which might lower the dark current in cells with these complexes. (2) The steric effect of [**5**](PF_6)$_2$ and [**6**](PF_6)$_2$ might suppress the dark current due to their steric bulk, as discussed above.

Electron recombination lifetimes τ of cells with [**1**](PF_6)$_2$ – [**6**](PF_6)$_2$ and N719 were determined experimentally by intensity-modulated photovoltage spectroscopy and the results corroborate the rationals derived from the dark current measurements (Figure 13).[101,102] Cells with [**1**](PF_6)$_2$ – [**6**](PF_6)$_2$ feature significantly smaller recombination lifetimes than the cell with N719. Because low recombination lifetimes result in charge carrier losses and, hence, in smaller short-circuit photocurrents,[4] the observed recombination dynamics explains the poor performance of cells with complexes [**1**](PF_6)$_2$ – [**6**](PF_6)$_2$ compared with the cell with N719 (Table 3). The cell with [**4**](PF_6)$_2$ features the smallest recombination rate constant among our bis(tridentate) complexes, followed by the cell with [**2**](PF_6)$_2$ (Figure 12 and Figure 13). This might again be due to the high dye loading of [**4**](PF_6)$_2$ [and [**2**](PF_6)$_2$] as discussed above (Table 3).[96] The lower dye loadings of [**1**](PF_6)$_2$, [**3**](PF_6)$_2$, [**5**](PF_6)$_2$, and [**6**](PF_6)$_2$ cannot effectively protect the TiO_2 surface from I_3^- and might be responsible for the high recombination rates. Successful strategies to suppress recombination are manifold and include the use of additional oxidic blocking layers, TiO_2 underlayers, coadsorbents, and sterically demanding dyes as surface protection.[96,103,104]

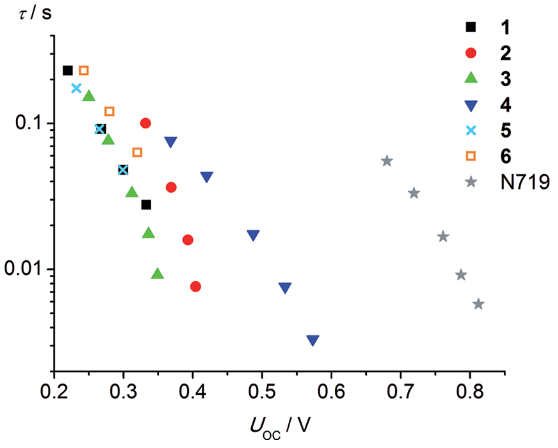

Figure 13. Electron recombination lifetimes τ vs. the open-circuit voltage U_{OC} of DSSCs with complexes [**1**](PF_6)$_2$ – [**6**](PF_6)$_2$ and N719.

Conclusions

Push-pull substituted heteroleptic bis(tridentate) ruthenium(II) polypyridine chromophores [**1**](PF_6)$_2$ – [**3**](PF_6)$_2$ (Figure 1) have been synthesized and fully characterized by ESI and HR-ESI mass spectrometry, infrared, ^{1}H, ^{13}C and ^{15}N NMR 1D and 2D spectroscopy, elemental analysis, electrochemistry, UV/Vis absorption and emission spectroscopy. The pronounced donor–acceptor substitution induces a small HOMO–LUMO gap, which shifts the absorption to lower energy (up to λ_{max} = 544 nm and extending to 720 nm). The push-pull character is introduced by a tpy acceptor ligand featuring one or three carboxylic acid functionalities as electron-withdrawing components and a tpy/ddpd donor ligand featuring two or three amino functionalities as electron-donating components. DFT calculations show spatially separated and orthogonal frontier orbitals with a high electronic directionality. Irradiation experiments reveal a high photostability for our bis(tridentate) complexes under conditions where N719 and tris(bidentate) [Ru(bpy)$_3$](PF_6)$_2$ undergo photodecomposition. Oxidation experiments revealed a superior stability of bis(tridentate) complexes as compared with N719. Complexes [**1**](PF_6)$_2$ – [**6**](PF_6)$_2$ (Figure 1) were tested as photosensitizers for TiO_2 in dye-sensitized solar cells with an I^-/I_3^- redox electrolyte. For the first time, 2,2′-bipyridine groups were used as anchors to TiO_2 {[**5**](PF_6)$_2$ and [**6**](PF_6)$_2$}. Power conversion efficiencies up to η = 0.26% under full AM 1.5 were obtained compared to η = 5.0% for the standard sensitizer N719 under our conditions. The twofold positive charge of our complexes contrasts with the twofold negative charge of N719. Consequently, the concentration of I_3^- near the TiO_2 electrode is increased and favors electron recombination. High dark currents and high recombination rates were measured for DSSCs with complexes [**1**](PF_6)$_2$ – [**6**](PF_6)$_2$, which rationalize the low cell performances.

Future perspectives are the use of negatively charged, cyclometalated, tridentate ligands, alkylated ligands, or triarylamine substituted ligands derived from tpy and ddpd, which can be used to redshift and broaden the absorption spectrum, to increase the push-pull characteristics and to decrease the overall positive charge of our complexes while retaining the excellent photo- and redox-stability.

Experimental Section

General Procedures: Diethyl ether was distilled from sodium, and acetonitrile from CaH_2 under an argon atmosphere. All reagents were used without further treatment from commercial suppliers (Acros and Sigma–Aldrich). Microwave heating was performed with a Discover Benchmate Plus (CEM Synthesis) single-mode microwave cavity, producing continuous irradiation at 2.455 GHz with 100 W (maximum power). NMR spectra were recorded with a Bruker Avance DRX 400 spectrometer at 400.31 MHz (^{1}H), 100.66 MHz (^{13}C{^{1}H}), and 40.56 MHz (^{15}N). All resonances are reported in ppm vs. the solvent signal as an internal standard [CH_3CN (^{1}H, δ = 1.94 ppm; ^{13}C, δ = 1.24 ppm)] or vs. external CH_3NO_2 [90% in $CDCl_3$, δ = 380.23 ppm vs. NH_3(l)] and referenced to NH_3 (^{15}N, δ = 0 ppm). Figure 1 shows the atom numbering for NMR signal assignment. IR spectra were recorded with a BioRad Excalibur FTS 3100 spectrometer as CsI disks. Electrochemical experiments were carried out with a Bio Logic SP-50 voltammetric analyzer using platinum wires as counter- and working-electrodes and 0.01 M Ag/AgNO$_3$ as reference electrode. The measurements were performed with a scan rate of 50–333 mV s^{-1} for cyclic voltammetry experiments and 100–200 mV s^{-1} for square-wave voltammetry experiments using 0.1 M [nBu$_4$N](PF_6) as the supporting electrolyte and a 10^{-3} M solution of the sample in anhydrous and degassed CH_3CN. Potentials are referenced to the ferrocene/ferrocenium couple ($E_{1/2}$ = 86 ± 5 mV under our experimental conditions). UV/Vis/near-IR spectra were recorded with a Varian Cary 5000 or a Jasco V-670 spectrometer using 1.0 cm cells (Hellma, Suprasil). Emission spectra were recorded with a Varian Cary Eclipse spectrometer. Quantum yields were determined by comparing the areas under the emission spectra on an energy scale (cm^{-1}) recorded for optically matched solutions of the sample and the reference [Ru(bpy)$_3$]Cl$_2$ (Φ = 9.4% in deaerated CH_3CN).[105] ESI mass spectra were recorded with a Micromass Q-TOF-Ultima spectrometer. Elemental analyses were performed by the microanalytical laboratory of the chemical institutes of the University of Mainz.

Photostability: Photostability measurements were conducted at room temperature under an Ar atmosphere in 0.1 M [nBu$_4$N]I in CH_3CN/H_2O (98:2, v/v) at λ_{exc} = 400 and 500 nm, respectively. The concentrations of the solutions were adjusted to ensure the same absorption at the corresponding excitation wavelength. The concentrations of **[1^Et]**$(PF_6)_2$, **[4^Et]**$(PF_6)_2$, N719, and [Ru(bpy)$_3$]$(PF_6)_2$ for the irradiation at λ_{exc} = 400 nm were 3.94×10^{-5}, 1.97×10^{-5}, 0.82×10^{-5}, and 0.96×10^{-5} M and for the irradiation at λ_{exc} = 500 nm 3.83×10^{-6}, 1.02×10^{-6}, 2.23×10^{-6}, and 9.89×10^{-6} M, respectively. As light sources, a Bivar LED (108A-713–5059, 400 nm) and a Sloan LED (L5-BG1G, 500 nm) were used in combination with a 40 W supply. Photodecomposition products of [Ru(bpy)$_3$]$(PF_6)_2$ were found when [Ru(bpy)$_3$]$(PF_6)_2$ (9.4 mg, 0.011 mmol, 1.0 equiv.) and [nBu$_4$N]I (9.0 mg, 0.024 mmol, 2.2 equiv.) were dissolved in CD_3CN (1.0 mL) and irradiated for 5 d at λ_{exc} = 400 nm. Before and after irradiation, NMR spectra were measured and their analysis revealed the formation of non-coordinated 2,2′-bipyridine during the irradiation. ESI$^+$ mass spectra were measured with the same solution. Photodecomposition products of N719 were found when N719 (3.9 mg, 0.0033 mmol, 1.0 equiv.) and [nBu$_4$N]I (5.5 mg, 0.015 mmol, 4.5 equiv.) were dissolved in CD_3CN/H_2O (14:1, 0.75 mL) and irradiated for 4 d at λ_{exc} = 400 nm. Before and after irradiation, NMR spectra were measured and reveal the formation of a new complex, in which presumably both NCS^- ligands are substituted by I^- or H_2O. No signals with ruthenium isotope pattern could be found in FD, ESI$^+$, or ESI$^-$ mass spectra.

Redox Stability: The chemical stabilities of electrochemically oxidized complexes were measured at room temperature in a 10^{-3} M NaOH and 0.1 M [nBu$_4$N](PF_6) in CH_3CN/H_2O (98:2, v/v) with ruthenium complex concentrations of 2×10^{-4} M. The optical pathlength of the OTTLE cell was 1 mm. A platinum mesh was used as working electrode, a platinum wire as counter electrode, and 0.01 M $Ag/AgNO_3$ as reference electrode. Electrical potentials were applied for at least 2 min before UV/Vis spectra were recorded.

DFT Calculations: Calculations were performed by using the Gaussian09/DFT[106]series of programs. The B3LYP formulation of DFT was used, employing the LANL2DZ basis set.[106] No symmetry constraints were imposed on the molecules. The presence of energy minima was checked by analytical frequency calculations. The integral-equation-formalism polarizable continuum model (IEFPCM in CH_3CN) was employed for solvent modeling. In TD-DFT calculations, at least 50 singlet transitions ($n \geq 50$) were calculated. All calculations were performed without explicit counterions and solvent molecules.

Materials and Fabrication of Dye-Sensitized Solar Cells: A TiO_2 blocking layer was prepared by spin coating a 2 wt.-% solution of bis(ethyl acetoacetato)-diisopropoxide titanium(IV) in *n*-butanol onto a FTO glass (TEC 8, Pilkington) followed by sintering at 500 °C for 15 min. The nanostructured TiO_2 layer was fabricated by doctor blading commercial TiO_2 paste (18NR-T, Dyesol) onto the TiO_2 layered FTO substrate followed by sintering at 500 °C for 15 min. The TiO_2 particle size was around 20 nm and the TiO_2 layer thickness was 7 µm as measured by a surface profiler (alpha-step IQ, Tencor). The TiO_2 electrodes were dipped into 0.3 mM solutions of ruthenium complexes in acetonitrile/*tert*-butyl alcohol (1:1) for 18 h at 25 °C, washed with acetonitrile and dried with an air stream. Dye loadings on TiO_2 were determined by the absorption difference of the dipping solution before and after dipping of a TiO_2 layer with a defined area of 2.6 cm^2. The N719 dye, bis(tetra-*n*-butylammonium)-*cis*-di(isothiocyanato)bis(2,2′-bipyridyl-4,4′-dicarboxylato)ruthenium(II), (Solaronix) was used as reference. For cell measurements, an active TiO_2 area of 0.25 cm^2 was used. Pt counter electrodes were fabricated by thermal decomposition of 0.01 M H_2PtCl_6 (Sigma–Aldrich) in isopropanol (Sigma–Aldich) and were spun onto FTO substrates followed by sintering at 500 °C for 15 min. Two small holes were made in the Pt counter electrodes with a drill. A Surlyn film (25 µm, Solaronix) was sandwiched between the TiO_2 and the Pt electrode. The electrolyte was filled into the cell through one of the two holes and sealed with a Surlyn film and a cover glass. The electrolyte is a mixture of 1-methyl-3-propylimidazolium iodide (0.6 M) and iodine (0.05 M) in acetonitrile.

Characterization: The current-voltage curves of the cells were measured with a Keighley Model 2400 source meter and a solar simulator with a 300 W xenon arc-lamp (Newport) under 1 sun illumination (AM 1.5, 100 mW cm^{-2}). The light intensity was calibrated by a silicon solar cell (PV measurements, Inc.) A shading mask was placed on the residual area of the front side FTO substrate except for the 0.25 cm^2 TiO_2 active area to prevent overestimation of the power conversion efficiency. Electron recombination lifetimes were characterized by intensity-modulated photovoltage spectroscopy using IM6 (Zahner) under an open circuit condition. A white light-emitting diode (LED, λ_{emiss} = 603 nm, $\Delta\lambda$ = 105 nm) was used as the modulated light source to ensure a homogeneous distribution of the illumination of the TiO_2 photoanodes. The applied light intensities ranged from 250 to 7 W m^{-2}.

Syntheses: The syntheses of **[4]**$(PF_6)_2$ – **[6]**$(PF_6)_2$ have been reported previously.[45,49,50,62]

[Ru(ddpd)(HOOC-tpy)]$(PF_6)_2$ ([1]$(PF_6)_2$): [Ru(ddpd)(EtOOC-tpy)]$(PF_6)_2$[55] (119.6 mg, 0.121 mmol, 1.0 equiv.) was dissolved in CH_3CN (20 mL) and a mixture of conc. H_2SO_4 (20 mL) and water (50 mL) was added. The solution was heated to reflux (15 h). After cooling to room temperature, the mixture was neutralized with saturated NaOH solution and the solvent was removed under reduced pressure. CH_3CN (100 mL) was added, the suspension was ultrasonicated (1 min), filtered, and washed with CH_3CN (75 mL). The solvent was removed under reduced pressure and the precipitate was dissolved in water (10 mL). The pH was adjusted to 1.0 with conc. H_2SO_4. The addition of an acidic aqueous solution of [NH_4](PF_6) (127.8 mg, 0.785 mmol, 6.5 equiv; 5 mL water; the pH was adjusted to 1.0 with conc. H_2SO_4) led to precipitation of a dark-purple solid, which was filtered and washed with cold water (ca. 10 mL). The solid was dissolved in CH_3CN (1 mL) and precipitated by the addition of Et_2O (10 mL). After filtration, washing with Et_2O (10 mL), and drying under reduced pressure a dark-purple solid was obtained, yield 88.3 mg (0.092 mmol, 76 %). ^{1}H NMR (CD_3CN, 300 K): δ = 8.99 (s, 2 H, H-2), 8.56 (m, 2 H, H-5), 8.27 (t, $^3J_{H,H}$ = 8.2 Hz, 1 H, H-16), 8.11 (m, 2 H, H-8), 8.01 (m, 2 H, H-6), 7.61 (m, 2 H, H-11), 7.56 (d, $^3J_{H,H}$ = 8.2 Hz, 2 H, H-15), 7.47 (m, 2 H, H-7), 7.17 (m, 2 H, H-12), 6.58 (m, 2 H, H-10), 6.44 (m, 2 H, H-9), 3.47 (s, 6 H, CH_3N) ppm, no resonance for OH was observed. $^{13}C\{^1H\}$ NMR (CD_3CN, 300 K): δ = 165.7 (s, C=O), 159.8 (s, C-13), 159.5 (s, C-3), 158.7 (s, C-4), 157.2 (s, C-14), 155.1 (s, C-8), 149.4 (s, C-9), 141.7 (s, C-16), 140.1 (s, C-11), 139.1 (s, C-6), 137.1 (s, C-1), 127.9 (s, C-7), 125.7 (s, C-5), 124.1 (s, C-2), 121.4 (s, C-10), 116.3 (s, C-12), 113.5 (s, C-15), 41.8 (s, CH_3N) ppm. ^{1}H-^{15}N HMBC (CD_3CN, 300 K): δ = 293.6 (N^e), 238.3 (N^d), 218.4 (N^c), 212.1 (N^a), 92.1 (N^b) ppm. MS (ESI$^+$): *m/z* (%) = 335.1 (27) $[M - 2\,PF_6]^{2+}$, 625.1 (7) $[M - H - CO_2 - PF_6]^+$, 815.1 (100) $[M - PF_6]^+$. HRMS (ESI$^+$): *m/z* calcd. for $C_{33}H_{28}F_6N_8O_2P^{96}Ru^+$ 809.1053; found 809.1056. IR (CsI): $\tilde{\nu}$ = 3443 (br., m, OH), 3088 (w, CH), 2926 (w, CH), 1728 (m, C=O), 1601 (s, C=N), 1582 (m, C=N), 1489 (m, C=N), 1450 (s), 1364 (m), 1341 (m), 1279 (m), 1234 (m), 1138 (m), 1097 (m), 1043 (w), 1022 (w), 949 (w), 839 (vs, PF), 798 (m), 777 (m), 752 (m), 559 (s), 527 (w) cm^{-1}. UV/Vis (CH_3CN): λ_{abs} (ε, $\mathrm{M}^{-1}\,cm^{-1}$) = 517 (8110), 319 (31200), 279 (37600), 221 (37500) nm. Emission (CH_3CN, 295 K, λ_{exc} = 517 nm): λ_{emiss} = 732 nm. Φ(CH_3CN, λ_{exc} = 468 nm, 295 K): 0.068 %. CV (CH_3CN): $E_{1/2}$ = +0.81 (1e, rev.), –1.50 (1e, irrev.) V vs. Fc/Fc$^+$. $C_{33}H_{28}F_{12}N_8O_2P_2Ru\cdot0.8H_2O\cdot0.3Et_2O$: calcd. C 41.23, H 3.30, N 11.25; found C 40.94, H 2.99, N 10.87.

[Ru(ddpd){(HOOC)$_3$-tpy}](PF$_6$)$_2$ ([2](PF$_6$)$_2$): [Ru(ddpd){(MeOOC)$_3$-tpy}](PF$_6$)$_2$[41] (114.7 mg, 0.1053 mmol, 1.0 equiv.) was dissolved in CH_3CN (4 mL) and a mixture of conc. H_2SO_4 (4 mL) and water (10 mL) was added. The solution was heated to reflux (20 h). After cooling to room temperature, CH_3CN was removed under reduced pressure. The pH was adjusted to 1.0 with saturated aqueous NaOH solution. The addition of an acidic aqueous solution of [NH$_4$](PF$_6$) (646.0 mg, 3.963 mmol, 37.6 equiv; 10 mL water; the pH was adjusted to 1.0 with conc. H_2SO_4) led to the precipitation of a dark-purple solid, which was filtered and washed with an acidic aqueous solution of [NH$_4$](PF$_6$) (20.0 mg, 0.123 mmol, 1.2 equiv; 20 mL water; the pH was adjusted to 1.0 with conc. H_2SO_4). The solid was dried under reduced pressure to give a dark-purple powder, yield 55.5 mg (0.053 mmol, 50 %). ^{1}H NMR (CD_3CN, 300 K): δ = 9.15 (s, 2 H, H-2), 8.97 (m, 2 H, H-5), 8.29 (t, $^3J_{H,H}$ = 8.2 Hz, 1 H, H-16), 8.26 (m, 2 H, H-8), 7.89 (m, 2 H, H-7), 7.61 (m, 2 H, H-11), 7.58 (d, $^3J_{H,H}$ = 8.2 Hz, 2 H, H-15), 7.18 (m, 2 H, H-12), 6.56 (m, 2 H, H-10), 6.36 (m, 2 H, H-9), 3.47 (s, 6 H, CH_3N) ppm, no resonance for OH was observed. ^{13}C{^{1}H} NMR (CD_3CN, 300 K): δ = 165.1 (s, C=O^{center}), 164.7 (s, C=O^{outer}), 159.7 (s, C-3), 159.6 (s, C-13), 159.2 (s, C-4), 157.1 (s, C-14), 155.8 (s, C-8), 149.2 (s, C-9), 142.1 (s, C-16), 140.4 (s, C-11), 140.1 (s, C-6), 136.6 (s, C-1), 127.1 (s, C-7), 125.0 (s, C-2), 124.9 (s, C-5), 121.6 (s, C-10), 116.6 (s, C-12), 113.7 (s, C-15), 41.7 (s, CH_3N) ppm. ^{1}H-^{15}N HMBC (CD_3CN, 300 K): δ = 293.9 (N^e), 249.5 (N^d), 216.3 (N^c), 209.0 (N^a) ppm, N^b was not observed. MS (ESI$^+$): *m/z* (%) = 379.1 (100) [*M* – 2 PF$_6$]$^{2+}$, 903.1 (80) [*M* – PF$_6$]$^+$. HRMS (ESI$^+$): *m/z* calcd. for $C_{35}H_{28}F_6N_8O_6P^{96}Ru^+$ 897.0850; found 897.0836. IR (CsI): $\tilde{\nu}$ = 3440 (br., m, OH), 3105 (w, CH), 2928 (w, CH), 2855 (w, CH), 1726 (m, C=O), 1605 (m, C=N), 1543 (w, C=N), 1489 (w, C=N), 1450 (m), 1404 (m), 1360 (vs), 1234 (s), 1138 (m), 1115 (m), 1099 (s), 843 (vs, PF), 800 (w), 777 (m), 752 (w), 679 (w), 615 (w), 559 (w) cm^{-1}. UV/Vis (CH_3CN): λ_{abs} (ε, $\mathrm{M}^{-1}\,cm^{-1}$) = 537 (6600), 473 (5820), 340 (34400), 291 (37100), 211 (55300) nm. Emission (CH_3CN, 295 K, λ_{exc} = 537 nm): λ_{emiss} = 743 nm. Φ(CH_3CN, λ_{exc} = 467.5 nm, 295 K): 0.59 %. CV (CH_3CN): $E_{1/2}$ = +0.87 (1e, rev.), –1.37 (1e, irrev.) V vs. Fc/Fc$^+$. $C_{35}H_{28}F_{12}N_8O_6P_2Ru\cdot0.3H_2O$: calcd. C 39.92, H 2.74, N 10.64; found C 40.51, H 3.36, N 10.36.

[Ru(ddpd-NH$_2$){(HOOC)$_3$-tpy}](PF$_6$)$_2$ ([3](PF$_6$)$_2$): {(MeOOC)$_3$-tpy}RuCl$_3$[13,69–71] (222.3 mg, 0.3616 mmol, 1.00 equiv.) and ddpd-4′-phthalimide[41] (162.7 mg, 0.3728 mmol, 1.03 equiv.) were suspended in methanol (20 mL), ultrasonicated (1 min), and *N*-ethylmorpholine (0.40 mL, 3.2 mmol, 8.7 equiv.) was added. The dark-green to brown mixture was heated to reflux in a laboratory microwave oven for 45 min (75 °C). After cooling to room temperature, the mixture was filtered through Celite (1.5 cm; Ø 3.0 cm) and rinsed with methanol. The solvent was removed under reduced pressure and the residue was dissolved in conc. HCl/H_2O (2:1, 150 mL) and heated to reflux (15 h). After cooling to room temperature, the pH was carefully adjusted to 0.9 with saturated NaOH solution. The addition of an acidic aqueous solution of [NH$_4$](PF$_6$) (1.0 g, 6.1 mmol, 17 equiv., 100 mL H_2O, adjusted to pH 0.9 with conc. H_2SO_4) led to the precipitation of a dark-purple solid, which was filtered and washed with an acidic aqueous solution of [NH$_4$](PF$_6$) (100 mg, 0.613 mmol, 1.7 equiv., 100 mL H_2O, adjusted to pH 0.9 with conc. H_2SO_4). The solid was dried under reduced pressure to give a dark-purple powder, yield 95.1 mg (0.0895 mmol, 25 %). ^{1}H NMR (CD_3CN, 300 K): δ = 9.12 (s, 2 H, H-2), 8.94 (m, 2 H, H-5), 8.30 (m, 2 H, H-8), 7.89 (m, 2 H, H-7), 7.58 (m, 2 H, H-11), 7.12 (m, 2 H, H-12), 6.81 (s, 2 H, H-15), 6.52 (m, 2 H, H-10), 6.29 (m, 2 H, H-9), 5.75 (br. s, 2 H, NH$_2$), 3.36 (s, 6 H, CH_3N) ppm, no resonance for OH was observed. ^{13}C{^{1}H} NMR (CD_3CN, 300 K): δ = 165.3 (s, C=O^{center}), 164.8 (s, C=O^{outer}), 160.0 (s, C-13), 159.8 (s, C-4), 159.5 (s, C-3), 159.3 (s, C-16), 156.7 (s, C-14), 155.7 (s, C-8), 149.2 (s, C-9), 140.3 (s, C-11), 139.7 (s, C-6), 135.5 (s, C-1), 127.0 (s, C-7), 124.9 (s, C-2), 124.7 (s, C-5), 121.2 (s, C-10), 116.5 (s, C-12), 98.8 (s, C-15), 41.3 (s, CH_3N) ppm. ^{1}H-^{15}N HMBC (CD_3CN, 300 K): δ = 296.9 (N^e), 249.9 (N^d), 210.0 (N^a), 181.6 (N^c), 72.2 (NH$_2$) ppm, N^b was not observed. MS (ESI$^+$): *m/z* (%) = 386.6 (38) [*M* – 2 PF$_6$]$^{2+}$, 918.1 (100) [*M* – PF$_6$]$^+$. HRMS (ESI$^+$): *m/z* calcd. for $C_{35}H_{29}F_6N_9O_6P^{96}Ru^+$ 912.0959; found 912.0914. IR (CsI): $\tilde{\nu}$ = 3443 (br., s, OH), 3098 (w, CH), 2959 (w, CH), 2926 (w, CH), 2855 (w, CH), 1713 (m, C=O), 1605 (vs, NH, C=N), 1539 (m, C=N), 1462 (s), 1437 (m), 1404 (s), 1360 (vs), 1234 (m), 1167 (m), 1117 (m), 1097 (vs), 968 (w), 841 (vs, PF), 781 (m), 756 (m), 727 (w), 696 (w), 683 (w), 667 (w), 648 (w), 613 (s), 561 (s), 530 (w), 505 (w), 482 (w), 451 (w), 347 (w) cm^{-1}. UV/Vis (CH_3CN): λ_{abs} (ε, $\mathrm{M}^{-1}\,cm^{-1}$) = 544 (6690), 480 (5090), 340 (30400), 292 (34400), 217 (59900) nm. Emission (CH_3CN, 295 K, λ_{exc} = 544 nm): λ_{emiss} = 771 nm. Φ(CH_3CN, λ_{exc} = 509 nm, 295 K): 0.067 %. CV (CH_3CN): $E_{1/2}$ = +0.71 (1e, rev.), –1.53 (1e, irrev.) V vs. Fc/Fc$^+$. $C_{35}H_{29}F_{12}N_9O_6P_2Ru\cdot3CH_3OH$: calcd. C 39.39, H 3.57, N 10.88; found C 39.96, H 3.67, N 11.22.

Supporting Information (see footnote on the first page of this article): Tabulated ^{1}H, ^{13}C and ^{15}N NMR chemical shifts in CD_3CN; cyclic and square-wave voltammograms of [**1**](PF$_6$)$_2$ – [**3**](PF$_6$)$_2$; spin densities of [**1**]$^+$ – [**6**]$^+$ and reduced N719; frontier molecular orbitals of [**1**]$^{2+}$ – [**6**]$^{2+}$ and N719. ^{1}H NMR spectra of [Ru(bpy)$_3$](PF$_6$)$_2$/[*n*Bu$_4$N]I before and after irradiation. ESI mass spectrum of [Ru(bpy)$_3$](PF$_6$)$_2$/[*n*Bu$_4$N]I after irradiation. ^{1}H NMR spectra of N719/[*n*Bu$_4$N]I before and after irradiation. UV/Vis spectra of the electrochemical oxidation and back reduction of [**1**](PF$_6$)$_2$; [Ru(bpy)$_3$](PF$_6$)$_2$ and N719 in the presence of NaOH; IPCE plots of cells with [**1**](PF$_6$)$_2$ – [**6**](PF$_6$)$_2$ and N719; DFT (B3LYP/LANL2DZ, IEFPCM, CH_3CN) optimized geometries of [**1**]$^{2+}$ – [**6**]$^{2+}$ and N719 (singlet) and [**1**]$^{3+}$ – [**6**]$^{3+}$, and oxidized N719 (doublet); results of TD-DFT calculations of [**1**]$^{2+}$ – [**6**]$^{2+}$ and N719 (singlet).

Acknowledgments

This work was supported by the International Research Training Group (IRTG 1404): Self Organized Materials for Optoelectronics supported by the Deutsche Forschungsgemeinschaft (DFG).

---

[1] B. O'Regan, M. Grätzel, *Nature* **1991**, *353*, 737–740.
[2] A. Hagfeld, G. Boschloo, L. Sun, L. Kloo, H. Pettersson, *Chem. Rev.* **2010**, *110*, 6595–6663.
[3] A. Reynal, E. Palomares, *Eur. J. Inorg. Chem.* **2011**, *29*, 4509–4526.
[4] J.-F. Yin, M. Velayudham, D. Bhattacharya, H.-C. Lin, K.-L. Lu, *Coord. Chem. Rev.* **2012**, *256*, 3008–3035.
[5] P. G. Bomben, K. C. D. Robson, B. D. Koivisto, C. P. Berlinguette, *Coord. Chem. Rev.* **2012**, *256*, 1438–1450.

[6] C. A. Bignozzi, R. Argazzi, R. Boaretto, E. Busatto, S. Carli, F. Ronconi, S. Caramori, *Coord. Chem. Rev.* **2013**, *257*, 1472–1492.

[7] B. Bozic-Weber, E. C. Constable, C. E. Housecroft, *Coord. Chem. Rev.* **2013**, *257*, 3089–3106.

[8] T. Chen, L. Qiu, Z. Yang, H. Peng, *Chem. Soc. Rev.* **2013**, *42*, 5031–5041.

[9] A. Yella, H.-W. Lee, H. N. Tsao, C. Yi, A. K. Chandiran, M. K. Nazeeruddin, E. W.-G. Diau, C.-Y. Yeh, S. M. Zakeeruddin, M. Grätzel, *Science* **2011**, *334*, 629–634.

[10] S. Campagna, F. Puntoriero, F. Nastasi, G. Bergamini, V. Balzani, *Top. Curr. Chem.* **2007**, *280*, 117–214.

[11] M. K. Nazeeruddin, S. M. Zakeeruddin, R. Humphry-Baker, M. Jirousek, P. Liska, N. Vlachopoulos, V. Shklover, C.-H. Fischer, M. Grätzel, *Inorg. Chem.* **1999**, *38*, 6298–6305.

[12] M. K. Nazeeruddin, F. D. Angelis, S. Fantacci, A. Selloni, G. Viscardi, P. Liska, S. Ito, B. Takeru, M. Grätzel, *J. Am. Chem. Soc.* **2005**, *127*, 16835–16847.

[13] M. K. Nazeeruddin, P. Péchy, T. Renouard, S. M. Zakeeruddin, R. Humphrey-Baker, P. Comte, P. Liska, L. Cevey, E. Costa, V. Shklover, L. Spiccia, G. B. Deacon, C. A. Bignozzi, M. Grätzel, *J. Am. Chem. Soc.* **2001**, *123*, 1613–1624.

[14] T. P. Brewster, W. Ding, N. D. Schley, N. Hazari, V. S. Batista, R. H. Crabtree, *Inorg. Chem.* **2011**, *50*, 11938–11946.

[15] S. Betanzos-Lara, L. Salassa, A. Habtemariam, O. Novakova, A. M. Pizarro, G. J. Clarkson, B. Liskova, V. Brabec, P. J. Sadler, *Organometallics* **2012**, *31*, 3466–3479.

[16] S. Kämper, A. Paretzki, J. Fiedler, S. Záliš, W. Kaim, *Inorg. Chem.* **2012**, *51*, 2097–2104.

[17] G. Xue, Y. Guo, T. Yu, J. Guan, X. Yu, J. Zhang, J. Liu, Z. Zou, *Int. J. Electrochem. Sci.* **2012**, *7*, 1496–1511.

[18] A. Bahreman, B. Limburg, M. A. Siegler, E. Bouwman, S. Bonnet, *Inorg. Chem.* **2013**, *52*, 9456–9469.

[19] P. T. Nguyen, B. X. T. Lam, A. R. Andersen, P. E. Hansen, T. Lund, *Eur. J. Inorg. Chem.* **2011**, 2533–2539.

[20] C. Dragonetti, A. Valore, A. Colombo, D. Roberto, V. Trifiletti, N. Manfredi, M. M. Salamone, R. Ruffo, A. Abbotto, *J. Organomet. Chem.* **2012**, *714*, 88–93.

[21] M. M. R. Choudhuri, R. J. Crutchley, *Inorg. Chem.* **2013**, *52*, 14404–14410.

[22] C.-H. Siu, C.-L. Ho, J. He, T. Chen, X. Cui, J. Zhao, W.-Y. Wong, *J. Organomet. Chem.* **2013**, *748*, 75–83.

[23] T. Bessho, E. Yoneda, J.-H. Yum, M. Guglielmi, I. Tavernelli, H. Imai, U. Rothlisberger, M. K. Nazeeruddin, M. Grätzel, *J. Am. Chem. Soc.* **2009**, *131*, 5930–5934.

[24] K.-L. Wu, H.-C. Hsu, K. Chen, Y. Chi, M.-W. Chung, W.-H. Liu, P.-T. Chou, *Chem. Commun.* **2010**, *46*, 5124–5126.

[25] C. E. Welby, C. R. Rice, P. I. P. Elliott, *Angew. Chem. Int. Ed.* **2013**, *52*, 10826–10829; *Angew. Chem.* **2013**, *125*, 11026–11029.

[26] K. Garg, J. T. Engle, C. J. Ziegler, J. J. Rack, *Chem. Eur. J.* **2013**, *19*, 11686–11695.

[27] J. D. Slinker, J. Rivnay, J. S. Moskowitz, J. B. Parker, S. Bernhard, H. D. Abruña, G. G. Malliaras, *J. Mater. Chem.* **2007**, *17*, 2976–2988.

[28] J. D. Slinker, J.-S. Kim, S. Flores-Torres, J. H. Delcamp, H. D. Abruña, R. H. Friend, G. G. Malliaras, *J. Mater. Chem.* **2007**, *17*, 76–81.

[29] L. J. Soltzberg, J. D. Slinker, S. Flores-Torres, D. A. Bernards, G. G. Malliaras, H. D. Abruña, J.-S. Kim, R. H. Friend, M. D. Kaplan, V. Goldberg, *J. Am. Chem. Soc.* **2006**, *128*, 7761–7764.

[30] G. Kalyuzhny, M. Buda, J. McNeill, P. Barbara, A. J. Bard, *J. Am. Chem. Soc.* **2003**, *125*, 6272–6283.

[31] C. Fu, M. Wenzel, E. Treutlein, K. Harms, E. Meggers, *Inorg. Chem.* **2012**, *51*, 10004–10011.

[32] E. Meggers, *Chem. Eur. J.* **2010**, *16*, 752–758.

[33] M. Maestri, N. Armaroli, V. Balzani, E. C. Constable, A. M. W. Cargill Thompson, *Inorg. Chem.* **1995**, *34*, 2759–2767.

[34] R. Hogg, R. G. Wilkins, *J. Chem. Soc.* **1962**, 341–350.

[35] R. H. Holyer, C. D. Hubbard, S. F. A. Kettle, R. G. Wilkins, *Inorg. Chem.* **1966**, *5*, 622–625.

[36] J.-P. Sauvage, J.-P. Collin, J.-C. Chambron, S. Guillerez, C. Coudret, V. Balzani, F. Barigelletti, L. D. Cola, L. Flamigni, *Chem. Rev.* **1994**, *94*, 993–1019.

[37] L. Hammarström, O. Johansson, *Coord. Chem. Rev.* **2010**, *254*, 2546–2559.

[38] Y. Liu, R. Hammitt, D. A. Lutterman, R. P. Thummel, C. Turro, *Inorg. Chem.* **2007**, *46*, 6011–6021.

[39] T. Banerjee, S. Kaniyankandy, A. Das, H. N. Ghosh, *Inorg. Chem.* **2013**, *52*, 5366–5377.

[40] E. Jakubikova, R. C. Snoeberger, V. S. Batista, R. L. Martin, E. R. Batista, *J. Phys. Chem. A* **2009**, *113*, 12532–12540.

[41] A. Breivogel, M. Meister, C. Förster, F. Laquei, K. Heinze, *Chem. Eur. J.* **2013**, *19*, 13745–13760.

[42] H. J. Bolink, L. Cappelli, E. Coronado, P. Gaviña, *Inorg. Chem.* **2005**, *44*, 5966–5968.

[43] S. H. Wadman, J. M. Kroon, K. Bakker, M. Lutz, A. L. Spek, G. P. M. van Klink, G. van Koten, *Chem. Commun.* **2007**, *19*, 1907–1909.

[44] C. Houarner-Rassin, F. Chaignon, C. She, D. Stockwell, E. Blart, P. Buvat, T. Lian, F. Odobel, *J. Photochem. Photobiol. A* **2007**, *192*, 56–65.

[45] K. Heinze, K. Hempel, M. Beckmann, *Eur. J. Inorg. Chem.* **2006**, 2040–2050.

[46] A. Breivogel, K. Hempel, K. Heinze, *Inorg. Chim. Acta* **2011**, *374*, 152–162.

[47] K. Heinze, K. Hempel, A. Breivogel, *Z. Anorg. Allg. Chem.* **2009**, *635*, 2541–2549.

[48] R. J. Kumar, S. Karlsson, D. Streich, A. R. Jensen, M. Jäger, H.-C. Becker, J. Bergquist, O. Johansson, L. Hammarström, *Chem. Eur. J.* **2010**, *16*, 2830–2842.

[49] J. Dietrich, U. Thorenz, C. Förster, K. Heinze, *Inorg. Chem.* **2013**, *52*, 1248–1264.

[50] J. Dietrich, A. Wünsche von Leupoldt, M. Grabolle, U. Resch-Genger, K. Heinze, *Eur. J. Inorg. Chem.* **2013**, 3009–3019.

[51] L. zur Borg, A. L. Domanski, A. Breivogel, M. Bürger, R. Berger, K. Heinze, R. Zentel, *J. Mater. Chem.* **2013**, *1*, 1223–1230.

[52] T. J. Meyer, *Pure Appl. Chem.* **1986**, *58*, 1193–1206.

[53] J. V. Caspar, T. J. Meyer, *J. Am. Chem. Soc.* **1983**, *105*, 5583–5590.

[54] J. V. Caspar, T. J. Meyer, *J. Phys. Chem.* **1983**, *87*, 952–957.

[55] A. Breivogel, C. Förster, K. Heinze, *Inorg. Chem.* **2010**, *49*, 7052–7056.

[56] B. D. Koivisto, K. C. D. Robson, C. P. Berlinguette, *Inorg. Chem.* **2009**, *48*, 9644–9652.

[57] K. C. D. Robson, B. D. Koivisto, A. Yella, B. Sporinova, M. K. Nazeeruddin, T. Baumgartner, M. Grätzel, C. P. Berlinguette, *Inorg. Chem.* **2011**, *50*, 5494–5508.

[58] C.-C. Chou, K.-L. Wu, Y. Chi, W.-P. Hu, S. J. Yu, G.-H. Lee, C.-L. Lin, P.-T. Chou, *Angew. Chem. Int. Ed.* **2011**, *50*, 2054–2058; *Angew. Chem.* **2011**, *123*, 2102–2106.

[59] C.-C. Chou, F.-C. Hu, H.-H. Yeh, H.-P. Wu, Y. Chi, J. N. Clifford, E. Palomares, S.-H. Liu, P.-T. Chou, G.-H. Lee, *Angew. Chem. Int. Ed.* **2014**, *53*, 178–183; *Angew. Chem.* **2014**, *126*, 182–187.

[60] C.-W. Hsu, S.-T. Ho, K.-L. Wu, Y. Chi, S.-H. Liu, P.-T. Chou, *Energy Environ. Sci.* **2012**, *5*, 7549–7554.

[61] B. Schulze, D. Escudero, C. Friebe, R. Siebert, H. Görls, S. Sinn, M. Thomas, S. Mai, J. Popp, B. Dietzek, L. González, U. S. Schubert, *Chem. Eur. J.* **2012**, *18*, 4010–4025.

[62] K. Heinze, K. Hempel, S. Tschierlei, M. Schmitt, J. Popp, S. Rau, *Eur. J. Inorg. Chem.* **2009**, 3119–3126.

[63] W. B. Heuer, H.-L. Xia, W. Ward, Z. Zhou, W. H. Pearson, M. A. Siegler, A. A. N. Sarjeant, M. Abrahamsson, G. J. Meyer, *Inorg. Chem.* **2012**, *51*, 3981–3988.

[64] S. Zhang, Y. Peng, W. Jiang, X. Liu, X. Song, B. Pan, H.-Q. Yu, *Chem. Commun.* **2014**, *50*, 1086–1088.

[65] W. R. McNamara, R. C. Snoeberger III, G. Li, J. M. Schleicher, C. W. Cady, M. Poyatos, C. A. Schmuttenmaer, R. H.

Crabtree, G. W. Brudvig, V. S. Batista, *J. Am. Chem. Soc.* **2008**, *130*, 14329–14338.

[66] T. Banerjee, S. Rawalekar, A. Das, H. N. Ghosh, *Eur. J. Inorg. Chem.* **2011**, 4187–4197.

[67] E. Franzmann, F. Khalil, C. Weidmann, M. Schröder, M. Rohnke, J. Janek, B. M. Smarsly, W. Maison, *Chem. Eur. J.* **2011**, *17*, 8596–8603.

[68] M. I. Asghar, K. Miettunen, J. Halme, P. Vahermaa, M. Toivola, K. Aitola, P. Lund, *Energy Environ. Sci.* **2010**, *3*, 418–426.

[69] J. Dehaudt, J. Husson, L. Guyard, *Green Chem.* **2011**, *13*, 3337–3340.

[70] L. Giribabu, T. Bessho, M. Srinivasu, C. Vijaykumar, Y. Soujanya, V. G. Reddy, P. Y. Reddy, J.-H. Yum, M. Grätzel, M. K. Nazeeruddin, *Dalton Trans.* **2011**, *40*, 4497–4504.

[71] M. K. Nazeeruddin, P. Péchy, M. Grätzel, *Chem. Commun.* **1997**, *18*, 1705–1706.

[72] M. Hesse, H. Meier, B. Zeeh, *Spektroskopische Methoden in der Organischen Chemie*, Thieme, Stuttgart, Germany, **1991**.

[73] W.-S. Han, J.-K. Han, H.-Y. Kim, M. J. Choi, Y.-S. Kang, C. Pac, S. O. Kang, *Inorg. Chem.* **2011**, *50*, 3271–3280.

[74] F. D. Angelis, S. Fantacci, E. Mosconi, M. K. Nazeeruddin, M. Grätzel, *J. Phys. Chem. C* **2011**, *115*, 8825–8831.

[75] A. Breivogel, M. Park, D. Lee, S. Klassen, A. Kühnle, C. Lee, K. Char, K. Heinze, *Eur. J. Inorg. Chem.* **2014**, 288–295.

[76] G. R. Desiraju, *Angew. Chem. Int. Ed. Engl.* **1995**, *34*, 2311–2327; *Angew. Chem.* **1995**, *107*, 2541–2558.

[77] K. Heinze, K. Hempel, *Chem. Eur. J.* **2009**, *15*, 1346–1358.

[78] C. Turro, S. H. Bossmann, Y. Jenkins, J. K. Barton, N. J. Turro, *J. Am. Chem. Soc.* **1995**, *117*, 9026–9032.

[79] Y. Nosenko, G. Wiosna-Sałyga, M. Kunitski, I. Petkova, A. Singh, W. J. Buma, R. P. Thummel, B. Brutschy, J. Waluk, *Angew. Chem. Int. Ed.* **2008**, *47*, 6037–6040; *Angew. Chem.* **2008**, *120*, 6126–6129.

[80] M. Marazzi, U. Sancho, O. Castaño, W. Domcke, L. M. Frutos, *J. Phys. Chem. Lett.* **2010**, *1*, 425–428.

[81] G. Y. Zheng, Y. Wang, D. P. Rillema, *Inorg. Chem.* **1996**, *35*, 7118–7123.

[82] P. A. Lay, W. H. F. Sasse, *Inorg. Chem.* **1984**, *23*, 4125–4127.

[83] R. J. Watts, *J. Chem. Educ.* **1983**, *60*, 834–842.

[84] B. Durham, J. V. Caspar, J. K. Nagle, T. J. Meyer, *J. Am. Chem. Soc.* **1982**, *104*, 4803–4810.

[85] Z. J. Fuller, W. D. Bare, K. A. Kneas, W.-Y. Xu, J. N. Demas, B. A. DeGraff, *Anal. Chem.* **2003**, *75*, 2670–2677.

[86] W. M. Wallace, P. E. Hoggard, *Inorg. Chem.* **1979**, *18*, 2934–2935.

[87] T. E. Keyes, E. Gicquel, L. Guerin, R. J. Forster, V. Hultgren, A. M. Bond, A. G. Wedd, *Inorg. Chem.* **2003**, *42*, 7897–7905.

[88] M. Abrahamsson, M. Jäger, R. J. Kumar, T. Österman, P. Persson, H.-C. Becker, O. Johansson, L. Hammarström, *J. Am. Chem. Soc.* **2008**, *130*, 15533–15542.

[89] O. Kohle, M. Grätzel, A. F. Meyer, T. B. Meyer, *Adv. Mater.* **1997**, *9*, 904–906.

[90] G. Wolfbauer, A. M. Bond, D. R. MacFarlane, *Inorg. Chem.* **1999**, *38*, 3836–3846.

[91] G. Boschloo, A. Hagfeld, *Acc. Chem. Res.* **2009**, *42*, 1819–1826.

[92] Y. Ooyama, T. Nagano, S. Inoue, I. Imae, K. Komaguchi, J. Ohshita, Y. Harima, *Chem. Eur. J.* **2011**, *17*, 14837–14843.

[93] Y. Ooyama, S. Inoue, T. Nagano, K. Kushimoto, J. Oshita, I. Imae, K. Komaguchi, Y. Harima, *Angew. Chem. Int. Ed.* **2011**, *50*, 7429–7433; *Angew. Chem.* **2011**, *123*, 7567–7571.

[94] S. H. Wadman, J. M. Kroon, K. Bakker, M. Lutz, A. L. Spek, G. P. M. van Klink, G. van Koten, *Chem. Commun.* **2007**, 1907–1909.

[95] A. J. Frank, N. Kopidakis, J. van de Lagemaat, *Coord. Chem. Rev.* **2004**, *248*, 1165–1179.

[96] S. Ito, P. Liska, P. Comte, R. Charvet, P. Péchy, U. Bach, L. Schmidt-Mende, S. M. Zakeeruddin, A. Kay, M. K. Nazeeruddin, M. Grätzel, *Chem. Commun.* **2005**, 4351–4353.

[97] S. A. Haque, Y. Tachibana, R. L. Willis, J. E. Moser, M. Grätzel, D. R. Klug, J. R. Durrant, *J. Phys. Chem. B* **2000**, *104*, 538–547.

[98] S. Caramori, J. Husson, M. Beley, C. A. Bignozzi, R. Argazzi, P. C. Gros, *Chem. Eur. J.* **2010**, *16*, 2611–2618.

[99] M. K. Nazeeruddin, R. Humphry-Baker, P. Liska, M. Grätzel, *J. Phys. Chem. B* **2003**, *107*, 8981–8987.

[100] G. Pizzoli, M. G. Lobello, B. Carlotti, F. Elisei, M. K. Nazeeruddin, G. Vitillaro, F. D. Angelis, *Dalton Trans.* **2012**, *41*, 11841–11848.

[101] G. Schlichthörl, S. Y. Huang, J. Sprague, A. J. Frank, *J. Phys. Chem. B* **1997**, *101*, 8141–8155.

[102] J. Bisquert, F. Fabregat-Santiago, I. Mora-Seró, G. Garcia-Belmonte, S. Giménez, *J. Phys. Chem. A* **2009**, *113*, 17278–17290.

[103] E. Palomares, J. N. Clifford, S. A. Haque, T. Lutz, J. R. Durrant, *Chem. Commun.* **2002**, 1464–1465.

[104] Y.-G. Lee, S. Park, W. Cho, T. Son, P. Sudhagar, J. H. Jung, S. Wooh, K. Char, Y. S. Kang, *J. Phys. Chem. C* **2012**, *116*, 6770–6777.

[105] K. Suzuki, A. Kobayashi, S. Kaneko, K. Takehira, T. Yoshihara, H. Ishida, Y. Shiina, S. Oishi, S. Tobita, *Phys. Chem. Chem. Phys.* **2009**, *11*, 9850–9860.

[106] M. J. Frisch, G. W. Trucks, H. B. Schlegel, G. E. Scuseria, M. A. Robb, J. R. Cheeseman, G. Scalmani, V. Barone, B. Mennucci, G. A. Petersson, H. Nakatsuji, M. Caricato, X. Li, H. P. Hratchian, A. F. Izmaylov, J. Bloino, G. Zheng, J. L. Sonnenberg, M. Hada, M. Ehara, K. Toyota, R. Fukuda, J. Hasegawa, M. Ishida, T. Nakajima, Y. Honda, O. Kitao, H. Nakai, T. Vreven, J. A. Montgomery Jr., J. E. Peralta, F. Ogliaro, M. Bearpark, J. J. Heyd, E. Brothers, K. N. Kudin, V. N. Staroverov, R. Kobayashi, J. Normand, K. Raghavachari, A. Rendell, J. C. Burant, S. S. Iyengar, J. Tomasi, M. Cossi, N. Rega, J. M. Millam, M. Klene, J. E. Knox, J. B. Cross, V. Bakken, C. Adamo, J. Jaramillo, R. Gomperts, R. E. Stratmann, O. Yazyev, A. J. Austin, R. Cammi, C. Pomelli, J. W. Ochterski, R. L. Martin, K. Morokuma, V. G. Zakrzewski, G. A. Voth, P. Salvador, J. J. Dannenberg, S. Dapprich, A. D. Daniels, O. Farkas, J. B. Foresman, J. V. Ortiz, J. Cioslowski, D. J. Fox, *Gaussian 09*, revision A.02, Gaussian, Inc., Wallingford CT, **2009**.

Received: February 21, 2014
Published Online: April 28, 2014

10 Supporting Information

10.1 Explanatory Notes for the Supporting Information

In the following the full supporting information of all manuscripts and publications is reproduced herein expect published DFT optimized cartesian coordinates and published results of TD-DFT calculations. This is for the sake of clarity. The data can be found in the online supporting information of the respective journal.

10.2 Thermal and Photo Reactivity of a Donor-Acceptor-Substituted Bis(terpyridine) Ruthenium(III) Complex in Acidic Solutions

A. Breivogel, K. Heinze.

-to be submitted-

Thermal and Photo Reactivity of a Donor-Acceptor-Substituted Bis(terpyridine) Ruthenium(III) Complex in Acidic Solutions

Aaron Breivogel, and Katja Heinze*

Supporting Information

Table of Contents:

1) Figures S1 – S8

2) Preparation and characterization of the $IrCl(PEt_3)_3$ solution and Figure S9.

3) DFT (B3LYP/LANL2DZ, IEFPCM, H_2O) optimized geometries of $[\mathbf{1}]^{2+}$, $[\mathbf{1}]^{3+}$, $[\mathbf{1} – H]^{2+}$, $[\mathbf{1} – 2 H]^{+}$, $[Ru(\kappa^2\text{-}H_2N\text{-tpy})(\kappa^3\text{-HOOC-tpy})(H_2O)]^{3+}$ and "$[Ru(\kappa^3\text{-}H_2N\text{-tpy})(\kappa^3\text{-HOOC-tpy})]^{3+} + H_2O$".

4) Results of TD-DFT calculations of $[\mathbf{1}]^{2+}$ and $[\mathbf{1}]^{3+}$.

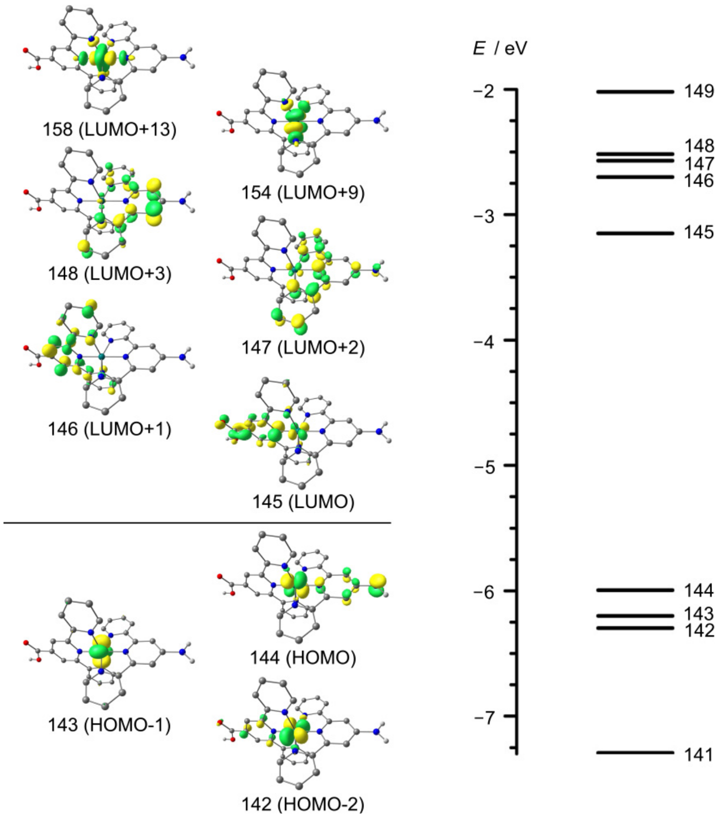

Figure S1. Relevant DFT-calculated Kohn-Sham frontier molecular orbitals (B3LYP/LANL2DZ, IEFPCM, H_2O, contour value 0.06 a.u., CH hydrogen atoms omitted) and energy levels of frontier molecular orbitals of $[\mathbf{1}]^{2+}$.

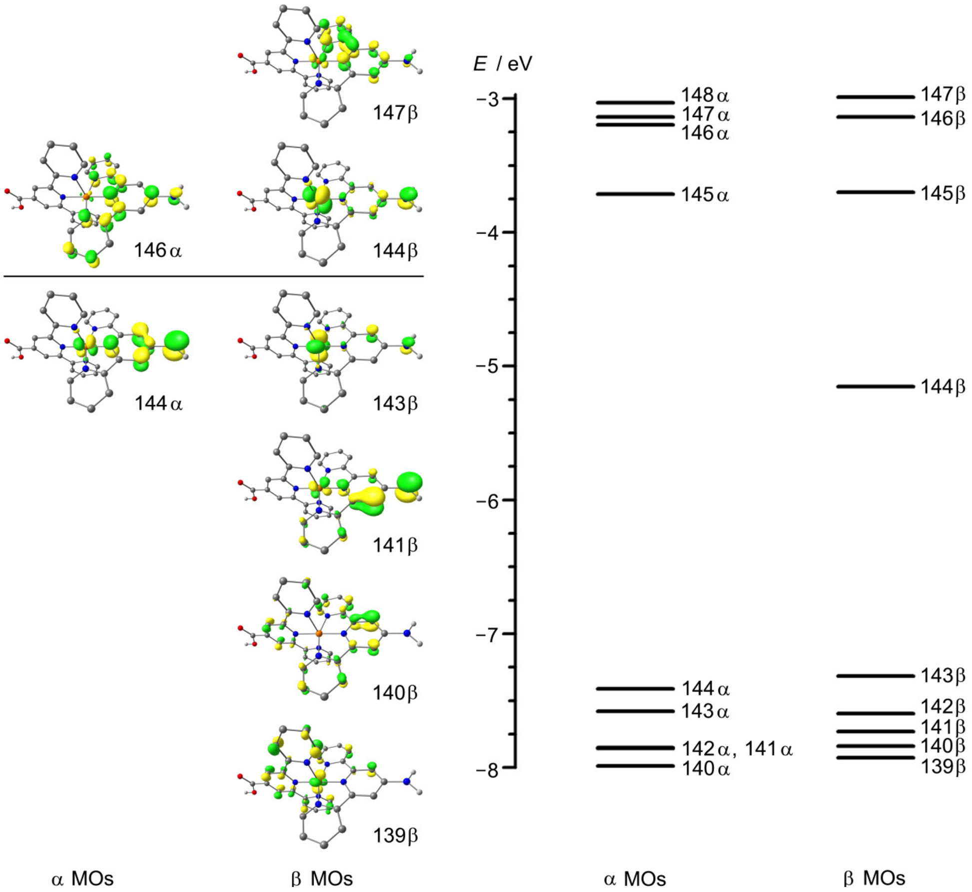

Figure S2. Relevant DFT-calculated Kohn-Sham frontier molecular orbitals (B3LYP/LANL2DZ, IEFPCM, H_2O, contour value 0.06 a.u., CH hydrogen atoms omitted) and energy levels of frontier molecular orbitals of $[\mathbf{1}]^{3+}$.

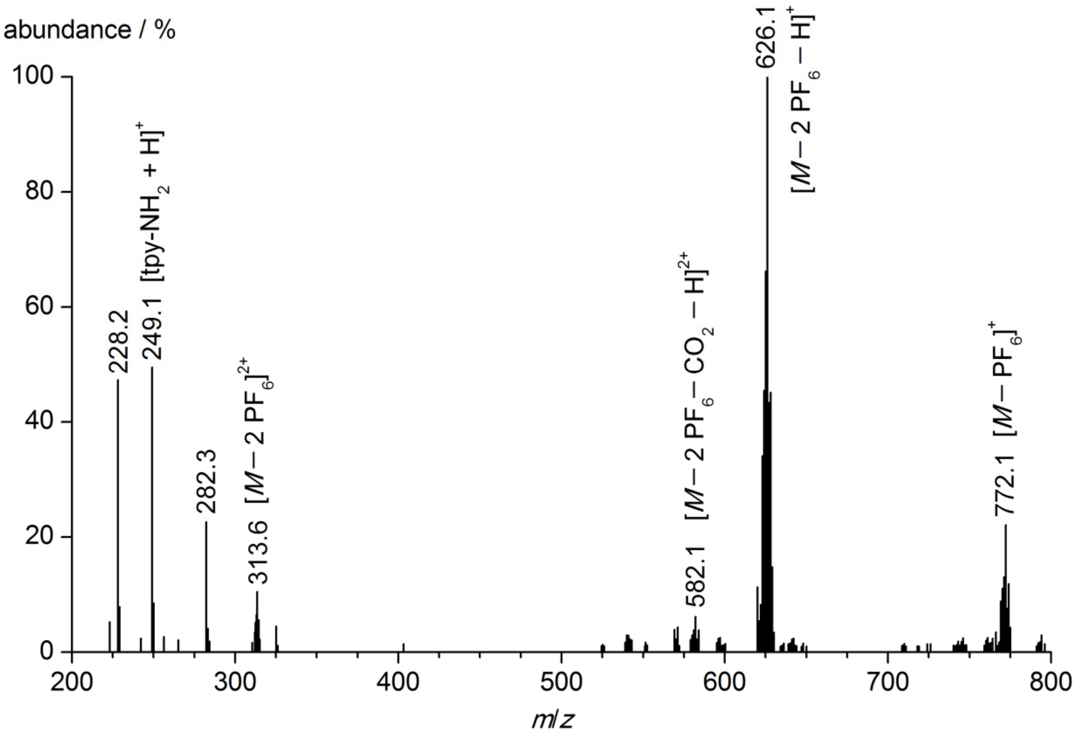

Figure S3. ESI$^+$ mass spectrum of [**1**](PF$_6$)$_2$ 0.5 M TFA in CH$_3$CN:H$_2$O (200:1) before addition of (NH$_4$)$_2$[Ce(NO$_3$)$_6$].

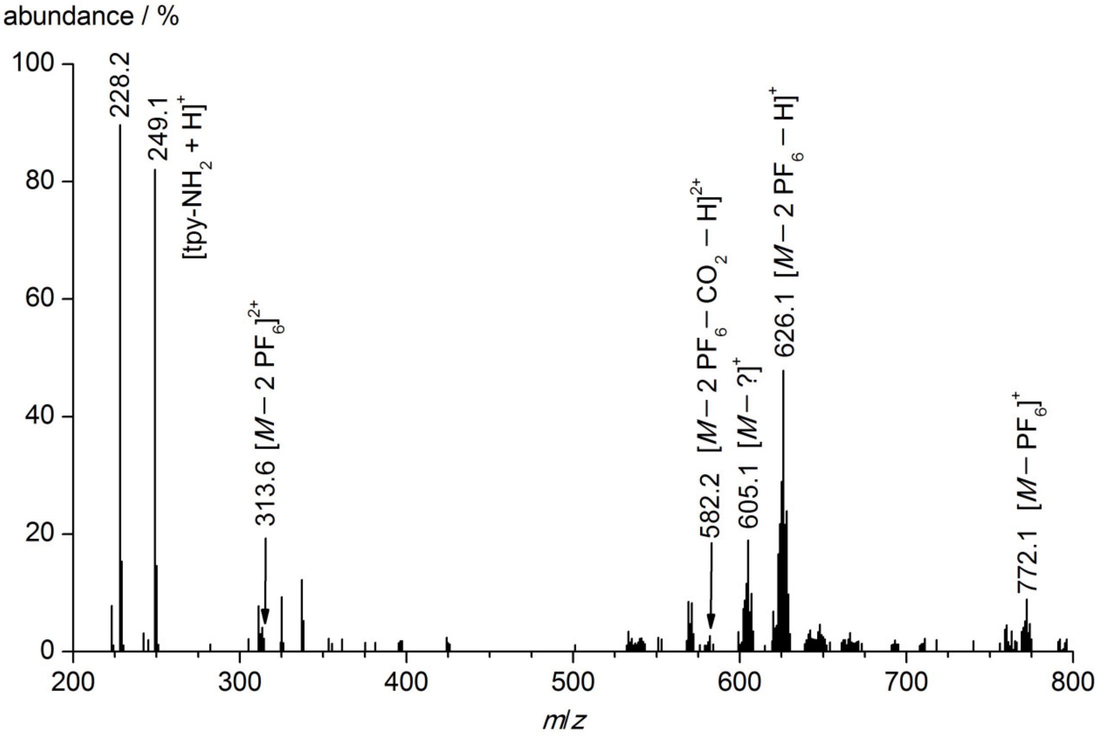

Figure S4. ESI$^+$ mass spectrum of [**1**](PF$_6$)$_2$ 0.5 M TFA in CH$_3$CN:H$_2$O (200:1) 2 d after oxidation with 2.0 equiv (NH$_4$)$_2$[Ce(NO$_3$)$_6$].

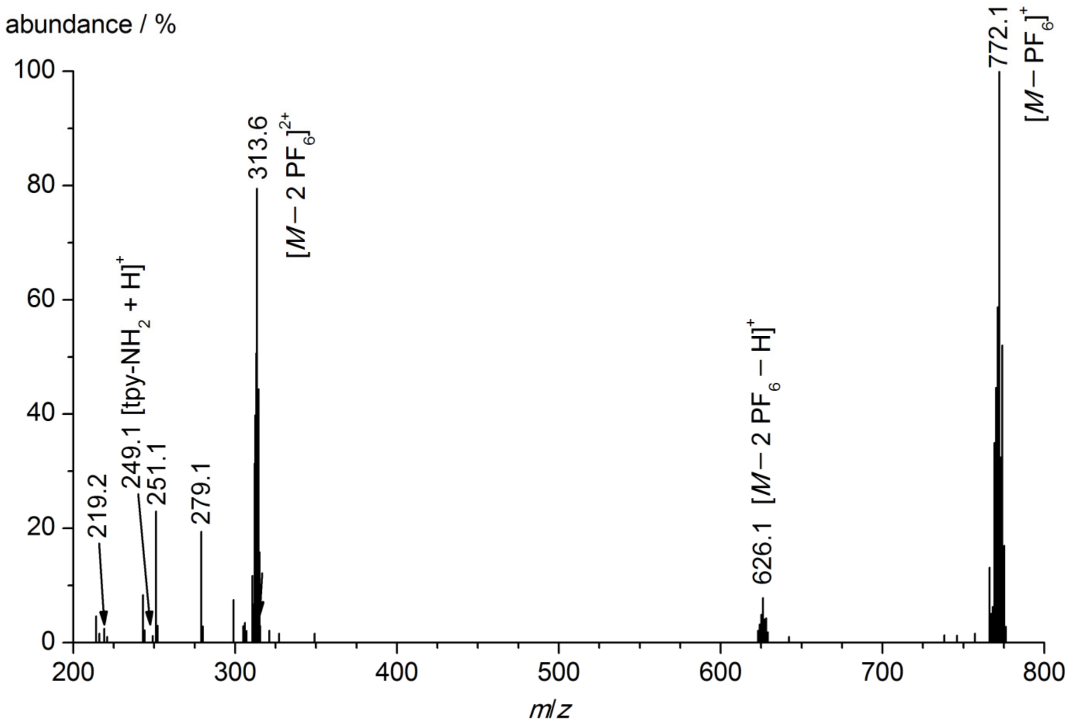

Figure S5. ESI$^+$ mass spectrum of [**1**]$(PF_6)_2$ in 0.5 M HNO_3 in H_2O before addition of $(NH_4)_2[Ce(NO_3)_6]$.

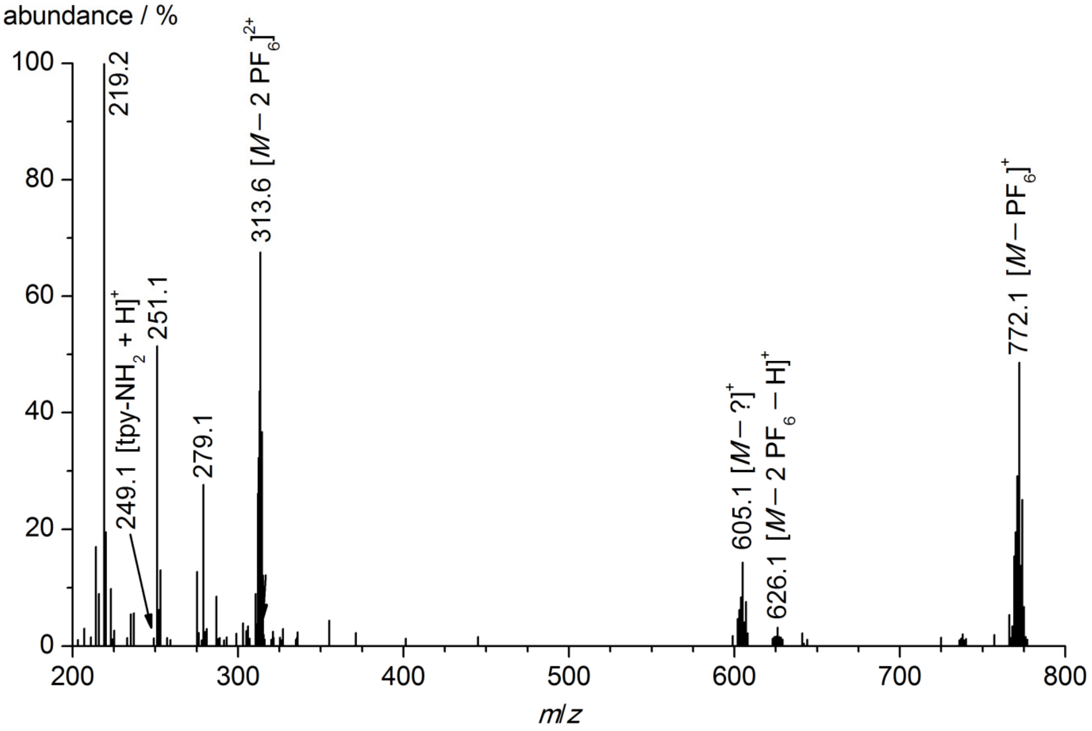

Figure S6. ESI$^+$ mass spectrum of [**1**]$(PF_6)_2$ in 0.5 M HNO_3 in H_2O 2 d after oxidation with 2.0 equiv $(NH_4)_2[Ce(NO_3)_6]$.

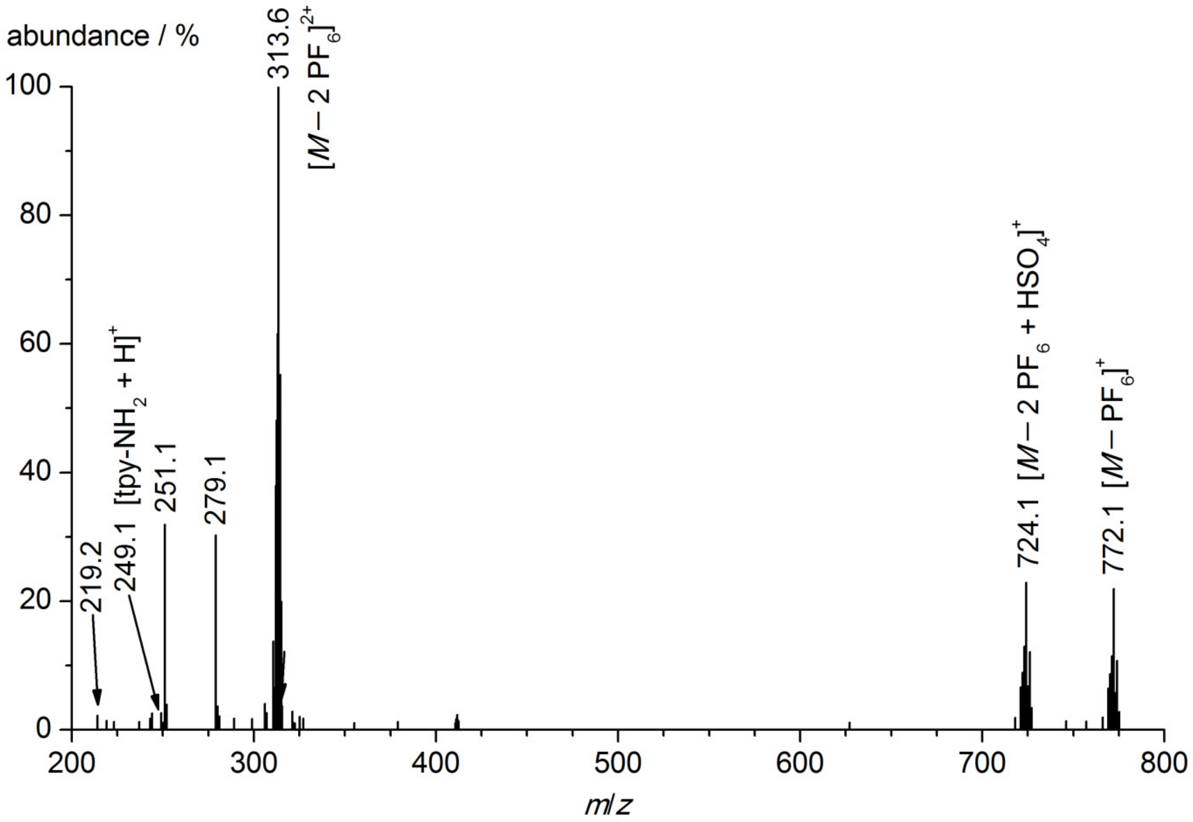

Figure S7. ESI$^+$ mass spectrum of [**1**]$(PF_6)_2$ in 0.1 M H_2SO_4 in H_2O before addition of $Ce(SO_4)_2$ • 4 H_2O.

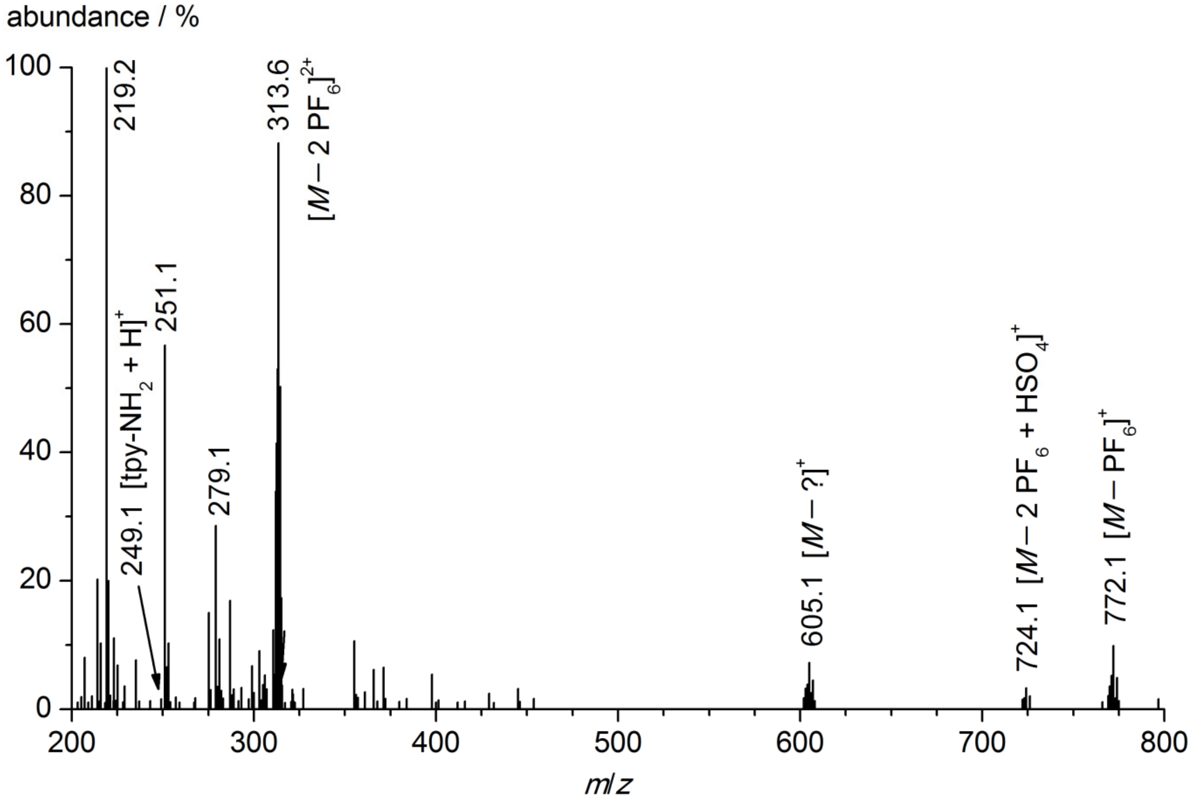

Figure S8. ESI$^+$ mass spectrum of [**1**]$(PF_6)_2$ in 0.1 M H_2SO_4 in H_2O 2 d after oxidation with 2.0 equiv $Ce(SO_4)_2$ • 4 H_2O.

Preparation of the IrCl(PEt$_3$)$_3$ solution[1]**:** [Ir(COE)$_2$Cl]$_2$ (178.3 mg, 0.199 mmol, 1.0 equiv) was dissolved in abs. THF (17 ml; COE = cyclooctene). The orange solution turned red when a solution of PEt$_3$ (1 M in THF, 1.2 ml, 1.2 mmol, 6.0 equiv) was added. The mixture was stirred for 4 h at room temperature. Then the solvent and excess PEt$_3$ were removed under reduced pressure. The red solid was dissolved in 7.2 ml d$_8$-THF and a red solution of IrCl(PEt$_3$)$_3$ was obtained (55 mM). IrCl(PEt$_3$)$_3$ reversibly reacts with O$_2$ under formation of IrCl(O$_2$)(PEt$_3$)$_3$.[2] Figure S9 shows ^{31}P-NMR spectra before and after bubbling an excess of air through the solution.

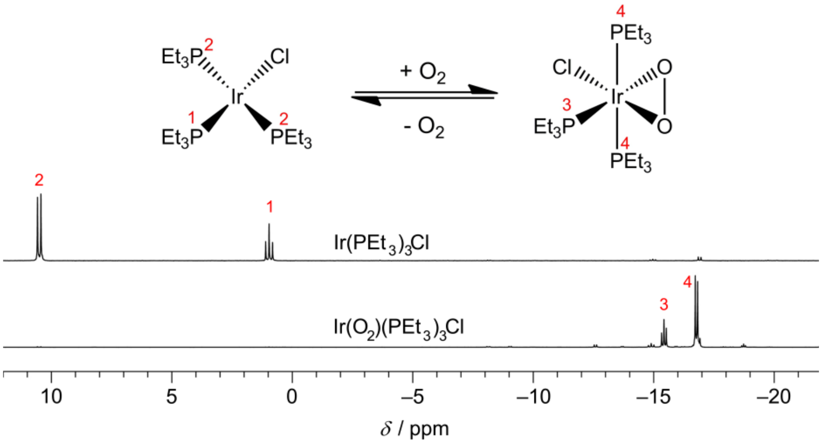

Figure S9. ^{31}P-NMR spectra, structures and phosphorus atom numbering of IrCl(PEt$_3$)$_3$ and IrCl(O$_2$)(PEt$_3$)$_3$ in d$_8$-THF.

IrCl(PEt$_3$)$_3$ and its oxygen adduct IrCl(O$_2$)(PEt$_3$)$_3$ show the following ^{31}P-NMR characteristics in accordance with literature data[2]:

IrCl(PEt$_3$)$_3$: ^{31}P-NMR (d$_8$-THF, 162 MHz): δ = 10.5 (d, 24.0 Hz, 2 P, P^2), 9.0 ppm (t, 24.0 Hz, 1 P, P^1).
IrCl(O$_2$)(PEt$_3$)$_3$: ^{31}P-NMR (d$_8$-THF, 162 MHz): δ = –15.5 (t, 15.6 Hz, 1 P, P^3), –16.8 ppm (d, 15.6 Hz, 2 P, P^4).

[1] A. L. Casalnuovo, J. C. Calabrese, D. Milstein, *J. Am. Chem. Soc.* **1988**, *110*, 6738–6744.
[2] S. W. Kohl, L. Weiner, L. Schwartsburd, L. Konstantinovski, L. J. W. Shimon, Y. Ben-David, M. A. Iron, D. Milstein, *Science* **2009**, *324*, 74–77.

DFT-optimized Cartesian Coordinates of [1]$^{2+}$ (singlet) in H$_2$O in Å.

6	2.345932000	1.227034000	0.000056000
6	3.745880000	1.259502000	0.000365000
6	4.457632000	0.040748000	-0.000607000
6	3.767095000	-1.189673000	-0.001892000
6	2.365520000	-1.177243000	-0.002196000
7	1.693729000	0.019176000	-0.001193000
1	4.294158000	2.194070000	0.001415000
1	4.324431000	-2.117441000	-0.002560000
6	-0.835580000	3.076620000	0.002348000
6	-0.460851000	4.427858000	0.003143000
6	0.907443000	4.756607000	0.002939000
6	1.858166000	3.722892000	0.001951000
6	1.429494000	2.385531000	0.001186000
7	0.079193000	2.072608000	0.001377000
1	1.227783000	5.793175000	0.003513000
1	-1.878145000	2.782458000	0.002503000
1	-1.226559000	5.195430000	0.003888000
1	2.916408000	3.956674000	0.001746000
6	1.467855000	-2.350346000	-0.003413000
6	1.917532000	-3.680929000	-0.004957000
6	0.983156000	-4.729462000	-0.006189000

6	-0.390209000	-4.422276000	-0.005929000
6	-0.786061000	-3.077170000	-0.004353000
7	0.112761000	-2.058854000	-0.003045000
1	1.319705000	-5.760874000	-0.007345000
1	2.979327000	-3.898074000	-0.005214000
1	-1.143852000	-5.201712000	-0.006903000
1	-1.833062000	-2.799455000	-0.004113000
6	-2.983720000	-0.020585000	1.194604000
6	-4.378794000	-0.033018000	1.229899000
6	-5.109048000	-0.038835000	0.003570000
6	-4.380885000	-0.030577000	-1.223984000
6	-2.985756000	-0.018227000	-1.190997000
7	-2.317904000	-0.013952000	0.001238000
1	-4.913161000	-0.038252000	2.173097000
1	-4.916806000	-0.033900000	-2.166312000
6	0.186433000	0.006603000	3.076521000
6	-0.199143000	0.003739000	4.424349000
6	-1.569786000	-0.007922000	4.740206000
6	-2.510304000	-0.016414000	3.696871000
6	-2.072287000	-0.012993000	2.363113000
7	-0.719180000	-0.001370000	2.063633000
1	-1.900198000	-0.010319000	5.773655000
1	1.232300000	0.015463000	2.794756000
1	0.560457000	0.010505000	5.197878000
1	-3.570482000	-0.025372000	3.920904000
6	-2.076289000	-0.008267000	-2.361029000
6	-2.516561000	-0.009302000	-3.694056000
6	-1.577793000	0.001323000	-4.738951000
6	-0.206622000	0.012755000	-4.425363000
6	0.181212000	0.013196000	-3.078183000
7	-0.722688000	0.003047000	-2.063788000
1	-1.909929000	0.000720000	-5.771849000
1	-3.577117000	-0.018091000	-3.916305000
1	0.551691000	0.021151000	-5.200140000
1	1.227546000	0.021834000	-2.798148000
44	-0.295512000	0.003541000	-0.000426000
8	6.613661000	1.148068000	0.000993000
6	5.945539000	0.095901000	-0.000097000
8	6.523325000	-1.152892000	-0.000961000
7	-6.479088000	-0.052174000	0.004733000
1	-7.003176000	-0.059026000	0.869213000
1	7.507019000	-1.110604000	-0.000592000
1	-7.004664000	-0.057368000	-0.858853000

DFT-optimized Cartesian Coordinates of $[1]^{3+}$ (doublet) in H_2O in Å.

6	2.339086000	1.039146000	-0.685533000
6	3.739758000	1.074493000	-0.729207000
6	4.463091000	0.088631000	-0.031293000
6	3.792121000	-0.906525000	0.704129000
6	2.389118000	-0.896918000	0.720919000
7	1.708088000	0.061586000	0.028784000
1	4.274110000	1.835121000	-1.284964000
1	4.359712000	-1.655902000	1.239366000
6	-0.870021000	2.516129000	-1.690720000
6	-0.520860000	3.628289000	-2.470061000
6	0.838217000	3.912334000	-2.686782000
6	1.812614000	3.076093000	-2.115372000
6	1.411503000	1.975842000	-1.345461000
7	0.072179000	1.705452000	-1.144978000
1	1.136203000	4.766336000	-3.285152000
1	-1.907136000	2.268239000	-1.506695000

1	-1.303911000	4.248245000	-2.890377000
1	2.865052000	3.282726000	-2.267564000
6	1.510705000	-1.837403000	1.440767000
6	1.968807000	-2.888834000	2.246231000
6	1.038235000	-3.711290000	2.904151000
6	-0.334712000	-3.458362000	2.743588000
6	-0.742064000	-2.392859000	1.927970000
7	0.158100000	-1.603877000	1.287274000
1	1.380219000	-4.528150000	3.530181000
1	3.031124000	-3.064935000	2.364798000
1	-1.084390000	-4.066563000	3.235833000
1	-1.791538000	-2.172277000	1.781441000
6	-3.047620000	0.619232000	0.881476000
6	-4.430285000	0.593050000	0.841876000
6	-5.087221000	-0.159489000	-0.190182000
6	-4.289174000	-0.867637000	-1.153707000
6	-2.910685000	-0.811622000	-1.062421000
7	-2.311269000	-0.076752000	-0.058078000
1	-5.023263000	1.128601000	1.573175000
1	-4.777814000	-1.434219000	-1.936843000
6	0.018097000	1.834016000	2.523547000
6	-0.439460000	2.620729000	3.592072000
6	-1.822798000	2.765103000	3.788306000
6	-2.711738000	2.117848000	2.911674000
6	-2.202654000	1.343295000	1.860725000
7	-0.837079000	1.211158000	1.676822000
1	-2.205606000	3.367499000	4.604990000
1	1.077151000	1.701628000	2.342299000
1	0.278919000	3.102258000	4.245130000
1	-3.781402000	2.219432000	3.050170000
6	-1.938074000	-1.482072000	-1.960884000
6	-2.305505000	-2.297673000	-3.038495000
6	-1.305970000	-2.894669000	-3.828407000
6	0.043684000	-2.662829000	-3.516973000
6	0.357266000	-1.838748000	-2.424889000
7	-0.604120000	-1.259323000	-1.665899000
1	-1.580086000	-3.527515000	-4.665550000
1	-3.350693000	-2.471569000	-3.263944000
1	0.844059000	-3.105619000	-4.098027000
1	1.386567000	-1.643156000	-2.153487000
44	-0.343847000	-0.000946000	0.018047000
8	6.602531000	0.991666000	-0.722116000
6	5.958249000	0.132976000	-0.095147000
8	6.538920000	-0.884108000	0.616252000
7	-6.436200000	-0.202405000	-0.258185000
1	-7.017448000	0.294498000	0.407405000
1	7.522858000	-0.865411000	0.579343000
1	-6.913190000	-0.730631000	-0.980240000

DFT-optimized Cartesian Coordinates of [1 – H]$^{2+}$ (doublet) in H_2O in Å.

6	2.377101000	1.013332000	-0.668955000
6	3.778779000	1.032189000	-0.707309000
6	4.499932000	0.046337000	-0.005207000
6	3.804674000	-0.934696000	0.729049000
6	2.402460000	-0.916682000	0.739834000
7	1.729948000	0.044846000	0.042725000
1	4.332688000	1.780679000	-1.260428000
1	4.378176000	-1.678981000	1.267726000
6	-0.815690000	2.534668000	-1.673416000
6	-0.452427000	3.644414000	-2.448336000
6	0.911256000	3.910439000	-2.663619000

6	1.874029000	3.059699000	-2.095083000
6	1.459640000	1.961031000	-1.328811000
7	0.116285000	1.708595000	-1.131234000
1	1.220599000	4.762803000	-3.258818000
1	-1.855851000	2.298766000	-1.490046000
1	-1.226746000	4.276672000	-2.866608000
1	2.929768000	3.251271000	-2.244188000
6	1.509866000	-1.846644000	1.457062000
6	1.953317000	-2.901940000	2.266703000
6	1.012825000	-3.713664000	2.922773000
6	-0.357869000	-3.447628000	2.757825000
6	-0.750971000	-2.380043000	1.939338000
7	0.159778000	-1.601642000	1.298906000
1	1.344533000	-4.533049000	3.551294000
1	3.013989000	-3.086564000	2.386990000
1	-1.114994000	-4.047645000	3.248808000
1	-1.797636000	-2.148704000	1.788300000
6	-3.032962000	0.627495000	0.862096000
6	-4.416298000	0.605842000	0.813787000
6	-5.068218000	-0.143749000	-0.222693000
6	-4.266087000	-0.854059000	-1.180787000
6	-2.887331000	-0.801402000	-1.080521000
7	-2.294076000	-0.068959000	-0.072864000
1	-5.012413000	1.142796000	1.541590000
1	-4.751239000	-1.419283000	-1.967160000
6	0.029757000	1.828567000	2.522308000
6	-0.430115000	2.615938000	3.589357000
6	-1.814093000	2.765139000	3.778739000
6	-2.701323000	2.122518000	2.896947000
6	-2.190164000	1.347003000	1.847485000
7	-0.823870000	1.209909000	1.671169000
1	-2.198623000	3.368026000	4.594306000
1	1.088873000	1.690885000	2.344345000
1	0.286557000	3.094241000	4.246710000
1	-3.771319000	2.228142000	3.030107000
6	-1.909434000	-1.473442000	-1.974149000
6	-2.272431000	-2.284210000	-3.056914000
6	-1.269700000	-2.880764000	-3.843416000
6	0.078902000	-2.653131000	-3.524219000
6	0.388300000	-1.833973000	-2.427108000
7	-0.576011000	-1.255765000	-1.670987000
1	-1.540785000	-3.509708000	-4.684539000
1	-3.316721000	-2.454269000	-3.289473000
1	0.881218000	-3.095220000	-4.103176000
1	1.416090000	-1.639839000	-2.148383000
44	-0.323185000	-0.001760000	0.017989000
8	6.591218000	0.958849000	-0.754994000
6	6.036521000	0.042728000	-0.037284000
8	6.615892000	-0.876875000	0.656064000
7	-6.418193000	-0.182116000	-0.300060000
1	-7.001617000	0.316883000	0.361604000
1	-6.891791000	-0.708194000	-1.025488000

DFT-optimized Cartesian Coordinates of [1 – 2 H]$^+$ (doublet) in H_2O in Å.

6	-2.354807000	1.196201000	-0.007843000
6	-3.757813000	1.218302000	-0.010102000
6	-4.466861000	-0.000135000	-0.005773000
6	-3.757735000	-1.218517000	0.000699000
6	-2.354733000	-1.196312000	0.002612000
7	-1.695544000	-0.000031000	-0.001650000
1	-4.321707000	2.143137000	-0.015157000

1	-4.321581000	-2.143390000	0.004068000
6	0.814288000	3.071276000	-0.012058000
6	0.428859000	4.419245000	-0.017688000
6	-0.941394000	4.736782000	-0.020334000
6	-1.884451000	3.695719000	-0.017261000
6	-1.446611000	2.362234000	-0.011613000
7	-0.095461000	2.062843000	-0.009040000
1	-1.269644000	5.770826000	-0.024615000
1	1.859463000	2.787636000	-0.009721000
1	1.189413000	5.191677000	-0.019843000
1	-2.944772000	3.918674000	-0.019121000
6	-1.446470000	-2.362279000	0.009083000
6	-1.884229000	-3.695790000	0.014471000
6	-0.941108000	-4.736782000	0.020679000
6	0.429123000	-4.419148000	0.021477000
6	0.814470000	-3.071153000	0.015905000
7	-0.095338000	-2.062792000	0.009738000
1	-1.269298000	-5.770846000	0.024875000
1	-2.944536000	-3.918823000	0.013913000
1	1.189723000	-5.191522000	0.026302000
1	1.859626000	-2.787437000	0.016529000
6	2.979720000	-0.005418000	-1.204260000
6	4.364031000	-0.005644000	-1.232273000
6	5.116919000	-0.000040000	0.011111000
6	4.358481000	0.005494000	1.246991000
6	2.975382000	0.005363000	1.215383000
7	2.301977000	0.000008000	0.003738000
1	4.905951000	-0.009971000	-2.172394000
1	4.912872000	0.009684000	2.178052000
6	-0.193729000	-0.014215000	-3.076047000
6	0.187173000	-0.019897000	-4.425185000
6	1.557023000	-0.020809000	-4.745541000
6	2.503148000	-0.016126000	-3.707298000
6	2.068620000	-0.010564000	-2.372521000
7	0.718137000	-0.009543000	-2.070252000
1	1.882783000	-0.025092000	-5.780445000
1	-1.237848000	-0.013372000	-2.788110000
1	-0.574772000	-0.023451000	-5.196265000
1	3.562311000	-0.016789000	-3.936209000
6	2.060991000	0.010606000	2.380080000
6	2.491948000	0.016236000	3.716115000
6	1.542977000	0.021022000	4.751569000
6	0.173804000	0.020174000	4.427349000
6	-0.203363000	0.014447000	3.077285000
7	0.711419000	0.009660000	2.073878000
1	1.865813000	0.025325000	5.787407000
1	3.550763000	0.016859000	3.946666000
1	-0.590193000	0.023813000	5.196413000
1	-1.246694000	0.013669000	2.786490000
44	0.333881000	0.000043000	0.001077000
8	-6.574519000	1.156473000	-0.016102000
6	-6.002325000	-0.000205000	-0.008205000
8	-6.574424000	-1.156942000	-0.002256000
7	6.461372000	0.000483000	0.093263000
1	6.909218000	-0.003548000	-0.837938000

DFT-optimized Cartesian Coordinates of $[\mathrm{Ru}(\kappa^2\text{-}\mathrm{H_2N}\text{-tpy})(\kappa^3\text{-HOOC-tpy})(\mathrm{H_2O})]^{3+}$ (doublet) in H_2O in Å.

6	-2.528788000	1.228951000	0.418211000
6	-3.909906000	1.429337000	0.292727000
6	-4.663957000	0.494960000	-0.445550000
6	-4.046609000	-0.620696000	-1.041993000

6	-2.657994000	-0.776191000	-0.898003000
7	-1.953797000	0.146242000	-0.183950000
1	-4.408483000	2.275737000	0.748936000
1	-4.643985000	-1.331892000	-1.596759000
6	0.683358000	2.283634000	1.883320000
6	0.372386000	3.429128000	2.631127000
6	-0.953381000	3.895736000	2.641661000
6	-1.937778000	3.202500000	1.912813000
6	-1.575857000	2.063867000	1.182525000
7	-0.262537000	1.625177000	1.169014000
1	-1.221987000	4.778825000	3.211402000
1	1.688148000	1.882230000	1.848526000
1	1.154026000	3.932794000	3.187483000
1	-2.965298000	3.545625000	1.924453000
6	-1.824848000	-1.864522000	-1.451941000
6	-2.330202000	-2.917305000	-2.226683000
6	-1.450185000	-3.897822000	-2.718466000
6	-0.079482000	-3.800227000	-2.426121000
6	0.373921000	-2.726802000	-1.644173000
7	-0.473209000	-1.783765000	-1.165758000
1	-1.830102000	-4.716559000	-3.319897000
1	-3.388230000	-2.977353000	-2.450535000
1	0.631625000	-4.531388000	-2.792107000
1	1.423898000	-2.615033000	-1.409338000
6	3.304158000	0.166376000	-0.518955000
6	4.510538000	-0.535635000	-0.597531000
6	4.681222000	-1.784593000	0.060298000
6	3.609722000	-2.209525000	0.888128000
6	2.420439000	-1.485856000	0.912420000
7	2.200061000	-0.349962000	0.142437000
1	5.331280000	-0.123520000	-1.172155000
1	3.716651000	-3.109497000	1.479880000
6	2.427899000	3.347346000	-2.357521000
6	3.549567000	4.154001000	-2.151006000
6	4.593837000	3.649120000	-1.355117000
6	4.495429000	2.356194000	-0.812246000
6	3.356709000	1.564184000	-1.067155000
7	2.359939000	2.100697000	-1.824780000
1	5.471321000	4.253482000	-1.150859000
1	1.572141000	3.670270000	-2.937676000
1	3.591412000	5.144527000	-2.586942000
1	5.284802000	1.974548000	-0.177881000
6	1.317649000	-1.878965000	1.823163000
6	1.471468000	-2.789569000	2.883975000
6	0.385474000	-3.058858000	3.731184000
6	-0.841545000	-2.407317000	3.508316000
6	-0.941817000	-1.514641000	2.437171000
7	0.112656000	-1.259215000	1.617457000
1	0.498477000	-3.757566000	4.553268000
1	2.423144000	-3.270993000	3.066529000
1	-1.701695000	-2.582299000	4.143589000
1	-1.868951000	-0.997756000	2.228411000
8	-6.736137000	1.691419000	-0.066289000
6	-6.138487000	0.725137000	-0.570846000
8	-6.756588000	-0.250871000	-1.307343000
7	5.826583000	-2.506240000	-0.062788000
1	6.589812000	-2.185984000	-0.645036000
1	-7.727119000	-0.108508000	-1.396256000
1	5.949974000	-3.385040000	0.423616000
44	0.036013000	-0.039396000	-0.068002000
1	1.405432000	1.560687000	-1.950646000
1	-0.632442000	1.154297000	-2.318534000

8	0.163482000	0.948394000	-1.789268000

DFT-optimized Cartesian Coordinates of "["[Ru(κ^3-H_2N-tpy)(κ^3-HOOC-tpy)]$^{3+}$ + H_2O" (doublet) in H_2O in Å.

6	-2.255210000	-0.095835000	1.223861000
6	-3.650869000	-0.213871000	1.263436000
6	-4.352203000	-0.352928000	0.051528000
6	-3.664856000	-0.359978000	-1.175894000
6	-2.267526000	-0.239205000	-1.161610000
7	-1.606993000	-0.124922000	0.024696000
1	-4.198513000	-0.199847000	2.197784000
1	-4.215626000	-0.456252000	-2.102223000
6	0.913505000	0.320855000	3.036137000
6	0.542108000	0.422064000	4.384127000
6	-0.818827000	0.343315000	4.725933000
6	-1.772659000	0.166624000	3.709140000
6	-1.350186000	0.068565000	2.376245000
7	-0.008627000	0.142659000	2.055567000
1	-1.133978000	0.420366000	5.760855000
1	1.952730000	0.374394000	2.738704000
1	1.308905000	0.559883000	5.137311000
1	-2.826241000	0.110511000	3.954979000
6	-1.375578000	-0.211890000	-2.334963000
6	-1.815668000	-0.269762000	-3.664347000
6	-0.876133000	-0.205182000	-4.707376000
6	0.488346000	-0.079824000	-4.394309000
6	0.877645000	-0.025441000	-3.048579000
7	-0.030773000	-0.095555000	-2.041625000
1	-1.204456000	-0.248190000	-5.740169000
1	-2.872190000	-0.358562000	-3.886303000
1	1.244806000	-0.023699000	-5.168222000
1	1.920351000	0.067206000	-2.773297000
6	3.099225000	1.124915000	-0.074121000
6	4.483456000	1.138899000	-0.090854000
6	5.196291000	-0.105422000	-0.040146000
6	4.451911000	-1.333381000	0.029301000
6	3.069604000	-1.286935000	0.044486000
7	2.415814000	-0.072657000	-0.007984000
1	5.033477000	2.070725000	-0.143121000
1	4.982617000	-2.276917000	0.071320000
6	-0.060849000	3.023940000	-0.153708000
6	0.346765000	4.367920000	-0.221378000
6	1.716705000	4.674036000	-0.239845000
6	2.653187000	3.625604000	-0.191422000
6	2.200720000	2.301892000	-0.124946000
7	0.845346000	2.015785000	-0.106177000
1	2.054651000	5.703596000	-0.291398000
1	-1.118800000	2.769000000	-0.140813000
1	-0.406591000	5.146489000	-0.258323000
1	3.714626000	3.842180000	-0.206062000
6	2.149367000	-2.449583000	0.118917000
6	2.578941000	-3.781044000	0.183758000
6	1.626757000	-4.814077000	0.258936000
6	0.260664000	-4.488407000	0.268815000
6	-0.115910000	-3.138206000	0.200623000
7	0.799652000	-2.141823000	0.125458000
1	1.949336000	-5.848437000	0.309737000
1	3.636022000	-4.017704000	0.177936000
1	-0.504494000	-5.253548000	0.327689000
1	-1.159546000	-2.851759000	0.207584000
8	-6.499764000	-0.485589000	1.165080000

6	-5.841697000	-0.478822000	0.109796000
8	-6.405690000	-0.583527000	-1.135486000
7	6.548310000	-0.126336000	-0.057280000
1	7.091070000	0.728159000	-0.105680000
1	-7.386821000	-0.663704000	-1.105979000
1	7.064845000	-0.997689000	-0.024643000
44	0.442632000	-0.052313000	0.009353000
1	-3.656912000	3.048101000	-0.982642000
1	-3.654450000	3.192280000	0.606575000
8	-3.151029000	2.868133000	-0.165969000

Results of the TD-DFT (singlet) calculation of $[1]^{2+}$ in H_2O.

```
Excited State   1:      Singlet-A      1.9750 eV  627.78 nm  f=0.0000  <S**2>=0.000
     141 ->145        -0.10870
     144 ->145         0.69246
Excited State   2:      Singlet-A      2.1153 eV  586.12 nm  f=0.0052  <S**2>=0.000
     143 ->145         0.69916
Excited State   3:      Singlet-A      2.5469 eV  486.80 nm  f=0.1455  <S**2>=0.000
     142 ->145         0.57686
     143 ->146         0.31690
     143 ->148        -0.11544
     144 ->147         0.20329
Excited State   4:      Singlet-A      2.5876 eV  479.15 nm  f=0.0007  <S**2>=0.000
     144 ->146         0.68512
     144 ->148        -0.12805
Excited State   5:      Singlet-A      2.7334 eV  453.59 nm  f=0.0001  <S**2>=0.000
     143 ->147         0.51478
     144 ->146         0.12725
     144 ->148         0.45975
Excited State   6:      Singlet-A      2.7443 eV  451.79 nm  f=0.0721  <S**2>=0.000
     143 ->146        -0.24029
     143 ->148         0.27371
     144 ->147         0.59561
Excited State   7:      Singlet-A      2.7968 eV  443.31 nm  f=0.0831  <S**2>=0.000
     143 ->147        -0.47471
     144 ->148         0.50770
Excited State   8:      Singlet-A      2.8227 eV  439.25 nm  f=0.0399  <S**2>=0.000
     142 ->146         0.68338
     142 ->148        -0.13124
Excited State   9:      Singlet-A      2.8327 eV  437.69 nm  f=0.0000  <S**2>=0.000
     142 ->147         0.70338
Excited State  10:      Singlet-A      2.8766 eV  431.00 nm  f=0.1498  <S**2>=0.000
     142 ->145        -0.23294
     143 ->146         0.55124
     143 ->148         0.35878
Excited State  11:      Singlet-A      2.9978 eV  413.59 nm  f=0.0002  <S**2>=0.000
     142 ->146         0.13946
     142 ->148         0.68534
Excited State  12:      Singlet-A      3.2041 eV  386.95 nm  f=0.0000  <S**2>=0.000
     142 ->145         0.26190
     143 ->146        -0.17335
     143 ->148         0.51695
     143 ->153         0.19386
     144 ->147        -0.27442
Excited State  13:      Singlet-A      3.3095 eV  374.63 nm  f=0.0000  <S**2>=0.000
     144 ->149         0.69057
Excited State  14:      Singlet-A      3.5000 eV  354.24 nm  f=0.0025  <S**2>=0.000
     144 ->150         0.70082
Excited State  15:      Singlet-A      3.5055 eV  353.69 nm  f=0.0000  <S**2>=0.000
     143 ->154         0.68831
Excited State  16:      Singlet-A      3.5162 eV  352.61 nm  f=0.0227  <S**2>=0.000
```

```
     139 ->145        -0.25148
     143 ->149         0.64439
 Excited State  17:      Singlet-A      3.6070 eV  343.73 nm  f=0.0000  <S**2>=0.000
     141 ->145         0.69083
     144 ->145         0.10958
 Excited State  18:      Singlet-A      3.6122 eV  343.24 nm  f=0.0862  <S**2>=0.000
     142 ->149         0.68142
 Excited State  19:      Singlet-A      3.6767 eV  337.22 nm  f=0.0172  <S**2>=0.000
     140 ->145         0.68809
     143 ->149         0.10246
 Excited State  20:      Singlet-A      3.6851 eV  336.45 nm  f=0.0047  <S**2>=0.000
     143 ->150         0.18307
     144 ->151         0.67215
 Excited State  21:      Singlet-A      3.6985 eV  335.23 nm  f=0.0019  <S**2>=0.000
     142 ->154        -0.16061
     144 ->153         0.67319
 Excited State  22:      Singlet-A      3.7257 eV  332.78 nm  f=0.0433  <S**2>=0.000
     143 ->150         0.66581
     144 ->151        -0.19306
 Excited State  23:      Singlet-A      3.7552 eV  330.17 nm  f=0.0536  <S**2>=0.000
     139 ->145        -0.30303
     142 ->150         0.53909
     142 ->153        -0.12772
     143 ->149        -0.10597
     144 ->154        -0.25204
 Excited State  24:      Singlet-A      3.7665 eV  329.18 nm  f=0.2028  <S**2>=0.000
     139 ->145         0.52022
     142 ->150         0.20038
     143 ->149         0.22205
     143 ->152        -0.17578
     144 ->154        -0.23572
     144 ->158        -0.13462
 Excited State  25:      Singlet-A      3.7762 eV  328.33 nm  f=0.0000  <S**2>=0.000
     144 ->152         0.69464
 Excited State  26:      Singlet-A      3.7887 eV  327.25 nm  f=0.0455  <S**2>=0.000
     139 ->145         0.10903
     141 ->154        -0.12333
     142 ->150         0.40099
     142 ->153         0.15864
     144 ->154         0.47164
     144 ->158         0.17466
 Excited State  27:      Singlet-A      3.8519 eV  321.88 nm  f=0.0173  <S**2>=0.000
     140 ->147         0.23051
     143 ->151         0.65801
 Excited State  28:      Singlet-A      3.9279 eV  315.65 nm  f=0.0000  <S**2>=0.000
     142 ->151         0.70602
 Excited State  29:      Singlet-A      3.9370 eV  314.92 nm  f=0.0001  <S**2>=0.000
     142 ->154         0.62189
     142 ->158        -0.26124
     144 ->153         0.15388
 Excited State  30:      Singlet-A      3.9710 eV  312.23 nm  f=0.0709  <S**2>=0.000
     139 ->145         0.17217
     142 ->153        -0.44057
     143 ->152         0.48006
     144 ->154         0.10257
     144 ->158         0.14432
 Excited State  31:      Singlet-A      3.9882 eV  310.88 nm  f=0.0706  <S**2>=0.000
     139 ->145         0.11096
     142 ->153         0.45465
     143 ->152         0.45862
     144 ->158        -0.21776
 Excited State  32:      Singlet-A      4.0502 eV  306.12 nm  f=0.0085  <S**2>=0.000
```

```
      142 ->152         0.69614
 Excited State  33:      Singlet-A      4.0790 eV  303.95 nm  f=0.0377  <S**2>=0.000
      140 ->147         0.15337
      141 ->146         0.58621
      141 ->148         0.32934
      143 ->151        -0.11653
 Excited State  34:      Singlet-A      4.1049 eV  302.04 nm  f=0.0022  <S**2>=0.000
      140 ->146        -0.11582
      141 ->147         0.54619
      143 ->153         0.37082
      144 ->147         0.11367
      144 ->155        -0.10703
 Excited State  35:      Singlet-A      4.1417 eV  299.35 nm  f=0.0818  <S**2>=0.000
      140 ->147         0.26880
      141 ->146        -0.37987
      141 ->148         0.50095
      143 ->151        -0.12920
 Excited State  36:      Singlet-A      4.1720 eV  297.18 nm  f=0.0001  <S**2>=0.000
      139 ->146        -0.13244
      140 ->146         0.66731
      140 ->148        -0.12635
      141 ->147         0.12697
 Excited State  37:      Singlet-A      4.2541 eV  291.45 nm  f=0.3151  <S**2>=0.000
      140 ->147         0.57867
      141 ->148        -0.34301
      143 ->151        -0.16253
 Excited State  38:      Singlet-A      4.2675 eV  290.53 nm  f=0.0008  <S**2>=0.000
      136 ->145         0.65669
      136 ->149         0.22666
 Excited State  39:      Singlet-A      4.2763 eV  289.94 nm  f=0.0130  <S**2>=0.000
      141 ->158        -0.16381
      142 ->153         0.20544
      144 ->154        -0.30325
      144 ->158         0.56756
 Excited State  40:      Singlet-A      4.2922 eV  288.86 nm  f=0.0180  <S**2>=0.000
      140 ->146         0.10292
      140 ->148         0.19368
      141 ->147        -0.37843
      142 ->145        -0.12919
      143 ->153         0.49101
 Excited State  41:      Singlet-A      4.3518 eV  284.90 nm  f=0.0465  <S**2>=0.000
      139 ->147         0.70015
 Excited State  42:      Singlet-A      4.4032 eV  281.58 nm  f=0.0314  <S**2>=0.000
      137 ->145        -0.20112
      139 ->146         0.51274
      139 ->148         0.38877
      140 ->146         0.10739
      140 ->148         0.15620
 Excited State  43:      Singlet-A      4.4537 eV  278.39 nm  f=0.0000  <S**2>=0.000
      138 ->145         0.70297
 Excited State  44:      Singlet-A      4.4662 eV  277.60 nm  f=0.0925  <S**2>=0.000
      137 ->145         0.30491
      139 ->146        -0.30659
      139 ->148         0.49830
      140 ->148         0.22595
 Excited State  45:      Singlet-A      4.5271 eV  273.87 nm  f=0.1573  <S**2>=0.000
      139 ->148        -0.26896
      140 ->148         0.57427
      141 ->147         0.14123
      143 ->153        -0.18681
      144 ->155        -0.12126
 Excited State  46:      Singlet-A      4.6147 eV  268.67 nm  f=0.0024  <S**2>=0.000
```

```
     142 ->154         0.25091
     142 ->158         0.64013
 Excited State  47:      Singlet-A      4.6307 eV  267.74 nm  f=0.3221  <S**2>=0.000
     137 ->145         0.58807
     139 ->146         0.30995
     139 ->148        -0.11426
 Excited State  48:      Singlet-A      4.7889 eV  258.90 nm  f=0.0000  <S**2>=0.000
     141 ->149         0.67820
     143 ->158        -0.14964
 Excited State  49:      Singlet-A      4.8280 eV  256.80 nm  f=0.0000  <S**2>=0.000
     141 ->149         0.15706
     143 ->158         0.66443
 Excited State  50:      Singlet-A      4.8325 eV  256.56 nm  f=0.0156  <S**2>=0.000
     139 ->149         0.32655
     140 ->149         0.60284
```

Results of the TD-DFT (doublet) calculation of $[1]^{3+}$ in H_2O.

```
 Excited State   1:  2.008-A      0.3658 eV 3388.97 nm  f=0.0009  <S**2>=0.758
     139B ->144B        0.26181
     141B ->144B       -0.19275
     143B ->144B        0.91551
     143B ->147B       -0.10577
 Excited State   2:  2.007-A      0.5367 eV 2310.28 nm  f=0.0000  <S**2>=0.757
     127B ->144B        0.10736
     137B ->144B       -0.10498
     142B ->144B        0.96680
     142B ->147B       -0.11855
  Excited State   3:  2.122-A      1.8129 eV  683.89 nm  f=0.1535  <S**2>=0.876
     144A ->146A        0.18133
     141B ->144B        0.93145
     143B ->144B        0.21801
  Excited State   4:  2.110-A      1.8555 eV  668.19 nm  f=0.0118  <S**2>=0.863
     139B ->144B        0.48220
     140B ->144B        0.83199
     143B ->144B       -0.20153
  Excited State   5:  2.042-A      2.0387 eV  608.17 nm  f=0.0011  <S**2>=0.793
     139B ->144B        0.81370
     140B ->144B       -0.52923
     141B ->144B        0.13497
     143B ->144B       -0.17997
  Excited State   6:  3.092-A      2.6440 eV  468.92 nm  f=0.0061  <S**2>=2.140
     140A ->147A        0.12066
     141A ->145A       -0.18966
     141A ->147A        0.16086
     142A ->145A       -0.29651
     143A ->145A        0.11777
     143A ->147A       -0.16660
     138B ->144B        0.53468
     139B ->146B       -0.17131
     140B ->146B        0.16444
     142B ->145B        0.50119
     143B ->145B       -0.25299
     143B ->146B        0.15189
  Excited State   7:  2.586-A      2.6460 eV  468.58 nm  f=0.0013  <S**2>=1.422
     141A ->145A        0.14130
     141A ->147A       -0.11314
     142A ->145A        0.22506
     138B ->144B        0.81745
     139B ->146B        0.10435
     140B ->146B       -0.11907
     142B ->145B       -0.28673
```

```
      143B ->145B        0.18022
      143B ->146B       -0.10932
 Excited State   8:  3.309-A      2.6728 eV  463.88 nm  f=0.0006  <S**2>=2.488
      142A ->145A       -0.23286
      143A ->145A       -0.31601
      140B ->145B        0.21285
      141B ->145B       -0.13785
      142B ->145B        0.23888
      143B ->145B        0.77350
 Excited State   9:  2.050-A      2.7676 eV  447.98 nm  f=0.0000  <S**2>=0.801
      137B ->144B        0.98046
      142B ->144B        0.12704
 Excited State  10:  3.456-A      2.8968 eV  428.00 nm  f=0.0000  <S**2>=2.737
      128A ->150A       -0.11573
      140A ->149A        0.10119
      140A ->150A       -0.29653
      143A ->149A        0.18061
      143A ->150A       -0.51427
      144A ->150A       -0.16550
      139B ->152B        0.19455
      141B ->152B       -0.12517
      143B ->149B       -0.10247
      143B ->152B        0.58235
      143B ->154B        0.27497
 Excited State  11:  2.568-A      2.9434 eV  421.23 nm  f=0.0001  <S**2>=1.398
      141A ->145A       -0.28017
      142A ->145A        0.14813
      143A ->145A        0.69651
      144A ->145A        0.16119
      139B ->145B        0.28202
      140B ->145B       -0.16188
      143B ->145B        0.47082
 Excited State  12:  3.417-A      3.0158 eV  411.11 nm  f=0.0075  <S**2>=2.669
      138A ->145A        0.14716
      140A ->147A       -0.11423
      141A ->147A       -0.25876
      142A ->145A       -0.23245
      142A ->147A        0.12603
      143A ->146A        0.13532
      143A ->147A        0.33923
      143A ->148A       -0.13566
      137B ->145B       -0.13941
      139B ->146B        0.19530
      140B ->146B       -0.24146
      140B ->147B       -0.10522
      142B ->145B        0.49361
      143B ->146B       -0.37841
      143B ->148B       -0.11454
 Excited State  13:  3.373-A      3.0429 eV  407.46 nm  f=0.0059  <S**2>=2.594
      136A ->146A       -0.13093
      139A ->146A        0.15298
      140A ->148A       -0.16651
      141A ->148A        0.33865
      142A ->148A       -0.13341
      143A ->147A        0.12169
      143A ->148A        0.37896
      144A ->146A        0.11787
      144A ->148A        0.17445
      134B ->144B        0.13486
      138B ->144B        0.13186
      138B ->147B       -0.15508
      139B ->147B        0.13004
```

```
     139B ->148B       -0.11718
     140B ->147B        0.21938
     140B ->148B       -0.29254
     141B ->148B       -0.10323
     142B ->145B        0.14644
     143B ->146B       -0.10926
     143B ->147B       -0.24039
     143B ->148B        0.33938
 Excited State  14:  3.217-A      3.0813 eV  402.38 nm  f=0.0054  <S**2>=2.337
     139A ->148A        0.14126
     141A ->146A        0.19346
     143A ->146A        0.34775
     143A ->147A       -0.12636
     143A ->148A        0.10827
     144A ->145A       -0.24086
     144A ->146A        0.27921
     144A ->148A       -0.20096
     135B ->144B       -0.26193
     138B ->148B       -0.12251
     139B ->144B        0.10581
     140B ->147B       -0.12880
     141B ->148B       -0.19969
     143B ->147B        0.47774
     143B ->148B        0.19931
 Excited State  15:  2.510-A      3.0832 eV  402.13 nm  f=0.0002  <S**2>=1.325
     136A ->145A        0.10065
     139A ->145A        0.13035
     140A ->145A        0.15936
     141A ->145A        0.13064
     144A ->145A        0.89167
     139B ->145B       -0.15911
     140B ->145B        0.11879
     143B ->147B        0.13156
 Excited State  16:  3.055-A      3.1709 eV  391.00 nm  f=0.0008  <S**2>=2.083
     140A ->145A        0.45147
     141A ->145A        0.28698
     142A ->145A       -0.13040
     143A ->145A        0.53433
     144A ->145A       -0.24683
     139B ->145B       -0.40701
     140B ->145B        0.33275
     142B ->146B        0.10895
 Excited State  17:  3.453-A      3.1864 eV  389.11 nm  f=0.0010  <S**2>=2.731
     127A ->150A       -0.10798
     138A ->150A        0.10979
     141A ->150A       -0.24585
     142A ->149A        0.20008
     142A ->150A       -0.57020
     142B ->149B       -0.10855
     142B ->152B        0.61066
     142B ->154B        0.28870
 Excited State  18:  2.041-A      3.2040 eV  386.96 nm  f=0.0000  <S**2>=0.792
     136B ->144B        0.99860
 Excited State  19:  2.304-A      3.2309 eV  383.74 nm  f=0.0252  <S**2>=1.078
     142A ->145A        0.11810
     144A ->146A        0.42397
     134B ->144B       -0.22185
     135B ->144B        0.79032
     141B ->147B        0.13368
     143B ->147B        0.17595
 Excited State  20:  2.543-A      3.2503 eV  381.45 nm  f=0.0239  <S**2>=1.367
     139A ->148A        0.10151
```

```
     141A ->146A        0.13863
     143A ->146A        0.25853
     144A ->146A       -0.46182
     144A ->148A       -0.24144
     134B ->144B        0.43694
     135B ->144B        0.48031
     141B ->144B        0.13202
     141B ->148B       -0.28629
 Excited State  21:  2.809-A      3.3091 eV  374.68 nm  f=0.0256  <S**2>=1.723
     141A ->145A        0.11404
     141A ->148A       -0.11786
     142A ->145A        0.27456
     143A ->146A        0.11624
     143A ->148A       -0.15315
     144A ->148A        0.53025
     131B ->144B       -0.12220
     134B ->144B        0.40026
     141B ->147B       -0.17554
     141B ->148B        0.29260
     142B ->145B        0.19186
     143B ->147B        0.16959
     143B ->148B        0.31225
 Excited State  22:  2.538-A      3.3234 eV  373.07 nm  f=0.0714  <S**2>=1.360
     141A ->145A        0.18912
     142A ->145A        0.45056
     143A ->146A       -0.19706
     144A ->146A        0.22140
     144A ->148A       -0.36023
     126B ->144B       -0.10475
     134B ->144B        0.35127
     135B ->144B       -0.18647
     141B ->147B        0.22787
     142B ->145B        0.32912
     143B ->146B        0.29040
     143B ->148B       -0.17173
 Excited State  23:  2.083-A      3.3374 eV  371.50 nm  f=0.0008  <S**2>=0.835
     127B ->144B       -0.16182
     128B ->144B       -0.10050
     130B ->144B        0.16340
     132B ->144B       -0.15240
     133B ->144B        0.91000
     134B ->144B       -0.13166
     142B ->144B        0.10096
     142B ->147B        0.12584
 Excited State  24:  2.034-A      3.3931 eV  365.40 nm  f=0.0001  <S**2>=0.784
     128A ->150A        0.10177
     140A ->150A        0.30191
     143A ->149A       -0.19602
     143A ->150A        0.57043
     143A ->155A       -0.11938
     144A ->150A        0.13240
     139B ->152B        0.16283
     141B ->145B       -0.10377
     141B ->152B       -0.10802
     143B ->149B       -0.11152
     143B ->152B        0.53291
     143B ->154B        0.24984
 Excited State  25:  2.375-A      3.4026 eV  364.38 nm  f=0.0004  <S**2>=1.160
     141A ->145A       -0.12162
     142A ->145A       -0.31509
     143A ->146A       -0.28799
     144A ->146A        0.15601
```

```
    133B ->144B        0.11419
    134B ->144B        0.57490
    139B ->146B       -0.12350
    141B ->147B        0.12836
    141B ->148B        0.10331
    142B ->145B       -0.28324
    143B ->146B       -0.39710
    143B ->147B        0.18850
    143B ->148B       -0.12237
 Excited State  26:  2.279-A      3.5016 eV  354.08 nm  f=0.0192  <S**2>=1.049
    141A ->146A       -0.17362
    142A ->150A       -0.10596
    143A ->146A       -0.44952
    143A ->147A        0.13111
    144A ->146A       -0.34208
    144A ->148A       -0.18543
    128B ->144B       -0.12354
    129B ->144B       -0.10320
    134B ->144B       -0.15452
    139B ->147B        0.16466
    140B ->147B        0.12409
    141B ->148B       -0.11907
    143B ->144B        0.13443
    143B ->147B        0.49394
    143B ->148B        0.34590
 Excited State  27:  2.826-A      3.5159 eV  352.64 nm  f=0.0056  <S**2>=1.746
    140A ->145A        0.10080
    141A ->145A        0.13970
    140B ->145B       -0.12894
    141B ->145B        0.92432
    142B ->146B        0.15841
    143B ->145B        0.16012
 Excited State  28:  2.274-A      3.5402 eV  350.22 nm  f=0.0357  <S**2>=1.042
    136A ->150A       -0.11486
    139A ->150A       -0.12264
    140A ->145A        0.21511
    141A ->145A        0.37874
    142A ->145A       -0.12406
    144A ->149A        0.10654
    144A ->150A       -0.28530
    139B ->145B        0.29855
    140B ->145B       -0.46496
    141B ->145B       -0.29446
    142B ->146B        0.47264
 Excited State  29:  2.935-A      3.5863 eV  345.72 nm  f=0.0298  <S**2>=1.904
    140A ->147A       -0.20064
    141A ->147A       -0.14104
    142A ->145A       -0.36314
    142A ->147A        0.10984
    143A ->148A        0.14571
    144A ->150A       -0.17518
    126B ->144B        0.10141
    134B ->144B        0.13766
    139B ->146B        0.33439
    140B ->146B       -0.19878
    142B ->145B       -0.12745
    142B ->146B       -0.17647
    143B ->146B        0.59614
    143B ->147B        0.15818
 Excited State  30:  2.614-A      3.5994 eV  344.45 nm  f=0.0042  <S**2>=1.458
    133A ->150A        0.12250
    136A ->150A        0.18790
```

```
     139A ->150A        0.20730
     141A ->145A       -0.12436
     143A ->150A       -0.10825
     144A ->149A       -0.18908
     144A ->150A        0.50478
     133B ->144B        0.12475
     139B ->146B        0.11905
     142B ->146B        0.51083
     142B ->147B       -0.28502
     142B ->148B       -0.11665
     143B ->146B        0.19046
 Excited State  31:  2.761-A      3.6193 eV  342.56 nm  f=0.0183  <S**2>=1.656
     136A ->150A        0.11842
     139A ->150A        0.13189
     141A ->145A        0.18827
     142A ->146A        0.16014
     144A ->149A       -0.11672
     144A ->150A        0.32618
     127B ->144B       -0.16047
     133B ->144B       -0.21421
     139B ->145B        0.12364
     140B ->145B       -0.15368
     142B ->144B        0.13619
     142B ->147B        0.64238
     142B ->148B        0.35417
 Excited State  32:  3.373-A      3.6349 eV  341.09 nm  f=0.0033  <S**2>=2.595
     140A ->145A       -0.29119
     141A ->145A        0.36535
     142A ->145A       -0.13490
     143A ->145A        0.16462
     139B ->145B        0.58287
     140B ->145B        0.54706
     143B ->145B       -0.14313
 Excited State  33:  2.477-A      3.6474 eV  339.93 nm  f=0.0154  <S**2>=1.284
     140A ->145A       -0.30875
     141A ->145A        0.51338
     142A ->145A       -0.19004
     142A ->147A        0.15467
     143A ->145A        0.12840
     144A ->150A        0.18833
     139B ->145B       -0.23445
     140B ->145B       -0.39499
     142B ->146B       -0.39712
     142B ->147B       -0.18493
     142B ->148B       -0.20720
 Excited State  34:  3.158-A      3.6584 eV  338.90 nm  f=0.0095  <S**2>=2.243
     139A ->148A       -0.18786
     140A ->146A        0.41850
     140A ->148A       -0.11131
     141A ->146A       -0.29707
     143A ->146A        0.46315
     144A ->147A        0.10864
     144A ->148A       -0.17145
     139B ->147B        0.28695
     140B ->147B        0.36175
     141B ->148B        0.10902
     143B ->147B        0.12838
     143B ->148B       -0.21507
 Excited State  35:  2.823-A      3.6680 eV  338.02 nm  f=0.0178  <S**2>=1.743
     139A ->146A       -0.10496
     139A ->148A       -0.10190
     140A ->147A       -0.12715
```

```
     140A ->148A        0.18342
     141A ->148A       -0.14974
     143A ->146A        0.16940
     143A ->147A       -0.22174
     144A ->147A       -0.21358
     144A ->148A       -0.31514
     139B ->148B        0.20734
     140B ->146B       -0.10778
     140B ->148B        0.23925
     141B ->147B        0.14980
     141B ->148B        0.16854
     143B ->146B       -0.14723
     143B ->147B       -0.33599
     143B ->148B        0.49374
 Excited State  36:  2.777-A      3.6886 eV  336.13 nm  f=0.0863  <S**2>=1.678
     138A ->147A        0.11174
     140A ->145A        0.57849
     141A ->147A        0.13170
     142A ->147A        0.27901
     143A ->145A       -0.18413
     144A ->150A        0.16844
     130B ->144B       -0.10100
     137B ->146B       -0.10745
     139B ->145B        0.34466
     142B ->146B       -0.36306
     143B ->149B        0.18611
 Excited State  37:  3.466-A      3.6975 eV  335.32 nm  f=0.0002  <S**2>=2.754
     137A ->145A        0.64327
     137A ->149A        0.25929
     137A ->154A       -0.13375
     137A ->159A        0.12887
     136B ->145B       -0.60761
     136B ->149B       -0.25818
     136B ->154B        0.10442
     136B ->159B       -0.12562
 Excited State  38:  2.322-A      3.7110 eV  334.10 nm  f=0.0010  <S**2>=1.098
     139A ->147A        0.12243
     144A ->146A        0.18867
     144A ->147A        0.90395
     144A ->148A       -0.15602
     143B ->148B        0.16108
 Excited State  39:  3.396-A      3.7378 eV  331.70 nm  f=0.0095  <S**2>=2.633
     140A ->145A        0.18296
     140A ->155A       -0.25395
     141A ->155A        0.10023
     142A ->155A        0.20584
     143A ->149A        0.11905
     143A ->155A       -0.46898
     144A ->155A       -0.14945
     139B ->155B        0.17325
     141B ->155B       -0.10650
     142B ->146B       -0.10470
     142B ->147B       -0.13903
     142B ->148B       -0.10181
     142B ->155B       -0.24661
     143B ->149B       -0.10726
     143B ->155B        0.54683
 Excited State  40:  3.333-A      3.7452 eV  331.04 nm  f=0.0205  <S**2>=2.527
     134A ->151A       -0.11770
     135A ->149A       -0.10684
     138A ->147A       -0.25401
     140A ->145A        0.32754
```

```
     140A ->154A        0.16247
     141A ->145A       -0.12597
     141A ->154A        0.13172
     142A ->155A       -0.13700
     143A ->149A        0.21694
     143A ->150A        0.11130
     143A ->155A        0.16223
     133B ->150B        0.10704
     135B ->149B       -0.10232
     137B ->146B        0.25566
     139B ->154B       -0.17266
     140B ->145B       -0.16789
     140B ->154B        0.11571
     142B ->146B       -0.16583
     142B ->148B       -0.10768
     142B ->150B        0.10288
     142B ->155B        0.16464
     143B ->149B       -0.28288
     143B ->155B       -0.19713
 Excited State  41:  3.450-A      3.7580 eV  329.92 nm  f=0.0000  <S**2>=2.726
     128A ->155A       -0.10066
     138A ->155A        0.10536
     140A ->155A       -0.14790
     141A ->155A       -0.22194
     142A ->155A       -0.52854
     143A ->155A       -0.21703
     142B ->152B        0.12443
     142B ->155B        0.63175
     143B ->155B        0.26339
 Excited State  42:  2.522-A      3.7653 eV  329.28 nm  f=0.0007  <S**2>=1.340
     141A ->146A        0.36079
     142A ->146A        0.87440
     142A ->147A       -0.12800
     142B ->147B       -0.19219
 Excited State  43:  2.765-A      3.8051 eV  325.84 nm  f=0.0352  <S**2>=1.661
     139A ->146A       -0.10283
     140A ->147A        0.36154
     140A ->148A        0.11157
     141A ->147A        0.18067
     141A ->148A       -0.12315
     142A ->147A       -0.11645
     143A ->146A        0.15224
     143A ->147A        0.61337
     143A ->148A        0.13632
     144A ->147A       -0.14239
     126B ->144B        0.10614
     131B ->144B        0.13066
     137B ->145B       -0.10879
     139B ->146B       -0.13749
     142B ->145B       -0.11047
     143B ->146B        0.18770
     143B ->148B        0.14781
     143B ->150B        0.15292
 Excited State  44:  2.209-A      3.8087 eV  325.53 nm  f=0.0013  <S**2>=0.970
     142A ->147A        0.12262
     127B ->144B       -0.35135
     128B ->144B       -0.25294
     130B ->144B        0.75166
     132B ->144B        0.28978
     133B ->144B       -0.14389
     142B ->147B       -0.26924
 Excited State  45:  2.938-A      3.8446 eV  322.49 nm  f=0.0012  <S**2>=1.908
```

```
     130B ->144B       -0.14613
     132B ->144B       -0.14972
     142B ->146B       -0.17132
     142B ->147B       -0.48784
     142B ->148B        0.79837
 Excited State  46:  3.257-A      3.8510 eV  321.95 nm  f=0.0062  <S**2>=2.402
     129A ->147A       -0.10828
     138A ->145A        0.49979
     140A ->148A       -0.10099
     143A ->147A       -0.35202
     143A ->148A       -0.14291
     131B ->144B        0.27412
     137B ->145B       -0.47258
     143B ->148B        0.12364
     143B ->150B        0.11168
 Excited State  47:  2.226-A      3.8702 eV  320.36 nm  f=0.0007  <S**2>=0.989
     144A ->148A        0.22108
     127B ->144B        0.10916
     128B ->144B       -0.18069
     129B ->144B       -0.57438
     131B ->144B        0.67093
     132B ->144B        0.11771
 Excited State  48:  2.427-A      3.8839 eV  319.22 nm  f=0.0291  <S**2>=1.222
     138A ->145A        0.14483
     139A ->146A       -0.10668
     140A ->148A        0.26634
     141A ->148A       -0.16837
     143A ->147A       -0.15474
     143A ->148A        0.48991
     144A ->146A       -0.14148
     144A ->147A        0.10203
     144A ->148A        0.22580
     126B ->144B       -0.36068
     128B ->144B       -0.10106
     131B ->144B       -0.15619
     134B ->144B       -0.17491
     141B ->147B        0.22403
     143B ->147B        0.10495
     143B ->148B       -0.30332
     143B ->153B       -0.12053
 Excited State  49:  2.314-A      3.8992 eV  317.97 nm  f=0.0201  <S**2>=1.089
     138A ->145A       -0.13695
     142A ->150A        0.17608
     144A ->146A       -0.17155
     126B ->144B       -0.25726
     127B ->144B       -0.23415
     128B ->144B        0.45334
     129B ->144B        0.35388
     131B ->144B        0.38179
     137B ->145B        0.14624
     141B ->146B       -0.10928
     141B ->147B        0.24331
     142B ->152B        0.14495
     143B ->147B        0.22593
     143B ->148B        0.12755
 Excited State  50:  2.154-A      3.9215 eV  316.16 nm  f=0.0289  <S**2>=0.910
     141A ->147A        0.15542
     142A ->147A        0.36853
     127B ->144B        0.34077
     128B ->144B        0.16720
     129B ->144B        0.10568
     132B ->144B        0.69256
```

```
      133B ->144B        0.17356
      139B ->145B       -0.10195
      142B ->146B        0.11614
      142B ->147B        0.15366
      142B ->148B        0.26673
 Excited State  51:  2.394-A      3.9244 eV  315.93 nm  f=0.0965  <S**2>=1.182
      141A ->147A        0.30638
      142A ->147A        0.66361
      142A ->148A       -0.16198
      125B ->144B        0.10804
      127B ->144B       -0.15008
      132B ->144B       -0.42499
      139B ->145B       -0.19845
      142B ->146B        0.20020
      143B ->149B       -0.14801
 Excited State  52:  2.739-A      3.9655 eV  312.66 nm  f=0.0402  <S**2>=1.626
      139A ->146A       -0.12540
      140A ->146A       -0.20781
      140A ->148A       -0.16260
      141A ->146A        0.21919
      141A ->148A        0.13269
      142A ->150A       -0.14352
      143A ->146A        0.16728
      143A ->148A       -0.26217
      144A ->146A       -0.14711
      126B ->144B       -0.32354
      128B ->144B       -0.13151
      129B ->144B       -0.18135
      131B ->144B       -0.16104
      139B ->148B       -0.16561
      140B ->148B       -0.18914
      141B ->146B       -0.20796
      141B ->147B        0.29384
      141B ->148B        0.34341
      142B ->152B       -0.12462
      143B ->151B       -0.12138
 Excited State  53:  2.503-A      3.9753 eV  311.89 nm  f=0.0059  <S**2>=1.316
      136A ->146A       -0.13336
      140A ->146A        0.11917
      141A ->146A       -0.19471
      143A ->148A       -0.36754
      144A ->146A       -0.16950
      144A ->148A        0.18623
      126B ->144B        0.45307
      131B ->144B       -0.14979
      141B ->147B        0.51021
      141B ->148B       -0.21789
 Excited State  54:  3.311-A      4.0051 eV  309.57 nm  f=0.0049  <S**2>=2.490
      132A ->145A        0.15641
      132A ->149A        0.12483
      134A ->145A        0.29438
      138A ->145A        0.15843
      140A ->151A        0.19437
      141A ->149A       -0.11071
      141A ->151A        0.12494
      142A ->149A       -0.21829
      143A ->147A        0.22278
      129B ->144B        0.12747
      132B ->145B       -0.16498
      132B ->149B       -0.12798
      133B ->145B       -0.26674
      137B ->145B       -0.15199
```

```
    139B ->146B        0.10199
    139B ->150B       -0.20995
    139B ->153B       -0.10561
    141B ->148B        0.12681
    142B ->149B        0.30895
    142B ->154B        0.12201
    143B ->146B       -0.13536
    143B ->150B       -0.17778
 Excited State  55:  2.718-A      4.0237 eV  308.14 nm  f=0.0114  <S**2>=1.597
    139A ->153A        0.10836
    140A ->146A       -0.15173
    141A ->146A        0.25316
    142A ->146A       -0.10731
    142A ->150A        0.20843
    143A ->147A       -0.15705
    143A ->148A        0.13646
    144A ->146A       -0.12593
    126B ->144B        0.38296
    141B ->146B       -0.14067
    141B ->147B       -0.21697
    141B ->148B        0.25991
    142B ->145B        0.10339
    142B ->149B       -0.14865
    142B ->152B        0.17652
    143B ->147B        0.21236
    143B ->148B       -0.12593
    143B ->153B       -0.11587
 Excited State  56:  2.019-A      4.0289 eV  307.73 nm  f=0.0002  <S**2>=0.770
    137A ->145A        0.64634
    137A ->149A        0.18379
    136B ->145B        0.67950
    136B ->149B        0.20658
 Excited State  57:  2.689-A      4.0349 eV  307.28 nm  f=0.0010  <S**2>=1.558
    141A ->148A        0.35548
    142A ->147A        0.19693
    142A ->148A        0.87458
 Excited State  58:  2.051-A      4.0492 eV  306.19 nm  f=0.0062  <S**2>=0.802
    125B ->144B        0.95603
 Excited State  59:  3.050-A      4.0678 eV  304.80 nm  f=0.0062  <S**2>=2.076
    136A ->146A       -0.12208
    139A ->146A        0.15437
    139A ->153A        0.14009
    140A ->146A       -0.13591
    140A ->152A        0.13766
    140A ->153A        0.10349
    141A ->146A       -0.12472
    141A ->152A       -0.10565
    142A ->150A       -0.22421
    143A ->146A        0.19952
    143A ->148A       -0.19711
    144A ->146A        0.10711
    129B ->144B        0.20436
    131B ->144B        0.11234
    138B ->147B       -0.16480
    139B ->151B       -0.12833
    140B ->147B       -0.10423
    140B ->151B       -0.14392
    141B ->146B        0.35275
    141B ->147B       -0.11529
    141B ->148B       -0.12909
    142B ->149B        0.11148
    142B ->152B       -0.19646
```

```
     142B ->154B       -0.10080
     143B ->150B        0.12599
 Excited State  60:  3.132-A      4.0812 eV  303.79 nm  f=0.0001  <S**2>=2.203
     133A ->152A       -0.10326
     135A ->152A       -0.10262
     136A ->146A       -0.13549
     136A ->148A       -0.10159
     139A ->145A       -0.23108
     139A ->151A        0.10056
     139A ->152A        0.15657
     139A ->153A       -0.11200
     140A ->146A        0.14086
     140A ->152A       -0.19190
     141A ->152A        0.14773
     142A ->150A       -0.10994
     143A ->146A       -0.16387
     143A ->148A       -0.14467
     144A ->148A       -0.13196
     128B ->144B       -0.20324
     129B ->144B        0.15514
     131B ->144B        0.20987
     134B ->151B        0.11672
     138B ->148B       -0.17519
     138B ->151B        0.11449
     139B ->151B        0.12935
     140B ->151B        0.15711
     141B ->148B        0.31767
     141B ->151B        0.13669
     143B ->148B       -0.14230
     143B ->150B        0.13719
     143B ->151B        0.10782
 Excited State  61:  2.588-A      4.0844 eV  303.55 nm  f=0.0007  <S**2>=1.424
     132A ->145A       -0.12337
     139A ->145A        0.59235
     141A ->149A        0.10050
     142A ->150A       -0.15796
     144A ->145A       -0.10548
     126B ->144B        0.11688
     128B ->144B       -0.34539
     129B ->144B        0.38471
     130B ->144B       -0.10387
     131B ->144B        0.24084
     132B ->145B        0.12647
     142B ->152B       -0.19048
 Excited State  62:  2.789-A      4.0861 eV  303.43 nm  f=0.0006  <S**2>=1.694
     132A ->145A        0.11667
     136A ->145A        0.11366
     139A ->145A        0.71376
     143A ->148A       -0.12850
     144A ->145A       -0.12884
     126B ->144B       -0.12265
     128B ->144B        0.22951
     129B ->144B       -0.27611
     131B ->144B       -0.13675
     132B ->145B       -0.12010
     142B ->152B        0.12196
     143B ->150B        0.10416
 Excited State  63:  2.488-A      4.1145 eV  301.34 nm  f=0.0017  <S**2>=1.297
     132A ->145A       -0.12135
     138A ->145A        0.12791
     141A ->146A       -0.12435
     142A ->150A       -0.23544
```

```
     126B ->144B        0.24598
     128B ->144B        0.50058
     129B ->144B       -0.25998
     130B ->144B        0.16130
     132B ->145B        0.12188
     137B ->145B       -0.12155
     140B ->146B        0.12111
     141B ->146B        0.21408
     141B ->148B        0.26917
     142B ->152B       -0.26366
     142B ->155B        0.11047
 Excited State  64:  3.179-A      4.1204 eV  300.91 nm  f=0.0003  <S**2>=2.276
     132A ->145A        0.16139
     138A ->145A       -0.10365
     138A ->151A        0.13255
     140A ->149A       -0.20251
     140A ->153A       -0.11875
     140A ->154A       -0.10243
     141A ->149A       -0.17477
     142A ->149A        0.15468
     142A ->151A        0.17422
     142A ->154A        0.10679
     143A ->147A       -0.11601
     143A ->148A        0.19635
     143A ->149A        0.12815
     126B ->144B        0.27814
     132B ->145B       -0.15955
     137B ->145B        0.10702
     137B ->150B       -0.13540
     139B ->149B        0.25281
     139B ->153B        0.10290
     139B ->154B        0.10281
     140B ->149B       -0.19758
     140B ->150B       -0.10581
     141B ->148B        0.12520
     142B ->150B       -0.17554
     142B ->154B       -0.12790
 Excited State  65:  2.783-A      4.1295 eV  300.24 nm  f=0.0018  <S**2>=1.687
     141A ->146A        0.17493
     142A ->150A        0.16157
     128B ->144B       -0.14733
     141B ->146B        0.80602
     141B ->147B        0.26150
     141B ->148B        0.20991
     142B ->152B        0.17191
     142B ->155B       -0.10565
 Excited State  66:  3.387-A      4.1391 eV  299.54 nm  f=0.0003  <S**2>=2.617
     132A ->145A       -0.21381
     134A ->145A       -0.15884
     134A ->149A       -0.11021
     138A ->145A        0.12801
     138A ->151A        0.13832
     140A ->149A       -0.19759
     140A ->151A        0.12934
     140A ->153A        0.10493
     140A ->154A       -0.11581
     141A ->149A       -0.19562
     141A ->151A        0.16229
     141A ->154A       -0.12213
     142A ->145A       -0.10977
     142A ->149A        0.10541
     143A ->148A       -0.11228
```

```
     143A ->149A        0.14117
     126B ->144B       -0.14763
     128B ->145B        0.11664
     132B ->145B        0.21718
     133B ->145B        0.12991
     133B ->149B        0.10470
     137B ->145B       -0.13612
     137B ->150B       -0.13956
     139B ->149B        0.24427
     139B ->150B       -0.13342
     139B ->154B        0.11977
     140B ->149B       -0.19798
     140B ->150B        0.10784
     142B ->150B       -0.18195
     142B ->154B        0.12882
     143B ->149B       -0.11385
 Excited State  67:  2.569-A      4.1651 eV  297.67 nm  f=0.0665  <S**2>=1.400
     139A ->146A        0.12497
     140A ->146A        0.26503
     141A ->146A        0.49833
     141A ->147A       -0.15492
     142A ->146A       -0.21857
     142A ->150A       -0.20259
     144A ->148A        0.13259
     126B ->144B        0.11553
     128B ->144B        0.17170
     138B ->147B       -0.10374
     139B ->146B       -0.17327
     139B ->147B        0.10190
     140B ->146B       -0.29657
     140B ->147B        0.24698
     140B ->148B        0.15773
     141B ->147B        0.19404
     141B ->148B       -0.15188
     142B ->152B       -0.20255
 Excited State  68:  2.856-A      4.1918 eV  295.78 nm  f=0.0591  <S**2>=1.789
     139A ->146A       -0.12673
     140A ->146A        0.60398
     140A ->147A       -0.17175
     141A ->146A        0.23564
     142A ->146A       -0.12058
     142A ->155A        0.16609
     143A ->146A       -0.11624
     139B ->146B        0.24820
     140B ->146B        0.35981
     140B ->147B       -0.23868
     140B ->151B       -0.11608
     140B ->153B       -0.10021
     142B ->155B        0.17846
 Excited State  69:  3.101-A      4.2227 eV  293.61 nm  f=0.0277  <S**2>=2.154
     136A ->146A       -0.20851
     139A ->146A        0.44415
     139A ->152A       -0.18767
     140A ->151A        0.12571
     140A ->153A       -0.16174
     141A ->147A       -0.10989
     141A ->151A       -0.14346
     141A ->153A        0.17546
     143A ->153A        0.11441
     144A ->146A       -0.11719
     138B ->147B       -0.27336
     138B ->148B       -0.17594
```

```
     138B ->151B       -0.13934
     139B ->146B        0.15339
     139B ->150B       -0.12877
     139B ->153B        0.14938
     140B ->146B        0.29286
     140B ->147B       -0.11842
     140B ->150B       -0.16470
     140B ->153B        0.18835
     141B ->147B        0.10445
     141B ->148B        0.11653
     141B ->151B       -0.15884
 Excited State  70:  3.246-A      4.2300 eV  293.11 nm  f=0.0199  <S**2>=2.383
     140A ->146A       -0.21909
     140A ->147A       -0.34913
     141A ->146A        0.11548
     141A ->147A        0.39785
     141A ->148A       -0.12828
     142A ->147A       -0.15349
     142A ->155A       -0.17063
     143A ->147A        0.14109
     143A ->151A        0.10231
     139B ->146B        0.26329
     139B ->147B        0.17175
     139B ->148B        0.10674
     140B ->146B        0.33095
     140B ->147B        0.21459
     140B ->148B        0.24457
     142B ->155B       -0.16454
     143B ->150B       -0.13373
 Excited State  71:  2.209-A      4.2521 eV  291.58 nm  f=0.0020  <S**2>=0.970
     139A ->146A        0.10703
     140A ->147A       -0.37566
     141A ->147A        0.42460
     141A ->148A       -0.10522
     141A ->155A        0.11126
     142A ->147A       -0.15640
     142A ->155A        0.25740
     139B ->146B       -0.30938
     139B ->148B       -0.10106
     140B ->146B       -0.42017
     140B ->147B       -0.21284
     140B ->148B       -0.16871
     142B ->155B        0.25080
     143B ->150B       -0.14360
 Excited State  72:  2.863-A      4.2600 eV  291.04 nm  f=0.0224  <S**2>=1.799
     135A ->145A       -0.11163
     138A ->147A       -0.21359
     141A ->154A        0.12052
     142A ->147A        0.10760
     143A ->154A       -0.13767
     127B ->144B        0.41623
     130B ->144B        0.30757
     132B ->144B       -0.24085
     133B ->146B        0.10094
     137B ->146B        0.18721
     140B ->154B        0.10341
     143B ->149B        0.54828
     143B ->154B        0.17971
 Excited State  73:  2.541-A      4.2694 eV  290.40 nm  f=0.0155  <S**2>=1.364
     138A ->147A        0.17647
     143A ->154A        0.10551
     127B ->144B        0.58251
```

```
    129B ->144B        0.11268
    130B ->144B        0.41237
    132B ->144B       -0.31152
    137B ->146B       -0.15769
    143B ->149B       -0.37347
    143B ->154B       -0.14217
 Excited State  74:  2.222-A      4.2808 eV  289.63 nm  f=0.0811  <S**2>=0.984
    127A ->155A        0.10044
    140A ->146A       -0.17415
    140A ->147A        0.10329
    141A ->146A        0.10222
    141A ->155A        0.22329
    142A ->155A        0.51792
    139B ->146B        0.17176
    140B ->147B        0.38033
    140B ->148B        0.23083
    142B ->155B        0.49974
    143B ->150B        0.10645
    143B ->151B       -0.11449
 Excited State  75:  3.008-A      4.3215 eV  286.90 nm  f=0.0358  <S**2>=2.012
    139A ->152A       -0.11923
    140A ->147A       -0.17581
    140A ->148A        0.18260
    141A ->147A        0.29579
    141A ->148A        0.14613
    141A ->153A        0.11128
    142A ->147A       -0.12547
    143A ->151A       -0.18631
    137B ->145B        0.16731
    138B ->151B       -0.11928
    139B ->146B        0.31570
    139B ->147B       -0.39011
    139B ->148B       -0.11540
    140B ->147B        0.19454
    140B ->153B        0.14378
    141B ->151B       -0.10188
    143B ->150B        0.43887
 Excited State  76:  2.838-A      4.3436 eV  285.44 nm  f=0.0123  <S**2>=1.764
    138A ->145A       -0.11021
    139A ->146A       -0.16575
    140A ->146A       -0.13680
    140A ->147A       -0.19616
    140A ->148A        0.31433
    141A ->148A        0.30441
    142A ->148A       -0.13891
    143A ->151A       -0.11969
    139B ->146B       -0.19194
    139B ->147B        0.50444
    139B ->148B        0.28746
    140B ->146B        0.19613
    140B ->147B       -0.22524
    140B ->148B       -0.14246
    143B ->150B        0.23501
    143B ->153B       -0.10032
 Excited State  77:  2.879-A      4.3519 eV  284.90 nm  f=0.0001  <S**2>=1.822
    138B ->145B        0.99330
 Excited State  78:  2.036-A      4.3658 eV  283.99 nm  f=0.0001  <S**2>=0.787
    126A ->155A        0.12605
    133A ->155A        0.17086
    136A ->155A        0.25666
    139A ->155A        0.29818
    143A ->155A       -0.16950
```

```
      144A ->150A       -0.12028
      144A ->155A        0.78030
      123B ->144B        0.14194
      124B ->144B        0.22187
 Excited State  79:  3.078-A      4.3692 eV  283.77 nm  f=0.0120  <S**2>=2.119
      138A ->145A        0.11645
      140A ->147A        0.24166
      140A ->148A        0.44758
      141A ->148A        0.45982
      141A ->151A       -0.12712
      142A ->148A       -0.20822
      143A ->148A       -0.14711
      143A ->151A        0.15075
      139B ->147B       -0.18506
      140B ->150B       -0.14813
      142B ->149B       -0.17179
      143B ->150B       -0.35447
      143B ->153B       -0.13693
 Excited State  80:  2.159-A      4.3897 eV  282.45 nm  f=0.0325  <S**2>=0.916
      138A ->145A        0.34927
      140A ->147A        0.41559
      141A ->147A        0.25083
      142A ->147A       -0.12201
      143A ->147A       -0.12504
      137B ->145B        0.33908
      139B ->146B        0.37677
      139B ->147B        0.40396
      140B ->146B       -0.23398
      140B ->147B       -0.25946
 Excited State  81:  2.702-A      4.4287 eV  279.96 nm  f=0.0624  <S**2>=1.575
      134A ->147A        0.19963
      135A ->145A        0.26122
      143A ->149A        0.43277
      143A ->150A        0.13606
      143A ->154A        0.10490
      144A ->149A        0.26732
      133B ->146B       -0.18102
      135B ->145B        0.33007
      135B ->149B       -0.10742
      139B ->154B        0.10900
      143B ->149B        0.49571
 Excited State  82:  2.554-A      4.4343 eV  279.60 nm  f=0.0236  <S**2>=1.380
      138A ->145A        0.13101
      139A ->146A       -0.14113
      140A ->147A        0.14366
      140A ->148A       -0.27191
      141A ->148A       -0.14505
      143A ->153A        0.13076
      139B ->147B       -0.17781
      139B ->148B        0.63204
      140B ->147B        0.17801
      140B ->148B       -0.45826
      142B ->149B       -0.10003
      143B ->153B       -0.14311
 Excited State  83:  3.190-A      4.4402 eV  279.23 nm  f=0.0136  <S**2>=2.294
      132A ->145A        0.21258
      134A ->145A       -0.15895
      135A ->147A       -0.10424
      136A ->146A        0.11862
      139A ->146A        0.29868
      140A ->148A        0.23586
      141A ->151A        0.10681
```

```
     143A ->151A       -0.10056
     143A ->152A       -0.10056
     143A ->153A       -0.13777
     132B ->145B       -0.20989
     133B ->145B        0.18642
     137B ->145B        0.11025
     139B ->147B       -0.12013
     139B ->148B        0.31259
     140B ->147B        0.12140
     140B ->148B       -0.13192
     140B ->150B        0.13476
     141B ->147B        0.11911
     143B ->150B       -0.25557
     143B ->151B        0.17861
     143B ->153B        0.30253
 Excited State  84:  3.341-A      4.4511 eV  278.55 nm  f=0.0177  <S**2>=2.540
     132A ->145A       -0.12606
     133A ->148A        0.11114
     135A ->146A        0.19576
     136A ->148A       -0.10989
     136A ->153A       -0.10666
     140A ->146A       -0.16657
     141A ->152A       -0.16522
     143A ->152A       -0.34218
     132B ->145B        0.12362
     134B ->148B        0.12405
     135B ->147B       -0.12007
     138B ->153B        0.12084
     139B ->148B       -0.10942
     140B ->148B        0.12587
     140B ->151B       -0.17403
     141B ->151B       -0.16922
     143B ->151B        0.54188
 Excited State  85:  2.569-A      4.4547 eV  278.32 nm  f=0.0011  <S**2>=1.399
     136A ->145A       -0.58339
     139A ->145A        0.17775
     144A ->149A        0.66295
     144A ->150A        0.22591
 Excited State  86:  2.910-A      4.4593 eV  278.03 nm  f=0.0361  <S**2>=1.868
     127A ->145A        0.12982
     130A ->145A        0.16889
     132A ->145A       -0.21059
     132A ->149A       -0.12791
     138A ->145A        0.23258
     140A ->151A       -0.10904
     127B ->145B       -0.12699
     130B ->145B       -0.16055
     132B ->145B        0.20722
     132B ->149B        0.14522
     137B ->145B        0.36494
     139B ->147B       -0.10288
     139B ->148B        0.14994
     142B ->149B        0.52624
     142B ->152B        0.12077
     143B ->150B       -0.17620
 Excited State  87:  2.700-A      4.4817 eV  276.65 nm  f=0.1190  <S**2>=1.573
     132A ->145A       -0.17189
     134A ->145A        0.13280
     136A ->146A        0.18288
     138A ->145A       -0.24382
     139A ->146A        0.28558
     140A ->147A        0.13124
```

```
      140A ->148A        0.37536
      141A ->148A       -0.11526
      143A ->151A        0.21715
      122B ->144B       -0.11099
      132B ->145B        0.16630
      133B ->145B       -0.18889
      137B ->145B       -0.25194
      140B ->148B       -0.30383
      141B ->147B        0.11250
      143B ->150B        0.24033
      143B ->153B        0.15732
 Excited State  88:  2.598-A      4.5121 eV  274.78 nm  f=0.0013  <S**2>=1.437
      136A ->145A        0.70991
      139A ->145A       -0.10155
      143A ->149A       -0.11453
      143A ->155A        0.11739
      144A ->149A        0.56273
      144A ->150A        0.17928
      143B ->155B        0.11862
 Excited State  89:  2.401-A      4.5163 eV  274.53 nm  f=0.0349  <S**2>=1.191
      130A ->145A        0.10477
      136A ->145A       -0.11108
      138A ->145A       -0.26169
      140A ->148A       -0.23963
      141A ->147A        0.10065
      141A ->148A        0.29639
      142A ->148A       -0.11674
      142A ->149A       -0.13102
      143A ->148A        0.16153
      143A ->151A       -0.10646
      144A ->146A       -0.10854
      144A ->149A       -0.10004
      144A ->152A        0.13601
      122B ->144B        0.10771
      137B ->145B       -0.18593
      139B ->146B        0.10375
      139B ->147B       -0.10671
      139B ->148B        0.36946
      140B ->146B       -0.13153
      140B ->147B       -0.20835
      140B ->148B        0.27929
      142B ->149B       -0.13532
      143B ->153B        0.29833
 Excited State  90:  3.196-A      4.5385 eV  273.18 nm  f=0.0002  <S**2>=2.303
      129A ->146A        0.11800
      131A ->146A       -0.11646
      136A ->148A       -0.14924
      139A ->148A        0.60922
      139A ->151A       -0.10710
      139A ->153A        0.12019
      140A ->146A        0.15123
      140A ->152A        0.13514
      141A ->146A       -0.11890
      141A ->152A       -0.15285
      129B ->147B        0.10274
      138B ->147B        0.18693
      138B ->148B       -0.28227
      139B ->147B        0.15042
      139B ->151B       -0.14359
      140B ->147B        0.11894
      140B ->151B       -0.16801
      143B ->151B       -0.26655
```

```
 Excited State  91:  2.711-A      4.5748 eV  271.02 nm  f=0.0688  <S**2>=1.587
     134A ->145A       -0.20608
     138A ->145A       -0.13728
     141A ->147A        0.11993
     143A ->151A        0.42463
     144A ->151A        0.33811
     130B ->145B        0.11634
     133B ->145B        0.14067
     137B ->145B       -0.18684
     139B ->148B        0.10836
     142B ->149B        0.53096
     143B ->150B        0.13617
 Excited State  92:  3.094-A      4.5811 eV  270.64 nm  f=0.0185  <S**2>=2.143
     134A ->147A       -0.17682
     135A ->145A       -0.38755
     138A ->147A        0.10494
     143A ->149A        0.62221
     143A ->150A        0.17525
     143A ->154A        0.14245
     133B ->146B        0.18466
     135B ->145B       -0.29284
     137B ->146B       -0.13203
     142B ->150B        0.14330
     143B ->154B       -0.19919
 Excited State  93:  2.707-A      4.6008 eV  269.48 nm  f=0.0389  <S**2>=1.581
     127A ->145A        0.11175
     130A ->145A        0.16220
     136A ->146A       -0.20034
     138A ->145A       -0.10954
     139A ->146A       -0.23619
     139A ->147A       -0.12527
     141A ->148A       -0.13819
     142A ->149A       -0.21082
     143A ->153A       -0.10485
     144A ->151A        0.58161
     127B ->145B       -0.12052
     130B ->145B       -0.16121
     133B ->145B        0.10515
     140B ->148B       -0.13258
     141B ->148B       -0.10251
     142B ->149B       -0.18239
     143B ->150B       -0.24949
 Excited State  94:  2.872-A      4.6015 eV  269.44 nm  f=0.0536  <S**2>=1.812
     134A ->145A        0.19110
     135A ->147A        0.11324
     136A ->146A       -0.11210
     138A ->145A        0.27870
     141A ->147A       -0.13741
     142A ->149A        0.19786
     143A ->153A       -0.23649
     144A ->151A        0.38355
     144A ->152A        0.12014
     133B ->145B       -0.21439
     135B ->146B        0.10520
     137B ->145B        0.20015
     139B ->146B       -0.16383
     142B ->149B       -0.19314
     143B ->150B        0.26265
     143B ->151B       -0.10393
     143B ->153B        0.30913
 Excited State  95:  2.548-A      4.6265 eV  267.99 nm  f=0.1021  <S**2>=1.373
     136A ->146A        0.30207
```

```
     139A ->146A        0.26549
     139A ->147A       -0.16673
     140A ->148A       -0.12904
     141A ->148A        0.13460
     143A ->151A       -0.29917
     143A ->153A        0.28562
     144A ->151A        0.52475
     144A ->152A       -0.11590
     122B ->144B       -0.11257
     138B ->147B        0.18531
     140B ->148B        0.11500
     141B ->147B        0.11117
     141B ->148B        0.15244
     143B ->153B       -0.16342
 Excited State  96:  2.082-A      4.6441 eV  266.97 nm  f=0.0010  <S**2>=0.834
     136A ->145A       -0.23454
     140A ->155A        0.25092
     143A ->150A        0.14326
     143A ->155A        0.58385
     144A ->155A        0.11239
     124B ->144B       -0.19452
     127B ->144B        0.12060
     139B ->155B        0.13940
     141B ->152B       -0.10369
     141B ->155B       -0.11807
     142B ->150B        0.11415
     143B ->152B        0.10675
     143B ->155B        0.56539
 Excited State  97:  2.851-A      4.6627 eV  265.90 nm  f=0.0034  <S**2>=1.782
     143A ->149A       -0.14332
     137B ->150B       -0.12221
     139B ->149B        0.16334
     140B ->149B       -0.15450
     142B ->150B        0.86334
     142B ->153B       -0.15165
     143B ->154B       -0.15530
 Excited State  98:  2.913-A      4.6745 eV  265.23 nm  f=0.0064  <S**2>=1.872
     143A ->149A        0.17966
     124B ->144B       -0.10228
     137B ->146B       -0.19861
     139B ->149B       -0.11100
     140B ->149B        0.11050
     142B ->150B        0.23332
     142B ->153B       -0.10621
     143B ->149B       -0.15621
     143B ->151B       -0.10205
     143B ->152B       -0.37767
     143B ->154B        0.72252
 Excited State  99:  3.075-A      4.6797 eV  264.94 nm  f=0.0586  <S**2>=2.114
     133A ->148A       -0.16222
     135A ->146A       -0.25219
     136A ->148A        0.29142
     139A ->146A       -0.10418
     139A ->148A        0.38242
     144A ->152A       -0.18505
     134B ->147B        0.16947
     134B ->148B       -0.17036
     135B ->147B        0.24952
     139B ->147B        0.11034
     143B ->151B        0.50098
     143B ->153B        0.25307
     143B ->154B        0.12899
```

10.3 Dinuclear Bis(terpyridine)ruthenium(II) Complexes by Amide Coupling of Ruthenium Amino Acids: Synthesis and Properties

A. Breivogel, K. Hempel, K. Heinze, *Inorg. Chim. Acta* **2011**, *374*, 152–162.

DOI: 10.1016/j.ica.2011.03.046

DFT-optimized (B3LYP/LANL2DZ) cartesian coordinates of **3a** and **3b** (singlet) and **1b**$^+$, **3a**$^+$ and **3b**$^+$ (doublet) can be found in the online supporting information.

.

Dinuclear Bis(terpyridine)ruthenium(II) Complexes by Amide Coupling of Ruthenium Amino Acids: Synthesis and Properties

Aaron Breivogel[a], Klaus Hempel[b], Katja Heinze*[a]

Supporting Information

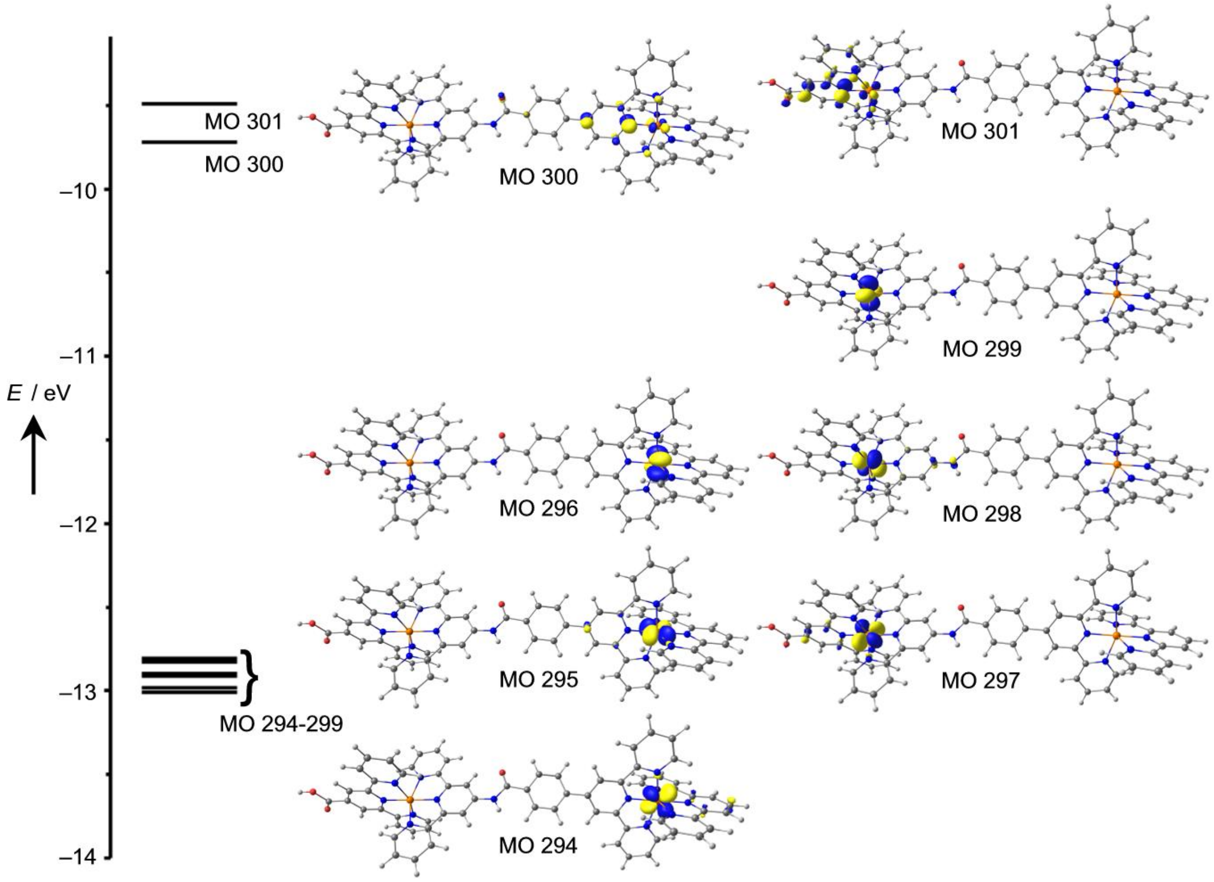

Fig. S1. MO scheme of **3a** (contour level 0.07 a.u.).

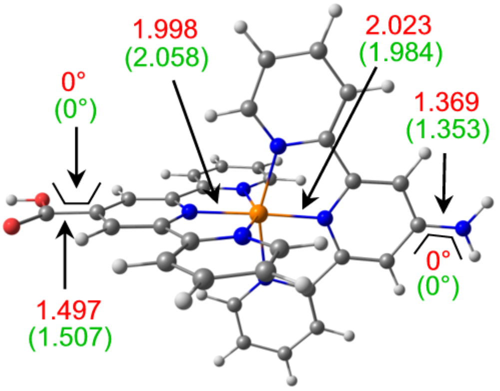

Fig. S2. Relevant DFT calculated metrical parameters of a model of **1b** (red) and **[1b]**$^+$ (green, in parentheses) (distances in Å).

10.4 Light-induced Charge Separation in a Donor-Chromophore-Acceptor Nanocomposite Poly[TPA-Ru(tpy)$_2$]@ZnO

L. zur Borg, A. L. Domanski, A. Breivogel, M. Bürger, R. Berger, K. Heinze, R. Zentel, *J. Mater. Chem. C* **2013**, *1*, 1223–1230.

DOI: 10.1039/c2tc00535b

Supporting Information

Light-Induced Charge Separation in a Donor-Chromophore-Acceptor Nanocomposite Poly[TPA-Ru(tpy)$_2$]@ZnO

Fig. S1 FT-IR spectrum of [(H_2N-CH_2-CONH-tpy)Ru(tpy-CONH-CH_2-COOH)](PF_6)$_2$ (A).

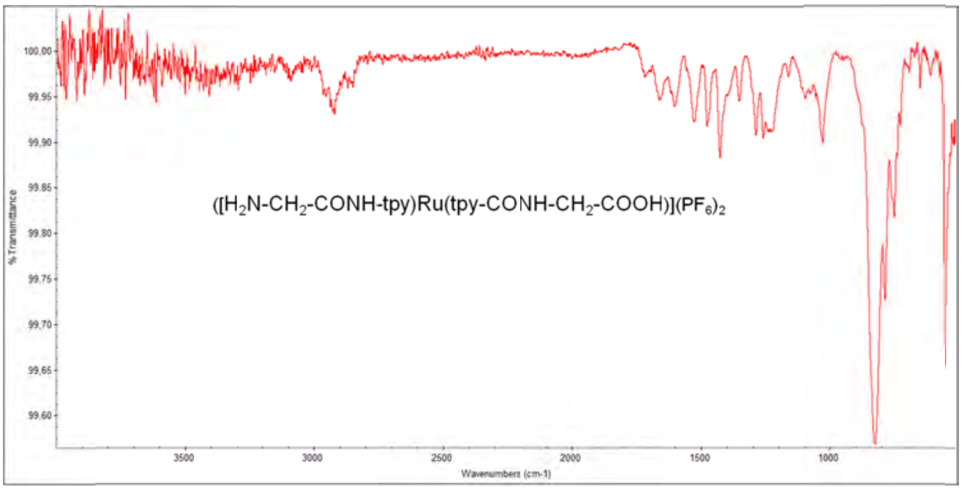

Fig. S2 FT-IR spectra of P2 and P3a and 3b.

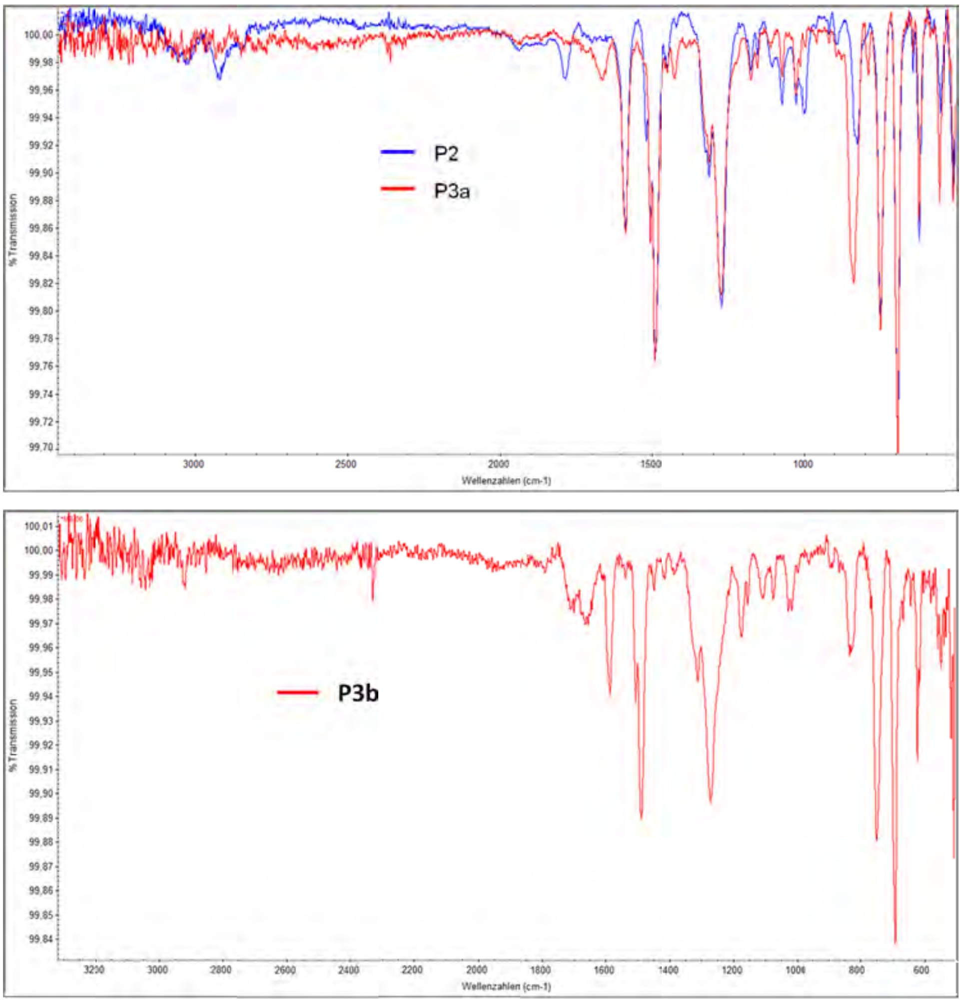

Fig. S3 ^{19}F NMR spectra of P2 and P3a in $CDCl_3$.

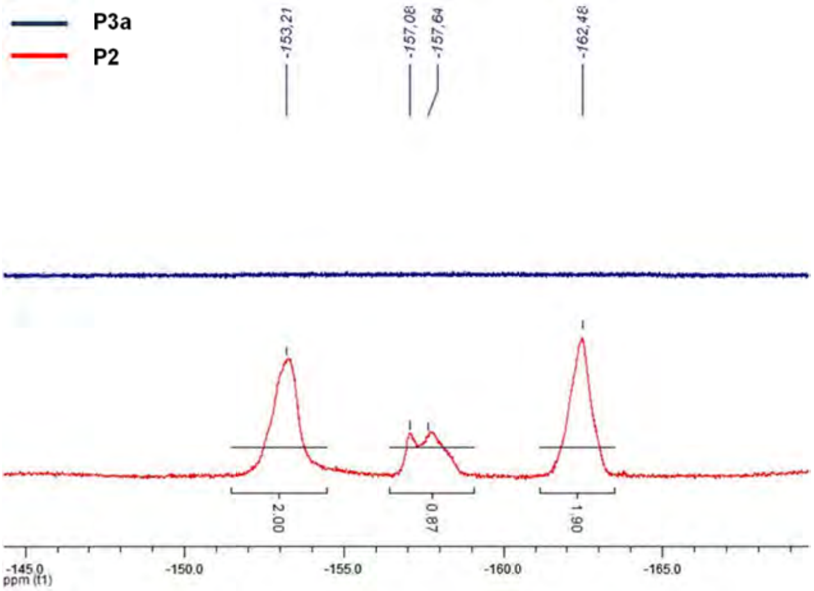

Fig. S4 TEM images of a) pristine ZnO. b) and c) P3a@ZnO, drop cast from THF.

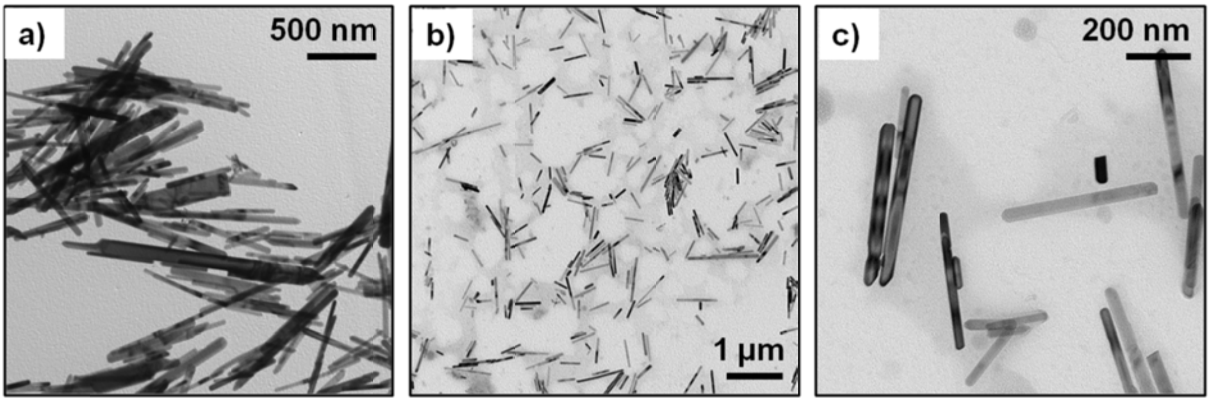

Fig. S5 Topography image of P3a@ZnO.

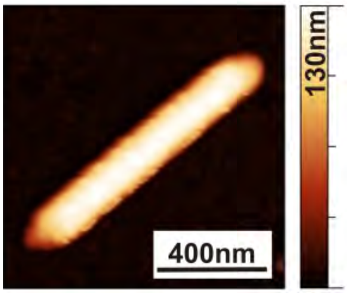

Fig. S6 KPFM images of P3b@ZnO. a) Topography b) Surface potential map recorded in darkness. c) Surface potential map recorded under laser illumination of a wavelength of 488 nm. d) Line profile of the surface potential across the particle indicated by the line in the respective surface potential map. No photo-response was observed for this D-A system.

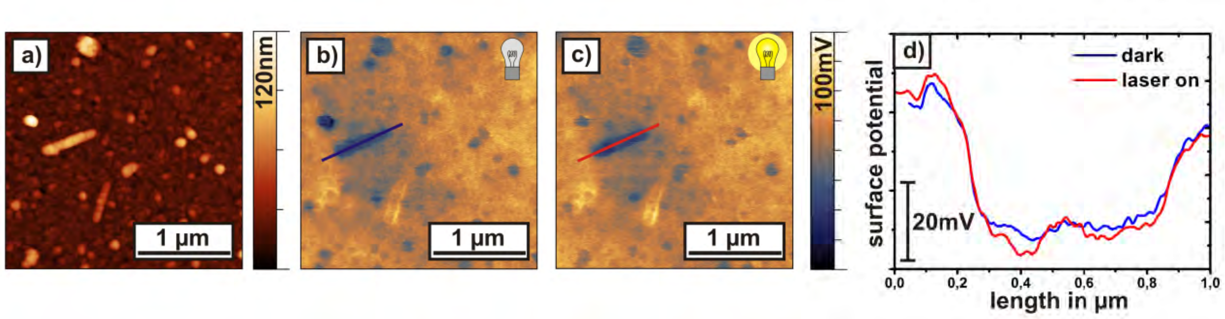

Fig. S7 Atom numbering of A used for NMR assignments.

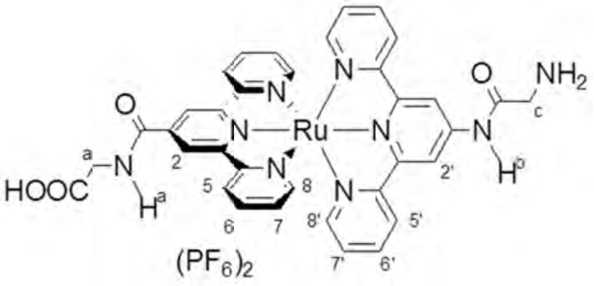

Fig. S8 UV-Vis spectrum of P3b in THF.

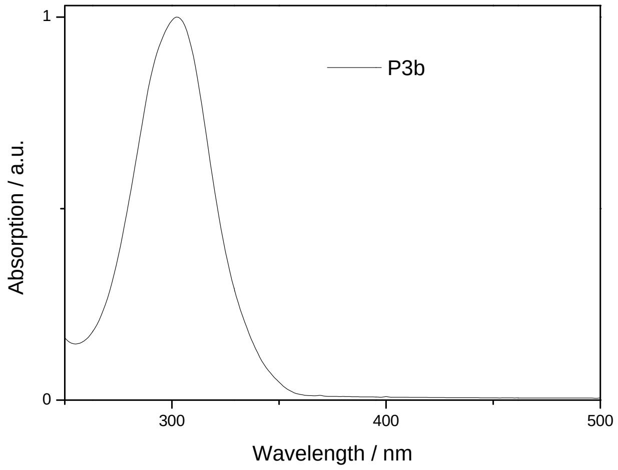

10.5 A Heteroleptic Bis(tridentate)ruthenium(II) Polypyridine Complex with Improved Photophysical Properties and Integrated Functionalizability

A. Breivogel, C. Förster, K. Heinze, *Inorg. Chem.* **2010**, *49*, 7052–7056.

DOI: 10.1021/ic1007236

DFT-optimized (B3LYP/LANL2DZ, IEFPCM in CH_3CN) cartesian coordinates of *cis*-*fac*-$[Ru(ddpd)_2]^{2+}$, *trans*-*fac*-$[Ru(ddpd)_2]^{2+}$, *mer*-$[Ru(ddpd)_2]^{2+}$, $[\mathbf{8}]^{2+}$ (singlet ground state and ^{3}MLCT state) and results of the TD-DFT (B3LYP/LANL2DZ, gasphase and IEFPCM in CH_3CN) calculation of $[\mathbf{8}]^{2+}$ (singlet) can be found in the online supporting information.

A Heteroleptic Bis(tridentate)ruthenium(II) Polypyridine Complex with Improved Photophysical Properties and Integrated Functionalizability

*Aaron Breivogel, Christoph Förster, Katja Heinze**

Supporting Information

- **X-ray crystal data of 8**
- **Spectroscopic data of 8**
- **Cartesian Coordinates of *cis-fac*-[Ru(ddpd)$_2$]$^{2+}$, *trans-fac*-[Ru(ddpd)$_2$]$^{2+}$, *mer*-[Ru(ddpd)$_2$]$^{2+}$, 8 (singlet ground state), 8 (^{3}MLCT state)**
- **Graphical representation of the frontier orbitals of 8**
- **Results of the TD-DFT (singlets) calculation of 8 (gas phase)**
- **Results of the TD-DFT (singlets) calculation of 8 (CH$_3$CN).**
- **Cartesian Coordinates of Ni(CO)$_3$L complexes (L = κ*N*(central pyridine)-ddpd, κ*N*(terminal pyridine)-ddpd, NMe$_3$, NHC (1,3-dimethyl-2,3-dihydro-1*H*-imidazol-2-ylidene), PMe$_3$, PH$_3$, PF$_3$, pyridine, methyl(1-methyl-1H-pyridin-2-ylidene)amine)**

Figure S1. Atom numbering of the dication of **8**.

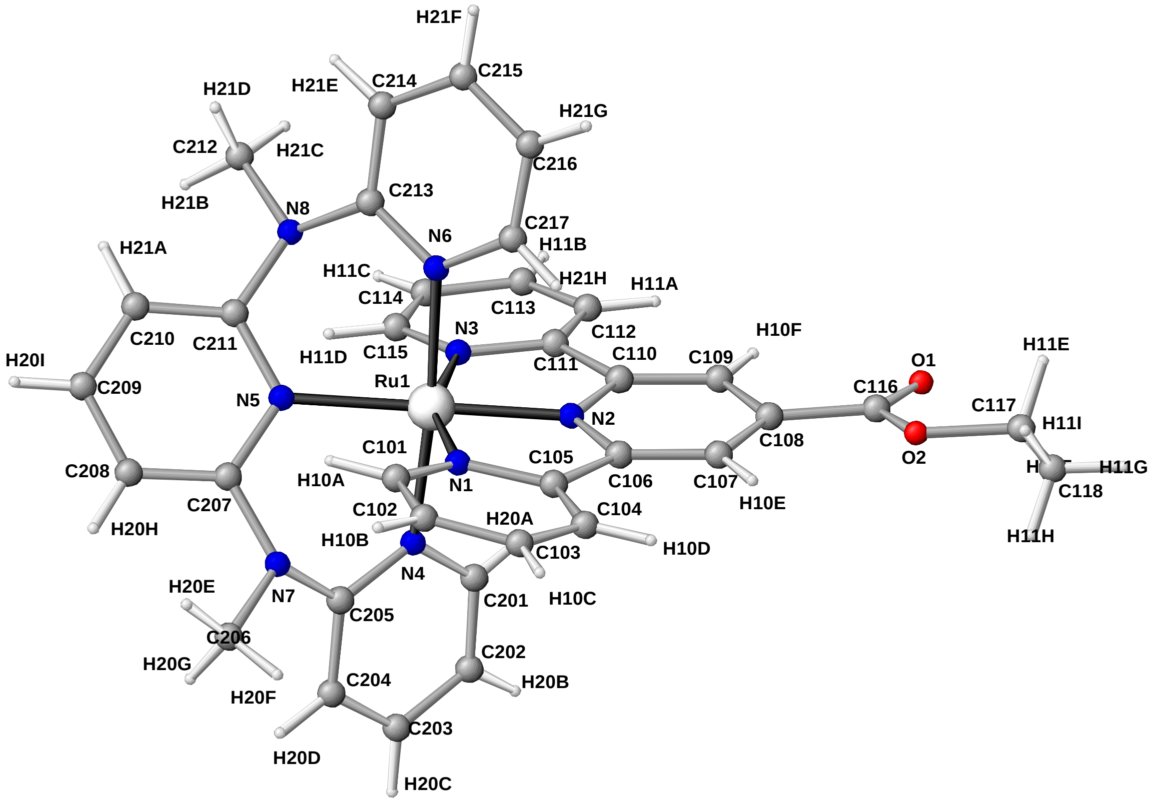

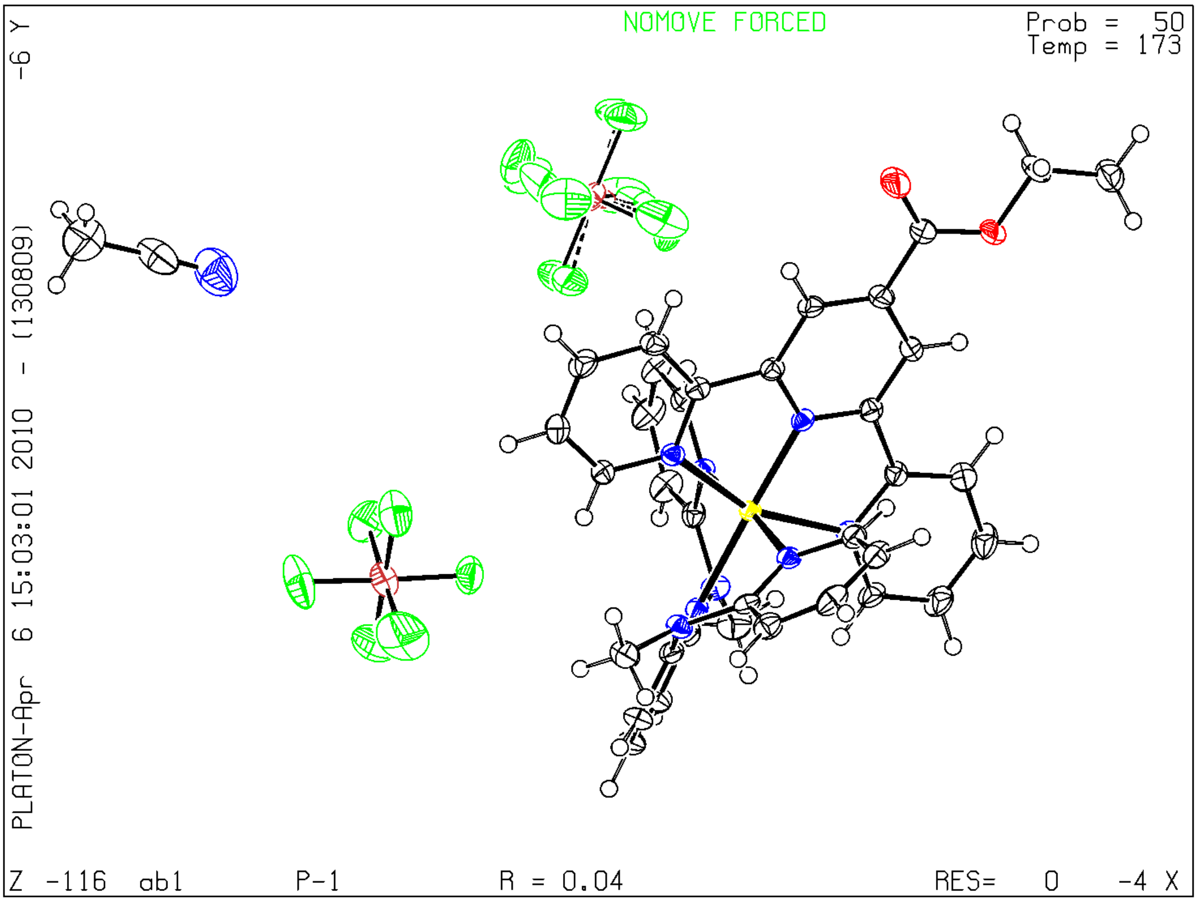

Table S1. Crystal and structure refinement data for **8**.

	8
Empirical formula	$C_{37}H_{35}F_{12}N_9O_2P_2Ru$
Formula weight	1028.75
Crystal color, habit	orange-brown plate
Crystal dimensions / mm	0.20 × 0.20 × 0.10
Crystal system	triclinic
Space group	*P*1-bar
a / Å	11.9005(9)
b / Å	13.2663(10)
c / Å	14.7564(11)
α / °	68.413(2)
β / °	73.337(2)
γ / °	73.704(2)
V / $Å^3$	2034.8(3)
Z	2
F(000)	1036
Density (calcd) / g cm^{-3}	1.679
Absorption coefficient μ / mm^{-1}	0.567 (MULABS)
Theta range / °	1.52 – 28.12
Index ranges	$-15 \leq h \leq 15$ $-17 \leq k \leq 17$ $-19 \leq l \leq 19$
Reflections collected	44719
Independent reflections	9793 (R_{int} = 0.1026)
Observed reflections	9793
Parameters	632
Max. / min. transmission	1.2702 / 0.8205
Goodness-of-fit on F^2	0.931
Largest difference peak and hole / e $Å^{-3}$	0.51 / –1.26
R_1 ($I > 2\sigma(I)$)	0.0391
R_1 (all data)	0.0781
wR_2 ($I > 2\sigma(I)$)	0.0614
wR_2 (all data)	0.0842

Table S2. Bond lengths / Å and angles / ° of **8**.

Ru(1)-N(2)	1.944(2)
Ru(1)-N(6)	2.072(2)
Ru(1)-N(4)	2.076(2)
Ru(1)-N(3)	2.078(2)
Ru(1)-N(5)	2.078(2)
Ru(1)-N(1)	2.079(2)
N(1)-C(101)	1.348(3)
N(1)-C(105)	1.378(3)
N(2)-C(110)	1.360(3)
N(2)-C(106)	1.366(3)
N(3)-C(115)	1.349(3)
N(3)-C(111)	1.373(3)
C(101)-C(102)	1.378(4)
C(101)-H(10A)	0.9500
C(102)-C(103)	1.382(4)
C(102)-H(10B)	0.9500
C(103)-C(104)	1.384(4)
C(103)-H(10C)	0.9500
C(104)-C(105)	1.379(4)
C(104)-H(10D)	0.9500
C(105)-C(106)	1.479(4)
C(106)-C(107)	1.376(3)
C(107)-C(108)	1.388(4)
C(107)-H(10E)	0.9500
C(108)-C(109)	1.397(4)
C(108)-C(116)	1.488(4)
C(109)-C(110)	1.379(3)
C(109)-H(10F)	0.9500
C(110)-C(111)	1.476(4)
C(111)-C(112)	1.382(4)
C(112)-C(113)	1.381(4)
C(112)-H(11A)	0.9500
C(113)-C(114)	1.383(4)
C(113)-H(11B)	0.9500
C(114)-C(115)	1.373(4)
C(114)-H(11C)	0.9500
C(115)-H(11D)	0.9500
C(116)-O(1)	1.210(3)
C(116)-O(2)	1.329(3)
C(117)-O(2)	1.457(3)
C(117)-C(118)	1.497(4)
C(117)-H(11E)	0.9900
C(117)-H(11F)	0.9900
C(118)-H(11G)	0.9800
C(118)-H(11H)	0.9800
C(118)-H(11I)	0.9800
N(4)-C(201)	1.352(3)
N(4)-C(205)	1.357(3)
N(5)-C(211)	1.360(3)
N(5)-C(207)	1.361(3)
N(6)-C(213)	1.349(3)
N(6)-C(217)	1.359(3)
C(201)-C(202)	1.363(4)
C(201)-H(20A)	0.9500
C(202)-C(203)	1.374(4)
C(202)-H(20B)	0.9500
C(203)-C(204)	1.375(4)
C(203)-H(20C)	0.9500
C(204)-C(205)	1.391(4)
C(204)-H(20D)	0.9500
C(205)-N(7)	1.401(3)
N(7)-C(207)	1.412(3)
N(7)-C(206)	1.473(3)
C(206)-H(20E)	0.9800
C(206)-H(20F)	0.9800
C(206)-H(20G)	0.9800
C(207)-C(208)	1.384(4)
C(208)-C(209)	1.378(4)

C(208)-H(20H)	0.9500
C(209)-C(210)	1.370(4)
C(209)-H(20I)	0.9500
C(210)-C(211)	1.381(3)
C(210)-H(21A)	0.9500
C(211)-N(8)	1.410(3)
N(8)-C(213)	1.407(3)
N(8)-C(212)	1.478(3)
C(212)-H(21B)	0.9800
C(212)-H(21C)	0.9800
C(212)-H(21D)	0.9800
C(213)-C(214)	1.395(3)
C(214)-C(215)	1.370(4)
C(214)-H(21E)	0.9500
C(215)-C(216)	1.387(4)
C(215)-H(21F)	0.9500
C(216)-C(217)	1.367(4)
C(216)-H(21G)	0.9500
C(217)-H(21H)	0.9500
P(1)-F(13)	1.565(5)
P(1)-F(16)	1.576(4)
P(1)-F(15)	1.582(5)
P(1)-F(14)	1.587(5)
P(1)-F(12)	1.598(5)
P(1)-F(11)	1.603(5)
P(1A)-F(14A)	1.566(12)
P(1A)-F(15A)	1.582(12)
P(1A)-F(16A)	1.582(12)
P(1A)-F(13A)	1.583(13)
P(1A)-F(12A)	1.589(13)
P(1A)-F(11A)	1.610(13)
P(2)-F(26)	1.571(2)
P(2)-F(24)	1.583(2)
P(2)-F(23)	1.595(2)
P(2)-F(25)	1.597(2)
P(2)-F(22)	1.602(2)
P(2)-F(21)	1.6022(18)
N(300)-C(301)	1.134(5)
C(301)-C(302)	1.452(6)
C(302)-H(30A)	0.9800
C(302)-H(30B)	0.9800
C(302)-H(30C)	0.9800

N(2)-Ru(1)-N(6)	91.95(8)
N(2)-Ru(1)-N(4)	92.92(8)
N(6)-Ru(1)-N(4)	174.70(8)
N(2)-Ru(1)-N(3)	79.57(8)
N(6)-Ru(1)-N(3)	88.88(8)
N(4)-Ru(1)-N(3)	89.94(8)
N(2)-Ru(1)-N(5)	178.29(9)
N(6)-Ru(1)-N(5)	87.68(8)
N(4)-Ru(1)-N(5)	87.51(8)
N(3)-Ru(1)-N(5)	102.09(8)
N(2)-Ru(1)-N(1)	79.68(8)
N(6)-Ru(1)-N(1)	90.94(8)
N(4)-Ru(1)-N(1)	92.00(8)
N(3)-Ru(1)-N(1)	159.22(8)
N(5)-Ru(1)-N(1)	98.66(8)
C(101)-N(1)-C(105)	117.4(2)
C(101)-N(1)-Ru(1)	129.34(19)
C(105)-N(1)-Ru(1)	113.22(16)
C(110)-N(2)-C(106)	121.1(2)
C(110)-N(2)-Ru(1)	119.27(17)
C(106)-N(2)-Ru(1)	119.59(17)
C(115)-N(3)-C(111)	116.7(2)
C(115)-N(3)-Ru(1)	129.85(18)
C(111)-N(3)-Ru(1)	113.38(16)
N(1)-C(101)-C(102)	123.1(3)
N(1)-C(101)-H(10A)	118.5
C(102)-C(101)-H(10A)	118.5
C(101)-C(102)-C(103)	119.2(3)

C(101)-C(102)-H(10B)	120.4
C(103)-C(102)-H(10B)	120.4
C(102)-C(103)-C(104)	118.8(3)
C(102)-C(103)-H(10C)	120.6
C(104)-C(103)-H(10C)	120.6
C(105)-C(104)-C(103)	119.8(3)
C(105)-C(104)-H(10D)	120.1
C(103)-C(104)-H(10D)	120.1
N(1)-C(105)-C(104)	121.6(2)
N(1)-C(105)-C(106)	114.7(2)
C(104)-C(105)-C(106)	123.7(2)
N(2)-C(106)-C(107)	120.3(2)
N(2)-C(106)-C(105)	112.6(2)
C(107)-C(106)-C(105)	126.8(2)
C(106)-C(107)-C(108)	119.4(2)
C(106)-C(107)-H(10E)	120.3
C(108)-C(107)-H(10E)	120.3
C(107)-C(108)-C(109)	119.7(2)
C(107)-C(108)-C(116)	122.7(2)
C(109)-C(108)-C(116)	117.5(2)
C(110)-C(109)-C(108)	119.4(2)
C(110)-C(109)-H(10F)	120.3
C(108)-C(109)-H(10F)	120.3
N(2)-C(110)-C(109)	120.1(2)
N(2)-C(110)-C(111)	113.0(2)
C(109)-C(110)-C(111)	126.9(2)
N(3)-C(111)-C(112)	122.1(2)
N(3)-C(111)-C(110)	114.5(2)
C(112)-C(111)-C(110)	123.4(2)
C(113)-C(112)-C(111)	119.9(3)
C(113)-C(112)-H(11A)	120.1
C(111)-C(112)-H(11A)	120.1
C(112)-C(113)-C(114)	118.3(3)
C(112)-C(113)-H(11B)	120.9
C(114)-C(113)-H(11B)	120.9
C(115)-C(114)-C(113)	119.6(3)
C(115)-C(114)-H(11C)	120.2
C(113)-C(114)-H(11C)	120.2
N(3)-C(115)-C(114)	123.4(3)
N(3)-C(115)-H(11D)	118.3
C(114)-C(115)-H(11D)	118.3
O(1)-C(116)-O(2)	124.4(2)
O(1)-C(116)-C(108)	122.8(3)
O(2)-C(116)-C(108)	112.8(2)
O(2)-C(117)-C(118)	107.5(2)
O(2)-C(117)-H(11E)	110.2
C(118)-C(117)-H(11E)	110.2
O(2)-C(117)-H(11F)	110.2
C(118)-C(117)-H(11F)	110.2
H(11E)-C(117)-H(11F)	108.5
C(117)-C(118)-H(11G)	109.5
C(117)-C(118)-H(11H)	109.5
H(11G)-C(118)-H(11H)	109.5
C(117)-C(118)-H(11I)	109.5
H(11G)-C(118)-H(11I)	109.5
H(11H)-C(118)-H(11I)	109.5
C(116)-O(2)-C(117)	115.3(2)
C(201)-N(4)-C(205)	117.9(2)
C(201)-N(4)-Ru(1)	121.68(17)
C(205)-N(4)-Ru(1)	120.40(17)
C(211)-N(5)-C(207)	117.8(2)
C(211)-N(5)-Ru(1)	121.56(16)
C(207)-N(5)-Ru(1)	120.61(18)
C(213)-N(6)-C(217)	117.9(2)
C(213)-N(6)-Ru(1)	121.10(16)
C(217)-N(6)-Ru(1)	120.51(18)
N(4)-C(201)-C(202)	123.7(3)
N(4)-C(201)-H(20A)	118.1
C(202)-C(201)-H(20A)	118.1
C(201)-C(202)-C(203)	118.3(3)
C(201)-C(202)-H(20B)	120.8

C(203)-C(202)-H(20B)	120.8
C(202)-C(203)-C(204)	119.5(3)
C(202)-C(203)-H(20C)	120.3
C(204)-C(203)-H(20C)	120.3
C(203)-C(204)-C(205)	120.0(3)
C(203)-C(204)-H(20D)	120.0
C(205)-C(204)-H(20D)	120.0
N(4)-C(205)-C(204)	120.6(2)
N(4)-C(205)-N(7)	117.9(2)
C(204)-C(205)-N(7)	121.5(2)
C(205)-N(7)-C(207)	121.9(2)
C(205)-N(7)-C(206)	115.7(2)
C(207)-N(7)-C(206)	115.8(2)
N(7)-C(206)-H(20E)	109.5
N(7)-C(206)-H(20F)	109.5
H(20E)-C(206)-H(20F)	109.5
N(7)-C(206)-H(20G)	109.5
H(20E)-C(206)-H(20G)	109.5
H(20F)-C(206)-H(20G)	109.5
N(5)-C(207)-C(208)	122.4(2)
N(5)-C(207)-N(7)	117.2(2)
C(208)-C(207)-N(7)	120.4(2)
C(209)-C(208)-C(207)	118.7(3)
C(209)-C(208)-H(20H)	120.7
C(207)-C(208)-H(20H)	120.7
C(210)-C(209)-C(208)	119.7(3)
C(210)-C(209)-H(20I)	120.2
C(208)-C(209)-H(20I)	120.2
C(209)-C(210)-C(211)	119.7(3)
C(209)-C(210)-H(21A)	120.2
C(211)-C(210)-H(21A)	120.2
N(5)-C(211)-C(210)	121.8(2)
N(5)-C(211)-N(8)	117.5(2)
C(210)-C(211)-N(8)	120.7(2)
C(213)-N(8)-C(211)	123.0(2)
C(213)-N(8)-C(212)	116.0(2)
C(211)-N(8)-C(212)	115.5(2)
N(8)-C(212)-H(21B)	109.5
N(8)-C(212)-H(21C)	109.5
H(21B)-C(212)-H(21C)	109.5
N(8)-C(212)-H(21D)	109.5
H(21B)-C(212)-H(21D)	109.5
H(21C)-C(212)-H(21D)	109.5
N(6)-C(213)-C(214)	121.0(2)
N(6)-C(213)-N(8)	118.5(2)
C(214)-C(213)-N(8)	120.5(2)
C(215)-C(214)-C(213)	119.9(3)
C(215)-C(214)-H(21E)	120.0
C(213)-C(214)-H(21E)	120.0
C(214)-C(215)-C(216)	119.4(3)
C(214)-C(215)-H(21F)	120.3
C(216)-C(215)-H(21F)	120.3
C(217)-C(216)-C(215)	118.2(3)
C(217)-C(216)-H(21G)	120.9
C(215)-C(216)-H(21G)	120.9
N(6)-C(217)-C(216)	123.4(3)
N(6)-C(217)-H(21H)	118.3
C(216)-C(217)-H(21H)	118.3
F(13)-P(1)-F(16)	89.8(4)
F(13)-P(1)-F(15)	179.2(4)
F(16)-P(1)-F(15)	91.0(4)
F(13)-P(1)-F(14)	89.8(4)
F(16)-P(1)-F(14)	179.6(4)
F(15)-P(1)-F(14)	89.4(4)
F(13)-P(1)-F(12)	89.9(5)
F(16)-P(1)-F(12)	89.7(4)
F(15)-P(1)-F(12)	90.2(4)
F(14)-P(1)-F(12)	90.3(4)
F(13)-P(1)-F(11)	90.6(5)
F(16)-P(1)-F(11)	90.6(5)
F(15)-P(1)-F(11)	89.3(5)

F(14)-P(1)-F(11)	89.5(5)
F(12)-P(1)-F(11)	179.4(6)
F(14A)-P(1A)-F(15A)	92.3(12)
F(14A)-P(1A)-F(16A)	175.2(12)
F(15A)-P(1A)-F(16A)	92.3(11)
F(14A)-P(1A)-F(13A)	90.4(11)
F(15A)-P(1A)-F(13A)	177.1(13)
F(16A)-P(1A)-F(13A)	85.0(11)
F(14A)-P(1A)-F(12A)	90.2(12)
F(15A)-P(1A)-F(12A)	93.1(12)
F(16A)-P(1A)-F(12A)	91.1(13)
F(13A)-P(1A)-F(12A)	87.9(12)
F(14A)-P(1A)-F(11A)	89.0(13)
F(15A)-P(1A)-F(11A)	89.3(13)
F(16A)-P(1A)-F(11A)	89.5(12)
F(13A)-P(1A)-F(11A)	89.8(13)
F(12A)-P(1A)-F(11A)	177.6(16)
F(26)-P(2)-F(24)	91.86(14)
F(26)-P(2)-F(23)	178.61(13)
F(24)-P(2)-F(23)	89.13(12)
F(26)-P(2)-F(25)	91.54(14)
F(24)-P(2)-F(25)	91.20(12)
F(23)-P(2)-F(25)	89.41(12)
F(26)-P(2)-F(22)	90.24(14)
F(24)-P(2)-F(22	)177.72(13)
F(23)-P(2)-F(22)	88.76(12)
F(25)-P(2)-F(22)	89.65(12)
F(26)-P(2)-F(21)	89.96(12)
F(24)-P(2)-F(21)	89.76(11)
F(23)-P(2)-F(21)	89.07(10)
F(25)-P(2)-F(21)	178.18(13)
F(22)-P(2)-F(21)	89.33(10)
N(300)-C(301)-C(302)	176.9(5)
C(301)-C(302)-H(30A)	109.5
C(301)-C(302)-H(30B)	109.5
H(30A)-C(302)-H(30B)	109.5
C(301)-C(302)-H(30C)	109.5
H(30A)-C(302)-H(30C)	109.5
H(30B)-C(302)-H(30C)	109.5

Figure S2. IR spectrum of **8** in KBr.

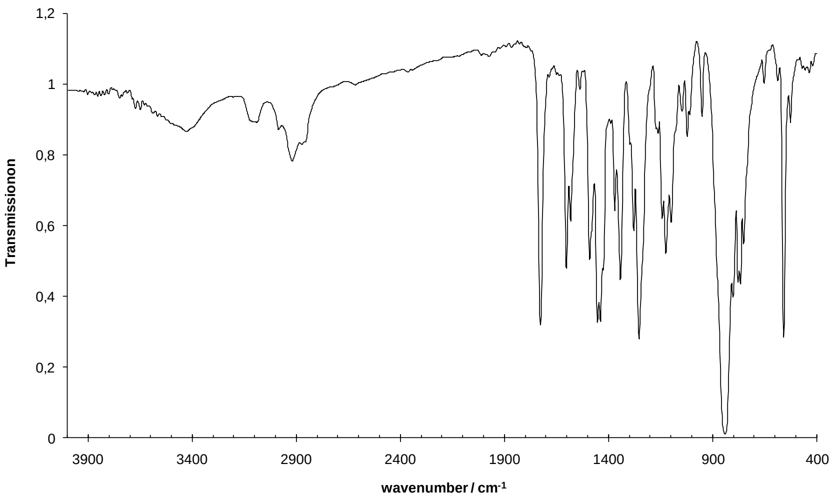

Figure S3. UV/Vis absorption and emission spectrum (λ_{exc} = 517 nm) of **8** in CH$_3$CN at 295 K.

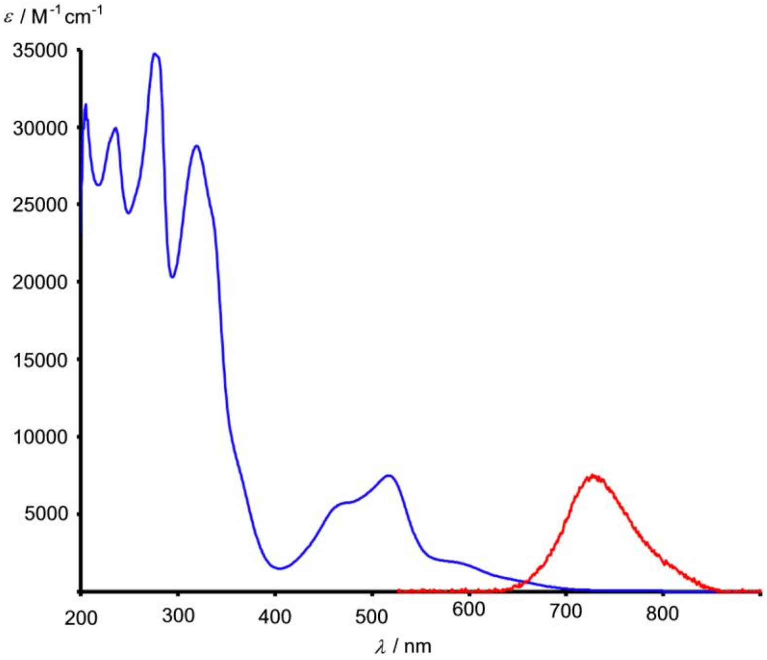

Figure S4. ^{1}H NMR spectrum of **8** in CD_3CN (top: full spectrum; bottom: zoom).

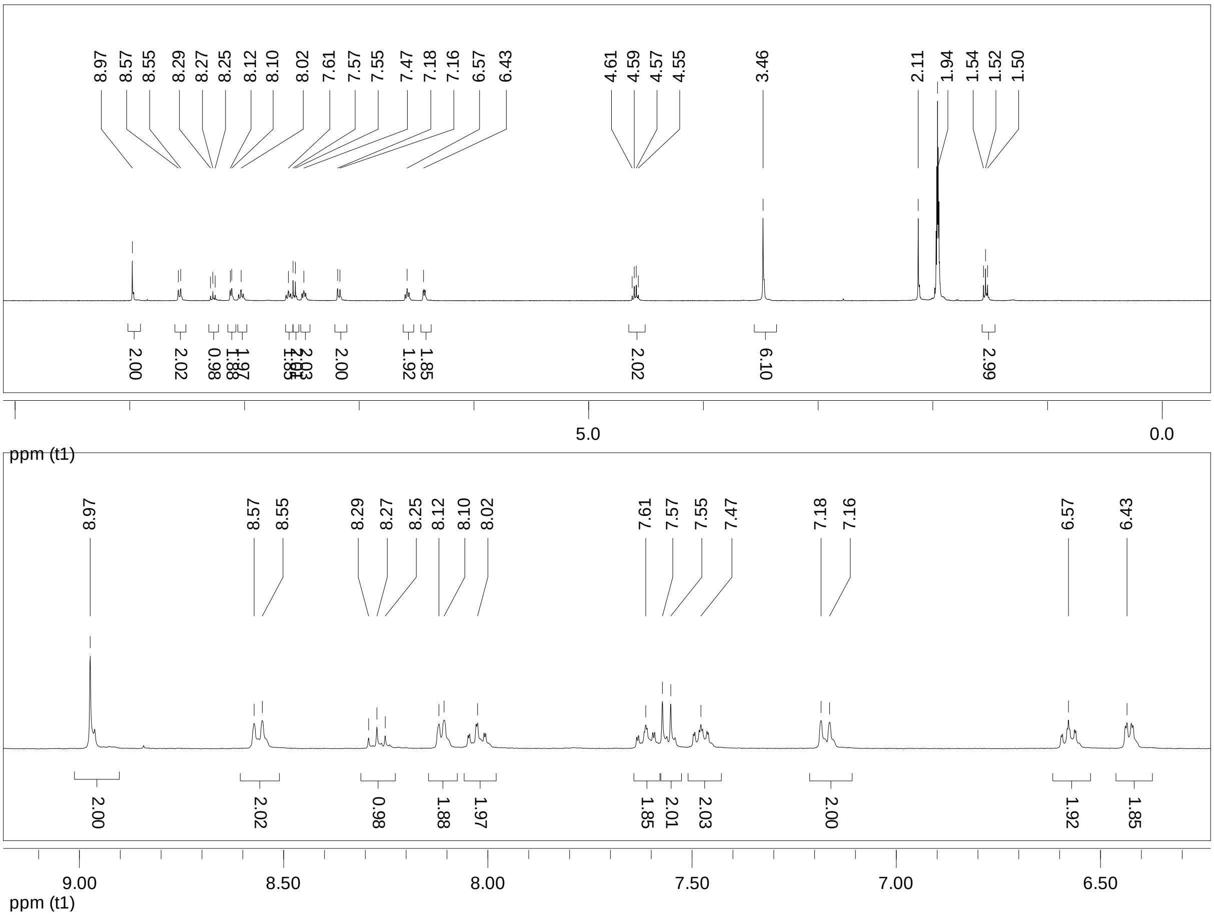

Figure S5. $^{13}C\{^1H\}$ NMR spectrum of **8** in CD_3CN (top: full spectrum; bottom: zoom).

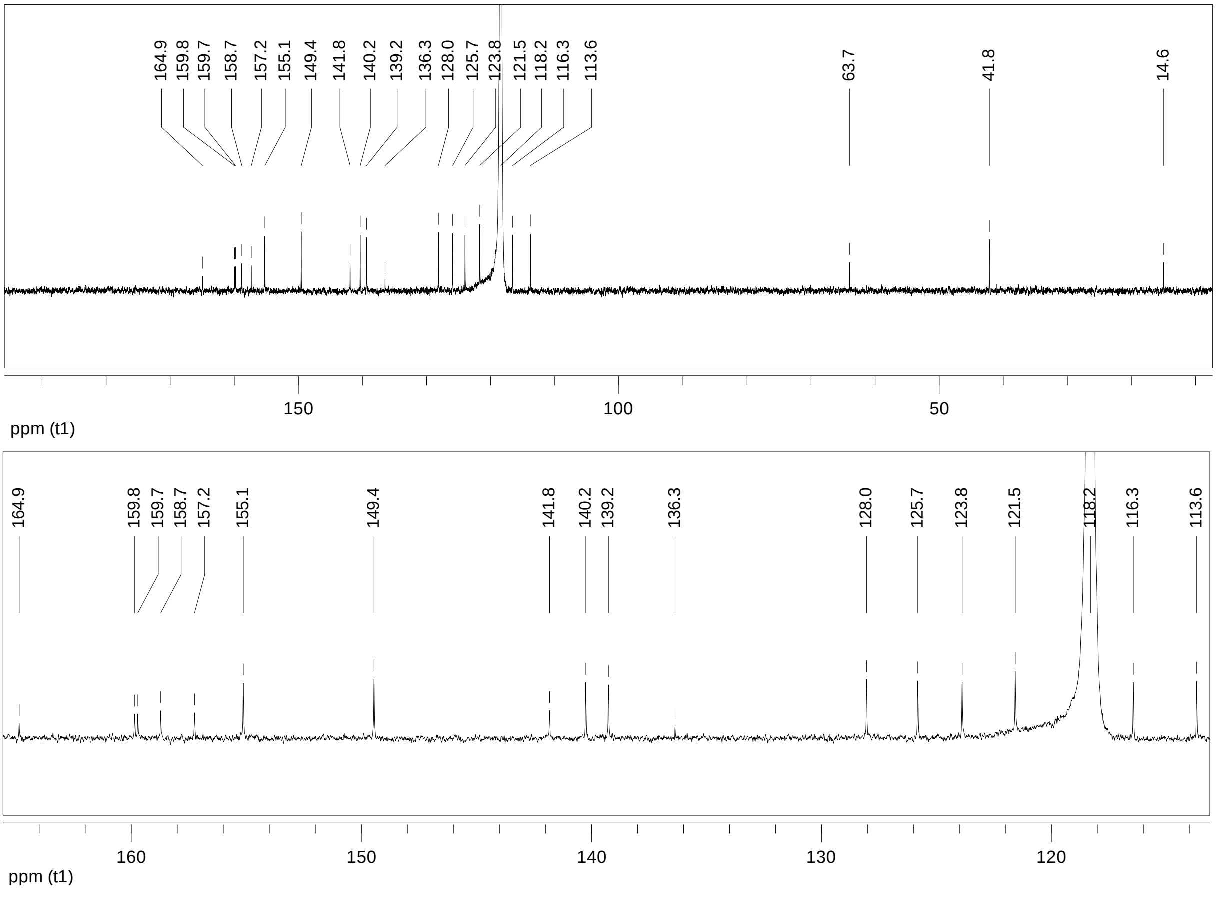

Figure S6. HH-COSY of **8** in CD_3CN.

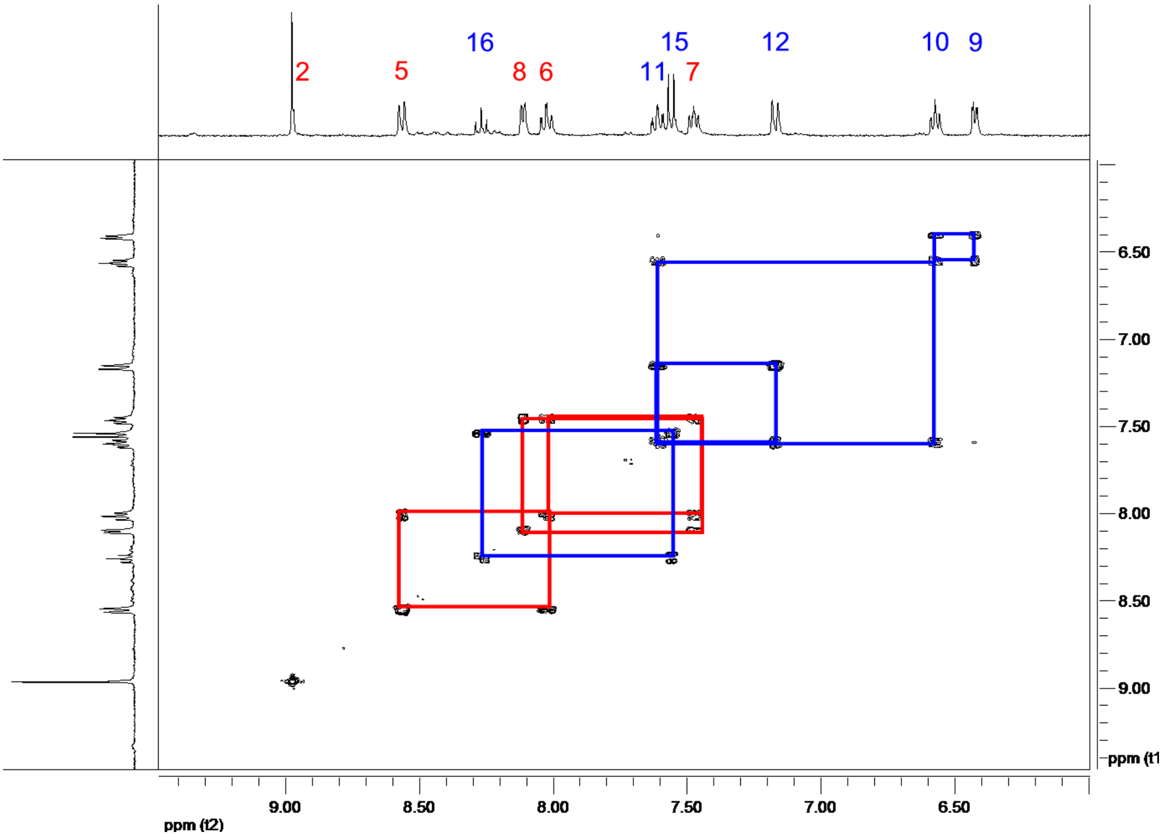

Figure S7. NOESY of **8** in CD_3CN.

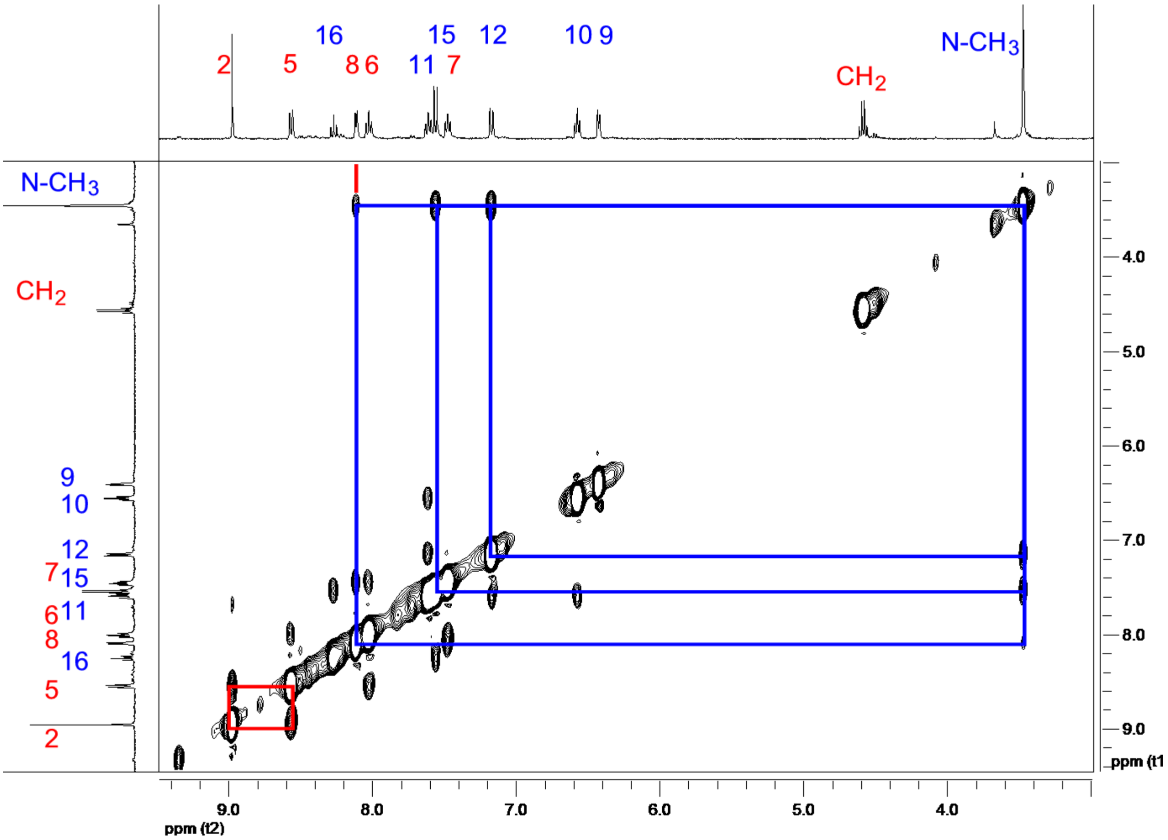

Figure S8. CH-COSY of **8** in CD$_3$CN.

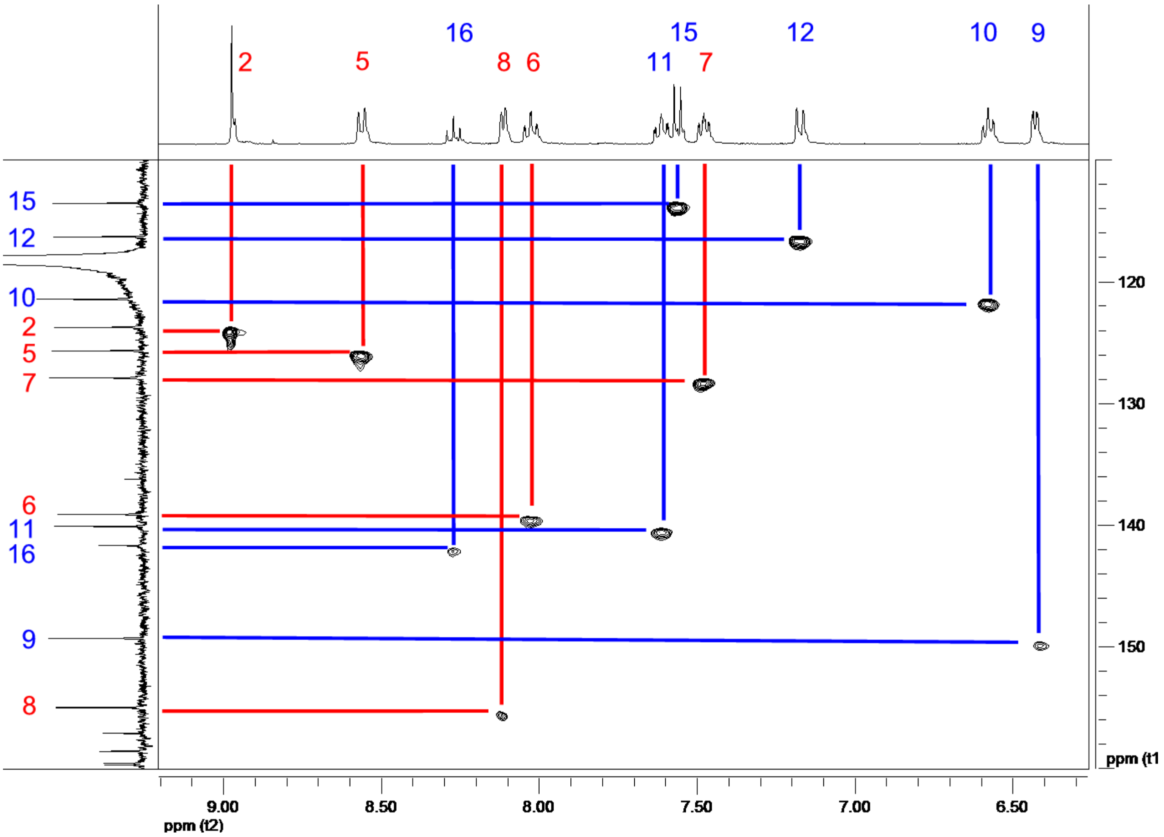

Figure S9. ^{13}C-^{1}H HMBC of **8** in CD$_3$CN.

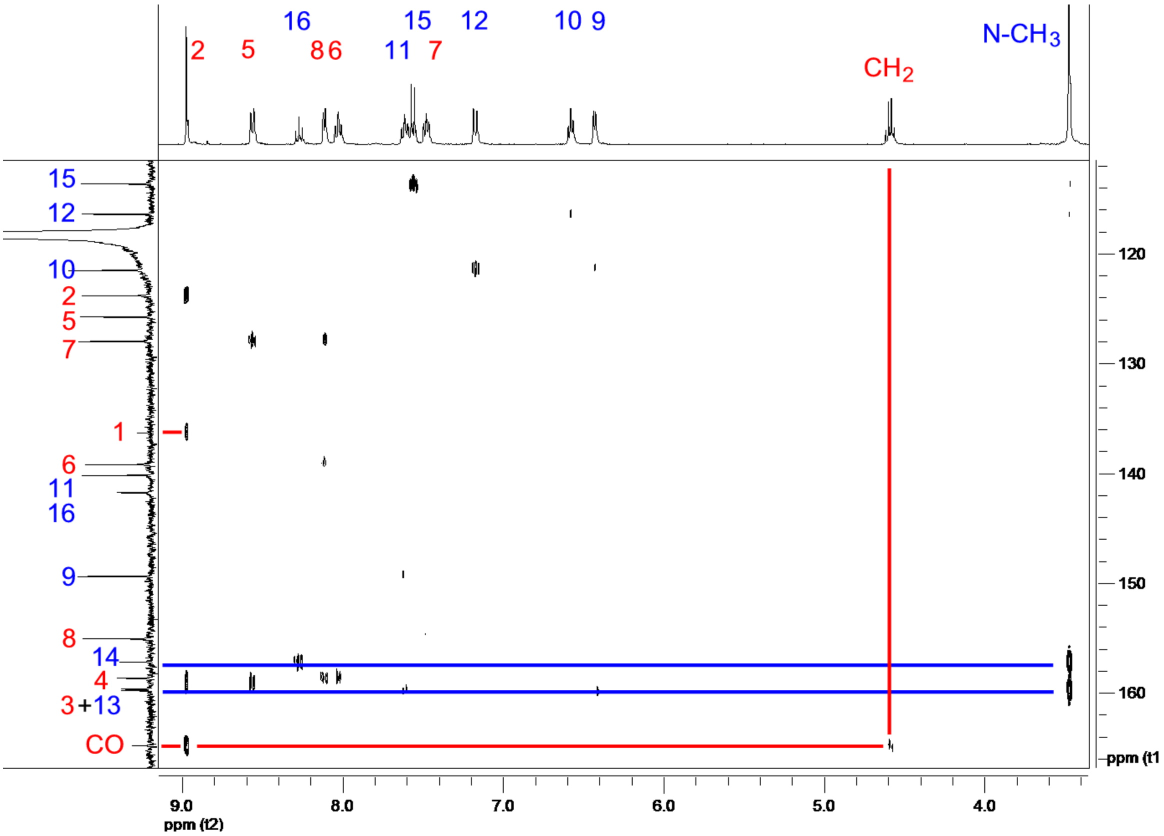

Figure S10. ^{15}N-^{1}H HMBC of **8** in CD_3CN.

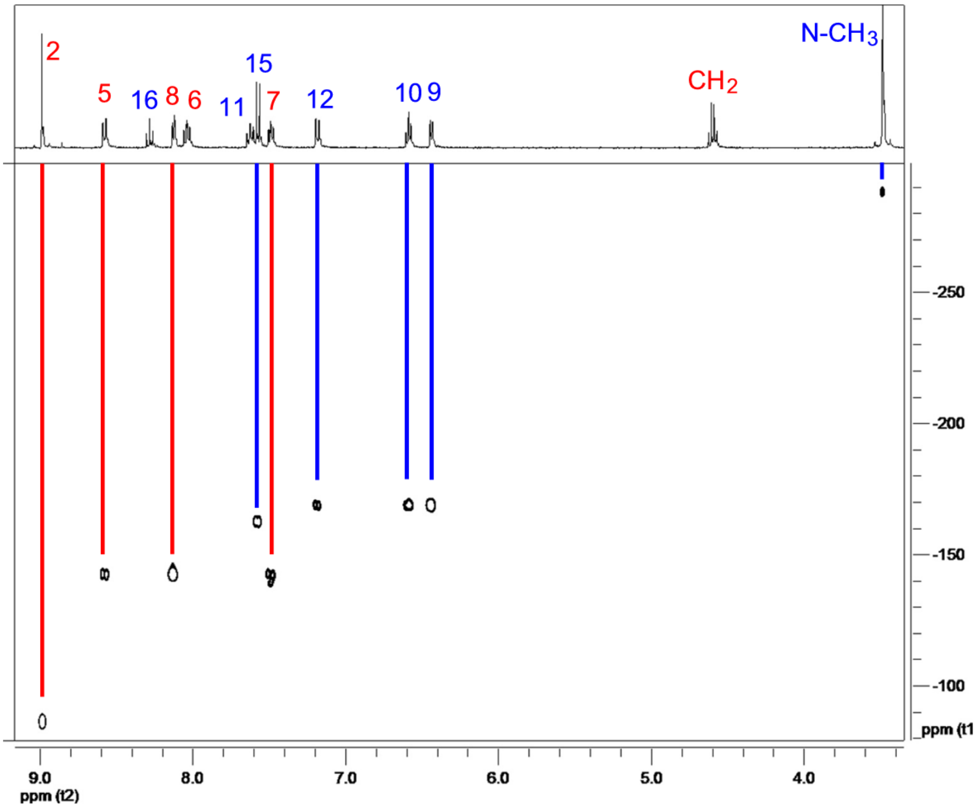

Graphical representation of some relevant frontier orbitals of 8.

#MO	*E* / eV	contour value 0.06 a.u.	qualitative description
160	-11.884	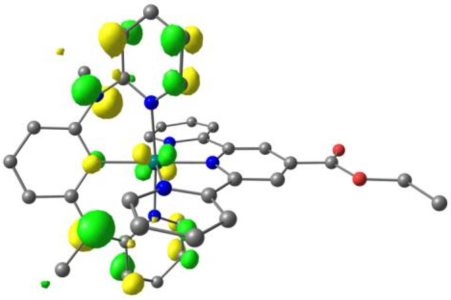	**ddpd (NMe+py$_{\text{terminal}}$)** + d_{yz}
161	-11.352	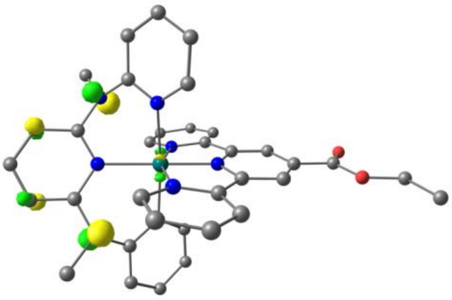	**ddpd (NMe+py$_{\text{central}}$)** + d_{xy}
162	-11.083	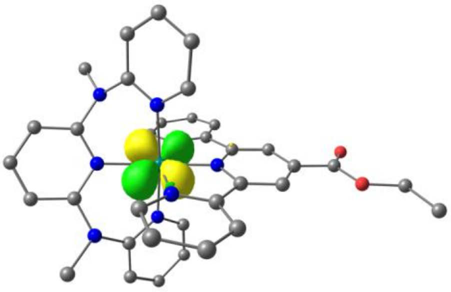	**d_{xz}**
163	-10.838	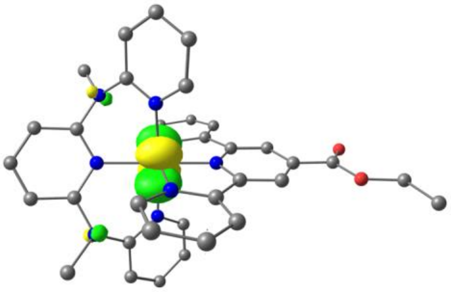	ddpd (NMe) + **d_{xy}**
164	-10.798 (HOMO)	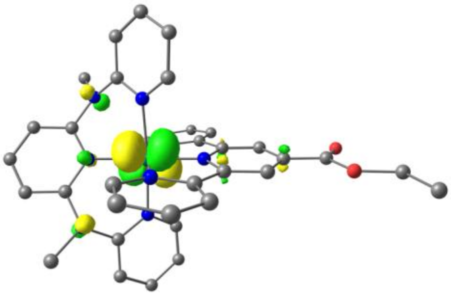	ddpd (NMe) + **d_{yz}**

165	-7.779 (LUMO)	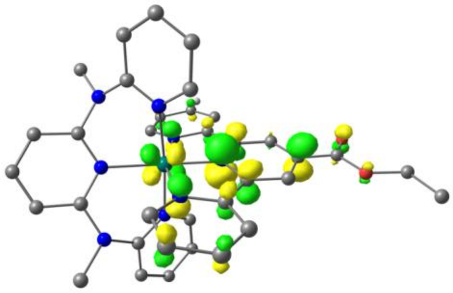	π*(tpy-COOEt)
166	-7.424	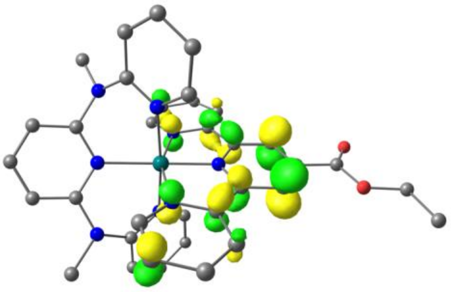	π*(tpy-COOEt)
167	-6.618	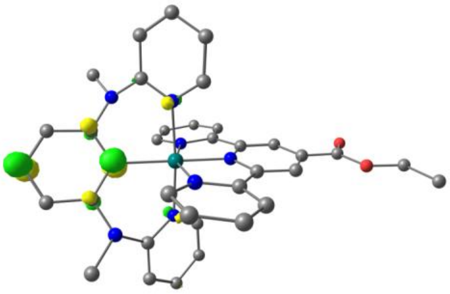	π*(ddpd)
168	-6.577	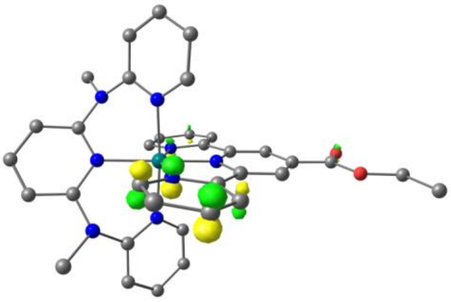	π*(tpy-COOEt)
169	-6.548		π*(tpy-COOEt+ddpd)
170	-6.452	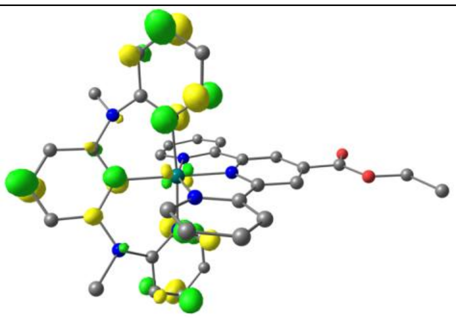	π*(ddpd)

171	-6.357	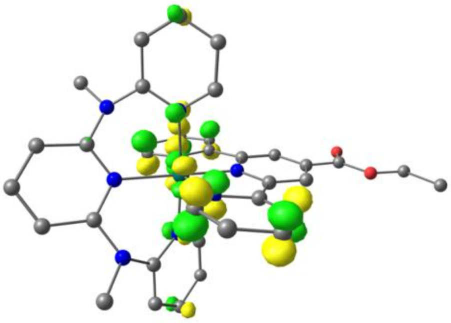	π*(tpy-COOEt+ddpd)
172	-6.187		π*(tpy-COOEt)
173	-6.020		π*(ddpd)
174	-5.723		π*(ddpd)
175	-5.679	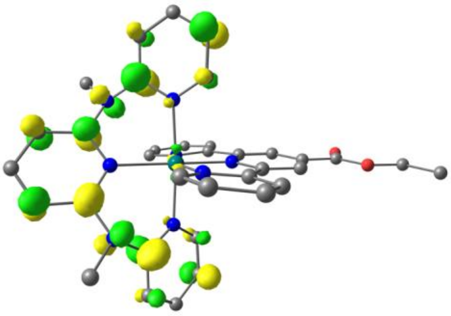	π*(ddpd)
176	-5.110	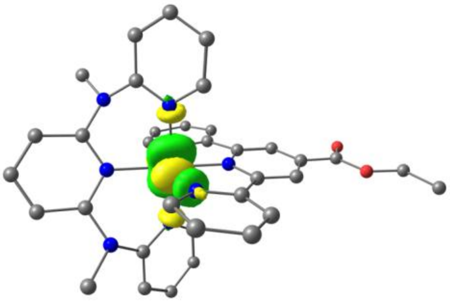	$\mathbf{d_{x^2-y^2}}$
177	-4.794		π*(tpy-COOEt)
178	-4.619	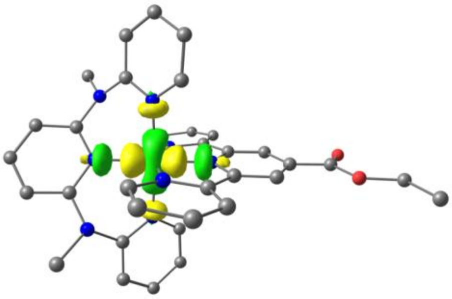	$\mathbf{d_{z^2}}$

Cartesian Coordinates of Ni(CO)$_3$L complexes

L = κ*N*(central pyridine)-ddpd: $\tilde{\nu}$ = 2017 cm^{-1}; d(C-O) = 1.1776 Å

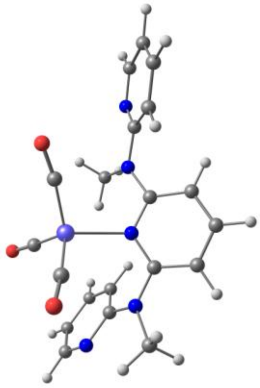

6	-1.192199000	1.057845000	-0.602639000
6	-1.697181000	2.378356000	-0.678960000
6	-0.825367000	3.446807000	-0.438169000
6	0.535284000	3.204164000	-0.201082000
6	0.989100000	1.865741000	-0.169386000
7	0.113752000	0.811282000	-0.268176000
1	-2.728587000	2.551799000	-0.958313000
1	1.235503000	4.022932000	-0.094502000
6	-5.473083000	-0.958263000	-1.281627000
6	-6.146247000	-0.278924000	-0.254916000
6	-5.377153000	0.527369000	0.612285000
6	-3.995895000	0.635688000	0.417157000
6	-3.402769000	-0.066240000	-0.666871000
7	-4.137655000	-0.856671000	-1.490775000
1	-5.845745000	1.047151000	1.443935000
1	-6.008550000	-1.610381000	-1.967309000
1	-7.218301000	-0.389967000	-0.128411000
1	-3.386454000	1.215258000	1.101170000
6	3.040139000	0.557851000	-0.674111000
6	2.548525000	0.002814000	-1.884719000
6	3.311231000	-0.975008000	-2.534425000
6	4.542699000	-1.385650000	-1.982674000
6	4.958791000	-0.771504000	-0.791233000
7	4.230954000	0.174948000	-0.152067000
1	2.951583000	-1.409635000	-3.463633000
1	1.608958000	0.338984000	-2.304192000
1	5.154917000	-2.145707000	-2.456725000
1	5.902433000	-1.037881000	-0.321846000
7	-2.008536000	-0.051463000	-0.909034000
6	-1.454588000	-1.144950000	-1.744886000
1	-0.367283000	-1.103242000	-1.694291000
1	-1.795653000	-2.112858000	-1.369475000
1	-1.798518000	-1.043614000	-2.780800000
7	2.355807000	1.593773000	0.018702000
6	3.157844000	2.527373000	0.842551000
1	2.571550000	2.862134000	1.703304000
1	4.037020000	1.987238000	1.192814000
1	3.487830000	3.402031000	0.262402000
1	-1.192113000	4.468281000	-0.496084000
28	0.485328000	-0.897765000	1.134868000
6	-1.150388000	-1.362065000	1.777693000
6	1.504902000	-0.140656000	2.438177000
6	1.314170000	-2.312051000	0.352032000
8	-2.130302000	-1.759076000	2.297063000
8	2.144125000	0.250679000	3.346037000
8	1.835560000	-3.299150000	-0.023109000

L = κ*N*(terminal pyridine)-ddpd: $\tilde{\nu}$ = 2016 cm^{-1}; d(C-O) = 1.1780 Å

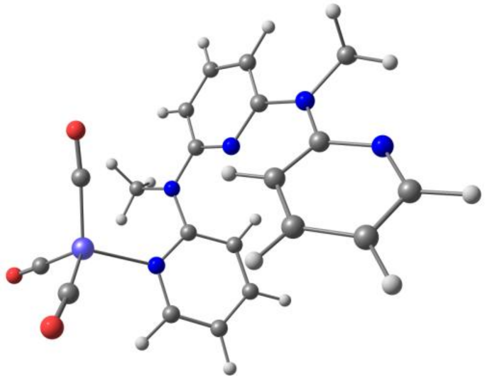

6	-2.738332000	1.560588000	-0.186873000
6	-3.012743000	2.931350000	-0.457625000
6	-1.997339000	3.866410000	-0.217368000
6	-0.745507000	3.468484000	0.279624000
6	-0.552959000	2.085098000	0.515395000
7	-1.528110000	1.175449000	0.284611000
1	-3.964883000	3.252281000	-0.856848000
1	0.031290000	4.197700000	0.466482000
6	-4.447703000	-2.956659000	-0.249348000
6	-3.243545000	-3.600233000	-0.571880000
6	-2.121379000	-2.785573000	-0.832208000
6	-2.231142000	-1.391457000	-0.754678000
6	-3.489759000	-0.823767000	-0.417448000
7	-4.570423000	-1.610624000	-0.174332000
1	-1.166782000	-3.230798000	-1.101512000
1	-5.351406000	-3.525300000	-0.042735000
1	-3.189562000	-4.683032000	-0.624343000
1	-1.377504000	-0.756595000	-0.934651000
6	0.790332000	0.276276000	1.523583000
6	-0.109657000	-0.161232000	2.524586000
6	0.088290000	-1.399677000	3.140482000
6	1.199453000	-2.182246000	2.761478000
6	2.036526000	-1.700322000	1.752561000
7	1.826899000	-0.510169000	1.113385000
1	-0.595247000	-1.741432000	3.912634000
1	-0.939140000	0.476955000	2.801142000
1	1.407794000	-3.140147000	3.226517000
1	2.895712000	-2.270938000	1.419187000
7	-3.731575000	0.581361000	-0.374195000
6	-5.126955000	1.045590000	-0.540957000
1	-5.273430000	1.517152000	-1.522974000
1	-5.777095000	0.176909000	-0.455264000
1	-5.388039000	1.764344000	0.244408000
7	0.681281000	1.582486000	0.973534000
6	1.830164000	2.497523000	1.119693000
1	1.645656000	3.239585000	1.911368000
1	2.714485000	1.916006000	1.381052000
1	2.037042000	3.023169000	0.181172000
1	-2.181427000	4.918039000	-0.422480000
28	2.897774000	-0.278308000	-0.705140000
6	1.970163000	0.849428000	-1.792671000
6	4.564682000	0.324220000	-0.311884000
6	2.946051000	-1.940390000	-1.447871000
8	5.665810000	0.700454000	-0.125179000
8	3.019127000	-2.969049000	-2.017776000
8	1.432128000	1.562188000	-2.559520000

L = NH_3: $\tilde{\nu} = 2022\ cm^{-1}$; d(C-O) = 1.1779 Å

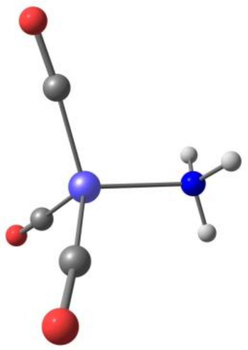

7	0.010502000	0.006530000	2.247972000
28	0.000827000	-0.000425000	0.113981000
6	1.741517000	-0.076465000	-0.406532000
6	-0.938262000	-1.471886000	-0.395239000
6	-0.808274000	1.544182000	-0.401231000
8	-1.537721000	-2.401312000	-0.800521000
8	-1.320030000	2.523850000	-0.808483000
8	2.844968000	-0.126842000	-0.815548000
1	0.439625000	-0.861521000	2.565872000
1	0.551497000	0.813916000	2.554989000
1	-0.955418000	0.073256000	2.566290000

L = CH_3CN: $\tilde{\nu} = 2029\ cm^{-1}$; d(C-O) = 1.1759 Å

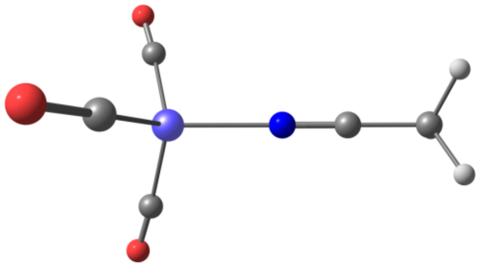

28	-0.493126000	0.000188000	0.000042000
6	-1.019284000	-0.764509000	1.570875000
6	-1.014613000	-0.978525000	-1.448953000
6	-1.013966000	1.744563000	-0.124384000
8	-1.422046000	-1.248258000	2.564164000
8	-1.414117000	-1.597775000	-2.365347000
8	-1.413083000	2.847898000	-0.203117000
6	4.191001000	-0.001721000	0.002217000
1	4.571096000	0.593705000	0.839816000
1	4.570675000	-1.024970000	0.099109000
1	4.570967000	0.425908000	-0.932317000
6	2.726395000	-0.001323000	0.002291000
7	1.553079000	-0.000820000	0.002048000

L = CH_3NC: $\tilde{\nu}$ = 2026 cm^{-1}; d(C-O) = 1.1746 Å

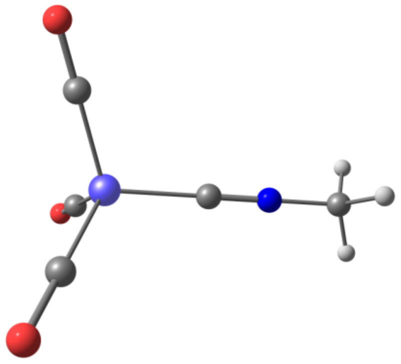

28	-0.457112000	0.000276000	-0.000197000
6	-1.034001000	-0.136895000	1.734395000
6	-1.028171000	-1.436217000	-0.985532000
6	-1.035554000	1.569530000	-0.750348000
6	1.459999000	0.002733000	0.000894000
8	-1.406675000	-0.225082000	2.844827000
8	-1.397053000	-2.356070000	-1.616016000
8	-1.409862000	2.574065000	-1.230495000
7	2.645858000	0.003477000	0.001129000
6	4.076084000	0.003322000	0.001596000
1	4.452180000	0.841387000	0.598785000
1	4.451976000	-0.932919000	0.428959000
1	4.452567000	0.101326000	-1.022680000

L = NMe_3: $\tilde{\nu}$ = 2018 cm^{-1}; d(C-O) = 1:1783 Å

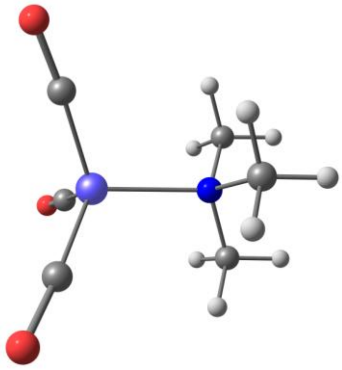

7	1.630255000	-0.002271000	0.000256000
28	-0.533608000	0.001320000	-0.000344000
6	-1.061949000	1.729122000	-0.180847000
6	-1.067140000	-1.018648000	-1.404455000
6	-1.067223000	-0.705530000	1.584770000
8	-1.493372000	-1.666204000	-2.291811000
8	-1.492311000	-1.152815000	2.588585000
8	-1.483529000	2.823384000	-0.295984000
6	2.126237000	0.542377000	-1.302423000
1	1.755592000	1.562183000	-1.438914000
1	3.230184000	0.553920000	-1.333168000
1	1.754163000	-0.075589000	-2.124431000
6	2.126374000	0.852475000	1.124144000
1	1.754058000	0.461197000	2.075083000
1	3.230298000	0.872020000	1.151229000
1	1.755971000	1.873940000	1.000063000
6	2.122907000	-1.404137000	0.178729000
1	1.743234000	-2.032970000	-0.631549000
1	3.226735000	-1.440883000	0.174784000
1	1.757468000	-1.803735000	1.128904000

L = NHC (1,3-dimethyl-2,3-dihydro-1*H*-imidazol-2-ylidene): $\tilde{\nu}$ = 2003 cm^{-1}; d(C-O) = 1.1795 Å

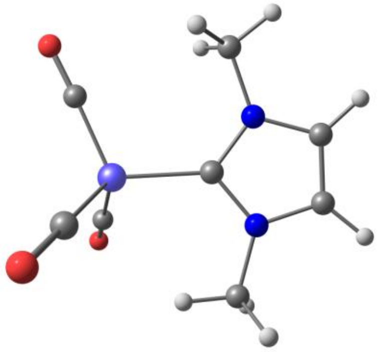

28	-0.999909000	-0.038726000	0.005330000
6	-1.773367000	1.604051000	-0.131304000
6	-1.488999000	-1.035589000	-1.439149000
6	-1.488024000	-0.803448000	1.584151000
8	-1.794347000	-1.667664000	-2.386652000
8	-1.790182000	-1.283721000	2.617791000
8	-2.315954000	2.648117000	-0.221294000
6	0.999683000	0.065109000	-0.000221000
6	3.185074000	0.815152000	-0.016069000
6	3.226755000	-0.553869000	-0.011355000
1	3.982625000	1.540060000	-0.021738000
1	4.066378000	-1.229766000	-0.013203000
7	1.827590000	1.176617000	-0.008208000
7	1.893589000	-0.995136000	0.000280000
6	1.352213000	2.566868000	-0.007142000
1	0.778788000	2.775658000	-0.914669000
1	0.714855000	2.748781000	0.862212000
1	2.212862000	3.241013000	0.034267000
6	1.513720000	-2.412900000	0.000235000
1	0.435997000	-2.484981000	0.146771000
1	1.776067000	-2.882138000	-0.955295000
1	2.023158000	-2.940771000	0.814279000

L = PMe_3: $\tilde{\nu}$ = 2017 cm^{-1}; d(C-O) = 1.1774 Å

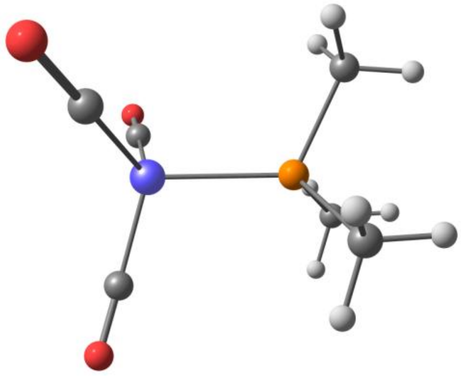

28	-0.847940000	0.002154000	-0.000741000
6	-1.341633000	-0.783905000	1.560879000
6	-1.340990000	1.747530000	-0.102242000
6	-1.337773000	-0.961554000	-1.460422000
8	-1.677544000	2.873887000	-0.168144000
8	-1.671240000	-1.583737000	-2.402781000
8	-1.678242000	-1.294500000	2.567013000
6	2.364086000	0.807528000	1.490935000
1	2.045422000	0.296488000	2.405199000
1	3.456268000	0.754842000	1.407903000
1	2.056757000	1.856181000	1.558346000
6	2.354032000	-1.696646000	-0.041598000
1	2.038980000	-2.228499000	-0.945164000
1	3.447198000	-1.608441000	-0.035660000
1	2.033777000	-2.278701000	0.828799000
6	2.368328000	0.883224000	-1.443663000
1	2.050087000	1.930604000	-1.464236000
1	3.460359000	0.838070000	-1.354179000
1	2.062725000	0.412731000	-2.383810000
15	1.527376000	0.001609000	0.000767000

L = PH_3: $\tilde{\nu}$ = 2033 cm^{-1}; d(C-O) = 1.1752 Å

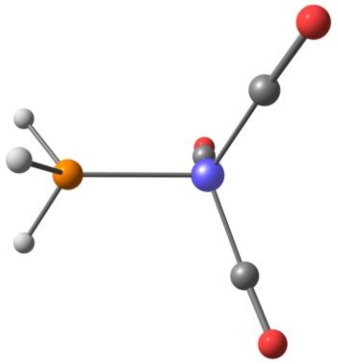

28	0.181192000	0.001745000	-0.000798000
6	0.650749000	1.739721000	-0.271771000
6	0.683806000	-0.626292000	1.632568000
6	0.676566000	-1.092629000	-1.368541000
8	1.054681000	-1.027119000	2.673219000
8	1.043177000	-1.789048000	-2.241334000
8	1.000852000	2.848351000	-0.443658000
15	-2.210295000	-0.022743000	0.008572000
1	-2.911744000	-1.101275000	0.643921000
1	-2.933601000	1.053412000	0.623122000
1	-2.930017000	-0.042118000	-1.232625000

L = PF_3: $\tilde{\nu}$ = 2068 cm^{-1}; d(C-O) = 1.1682 Å

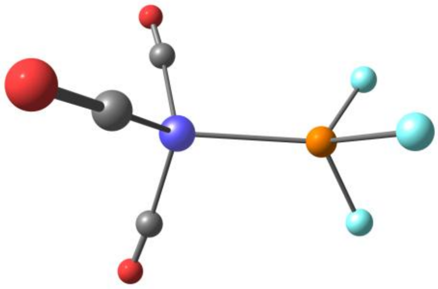

28	0.795350000	0.000773000	-0.000169000
6	1.307127000	-0.688236000	1.624481000
6	1.307109000	-1.061834000	-1.409283000
6	1.301104000	1.753870000	-0.215532000
8	1.705158000	-1.723465000	-2.285942000
8	1.695383000	2.845303000	-0.349779000
8	1.705110000	-1.117212000	2.635532000
15	-1.506495000	-0.002249000	0.000480000
9	-2.371505000	-0.585592000	1.348650000
9	-2.370092000	1.457763000	-0.168657000
9	-2.370584000	-0.877472000	-1.179874000

L = pyridine: $\tilde{\nu}$ = 2020 cm^{-1}; d(C-O) = 1.1765 Å

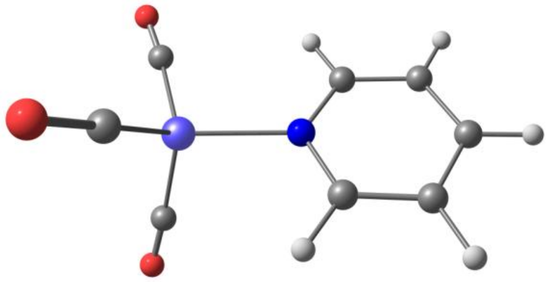

6	-1.756714000	-1.132832000	0.000494000
6	-3.159507000	-1.176693000	0.000397000
6	-3.879971000	0.032151000	-0.000549000
6	-3.163814000	1.243057000	-0.001302000
6	-1.760138000	1.204903000	-0.001153000
7	-1.059619000	0.037248000	-0.000313000
1	-4.966436000	0.030146000	-0.000682000
1	-3.666515000	-2.136425000	0.001040000
1	-3.674181000	2.201019000	-0.002007000
1	-1.176271000	2.118286000	-0.001691000
28	1.025497000	-0.002772000	-0.000123000
6	1.524415000	-0.872345000	1.519160000
6	1.524310000	-0.900744000	-1.502698000
6	1.643434000	1.707106000	-0.015834000
8	1.906568000	-1.474600000	-2.457106000
8	2.128279000	2.780695000	-0.025176000
8	1.905281000	-1.428758000	2.484359000
1	-1.166273000	-2.042450000	0.001276000

Correlation of *A_1* stretching frequencies with C-O distances in Ni(CO)$_3$L complexes

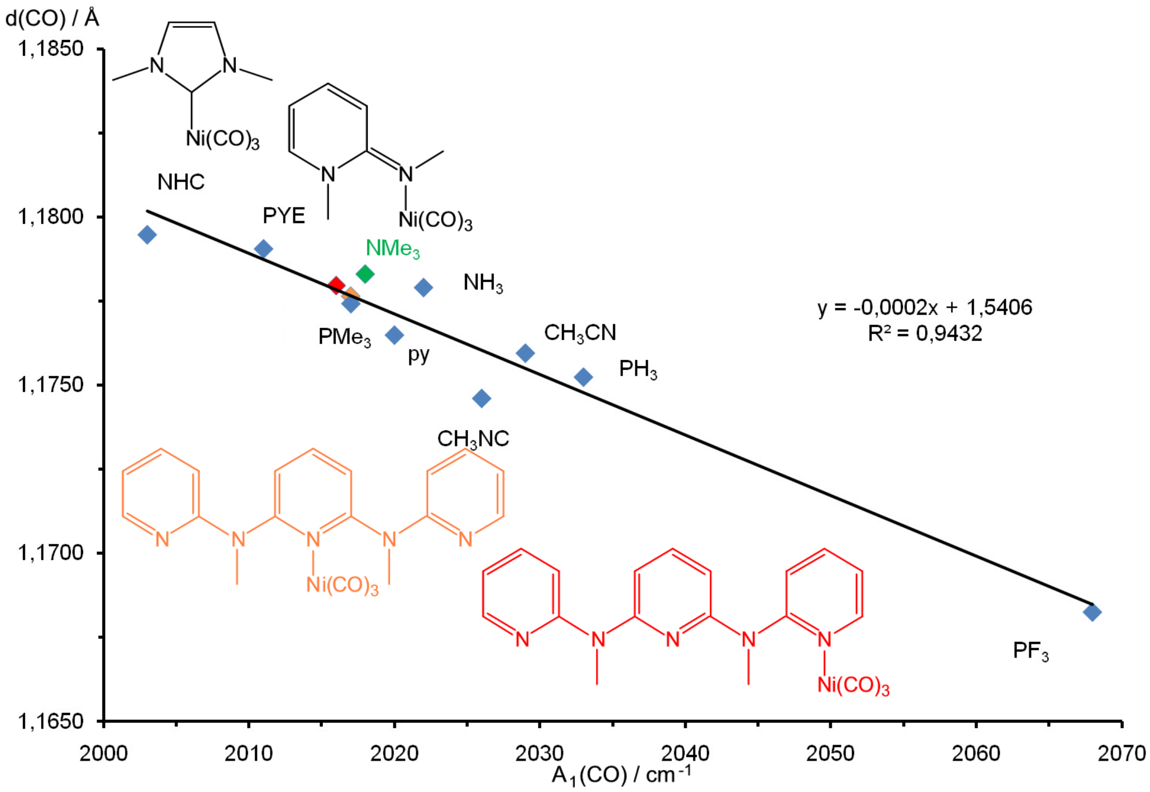

10.6 Excited State Tuning of Bis(tridentate) Ruthenium(II) Polypyridine Chromophores by Push-Pull Effects and Bite Angle Optimization: A Comprehensive Experimental and Theoretical Study

A. Breivogel, M. Meister, C. Förster, F. Laquai, K. Heinze, *Chem. Eur. J.* **2013**, *19*, 13745–13760.

DOI: 10.1002/chem.201302231

DFT-optimized (B3LYP/LANL2DZ, IEFPCM in CH_3CN) cartesian coordinates of [**1** – **7**]^{0} (singlet and triplet), [**1** – **7**]$^{+}$ [**1** – **7**]$^{2+}$ (singlet ground state and ^{3}MLCT state), [**1** – **7**]$^{2+}$ (^{3}MC and ^{3}TS state, except for [**4**]$^{2+}$), [**1** – **7**]$^{3+}$, [**1** – **7**]$^{4+}$ and results of the TD-DFT (B3LYP/LANL2DZ, IEFPCM in CH_3CN) calculation of [**1** – **7**]$^{2+}$ (singlet) can be found in the online supporting information.

CHEMISTRY
A EUROPEAN JOURNAL

Supporting Information

Excited State Tuning of Bis(tridentate) Ruthenium(II) Polypyridine Chromophores by Push–Pull Effects and Bite Angle Optimization: A Comprehensive Experimental and Theoretical Study

Aaron Breivogel,[a] Michael Meister,[b] Christoph Förster,[a] Frédéric Laquai,[b] and Katja Heinze*[a]

chem_201302231_sm_miscellaneous_information.pdf

Table of Contents:

1) Description of the synthetic strategy and syntheses of **8**, 4-amino-2,6-dibromopyridine, **9** and **10**
2) Figures S1 – S49
3) Tables S1 – S11
4) DFT (B3LYP/LANL2DZ, IEFPCM in CH_3CN) optimized geometries of **[1 – 7]^{0}** (singlet and triplet), **[1]** – **[7]**$^{+}$ (doublet), **[1]** – **[7]**$^{2+}$ (singlet, ^{3}MLCT, ^{3}MC (not for **[4]**$^{2+}$), ^{3}TS (not for **[4]**$^{2+}$)), **[1]** – **[7]**$^{3+}$ (doublet) and **[1]** – **[7]**$^{4+}$ (triplet)
5) Results of TD-DFT calculations of **[1]** – **[7]**$^{2+}$ (singlet)

Synthesis strategy. Initial attempts to synthesize an amino substituted ddpd ligand analogously to the straightforward synthesis of **11** in a metal free amination using 4-amino-2,6-dibromopyridine or 4-amino-2,6-dichloropyridine and *N*-methylpyridine-2-ylamine failed although a similar procedure for the amination of 4-amino-2,6-dichloropyridine with pyrrolidine had been reported.[1] This is probably due to the electron donating character of the NH_2 group which prevents a nucleophilic attack of *N*-methylpyridine-2-ylamine Furthermore, the amine group itself can act as nucleophile. Hence, a strategy is necessary to prevent nucleophilic reactivity of the primary amino group and to activate the dibromopyridine. Attempts to employ a nitro group as latent amine by using 2,6-dibromo-4-nitropyridine in a metal free amination reaction with *N*-methylpyridine-2-ylamine using sodium hydride as base only resulted in *ipso* substitution of the nitro group before the desired bromine substitution.[1,2,3,4] Finally, we chose the phthalimido group as protecting group because of its less electron withdrawing character compared to the nitro group which should inhibit the undesired *ipso* substitution. The phthalimido protecting group is introduced straightforwardly by treating 4-amino-2,6-dichloropyridine or its dibromo derivative with phthalic anhydride giving *N*-protected **8** and **9** in 56 % and 65 % yield, respectively. Amination of **8** or **9** with *N*-methylpyridine-2-ylamine using sodium hydride or potassium bis(trimethylsilyl) amide (KHMDS) as base in dioxane or in *N*-methylpyridine-2-ylamine as solvent using different reaction times and temperatures without a metal catalyst did not yield the desired ligand **10**. However, using $Pd_2(dba)_3$ (dba = dibenzylidene acetone) together with $P(^t\mathrm{Bu})_3$ as precatalyst and $KO^t\mathrm{Bu}$ as base **10** is successfully obtained from **8** or **9** in 5 % and 26 % yields, respectively (Scheme 2). Harsher reaction conditions are required for the chloro compound **8** compared to the bromo derivative **9** due to the lower reactivity of the chloro derivative **8** in the oxidative addition to the catalytically active palladium species. However, the starting material for **8**, 4-amino-2,6-dichloropyridine, is commercially available while the bromo derivative 4-amino-2,6-dibromopyridine, has to be prepared in three steps from 2,6-dibromopyridine rendering the dichloro starting material attractive in spite of its lower reactivity.[5,6]

Synthesis of 2,6-dichloro-4-phthalimidopyridine (8). Phthalic anhydride (2.338 g, 15.78 mmol, 1.0 equiv) and 4-amino-2,6-dichloropyridine (3.287 g, 20.17 mmol, 1.3 equiv) were placed in a flask and acetic acid (100 ml) was added. The mixture was stirred at room temperature and ultrasonicated until the starting materials were completely dissolved. The yellow solution was heated to reflux for 6 h and cooled to room temperature. During the cooling process a colorless solid precipitated. The solid was filtered, washed with 60 ml of petroleum ether 40 – 60 and dried under reduced pressure. A colourless solid was obtained. Single crystals for X-ray diffraction analysis were obtained by slow evaporation of an acetone solution of **8**. Yield: 2.609 g (8.9 mmol, 56%). ^{1}H NMR (d_6-DMSO, 300 K): δ = 8.06-8.04 (m, 2 H, H^2), 7.98-7.96 (m, 2 H, H^1), 7.80 (s, 2 H, H^6) ppm. $^{13}C\{^1H\}$ NMR (d_6-DMSO, 300 K): δ = 165.5 (C^4), 149.4 (s, C^7), 144.1 (s, C^5), 135.3 (s, C^1), 131.0 (s, C^3), 124.0 (s, C^2), 119.3 (s, C^6) ppm. ^1H-^{15}N HMBC (d_6-DMSO, 300 K): δ = 294.1 (N^a), 167.6 (N^b) ppm. MS (FD): *m/z* 292.3 (100%) $[M]^+$. IR (CsI): $\tilde{\nu}$ 3130 (w, CH), 3099 (w, CH), 1788 (m, C=O), 1761 (m, C=O), 1736 (vs, C=O), 1580 (vs, C=N), 1549 (s, C=N), 1468 (w), 1433 (s), 1377 (vs), 1354 (vs, C-N), 1232 (s, C-N), 1167 (m, C-N), 1143 (w, C-N), 1121 (w, C-N), 1097 (m, C-N, C-Cl), 1074 (m, C-N, C-Cl), 988 (w), 932 (w), 885 (w, C=C), 858 (m, C=C), 824 (m, C=C), 798 (w, C=C), 789 (w), 714 (s), 663 (w), 638 (m), 613 (w), 596 (w), 532 (w), 453 (w), 361 (w), 270 (w) cm^{-1}. Elemental analysis calcd (%) for $C_{13}H_6Cl_2N_2O_2$: C 53.27, H 2.06, N 9.56; found: C 52.90, H 2.20, N 8.92.

Synthesis of 4-amino-2,6-dibromopyridine. 4-amino-2,6-Dibromopyridine was synthesized by modification of a literature procedure.[5] 2,6-Dibromo-4-nitropyridine-*N*-oxide[6] (303 mg, 1.08 mmol, 1.0 equiv) and iron powder (301 mg, 5.39 mmol, 5.0 equiv) were suspended in acetic acid. The grey suspension was heated to 100 °C and stirred for 1 h. During the heating process the mixture turned brown. After cooling to room temperature the mixture was cooled with an ice bath and the pH was adjusted to 14 with a concentrated NaOH solution. The mixture was extracted with diethylether (5 × 10 – 15 ml). The combined organic phases were dried over Na_2SO_4, filtered and the solvent was removed in vacuo. A colorless solid was obtained. Yield: 0.24 g, (0.95 mmol, 88%). ^{1}H NMR (CD_2Cl_2, 300 K): δ = 6.69 (s, 2 H, $H^{aromatic}$), 4.43 (s, 2 H, NH_2) ppm. MS (FD): *m/z* 251.9 (100%) $[M]^+$.

Synthesis of 2,6-dibromo-4-phthalimidopyridine (9). Phthalic anhydride (2.80 g, 18.9 mmol, 1.0 equiv) and 4-amino-2,6-dibromopyridine (5.94 g, 23.6 mmol, 1.2 equiv) were placed in a flask and acetic acid (150 ml) was added. The mixture was stirred at room temperature and ultrasonicated. The starting materials did not dissolve completely. The yellowish suspension was heated to reflux for 6 h. Before starting to reflux, all the components were dissolved (at 60-70 °C) and a yellow solution was obtained. The mixture was cooled to room temperature. During the cooling process a colorless solid precipitated. The solid was filtered, washed with 50 ml of petroleum ether 40 – 60 and dried in a vacuo. A colorless solid was obtained. Single crystals for X-ray diffraction analysis were obtained by slow evaporation of an acetone solution of **9**. Yield: 4.67 g (12.2 mmol, 65%). ^{1}H NMR (d_6-DMSO, 300 K): δ = 8.06-8.03 (m, 2 H, H^2), 7.98-7.95 (m, 2 H, H^1), 7.94 (s, 2 H, H^6) ppm. ^{13}C{^{1}H} NMR (d_6-DMSO, 300 K): δ = 165.5 (C^4), 143.1 (s, C^5), 139.8 (s, C^7), 135.3 (s, C^1), 131.1 (s, C^3), 123.9 (s, C^2), 123.3 (s, C^6) ppm. ^{1}H-^{15}N HMBC (d_6-DMSO, 300 K): δ = 260.5 (N^a), 166.8 (N^b) ppm. MS (FD): *m*/*z* 382.1 (100%) [M]$^+$. IR (CsI): $\tilde{\nu}$ 3140 (w, CH), 3117 (w, CH), 3090 (w, CH), 3062 (w, CH), 1790 (vs, C=O), 1757 (s, C=O), 1734 (s, C=O), 1570 (s, C=N), 1535 (vs, C=N), 1468 (m, C=N), 1423 (vs), 1348 (vs, C-N), 1231 (vs, C-N), 1165 (s, C-N), 1126 (s, C-N), 1096 (s, C-N), 1070 (vs, C-N, C-Br), 1016 (w), 982 (m), 962 (w), 906 (w, C=C), 883 (m, C=C), 860 (s, C=C), 824 (w, C=C), 800 (m, C=C), 770 (s), 717 (vs), 665 (w), 635 (vs), 590 (m), 563 (w), 532 (m), 405 (w), 362 (m), 330 (w), 289 (w), 224 (w) cm^{-1}. Elemental analysis calcd (%) for $C_{13}H_6Br_2N_2O_2$: C 40.87, H 1.58, N 7.33; found: C 41.79, H 1.57, N 7.43.

Synthesis of ddpd-phthalimide (10) from 2,4-dibromo-4-phthalimidopyridine (9). Under an argon atmosphere KO*t*Bu (814.2 mg, 7.6 mmol, 2.6 equiv) was dissolved in absolute dioxane (50 ml). While adding methylaminopyridine (0.80 ml, 7.8 mmol, 2.8 equiv) the solution turned yellow. $Pd_2(dba)_3$ (128.2 mg, 0.14 mmol, 0.05 equiv) was added and a black suspension was obtained. Then a solution of P(^{t}Bu)$_3$ (1 M in toluene, 0.50 ml, 0.50 mmol, 0.18 equiv) was added and the reaction mixture turned into a green-brown solution. 2,6-Dibromo-4-phthalimidopyridine (**9**, 1.060 g, 2.8 mmol, 1.0 equiv) was added and dissolved completely. The green-brown solution was heated to 80 °C for 48 h. The reaction mixture was a brown solution containing a brown solid. The solvent was removed under reduced pressure. The residue was purified by column chromatography (silica gel, petroleum ether 40 – 60/ethyl acetate 1:2), yielding a light yellow solid. Yield: 312.1 mg (7.2 mmol, 26%). ^{1}H NMR (CD_3CN, 300 K): δ = 8.33 (m, 2 H, H^8), 7.90 (m, 2 H, H^{11}), 7.85 (s, 2 H, H^{12}), 7.64 (m, 2 H, H^6), 7.38 (m, 2 H, H^5), 6.96 (m, 2 H, H^7), 6.79 (s, 2 H, H^2), 3.55 (s, 6 H, CH_3) ppm. ^{13}C{^{1}H} NMR (CD_3CN, 300 K): δ = 167.6 (s, C^9) , 158.4 (s, C^4), 157.6 (s, C^3), 148.9 (s, C^8), 143.0 (s, C^1), 138.0 (s, C^6), 135.7 (s, C^{12}), 132.7 (s, C^{10}), 124.4 (s, C^{11}), 118.6 (s, C^7), 117.1 (s, C^5), 102.8 (s, C^2), 36.3 (s, CH_3) ppm. ^{1}H-^{15}N HMBC (CD_3CN, 300 K): δ = 287.9 (N$^{\text{pyridine,outer}}$), 250.1 (N$^{\text{pyridine,center}}$), 169.0 (N$^{\text{phthalimide}}$), 98.7 ($NCH_3$) ppm. MS (FD): *m*/*z* 436.5 (100%) [M]$^+$. HR-MS (ESI$^+$): Calcd for $C_{25}H_{20}N_6NaO_2^+$: *m*/*z* 459.1545. Obsd: *m*/*z* 459.1559. IR (CsI): $\tilde{\nu}$ 3055 (w, CH), 2957 (s, CH), 2926 (s, CH), 2854 (s, CH), 1768 (m, C=O), 1726 (vs, C=O), 1599 (s, C=N), 1472 (vs, CH_3, C=N), 1421 (vs, CH_3), 1364 (vs, C-N, CH_3), 1333 (s, C-N), 1290 (s, C-N), 1240 (s, C-N), 1175 (m, C-N), 1144 (m, C-N), 1111 (s, C-N), 1080 (m, C-N), 989 (m), 961 (w), 881 (m), 851 (w), 798 (m), 777 (s), 743 (m), 716 (s), 673 (w), 636 (w), 619 (m), 555 (w), 532 (w), 409 (w), 361 (w) cm^{-1}. Elemental analysis calcd (%) for $C_{25}H_{20}N_6O_2$: C 68.80, H 4.62, N 19.25; found: C 68.57, H 4.65, N 18.34.

Synthesis of ddpd-phthalimide (10) from 2,6-dichloro-4-phthalimidopyridine (8). Under an argon atmosphere KO*t*Bu (411.0 mg, 3.66 mmol, 2.6 equiv) was dissolved in absolute dioxane (50 ml). While adding methylaminopyridine (0.40 ml, 3.9 mmol, 2.8 equiv) the solution turned yellow. $Pd_2(dba)_3$ (66.8 mg, 0.073 mmol, 0.05 equiv) was added and a black suspension was obtained. Then a solution of P(^{t}Bu)$_3$ (1 M in toluene, 0.40 ml, 0.40 mmol, 0.30 equiv) was added and the reaction mixture turned into a green-brown solution. 2,6-Dichloro-4-phthalimidopyridine (**8**, 410.1 mg, 1.4 mmol, 1.0 equiv) was added and dissolved completely. The green-brown solution was heated (80 °C for 48 h). An aliquot was taken from the reaction mixture and filtered. An FD mass spectrum of the solution did not show a signal for the product, only signals of the starting materials could be found. Therefore, the heating of the mixture was continued (90 °C for 48 h). The reaction mixture now was a brown solution containing a brown solid. The solvent was removed under reduced pressure. The remaining dark brown oil was dissolved in very few dichloromethane and purified by column chromatography (silica gel, petroleum ether 40 – 60/ethyl acetate 1:2). A yellow oil was obtained, which was dissolved in THF (2 ml) and ice cold petroleum ether 40 – 60 was added. The mixture was stored at –30 °C for 18 h. The clear solution was decanted and the solid was dried in a vacuo and purified by column chromatography (silica gel, 1:3:0.05 petroleum ether 40-60/ethyl acetate/triethylamine). A light yellow solid was obtained. Yield: 19.2 mg (0.0669 mmol, 5%).

[1] M. Menichincheri, D. F. Bassini, M. Gude, M. Angiolini, *Tetrahedron Lett.* **2003**, *44*, 519–522.

[2] R. Shetty, D. Nguyen, D. Flubacher, F. Ruggle, A. Schumacher, M. Kelly, E. Michelotti, *Tetrahedron Lett.* **2007**, *48*, 113–117.

[3] H. Abe, N. Masuda, M. Waki, M. Inouye, *J. Am. Chem. Soc.* **2005**, *127*, 16189–16196.

[4] J. C. Rodriguez-Ubis, R. Sedano, G. Barroso, O. Juanes, E. Brunet, *Helv. Chim. Acta* **1997**, *80*, 86–96.

[5] M. van Ammers, H. J. den Hertog, *Recl. Trav. Chim. Pays-Bas* **1958**, *77*, 340–345.

[6] U. Neumann, F. Vögtle, *Chem. Ber.* **1989**, *122*, 589–591.

Figure S1. IR spectrum of **8** in CsI.

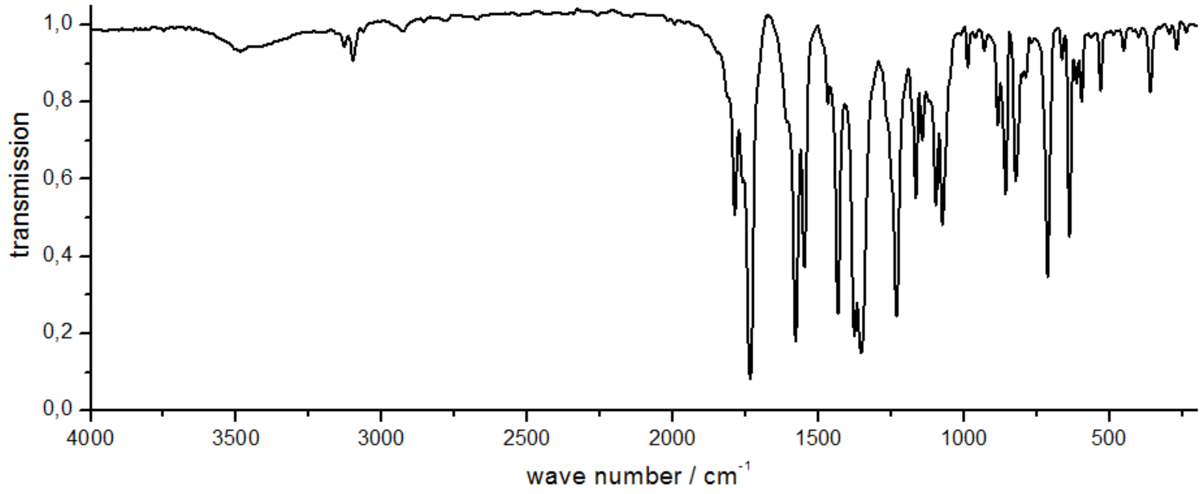

Figure S2. IR spectrum of **9** in CsI.

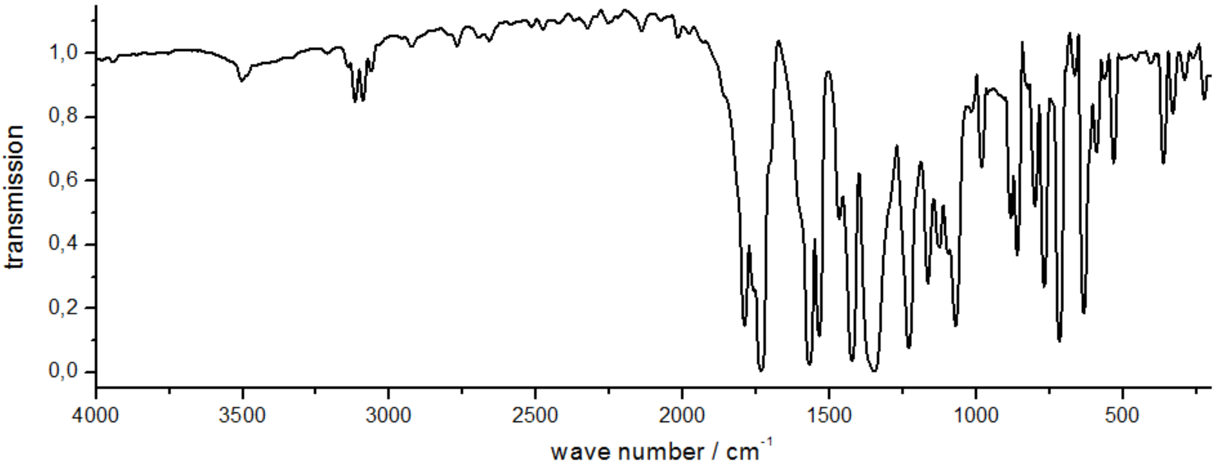

Figure S3. IR spectrum of **10** in CsI.

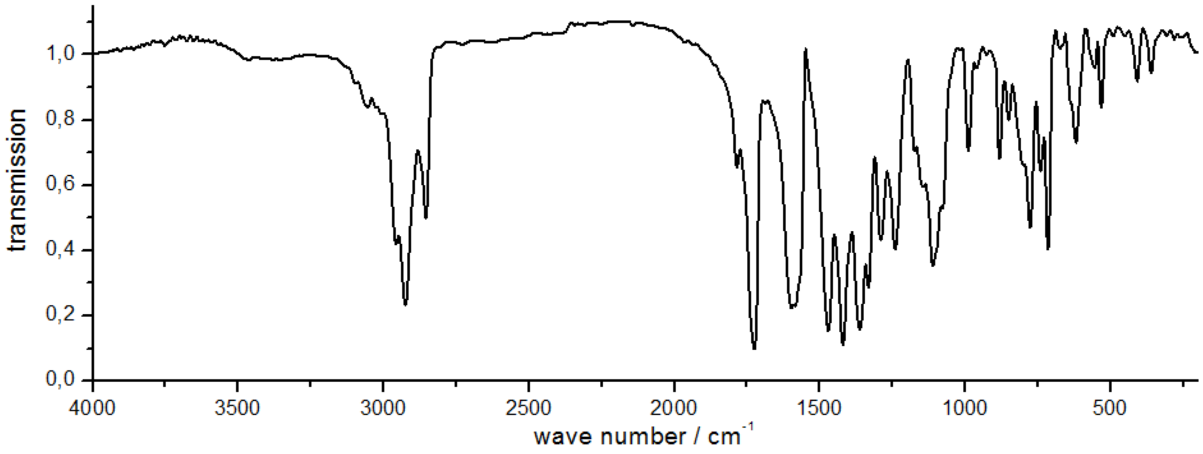

Figure S4. IR spectrum of **11** between KBr plates.

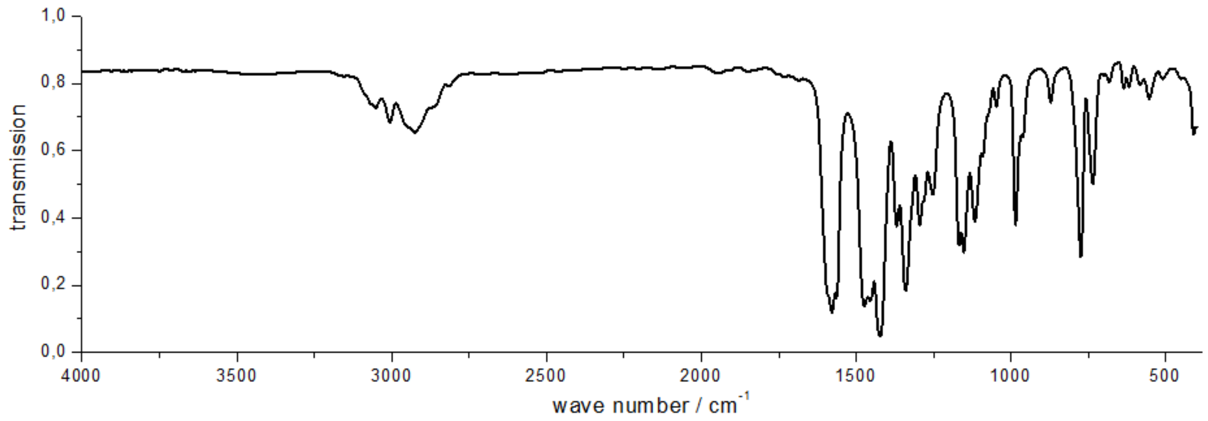

Figure S5. ^{1}H-NMR spectrum of **8** in d$_6$-DMSO (top: full spectrum; inset: zoom).

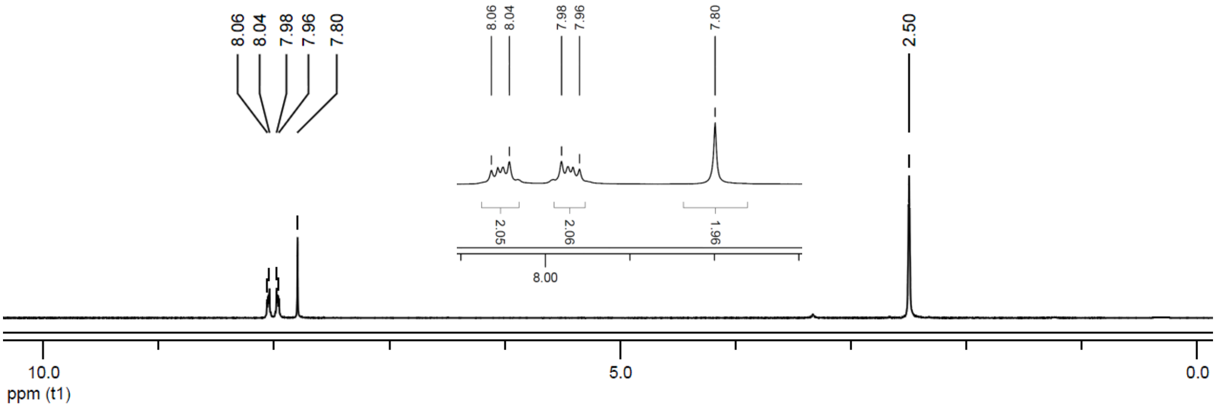

Figure S6. ^{1}H-NMR spectrum of **9** in d$_6$-DMSO (top: full spectrum; inset: zoom).

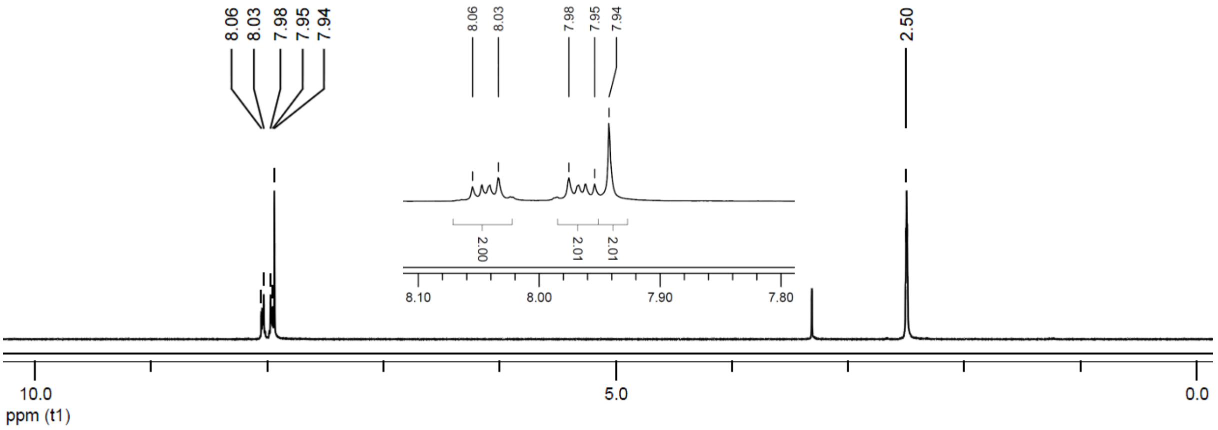

Figure S7. ^{1}H-NMR spectrum of **10** in CD_3CN (top: full spectrum; bottom: zoom).

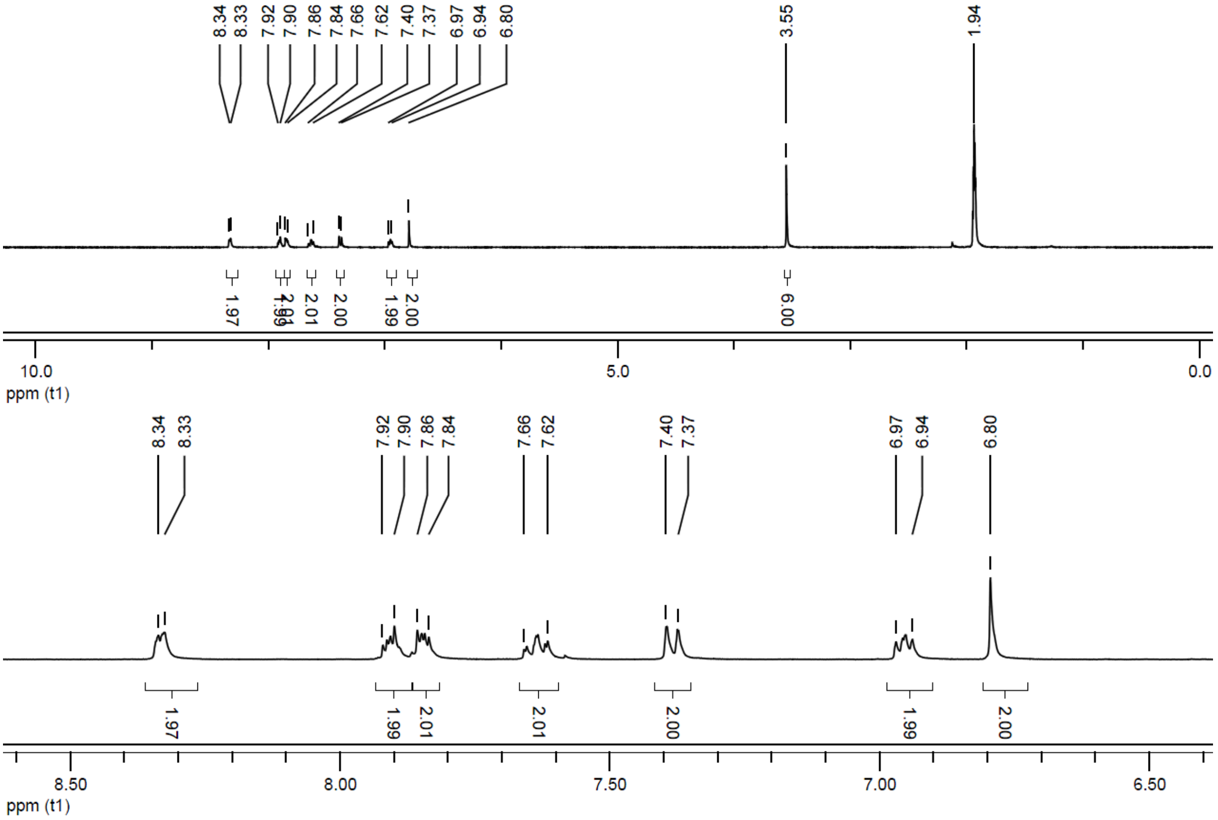

Figure S8. ^{1}H-NMR spectrum of **11** in CD_3CN (top: full spectrum; bottom: zoom).

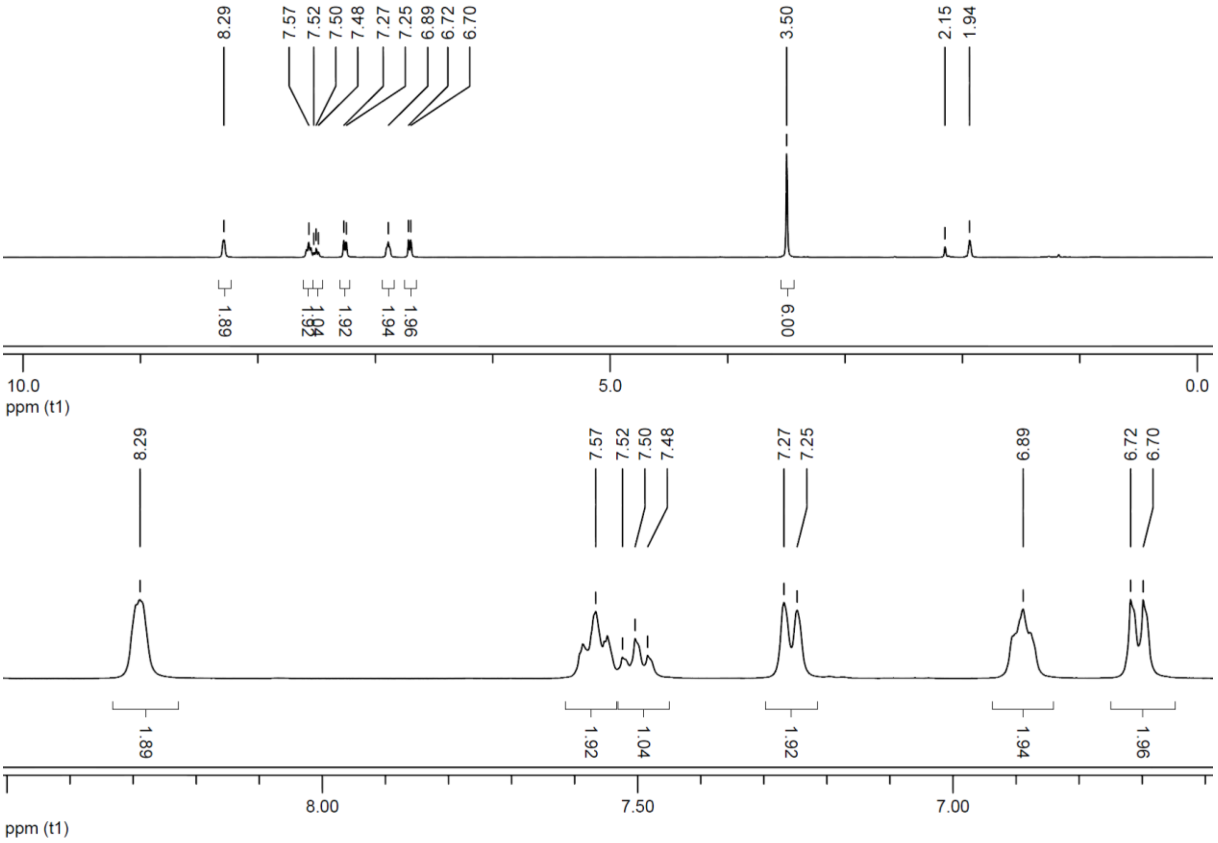

Figure S9. $^{13}C\{^1H\}$ NMR spectrum of **8** in d_6-DMSO.

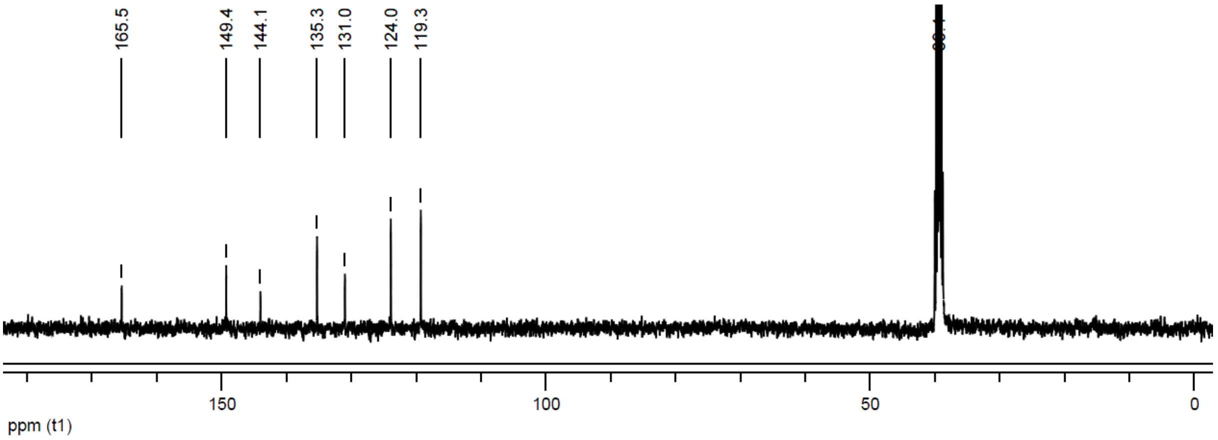

Figure S10. $^{13}C\{^1H\}$ NMR spectrum of **9** in d_6-DMSO.

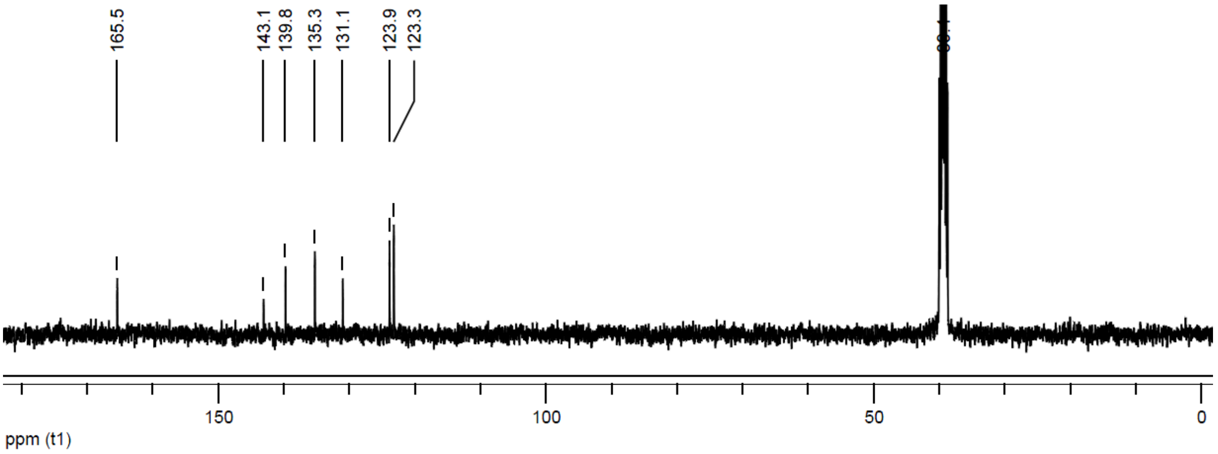

Figure S11. $^{13}C\{^1H\}$ NMR spectrum of **10** in CD_3CN.

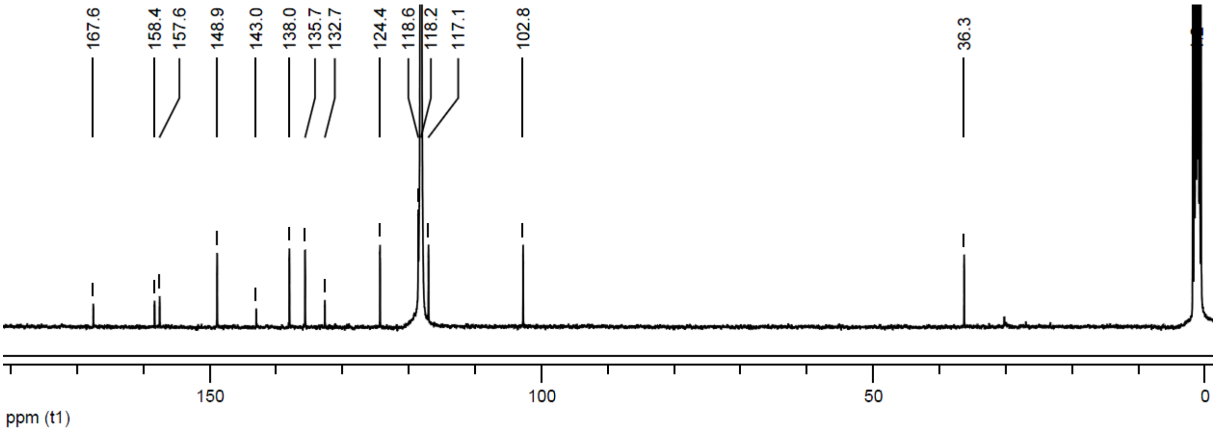

Figure S12. $^{13}C\{^{1}H\}$ NMR spectrum of **11** in CD_3CN.

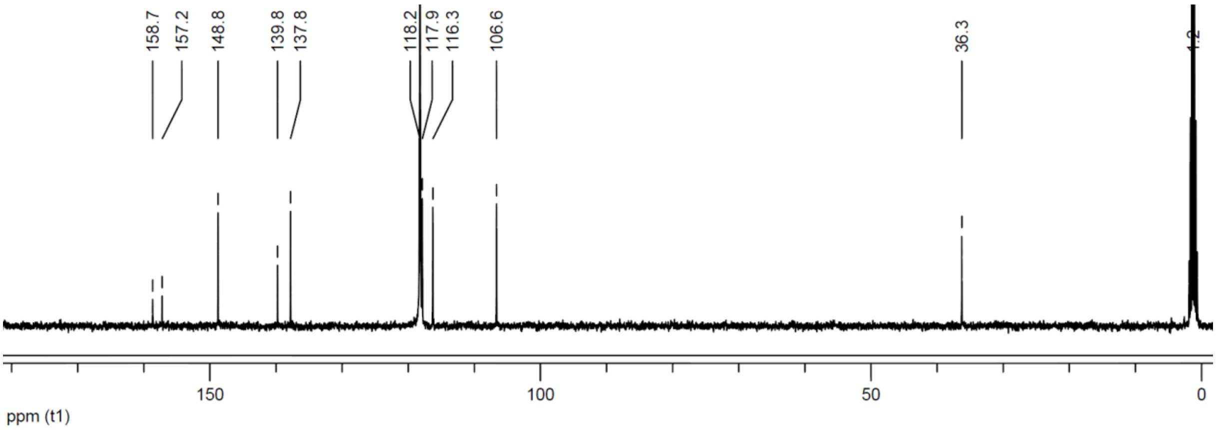

Figure S13. ^{15}N-^{1}H HMBC of **8** in d_6DMSO.

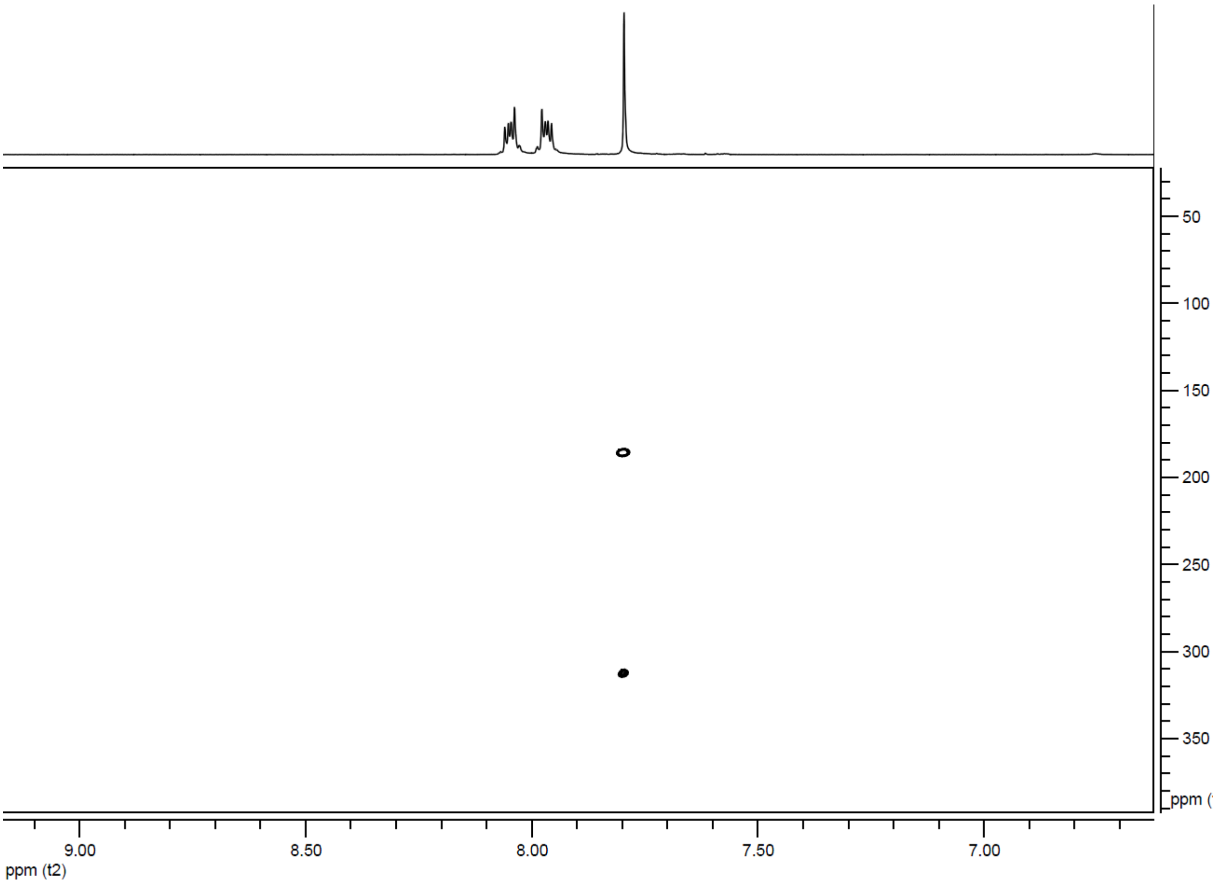

Figure S14. ^{15}N-^{1}H HMBC of **9** in d_6DMSO.

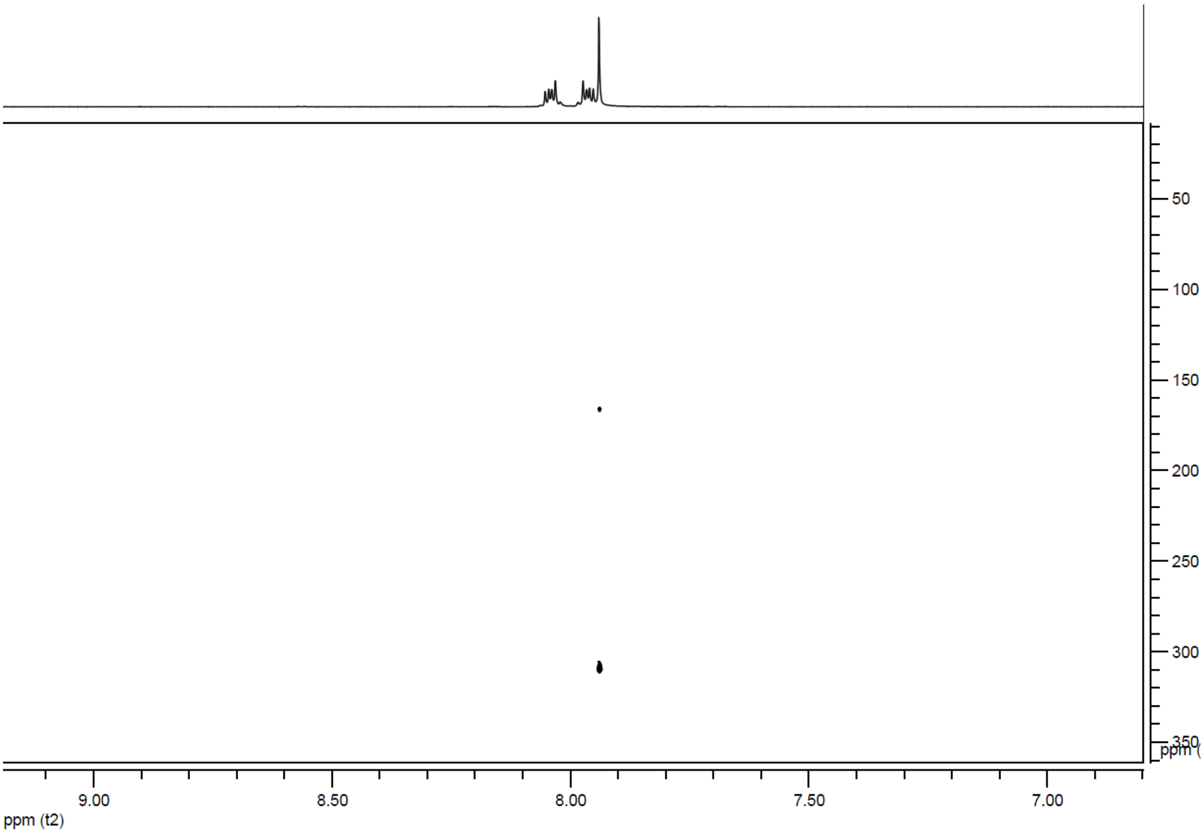

Figure S15. ^{15}N-^{1}H HMBC of **10** in CD_3CN.

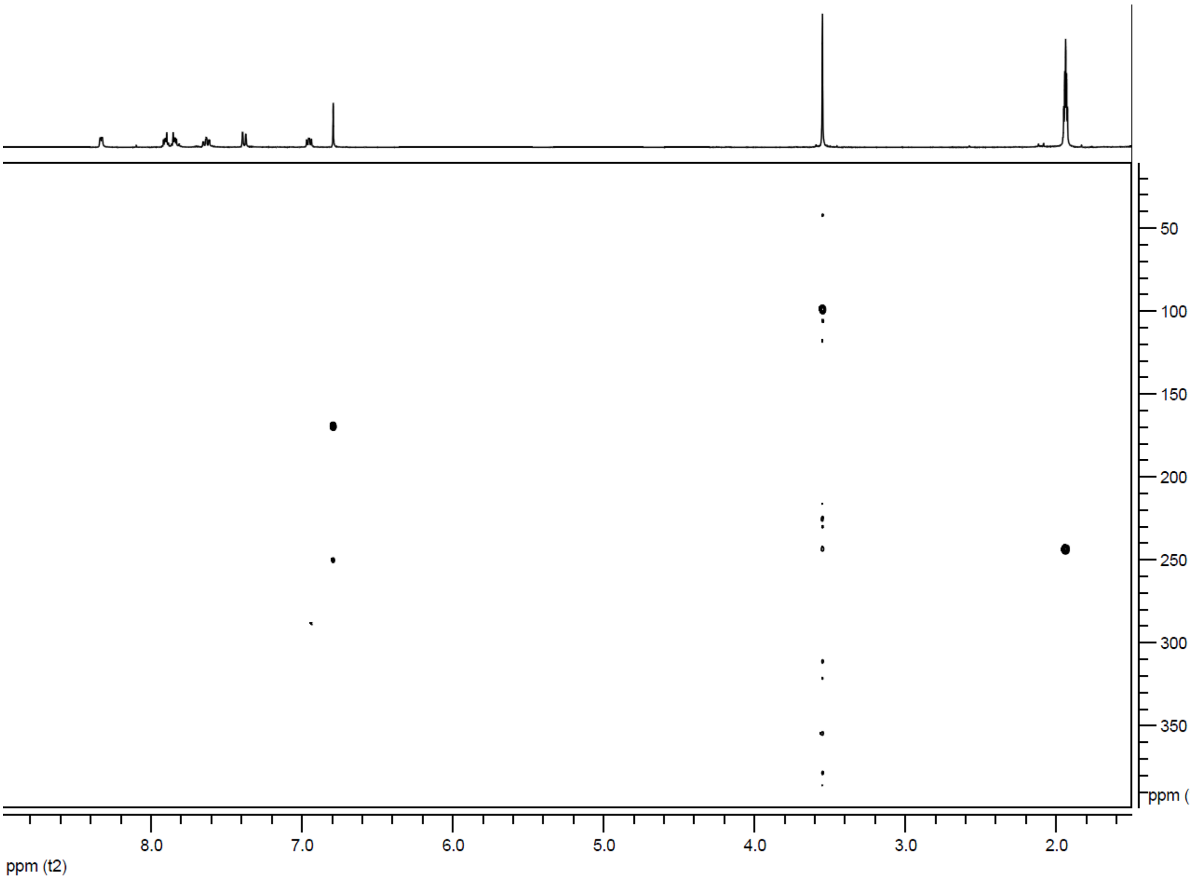

Figure S16. ^{15}N-^{1}H HMBC of **11** in CD_3CN.

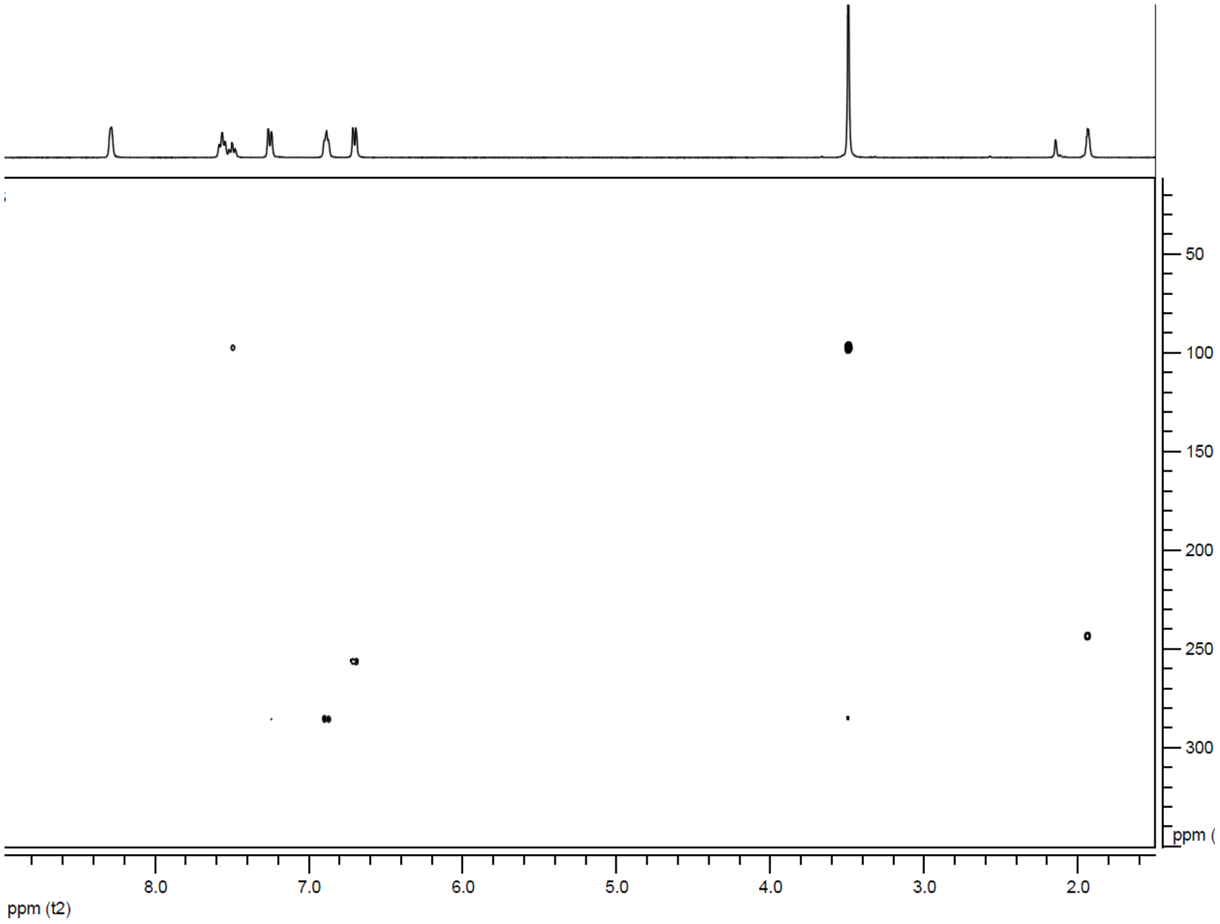

Figure S17. Ellipsoid view and atom numbering of **8** (50% probability, 296 K).

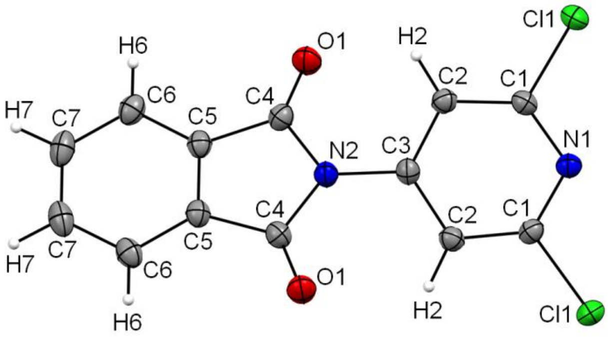

Figure S18. Ellipsoid view and atom numbering of **9** (50% probability, 173 K).

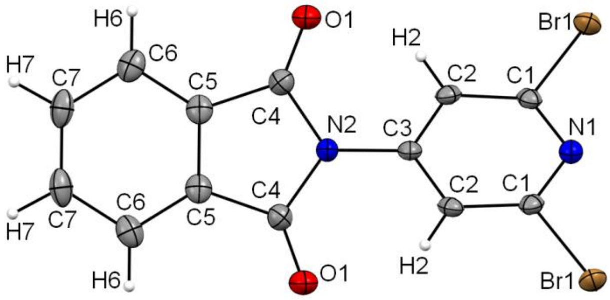

Figure S19. ^{1}H-NMR spectrum of **[2](PF$_6$)$_2$** in CD$_3$CN (top: full spectrum; bottom: zoom).

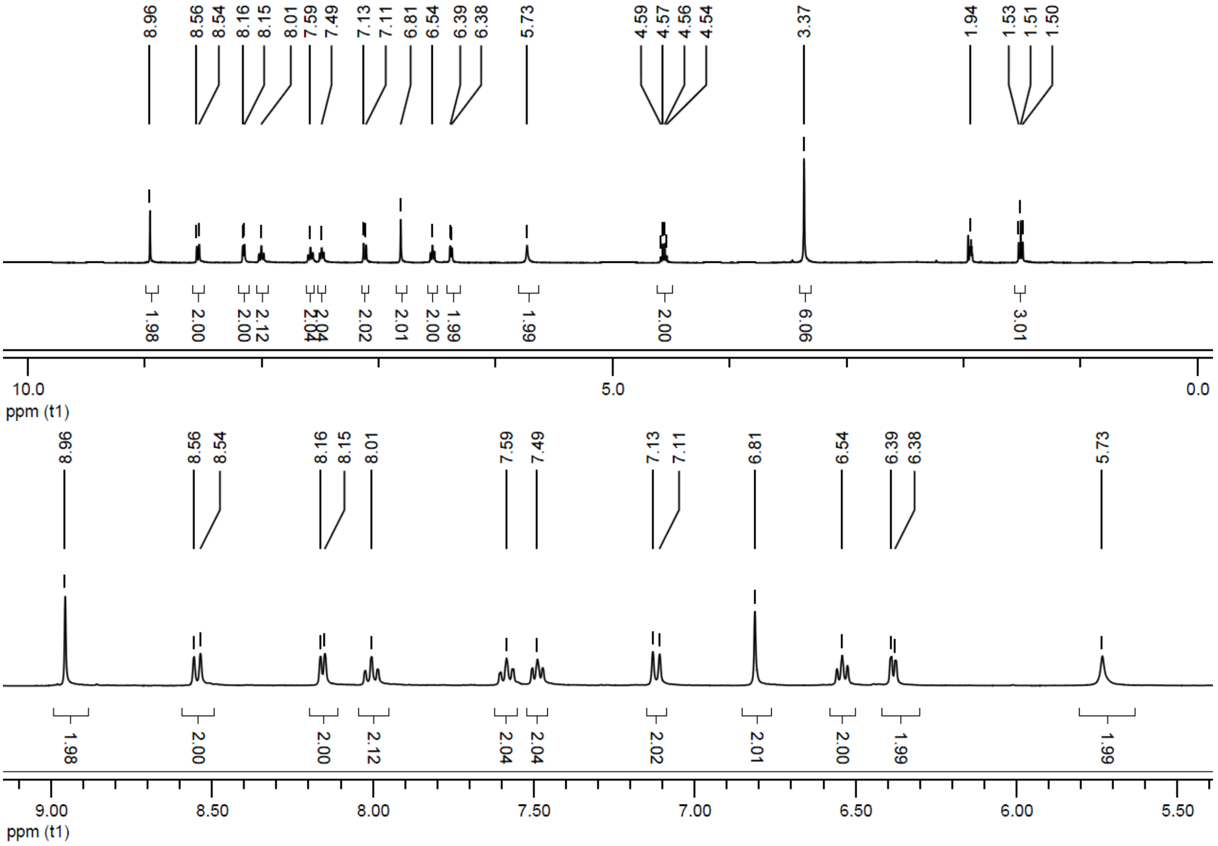

Figure S20. ^{1}H-NMR spectrum of **[3](PF$_6$)$_2$** in CD$_3$CN (top: full spectrum; bottom: zoom).

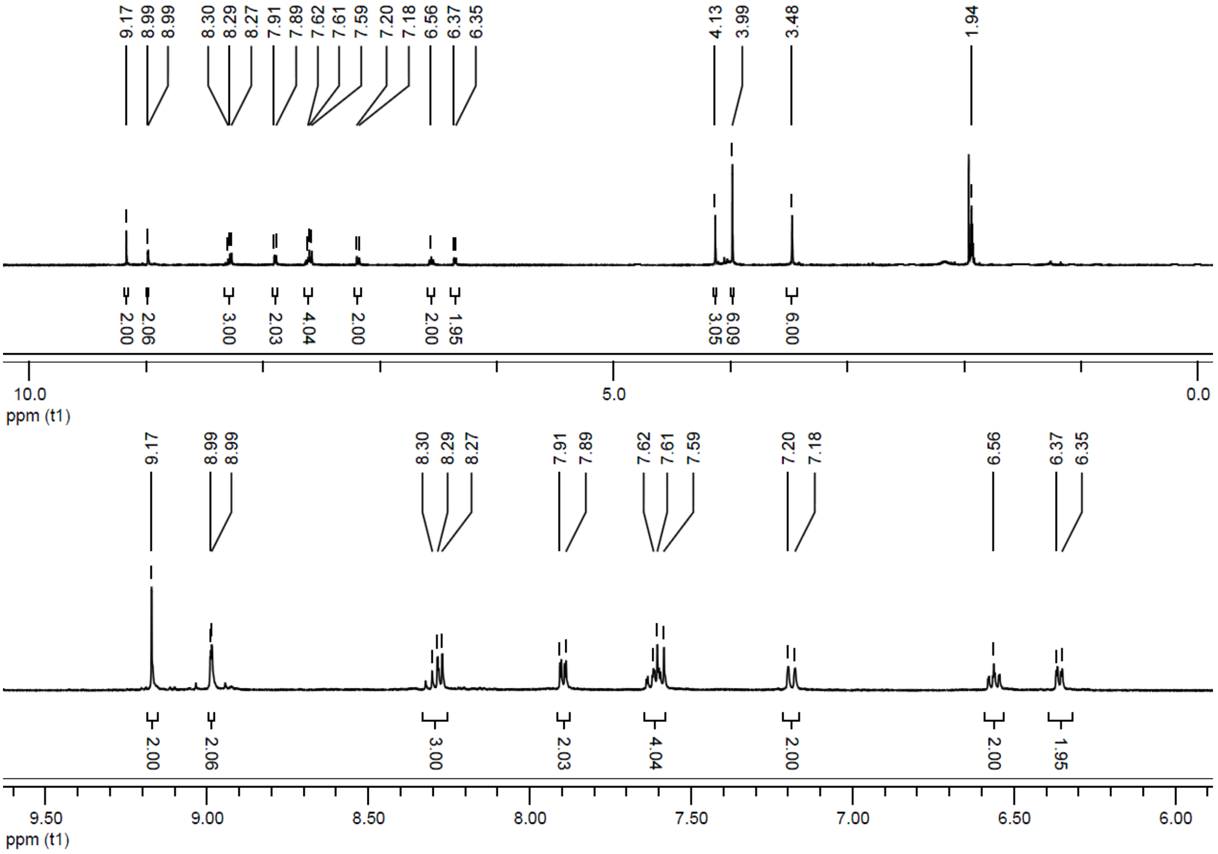

Figure S21. ^{1}H-NMR spectrum of **[4](PF$_6$)$_2$** in CD$_3$CN (top: full spectrum; bottom: zoom).

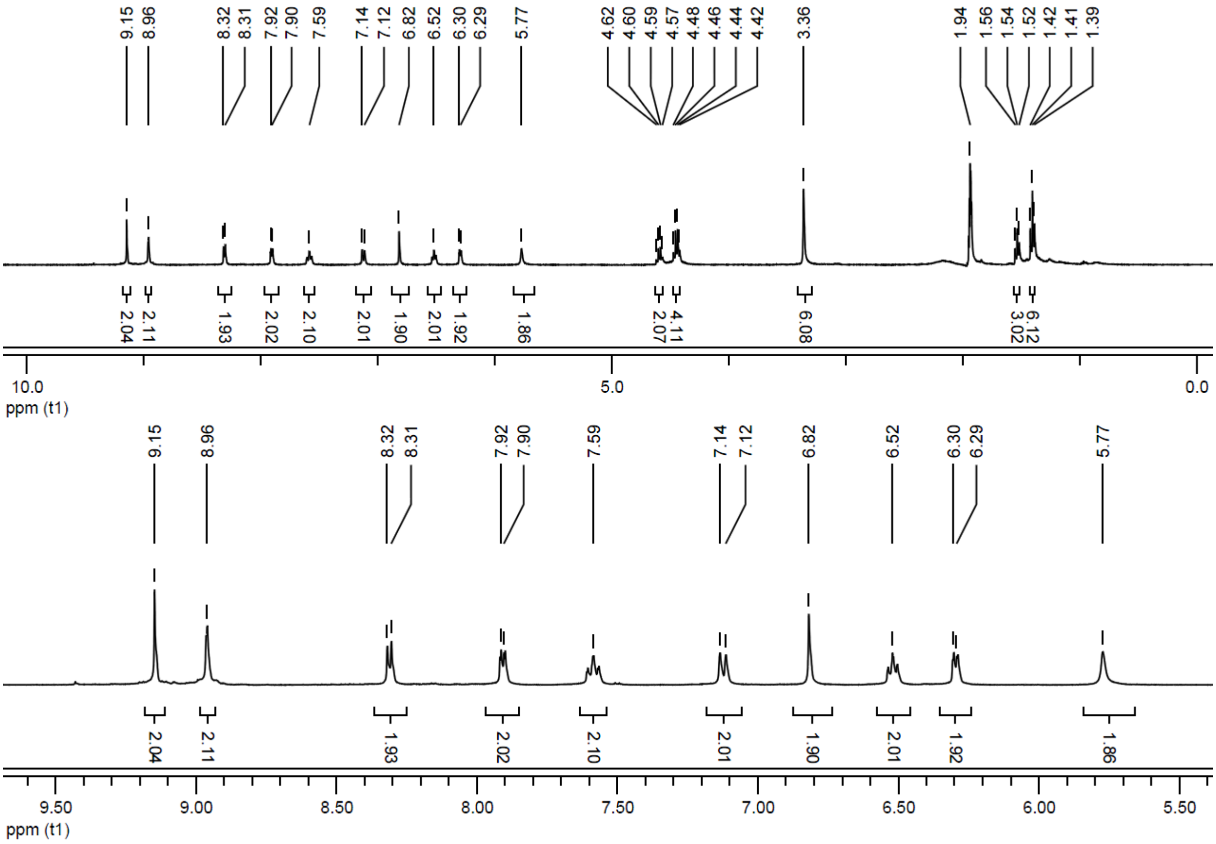

Figure S22. ^{13}C{^{1}H} NMR spectrum of **[2](PF$_6$)$_2$** in CD$_3$CN (top: full spectrum; bottom: zoom).

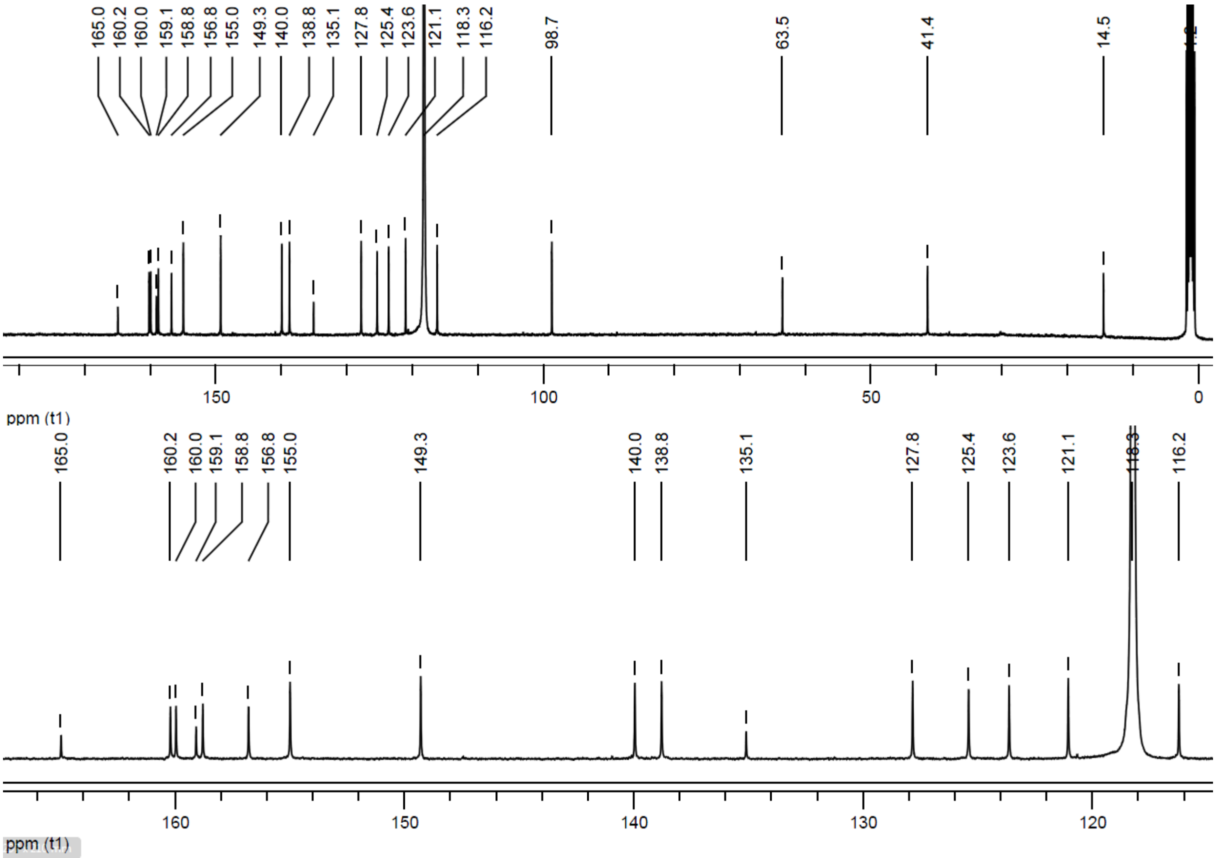

Figure S23. $^{13}C\{^{1}H\}$ NMR spectrum of **[3](PF$_6$)$_2$** in CD_3CN (top: full spectrum; bottom: zoom).

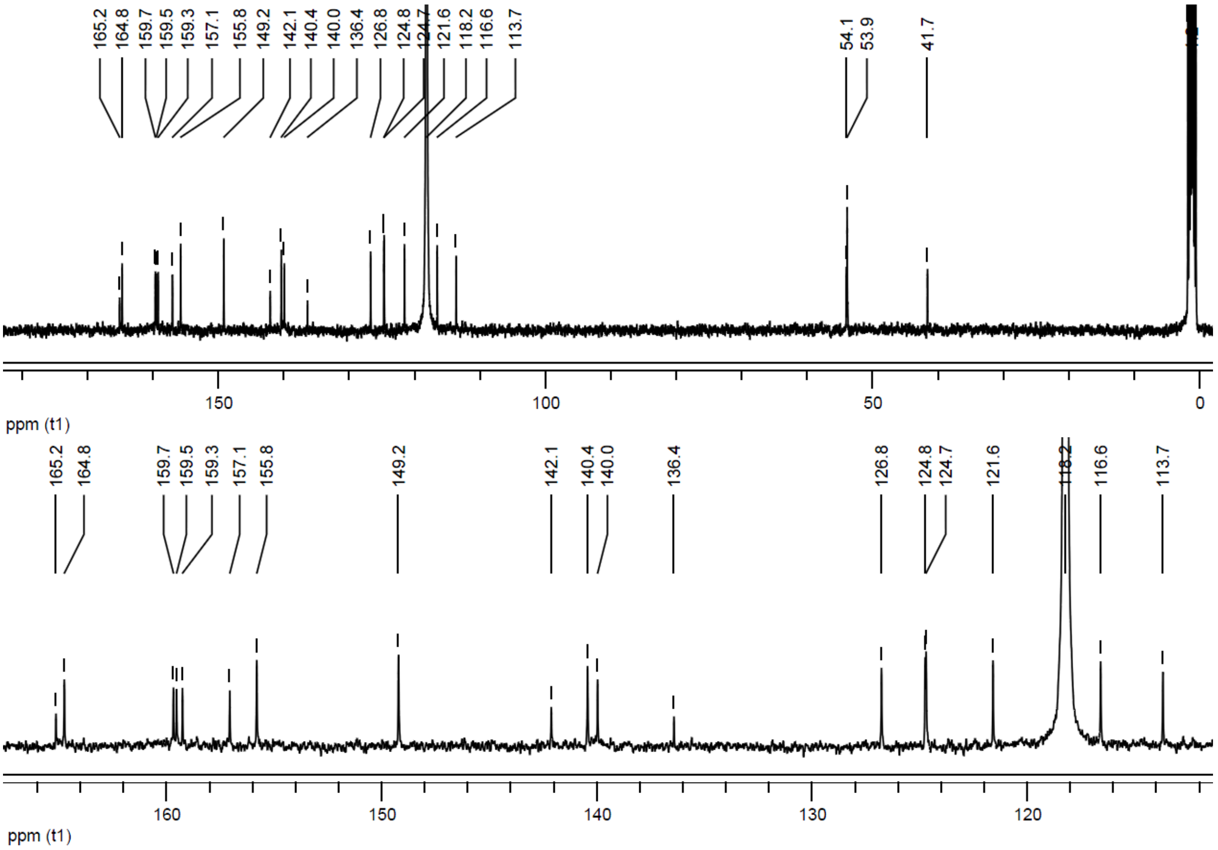

Figure S24. $^{13}C\{^{1}H\}$ NMR spectrum of **[4](PF$_6$)$_2$** in CD_3CN (top: full spectrum; bottom: zoom).

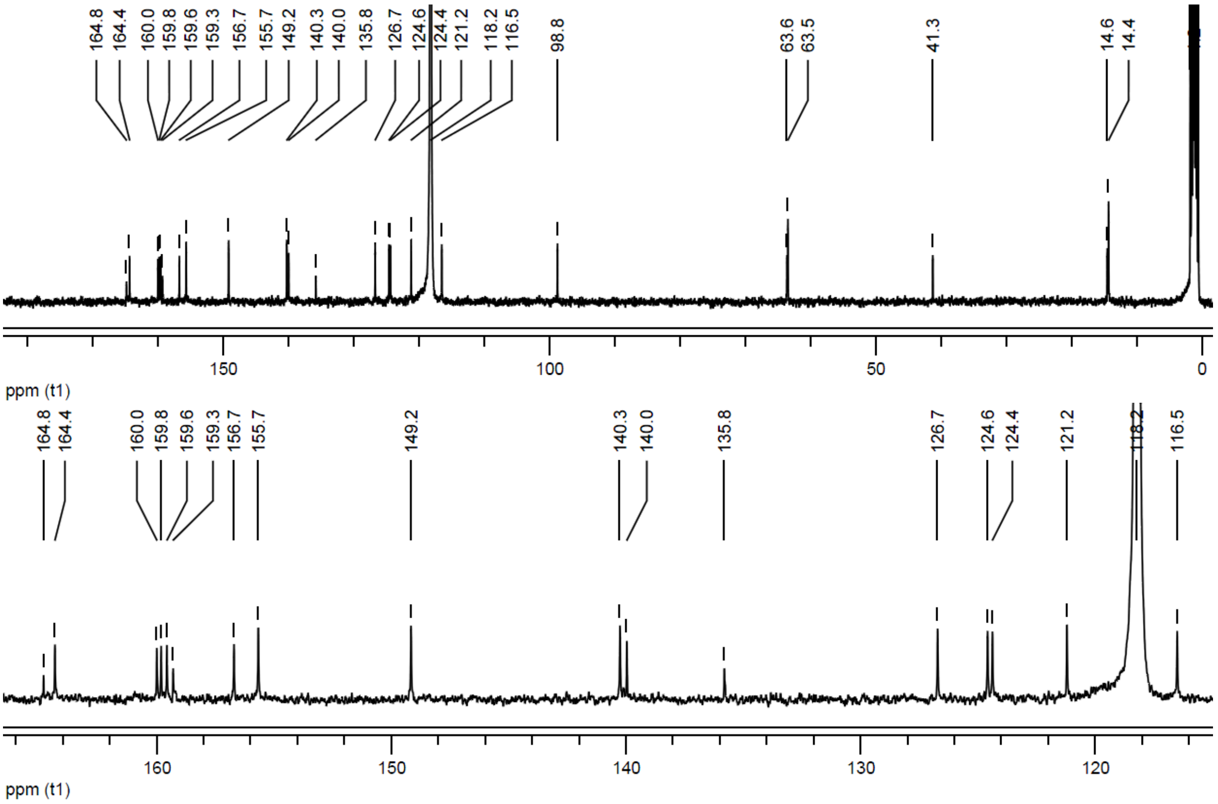

Figure S25. ^{15}N-^{1}H HMBC of **[2](PF$_6$)$_2$** in CD$_3$CN.

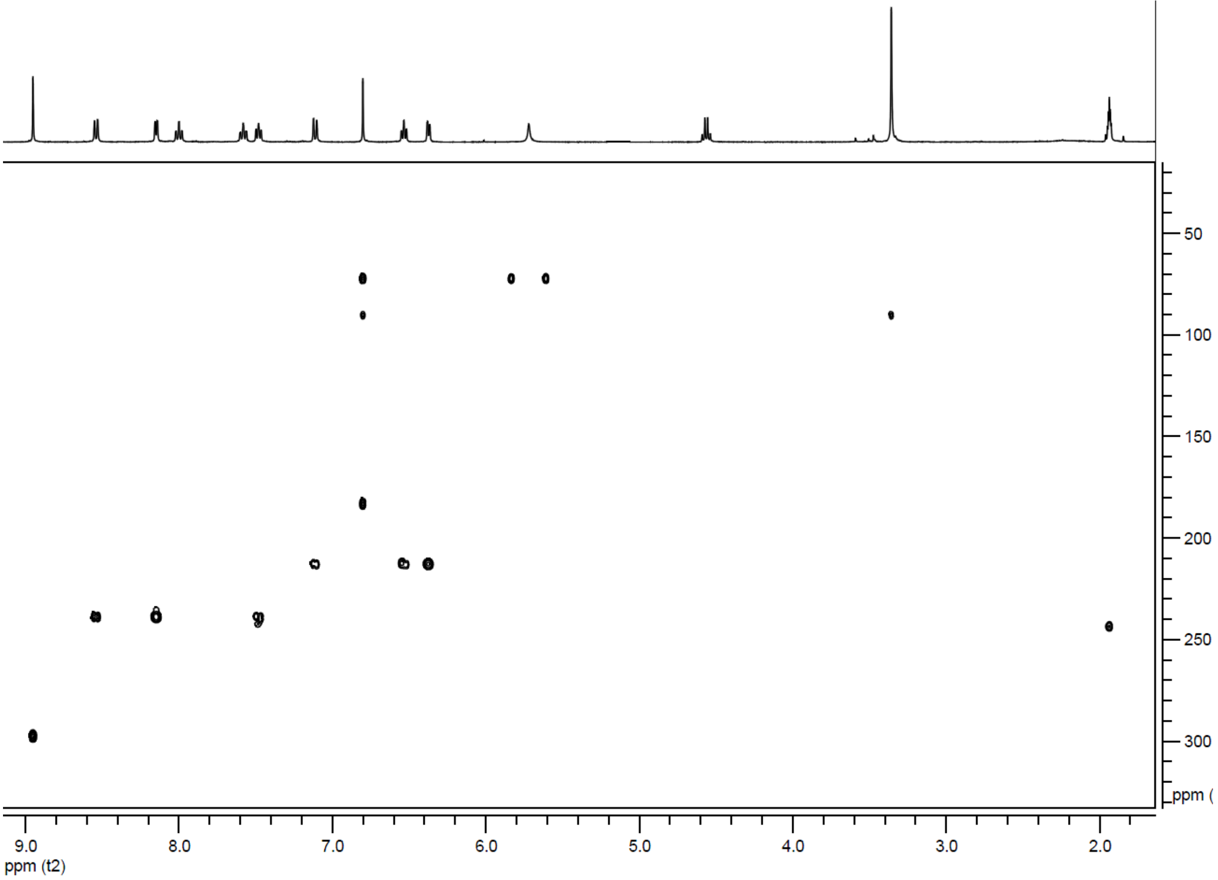

Figure S26. ^{15}N-^{1}H HMBC of **[3](PF$_6$)$_2$** in CD$_3$CN.

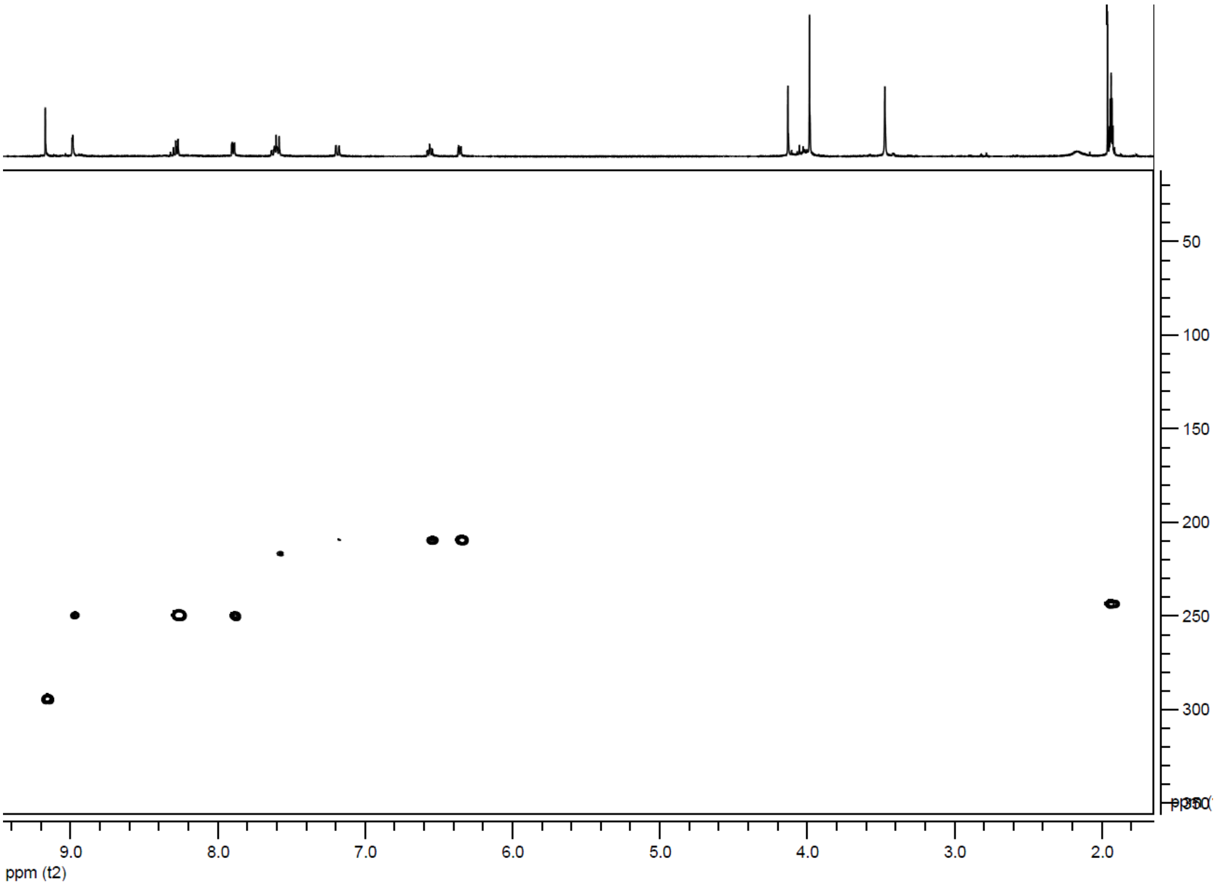

Figure S27. ^{15}N-^{1}H HMBC of **[4](PF$_6$)$_2$** in CD$_3$CN.

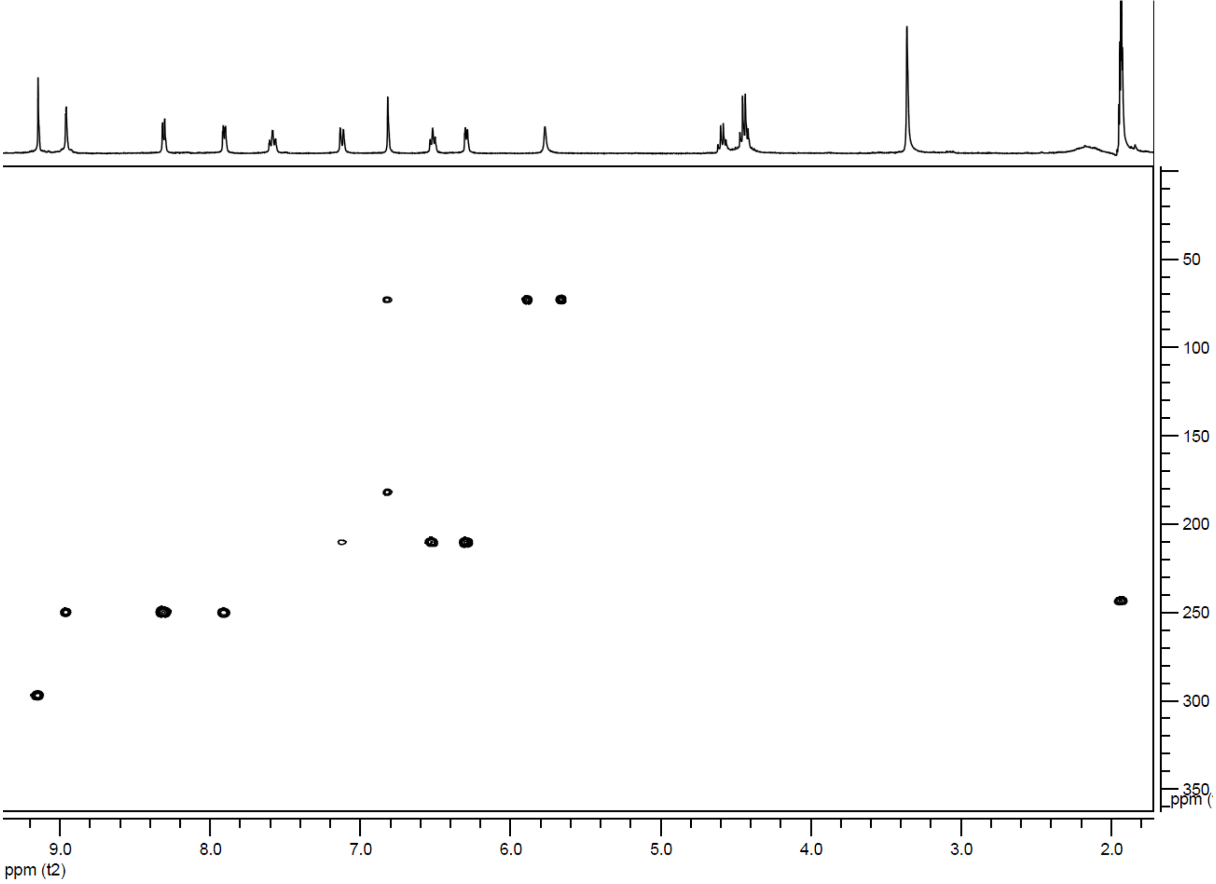

Figure S28. IR spectrum of **[2](PF$_6$)$_2$** in CsI.

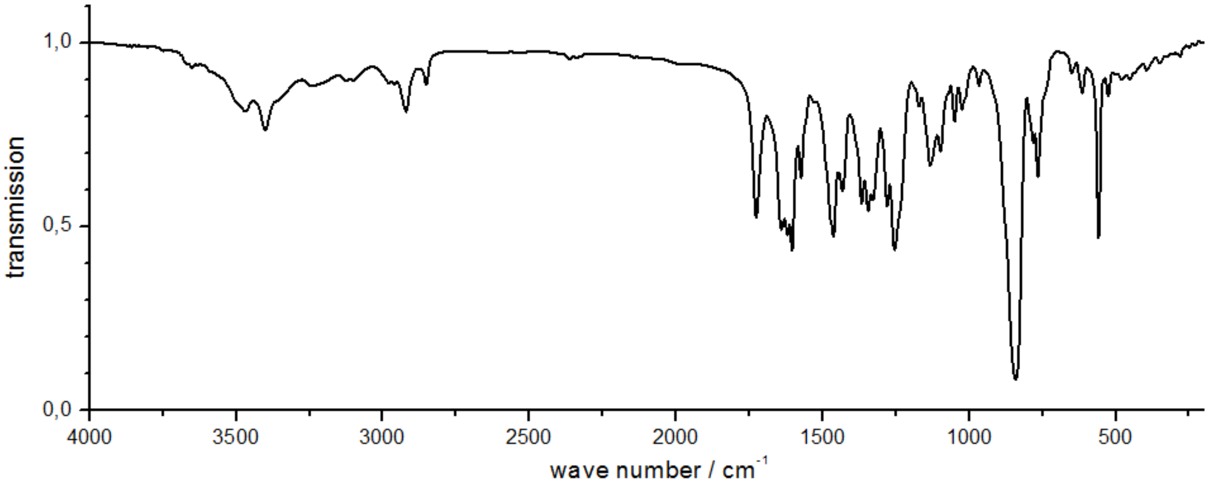

Figure S29. IR spectrum of **[3](PF$_6$)$_2$** in CsI.

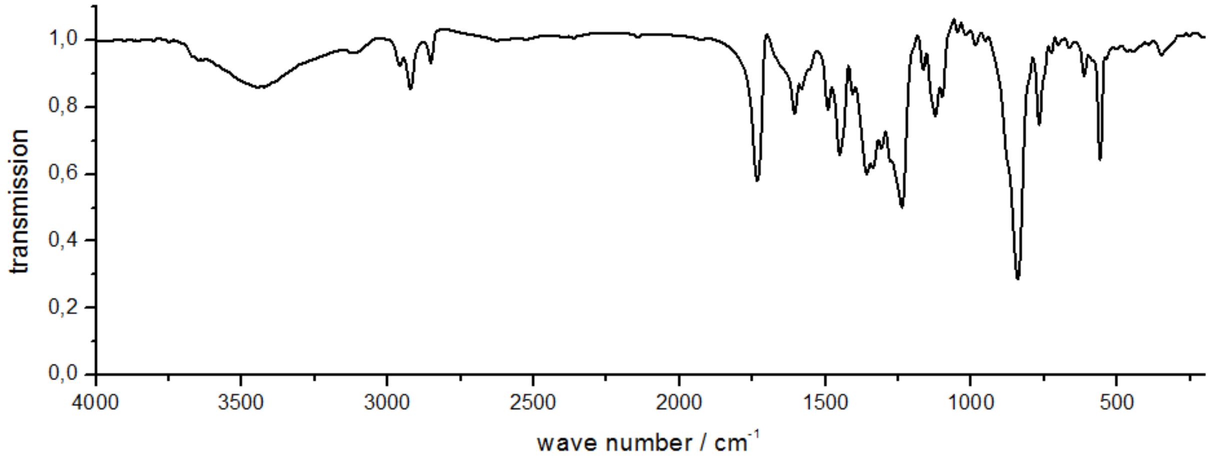

Figure S30. IR spectrum of **[4](PF$_6$)$_2$** in CsI.

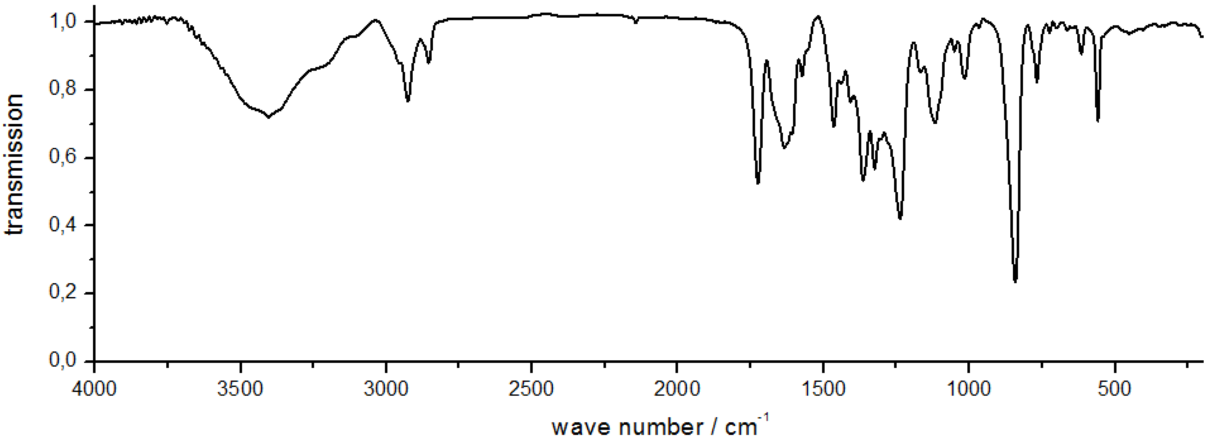

Figure S31. Ellipsoid view of **[2](PF$_6$)$_2$** (50% probability, 173 K).

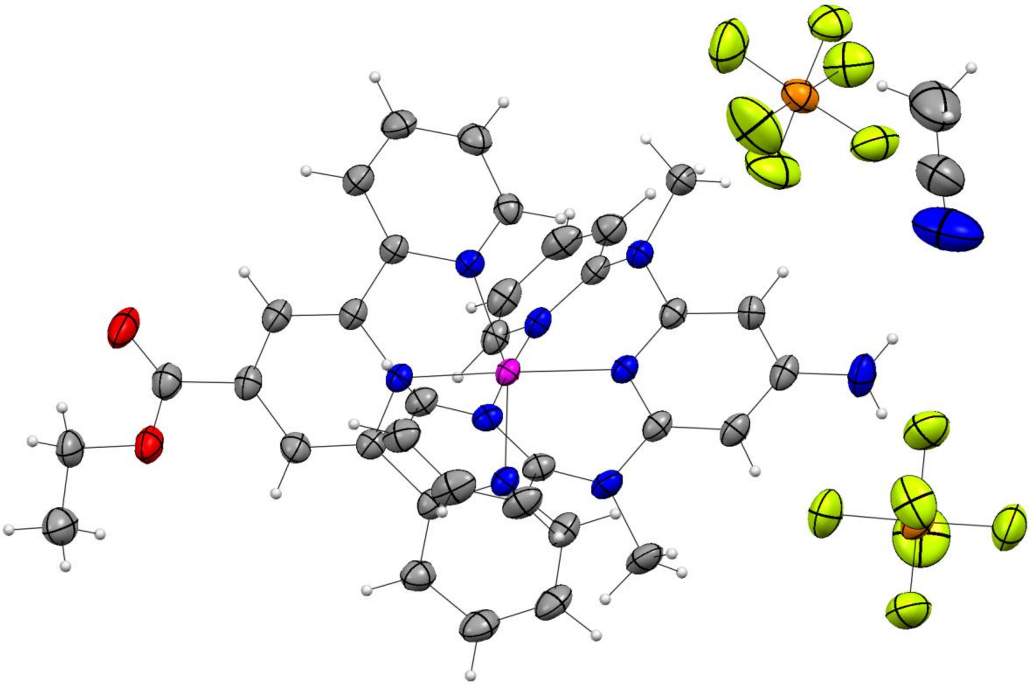

Figure S32. Ellipsoid view of **[3](PF$_6$)$_2$** (50% probability, 173 K).

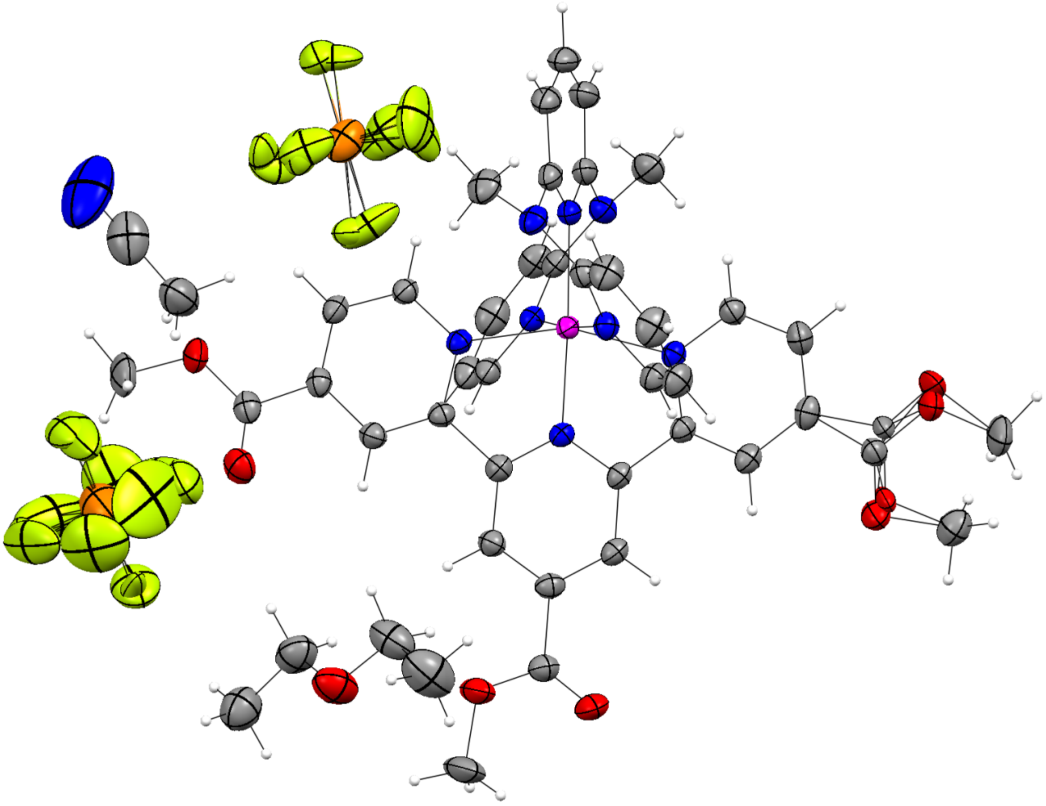

Figure S33. ^{1}H NMR spectra of selected signals of **[2](PF$_6$)$_2$** CD$_3$CN without and with Δ–TRISPHAT.

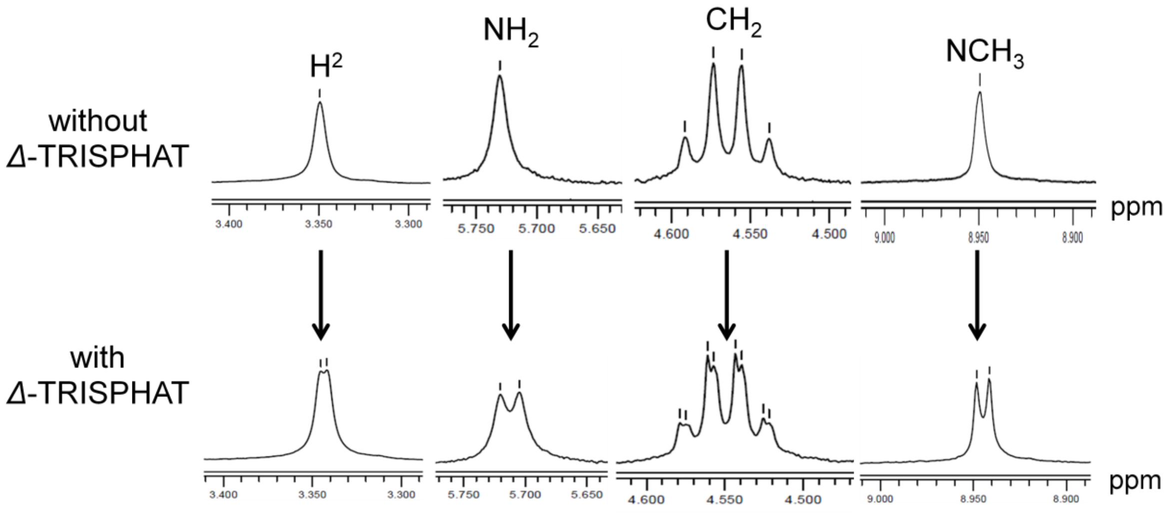

Figure S34. Cyclic voltammograms (CV) and square wave voltammograms (SWV) of **[1](PF$_6$)$_2$**[a].

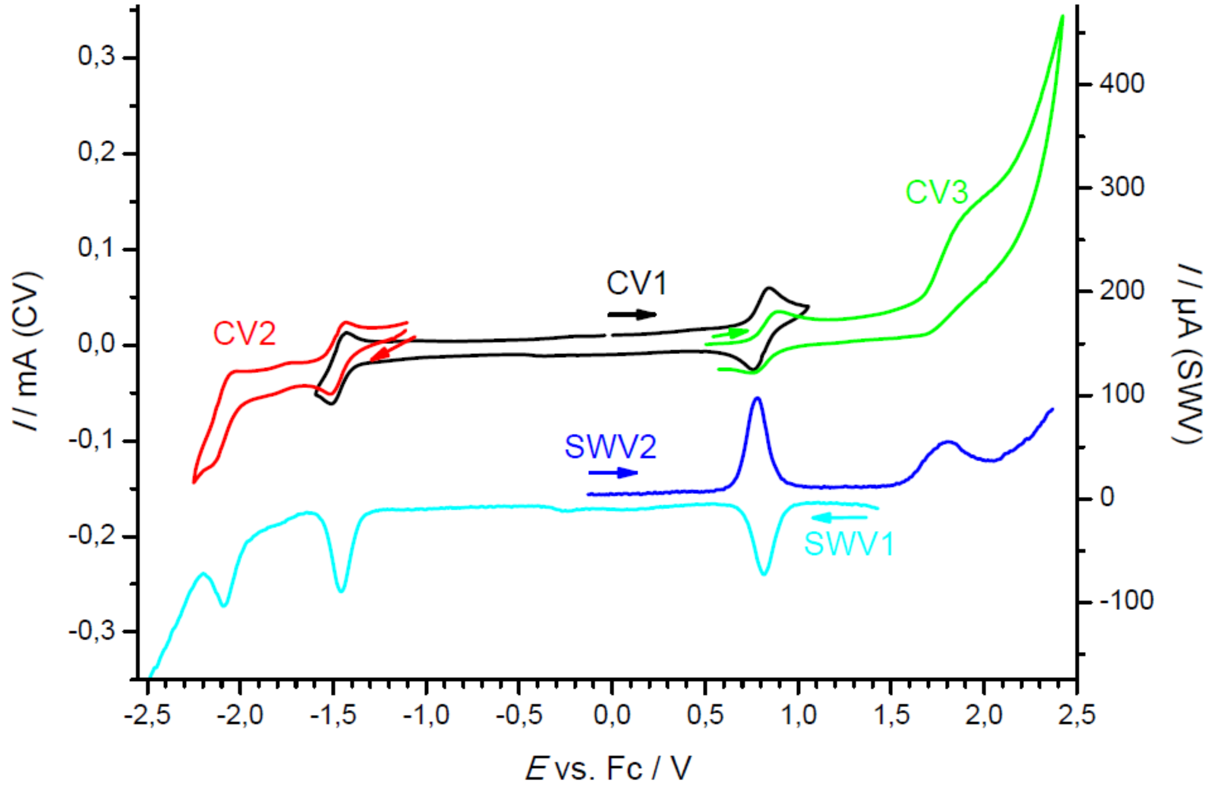

[a] in CH_3CN; 0.1 M (nBu$_4$)(PF$_6$); in V versus Fc/Fc$^+$.

Figure S35. Cyclic voltammograms (CV) and square wave voltammograms (SWV) of **[2](PF$_6$)$_2$**[a].

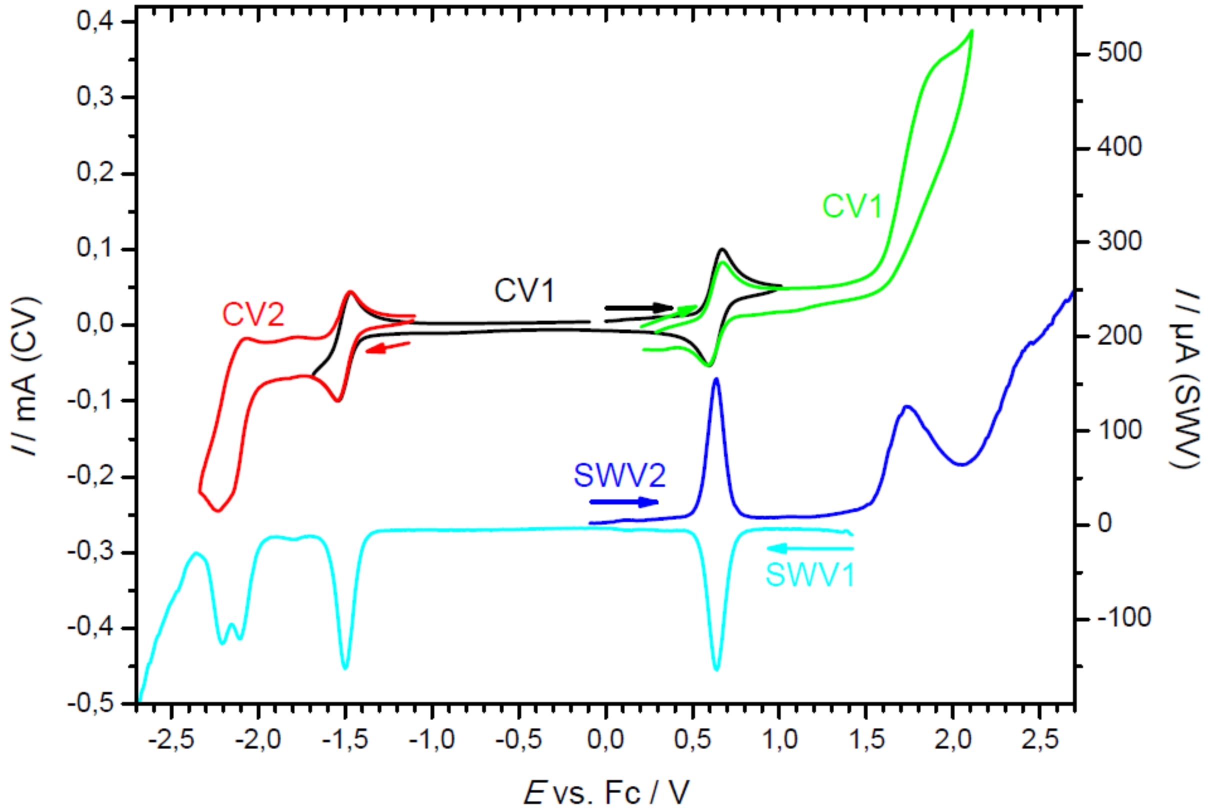

[a] in CH_3CN; 0.1 M (nBu$_4$)(PF$_6$); in V versus Fc/Fc$^+$.

Figure S36. Cyclic voltammograms (CV) and square wave voltammograms (SWV) of **[3](PF$_6$)$_2$**[a].

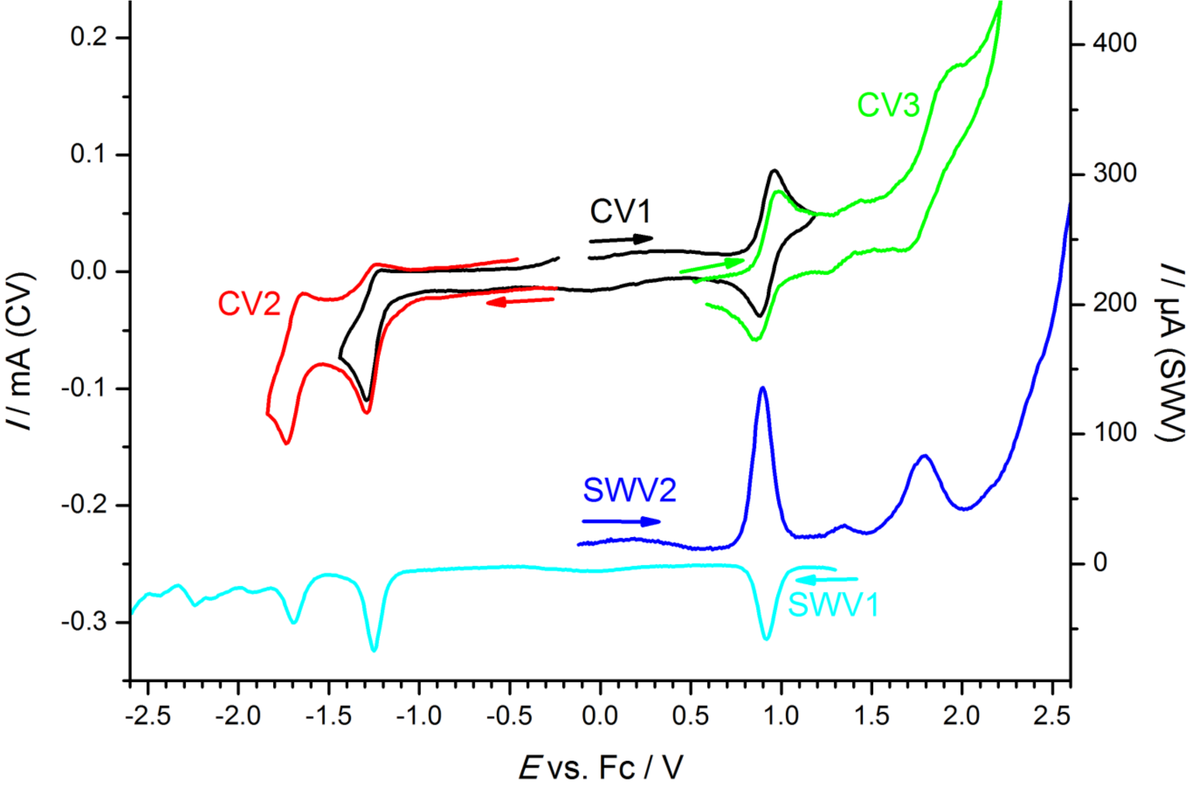

[a] in CH_3CN; 0.1 M (nBu$_4$)(PF$_6$); in V versus Fc/Fc$^+$.

Figure S37. Spin density of one-electron oxidized species **[1]**$^{3+}$ – **[4]**$^{3+}$ and reference compounds **[5]**$^{3+}$ – **[7]**$^{3+}$ in CH_3CN (b3lyp/lanl2dz, iefpcm, contour value 0.01 a. u.). Hydrogen atoms are omitted for clarity.

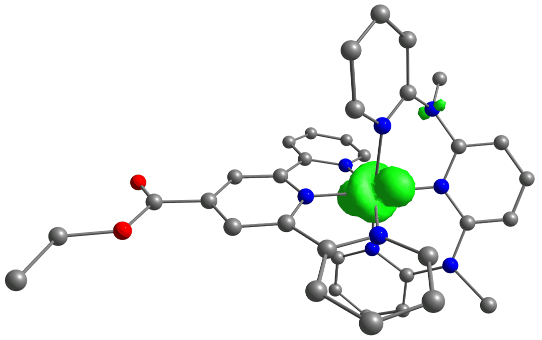

[1]$^{3+}$

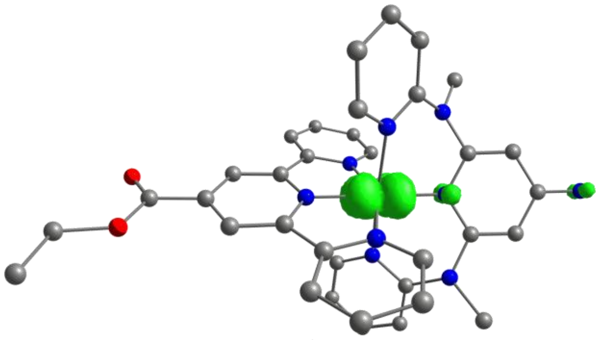

[2]$^{3+}$

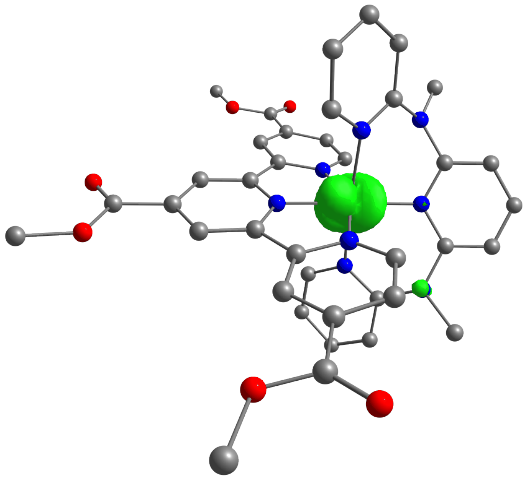

[3]$^{3+}$

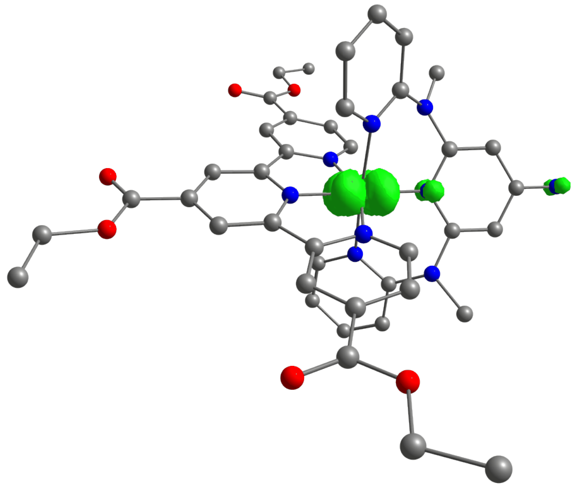

[4]$^{3+}$

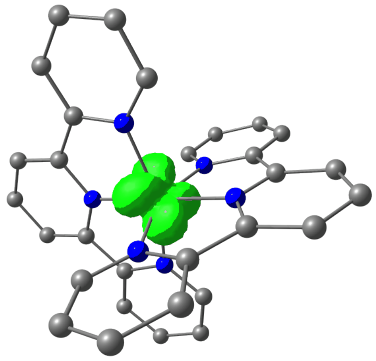

[5]$^{3+}$

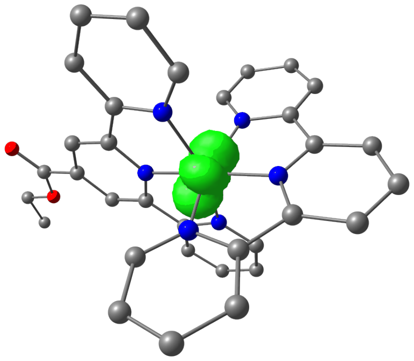

[6]$^{3+}$

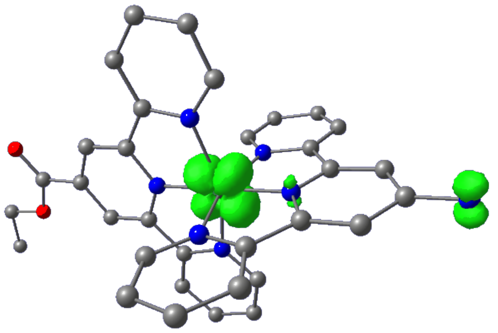

[7]$^{3+}$

Figure S38. Spin density of two-electron oxidized species **[1]**$^{4+}$ – **[4]**$^{4+}$ and reference compounds **[5]**$^{4+}$ – **[7]**$^{4+}$in CH_3CN (b3lyp/lanl2dz, iefpcm, contour value 0.01 a. u.). Hydrogen atoms are omitted for clarity.

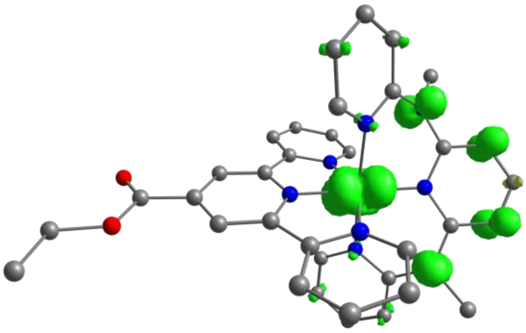

[1]$^{4+}$

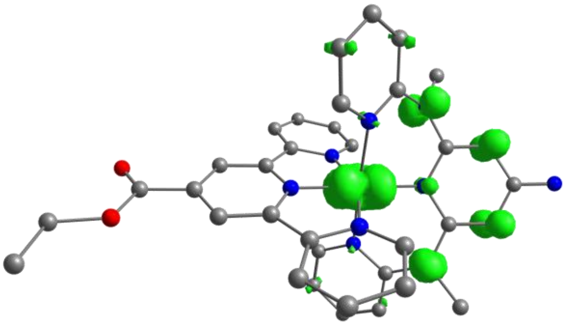

[2]$^{4+}$

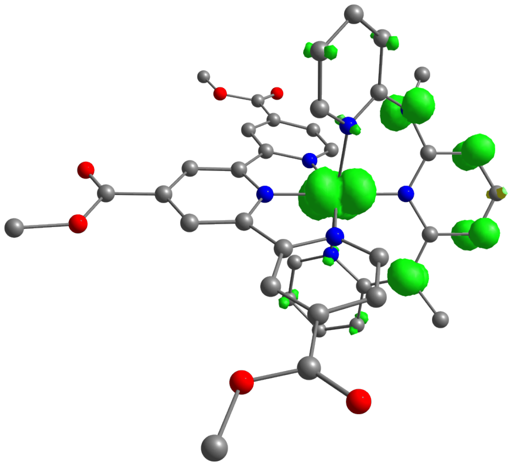

[3]$^{4+}$

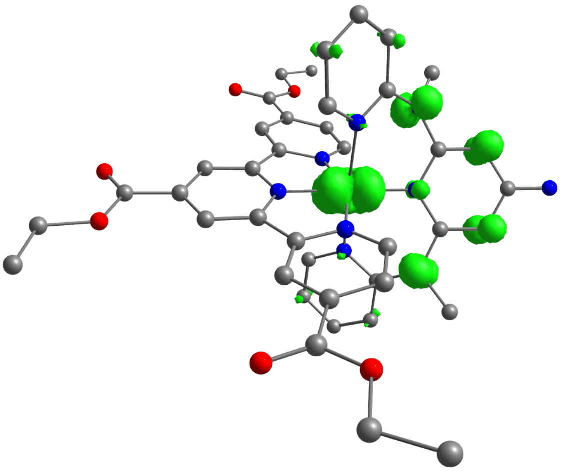

[4]$^{4+}$

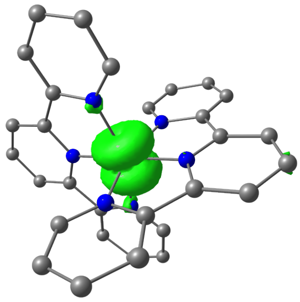

[5]$^{4+}$

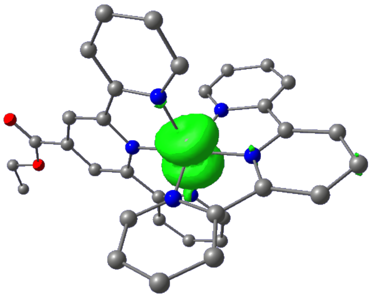

[6]$^{4+}$

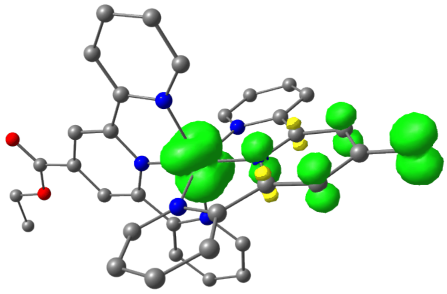

[7]$^{4+}$

Figure S39. Spin density of one-electron reduced species **[1]**$^+$ – **[4]**$^+$ and reference compounds **[5]**$^+$ – **[7]**$^+$ in CH_3CN (b3lyp/lanl2dz, iefpcm, contour value 0.01 a. u.). Hydrogen atoms are omitted for clarity.

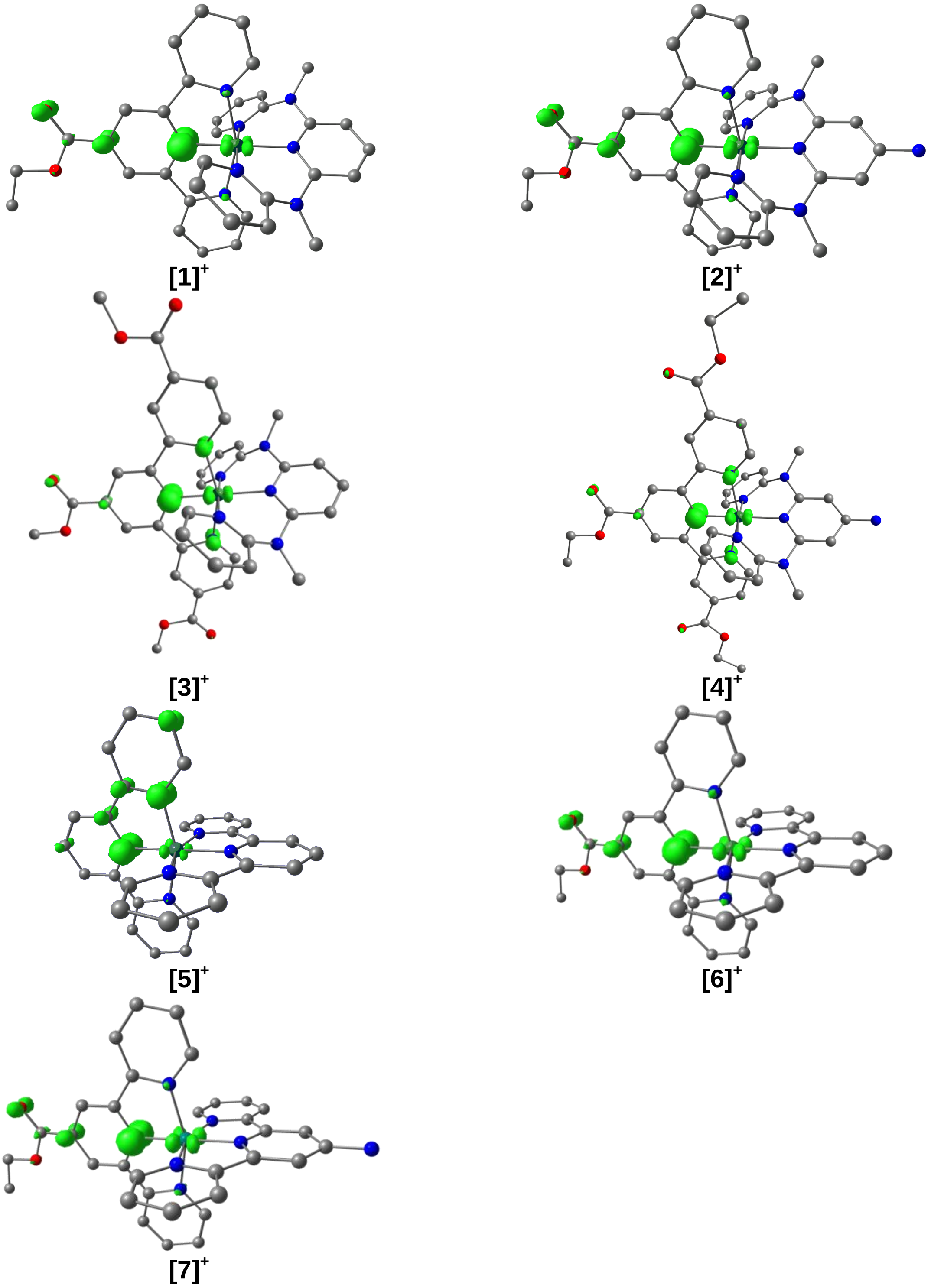

[1]$^+$ **[2]**$^+$

[3]$^+$ **[4]**$^+$

[5]$^+$ **[6]**$^+$

[7]$^+$

Figure S40. Two-electron reduced species **[1]**^{0} – **[4]**^{0} and reference compounds **[5]**^{0} – **[7]**^{0} CH_3CN (b3lyp/lanl2dz, iefpcm). Left: HOMOs of singlet species (M = 1, contour value 0.06 a. u.). Right: Spin density of triplet species (M = 3, contour value 0.01 a. u.). In parentheses is shown the relative energy of singlet and triplet species. Hydrogen atoms are omitted for clarity.

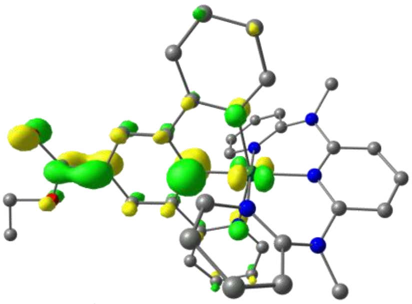

[1]^0 (singlet, 0 kJ mol^{-1})

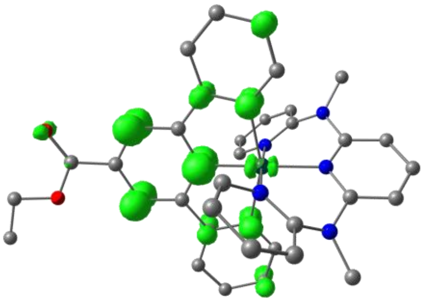

[1]^0 (triplet, 2.7 kJ mol^{-1})

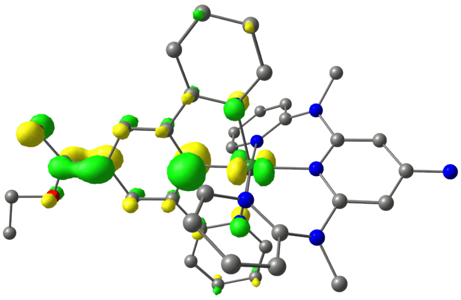

[2]^0 (singlet, 0 kJ mol^{-1})

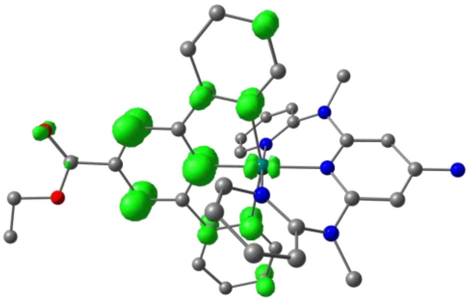

[2]^0 (triplet, 1.5 kJ mol^{-1})

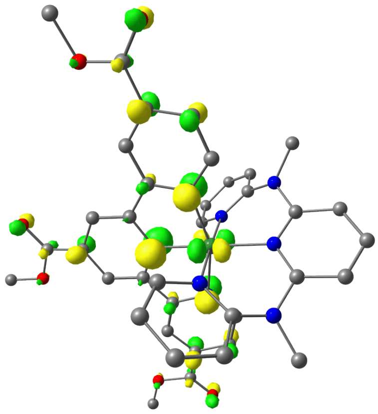

[3]^0 (singlet, 8.4 kJ mol^{-1})

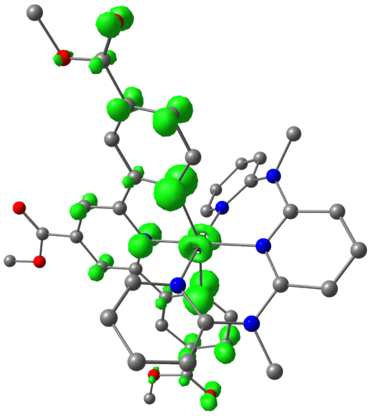

[3]^0 (triplet, 0 kJ mol^{-1})

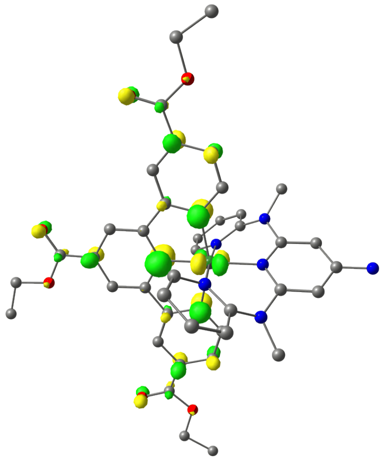

[4]^0 (singlet, 9.4 kJ mol^{-1})

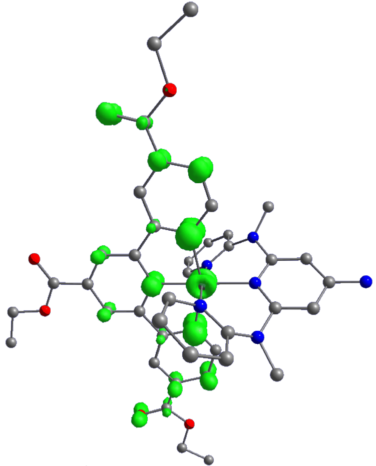

[4]^0 (triplet, 0 kJ mol^{-1})

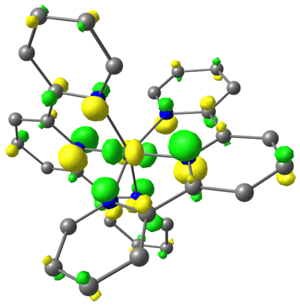

[5]^0 (singlet, 22.6 kJ mol^{-1})

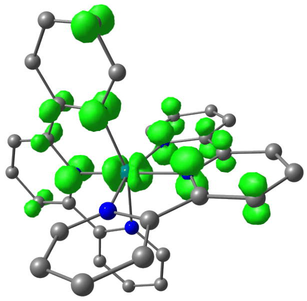

[5]^0 (triplet, 0 kJ mol^{-1})

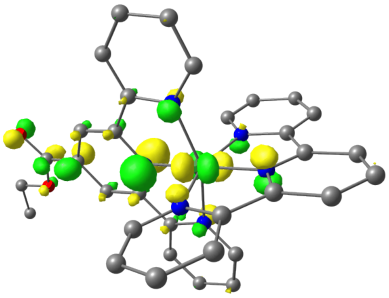

[6]^0 (singlet, 26.1 kJ mol^{-1})

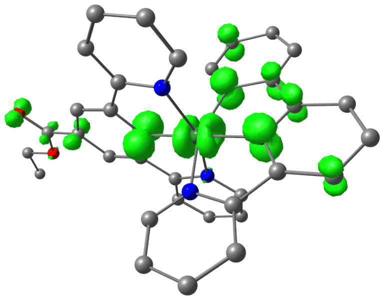

[6]^0 (triplet, 0 kJ mol^{-1})

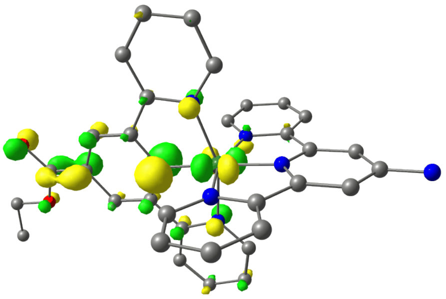

[7]^0 (singlet, 21.7 kJ mol^{-1})

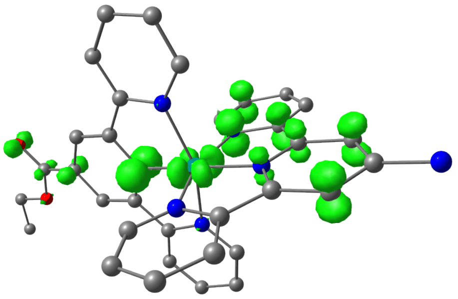

[7]^0 (triplet, 0 kJ mol^{-1})

Figure S41. X-band EPR spectrum of **[2]**$^{3+}$ in 0.5 M trifluoroacetic acid in CH_3CN at 77 K. Black: measurement; red: simulation.

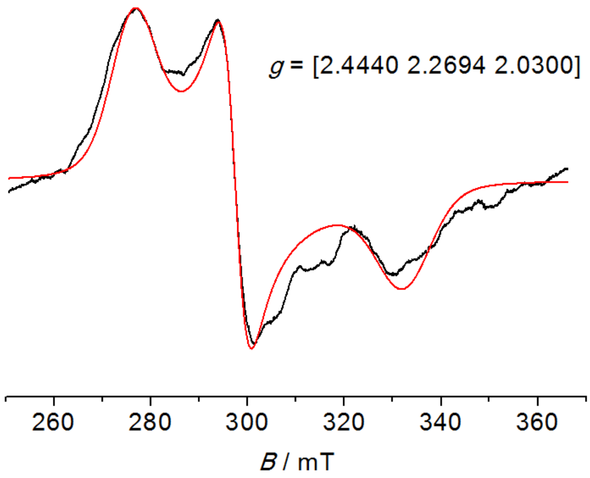

Figure S42. X-band EPR spectrum of **[2]**$^+$ in CH_3CN at 77 K. Black: measurement; red: simulation.

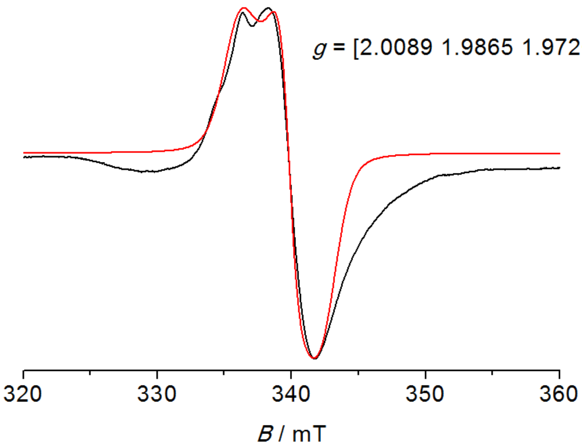

Figure S43. Transient absorption spectra of **[1](PF$_6$)$_2$** in PrCN at room temperature (pulse λ_{exc} = 425 nm, 1900 nJ).

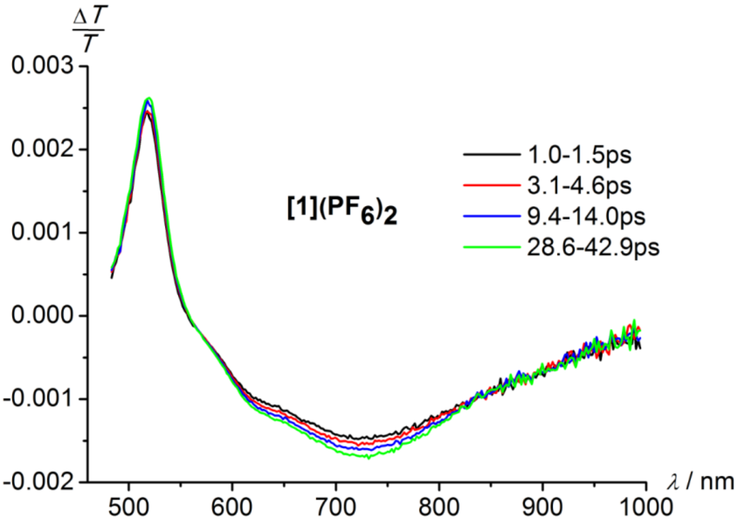

Figure S44. Transient absorption spectra of **[3](PF$_6$)$_2$** in PrCN at room temperature (pulse λ_{exc} = 400 nm, 2200 nJ).

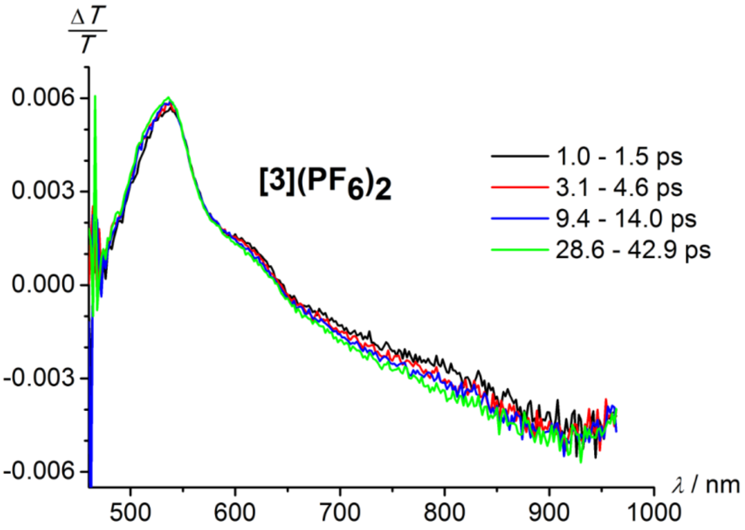

Figure S45. Transient absorption spectra of **[4](PF$_6$)$_2$** in PrCN at room temperature (pulse λ_{exc} = 420 nm, 3800 nJ).

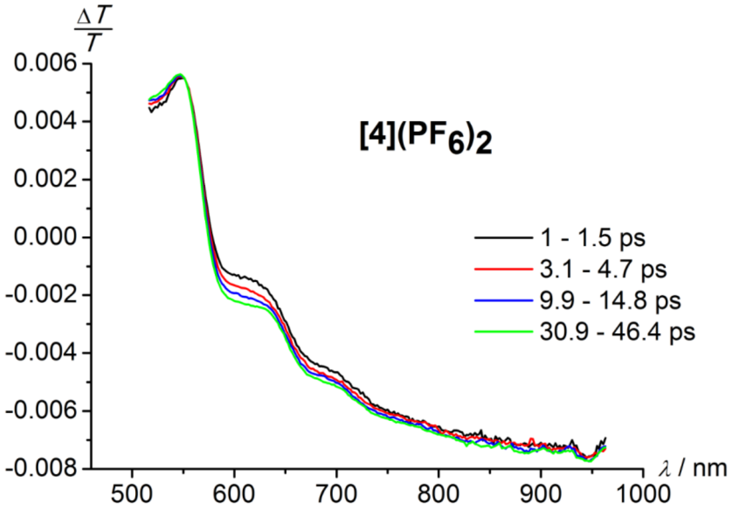

Figure S46. Transient absorption spectra of **[6](PF$_6$)$_2$** in PrCN at room temperature (pulse λ_{exc} = 425 nm, 2050 nJ).

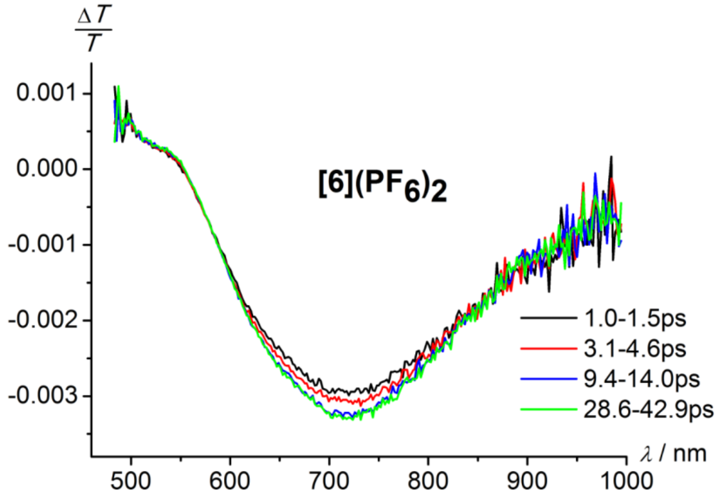

Figure S47. UV/Vis spectra of reduced and oxidized **[2](PF$_6$)$_2$** in different solvents.

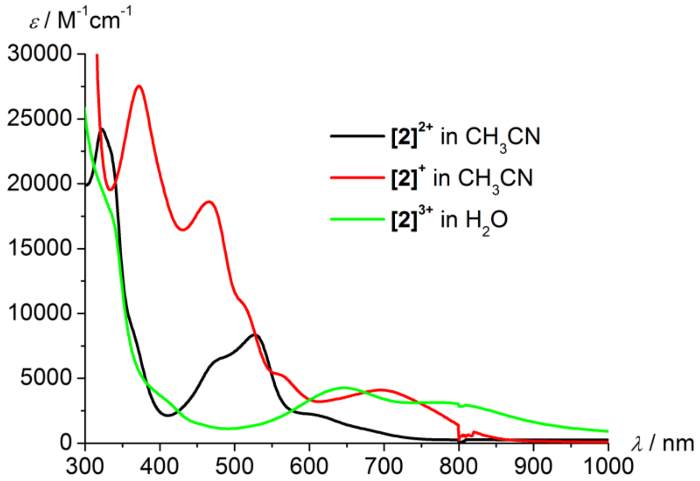

Figure S48. IR spectrum (CsI) of **[2^{D}](PF$_6$)$_2$**.

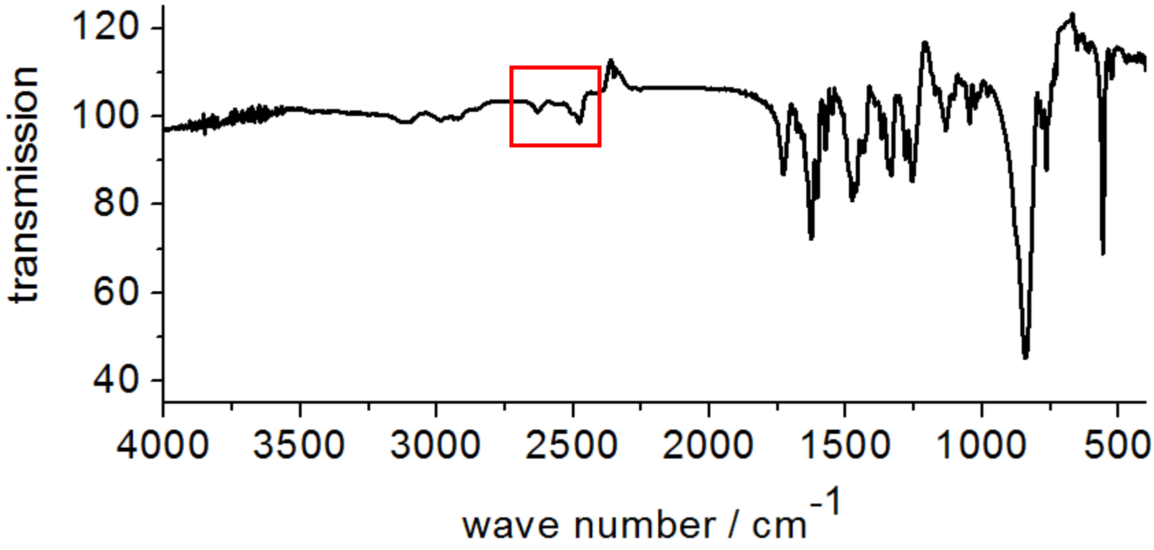

Figure S49. IR spectrum (CsI) of **[4^{D}](PF$_6$)$_2$**.

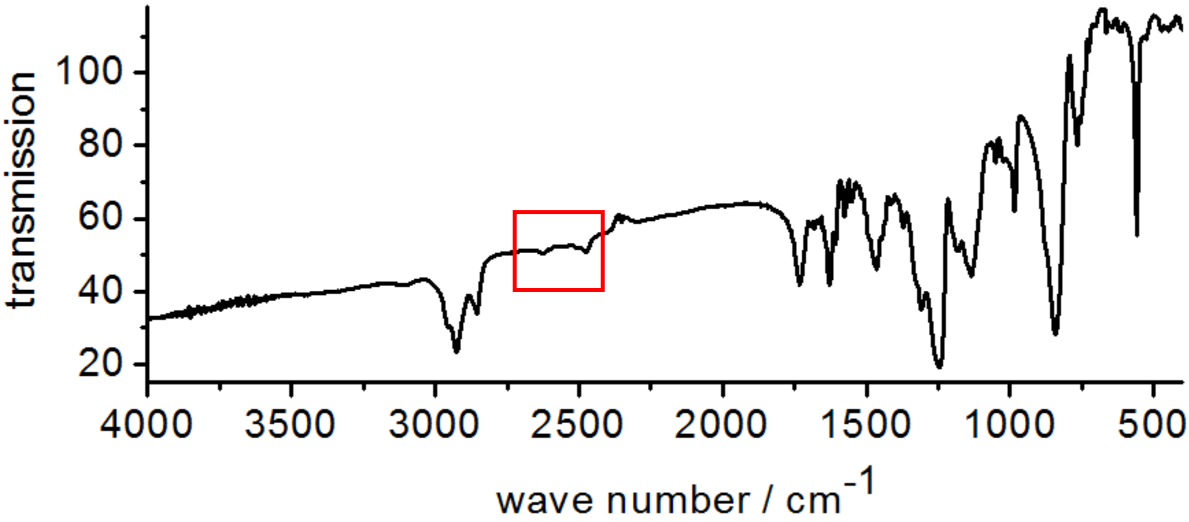

Table S1. Crystal and structure refinement data for **8** and **9** from X-ray analysis.

	8	**9**
Empirical formula	$C_{13}H_6Cl_2N_2O_2$	$C_{13}H_6Br_2N_2O_2$
Formula weight	293.10	382.02
Crystal color, habit	colourless block	colourless plate
Crystal dimensions / mm	0.85 x 0.52 x 0.30	0.98 x 0.37 x 0.10
Crystal system	orthorhombic	orthorhombic
Space group	Pbcn	Pbcn
a / Å	7.2514(5)	7.2704(14)
b / Å	12.1612(8)	12.246(2)
c / Å	13.5025(9)	14.167(3)
α / °	90	90
β / °	90	90
γ / °	90	90
V / Å^3	1190.73(14)	1261.3(4)
Z	4	4

F(000)	592	736
Density (calcd) / g cm^{-3}	1.635	2.012
Absorption coefficient μ / mm^{-1}	0.542 (MULABS)	6.424 (MULABS)
Theta range / °	3.02 – 27.94	2.88 – 27.87
Index ranges	$-9 \leq h \leq 9$	$-9 \leq h \leq 9$
	$-15 \leq k \leq 15$	$-16 \leq k \leq 16$
	$-17 \leq l \leq 17$	$-18 \leq l \leq 17$
Reflections collected	12886	11138
Independent reflections	1424 (R_{int} = 0.0868)	1513 (R_{int} = 0.1152)
Observed reflections	1424	1513
Parameters	89	88
Max. / min. transmission	0.8543 / 0.6558	0.5659 / 0.0616
Goodness-of-fit on F^2	1.080	1.048
Largest difference peak and hole / e Å^{-3}	0.385 / -0.360	1.258 / -1.038
R_1 (I>2σ(I))	0.0302	0.0478
R_1 (all data)	0.0331	0.0684
wR_2 (I>2σ(I))	0.0732	0.1316
wR_2 (all data)	0.0752	0.1494

Table S2. Bond lengths / Å and angles / ° of **8** from X-ray crystal analysis.

Cl(1)-C(1)	1.7376(11)
O(1)-C(4)	1.2038(14)
N(2)-C(3)	1.4163(19)
N(2)-C(4)#1	1.4232(13)
N(2)-C(4)	1.4232(13)
C(5)-C(5)#1	1.386(2)
C(5)-C(6)	1.3877(16)
C(5)-C(4)	1.4830(15)
C(1)-N(1)	1.3305(13)
C(1)-C(2)	1.3841(15)
C(2)-C(3)	1.3929(13)
C(2)-H(2)	0.9300
C(3)-C(2)#1	1.3929(13)
C(6)-C(7)	1.3928(17)
C(6)-H(6)	0.9300
C(7)-C(7)#1	1.395(3)
C(7)-H(7)	0.9300
N(1)-C(1)#1	1.3305(13)

C(3)-N(2)-C(4)#1	124.24(6)
C(3)-N(2)-C(4)	124.24(6)
C(4)#1-N(2)-C(4)	111.52(13)
C(5)#1-C(5)-C(6)	121.65(7)
C(5)#1-C(5)-C(4)	109.03(6)
C(6)-C(5)-C(4)	129.32(11)
N(1)-C(1)-C(2)	125.61(10)
N(1)-C(1)-Cl(1)	114.77(8)
C(2)-C(1)-Cl(1)	119.62(8)
C(1)-C(2)-C(3)	116.43(10)
C(1)-C(2)-H(2)	121.8
C(3)-C(2)-H(2)	121.8
O(1)-C(4)-N(2)	125.28(11)
O(1)-C(4)-C(5)	129.50(10)
N(2)-C(4)-C(5)	105.21(9)
C(2)#1-C(3)-C(2)	120.31(14)

C(2)#1-C(3)-N(2)	119.84(7)
C(2)-C(3)-N(2)	119.84(7)
C(5)-C(6)-C(7)	117.02(12)
C(5)-C(6)-H(6)	121.5
C(7)-C(6)-H(6)	121.5
C(6)-C(7)-C(7)#1	121.32(7)
C(6)-C(7)-H(7)	119.3
C(7)#1-C(7)-H(7)	119.3
C(1)#1-N(1)-C(1)	115.59(13)

Table S3. Bond lengths / Å and angles / ° of **9** from X-ray crystal analysis.

Br(1)-C(1)	1.899(5)
O(1)-C(4)	1.210(7)
N(1)-C(1)	1.329(6)
N(1)-C(1)#1	1.329(6)
N(2)-C(4)	1.419(6)
N(2)-C(4)#1	1.419(6)
N(2)-C(3)	1.423(9)
C(1)-C(2)	1.395(7)
C(2)-C(3)	1.389(6)
C(2)-H(2)	0.9500
C(3)-C(2)#1	1.389(6)
C(4)-C(5)	1.488(7)
C(5)-C(5)#1	1.374(11)
C(5)-C(6)	1.397(7)
C(6)-C(7)	1.403(8)
C(6)-H(6)	0.9500
C(7)-C(7)#1	1.372(13)
C(7)-H(7)	0.9500

C(1)-N(1)-C(1)#1	116.6(6)
C(4)-N(2)-C(4)#1	111.4(6)
C(4)-N(2)-C(3)	124.3(3)
C(4)#1-N(2)-C(3)	124.3(3)
N(1)-C(1)-C(2)	124.9(5)
N(1)-C(1)-Br(1)	115.6(4)
C(2)-C(1)-Br(1)	119.5(4)
C(3)-C(2)-C(1)	116.2(5)
C(3)-C(2)-H(2)	121.9
C(1)-C(2)-H(2)	121.9
C(2)#1-C(3)-C(2)	121.1(6)
C(2)#1-C(3)-N(2)	119.5(3)
C(2)-C(3)-N(2)	119.5(3)
O(1)-C(4)-N(2)	125.5(5)
O(1)-C(4)-C(5)	129.2(5)
N(2)-C(4)-C(5)	105.2(5)
C(5)#1-C(5)-C(6)	122.3(3)
C(5)#1-C(5)-C(4)	109.0(3)
C(6)-C(5)-C(4)	128.6(5)
C(5)-C(6)-C(7)	115.4(6)
C(5)-C(6)-H(6)	122.3
C(7)-C(6)-H(6)	122.3
C(7)#1-C(7)-C(6)	122.2(4)
C(7)#1-C(7)-H(7)	118.9
C(6)-C(7)-H(7)	118.9

Table S4. ^{1}H NMR data of $[1](PF_6)_2$ – $[4](PF_6)_2$ in CD_3CN, 400 MHz.

	$[1](PF_6)_2$	$[2](PF_6)_2$	$[3](PF_6)_2$	$[4](PF_6)_2$
H^2	8.97 (s, 2 H)	8.95 (s, 2 H)	9.17 (s, 2 H)	9.15 (s, 2 H)
H^5	8.56 (s, 2 H)	8.54 (s, 2 H)	8.99 (m, 2 H)	8.96 (m, 2 H)
H^6	8.02 (m, 2 H)	8.00 (m, 2 H)	-	-
H^7	7.47 (m, 2 H)	7.48 (m, 2 H)	7.91 (m, 2 H)	7.91 (m, 2 H)
H^8	8.11 (m, 2 H)	8.15 (m, 2 H)	8.28 (m, 2 H)	8.31 (m, 2 H)
H^9	6.42 (m, 2 H)	6.38 (m, 2 H)	6.36 (m, 2 H)	6.30 (m, 2 H)
H^{10}	6.57 (m, 2 H)	6.54 (m, 2 H)	6.56 (m, 2 H)	6.52 (m, 2 H)
H^{11}	7.61 (m, 2 H)	7.58 (m, 2 H)	7.62 (m, 2 H)	7.59 (m, 2 H)
H^{12}	7.17 (m, 2 H)	7.12 (m, 2 H)	7.19 (m, 2 H)	7.13 (m, 2 H)
H^{15}	7.56 (d, $^3J_{HH}$ = 8.2 Hz, 2 H)	6.80 (s, 2 H)	7.60 (d, $^3J_{HH}$ = 8.2 Hz, 2 H)	6.82 (s, 2 H)
H^{16}	8.27 (t, $^3J_{HH}$ = 8.2 Hz, 1 H)	-	8.30 (t, $^3J_{HH}$ = 8.2 Hz, 1 H)	-
NH_2	-	5.72 (br, s, 2 H)	-	5.77 (br, s, 2 H)
NCH_3	3.46 (s, 6 H)	3.36 (s, 6 H)	3.48 (s, 6 H)	3.36 (s, 6 H)
$CH_2C\underline{H}_3^{center}$	1.52 (t, $^3J_{HH}$ = 7.1 Hz, 3 H)	1.51 (t, $^3J_{HH}$ = 7.1 Hz, 3 H)	-	1.54 (t, $^3J_{HH}$ = 7.1 Hz, 3 H)
$CH_2C\underline{H}_3^{outer}$	-	-	-	1.41 (q, $^3J_{HH}$ = 7.1 Hz, 6 H)
$C\underline{H}_2CH_3^{center}$	4.58 (q, $^3J_{HH}$ = 7.1 Hz, 2 H)	4.57 (q, $^3J_{HH}$ = 7.1 Hz, 2 H)	-	4.60 (q, $^3J_{HH}$ = 7.1 Hz, 2 H)
$C\underline{H}_2CH_3^{outer}$	-	-	-	4.45 (q, $^3J_{HH}$ = 7.1 Hz, 4 H)
OCH_3^{center}	-	-	4.13 (s, 3 H)	-
OCH_3^{outer}	-	-	3.99 (s, 6 H)	-

Table S5. $^{13}C\{^1H\}$ NMR data of $[1](PF_6)_2$ – $[4](PF_6)_2$ in CD_3CN, 101 MHz.

	$[1](PF_6)_2$	$[2](PF_6)_2$	$[3](PF_6)_2$	$[4](PF_6)_2$
C^1	136.3	135.1	136.4	135.8
C^2	123.8	123.6	124.8	124.6
C^3	159.7	159.1	159.3	159.6
C^4	158.7	158.8	159.7	159.8
C^5	125.7	125.4	124.7	124.4
C^6	139.2	138.8	140.0	140.0
C^7	128.0	127.8	126.8	126.7
C^8	155.1	155.0	155.8	155.7
C^9	149.4	149.3	149.2	149.2
C^{10}	121.5	121.1	121.6	121.2
C^{11}	140.2	140.0	140.4	140.3
C^{12}	116.3	116.2	116.6	116.5
C^{13}	159.8	160.2	159.5	160.0
C^{14}	157.2	156.8	157.1	156.7
C^{15}	113.6	98.7	113.7	98.8
C^{16}	141.8	160.0	142.1	159.3
CO^{center}	164.9	165.0	165.2	164.8
CO^{outer}	-	-	164.8	164.4
NCH_3	41.8	41.4	41.7	41.3
$CH_2\underline{C}H_3^{center}$	14.6	14.5	-	14.6
$CH_2\underline{C}H_3^{outer}$	-	-	-	14.4
$\underline{C}H_2CH_3^{center}$	63.7	63.5	-	63.6
$\underline{C}H_2CH_3^{outer}$	-	-	-	63.5
OCH_3^{center}	-	-	54.1	-
OCH_3^{outer}	-	-	53.9	-

Table S6. ^{15}N NMR data of [1](PF_6)$_2$ – [4](PF_6)$_2$, 10 and 11 in CD_3CN, 41 MHz.

	[1](PF_6)$_2$	**[2](PF_6)$_2$**	**[3](PF_6)$_2$**	**[4](PF_6)$_2$**	**10**	**11**	EtOOC-tpy (in d_6-DMSO)
N^a	211.6	212.7	209.2	209.9	287.9	285.4	-
N^b	92.1	90.1	92.0	89.5	98.7	97.1	-
N^c	218.0	183.1	216.2	181.7	250.1	256.1	-
N^d	238.0	238.6	249.1	249.7	-	-	301.5
N^e	294.4	297.2	294.4	296.6	-	-	306.6
NH_2	-	72.1	-	72.7	-	-	-
phthalimide	-	-	-	-	169.0	-	-

Table S7. Crystal and structure refinement data for **[2](PF_6)$_2$** and **[3](PF_6)$_2$** from X-ray analysis.

	[2](PF_6)$_2$	**[3](PF_6)$_2$**
Empirical formula	$C_{37}H_{36}F_{12}N_{10}O_2P_2Ru$	$C_{44}H_{47}F_{12}N_9O_7P_2Ru$
Formula weight	1043.77	1204.92
Crystal color, habit	brown block	black block
Crystal dimensions / mm	0.43 x 0.20 x 0.17	0.25 x 0.11 x 0.11
Crystal system	triclinic	triclinic
Space group	$P\bar{1}$	$P\bar{1}$
a / Å	12.0041(5)	12.0767(3)
b / Å	13.4065(5)	15.4254(4)
c / Å	14.8818(6)	15.7197(4)
α / °	68.1070(10)	64.4150(10)
β / °	72.3710(10)	86.9760(10)
γ / °	73.7940(10)	69.4790(10)
V / Å^3	2080.16(14)	2456.73(11)
Z	2	2
F(000)	1052	1224
Density (calcd) / g cm^{-3}	1.666	1.629
Absorption coefficient μ / mm^{-1}	0.556 (MULABS)	0.490 (MULABS)
Theta range / °	1.51 – 27.97	2.45 – 27.98
Index ranges	$-15 \leq h \leq 15$	$-15 \leq h \leq 15$
	$-17 \leq k \leq 17$	$-20 \leq k \leq 17$
	$-19 \leq l \leq 19$	$-20 \leq l \leq 20$
Reflections collected	43817	45957
Independent reflections	9967 (R_{int} = 0.0373)	11811 (R_{int} = 0.0376)
Observed reflections	9967	11811
Parameters	585	841
Max. / min. transmission	0.910 / 0.875	0.9481 / 0.8873
Goodness-of-fit on F^2	1.019	0.944
Largest difference peak and hole / e Å^{-3}	0.837 / -0.398	0.453 / -0.331
R_1 (I>2σ(I))	0.0316	0.0300
R_1 (all data)	0.0414	0.0432
wR_2 (I>2σ(I))	0.0816	0.0704
wR_2 (all data)	0.0855	0.0745

Table S8. Bond lengths / Å and angles / ° of **[2](PF_6)$_2$** from X-ray crystal analysis.

Ru(1)-N(2)	1.9465(16)
Ru(1)-N(4)	2.0750(16)
Ru(1)-N(6)	2.0766(16)
Ru(1)-N(1)	2.0804(17)
Ru(1)-N(5)	2.0806(16)
Ru(1)-N(3)	2.0869(16)

N(1)-C(101)	1.348(3)
N(1)-C(105)	1.370(3)
N(2)-C(106)	1.366(3)
N(2)-C(110)	1.368(2)
N(3)-C(115)	1.343(3)
N(3)-C(111)	1.375(2)
N(4)-C(201)	1.354(3)
N(4)-C(205)	1.358(2)
N(5)-C(207)	1.362(2)
N(5)-C(211)	1.362(3)
N(6)-C(213)	1.350(3)
N(6)-C(217)	1.361(3)
N(7)-C(205)	1.403(3)
N(7)-C(207)	1.422(3)
N(7)-C(206)	1.479(2)
N(8)-C(213)	1.409(3)
N(8)-C(211)	1.416(2)
N(8)-C(212)	1.473(3)
N(9)-C(209)	1.364(3)
N(9)-H(9A)	0.8800
N(9)-H(9B)	0.8800
O(1)-C(116)	1.210(3)
O(2)-C(116)	1.323(3)
O(2)-C(117)	1.459(3)
C(101)-C(102)	1.390(3)
C(101)-H(101)	0.9500
C(102)-C(103)	1.378(4)
C(102)-H(102)	0.9500
C(103)-C(104)	1.388(3)
C(103)-H(103)	0.9500
C(104)-C(105)	1.384(3)
C(104)-H(104)	0.9500
C(105)-C(106)	1.481(3)
C(106)-C(107)	1.384(3)
C(107)-C(108)	1.394(3)
C(107)-H(107)	0.9500
C(108)-C(109)	1.399(3)
C(108)-C(116)	1.493(3)
C(109)-C(110)	1.380(3)
C(109)-H(109)	0.9500
C(110)-C(111)	1.480(3)
C(111)-C(112)	1.388(3)
C(112)-C(113)	1.378(3)
C(112)-H(112)	0.9500
C(113)-C(114)	1.382(3)
C(113)-H(113)	0.9500
C(114)-C(115)	1.388(3)
C(114)-H(114)	0.9500
C(115)-H(115)	0.9500
C(117)-C(118)	1.493(3)
C(117)-H(11A)	0.9900
C(117)-H(11B)	0.9900
C(118)-H(11C)	0.9800
C(118)-H(11D)	0.9800
C(118)-H(11E)	0.9800
C(201)-C(202)	1.372(3)

C(201)-H(201)	0.9500
C(202)-C(203)	1.387(3)
C(202)-H(202)	0.9500
C(203)-C(204)	1.376(3)
C(203)-H(203)	0.9500
C(204)-C(205)	1.397(3)
C(204)-H(204)	0.9500
C(206)-H(20A)	0.9800
C(206)-H(20B)	0.9800
C(206)-H(20C)	0.9800
C(207)-C(208)	1.372(3)
C(208)-C(209)	1.393(3)
C(208)-H(208)	0.9500
C(209)-C(210)	1.405(3)
C(210)-C(211)	1.376(3)
C(210)-H(210)	0.9500
C(212)-H(21A)	0.9800
C(212)-H(21B)	0.9800
C(212)-H(21C)	0.9800
C(213)-C(214)	1.404(3)
C(214)-C(215)	1.378(3)
C(214)-H(214)	0.9500
C(215)-C(216)	1.383(4)
C(215)-H(215)	0.9500
C(216)-C(217)	1.371(3)
C(216)-H(216)	0.9500
C(217)-H(217)	0.9500
P(1)-F(6)	1.571(2)
P(1)-F(4)	1.5809(19)
P(1)-F(5)	1.5899(19)
P(1)-F(2)	1.5952(17)
P(1)-F(3)	1.5961(18)
P(1)-F(1)	1.6037(16)
P(2)-F(10)	1.5770(18)
P(2)-F(12)	1.5845(18)
P(2)-F(9)	1.5905(17)
P(2)-F(7)	1.5956(17)
P(2)-F(11)	1.5980(16)
P(2)-F(8)	1.6127(17)
N(10)-C(300)	1.146(5)
C(300)-C(301)	1.418(5)
C(301)-H(30A)	0.9800
C(301)-H(30B)	0.9800
C(301)-H(30C)	0.9800
N(2)-Ru(1)-N(4)	92.88(7)
N(2)-Ru(1)-N(6)	92.02(6)
N(4)-Ru(1)-N(6)	174.83(6)
N(2)-Ru(1)-N(1)	79.80(7)
N(4)-Ru(1)-N(1)	91.53(6)
N(6)-Ru(1)-N(1)	90.94(7)
N(2)-Ru(1)-N(5)	178.19(7)
N(4)-Ru(1)-N(5)	87.33(6)
N(6)-Ru(1)-N(5)	87.83(6)
N(1)-Ru(1)-N(5)	98.39(6)
N(2)-Ru(1)-N(3)	79.74(7)

N(4)-Ru(1)-N(3)	90.38(6)
N(6)-Ru(1)-N(3)	88.88(6)
N(1)-Ru(1)-N(3)	159.53(7)
N(5)-Ru(1)-N(3)	102.05(6)
C(101)-N(1)-C(105)	117.89(18)
C(101)-N(1)-Ru(1)	128.94(15)
C(105)-N(1)-Ru(1)	113.13(13)
C(106)-N(2)-C(110)	121.29(17)
C(106)-N(2)-Ru(1)	119.25(13)
C(110)-N(2)-Ru(1)	119.39(14)
C(115)-N(3)-C(111)	117.73(17)
C(115)-N(3)-Ru(1)	129.36(14)
C(111)-N(3)-Ru(1)	112.90(13)
C(201)-N(4)-C(205)	117.78(17)
C(201)-N(4)-Ru(1)	121.55(13)
C(205)-N(4)-Ru(1)	120.62(14)
C(207)-N(5)-C(211)	116.83(17)
C(207)-N(5)-Ru(1)	121.21(14)
C(211)-N(5)-Ru(1)	121.82(12)
C(213)-N(6)-C(217)	118.09(17)
C(213)-N(6)-Ru(1)	121.02(13)
C(217)-N(6)-Ru(1)	120.63(14)
C(205)-N(7)-C(207)	122.30(17)
C(205)-N(7)-C(206)	116.09(17)
C(207)-N(7)-C(206)	115.46(17)
C(213)-N(8)-C(211)	122.15(17)
C(213)-N(8)-C(212)	116.24(17)
C(211)-N(8)-C(212)	115.65(16)
C(209)-N(9)-H(9A)	120.0
C(209)-N(9)-H(9B)	120.0
H(9A)-N(9)-H(9B)	120.0
C(116)-O(2)-C(117)	115.90(17)
N(1)-C(101)-C(102)	122.6(2)
N(1)-C(101)-H(101)	118.7
C(102)-C(101)-H(101)	118.7
C(103)-C(102)-C(101)	119.1(2)
C(103)-C(102)-H(102)	120.5
C(101)-C(102)-H(102)	120.5
C(102)-C(103)-C(104)	119.2(2)
C(102)-C(103)-H(103)	120.4
C(104)-C(103)-H(103)	120.4
C(105)-C(104)-C(103)	119.4(2)
C(105)-C(104)-H(104)	120.3
C(103)-C(104)-H(104)	120.3
N(1)-C(105)-C(104)	121.74(19)
N(1)-C(105)-C(106)	114.95(18)
C(104)-C(105)-C(106)	123.21(19)
N(2)-C(106)-C(107)	120.03(18)
N(2)-C(106)-C(105)	112.62(17)
C(107)-C(106)-C(105)	127.10(19)
C(106)-C(107)-C(108)	119.2(2)
C(106)-C(107)-H(107)	120.4
C(108)-C(107)-H(107)	120.4
C(107)-C(108)-C(109)	120.24(19)
C(107)-C(108)-C(116)	121.9(2)
C(109)-C(108)-C(116)	117.79(19)

C(110)-C(109)-C(108)	118.98(19)
C(110)-C(109)-H(109)	120.5
C(108)-C(109)-H(109)	120.5
N(2)-C(110)-C(109)	120.24(19)
N(2)-C(110)-C(111)	112.53(17)
C(109)-C(110)-C(111)	127.21(18)
N(3)-C(111)-C(112)	121.51(19)
N(3)-C(111)-C(110)	115.11(17)
C(112)-C(111)-C(110)	123.31(19)
C(113)-C(112)-C(111)	119.8(2)
C(113)-C(112)-H(112)	120.1
C(111)-C(112)-H(112)	120.1
C(112)-C(113)-C(114)	118.8(2)
C(112)-C(113)-H(113)	120.6
C(114)-C(113)-H(113)	120.6
C(113)-C(114)-C(115)	119.3(2)
C(113)-C(114)-H(114)	120.4
C(115)-C(114)-H(114)	120.4
N(3)-C(115)-C(114)	122.8(2)
N(3)-C(115)-H(115)	118.6
C(114)-C(115)-H(115)	118.6
O(1)-C(116)-O(2)	124.9(2)
O(1)-C(116)-C(108)	122.8(2)
O(2)-C(116)-C(108)	112.30(19)
O(2)-C(117)-C(118)	107.26(19)
O(2)-C(117)-H(11A)	110.3
C(118)-C(117)-H(11A)	110.3
O(2)-C(117)-H(11B)	110.3
C(118)-C(117)-H(11B)	110.3
H(11A)-C(117)-H(11B)	108.5
C(117)-C(118)-H(11C)	109.5
C(117)-C(118)-H(11D)	109.5
H(11C)-C(118)-H(11D)	109.5
C(117)-C(118)-H(11E)	109.5
H(11C)-C(118)-H(11E)	109.5
H(11D)-C(118)-H(11E)	109.5
N(4)-C(201)-C(202)	124.00(19)
N(4)-C(201)-H(201)	118.0
C(202)-C(201)-H(201)	118.0
C(201)-C(202)-C(203)	117.9(2)
C(201)-C(202)-H(202)	121.1
C(203)-C(202)-H(202)	121.1
C(204)-C(203)-C(202)	119.5(2)
C(204)-C(203)-H(203)	120.2
C(202)-C(203)-H(203)	120.2
C(203)-C(204)-C(205)	119.9(2)
C(203)-C(204)-H(204)	120.1
C(205)-C(204)-H(204)	120.1
N(4)-C(205)-C(204)	120.9(2)
N(4)-C(205)-N(7)	118.37(17)
C(204)-C(205)-N(7)	120.72(18)
N(7)-C(206)-H(20A)	109.5
N(7)-C(206)-H(20B)	109.5
H(20A)-C(206)-H(20B)	109.5
N(7)-C(206)-H(20C)	109.5
H(20A)-C(206)-H(20C)	109.5

H(20B)-C(206)-H(20C)	109.5
N(5)-C(207)-C(208)	123.4(2)
N(5)-C(207)-N(7)	117.05(17)
C(208)-C(207)-N(7)	119.52(17)
C(207)-C(208)-C(209)	119.52(19)
C(207)-C(208)-H(208)	120.2
C(209)-C(208)-H(208)	120.2
N(9)-C(209)-C(208)	121.0(2)
N(9)-C(209)-C(210)	121.3(2)
C(208)-C(209)-C(210)	117.75(19)
C(211)-C(210)-C(209)	119.6(2)
C(211)-C(210)-H(210)	120.2
C(209)-C(210)-H(210)	120.2
N(5)-C(211)-C(210)	122.87(18)
N(5)-C(211)-N(8)	117.20(17)
C(210)-C(211)-N(8)	119.93(19)
N(8)-C(212)-H(21A)	109.5
N(8)-C(212)-H(21B)	109.5
H(21A)-C(212)-H(21B)	109.5
N(8)-C(212)-H(21C)	109.5
H(21A)-C(212)-H(21C)	109.5
H(21B)-C(212)-H(21C)	109.5
N(6)-C(213)-C(214)	120.85(19)
N(6)-C(213)-N(8)	118.79(17)
C(214)-C(213)-N(8)	120.3(2)
C(215)-C(214)-C(213)	119.6(2)
C(215)-C(214)-H(214)	120.2
C(213)-C(214)-H(214)	120.2
C(214)-C(215)-C(216)	119.5(2)
C(214)-C(215)-H(215)	120.2
C(216)-C(215)-H(215)	120.2
C(217)-C(216)-C(215)	118.3(2)
C(217)-C(216)-H(216)	120.9
C(215)-C(216)-H(216)	120.9
N(6)-C(217)-C(216)	123.5(2)
N(6)-C(217)-H(217)	118.3
C(216)-C(217)-H(217)	118.3
F(6)-P(1)-F(4)	92.00(13)
F(6)-P(1)-F(5)	92.28(13)
F(4)-P(1)-F(5)	91.68(11)
F(6)-P(1)-F(2)	90.12(13)
F(4)-P(1)-F(2)	177.40(11)
F(5)-P(1)-F(2)	89.74(11)
F(6)-P(1)-F(3)	177.87(13)
F(4)-P(1)-F(3)	89.25(11)
F(5)-P(1)-F(3)	89.41(12)
F(2)-P(1)-F(3)	88.59(10)
F(6)-P(1)-F(1)	89.80(11)
F(4)-P(1)-F(1)	88.94(10)
F(5)-P(1)-F(1)	177.81(12)
F(2)-P(1)-F(1)	89.55(9)
F(3)-P(1)-F(1)	88.50(9)
F(10)-P(2)-F(12)	92.45(12)
F(10)-P(2)-F(9)	91.37(10)
F(12)-P(2)-F(9)	90.93(11)
F(10)-P(2)-F(7)	90.30(11)

F(12)-P(2)-F(7)	177.23(12)
F(9)-P(2)-F(7)	89.39(10)
F(10)-P(2)-F(11)	89.93(10)
F(12)-P(2)-F(11)	89.58(11)
F(9)-P(2)-F(11)	178.58(10)
F(7)-P(2)-F(11)	90.04(10)
F(10)-P(2)-F(8)	179.28(12)
F(12)-P(2)-F(8)	88.25(11)
F(9)-P(2)-F(8)	88.80(10)
F(7)-P(2)-F(8)	89.01(10)
F(11)-P(2)-F(8)	89.89(10)
N(10)-C(300)-C(301)	176.3(4)
C(300)-C(301)-H(30A)	109.5
C(300)-C(301)-H(30B)	109.5
H(30A)-C(301)-H(30B)	109.5
C(300)-C(301)-H(30C)	109.5
H(30A)-C(301)-H(30C)	109.5
H(30B)-C(301)-H(30C)	109.5

Table S9. Bond lengths / Å and angles / ° of **[3](PF$_6$)$_2$** from X-ray crystal analysis.

Ru(1)-N(2)	1.9481(14)
Ru(1)-N(1)	2.0777(15)
Ru(1)-N(8)	2.0784(15)
Ru(1)-N(4)	2.0800(15)
Ru(1)-N(6)	2.0858(15)
Ru(1)-N(3)	2.0921(15)
O(1)-C(4)	1.199(2)
O(2)-C(4)	1.328(2)
O(2)-C(5)	1.457(2)
N(1)-C(1)	1.349(2)
N(1)-C(7)	1.371(2)
N(2)-C(14)	1.359(2)
N(2)-C(8)	1.364(2)
N(3)-C(21)	1.344(2)
N(3)-C(15)	1.381(2)
N(4)-C(22)	1.352(2)
N(4)-C(26)	1.353(2)
N(5)-C(26)	1.409(2)
N(5)-C(28)	1.415(3)
N(5)-C(27)	1.471(3)
N(6)-C(32)	1.354(2)
N(6)-C(28)	1.358(2)
N(7)-C(34)	1.412(2)
N(7)-C(32)	1.412(3)
N(7)-C(33)	1.472(3)
N(8)-C(34)	1.345(2)
N(8)-C(38)	1.360(2)
C(1)-C(2)	1.383(3)
C(1)-H(1A)	0.9500
C(2)-C(3)	1.388(3)
C(2)-H(2A)	0.9500
C(3)-C(6)	1.388(3)
C(3)-C(4)	1.502(3)
C(5)-H(5A)	0.9800
C(5)-H(5B)	0.9800

C(5)-H(5C)	0.9800
C(6)-C(7)	1.387(3)
C(6)-H(6A)	0.9500
C(7)-C(8)	1.471(3)
C(8)-C(9)	1.371(3)
C(9)-C(10)	1.393(3)
C(9)-H(9A)	0.9500
C(10)-C(13)	1.389(3)
C(10)-C(11)	1.499(2)
C(11)-O(3)	1.195(2)
C(11)-O(4)	1.331(2)
O(4)-C(12)	1.448(2)
C(12)-H(12A)	0.9800
C(12)-H(12B)	0.9800
C(12)-H(12C)	0.9800
C(13)-C(14)	1.385(2)
C(13)-H(13A)	0.9500
C(14)-C(15)	1.474(3)
C(15)-C(16)	1.380(3)
C(16)-C(17)	1.383(3)
C(16)-H(16A)	0.9500
C(17)-C(20)	1.382(3)
C(17)-C(18)	1.508(4)
C(17)-C(18A)	1.518(9)
C(18)-O(5)	1.196(2)
C(18)-O(6)	1.332(2)
O(6)-C(19)	1.449(2)
C(19)-H(19A)	0.9800
C(19)-H(19B)	0.9800
C(19)-H(19C)	0.9800
C(18A)-O(5A)	1.196(2)
C(18A)-O(6A)	1.332(2)
O(6A)-C(19A)	1.448(2)
C(19A)-H(19D)	0.9800
C(19A)-H(19E)	0.9800
C(19A)-H(19F)	0.9800
C(20)-C(21)	1.391(3)
C(20)-H(20A)	0.9500
C(21)-H(21A)	0.9500
C(22)-C(23)	1.373(3)
C(22)-H(22A)	0.9500
C(23)-C(24)	1.382(3)
C(23)-H(23A)	0.9500
C(24)-C(25)	1.373(3)
C(24)-H(24A)	0.9500
C(25)-C(26)	1.393(3)
C(25)-H(25A)	0.9500
C(27)-H(27A)	0.9800
C(27)-H(27B)	0.9800
C(27)-H(27C)	0.9800
C(28)-C(29)	1.387(3)
C(29)-C(30)	1.368(3)
C(29)-H(29A)	0.9500
C(30)-C(31)	1.375(3)
C(30)-H(30A)	0.9500
C(31)-C(32)	1.391(3)

C(31)-H(31A)	0.9500
C(33)-H(33A)	0.9800
C(33)-H(33B)	0.9800
C(33)-H(33C)	0.9800
C(34)-C(35)	1.402(3)
C(35)-C(36)	1.370(3)
C(35)-H(35A)	0.9500
C(36)-C(37)	1.378(3)
C(36)-H(36A)	0.9500
C(37)-C(38)	1.370(3)
C(37)-H(37A)	0.9500
C(38)-H(38A)	0.9500
P(1)-F(4)	1.574(2)
P(1)-F(3)	1.586(2)
P(1)-F(1)	1.5881(19)
P(1)-F(6)	1.5973(19)
P(1)-F(2)	1.598(2)
P(1)-F(5)	1.604(2)
P(1A)-F(4A)	1.574(2)
P(1A)-F(3A)	1.586(2)
P(1A)-F(1A)	1.588(2)
P(1A)-F(6A)	1.597(2)
P(1A)-F(2A)	1.598(2)
P(1A)-F(5A)	1.604(2)
P(2)-F(9)	1.513(5)
P(2)-F(8)	1.536(4)
P(2)-F(12)	1.566(6)
P(2)-F(11)	1.595(4)
P(2)-F(10)	1.609(4)
P(2)-F(7)	1.619(7)
P(2A)-F(10A)	1.402(12)
P(2A)-F(7A)	1.38(2)
P(2A)-F(9A)	1.538(12)
P(2A)-F(11A)	1.590(12)
P(2A)-F(12A)	1.635(14)
P(2A)-F(8A)	1.668(12)
O(10)-C(41)	1.417(3)
O(10)-C(40)	1.422(3)
C(39)-C(40)	1.495(4)
C(39)-H(39A)	0.9800
C(39)-H(39B)	0.9800
C(39)-H(39C)	0.9800
C(40)-H(40A)	0.9900
C(40)-H(40B)	0.9900
C(41)-C(42)	1.504(4)
C(41)-H(41A)	0.9900
C(41)-H(41B)	0.9900
C(42)-H(42A)	0.9800
C(42)-H(42B)	0.9800
C(42)-H(42C)	0.9800
N(9)-C(44)	1.125(4)
C(43)-C(44)	1.438(4)
C(43)-H(43A)	0.9800
C(43)-H(43B)	0.9800
C(43)-H(43C)	0.9800

N(2)-Ru(1)-N(1)	79.84(6)
N(2)-Ru(1)-N(8)	93.08(6)
N(1)-Ru(1)-N(8)	89.97(6)
N(2)-Ru(1)-N(4)	92.05(6)
N(1)-Ru(1)-N(4)	92.08(6)
N(8)-Ru(1)-N(4)	174.74(6)
N(2)-Ru(1)-N(6)	177.18(6)
N(1)-Ru(1)-N(6)	97.43(6)
N(8)-Ru(1)-N(6)	87.59(6)
N(4)-Ru(1)-N(6)	87.34(6)
N(2)-Ru(1)-N(3)	79.31(6)
N(1)-Ru(1)-N(3)	159.10(6)
N(8)-Ru(1)-N(3)	89.80(6)
N(4)-Ru(1)-N(3)	90.00(6)
N(6)-Ru(1)-N(3)	103.44(6)
C(4)-O(2)-C(5)	115.64(18)
C(1)-N(1)-C(7)	117.70(16)
C(1)-N(1)-Ru(1)	129.52(12)
C(7)-N(1)-Ru(1)	112.73(12)
C(14)-N(2)-C(8)	120.91(15)
C(14)-N(2)-Ru(1)	120.10(12)
C(8)-N(2)-Ru(1)	118.98(12)
C(21)-N(3)-C(15)	117.11(16)
C(21)-N(3)-Ru(1)	130.17(13)
C(15)-N(3)-Ru(1)	112.71(11)
C(22)-N(4)-C(26)	117.40(16)
C(22)-N(4)-Ru(1)	122.10(13)
C(26)-N(4)-Ru(1)	120.49(13)
C(26)-N(5)-C(28)	121.22(16)
C(26)-N(5)-C(27)	115.79(17)
C(28)-N(5)-C(27)	116.66(17)
C(32)-N(6)-C(28)	118.19(16)
C(32)-N(6)-Ru(1)	121.50(13)
C(28)-N(6)-Ru(1)	120.20(13)
C(34)-N(7)-C(32)	121.66(16)
C(34)-N(7)-C(33)	115.71(17)
C(32)-N(7)-C(33)	115.80(16)
C(34)-N(8)-C(38)	117.85(16)
C(34)-N(8)-Ru(1)	121.45(12)
C(38)-N(8)-Ru(1)	120.59(13)
N(1)-C(1)-C(2)	122.74(17)
N(1)-C(1)-H(1A)	118.6
C(2)-C(1)-H(1A)	118.6
C(1)-C(2)-C(3)	119.48(18)
C(1)-C(2)-H(2A)	120.3
C(3)-C(2)-H(2A)	120.3
C(2)-C(3)-C(6)	118.35(17)
C(2)-C(3)-C(4)	123.74(18)
C(6)-C(3)-C(4)	117.89(18)
O(1)-C(4)-O(2)	125.59(19)
O(1)-C(4)-C(3)	122.97(19)
O(2)-C(4)-C(3)	111.43(18)
O(2)-C(5)-H(5A)	109.5
O(2)-C(5)-H(5B)	109.5
H(5A)-C(5)-H(5B)	109.5
O(2)-C(5)-H(5C)	109.5

H(5A)-C(5)-H(5C)	109.5
H(5B)-C(5)-H(5C)	109.5
C(7)-C(6)-C(3)	119.76(18)
C(7)-C(6)-H(6A)	120.1
C(3)-C(6)-H(6A)	120.1
N(1)-C(7)-C(6)	121.66(17)
N(1)-C(7)-C(8)	115.33(16)
C(6)-C(7)-C(8)	122.97(17)
N(2)-C(8)-C(9)	120.28(17)
N(2)-C(8)-C(7)	112.73(16)
C(9)-C(8)-C(7)	126.73(17)
C(8)-C(9)-C(10)	119.57(17)
C(8)-C(9)-H(9A)	120.2
C(10)-C(9)-H(9A)	120.2
C(13)-C(10)-C(9)	119.85(17)
C(13)-C(10)-C(11)	118.90(17)
C(9)-C(10)-C(11)	121.24(17)
O(3)-C(11)-O(4)	125.45(16)
O(3)-C(11)-C(10)	123.65(17)
O(4)-C(11)-C(10)	110.88(16)
C(11)-O(4)-C(12)	116.29(16)
O(4)-C(12)-H(12A)	109.5
O(4)-C(12)-H(12B)	109.5
H(12A)-C(12)-H(12B)	109.5
O(4)-C(12)-H(12C)	109.5
H(12A)-C(12)-H(12C)	109.5
H(12B)-C(12)-H(12C)	109.5
C(14)-C(13)-C(10)	118.96(17)
C(14)-C(13)-H(13A)	120.5
C(10)-C(13)-H(13A)	120.5
N(2)-C(14)-C(13)	120.40(16)
N(2)-C(14)-C(15)	112.48(15)
C(13)-C(14)-C(15)	127.10(17)
C(16)-C(15)-N(3)	121.88(17)
C(16)-C(15)-C(14)	122.94(17)
N(3)-C(15)-C(14)	115.16(16)
C(15)-C(16)-C(17)	120.03(18)
C(15)-C(16)-H(16A)	120.0
C(17)-C(16)-H(16A)	120.0
C(20)-C(17)-C(16)	118.53(18)
C(20)-C(17)-C(18)	127.3(2)
C(16)-C(17)-C(18)	114.1(2)
C(20)-C(17)-C(18A)	109.0(4)
C(16)-C(17)-C(18A)	132.5(4)
C(18)-C(17)-C(18A)	18.4(4)
O(5)-C(18)-O(6)	125.0(2)
O(5)-C(18)-C(17)	125.6(3)
O(6)-C(18)-C(17)	109.4(2)
C(18)-O(6)-C(19)	115.7(2)
O(6)-C(19)-H(19A)	109.5
O(6)-C(19)-H(19B)	109.5
H(19A)-C(19)-H(19B)	109.5
O(6)-C(19)-H(19C)	109.5
H(19A)-C(19)-H(19C)	109.5
H(19B)-C(19)-H(19C)	109.5
O(5A)-C(18A)-O(6A)	125.3(2)

O(5A)-C(18A)-C(17)	129.4(6)
O(6A)-C(18A)-C(17)	105.2(6)
C(18A)-O(6A)-C(19A)	116.0(2)
O(6A)-C(19A)-H(19D)	109.5
O(6A)-C(19A)-H(19E)	109.5
H(19D)-C(19A)-H(19E)	109.5
O(6A)-C(19A)-H(19F)	109.5
H(19D)-C(19A)-H(19F)	109.5
H(19E)-C(19A)-H(19F)	109.5
C(17)-C(20)-C(21)	119.28(18)
C(17)-C(20)-H(20A)	120.4
C(21)-C(20)-H(20A)	120.4
N(3)-C(21)-C(20)	123.08(18)
N(3)-C(21)-H(21A)	118.5
C(20)-C(21)-H(21A)	118.5
N(4)-C(22)-C(23)	123.84(19)
N(4)-C(22)-H(22A)	118.1
C(23)-C(22)-H(22A)	118.1
C(22)-C(23)-C(24)	118.2(2)
C(22)-C(23)-H(23A)	120.9
C(24)-C(23)-H(23A)	120.9
C(25)-C(24)-C(23)	119.3(2)
C(25)-C(24)-H(24A)	120.3
C(23)-C(24)-H(24A)	120.3
C(24)-C(25)-C(26)	119.7(2)
C(24)-C(25)-H(25A)	120.2
C(26)-C(25)-H(25A)	120.2
N(4)-C(26)-C(25)	121.50(18)
N(4)-C(26)-N(5)	117.52(17)
C(25)-C(26)-N(5)	120.95(18)
N(5)-C(27)-H(27A)	109.5
N(5)-C(27)-H(27B)	109.5
H(27A)-C(27)-H(27B)	109.5
N(5)-C(27)-H(27C)	109.5
H(27A)-C(27)-H(27C)	109.5
H(27B)-C(27)-H(27C)	109.5
N(6)-C(28)-C(29)	122.04(19)
N(6)-C(28)-N(5)	117.37(16)
C(29)-C(28)-N(5)	120.58(18)
C(30)-C(29)-C(28)	118.8(2)
C(30)-C(29)-H(29A)	120.6
C(28)-C(29)-H(29A)	120.6
C(29)-C(30)-C(31)	120.44(19)
C(29)-C(30)-H(30A)	119.8
C(31)-C(30)-H(30A)	119.8
C(30)-C(31)-C(32)	118.6(2)
C(30)-C(31)-H(31A)	120.7
C(32)-C(31)-H(31A)	120.7
N(6)-C(32)-C(31)	121.90(19)
N(6)-C(32)-N(7)	117.66(16)
C(31)-C(32)-N(7)	120.44(18)
N(7)-C(33)-H(33A)	109.5
N(7)-C(33)-H(33B)	109.5
H(33A)-C(33)-H(33B)	109.5
N(7)-C(33)-H(33C)	109.5
H(33A)-C(33)-H(33C)	109.5

H(33B)-C(33)-H(33C)	109.5
N(8)-C(34)-C(35)	121.21(18)
N(8)-C(34)-N(7)	118.32(17)
C(35)-C(34)-N(7)	120.43(18)
C(36)-C(35)-C(34)	119.4(2)
C(36)-C(35)-H(35A)	120.3
C(34)-C(35)-H(35A)	120.3
C(35)-C(36)-C(37)	119.9(2)
C(35)-C(36)-H(36A)	120.0
C(37)-C(36)-H(36A)	120.0
C(38)-C(37)-C(36)	118.14(19)
C(38)-C(37)-H(37A)	120.9
C(36)-C(37)-H(37A)	120.9
N(8)-C(38)-C(37)	123.48(19)
N(8)-C(38)-H(38A)	118.3
C(37)-C(38)-H(38A)	118.3
F(4)-P(1)-F(3)	91.47(14)
F(4)-P(1)-F(1)	91.13(17)
F(3)-P(1)-F(1)	89.86(12)
F(4)-P(1)-F(6)	89.95(16)
F(3)-P(1)-F(6)	90.52(13)
F(1)-P(1)-F(6)	178.84(17)
F(4)-P(1)-F(2)	178.42(13)
F(3)-P(1)-F(2)	89.90(13)
F(1)-P(1)-F(2)	89.67(14)
F(6)-P(1)-F(2)	89.24(14)
F(4)-P(1)-F(5)	88.87(15)
F(3)-P(1)-F(5)	179.53(17)
F(1)-P(1)-F(5)	90.46(11)
F(6)-P(1)-F(5)	89.16(12)
F(2)-P(1)-F(5)	89.76(15)
F(4A)-P(1A)-F(3A)	91.47(15)
F(4A)-P(1A)-F(1A)	91.12(17)
F(3A)-P(1A)-F(1A)	89.86(13)
F(4A)-P(1A)-F(6A)	89.96(16)
F(3A)-P(1A)-F(6A)	90.52(13)
F(1A)-P(1A)-F(6A)	178.84(17)
F(4A)-P(1A)-F(2A)	178.43(14)
F(3A)-P(1A)-F(2A)	89.90(14)
F(1A)-P(1A)-F(2A)	89.66(14)
F(6A)-P(1A)-F(2A)	89.24(14)
F(4A)-P(1A)-F(5A)	88.87(16)
F(3A)-P(1A)-F(5A)	179.54(16)
F(1A)-P(1A)-F(5A)	90.46(12)
F(6A)-P(1A)-F(5A)	89.16(12)
F(2A)-P(1A)-F(5A)	89.76(15)
F(9)-P(2)-F(8)	94.5(3)
F(9)-P(2)-F(12)	89.1(4)
F(8)-P(2)-F(12)	89.7(3)
F(9)-P(2)-F(11)	176.5(4)
F(8)-P(2)-F(11)	88.7(3)
F(12)-P(2)-F(11)	89.5(3)
F(9)-P(2)-F(10)	88.3(3)
F(8)-P(2)-F(10)	177.2(4)
F(12)-P(2)-F(10)	90.7(3)
F(11)-P(2)-F(10)	88.5(3)

F(9)-P(2)-F(7)	88.5(3)
F(8)-P(2)-F(7)	88.1(3)
F(12)-P(2)-F(7)	176.6(4)
F(11)-P(2)-F(7)	93.1(3)
F(10)-P(2)-F(7)	91.6(3)
F(10A)-P(2A)-F(7A)	85.5(13)
F(10A)-P(2A)-F(9A)	94.6(10)
F(7A)-P(2A)-F(9A)	92.0(11)
F(10A)-P(2A)-F(11A)	97.8(11)
F(7A)-P(2A)-F(11A)	91.1(11)
F(9A)-P(2A)-F(11A)	167.5(12)
F(10A)-P(2A)-F(12A)	88.6(9)
F(7A)-P(2A)-F(12A)	173.2(14)
F(9A)-P(2A)-F(12A)	91.8(7)
F(11A)-P(2A)-F(12A)	86.3(7)
F(10A)-P(2A)-F(8A)	177.5(10)
F(7A)-P(2A)-F(8A)	97.0(13)
F(9A)-P(2A)-F(8A)	85.0(10)
F(11A)-P(2A)-F(8A)	82.6(8)
F(12A)-P(2A)-F(8A)	88.9(7)
C(41)-O(10)-C(40)	113.1(2)
C(40)-C(39)-H(39A)	109.5
C(40)-C(39)-H(39B)	109.5
H(39A)-C(39)-H(39B)	109.5
C(40)-C(39)-H(39C)	109.5
H(39A)-C(39)-H(39C)	109.5
H(39B)-C(39)-H(39C)	109.5
O(10)-C(40)-C(39)	109.5(2)
O(10)-C(40)-H(40A)	109.8
C(39)-C(40)-H(40A)	109.8
O(10)-C(40)-H(40B)	109.8
C(39)-C(40)-H(40B)	109.8
H(40A)-C(40)-H(40B)	108.2
O(10)-C(41)-C(42)	110.8(2)
O(10)-C(41)-H(41A)	109.5
C(42)-C(41)-H(41A)	109.5
O(10)-C(41)-H(41B)	109.5
C(42)-C(41)-H(41B)	109.5
H(41A)-C(41)-H(41B)	108.1
C(41)-C(42)-H(42A)	109.5
C(41)-C(42)-H(42B)	109.5
H(42A)-C(42)-H(42B)	109.5
C(41)-C(42)-H(42C)	109.5
H(42A)-C(42)-H(42C)	109.5
H(42B)-C(42)-H(42C)	109.5
C(44)-C(43)-H(43A)	109.5
C(44)-C(43)-H(43B)	109.5
H(43A)-C(43)-H(43B)	109.5
C(44)-C(43)-H(43C)	109.5
H(43A)-C(43)-H(43C)	109.5
H(43B)-C(43)-H(43C)	109.5
N(9)-C(44)-C(43)	177.4(4)

	Ru-N1	Ru-N2	Ru-N3	Ru-N4	Ru-N5	Ru-N6	N1-Ru-N2	N2-Ru-N3	N4-Ru-N5	N5-Ru-N6	N1-C-C-N2	N2-C-C-N3
[1]$^{2+}$ - ^{1}GS	2.12	1.98	2.12	2.12	2.11	2.12	79.2	79.2	87.6	87.6	-1.4	-1.4
[1]$^{2+}$ - ^{3}MLCT	2.12	2.01	2.12	2.12	2.09	2.10	78.0	77.9	88.2	88.2	-1.5	-2.4
[1]$^{2+}$ - ^{3}TS	2.31	2.16	2.30	2.15	2.10	2.11	72.7	73.2	87.1	88.2	10.9	-17.9
[1]$^{2+}$ - ^{3}MC	2.36	2.23	2.38	2.13	2.11	2.11	71.1	71.2	87.9	87.9	1.9	-14.3
[2]$^{2+}$ - ^{1}GS	2.11	1.98	2.12	2.12	2.11	2.12	79.3	79.3	87.3	87.3	-1.3	-1.2
[2]$^{2+}$ - ^{3}MLCT	2.12	2.02	2.12	2.11	2.06	2.11	77.5	77.5	88.6	88.6	-1.8	-1.9
[2]$^{2+}$ - ^{3}TS	2.33	2.19	2.33	2.14	2.09	2.11	72.1	72.4	87.3	88.1	9.5	-17.9
[2]$^{2+}$ - ^{3}MC	2.37	2.23	2.38	2.12	2.09	2.11	71.0	71.2	87.4	87.7	-0.8	-13.6
[3]$^{2+}$ - ^{1}GS	2.11	1.98	2.11	2.12	2.11	2.12	79.3	79.3	87.6	87.5	-1.3	-1.2
[3]$^{2+}$ - ^{3}MLCT	2.11	2.02	2.11	2.12	2.09	2.10	77.9	77.8	88.2	88.3	-1.0	-2.8
[3]$^{2+}$ - ^{3}TS	2.35	2.19	2.35	2.14	2.10	2.11	71.3	71.8	87.1	87.6	3.3	-16.8
[3]$^{2+}$ - ^{3}MC	2.35	2.23	2.38	2.13	2.11	2.11	70.8	71.1	87.3	87.8	1.1	-14.1
[4]$^{2+}$ - ^{1}GS	2.11	1.98	2.11	2.12	2.11	2.12	79.3	79.4	87.3	87.3	-1.1	-0.9
[4]$^{2+}$ - ^{3}MLCT	2.11	2.03	2.11	2.11	2.05	2.11	77.5	77.5	88.6	88.6	-1.7	-1.7
[4]$^{2+}$ - ^{3}TS	n. a.	n. a.	n. a.	n. a.	n. a.	n. a.	n. a.	n. a.	n. a.	n. a.	n. a.	n. a.
[4]$^{2+}$ - ^{3}MC	n. a.	n. a.	n. a.	n. a.	n. a.	n. a.	n. a.	n. a.	n. a.	n. a.	n. a.	n. a.
[5]$^{2+}$ - ^{1}GS	2.11	2.01	2.11	2.11	2.01	2.11	78.9	78.9	78.9	78.9	0.0	0.0
[5]$^{2+}$ - ^{3}MLCT	2.10	2.05	2.10	2.12	1.98	2.10	77.6	77.6	79.7	79.5	-0.4	0.4
[5]$^{2+}$ - ^{3}TS	2.20	2.07	2.15	2.11	2.02	2.18	75.4	76.0	79.5	77.4	-10.6	11.2
[5]$^{2+}$ - ^{3}MC	2.36	2.16	2.35	2.14	2.01	2.15	72.6	72.6	79.2	77.8	-10.6	10.6
[6]$^{2+}$ - ^{1}GS	2.10	2.00	2.10	2.11	2.01	2.11	79.0	79.0	78.8	78.8	0.0	0.0
[6]$^{2+}$ - ^{3}MLCT	2.10	2.02	2.10	2.10	2.02	2.12	77.8	77.9	79.0	79.9	1.3	-1.7
[6]$^{2+}$ - ^{3}TS	2.25	2.10	2.25	2.18	2.02	2.13	74.3	74.5	77.4	79.4	12.2	-12.7
[6]$^{2+}$ - ^{3}MC	2.34	2.14	2.34	2.16	2.02	2.14	72.9	73.0	77.7	79.2	10.9	-11.0
[7]$^{2+}$ - ^{1}GS	2.10	1.99	2.10	2.11	2.02	2.11	79.2	79.2	78.4	78.4	0.0	0.0
[7]$^{2+}$ - ^{3}MLCT	2.11	2.04	2.10	2.11	1.99	2.12	77.0	77.1	79.4	79.8	0.3	-0.3
[7]$^{2+}$ - ^{3}TS	2.29	2.15	2.30	2.15	2.01	2.13	72.9	72.9	77.8	79.2	12.6	-12.8
[7]$^{2+}$ - ^{3}MC	2.33	2.17	2.33	2.14	2.01	2.13	72.2	72.3	77.9	79.1	11.2	-11.4

Table S10. Selected bond lengths / Å and angles / ° of DFT (B3LYP/LANL2DZ, IEFPCM in CH_3CN) calculated singlet ground state (^{1}GS) and triplet excited states (^{3}MLCT, ^{3}MC, ^{3}TS) of **[1]**$^{2+}$ – **[7]**$^{2+}$.

Table S11. Selected Mulliken spin densities of DFT (B3LYP/LANL2DZ, IEFPCM in CH_3CN) calculated triplet excited states (^{3}MLCT, ^{3}MC, ^{3}TS) of **[1]**$^{2+}$ – **[7]**$^{2+}$.

	Ru	ligand 1	ligand 2
		tpy	ddpd or second tpy
[1]$^{2+}$ - ^{3}MLCT	0.89	1.04	0.07
[1]$^{2+}$ - ^{3}TS	1.60	0.38	0.02
[1]$^{2+}$ - ^{3}MC	1.80	0.19	0.01
[2]$^{2+}$ - ^{3}MLCT	0.86	1.03	0.11
[2]$^{2+}$ - ^{3}TS	1.67	0.30	0.03
[2]$^{2+}$ - ^{3}MC	1.81	0.17	0.02
[3]$^{2+}$ - ^{3}MLCT	0.89	1.04	0.07
[3]$^{2+}$ - ^{3}TS	1.72	0.27	0.01
[3]$^{2+}$ - ^{3}MC	1.78	0.21	0.01
[4]$^{2+}$ - ^{3}MLCT	0.85	1.03	0.12
[4]$^{2+}$ - ^{3}TS	n. a.	n. a.	n. a.
[4]$^{2+}$ - ^{3}MC	n. a.	n. a.	n. a.
[5]$^{2+}$ - ^{3}MLCT	0.86	0.05	1.09
[5]$^{2+}$ - ^{3}TS	1.31	0.60	0.09
[5]$^{2+}$ - ^{3}MC	1.75	0.21	0.04
[6]$^{2+}$ - ^{3}MLCT	0.91	1.05	0.04
[6]$^{2+}$ - ^{3}TS	1.50	0.44	0.06
[6]$^{2+}$ - ^{3}MC	1.73	0.22	0.05
[7]$^{2+}$ - ^{3}MLCT	0.85	1.02	0.13
[7]$^{2+}$ - ^{3}TS	1.59	0.33	0.08
[7]$^{2+}$ - ^{3}MC	1.69	0.24	0.07

10.7 Push-Pull Design of Bis(tridentate) Ruthenium(II) Polypyridine Chromophores as Deep Red Light Emitters in Light-Emitting Electrochemical Cells

A. Breivogel, M. Park, D. Lee, S. Klassen, A. Kühnle, C. Lee, K. Char, K. Heinze, *Eur. J. Inorg. Chem.* **2014**, 288–295.

DOI: 10.1002/ejic.201301226

Eur. J. Inorg. Chem. **2013** · © WILEY-VCH Verlag GmbH & Co. KGaA, 69451 Weinheim, 2013 · ISSN 1099–0682

SUPPORTING INFORMATION

DOI: 10.1002/ejic.201301226

Title: Push-Pull Design of Bis(tridentate) Ruthenium(II) Polypyridine Chromophores as Deep Red Light Emitters in Light-Emitting Electrochemical Cells

Author(s): Aaron Breivogel, Myeongjin Park, Donggu Lee, Stefanie Klassen, Angelika Kühnle, Changhee Lee, Kookheon Char, Katja Heinze*

Table of Contents:

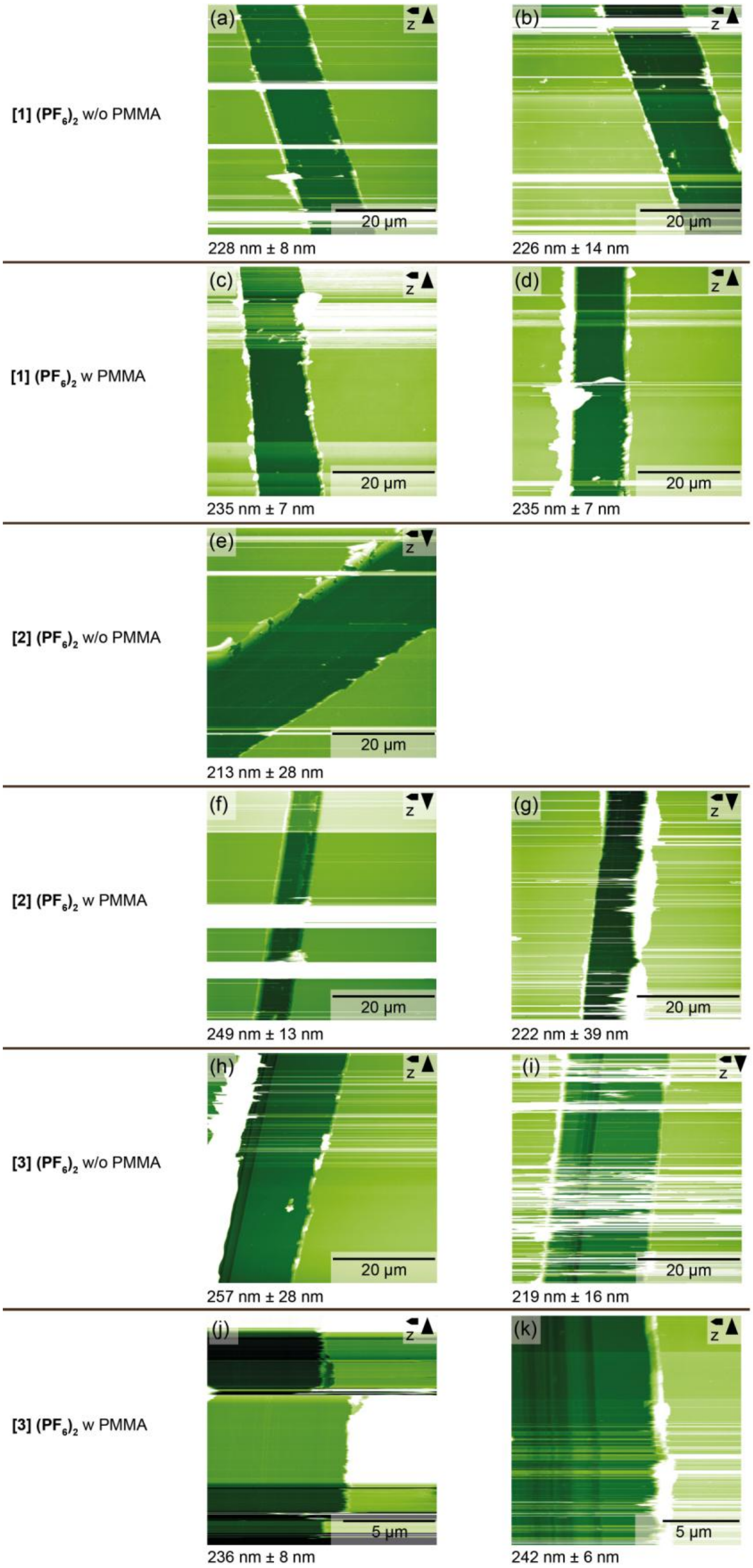

Figure S1. Representative intermittent contact mode images showing scratched PEDOT:PSS/ruthenium(II) complex:PMMA samples with varying compositions. The horizontal stipes arise from material attaching to and detaching from the cantilever tip. The given thickness values are determined by height histograms taken in areas without stripe artifacts.

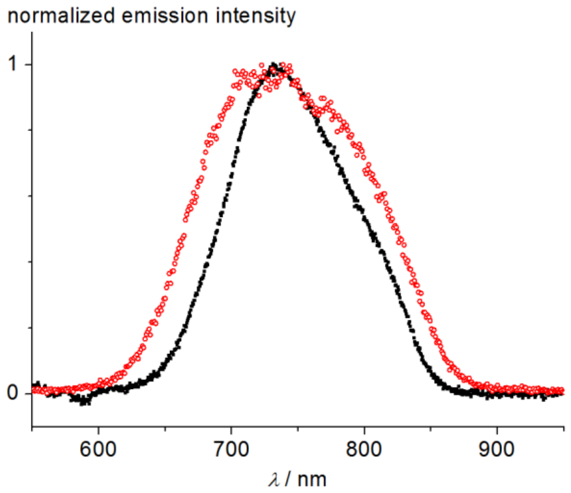

Figure S2. Normalized emission spectra of **[1](PF$_6$)$_2$** (black squares: CH$_3$CN solution at 297 K; red hollow circles: LEC with PMMA, 6 V.

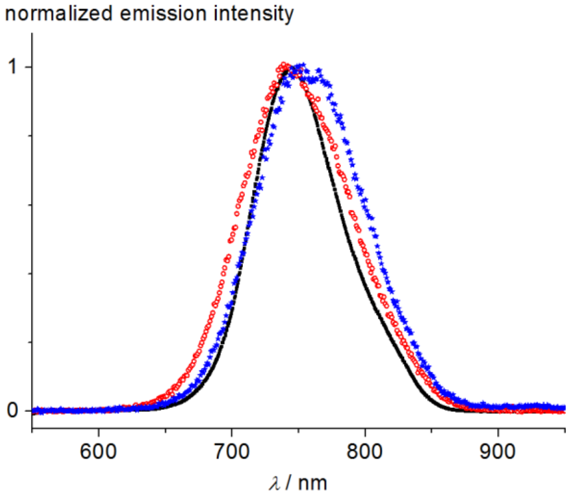

Figure S3. Normalized emission spectra of **[3](PF$_6$)$_2$** (black squares: CH$_3$CN solution at 297 K; red hollow circles: LEC with PMMA, 5 V; blue stars: LEC without PMMA, 4 V)

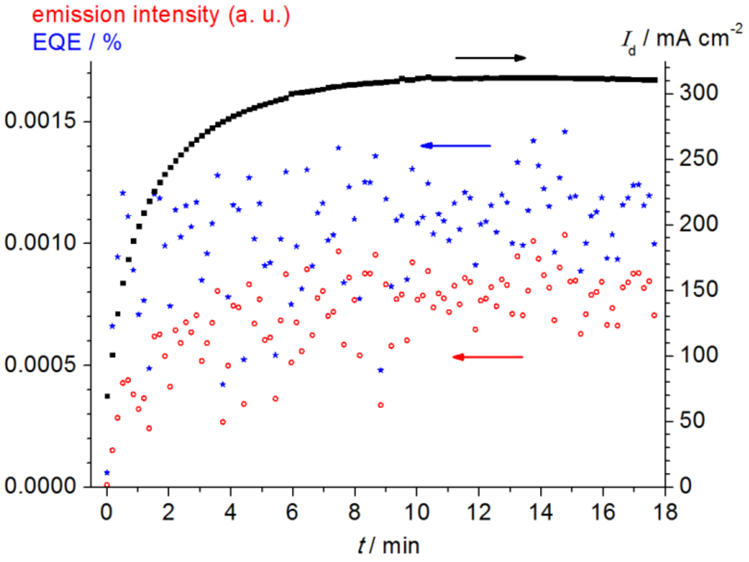

Figure S4. Current density (black squares), emission intensity (red hollow circles) and EQE (blue stars) *vs.* time in the LEC with **[1](PF$_6$)$_2$** with PMMA at an applied voltage of 4 V.

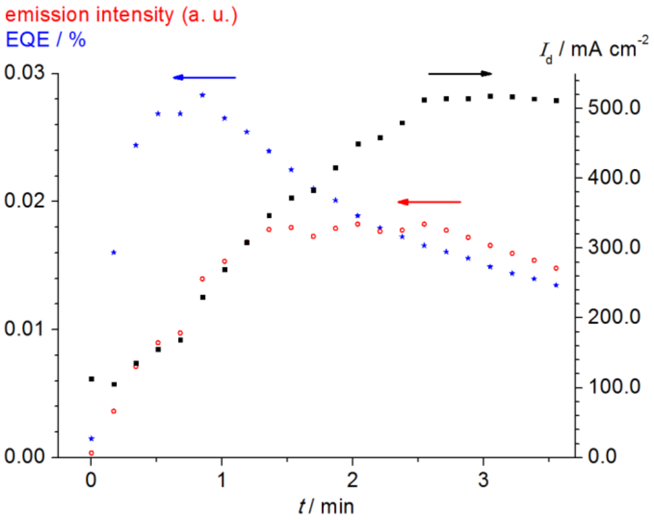

Figure S5. Current density (black squares), emission intensity (red hollow circles) and EQE (blue stars) *vs.* time in the LEC with **[2](PF$_6$)$_2$** with PMMA at an applied voltage of 6 V.

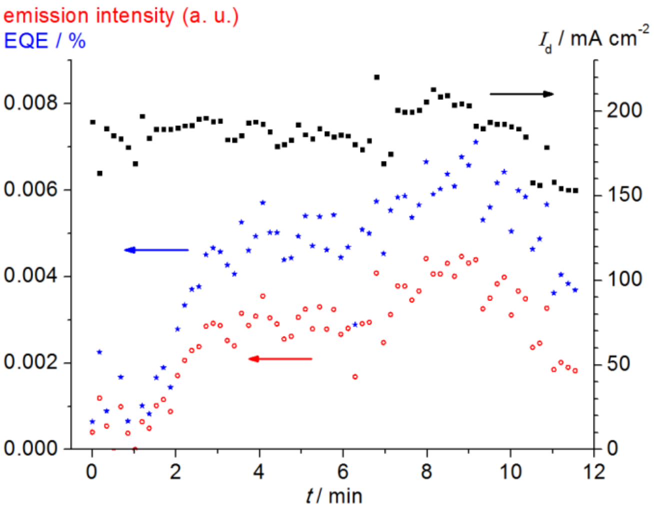

Figure S6. Current density (black squares), emission intensity (red hollow circles) and EQE (blue stars) *vs.* time in the LEC with **[3](PF$_6$)$_2$** without PMMA at an applied voltage of 4 V.

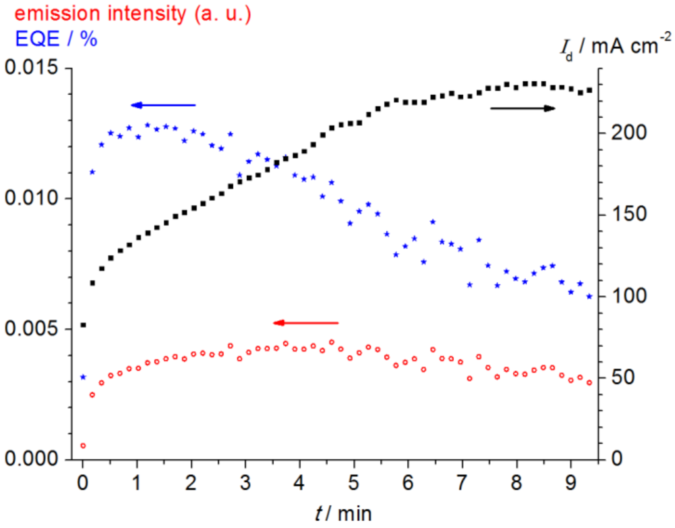

Figure S7. Current density (black squares), emission intensity (red hollow circles) and EQE (blue stars) *vs.* time in the LEC with **[3](PF$_6$)$_2$** with PMMA at an applied voltage of 5 V.

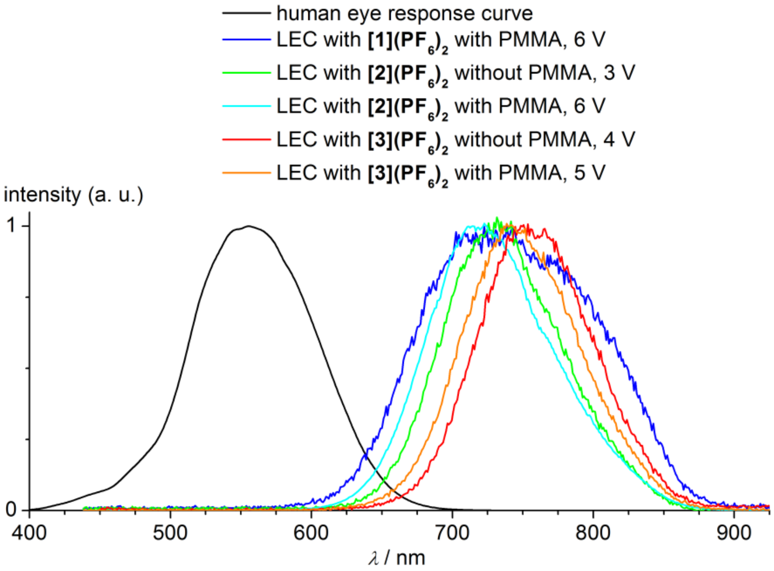

Figure S8. Comparison of the human eye response curve (photopic response curve) with normalized emission spectra of LECs of **[1](PF$_6$)$_2$** – **[3](PF$_6$)$_2$**.

10.8 Anchor-Functionalized Push-Pull-Substituted Bis(tridentate) Ruthenium(II) Polypyridine Chromophores: Photostability and Evaluation as Photosensitizers

A. Breivogel, S. Wooh, J. Dietrich, T. Y. Kim, Y. S. Kang, K. Char, K. Heinze, *Eur. J. Inorg. Chem.* **2014**, 2720–2734.

DOI: 10.1002/ejic.2014020919

DFT-optimized (B3LYP/LANL2DZ, IEFPCM in CH_3CN) cartesian coordinates of [**1** – **6**]$^{3+}$ and reduced N719 (doublet), [**1** – **6**]$^{2+}$ and N719 (singlet), [**1** – **6**]$^{3+}$ and oxidized N719 (doublet) and results of the TD-DFT (B3LYP/LANL2DZ, IEFPCM in CH_3CN) calculation of [**1** – **6**]$^{2+}$ (singlet) can be found in the online supporting information.

Eur. J. Inorg. Chem. **2014** · © WILEY-VCH Verlag GmbH & Co. KGaA, 69451 Weinheim, 2014 · ISSN 1099–0682

SUPPORTING INFORMATION

DOI: 10.1002/ejic.201402091

Title: Anchor-Functionalized Push-Pull-Substituted Bis(tridentate) Ruthenium(II) Polypyridine Chromophores: Photostability and Evaluation as Photosensitizers

Author(s): Aaron Breivogel, Sanghyuk Wooh, Jan Dietrich, Tea Yon Kim, Yong Soo Kang, Kookheon Char, Katja Heinze*

Table of Contents:

1) Tabulated ^{1}H, ^{13}C and ^{15}N NMR chemical shifts in CD_3CN (Tables S1 – S3).

2) Figures S1 – S13

3) DFT (B3LYP/LANL2DZ, IEFPCM, CH_3CN) optimized geometries of
    - [**1**]$^{2+}$ – [**6**]$^{2+}$ and N719 (singlet)
    - [**1**]$^{3+}$ – [**6**]$^{3+}$ and oxidized N719 (doublet)
    - [**1**]$^{+}$ – [**6**]$^{+}$ and reduced N719 (doublet)

4) Results of TD-DFT calculations of [**1**]$^{2+}$ – [**6**]$^{2+}$ and N719 (singlet).

Table S1. ^{1}H NMR data (δ / ppm) of [1]($PF_6)_2$ – [3]($PF_6)_2$ in CD_3CN, 400 MHz.

	$[\mathbf{1}](PF_6)_2$	$[\mathbf{2}](PF_6)_2$	$[\mathbf{3}](PF_6)_2$
H^2	8.99 (s, 2 H)	9.15 (s, 2 H)	9.12 (s, 2 H)
H^5	8.56 (m, 2 H)	8.97 (m, 2 H)	8.94 (m, 2 H)
H^6	8.01 (m, 2 H)	-	-
H^7	7.47 (m, 2 H)	7.89 (m, 2 H)	7.89 (m, 2 H)
H^8	8.11 (m, 2 H)	8.26 (m, 2 H)	8.30 (m, 2 H)
H^9	6.44 (m, 2 H)	6.36 (m, 2 H)	6.29 (m, 2 H)
H^{10}	6.58 (m, 2 H)	6.56 (m, 2 H)	6.52 (m, 2 H)
H^{11}	7.61 (m, 2 H)	7.61 (m, 2 H)	7.58 (m, 2 H)
H^{12}	7.17 (m, 2 H)	7.18 (m, 2 H)	7.12 (m, 2 H)
H^{15}	7.56 (d, $^3J_{HH}$ = 8.2 Hz, 2 H)	7.58 (d, $^3J_{HH}$ = 8.2 Hz, 2 H)	6.81 (s, 2 H)
H^{16}	8.27 (t, $^3J_{HH}$ = 8.2 Hz, 1 H)	8.29 (t, $^3J_{HH}$ = 8.2 Hz, 1 H)	-
NH_2	-	-	5.75 (br, s, 2 H)
NCH_3	3.47 (s, 6 H)	3.47 (s, 6 H)	3.36 (s, 6 H)

Table S2. ^{13}C{^{1}H} NMR data (δ / ppm) of [1]($PF_6)_2$ – [3]($PF_6)_2$ in CD_3CN, 101 MHz.

	$[\mathbf{1}](PF_6)_2$	$[\mathbf{2}](PF_6)_2$	$[\mathbf{3}](PF_6)_2$
C^1	137.1	136.6	135.5
C^2	124.1	125.0	124.9
C^3	159.5	159.7	159.5
C^4	158.7	159.2	159.8
C^5	125.7	124.9	124.7
C^6	139.1	140.1	139.7
C^7	127.9	127.1	127.0
C^8	155.1	155.8	155.7
C^9	149.4	149.2	149.2
C^{10}	121.4	121.6	121.2
C^{11}	140.1	140.4	140.3
C^{12}	116.3	116.6	116.5
C^{13}	159.8	159.6	160.0
C^{14}	157.2	157.1	156.7
C^{15}	113.5	113.7	98.8
C^{16}	141.7	142.1	159.3
CO^{center}	165.7	165.1	165.3
CO^{outer}	-	164.7	164.8
NCH_3	41.8	41.7	41.3

Table S3. ^{15}N NMR data (δ / ppm) of [1]($PF_6)_2$ – [3]($PF_6)_2$ in CD_3CN, 41 MHz.

	$[\mathbf{1}](PF_6)_2$	$[\mathbf{2}](PF_6)_2$	$[\mathbf{3}](PF_6)_2$
N^a	212.1	209.0	210.0
N^b	92.1	not observed	not observed
N^c	218.4	216.3	181.6
N^d	238.3	249.5	249.9
N^e	293.6	293.9	296.9
NH_2	-	-	72.2

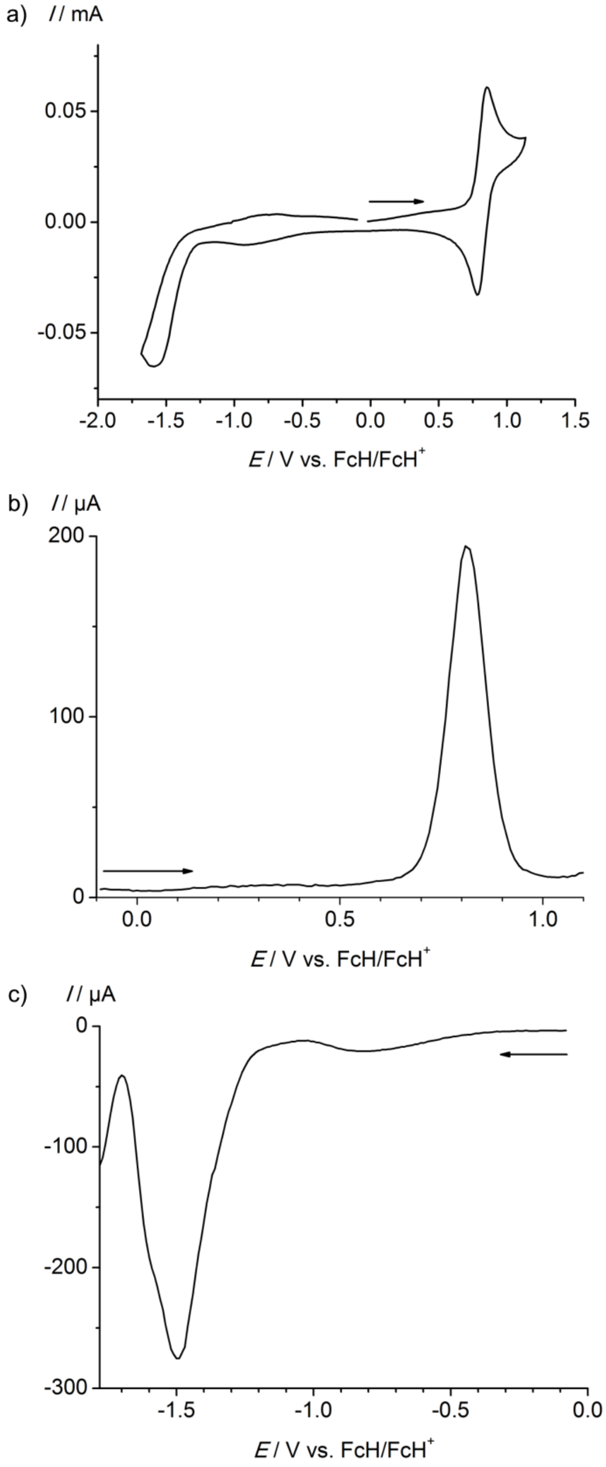

Figure S1. Cyclic voltammogram (a) and square wave voltammograms (b, c) of [1](PF_6)$_2$ in CH_3CN; 0.1 M [*n*-Bu_4](PF_6).

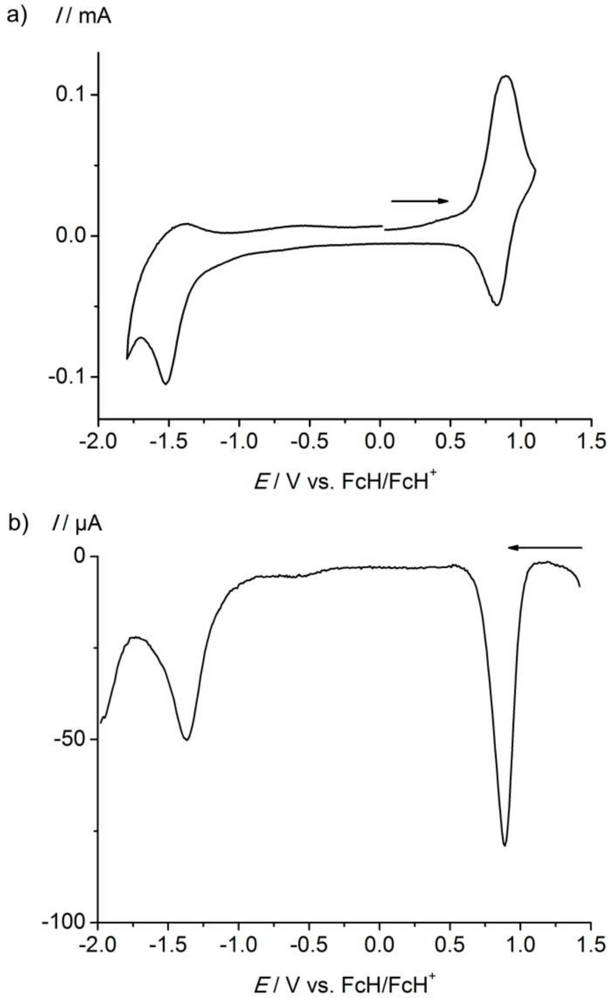

Figure S2. Cyclic voltammogram (a) and square wave voltammogram (b) of [2](PF_6)$_2$ in CH_3CN; 0.1 M [*n*-Bu_4](PF_6).

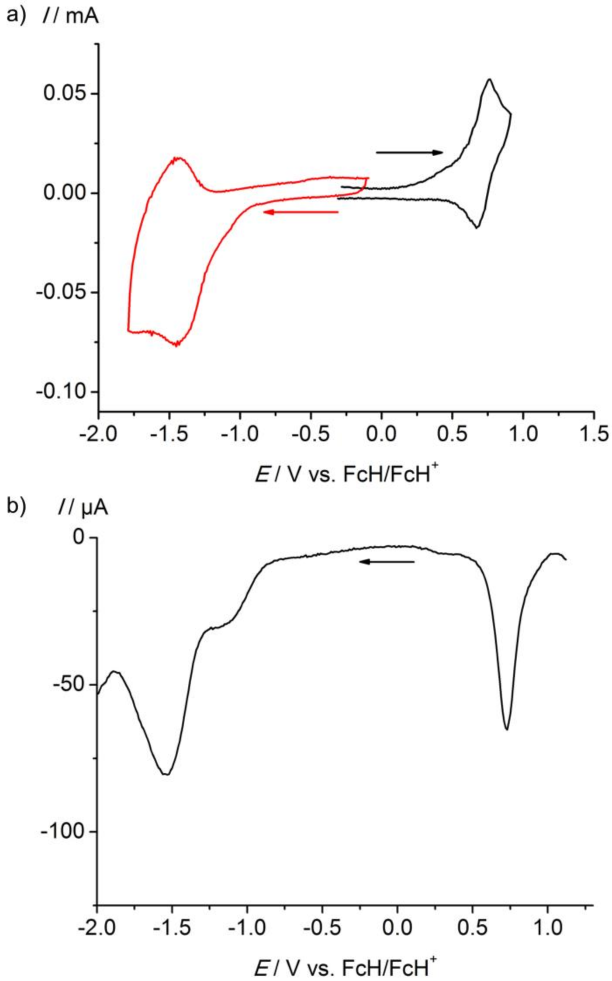

Figure S3. Cyclic voltammograms (a) and square wave voltammogram (b) of [3](PF_6)$_2$ in CH_3CN; 0.1 M [*n*-Bu_4](PF_6).

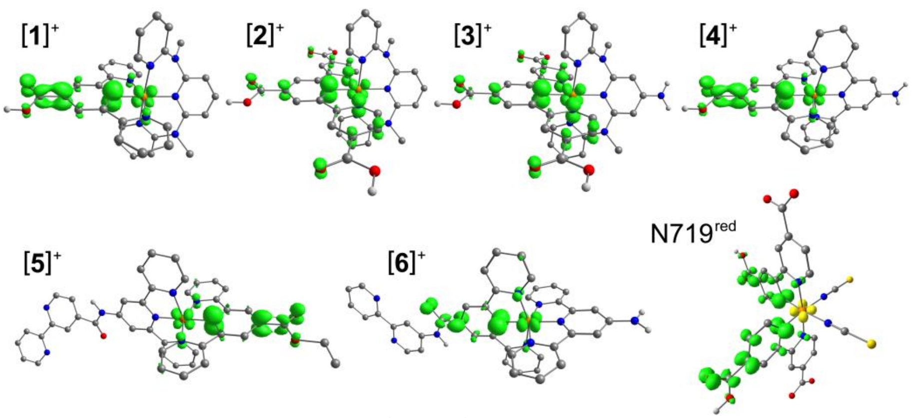

Figure S4. Spin densities of $[1]^+$ – $[6]^+$ and one-electron reduced N719 (contour value 0.005 a. u.; CH hydrogen atoms omitted).

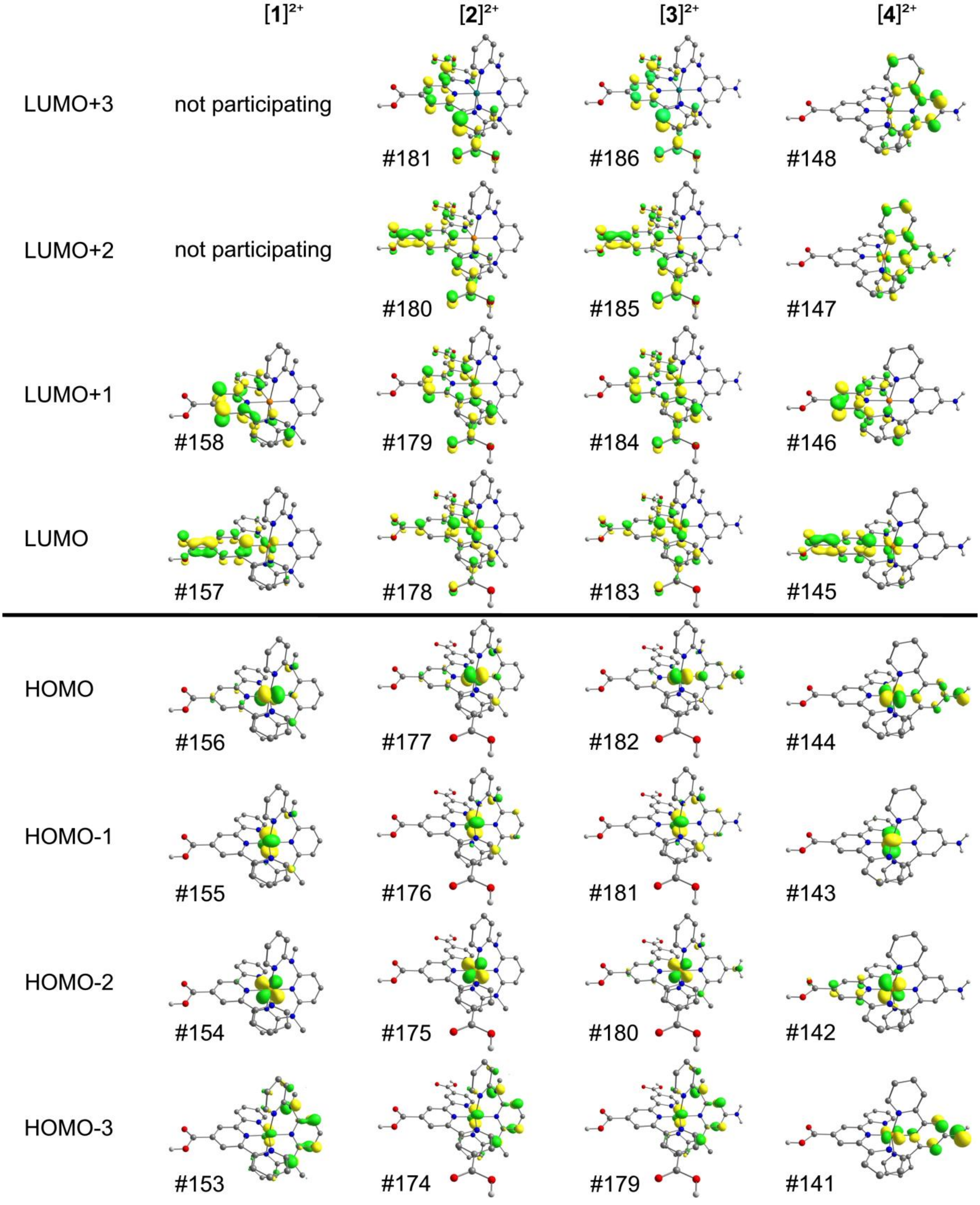

Figure S5. Relevant DFT calculated frontier orbitals (HOMO-3 to LUMO+3) of $[1]^{2+}$ – $[4]^{2+}$ for transitions with $\lambda > 400$ nm (contour value 0.06 a. u.; CH hydrogen atoms omitted).

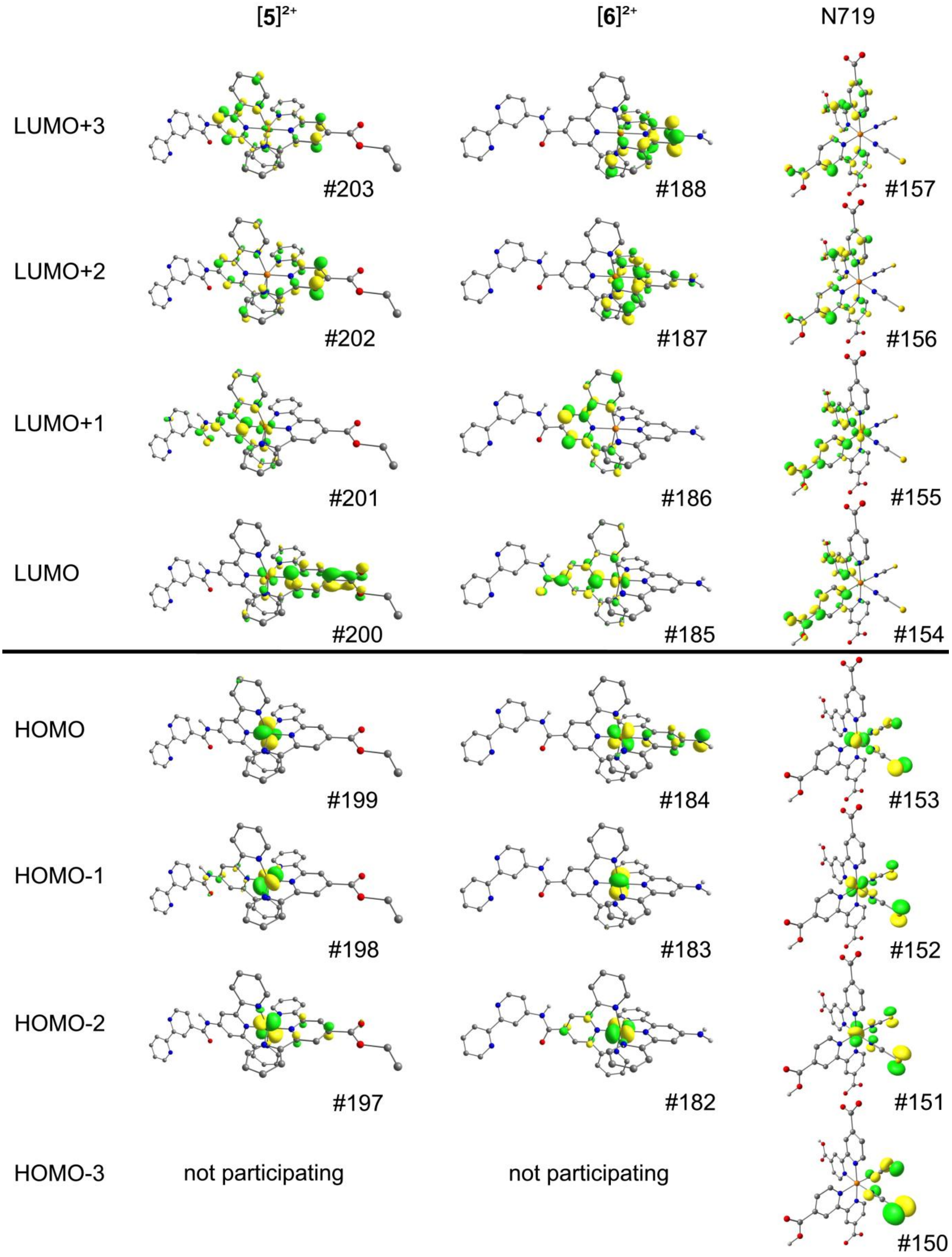

Figure S6. Relevant DFT calculated frontier orbitals (HOMO-3 to LUMO+3) of $[5]^{2+}$, $[6]^{2+}$ and N719 for transitions with λ > 400 nm (contour value 0.06 a. u.; CH hydrogen atoms omitted).

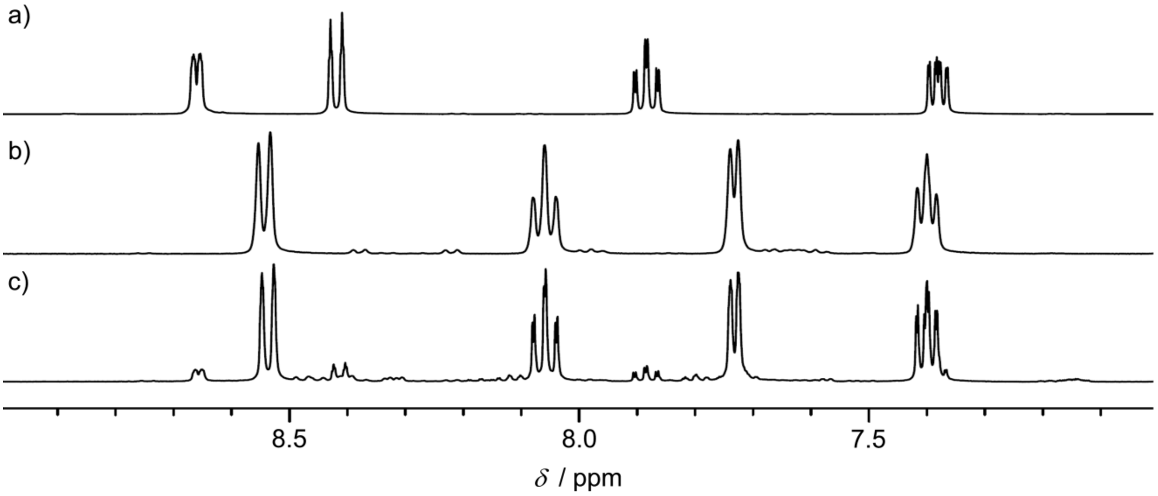

Figure S7. **^{1}H-NMR spectra in CD_3CN: a) free bpy and the mixture of $[Ru(bpy)_3](PF_6)_2$ and 2.2 equiv [*n*-Bu_4N]I b) before and c) after irradiation.**

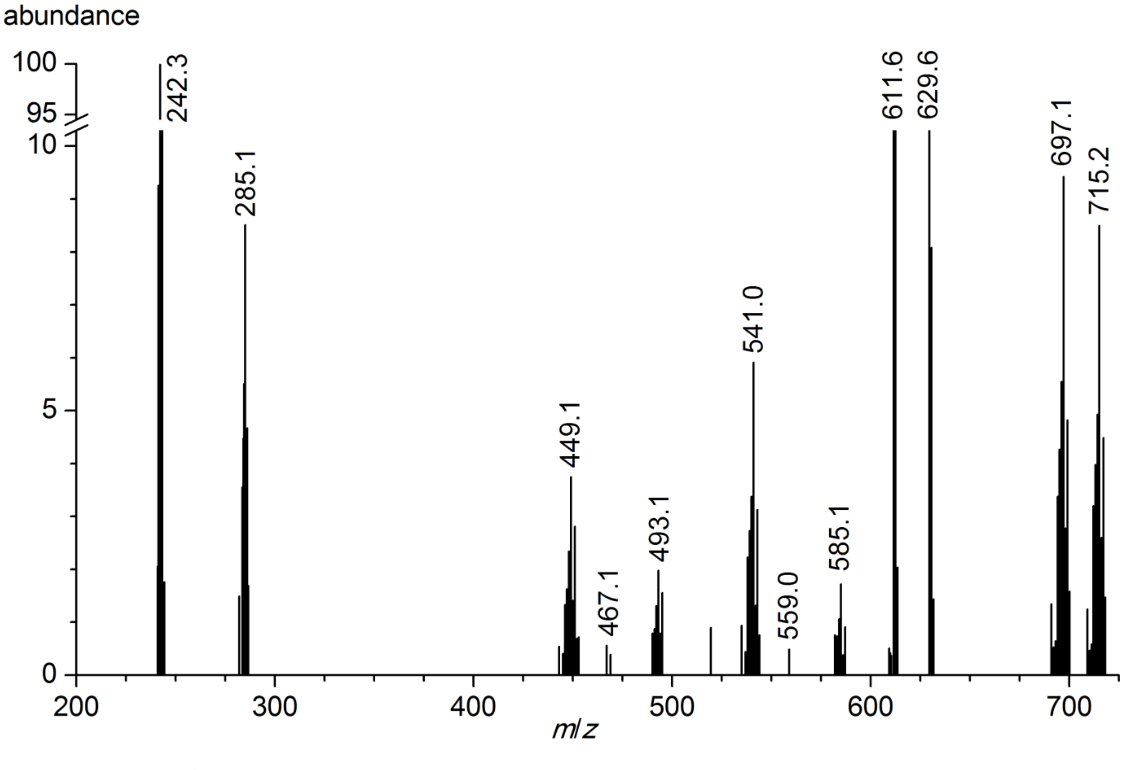

Figure S8. **ESI^+ mass spectrum of the mixture of $[Ru(bpy)_3](PF_6)_2$ and 2.2 equiv [*n*-Bu_4N]I in CD_3CN after irradiation.**

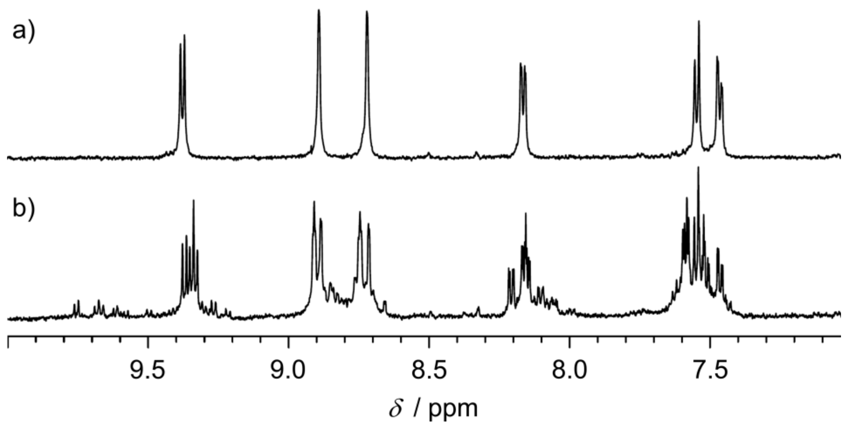

Figure S9. ^{1}H-NMR spectra in CD_3CN:H_2O (14:1): N719 and 4.5 equiv [*n*-Bu_4N]I a) before and b) after irradiation.

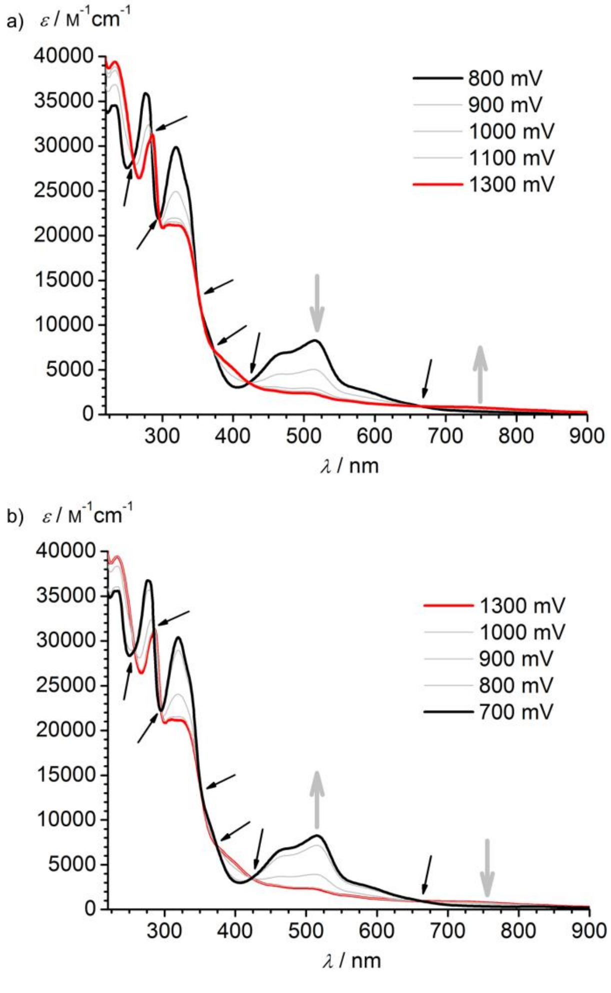

Figure S10. UV/Vis spectra of a) the electrochemical oxidation (E = 800 → 1300 mV) and b) back reduction (E = 1300 → 700 mV) of $[1^{Et}](PF_6)_2$ in an OTTLE cell in 10^{-3} M NaOH and 0.1 M [*n*-Bu_4N](PF_6) in CH_3CN:H_2O (98:2, *v*%). Black arrows indicate isosbestic points.

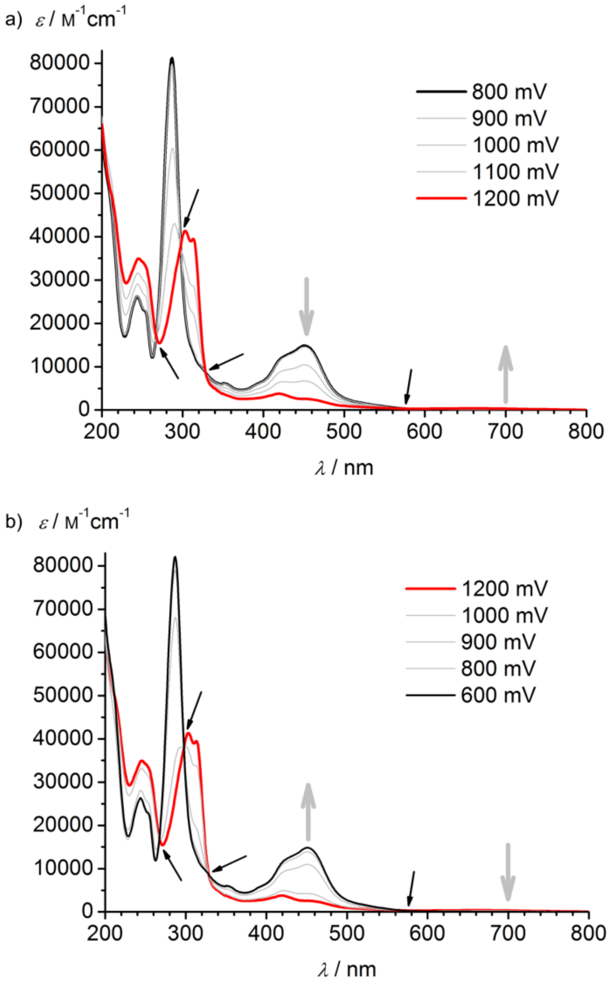

Figure S11. **UV/Vis spectra of a) the electrochemical oxidation (*E* = 800 → 1200 mV) and b) back reduction (*E* = 1200 → 600 mV) of [Ru(bpy)$_3$](PF$_6$)$_2$ in an OTTLE cell in 10^{-3} M NaOH and 0.1 M [*n*-Bu$_4$N](PF$_6$) in CH$_3$CN:H$_2$O (98:2, *v*%). Black arrows indicate isosbestic points.**

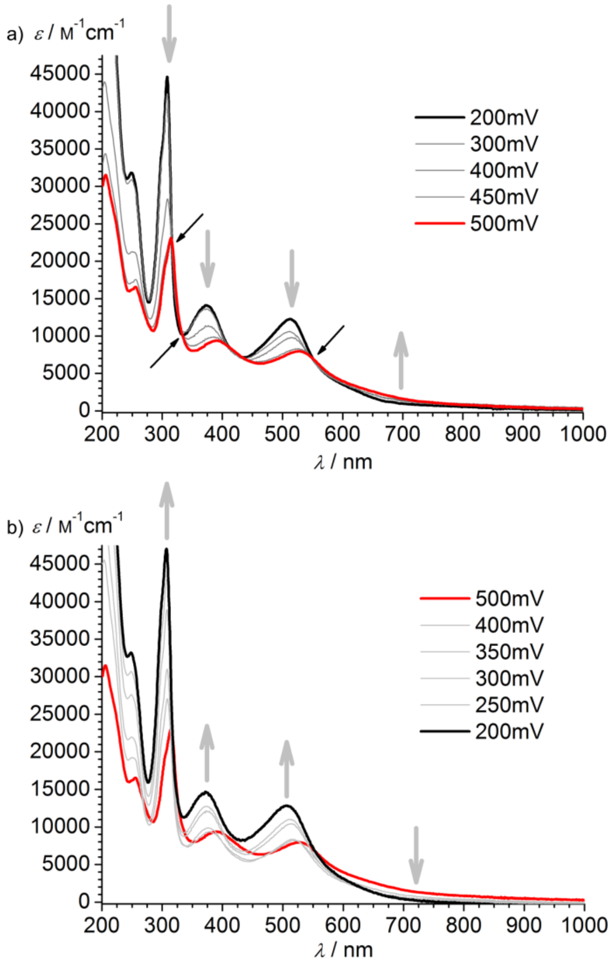

Figure S12. UV/Vis spectra of a) the electrochemical oxidation (E = 200 → 500 mV) and b) back reduction (E = 500 → 200 mV) of N719 in an OTTLE cell in 10^{-3} M NaOH and 0.1 M [*n*-Bu_4N](PF_6) in CH_3CN:H_2O (98:2, *v*%). Black arrows indicate isosbestic points.

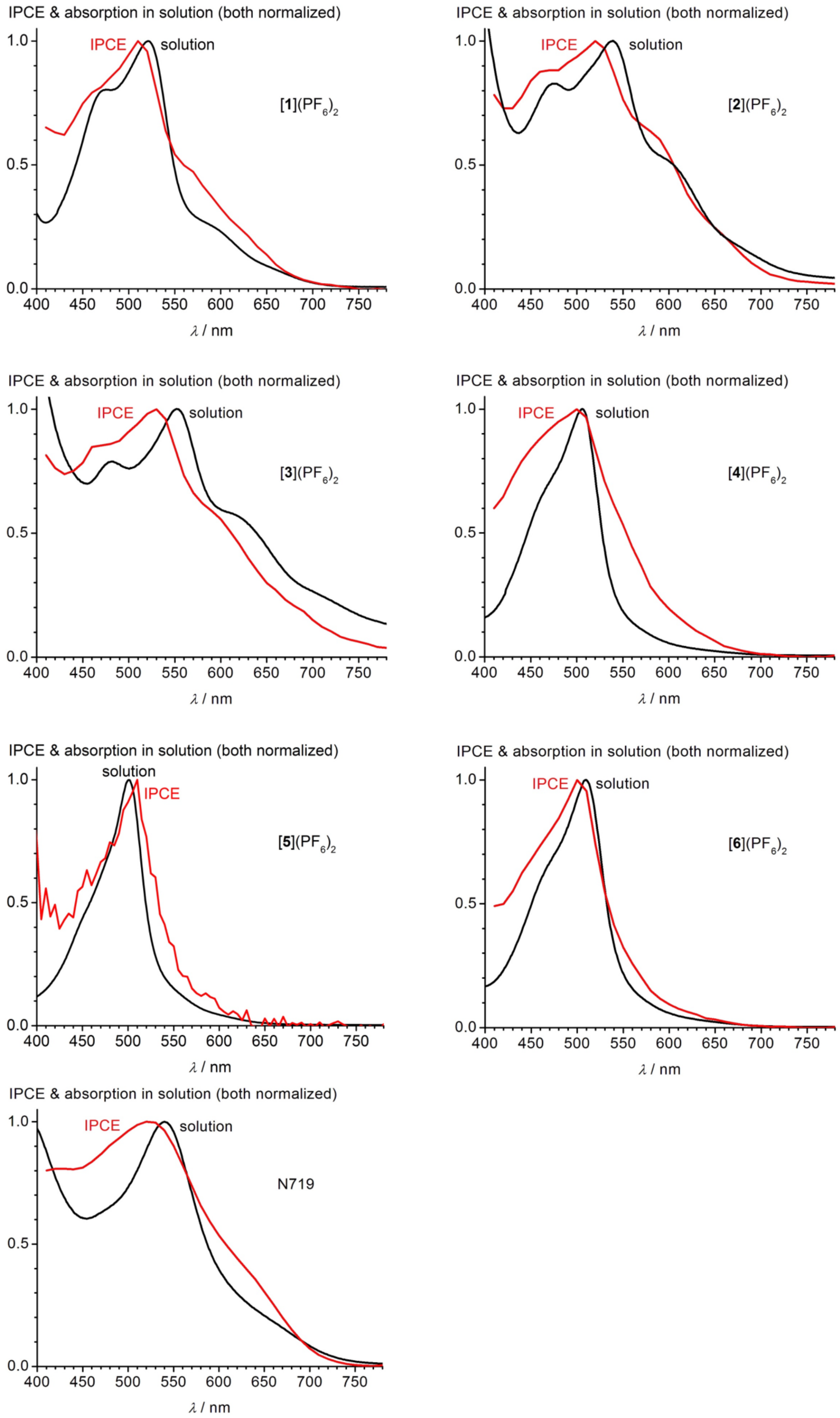

Figure S13. IPCE plots of cells with [1](PF$_6$)$_2$ – [6](PF$_6$)$_2$ and N719 and solution absorption spectra of the respective complexes in CH$_3$CN:^{t}BuOH (1:1).

11 Summary and Outlook

Polypyridine complexes of ruthenium(II) have unique and tunable electrochemical and photophysical properties such as high redox stability, visible light absorption, room temperature emission in fluid solution combined with high thermal and chemical robustness.[1] They are applied in a plethora of applications, e.g. dye-sensitized solar cells (DSSC),[2–4] light-emitting devices,[5–8] photodynamic therapy[9–11] and as photocatalysts for water splitting,[34,35] hydrogen production,[36–40] CO_2 reduction[38–40] and organic redox reactions.[39,41–45] One of the most famous ruthenium(II) polypyridine complexes is $[Ru(bpy)_3]^{2+}$ (bpy = 2,2'-bipyridine). Excitation of $[Ru(bpy)_3]^{2+}$ with visible light leads to instantaneous population of the ^{1}MLCT state followed by quantitative ISC to the ^{3}MLCT state (Figure 29a, MLCT = metal-to-ligand charge transfer, ISC = intersystem crossing).[1] At room temperature the ^{3}MLCT state is emissive with a long lifetime of $\tau_{RT} \approx 1$ µs and a high luminescence quantum yield of $\Phi_{RT} \approx 10\%$ which explains the use of $[Ru(bpy)_3]^{2+}$ as photoredox catalyst and as emitter in light-emitting devices.[47] The properties of $[Ru(bpy)_3]^{2+}$ can be fine tuned via ligand design. However, the intrinsic Δ, Λ chirality of tris(bidentate) $[Ru(bpy)_3]^{2+}$ leads to stereoisomers when the bpy ligands are substituted unsymmetrically which heavily complicates synthetic procedures.[48–50] In contrast, bis(tridentate) $[Ru(tpy)_2]^{2+}$ ($[\mathbf{1}]^{2+}$, Figure 30) is achiral, even in the case of unsymmetrical substitution of the tpy 4'-positions (tpy = 2,2';6',2''-terpyridine).[47] Furthermore, the stronger chelate effect is favorable in terms of chemical, photo and redox stability.[52,53,78] Unfortunatelly, $[Ru(tpy)_2]^{2+}$ features poor excited state properties ($\tau_{RT} \approx 0.1 – 0.2$ ns, $\Phi_{RT} \leq 0.0007\%$) due to effective radiationless deactivation of the ^{3}MLCT state via thermally accessible ^{3}MC states (Figure 29b, MC = metal-centered).[54–56]

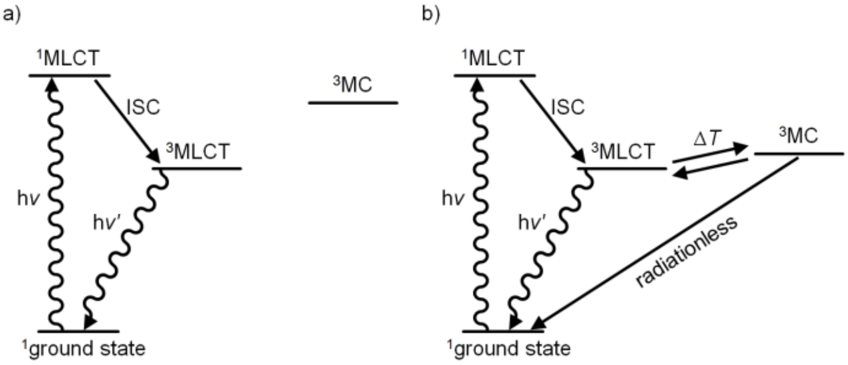

Figure 29. Qualitative Jablonski diagrams of a) $[Ru(bpy)_3]^{2+}$ and b) $[Ru(tpy)_2]^{2+}$ (MLCT = metal-to-ligand charge transfer, ISC = intersystem crossing, MC = metal-centered, bpy = 2,2'-bipyridine, tpy = 2,2';6',2''-terpyridine).

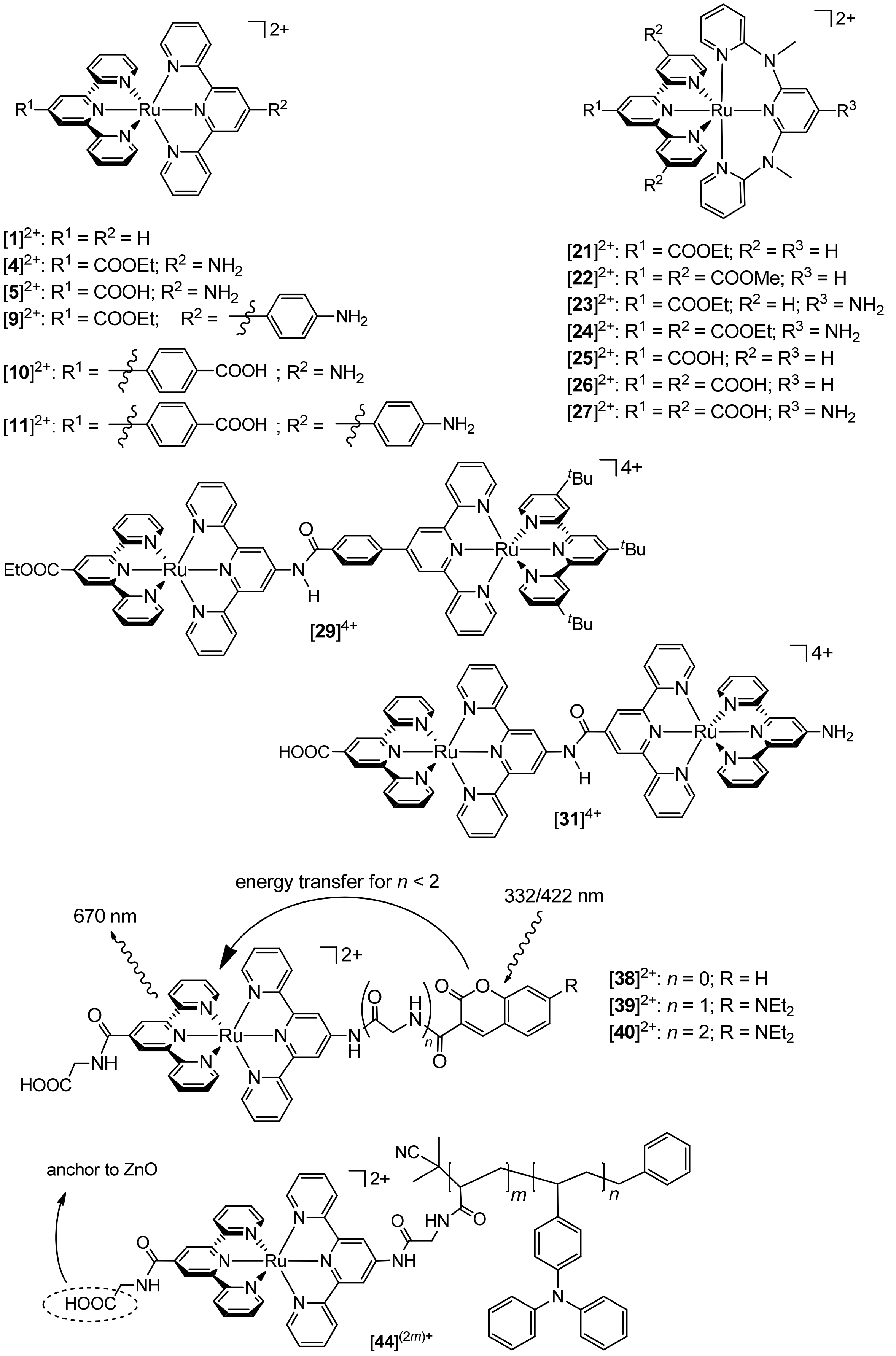

Figure 30. Bis(tridentate) polypyridine complexes of ruthenium(II) and their amide conjugates.

Amino acid ester [**4**]$^{2+}$ features substituents at the 4'-position of both tpy ligands (Figure 30). The electron-withdrawing COOEt group lowers the energy of the ^{3}MLCT state while the electron-donating NH_2 group shifts the ^{3}MC state to higher energy resulting in improved excited state properties ($\tau_{RT} \approx 34$ ns, $\Phi_{RT} = 0.27\%$).[61] [**4**]$^{2+}$ can be hydrolyzed to the carboxylic acid [**5**]$^{2+}$ (Figure 30) enabling selective functionalization either at the C- or at the N-terminus. The formal addition of *para*-phenylene spacers to [**4**]$^{2+}$/[**5**]$^{2+}$ results in complexes [**9** – **11**]$^{2+}$ (Figure 30).[62] [**9** – **11**]$^{2+}$ feature enhanced extinction coefficients compared to the respective *para*-phenylene-free complex ([**4**]$^{2+}$/[**5**]$^{2+}$). However, the ring planes of the phenylene ring and the central pyridyl ring of a tpy ligand are twisted which dilutes the effect of donor and acceptor substituents. Hence, ^{3}MLCT lifetimes and phosphorescence quantum yields of [**9** – **11**]$^{2+}$ are smaller compared to the *para*-phenylene-free analogues [**4**]$^{2+}$ and [**5**]$^{2+}$.

The N-Ru-N ligand bite angles of bis(terpyridine) complexes of ruthenium(II) are typically around 79°. Enlargement of the bite angles to 90° creates a stronger ligand field splitting due to the higher overlap between Ru d orbitals and pyridine nitrogen lone pairs. A stronger ligand field increases the ^{3}MC–^{3}MLCT energy difference making ^{3}MC states less accessible.[56] However, ligands with large bite angles can form stereoisomers (*mer*, *cis-fac*, *trans-fac*).[85]

In this work, complexes [**21**]$^{2+}$ and [**22**]$^{2+}$ (Figure 30) have been synthesized and characterized. In these complexes the problem of stereoisomers is overcome by the use of a tpy acceptor ligand in combination with a ddpd donor ligand (ddpd = *N*,*N*'-dimethyl-*N*,*N*'-dipyridin-2-ylpyridine-2,6-diamine) because the tpy ligand only allows for the *meridional* coordination. The ddpd ligand features N-Ru-N bite angles of 88°. The donor-acceptor substitution in [**21**]$^{2+}$ and [**22**]$^{2+}$ leads to small HOMO–LUMO gaps and spatially separated frontier orbitals which is favorable for low-energy absorption and the use as photosensitizers in dye-sensitized solar cells. The high ^{3}MLCT lifetimes and phosphorescence quantum yields of [**21**]$^{2+}$ ($\tau_{RT} = 722$ ns, $\Phi_{RT} = 0.45\%$) and [**22**]$^{2+}$ ($\tau_{RT} = 841$ ns, $\Phi_{RT} = 1.1\%$) confirm the effectiveness of the bite angle enlargement strategy.[57] [**23**]$^{2+}$ and [**24**]$^{2+}$ (Figure 30) feature additional NH_2 groups at the 4'-position of the ddpd ligand. The donor-acceptor substitution is even more pronounced inducing smaller HOMO–LUMO gaps compared to the NH_2-free analogues [**21**]$^{2+}$ and [**22**]$^{2+}$. However, ^{3}MLCT lifetimes and phosphorescence quantum yields of [**23**]$^{2+}$ ($\tau_{RT} = 149$ ns, $\Phi_{RT} = 0.042\%$) and [**24**]$^{2+}$ ($\tau_{RT} = 136$ ns, $\Phi_{RT} = 0.052\%$) are smaller compared to the NH_2-free analogues.[57] There are two reasons for this: The small HOMO-LUMO gap induces fast radiationless deactivation of the ^{3}MLCT state due to the energy gap law.[73,87,88] Secondly, the presence of high-energy oscillators (N–H) provides an additional path for radiationless deactivation to the ground state. Deuteration ($NH_2 \rightarrow ND_2$) removes this effect and enhances the quantum yields by a factor of about 2.[57] Excited states of [**4**]$^{2+}$ and [**21** – **24**]$^{2+}$ were studied experimentally by transient absorption measurements revealing excited state dynamics with a lifetime in the ps regime which might be associated with localization of the electron on the tpy-COOEt ligand, ISC or vibrational relaxation within $^{1/3}$MLCT states.[57] Lifetime and transient absorption experiments were measured in collaboration with the group of Dr. [redacted] together with Dr. [redacted]. ^{3}MC, ^{3}MLCT and the connecting transition state ^{3}TS were calculated via DFT methods and nicely explain the trends of experimental ^{3}MLCT lifetimes of [**1**]$^{2+}$, [**2**]$^{2+}$, [**4**]$^{2+}$ and [**21** – **24**]$^{2+}$ (DFT = density functional theory).[57] In the future [**21**]$^{2+}$ and [**22**]$^{2+}$ will be used as sensitizers for photoredox catalysis.

[**4**]$^{2+}$, [**21**]$^{2+}$ and [**22**]$^{2+}$ have been used and characterized as emitters in light-emitting electrochemical cells with an ITO/PEDOT:PSS/ruthenium(II) complex/Ag device structure in a collaboration with the groups of Prof. Dr. [redacted], Prof. Dr. [redacted] and Prof. Dr. [redacted] together with [redacted], [redacted] and [redacted]. Deep red light emission up to a maximum emission wavelength of 755 nm is achieved when an external voltage is applied. The small external quantum efficiencies (EQE) of ≤ 0.03% is rationalized by radiationless deactivation predicted by the energy gap law and by saturation and quenching effects in the emitting layer. The EQE increases by admixture of PMMA to the emitting ruthenium complexes.[107] Future work will be focused on the steric protection of the ruthenium core by bulky ligands to prevent self-quenching and the effect of counterion exchange.

Compared to $[Ru(bpy)_3]^{2+}$ bis(tridentate) complexes [**4**]$^{2+}$ and [**21**]$^{2+}$ feature an enhanced photostability in the presence of H_2O and coordinating I^- ions which is favorable for applications in DSSCs.[78] [**21**]$^{2+}$, [**22**]$^{2+}$ and [**24**]$^{2+}$ can be hydrolyzed to their respective carboxylic acids in order to obtain [**25** – **27**]$^{2+}$ (Figure 30). [**5**]$^{2+}$, derivatives of [**5**]$^{2+}$ featuring 2,2'-bipyridine anchor substituents (kindly donated by [redacted], AK [redacted]) and [**25** – **27**]$^{2+}$ have been incorporated as sensitizers in dye-sensitized solar cells with an I^-/I_3^- redox electrolyte. DSSC fabrication and characterization were conducted in collaborations with the groups of Prof. Dr. [redacted] and Prof. Dr. [redacted] together with Dr. [redacted] and [redacted]. The COOH and 2,2'-bipyridine groups serve as anchor to the nanoporous TiO_2 electrode. The incident photon-to-current efficiency (IPCE) follows the solution absorption spectrum of the complexes. Power conversion efficiencies of the cells remain low (η_{max} = 0.26%). This is ascribed to the twofold positive charge of the complexes which increases the I_3^- concentration near the TiO_2 electrode favoring electron recombination. This was shown by dark current measurements and electron recombination lifetime measurements. A twofold negatively charged ruthenium(II) complex (N719) was used as reference and reaches a power conversion efficiency of η = 5.03% under the same conditions.[78] Future perspectives include the reduction of the overall complex charge by negatively charged, cyclometalated, tridentate ligands. Triarylamine substituted ligands will be employed in order to further redshift the absorption spectrum and to enhance extinction coefficients. In addition, other redox electrolytes such as polypyridine complexes of $Co^{2+/3+}$ will be used in order to suppress electron recombination.

Dinuclear complexes [**29**]$^{4+}$ and [**31**]$^{4+}$ (Figure 30), kindly donated by Dr. [redacted] (AK [redacted]), have been synthesized from mononuclear complexes by standard solution peptide chemistry methods. The mixed valence behavior of the one-electron oxidized forms [**29**]$^{5+}$ and [**31**]$^{5+}$

has been studied. Electrochemical and UV/Vis/NIR spectroscopic measurements reveal that [**29**]$^{5+}$ and [**31**]$^{5+}$ are valence localized showing no metal-metal interaction (Robin-Day-Class I[94]). In both complexes, [**29**]$^{5+}$ and [**31**]$^{5+}$, the ruthenium center with the donor-substituted tpy ligand (^{t}Bu- or NH_2-substituents) is oxidized to ruthenium(III) while the other ruthenium(II) center remains unaffected.[26] This redox asymmetry vanishes when the substituents are adjusted and results will be reported in due course by [redacted] (AK [redacted]).[160]

Peptidic arrays such as [**38**]$^{2+}$, [**39**]$^{2+}$ and [**40**]$^{2+}$ (Figure 30) including amino acid [**5**]$^{2+}$ are also available via solid-phase peptide synthesis (SPPS). The bis(tpy) ruthenium(II) core of [**5**]$^{2+}$ is connected to coumarin chromophores via amide bridges consisting of a different number ($n = 0 - 2$) of glycine units.[18,20] For short amide bridges with $n = 0$ ([**38**]$^{2+}$) and $n = 1$ ([**39**]$^{2+}$; both kindly donated by Dr. [redacted], AK [redacted]) excitation of the coumarin chromophore leads to efficient energy transfer from the coumarin to the bis(tpy) ruthenium chromophore. This is evident from the phosphorescence of the ruthenium chromophore and the quenching of the coumarin fluorescence.[18] For longer bridges ($n = 2$; [**40**]$^{2+}$; prepared in this work) energy transfer is hampered which is evident from the intense fluorescence of the coumarin chromophore while no emission from the ruthenium chromophore is detected when the coumarin is excited.[20] Future applications deal with more sophisticated energy transfer systems featuring multichromophore systems for dye-sensitized solar cells and light-to-chemical energy conversion systems with 0 – 1 amino acids between the energy donor and the acceptor.

Amino acid [**5**]$^{2+}$ has been used as chromophore in light-induced charge separation in a donor-chromophore-acceptor nanocomposite in a collaboration with the groups of Prof. Dr. [redacted] and Dr. [redacted] together with Dr. [redacted], [redacted] and [redacted]. A TPA-containing block-copolymer acts as electron donor and ZnO nanorods as electron acceptor (TPA = triphenylamine). In this work [**5**]$^{2+}$ is functionalized by SPPS and connected to the TPA-containing block-copolymer (provided by Prof. Dr. [redacted] together with Dr. [redacted]) to obtain [**44**]$^{(2m)+}$ (Figure 30). The COOH groups serve as anchors to the ZnO nanorods. In [**44**]$^{(2m)+}$@ZnO the phosphorescence of the ruthenium(II) chromophore is completely quenched. Irradiation into the absorption band of the ruthenium(II) chromophore leads to electron injection into the ZnO nanorods. The electron holes are transferred to the TPA units of the block-copolymer. The positive charge of the polymer is detected by Kelvin probe force microscopy measured by the group of Dr. [redacted] together with [redacted].[100] In the future sophisticated nanoscale charge separation systems will be used in solid state dye-sensitized solar cells.

The ruthenium(II) complex [**5**]$^{2+}$ can be oxidized in acidic media by Ce^{IV} leading to the ruthenium(III) complex [**5**]$^{3+}$. [**5**]$^{3+}$ features a LMCT band around 730 nm. EPR spectra and DFT calculations reveal a ruthenium-centered oxidation with smaller contributions from the NH_2 nitrogen atom. After oxidation of [**5**]$^{2+}$ to [**5**]$^{3+}$ in acidic media, the ruthenium(III) complex undergoes slow spontaneous back reduction to [**5**]$^{2+}$ without addition of a reducing agent which is shown by mass spectrometry, UV/Vis and NMR spectroscopy. The rate of back reduction is enhanced in the presence of light. However, the responsible reducing agent is yet unidentified. The oxidation of H_2O to O_2 was ruled out by oxygen measurements using different methods. It is assumed that upon degradation a small fraction of [**5**]$^{3+}$ undergoes irreversible side reactions which provide enough electrons for the reduction of the majority (≈ 91 ± 3%) of [**5**]$^{3+}$ to [**5**]$^{2+}$. DFT calculations indicate that chelate decoordination and protonation of an outer pyridine ring of the tpy ligand in [**5**]$^{3+}$ in concert with the attack of water to the ruthenium atom might be responsible for irreversible side reactions such as ligand loss and oxidative ligand decomposition e.g. to CO_2. Further investigations are necessary to clarify the mechanism of the back reduction.[74]

12 List of Publications

A. Breivogel, K. Heinze, **2014**, to be submitted. Thermal and Photo Reactivity of a Donor-Acceptor-Substituted Bis(terpyridine) Ruthenium(III) Complex in Acidic Solutions.

A. Breivogel, C. Kreitner, K. Heinze, *Eur. J. Inorg. Chem.* **2014**, accepted. Redox and Photochemistry of Bis(terpyridine)ruthenium(II) Amino Acids and their Amide Conjugates – from Understanding to Applications.

A. Breivogel, S. Wooh, J. Dietrich, T. Y. Kim. Y. S. Kang, K. Char, K. Heinze, *Eur. J. Inorg. Chem.* **2014**, 2720–2734. Anchor-Functionalized Push-Pull-Substituted Bis(tridentate) Ruthenium(II) Polypyridine Chromophores: Photostability and Evaluation as Photosensitizers. DOI: 10.1002/ejic.201402091.

A. Breivogel, M. Park, D. Lee, S. Klassen, A. Kühnle, C. Lee, K. Char, K. Heinze, *Eur. J. Inorg. Chem.* **2014**, 288–295. Push-Pull Design of Bis(tridentate) Ruthenium(II) Polypyridine Chromophores as Deep Red Light Emitters in Light-Emitting Electrochemical Cells. DOI: 10.1002/ejic.201301226.

A. Breivogel, M. Meister, C. Förster, F. Laquai, K. Heinze, *Chem. Eur. J.* **2013**, *19*, 13745–13760. Excited State Tuning of Bis(tridentate) Ruthenium(II) Polypyridine Chromophores by Push-Pull Effects and Bite Angle Optimization: A Comprehensive Experimental and Theoretical Study. DOI: 10.1002/chem.201302231.

L. zur Borg, A. L. Domanski, A. Breivogel, M. Bürger, R. Berger, K. Heinze, R. Zentel, *J. Mater. Chem. C* **2013**, *1*, 1223–1230. Light-induced Charge Separation in a Donor-Chromophore-Acceptor Nanocomposite Poly[TPA-Ru(tpy)$_2$]@ZnO. DOI: 10.1039/c2tc00535b.

A. Breivogel, K. Hempel, K. Heinze, *Inorg. Chim. Acta* **2011**, *374*, 152–162. Dinuclear Bis(terpyridine)ruthenium(II) Complexes by Amide Coupling of Ruthenium Amino Acids: Synthesis and Properties. DOI: 10.1016/j.ica.2011.03.046.

A. Breivogel, C. Förster, K. Heinze, *Inorg. Chem.* **2010**, *49*, 7052–7056. A Heteroleptic Bis(tridentate)ruthenium(II) Polypyridine Complex with Improved Photophysical Properties and Integrated Functionalizability. DOI: 10.1021/ic1007236.

K. Heinze, K. Hempel, A. Breivogel, *Z. Anorg. Allg. Chem.* **2009**, *635*, 2541–2549. Synthesis and Characterization of Extended Bis(terpyridine)ruthenium Amino Acids. DOI: 10.1002/zaac.200900303.

13 Oral and Poster Presentations

03.2014	Poster *Novel Iron(II) Complexes – A Way to 3d Metal Complex Chromophores* at the Koordinationschemiker-Treffen in Kaiserslautern
08.2013	Oral presentation *Ruthenium Complexes for Applications in Solar Cells and Light-Emitting Devices* at Laytec in Berlin
03.2013	Oral presentation *Ruthenium Complexes for Applications in Solar Cells and Light-Emitting Devices* at the Seoul National University in Seoul (South Korea)
02.2013	Poster *New Ruthenium Chromophores for Solar Cells and Light-Emitting Devices* at the IRTG conference in Seoul (South Korea)
09.2012	Oral presentation *Molecular Ruthenium Chromophores* at the Seoul National University in Seoul (South Korea)
02.2012	Poster *Light-Induced Charge Separation in a ZnO-Bis(terpyridine)ruthenium-TPA Polymer Composite* at the Koordinationschemiker-Treffen in Dortmund
11.2011	Poster *Light-Induced Charge Separation in a ZnO-Bis(terpyridine)ruthenium-TPA Polymer Composite* at the pacific polymer conference in Jeju (South Korea)
07.2011	Oral presentation *Novel Ruthenium Chromophores with Optimized Properties* in the Max-Planck-Institut für Polymerforschung in Mainz
06.2011	Oral presentation *Novel Ruthenium Chromophores with Optimized Properties* at the IRTG conference in Mainz
01.2011	Poster *New Ruthenium Chromophores with Optimized Properties* at the IRTG conference in Seoul (South Korea)
02.2010	Poster *Neue Rutheniumchromophore mit maßgeschneiderten Eigenschaften* at the Koordinationschemiker-Treffen in Mainz
02.2009	Oral presentation *Solid-Phase Synthesis of Peptide Libraries Combining α-Amino Acids with Inorganic and Organic Chromophores* at the Koordinationschemiker-Treffen in Erlangen

14 Acknowledgment/Dank

Ich danke....

...besonders Prof. Dr. [redacted] für die Promotionsstelle in ihrem Arbeitskreis, die spannenden Themen und für die exzellente wissenschaftliche Betreuung.

...Prof. Dr. [redacted] für die 6-monatige, freundliche Aufnahme in seinem Arbeitskreis in der Seoul National University in Seoul.

...meinen Kooperationspartnern Prof. Dr. [redacted], Prof. Dr. [redacted], Prof. Dr. [redacted], Prof. Dr. [redacted], Prof. Dr. [redacted], Dr. [redacted], Dr. [redacted], Dr. [redacted], Dr. [redacted], Dr. [redacted], Dr. [redacted], Dr. [redacted], [redacted], [redacted], [redacted], [redacted], [redacted], [redacted], [redacted] und [redacted] für die erfolgreiche und interessante Zusammenarbeit.

...dem gesamten Arbeitskreis [redacted] für die gegenseitige Unterstützung, die Diskussionen und die gute Stimmung im Labor ("immer cool keepen").

…meinen Arbeitskollegen [redacted] (Stichwort: Käsebrot) und [redacted] (Ey, was guckst du?) für die Freundschaft und die gemeinsamen Freizeitaktivitäten.

...dem "IRTG 1404 - Self Organized Materials for Optoelectronics" von der Deutschen Forschungsgemeinschaft für die Finanzierung und die einzigartigen Auslandserfahrungen.

...Dr. [redacted] für das Lösen der Kristallstrukturen.

...Dr. [redacted] für die großartige Unterstützung bei den NMR-Experimenten.

...Dr. [redacted] und [redacted] für das Messen der Massenspektren.

...dem Mikroanalytischen Labor des Institutes für Organische Chemie.

...meinen Forschungspraktikanten [redacted], [redacted], [redacted], [redacted], [redacted], [redacted], [redacted], [redacted] und [redacted].

...Dr. [redacted] und Dr. [redacted] für die Hilfe beim Sprung in die koreanische Kultur.

...meinen Eltern dafür, dass sie immer zu mir halten und sowieso für alles.

...meiner Oma für die große Fürsorge.

...meiner Schwester [redacted] für den geschwisterlichen Zusammenhalt.

...meiner Freundin [redacted] für all die schönen Momente.

15 Literature

[1] S. Campagna, F. Puntoriero, F. Nastasi, G. Bergamini, V. Balzani, *Top. Curr. Chem.* **2007**, *280*, 117–214.

[2] B. O'Regan, M. Grätzel, *Nature* **1991**, *353*, 737–740.

[3] J.-F. Yin, M. Velayudham, D. Bhattacharya, H.-C. Lin, K.-L. Lu, *Coord. Chem. Rev.* **2012**, *256*, 3008–3035.

[4] P. G. Bomben, K. C. D. Robson, B. D. Koivisto, C. P. Berlinguette, *Coord. Chem. Rev.* **2012**, *256*, 1438–1450.

[5] R. D. Costa, E. Ortí, H. J. Bolink, F. Monti, G. Accorsi, N. Armaroli, *Angew. Chem.* **2012**, *124*, 8300-8334; *Angew. Chem. Int. Ed.* **2012**, *51*, 8178–8211.

[6] P. Dreyse, B. Loeb, M. Soto-Arriaza, D. Tordera, E. Ortí, J. J. Serrano-Pérez, H. J. Bolink, *Dalton Trans.* **2013**, *42*, 15502–15513.

[7] H. J. Bolink, E. Coronado, R. D. Costa, P. Gaviña, E. Ortí, S. Tatay, *Inorg. Chem.* **2009**, *48*, 3907–3909.

[8] H. J. Bolink, L. Cappelli, E. Coronado, P. Gaviña, *Inorg. Chem.* **2005**, *44*, 5966–5968.

[9] L. Marcélis, J. Ghesquière, K. Garnir, A. K.-D. Mesmaeker, C. Moucheron, *Coord. Chem. Rev.* **2012**, *256*, 1569–1582.

[10] M. R. Gill, J. A. Thomas, *Chem. Soc. Rev.* **2012**, *41*, 3179–3192.

[11] H. Komatsu, K. Yoshihara, H. Yamada, Y. Kimura, A. Son, S.-i. Nishimoto, K. Tanabe, *Chem. Eur. J.* **2013**, *19*, 1971–1977.

[12] D. Maity, C. Bhaumik, D. Mondal, S. Baitalik, *Dalton Trans.* **2014**, *43,* 1829–1845.

[13] Z.-B. Zheng, Z.-M. Duan, Y.-Y. Ma, K.-Z. Wang, *Inorg. Chem.* **2013**, *52*, 2306–2316.

[14] M. Li, Q. Liang, M. Zheng, C. Fang, S. Peng, M. Zhao, *Dalton Trans.* **2013**, *42*, 13509–13515.

[15] S. A. Poteet, F. M. MacDonnell, *Dalton Trans.* **2013**, *42*, 13305–13307.

[16] H. Chen, X. Li, Y. Wu, W. Gao, R. Bai, *Dalton Trans.* **2012**, *41*, 13292–13297.

[17] R. Zhang, Z. Ye, G. Wang, W. Zhang, J. Yuan, *Chem. Eur. J.* **2010**, *16*, 6884–6891.

[18] K. Heinze, K. Hempel, *Chem. Eur. J.* **2009**, *15*, 1346–1358.

[19] R. Horvath, J. Lombard, J.-C. Leprêtre, M.-N. Collomb, A. Deronizer, J. Chauvin, K. C. Gordon, *Dalton Trans.* **2013**, *42*, 16527–16537.

[20] A. Breivogel, C. Kreitner, K. Heinze, *Eur. J. Inorg. Chem.* **2014**, accepted.

[21] S. Roeser, M. Z. Ertem, C. Cady, R. Lomoth, J. Benet-Buchholz, L. Hammarström, B. Sarkar, W. Kaim, C. J. Cramer, A. Llobet, *Inorg. Chem.* **2012**, *51*, 320–327.

[22] L.-Z. Sui, W.-W. Yang, C.-J. Yao, H.-Y. Xie, Y.-W. Zhong, *Inorg. Chem.* **2012**, *51*, 1590–1598.

[23] O. S. Wenger, *Chem. Soc. Rev.* **2012**, *41*, 3772–3779.

[24] H.-J. Nie, X. Chen, C.-J. Yao, Y.-W. Zhong, G. R. Hutchison, J. Yao, *Chem. Eur. J.* **2012**, *18*, 14497–14509.

[25] C.-J. Yao, Y.-W. Zhong, J. Yao, *Inorg. Chem.* **2013**, *52*, 4040–4045.

[26] A. Breivogel, K. Hempel, K. Heinze, *Inorg. Chim. Acta* **2011**, *374*, 152–162.

[27] P. Ceroni, *Chem. Eur. J.* **2011**, *17*, 9560–9564.

[28] T. N. Singh-Rachford, F. N. Castellano, *Coord. Chem. Rev.* **2010**, *254*, 2560–2573.

[29] W. Wu, S. Ji, W. Wu, J. Shao, H. Guo, T. D. James, J. Zhao, *Chem. Eur. J.* **2012**, *18*, 4953–4964.

[30] P. Hanczyc, B. Norden, M. Samoc, *Dalten Trans.* **2012**, *41*, 3123–3125.

[31] P. Ceroni, G. Bergamini, V. Balzani, *Angew. Chem.* **2009**, *121*, 8668–8670; *Angew. Chem. Int. Ed.* **2009**, *48*, 8516–8518.

[32] J. Lee, H. Chang, S. Kim, G. S. Bang, H. Lee, *Angew. Chem.* **2009**, *121*, 8653–8656; *Angew. Chem. Int. Ed.* **2009**, *48*, 8501–8504.

[33] K. Terada, K. Kanaizuka, V. M. Iyer, M. Sannodo, S. Saito, K. Kobayashi, M.-a. Haga, *Angew. Chem.* **2011**, *123*, 6411–6415; *Angew. Chem. Int. Ed.* **2011**, *50*, 6287–6291.

[34] R. H. Crabtree *Energy Production and Storage: Inorganic Chemical Strategies for a Warming World*; Wiley-VCH: Weinheim, Germany, **2010**.

[35] X. Liu, F. Wang, *Coord. Chem. Rev.* **2012**, *256*, 1115–1136.

[36] W. T. Eckenhoff, R. Eisenberg, *Dalton Trans.* **2012**, *41*, 13004–13021.

[37] T. Stoll, M. Gennari, I. Serrano, J. Fortage, J. Chauvin, F. Odobel, M. Rebarz, O. Poizat, M. Sliwa, A. Deronizer, M.-N. Collomb, *Chem. Eur. J.* **2013**, *19*, 782–792.

[38] M. Schulz, M. Karnahl, M. Schwalbe, J. G. Vos, *Coord. Chem. Rev.* **2012**, *256*, 1682–1705.

[39] A. Inagaki, M. Akita, *Coord. Chem. Rev.* **2010**, *254*, 1220–1239.

[40] Z. Chen, P. Kang, M.-T. Zhang, T. J. Meyer, *Chem. Commun.* **2014**, *50*, 335–337.

[41] S. Ohzu, T. Ishizuka, Y. Hirai, S. Fukuzumi, T. Kojima, *Chem. Eur. J.* **2013**, *19*, 1563–1567.

[42] H. Nitadori, T. Takahashi, A. Inagaki, M. Akita, *Inorg. Chem.* **2012**, *51*, 51–62.

[43] P. Guillo, O. Hamelin, P. Batat, G. Jonusauskas, N. D. McClenaghan, S. Ménage, *Inorg. Chem.* **2012**, *51*, 2222–2230.

[44] F. Li, M. Yu, Y. Jiang, F. Huang, Y. Li, B. Zhang, L. Sun, *Chem. Commun.* **2011**, *47*, 8949–8951.

[45] D. Chao, W.-F. Fu, *Dalton Trans.* **2014**, *43*, 306–310.

[46] C. K. Prier, D. A. Rankic, D. W. C. MacMillan, *Chem. Rev.* **2013**, *113*, 5322–5363.

[47] A. Juris, V. Balzani, F. Barigelletti, S. Campagna, P. Belser, A. von Zelewsky, *Coord. Chem. Rev.* **1988**, *84*, 85–277.

[48] A. Reynal, E. Palomares, *Eur. J. Inorg. Chem.* **2011**, 4509–4526.

[49] C. Fu, M. Wenzel, E. Treutlein, K. Harms, E. Meggers, *Inorg. Chem.* **2012**, *51*, 10004–10011.

[50] E. Meggers, *Chem. Eur. J.* **2010**, *16*, 752–758.

[51] M. Maestri, N. Armaroli, V. Balzani, E. C. Constable, A. M. W. Cargill Thompson, *Inorg. Chem.* **1995**, *34*, 2759–2767.

[52] R. Hogg, R. G. Wilkins, *J. Chem. Soc.* **1962**, 341–350.

[53] R. H. Holyer, C. D. Hubbard, S. F. A. Kettle, R. G. Wilkins, *Inorg. Chem.* **1966**, *5*, 622–625.

[54] J.-P. Sauvage, J.-P. Collin, J.-C. Chambron, S. Guillerez, C. Coudret, V. Balzani, F. Barigelletti, L. D. Cola, L. Flamigni, *Chem. Rev.* **1994**, *94*, 993–1019.

[55] Y. Liu, R. Hammitt, D. A. Lutterman, R. P. Thummel, C. Turro, *Inorg. Chem.* **2007**, *46*, 6011–6021.

[56] L. Hammarström, O. Johansson, *Coord. Chem. Rev.* **2010**, *254*, 2546–2559.

[57] A. Breivogel, M. Meister, C. Förster, F. Laquai, K. Heinze, *Chem. Eur. J.* **2013**, *19*, 13745–13760.

[58] K. Suzuki, A. Kobayashi, S. Kaneko, K. Takehira, T. Yoshihara, H. Ishida, Y. Shiina, S. Oishi, S. Tobita, *Phys. Chem. Chem. Phys.* **2009**, *11*, 9850–9860.

[59] B. D. Koivisto, K. C. D. Robson, C. P. Berlinguette, *Inorg. Chem.* **2009**, *48*, 9644–9652.

[60] V. Duprez, M. Biancardo, F. C. Krebs, *Sol. Energy Mater. Sol. Cells* **2007**, *91*, 230–237.

[61] K. Heinze, K. Hempel, M. Beckmann, *Eur. J. Inorg. Chem.* **2006**, 2040–2050.

[62] K. Heinze, K. Hempel, A. Breivogel, *Z. Anorg. Allg. Chem.* **2009**, *635*, 2541–2549.

[63] K. Heinze, K. Hempel, S. Tschierlei, M. Schmitt, J. Popp, S. Rau, *Eur. J. Inorg. Chem.* **2009**, 3119–3126.

[64] Y.-Q. Fang, N. J. Taylor, G. S. Hanan, F. Loiseau, R. Passalacqua, S. Campagna, H. Nierengarten, A. V. Dorsselaer, *J. Am. Chem. Soc.* **2002**, *124*, 7912–7913.

[65] Y.-Q. Fang, N. J. Taylor, F. Laverdière, G. S. Hanan, F. Loiseau, F. Nastasi, S. Campagna, H. Nierengarten, E. Leize-Wagner, A. V. Dorsselaer, *Inorg. Chem.* **2007**, *46*, 2854–2863.

[66] A. Harriman, M. Hissler, A. Khatyr, R. Ziessel, *Chem. Commun.* **1999**, *8*, 735–736.

[67] M. Hissler, A. Harriman, A. Khatyr, R. Ziessel, *Chem. Eur. J.* **1999**, *5*, 3366–3381.

[68] A. C. Benniston, A. Harriman, D. J. Lawrie, A. Mayeux, *Phys. Chem. Chem. Phys.* **2004**, *6*, 51–57.

[69] D. G. Brown, N. Sanguantrakun, B. Schulze, U. S. Schubert, C. P. Berlinguette, *J. Am. Chem. Soc.* **2012**, *134*, 12354–12357.

[70] M. Abrahamsson, M. Jäger, T. Österman, L. Eriksson, P. Persson, H.-C. Becker, O. Johansson, L. Hammarström, *J. Am. Chem. Soc.* **2006**, *128*, 12616–12617.

[71] M. Abrahamsson, M. Jäger, R. J. Kumar, T. Österman, P. Persson, H.-C. Becker, O. Johansson, L. Hammarström, *J. Am. Chem. Soc.* **2008**, *130*, 15533–15542.

[72] F. Schramm, V. Meded, H. Fliegl, K. Fink, O. Fuhr, Z. Qu, W. Klopper, S. Finn, T. E. Keyes, M. Ruben, *Inorg. Chem.* **2009**, *48*, 5677–5684.

[73] J. V. Caspar, T. J. Meyer, *J. Am. Chem. Soc.* **1983**, *105*, 5583–5590.

[74] A. Breivogel, K. Heinze, **2014**, to be submitted.

[75] M. D. Kärkäs, T. Åkermark, H. Chen, J. Sun, B. Åkermark, *Angew. Chem.* **2013**, *125*, 4283–4287; *Angew. Chem. Int. Ed.* **2013**, *52*, 4189–4193.

[76] N. G. Connelly, W. E. Geiger, *Chem. Rev.* **1996**, *96*, 877–910.

[77] J. Dietrich, U. Thorenz, C. Förster, K. Heinze, *Inorg. Chem.* **2013**, *52*, 1248–1264.

[78] A. Breivogel, S. Wooh, J. Dietrich, T. Y. Kim, Y. S. Kang, K. Char, K. Heinze, *Eur. J. Inorg. Chem.* **2014**, 2720–2734.

[79] S. Ji, W. Wu, W. Wu, H. Guo, J. Zhao, *Angew. Chem.* **2011**, *123*, 1664–1667; *Angew. Chem. Int. Ed.* **2011**, *50*, 1626–1629.

[80] J. Wang, G. S. Hanan, F. Loiseau, S. Campagna, *Chem. Commun.* **2004**, *18*, 2068–2069.

[81] Y. Chi, P.-T. Chou, *Chem. Soc. Rev.* **2010**, *39*, 638–655.

[82] V. Friese, S. Nag, J. Wang, M.-P. Santoni, A. Rodrigue-Witchel, G. S. Hanan, F. Schaper, *Eur. J. Inorg. Chem.* **2011**, 39–44.

[83] W. Ghattas, H. Müller-Bunz, M. Albrecht, *Organometallics* **2010**, *29*, 6782–6789.

[84] G. A. Parada, L. A. Fredin, M.-P. Santoni, M. Jäger, R. Lomoth, L. Hammarström, O. Johansson, P. Persson, S. Ott, *Inorg. Chem.* **2013**, *52*, 5128–5137.

[85] M. Jäger, R. J. Kumar, H. Görls, J. Bergquist, O. Johansson, *Inorg. Chem.* **2009**, *48*, 3228–3238.

[86] A. Breivogel, C. Förster, K. Heinze, *Inorg. Chem.* **2010**, *49*, 7052–7056.

[87] T. J. Meyer, *Pure Appl. Chem.* **1986**, *58*, 1193–1206.

[88] J. V. Caspar, T. J. Meyer, *J. Phys. Chem.* **1983**, *87*, 952–957.

[89] R. J. Watts. *J. Chem. Educ.* **1983**, *60*, 834–842.

[90] B. Durham, J. V. Caspar, J. K. Nagle, T. J. Meyer, *J. Am. Chem. Soc.* **1982**, *104*, 4803–4810.

[91] Z. J. Fuller, W. D. Bare, K. A. Kneas, W.-Y. Xu, J. N. Demas, B. A. DeGraff, *Anal. Chem.* **2003**, *75*, 2670–2677.

[92] W. M. Wallace, P. E. Hoggard, *Inorg. Chem.* **1979**, *18*, 2934–2935.

[93] T. E. Keyes, E. Gicquel, L. Guerin, R. J. Forster, V. Hultgren, A. M. Bond, A. G. Wedd, *Inorg. Chem.* **2003**, *42*, 7897–7905.

[94] M. B. Robin, P. Day, *Adv. Inorg. Chem. Radiochem.* **1968**, *10*, 247–422.

[95] E. Bayer, *Angew. Chem.* **1991**, *103*, 117–133; *Angew. Chem. Int. Ed. Engl.* **1991**, *30*, 113–129.

[96] M. Grøtli, C. H. Gotfredsen, J. Rademann, J. Buchardt, A. J. Clark, J. Ø. Duus, M. Meldal, *J. Comb. Chem.* **2000**, *2*, 108–119.

[97] *Fmoc Solid Phase Peptide Synthesis* (Eds.: W. C. Chan, P. D. White), Oxford University Press, Oxford **2000**.

[98] A. Barbieri, B. Ventura, R. Ziessel, *Coord. Chem. Rev.* **2012**, *256*, 1732–1741.

[99] A. Barbieri, B. Ventura, F. Barigelletti, A. D. Nicola, M. Quesada, R. Ziessel, *Inorg. Chem.* **2004**, *43*, 7359–7368.

[100] L. zur Borg, A. L. Domanski, A. Breivogel, M. Bürger, R. Berger, K. Heinze, R. Zentel, *J. Mater. Chem. C* **2013**, *1*, 1223–1230.

[101] K. C. D. Robson, B. D. Koivisto, A. Yella, B. Sporinova, M. K. Nazeeruddin, T. Baumgartner, M. Grätzel, C. P. Berlinguette, *Inorg. Chem.* **2011**, *50*, 5494–5508.

[102] C.-C. Chou, K.-L. Wu, Y. Chi, W.-P. Hu, S. J. Yu, G.-H. Lee, C.-L. Lin, P.-T. Chou, *Angew. Chem.* **2011**, *123*, 2102–2106; *Angew. Chem. Int. Ed.* **2011**, *50*, 2054–2058.

[103] C.-C. Chou, F.-C. Hu, H.-H. Yeh, H.-P. Wu, Y. Chi, J. N. Clifford, E. Palomares, S.-H. Liu, P.-T. Chou, G.-H. Lee, *Angew. Chem.* **2014**, *126*, 182–187; *Angew. Chem. Int. Ed.* **2014**, *53*, 178–183.

[104] S. Caramori, J. Husson, M. Beley, C. A. Bignozzi, R. Argazzi, P. C. Gros, *Chem. Eur. J.* **2010**, *16*, 2611–2618.

[105] J. Dietrich, A. Wünsce von Leupoldt, M. Grabolle, U. Resch-Genger, K. Heinze, *Eur. J. Inorg. Chem.* **2013**, 3009–3019.

[106] W. Y. Ng. X. Gong, W. K. Chan, *Chem. Mater.* **1999**, *11*, 1165–1170.

[107] A. Breivogel, M. Park, D. Lee, S. Klassen, A. Kühnle, C. Lee, K. Char, K. Heinze, *Eur. J. Inorg. Chem.* **2014**, 288–295.

[108] A. Abbotto, N. Manfredi, *Dalton Trans.* **2011** *40*, 12421–12438.

[109] O. K. Varghese, C. A. Grimes, *Sol. Energy Mater. Sol. Cells* **2008**, *92*, 374–384.

[110] M. K. Nazeeruddin, P. Péchy, T. Renouard, S. M. Zakeeruddin, R. Humphrey-Baker, P. Comte, P. Liska, L. Cevey, E. Costa, V. Shklover, L. Spiccia, G. B. Deacon, C. A. Bignozzi, M. Grätzel, *J. Am. Chem. Soc.* **2001**, *123*, 1613–1624.

[111] M. K. Nazeeruddin, S. M. Zakeeruddin, R. Humphry-Baker, M. Jirousek, P. Liska, N. Vlachopoulos, V. Shklover, C.-H. Fischer, M. Grätzel, *Inorg. Chem.* **1999**, *38*, 6298–6305.

[112] M. K. Nazeeruddin, F. D. Angelis, S. Fantacci, A. Selloni, G. Viscardi, P. Liska, S. Ito, B. Takeru, M. Grätzel, *J. Am. Chem. Soc.* **2005**, *127*, 16835–16847.

[113] S. Ghosh, G. K. Chaitanya, K. Bhanuprakash, M. K. Nazeeruddin, M. Grätzel, P. Y. Reddy, *Inorg. Chem.* **2006**, *45*, 7600–7611.

[114] Y. Cao, Y. Bai, Q. Yu, Y. Cheng, S. Liu, D. Shi, F. Gao, P. Wang, *J. Phys. Chem. C* **2009**, *113*, 6290–6297.

[115] T. P. Brewster, W. Ding, N. D. Schley, N. Hazari, V. S. Batista, R. H. Crabtree, *Inorg. Chem.* **2011**, *50*, 11938–11946.

[116] S. Betanzos-Lara, L. Salassa, A. Habtemariam, O. Novakova, A. M. Pizarro, G. J. Clarkson, B. Liskova, V. Brabec, P. J. Sadler, *Organometallics* **2012**, *31*, 3466–3479.

[117] S. Kämper, A. Paretzki, J. Fiedler, S. Záliš, W. Kaim, *Inorg. Chem.* **2012**, *51*, 2097–2104.

[118] G. Xue, Y. Guo, T. Yu, J. Guan, X. Yu, J. Zhang, J. Liu, Z. Zou, *Int. J. Electrochem. Sci.* **2012**, *7*, 1496–1511.

[119] A. Bahreman, B. Limburg, M. A. Siegler, E. Bouwman, S. Bonnet, *Inorg. Chem.* **2013**, *52*, 9456–9469.

[120] P. T. Nguyen, B. X. T. Lam, A. R. Andersen, P. E. Hansen, T. Lund, *Eur. J. Inorg. Chem.* **2011**, 2533–2539.

[121] C. Dragonetti, A. Valore, A. Colombo, D. Roberto, V. Trifiletti, N. Manfredi, M. M. Salamone, R. Ruffo, A. Abbotto, *J. Organomet. Chem.* **2012**, *714*, 88–93.

[122] M. M. R. Choudhuri, R. J. Crutchley, *Inorg. Chem.* **2013**, *52*, 14404–14410.

[123] T. Bessho, E. Yoneda, J.-H. Yum, M. Guglielmi, I. Tavernelli, H. Imai, U. Rothlisberger, M. K. Nazeeruddin, M. Grätzel, *J. Am. Chem. Soc.* **2009**, *131*, 5930–5934.

[124] C.-H. Siu, C.-L. Ho, J. He, T. Chen, X. Cui, J. Zhao, W.-Y. Wong, *J. Organomet. Chem.* **2013**, *748*, 75–83.

[125] B. D. Koivisto, K. C. D. Robson, C. P. Berlinguette, *Inorg.Chem.* **2009**, *48*, 9644–9652.

[126] K. C. D. Robson, B. D. Koivisto, A. Yella, B. Sporinova, M. K. Nazeeruddin, T. Baumgartner, M. Grätzel, C. P. Berlinguette, *Inorg. Chem.* **2011**, *50*, 5495–5508.

[127] K.-L. Wu, H.-C. Hsu, K. Chen, Y. Chi, M.-W. Chung, W.-H. Liu, P.-T. Chou, *Chem. Commun.* **2010**, *46*, 5124–5126.

[128] C. E. Welby, C. R. Rice, P. I. P. Elliott, *Angew. Chem.* **2013**, *125*, 11026–11029; *Angew. Chem. Int. Ed.* **2013**, *52*, 10826–10829.

[129] K. Garg, J. T. Engle, C. J. Ziegler, J. J. Rack, *Chem. Eur. J.* **2013**, *19*, 11686–11695.

[130] C.-W. Hsu, S.-T. Ho, K.-L. Wu, Y. Chi, S.-H. Liu, P.-T. Chou, *Energy Environ. Sci.* **2012**, *5*, 7549–7554.

[131] B. Schulze, D. Escudero, C. Friebe, R. Siebert, H. Görls, S. Sinn, M. Thomas, S. Mai, J. Popp, B. Dietzek, L. González, U. S. Schubert, *Chem. Eur. J.* **2012**, *18*, 4010–4025.

[132] A. Yella, H.-W. Lee, H. N. Tsao, C. Yi, A. K. Chandiran, M. K. Nazeeruddin, E. W.-G. Diau, C.-Y. Yeh, S. M. Zakeeruddin, M. Grätzel, *Science* **2011**, *334*, 629–634.

[133] P. L. Burn, P. Meredith, *NPG Asia Materials* **2014**, 6, e79, DOI:10.1038/am.2013.74.

[134] H. J. Snaith, *J. Phys. Chem. Lett.* **2013**, *4*, 3623–3630.

[135] N.-G. Park, *J. Phys. Chem. Lett.* **2013**, *4*, 2423–2429.

[136] M. Liu, M. B. Johnston, H. J. Snaith, *Nature* **2013**, *501*, 395–398.

[137] Q. Pei, G. Yu, C. Zhang, Y. Yang, A. J. Heeger, *Science* **1995**, *269*, 1086–1088.

[138] Q. Pei, Y. Yang, G. Yu, C. Zhang, A. J. Heeger, *J. Am. Chem. Soc.* **1996**, *118*, 3922–3929.

[139] H. Xiang, J. Cheng, X. Ma, X. Zhou, J. J. Chruma, *Chem. Soc. Rev.* **2013**, *42*, 6128–6185.

[140] R. D. Costa, E. Ortí, H. J. Bolink, *Pure Appl. Chem.* **2011**, *83*, 2115–2128.

[141] J. Slinker, D. Bernards, P. L. Houston, H. D. Abruña, S. Bernhard, G. G. Malliaras, *Chem. Commun.* **2003**, *19*, 2392–2399.

[142] E. Holder, B. M. W. Langeveld, U. S. Schubert, *Adv. Mater.* **2005**, *17*, 1109–1121.

[143] J. D. Slinker, J. Rivnay, J. S. Moskowitz, J. B. Parker, S. Bernhard, H. D. Abruña, G. G. Malliaras, *J. Mater. Chem.* **2007**, *17*, 2976–2988.

[144] International Commission on Illumination (CIE), 1931.

[145] http://upload.wikimedia.org/wikipedia/commons/6/60/CIE1931xy_CIERGB.svg, 04.03.2014.

[146] P. Toivanen, J. Hovila, P. Kärhä, E. Ikonen, *Metrologia* **2000**, *37*, 527–530.

[147] P. Toivanen, P. Kärhä, F. Manoochehri, E. Ikonen, *Metrologia* **2000**, *37*, 131–140.

[148] A. P. Monkman, *ISRN Materials Science* **2013**, DOI:10.1155/2013670130.

[149] J. Wang, A. Chepelianskii, F. Gao, N. C. Greenham, *Nat. Commun.* **2012**, DOI:10.1038/ncomms2194.

[150] A. Köhler, H. Bässler, *Mater. Sci. Eng.* **2009**, R *66*, 71–109.

[151] H. Yersin, *Highly Efficient OLEDs with Phosphorescent Materials*; Wiley-VCH: Weinheim, Germany, **2008**.

[152] J.-K. Lee, D. S. Yoo, E. S. Handy, M. F. Rubner, *Appl. Phys. Lett.* **1996**, *69*, 1686–1688.

[153] C.-Y. Liu, A. J. Bard, *Appl. Phys. Lett.* **2005**, *87*, 061110.

[154] J. D. Slinker, J.-S. Kim, S. Flores-Torres, J. H. Delcamp, H. D. Abruña, R. H. Friend, G. G. Malliaras, *J. Mater. Chem.* **2007**, *17*, 76–81.

[155] L. J. Soltzberg, J. D. Slinker, S. Flores-Torres, D. A. Bernards, G. G. Malliaras, H. D. Abruña, J.-S. Kim, R. H. Friend, M. D. Kaplan, V. Goldberg, *J. Am. Chem. Soc.* **2006**, *128*, 7761–7764.

[156] G. Kalyuzhny, M. Buda, J. McNeill, P. Barbara, A. J. Bard, *J. Am. Chem. Soc.* **2003**, *125*, 6272–6283.

[157] H. Yersin, A. F. Rausch, R. Czerwieniec, T. Hofbeck, T. Fischer, *Coord. Chem. Rev.* **2011**, *255*, 2622–2652.

[158] S. Bernhard, J. A. Barron, P. L. Houston, H. D. Abruña, J. L. Ruglovksy, X. Gao, G. G. Malliaras, *J. Am. Chem. Soc.* **2002**, *124*, 13624–13628.

[159] T. Sajoto, P. I. Djurovich, A. B. Tamayo, J. Oxgaard, W. A. Goddard, M. E. Thompson, *J. Am. Chem. Soc.* **2009**, *131*, 9813–9822.

[160] C. Kreitner, K. Heinze, to be submitted.

Lebenslauf

Persönliche Daten

Name: Aaron Breivogel
Geburtsdatum: 18.03.1984
Geburtsort: Mainz
Nationalität: Deutsch

Promotionsarbeit

seit 08.2009	Promotionsarbeit in Chemie an der Johannes Gutenberg-Universität Mainz in der Arbeitsgruppe von Prof. Dr. [redacted] *Ruthenium-based Light Harvesting Complexes*
01.2011 – 12.2013	DFG-Stipendium im Rahmen des IRTG
08.2012 – 03.2013	Forschungsaufenthalt an der Seoul National University in Seoul (Südkorea) in der Arbeitsgruppe von Prof. Dr. [redacted]

Studium

04.2004 – 07.2009	Studium der Chemie an der Johannes Gutenberg-Universität Mainz mit den Schwerpunkten Physikalische, Organische, Anorganische und Analytische Chemie
10.2008 – 07.2009	Diplomarbeit in der Arbeitsgruppe von Prof. Dr. [redacted] *Ruthenium-basierte Lichtsammelkomplexe*
10.2007 – 02.2008	Forschungsaufenthalt an der Universidad de Valencia in Valencia (Spanien) in der Arbeitsgruppe von Prof. Dr. [redacted]

Zivildienst und Schulbildung

07.2003 – 04.2004	Zivildienst in der Rheinhessen-Fachklinik in Alzey
08.1994 – 03.2003	Allgemeine Hochschulreife am Elisabeth-Langgässer-Gymnasium in Alzey